2006

平成１８年度

金沢医科大学
共同研究成果報告書
奨励研究成果報告書

平成20年12月

金沢医科大学

はじめに

平成18年度金沢医科大学共同研究・奨励研究の成果報告書を発刊しましたのでお手元にお届けいたします。

本学では、平成15年度から若手研究者の育成を目的とした奨励研究や、学部、大学院、総合医学研究所、他大学等との有機的連携を目指す共同研究を展開することで本学研究の活性化を進めており、平成16年度までに共同研究に4研究課題、奨励研究に18研究課題を選定しております。また、平成17年度からは、奨励研究に萌芽的研究の枠を設けるなど研究の多様化にも対応しています。

本書は、平成18年度に学内公募で申請があった共同研究14件、奨励研究35件のうち、それぞれ6件、10件が採択された研究の成果をまとめたものであります。

今後、これらの共同研究と奨励研究を中心に学術研究がさらに発展し、本学の研究基盤が充実することを期待します。

最後に、本報告書の取りまとめの労をとられた研究業績評価委員会、研究推進センター事務課並びに関係各位に感謝します。

平成20年12月

金沢医科大学
学長　山田　裕一

目　　次

※研究者の所属・職名は、採択時のものとした。

平成１８年度

共同研究成果報告書

１．研究課題名：細胞膜リピッドラフト制御による新規抗癌剤および免疫抑制剤の開発
（研究番号　C2006-1）

２．キーワード：１）リピッドラフト（lipid rafts）
２）アポトーシス（apoptosis）
３）活性化シグナル（activation signal）
４）T 細胞（T cells）
５）スフィンゴミエリン（sphingomyelin）

３．研究代表者：梅原　久範・医学部・教　授・血液免疫制御学（血液免疫内科学）
研究分担者：岡崎　俊朗・鳥取大学・医学部・教　授・血液内科
南　　康博・神戸大学・医学部・教　授・ゲノム科学
金　　哲雄・医学部・助　教・血液免疫制御学（血液免疫内科学）

４．研 究 目 的

細胞膜からの活性化シグナル伝達の足場としてマイクロドメイン（ラフト）の存在が近年注目を浴びている。Fas 依存性アポトーシスにおいてもラフトの関与が証明され、ラフト凝集におけるセラミドの必要性が示唆されている。ある種の抗癌剤は Fas 依存性アポトーシスを誘導するが、薬剤耐性を獲得した場合この過程に障害が生じる。しかし、アポトーシスおよびラフト機能の解析において、細胞膜スフィンゴ脂質の解析はほとんどなされていなかった。我々は、下記に示す如く、スフィンゴミエリン合成酵素の遺伝子同定と、細胞膜スフィンゴミエリン欠失細胞および機能回復株を樹立しえた。ここに至り、アポトーシスにおける Fas およびラフトの凝集過程、DISC 形成過程、セラミド合成過程におけるスフィンゴミエリンの解析が可能となり、アポトーシスの詳細な解析と薬剤耐性機序の解明が可能となりえた。今回の研究課題では、世界に先駆けてアポトーシスおよび細胞活性化機構におけるラフト・フィンゴミエリンの機能を明らかにした。

５．研 究 計 画

A）スフィンゴミエリン欠失細胞株における Fas 誘導 apoptosis の解析

１）薬剤耐性を示す HL60 細胞株(WR/Mock)から調整した cDNA library を PIRES 2-EGFP ヒトベクターに組み込み、G418 およびグルコシルセラミド合成酵素阻害剤の存在下に、スフィンゴミエリン合成回復株(WR22)を樹立した。スフィンゴミエリン合成細胞および欠失細胞からスフィンゴミエリン合成酵素(SMS-1)をクローニングした（岡崎、梅原）。

２）WR22 および WR/Mock 細胞における細胞膜リピッドラフトを confocal microscopy による解析を行う（梅原、金）。

３）両細胞における Fas 誘導シグナルおよび T 細胞活性化シグナルの差異を検討する（梅原、南）。

４）細胞膜リピッドラフトを sucrose gradient による分離し組成の相違を解析する（梅原、金）。

５）ラフト分画における ganglioside GM1 量とスフィンゴミエリン量を比較検討する（梅原、岡崎）。

6）アポトーシスおよび活性化刺激によるラフト分画でのセラミド合成能を検討する（梅原、岡崎）。

B）スフィンゴミエリン欠失 T 細胞株の樹立と T 細胞活性化シグナルの解析

1）ヒト T 細胞株 Jurkat 細胞に SMS-1 遺伝子 Si-RNA を遺伝子導入し、スフィンゴミエリン合成低下株を樹立する(Jurkat/kd)（梅原、金）。

2）さらに限界希釈法および薬剤耐性機序を用いてスフィンゴミエリン合成低下株を樹立する(Jurkat/kd)（梅原、金）。

3）両細胞を抗 CD3 抗体で架橋刺激し、細胞増殖活性を MTT アッセイで評価する（梅原、岡崎、金）。

4）CD３架橋刺激によるラフト凝集能および TCR 凝集能を共焦点顕微鏡で検討する（梅原、岡崎、南）。

5）CD3 刺激細胞増殖において、Lck, Fyn などのチロシンキナーゼ活性化を in vitro kinase assay で、アダプター蛋白 LAT のリン酸化を抗 LAT 抗体の免疫沈降物を抗チロシンリン酸化抗体による免疫ブロット法で検討する（梅原、南）。

6）両細胞において CD3 分子のリピッドラフトへの移行量をショ糖比重密度勾配により分画したラフト内で検討する（梅原、金）。

6．研 究 成 果

A）スフィンゴミエリン欠失細胞株細胞株における Fas 誘導 apoptosis の解析

1）スフィンゴミエリン欠質細胞およびコントロール細胞を抗 Fas 抗体（CH11）で刺激し、apoptosis を sub G1 法で FACS で解析し、両細胞における apoptosis の差異を明らかにした。Fas 架橋刺激による、DISC 形成の検出、Caspase 活性の測定、ミトコンドリア膜電位の測定を行なった。

2）細胞膜 lipid raft の confocal microscopy による解析

スフィンゴミエリン欠失細胞株における lipid raft の形態および機能を明らかにした。細胞膜でのスフィンゴミエリンの局在を明らかにするために、スフィンゴミエリンに特異的に結合する MBP 結合 lysenin と PE 標識抗 MBP 抗体を用いて染色した。Fas 架橋刺激による Cluster 形成を FITC-, PE-標識 Fas 抗体で検出し、ラフト構成における ganglioside GM1 とスフィンゴミエリンおよび Fas の動態を明らかにした。 スフィンゴミエリン欠失細胞株では、Fas の凝集が抑制されていた。

3）Fas 誘導シグナルの差異の検討:Fas 架橋刺激に伴う、FADD、 Caspase-8 と Fas との結合を western blotting および免疫沈降法を用いて検討した。リピッドラフトを sucrose gradient 法により分画し、ganglioside GM1 量とスフィンゴミエリン量を比較検討した。Fas 刺激に伴う FADD や Caspase などのシグナル伝達物質の lipid raft への移行を検討した。スフィンゴミエリン欠失細胞では、Fas 刺激による caspase-8、 caspase-3 活性が抑制されていた。また、Fas に会合する FADD、 Caspase-8 量も低下していた。その結果 Fas によるアポトーシスがスフィンゴミエリン欠失細胞では障害されていることが明らかになった。

B）スフィンゴミエリン欠失Ｔ細胞株の樹立とＴ細胞活性化シグナルの解析

１）ヒトＴ細胞株 Jurkat 細胞に SMS-1 遺伝子 Si-RNA を遺伝子導入し、スフィンゴミエリン合成低下株（Jurkat/kd）の樹立に成功した。

２）両細胞を抗 CD3 抗体で架橋刺激し、細胞増殖活性を MTT アッセイで評価したところ、Jurkat/kd 細胞では有意に低下していた。

３）CD３架橋刺激によるラフト凝集能および TCR 凝集能を共焦点顕微鏡で検討したところ、Jurkat/kd 細胞では TCR 凝集能が有意に低下していた。

４）CD3 刺激細胞増殖において、Lck, Fyn などのチロシンキナーゼ活性化を in vitro kinase assay で、アダプター蛋白 LAT のリン酸化を抗 LAT 抗体の免疫沈降物を抗チロシンリン酸化抗体による免疫ブロット法で検討したところ、Jurkat/kd 細胞では細胞内チロシン化蛋白、LAT のチロシンリン酸化が有意に低下していた。

５）両細胞において CD3 分子のリピッドラフトへの移行量をショ糖比重密度勾配により検討したところ、Jurkat/kd 細胞では CD3 分子のリピッドラフトへの移行量が有意に低下していた。

７．研究の考察・今後の展開

上記の結果より、細胞膜スフィンゴミエリンはリピッドラフトの機能の本質を担う細胞膜脂質である事が明らかとなった。その欠質は、Fas を介した細胞のアポトーシスの障害、T 細胞レセプターを介した細胞活性化の障害に直結する結果を得た。今後は、細胞膜リピッドラフトを制御しうる薬物の検討に入り、抗がん剤抵抗性を獲得した腫瘍細胞をアポトーシスに引き込む手法を開発する。また、その逆に、リピッドラフト機能を抑制する手法で、自己免疫疾患の活性化Ｔ細胞を抑制する手法を検討する。現在、スフィンゴミエリン合成酵素(SMS1)ノックアウトマウスを使って、生体におけるリピッドラフトの重要性を解析中である。

８．研 究 発 表

Dong L, Masaki Y, Takegami T, Jin ZX, Huang CR, Fukushima T, Sawaki T, Kawanami T, Saeki T, Kitagawa K, Sugai S, Okazaki T, Hirose Y and Umehara H. Clonality analysis of lymphoproliferative disorders in patients with Sjögren's syndrome. Clin. Exp. Immunol. 2007; 150: 279-284. (MLDB)

Dong L, Masaki Y, Tanaka M, Fukushima T, Okazaki T and Umehara H. Sjögren's syndrome and lymphoma development. Curr. Immunol. Rev. 2007; 3: 289-296. (MLDB)

Umehara H, Tanaka M, Sawaki T, Jin ZX, Huang CR, Dong L, Kawanami T, Karasawa H, Masaki Y, Fukushima T, Hirose Y and Okazaki T. Fractalkine in rheumatoid arthritis and allied conditions. Mod. Rheumatol. 2006; 16: 124-130. (MLDB)

Clinical and Experimental Immunology ORIGINAL ARTICLE doi:10.1111/j.1365-2249.2007.03486.x

Clonality analysis of lymphoproliferative disorders in patients with Sjögren's syndrome

L. Dong,*§ Y. Masaki,* T. Takegami,† Z.-X. Jin,* C.-R. Huang,* T. Fukushima,* T. Sawaki,* T. Kawanami,* T. Saeki,¶ K. Kitagawa,‡ S. Sugai,* T. Okazaki,** Y. Hirose* and H. Umehara*

*Department of Hematology and Immunology, †Department of Molecular Oncology and Virology and ‡Department of Ophthalmology, Kanazawa Medical University, Ishikawa, Japan, §Department of Hematology and Immunology, Tongji Hospital, Huazhong University of Science and Technology, Wuhan, China., ¶Nagaoka Red Cross Hospital, Nagaoka, Niigata, Japan, and **Faculty of Medicine, Tottori University, Yonago, Tottori, Japan

Accepted for publication 17 July 2007
Correspondence: Yasufumi Masaki MD, PhD, Department of Hematology and Immunology, Kanazawa Medical University, 1–1 Daigaku, Uchinada, Ishikawa, 920–0293, Japan.
E-mail: yasum@kanazawa-med.ac.jp

Summary

The aim of this study was to clarify the nature of the clonal lymphocyte infiltration in Sjögren's syndrome (SS) patients associated with lymphoproliferative disorders. We examined B cell clonality in lymphoproliferative tissues from six primary SS patients associated with lymphoproliferative disorders or lymphoma by cloning and sequencing of the gene rearrangement of the immunoglobulin heavy chain complementarity determining region 3 (IgVH–CDR3). Three patients with sequential observation showed progressional clonal expansion with the presence of the same subclone in different tissues during the course of disease. Among them, one patient developed mucosa-associated lymphoid tissue (MALT) lymphoma in glandular parotid. The other three SS patients concomitant with malignant B cells lymphomas showed different clonal expansion of B cells between nodal sites and salivary glands. The cloanality analysis indicated that monoclonal B cell population could spread from one glandular site to another site during the course of SS, suggesting that the malignant clone may arise from the general abnormal microenvironment, not restricted to the glandular tissue, in some SS patients.

Keywords: clonality, lymphoproliferative disorders, Sjögren's syndrome

Introduction

Sjögren's syndrome (SS) is a systemic as well as an organ-specific autoimmune disease with destructive lymphocyte infiltration of salivary and lacrimal glands, which results in dry eyes and dry mouth. Myoepithelial sialadenitis (MESA) or lymphoepithelial lesion (LEL), consisting of T cell and B cell infilitration, are characteristic features of SS that may range from benign to malignant [1,2]. It has been estimated recently by a cohort study that patients with SS have a 16-fold increased risk of developing lymphoma [3]. Lymphomas that occur during the course of SS are mainly B cell lymphomas, the majority being of low-grade marginal zone type, particularly of mucosa-associated lymphoid tissue (MALT) origin, and develop most often from lymphoproliferative lesions in salivary and lacrimal glands [4,5].

Lymphoproliferative malignancy is the most alarming complication of SS [6]. It is suggested that patients with clonal expansion of B cells in their salivary glands are at high risk of developing lymphomas, and hypothesized that chronic exogenous or endogenous stimulation in MESA could play an important role in the lymphoproliferative process during the course of SS through restricted usage of immunoglobulin heavy chain complementarity determining region 3 (IgVH–CDR3) from MESA-associated clones [7,8]. However, predicting and diagnosing lymphoma by clonal analysis alone is unreliable [9,10]. To understand further the relationship between lymphocyte monoclonality and lymphoma development in SS patients, we studied the lymphocyte clonality by cloning and sequencing IgVH-CDR3 in lymphoproliferative tissues at multiple time-points from six SS patients who developed lymphoproliferative disorder (LPD) or lymphoma during the course of disease.

Materials and methods

Patients

Patient profiles are summarized in Table 1. All six patients satisfied the SS classification criteria of the American–European Community Classification Criteria [11]. Patient 1 (61 years old, male) was SS associated with LPD. He suffered

Table 1. Clinical, laboratory, histological features of patients with SS-ssociated pathological lymphocyte infiltration.

No.	A/S*	Dye eye/Dye mouth	RF/ANA	SSA/SSB	Salivary gland involvement†/ focus score‡	tissue biopsy	pathologic diagnosis
1	61/M	+/+	n.d/+	–/–	+/1.7	pancreas	pancreatitis
						L-submandibular gland	MESA
						R-submandibular gland	MESA
						lymph node (cervical)	LPD
						kidney	LPD
2	78/F	+/+	+/+	–/–	+/4.0	lacrimal gland	MESA
						MSG	MESA
						lacrimal gland	MESA
						MSG	Mikulicz' disease
3	79/F	+/+	+/+	+/–	+/1.0	R-parotid gland	MESA
						R-parotid gland	MESA
						L-parotid gland	MALT lymphoma
4	64/F	+/+	+/+	–/–	+/3.4	MSG	MESA
						LND	marginal zone B lymphoma
5	67/M	+/+	+/–	–/–	+/1.0	MSG	MESA
						LND	mantle cell lymphoma
6	85/M	+/+	–/–	–/–	+/1.0	MSG	MESA
						LND	mantle cell lymphoma

*: A/S means patient age/sex; †: + means at least one objective evidence of salivary gland involvement according to AECC criterion; ‡: + means focus score > 1.

MSG: minor salivary gland, MESA: myoepithelial sialadenitis, LND: lymph node, LPD: lymphoproliferative disorder.

initially from abdominal pain, with signs of enlargement of the pancreas at early onset of disease (1988). Malignancy of the pancreas was considered at that time and an operation was performed. The pathological diagnosis was pancreatitis with massive lymphocyte infiltration. About 1 year later the swellings of bilateral submandibular glands emerged (1989). Seven years later, he showed lymphoadenopathy and renal dysfunction (1996). He was diagnosed with so-called pseudolymphoma by histology and immunohistology study. Patient 2 (78 years old, female) showed bilateral enlargements of the lacrimal and parotid glands following the first onset of 1·5 years. Massive lymphocyte infiltration with MESA was proved, and Mikulicz's disease and SS were diagnosed at that time. Patient 3 (79 years old, female) was SS with MALT lymphoma development in the subsequent left parotid gland. Patients 4–6 were SS with nodal B cell lymphoma (Table 1). No steroids or other immunosuppressive mediations were taken at the time of sampling.

DNA extraction

Available specimens were studied from six patients, including the initial and subsequent biopsies of the tissues with sequential observation (Table 1). All patients provided informed consent and all the specimens were obtained as part of the diagnostic histological procedure. DNA extraction was performed by DEXPAT (DNA extraction from paraffin – embedded tissue) (Takara Biochemicals, Tokyo, Japan) and polymerase chain reaction (PCR) was performed on the soluble DNA. The integrity of the DNA following extraction from paraffin-embedded tissue sections was confirmed using control DNA primers for gene coding for the cell adhesion molecule E-cadherin (uvomorulin, chromosome 16q22), as described previously [12].

PCR for Ig monoclonanity

Determination of monoclonality through an evaluation of immunoglobulin heavy chain gene rearrangement is a commonly performed and useful diagnostic assay [13]. A modified seminested PCR technique was used to amplify the CDR3 region comprising the V–D–J region of the Ig heavy chain gene (IgVH–CDR3) [12]. For the first round of amplification, the framework 3 consensus primer (Fr3 5′-ACA CGG C[C/T] [G/C] TGT ATT ACT G-3′) and a downstream consensus primer directed at the joining region (LJH: 5′-TGA GGA GAC GGT GAC C-3′) were used. For the second round of PCR, the Fr3 primer was used in conjunction with an inner downstream primer (VLJH: 5′-GTG ACC AGG TNC CTT GGC CCC CAG-3′). In each round the PCR mixture (Takara Biochemicals) contained 50 μl total reaction mixture. The first PCR contained 100 ng of DNA and the second 2 μl of the first round reaction product. Reactions were carried out in a thermocycler (DNA Engine PT-200, Bio-Rad, Hercules, CA, USA), beginning with an initial denaturation of 98°C for 2 min preceding the addition of the DNA polymerase and terminated by an extension step of 72°C for 10 min. Thirty-one first-round and 31 second-round cycles consisting of

(a)

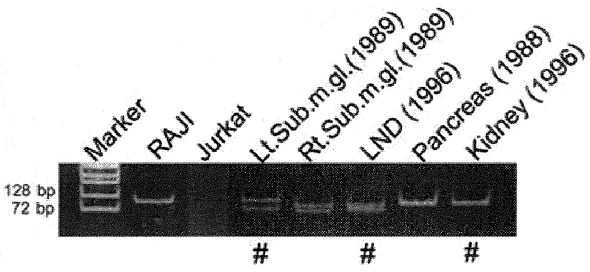

(b)

Tissue	Clone no.	CDR3
Pancreas (1988)	1	GQLGGRGGVRAEFGLDVWG
Lt. submandibular gl. (1989)	2	# ***LGSGWSRS***YYYGMDVWG
	3	APTPAVAVAVPYYYHGMDVWG
	4	EFRNLRYYYDSSGYQ*CF*YLGGRDLV
	5	ERTGPGAFDIWG
	6	GIADYYGMDVWG
Rt. submandibular gl (1989)	7	QTYYYDTEAYPPDTWG
	8	SGATEFHYYMEVWG
LND (1996)	9	# ***LGSGWSRS***YYYGMDVWG
	10	VSGSYFTV/SGFAFDVWG
	11	VSGSYFTV<u>K</u>SGFAFDVWG
Kidney (1996)	12	# ***LGSGWSRS***YYYGMDVWG

Fig. 1. B cell clonality of patient 1. (a) Polymerase chain reaction (PCR) results regarding B cell monoclonality; #the presence of the same subclone. (b) Sequences of PCR products: the same clone is shown in italics and bold type; 1 amino acid difference is underlined. *Clone 4 was a non-functional clone with a stop codon (Sub.m.gl: submandibular gland; LND: lymph node).

96°C for 1 min, 60°C for 1 min and 72°C for 1 min were performed. Use of the primers would be expected to generate a fragment of between 80 and 120 base pairs (bp) in length. The reaction products were analysed on a 10% non-denaturing polyacrylamide gel electrophoresis, stained with ethidium bromide and viewed under ultraviolet light. The dilution experiment by the mixture RAJI cells in normal peripheral blood mononuclear cells (PBMC) revealed that our method could detect one malignant RAJI cell in 10 000 PBMC by applying 100 ng genomic DNA (data not shown).

Cloning and sequencing of PCR products and intraclonal variation analysis

Bands corresponding to VH genes were isolated from 1·5% low-melting agarose gel, and the DNA was purified using a QIAquick PCR Purification Kit (Qiagen, Tokyo, Japan). Approximately 20 ng of purified DNA was cloned using the T-A Cloning Kit (Invitrogen, Tokyo, Japan). Up to 10 clones were picked up at random. Sequencing reactions were performed with M13 prime on the ABI 310 Genetic Analyser [7].

Results

Molecular analysis of B cell clonality

B cell clonality was studied by PCR in various involved tissues in six patients. In patient 1, oligoclonal or monoclonal B cell bands were found initially by PCR in tissues of pancreas (1988); 1 year later (1989) in the left and right submandibular glands, and subsequently 7 years later (1996) in the lymph node and kidney (Fig. 1a). After cloning and sequencing, five distinct B cell clones (including one non-functional rearrangement clone with stop code, clone 4 in Fig. 1b) were identified in the left submandibular glands, two distinct clones were observed in the right submandibular glands and one clone in the pancreas. Seven years later (1996), one of five clones in the left submandibular glands was also found in lymph node and kidney, and two clones with only one amino acid difference was identified in lymph node (Fig. 1b). Meanwhile, marked lymphocytic infiltration was identified by biopsy of the lymph node and kidney, although immunohistochemical staining did not show monoclonality. This case presented oligoclonal or monoclonal B cell expansion with the presence of one simimlar clone in glandular and extraglandular tissues during the course of SS.

In patient 2, swellings of bilateral lacrimal glands emerged twice. The first biopsies of lacrimal gland and minor salivary gland (MSG) revealed the polyclonal pattern of B cell expansion with mild lymphocyte infiltration identified by histology. After 1·5 years, the same size of B cell monoclonal bands were found by PCR in lacrimal gland and MSG (Fig. 2a). Sequence of CDR3 revealed that monoclonal B cells in the second biopsies of lacrimal glands and MSG were derived possibly from the same progenitor, because each had almost identical CDR3 with only one nucleotide difference, resulting in one amino acid difference (Fig. 2b). Histology of the second MSG showed massive lymphocyte infiltration with lymphoepithelial lesion. Mikulicz's disease type of SS

(a)

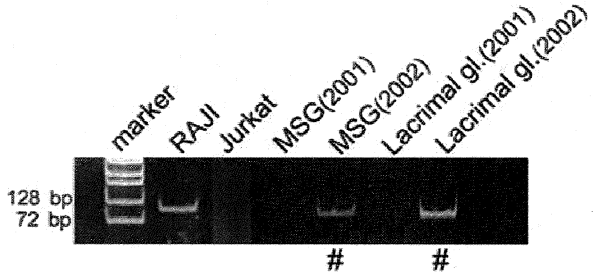

(b)

Tissue	Clone no.	CDR3
MSG (2002)	1	# ***EGT<u>P</u>D***AFDIWG
Lacrimal gl. (2002)	2	# ***EGT<u>R</u>D***AFDIWG

Fig. 2. B cell clonality of patient 2. (a) Polymerase chain reaction (PCR) results regarding B cell monoclonality; #the presence of the same subclone. (b) Sequences of PCR products: the same clone is shown in italics and bold type; 1 amino acid difference is underlined (MSG: minor salivary gland; gl. gland).

(a)

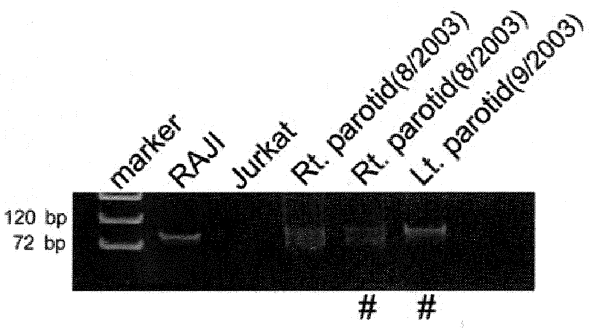

(b)

Tissue	Clone no.		CDR3
Rt. parotid gl. (8/2003)	1	#	***QTYCYDTEAYPDT***WG
	2		QTATFDH WG
Lt. parotid gl. (9/2003)	3	#	***QTYCYDTEAYPDT***WG

Fig. 3. B cell clonality of Patient 3. (a) Polymerase chain reaction (PCR) results of B cell monoclonality; #the presence of the same subclone. (b) Sequences of PCR products: the same clone is shown in italics and bold type.

was diagnosed at this time. This case may represent clonal progression from polyclonal to monoclonal B cell expansion in glandular tissues and development of the same clone in different tissues at the same onset.

In patient 3, one of the biopsies of the right parotid glands presented polyclonal B cell expansion, while another part of the same-side parotid glands was oligoclonal. About 1 month later, monoclonal B cells expansion was identified in the left parotid glands (Fig. 3a). DNA sequence of CDR3 identified that the sequential clone in left parotid glands is the same, with one of two clones in the initial right parotid gland (Fig. 3b). The sequential clone in the left parotid gland was proved to be MALT lymphoma by pathological diagnosis. Although it was difficult to draw a conclusion of clonal progression, we detected expansion of the same clone in a different site of the parotid glands within a 1-month interval.

Among three SS patients with nodal B cell lymphoma (patients 4–6), patient 4 (marginal zone B cell lymphoma) showed different monoclonal B cell bands between MSG and lymph node, while patients 5 and 6 (Mantle cell lymphoma) presented the same size of bands in MSG and lymph node (data not shown). Cloning and DNA sequencing data indicated different monoclonal lymphocytes expansion between MSG and lymph node, because each had a distinct IgH–CDR3 sequence (Fig. 4a).

IgH–CDR3 amino acid sequences

We compared the IgVH–CDR3 amino acid sequence of our cases to those presented on GenBank using the NCBI protein-BLAST program. By applying homology criteria by Bende *et al.*, i.e. CDR3 region at least seven amino acids, at least 75% amino acid sequence homology and a length difference between the CDR3 sequences not exceeding three amino acids, we found the conserved sequence motifs in CDR3 region between clone 7 in patient 1 and clone 1 in patient 3 (Fig. 4b) [14]. In addition, clones 6 and 8 from patient 1 showed homology to those reported on GenBank for patients with rheumatoid arthritis [15], and clone 5 to those patients with systemic lupus erythematosus [16].

Discussion

The risk for development of malignant lymphoma in SS patients was reported to be 16 times higher than in a comparable population [3]. It has been reported that salivary lymphoepithelial lesions from SS patients showed high frequent evidence of clonal immunoglobulin gene rearrangement and revealed morphological and/or immunophenotypic evidence of low-grade lymphoma [17,18]. Although many studies had tried to predict the progression to a malignant lymphoproliferative disorder by B cell clonality analysis in MESA-associated infiltrates, prediction and diagnosing of lymphoma still remain to be defined.

In this study, we analysed B cell clonality by focusing on the CDR3 region of IgVH. Because this region is unique to each B cell clone and specific to antigen recognition, the sequence of CDR3 offers the useful clonal signature of an individual B cell [13]. We observed clonal progression of B cells during lymphoma development in SS patients by sequence analysis of the variable region of IgH CDR3 gene. Patient 1 presented monoclonal B cell expansion in pancreas and oligoclonal B cell expansion in submandibular glands. In this patient, one identified subclone still existed in lymph node and kidney after 7 years (Fig. 1). Patient 2 showed progressive expansion of B cells from polyclonal to monoclonal in lacrimal glands and MSG with no evidence so far of malignancy. Sequence analysis indicates a strong possibility that clones in MSG (2002) and lacrimal gland (2002) might

(a)

Patient	Tissue	CDR3
P 4	MSG	SLTQLLMMLGMAMLEHIFRNPNG
	LND	GGTVTT YYYYGMDVWG
P 5	MSG	YCSGSCYSRLDFDPWG
	LND	DRVGAGGRWFDPWG
P 6	MSG	PSPYDSSGYYFDPWG
	LND	AVYDILTA DDSWWP

(b)

Patient	Tissue	CDR3
P 1	Right submandibular gl.clone 7	QTY Y YDTEAY P PDTWG
P 3	Parotid gl. clone 1	QTY C YDTEAY PDTWG

Fig. 4. (a) DNA sequence of the IgVH–CDR3 region between MSG and lymph node in three SS patients with nodal lymphoma. (b) Comparison of clone 7 in patient 1 and clone 1 in patient 3. The conserved sequences are framed.

Table 2. The literatures of monoclonality and lymphoma development.

Author	Year of Publication	Journal	Number of Cases	SS	Lymphoma	Same Clone†	Diferent Clone‡
Diss PC	1993	New Engl J Med	1	1SS→	MALT lymphoma	1	
Pablos JL	1994	Arthritis Rheum	14	1SS→	B cell neoplasm		1
Jordan R	1995	Oral Surg Oral Med Oral Pathol Oral Radiol Endod	11	4SS→	lymphoma	4§	
Lasota J	1997	Mod Pathol	1	1SS→	MALT lymphoma		1
De Vita S	1997	Arthritis Rheum	6	1SS→	Lympoma (DLB)	1	
Bathler DW	1998	Blood	7	5SS→	lymphoma	4	1
Aiello A	1999	Blood	1	1SS→	MALT lymphoma→FL	1	
Gellrich S	1999	Arthritis Rheum	2	0	0	0	0
Gasparotto D	2003	Arthritis Rheum	1	1SS→	Lymphoma (MZB)	1	
Hansen A	2006	Arthritis Rheum	1	1SS→	Lymphoma (MZB)	1	
			45	**16**		**13**	**3**

†Same clone: malignant clone is from the initial lymphoproliferative glandular tissues by PCR and/or sequence data to identify same monoclonal or mutated monoclonal B cell expansion with conserved amino acids sequence motifs in their CDR3. ‡Different clone: different size of monoclonal bands by PCR or same size bands with distinct lgVH-CDR3 between initial lymphoproliferation and lymphoma. §Without sequence data, the result is from PCR. DLB, diffuse large B cell lymphoma; FL, follicular lymphoma; MZB, marginal zone B cell lymphoma.

be derived from the same progenitor, because only one amino acid difference of CDR3 region was identified between MSG (2002) and lacrimal gland (2002) clone in this patient (Fig. 2). Although we had attempted to target PCR amplification of the longer VH–FR1 to clarify this possibility, we could not sequence the VH–FR1 sequence because of the poor amount of DNA. In patient 3 the sequential malignant clone in the left parotid glands was the same, with one of two clones in the initial right parotid gland (Fig. 3b), providing evidence of expansion of the same clone in different sites of parotid glands. Clonality analysis of these patients may suggest that monoclonal B cell population could spread from one glandular site to another site during the course of SS. Another possibility is that the microenvironment in SS may trigger monoclonal B cell proliferation, because the same clone was identified in different tissues during the course of disease. It has been reported that MESA and neoplastic B cell clones showed a marked VH gene restriction along with the similar CDR3 sequences, indicating that, even from different patients, MESA-associated clones may bind the same or similar antigens and are selected for clonal expansion [7]. In this regard, we found the conserved amino acids sequence motifs in CDR3 in different clones from patients 1 and 3 (Fig. 4b).

Recent studies have proposed that disturbed B cell biology, defects in apoptosis, T cell modulation, persistent antigenic stimulation and the effects of various molecules contribute to the development of lymphoma in SS. In particular, the B cell activating factor of the tumour necrosis factor family (BAFF) and a proliferation-inducing ligand (APRIL) have been receiving increasing attention because dysregulated BAFF expression in SS has been described to lead to disease progression and perpetuation of humoral autoimmunity [19]. BAFF is a member of the tumour necrosis factor (TNF) superfamily, also called B lymphocyte stimulator (BLys), which specifically regulates B lymphocyte proliferation and survival, and has emerged as a potential survival factor for B cell lymphomas. Continuous B cell activation resulting from increased BAFF may lead to the development of B cell lymphoma in SS [20]. Furthermore, it has been considered that gradual progression from polyclonal to monoclonal in lacrimal or minor salivary glands may lead to lymphoma development in SS patients. From a variety of studies on clonality analysis in SS patients, patients with the same and persistent monoclonal B cell expansion in follow-up biopsy specimens are at higher risk of developing lymphoma. Malignant clones may be brought from clones in initial lymphoproliferative glandular tissues (Table 2) [7,8,10,21–27]. In contrast to this classic story, patients 1 and 2 had been followed without evidence of lymphoma for more than 10 and 4 years, respectively. Although it remains to be determined whether they will develop into lymphoma over a longer follow-up period, the simple detection of B cell clonality cannot be used as a criterion for diagnosis of B cell lymphoma.

Our three patients with nodal lymphoma, who presented different B cell expansions between MSG and lymphoma tissue (lymph node), contradict this classic story. Additional steps such as genetic events and the effects of various molecules, possibly the BAFF/APRIL system, may be necessary for lymphoma development [19,28,29]. Our data sustain previous hypotheses [10] that microenvironments in SS may serve the conditions to sustain lymphoproliferation and transformation not only in salivary and lacrimal glands but also in extraglandular tissue, and malignant clones can arise from visceral organs and lymph nodes beyond its original target organ, the glandular tissues [10,28].

Acknowledgements

This work was supported by grants from the Japanese Ministry of Education, Culture, Sports, Science and Technology (13557160, 15024236, 15390313, 13877075 to H. U. and

17591060 to Y. M.), the Uehara Memorial Foundation (to H. U.), the Hokkoku Cancer Fund (to Y. M.) and the Kanazawa Medical University Research Foundation (C2006-1 to H. U. and S2004-16 to Y. M.).

References

1 Moutsopoulos HM, Chused TM, Mann DL *et al.* Sjogren's syndrome (Sicca syndrome): Curr Issues. Ann Intern Med 1980; **92**:212–26.

2 Bloch KJ, Buchanan WW, Wohl MJ, Bunim JJ. Sjogren's syndrome. A clinical, pathological, and serological study of sixty-two cases 1965. Medicine (Balt) 1992; **71**:386–401;discussion 401–3.

3 Theander E, Henriksson G, Ljungberg O, Mandl T, Manthorpe R, Jacobsson LT. Lymphoma and other malignancies in primary Sjogren's syndrome: a cohort study on cancer incidence and lymphoma predictors. Ann Rheum Dis 2006; **65**:796–803.

4 Isaacson PG, Spencer J. Malignant lymphoma and autoimmune disease. Histopathology 1993; **22**:509–10.

5 Manthorpe R, Bredberg A, Henriksson G, Larsson A. Progress and regression within primary Sjogren's syndrome. Scand J Rheumatol 2006; **35**:1–6.

6 Masaki Y, Sugai S. Lymphoproliferative disorders in Sjogren's syndrome. Autoimmun Rev 2004; **3**:175–82.

7 Bahler DW, Swerdlow SH. Clonal salivary gland infiltrates associated with myoepithelial sialadenitis (Sjogren's syndrome) begin as nonmalignant antigen-selected expansions. Blood 1998; **91**:1864–72.

8 De Vita S, Boiocchi M, Sorrentino D *et al.* Characterization of prelymphomatous stages of B cell lymphoproliferation in Sjogren's syndrome. Arthritis Rheum 1997; **40**:318–31.

9 De Re V, De Vita S, Carbone A *et al.* The relevance of VDJ PCR protocols in detecting B-cell clonal expansion in lymphomas and other lymphoproliferative disorders. Tumori 1995; **81**:405–9.

10 Gasparotto D, De Vita S, De Re V *et al.* Extrasalivary lymphoma development in Sjogren's syndrome: clonal evolution from parotid gland lymphoproliferation and role of local triggering. Arthritis Rheum 2003; **48**:3181–6.

11 Vitali C, Bombardieri S, Jonsson R *et al.* Classification criteria for Sjogren's syndrome: a revised version of the European criteria proposed by the American–European Consensus Group. Ann Rheum Dis 2002; **61**:554–8.

12 Jordan RC, Masaki Y, Takeshita S, Speight PM, Sugai S. High prevalence of B-cell monoclonality in labial gland biopsies of Japanese Sjogren's syndrome patients. Int J Hematol 1996; **64**:47–52.

13 Schwartz RS. Shattuck lecture: diversity of the immune repertoire and immunoregulation. N Engl J Med 2003; **348**:1017–26.

14 Bende RJ, Aarts WM, Riedl RG, de Jong D, Pals ST, van Noesel CJ. Among B cell non-Hodgkin's lymphomas, MALT lymphomas express a unique antibody repertoire with frequent rheumatoid factor reactivity. J Exp Med 2005; **201**:1229–41.

15 Miura Y, Chu CC, Dines DM, Asnis SE, Furie RA, Chiorazzi N. Diversification of the Ig variable region gene repertoire of synovial B lymphocytes by nucleotide insertion and deletion. Mol Med 2003; **9**:166–74.

16 Kwon YS, Chung J, Shin GT, Lee SY, Jang YJ. Variable region genes of human monoclonal autoantibodies to histones H2A and H2B from a systemic lupus erythematosus patient. Mol Immunol 2005; **42**:311–7.

17 De Re V, De Vita S, Gasparotto D *et al.* Salivary gland B cell lymphoproliferative disorders in Sjogren's syndrome present a restricted use of antigen receptor gene segments similar to those used by hepatitis C virus-associated non-Hodgkins's lymphomas. Eur J Immunol 2002; **32**:903–10.

18 Sugai S, Saito I, Masaki Y *et al.* Rearrangement of the rheumatoid factor-related germline gene Vg and bcl-2 expression in lymphoproliferative disorders in patients with Sjogren's syndrome. Clin Immunol Immunopathol 1994; **72**:181–6.

19 Szodoray P, Jonsson R. The BAFF/APRIL system in systemic autoimmune diseases with a special emphasis on Sjogren's syndrome. Scand J Immunol 2005; **62**:421–8.

20 Groom J, Kalled SL, Cutler AH *et al.* Association of BAFF/BLyS overexpression and altered B cell differentiation with Sjogren's syndrome. J Clin Invest 2002; **109**:59–68.

21 Diss TC, Peng H, Wotherspoon AC, Pan L, Speight PM, Isaacson PG. Brief report. a single neoplastic clone in sequential biopsy specimens from a patient with primary gastric-mucosa-associated lymphoid-tissue lymphoma and Sjogren's syndrome. N Engl J Med 1993; **329**:172–5.

22 Pablos JL, Carreira PE, Morillas L, Montalvo G, Ballestin C, Gomez-Reino JJ. Clonally expanded lymphocytes in the minor salivary glands of Sjogren's syndrome patients without lymphoproliferative disease. Arthritis Rheum 1994; **37**:1441–4.

23 Lasota J, Miettinen MM. Coexistence of different B-cell clones in consecutive lesions of low-grade MALT lymphoma of the salivary gland in Sjogren's disease. Mod Pathol 1997; **10**:872–8.

24 Jordan R, Diss TC, Lench NJ, Isaacson PG, Speight PM. Immunoglobulin gene rearrangements in lymphoplasmacytic infiltrates of labial salivary glands in Sjogren's syndrome. A possible predictor of lymphoma development. Oral Surg Oral Med Oral Pathol Oral Radiol Endod 1995; **79**:723–9.

25 Aiello AMQ, Diss TC *et al.* Simultaneous phenotypically distinct but clonally identical mucosa-associated lymphoid tissue and follicular lymphoma in a patient with Sjogren's syndrome. Blood 1999; **94**:2247–51.

26 Gellrich S, Rutz S, Borkowski A *et al.* Analysis of V(H)-D-J(H) gene transcripts in B cells infiltrating the salivary glands and lymph node tissues of patients with Sjogren's syndrome. Arthritis Rheum 1999; **42**:240–7.

27 Hansen A, Reiter K, Pruss A *et al.* Dissemination of a Sjogren's syndrome-associated extranodal marginal-zone B cell lymphoma: circulating lymphoma cells and invariant mutation pattern of nodal Ig heavy- and light-chain variable-region gene rearrangements. Arthritis Rheum 2006; **54**:127–37.

28 Mariette X. Lymphomas in patients with Sjogren's syndrome: review of the literature and physiopathologic hypothesis. Leuk Lymph 1999; **33**:93–9.

29 Sugai S, Masaki Y, Dong L. Lymphoproliferative disorders in patients with Sjogren's syndrome. Autoimmun Rev 2004; **3** (Suppl. 1):S67–9.

Sjögren's Syndrome and Lymphoma Development

Lingli Dong[1,2], Yasufumi Masaki[1], Masao Tanaka[1], Toshihiro Fukushima[1], Toshiro Okazaki[3] and Hisanori Umehara[*,1]

[1]*Division of Hematology and Immunology, Department of Internal Medicine, Kanazawa Medical University, Kahoku-gun, Ishikawa 920-0293, Japan*

[2]*Department of Hematology and Immunology, Tongji Hospital, Huazhong University of Science and Technology, Wuhan, Hubei, 430030, China*

[3]*Department of Clinical Laboratory Medicine/Hematology, Faculty of Medicine, Tottori University, Yonago, Tottori, 683-8504, Japan*

Abstract: Primary Sjögren's syndrome (pSS) is a systemic as well as an organ-specific autoimmune disease characterized by lymphocytic infiltration of the glandular epithelial tissue. It has been reported that pSS patients have a relatively increased risk for the development of lymphoma and various factors such as cytokine stimulation, environmental exposures and viral infections as well as genetic events may contribute to the development of lymphoma in pSS patients. Over the past few decades, numerous efforts have been undertaken to search for the relationship between lymphoma and pSS, for example advances in molecular biology for clonality analysis and well-linked register cohort studies for the predictive value of clinical, laboratory and histological findings. Despite this, mechanisms and prediction of lymphoma development in pSS patients still remain to be defined. In this review we have summarized the current knowledge concerning incidence and risk factors of lymphoma development in pSS patients. In addition, the most recent discoveries in the emergence and treatment of lymphoma in pSS patients and the possible mechanism of lymphoma development are also discussed.

Keywords: Sjögren's syndrome, lymphoproliferative disease, lymphoma.

INTRODUCTION

Sjögren's syndrome (SS) is chronic autoimmune disease characterized by destructive lymphocyte infiltration of salivary and lacrimal glands, which results in dry eyes and dry mouth. During disease progression, it may extend from an autoimmune exocrinopathy to systemic disorder including non-visceral (skin, arthralgia, myalgia, central and peripheral nervous system) and visceral (lung, heart, kidney, gastrointestinal and endocrine) involvement. SS may occur alone (primary SS; pSS), or in association with another auto-immune diseases including rheumatoid arthritis (RA), systemic lupus erythematosus (SLE) or scleroderma, defined as secondary SS. SS affects ~0.2-1.0% of general population with a female preponderance (female to male ratio nine to one) [1].

Despite extensive study of the underlying cause of SS, the pathogenesis remains obscure. In broad terms, the pathogenesis of SS is multifactorial and includes several different steps induced by so called danger signals such as foreign material (e.g. during infection), non-infectious (e.g. oxidative stress) and DNA damage [2]. These steps include: ①Initiation: an initial danger signal (either viral or non-viral) to the gland that leads to cellular necrosis or apoptosis with subsequent expression of the Ro/SS-A and/or La/SS-B proteins on the glandular-cell surface [3]. ②Establishment: Persistent abnormal immune responses such as T cell activation, autoantibody production by B cells and dysfunction of dendritic cells (DC) in the salivary gland establish the pathological lesion of SS. Increased expression of the cytotoxic T-lymphocyte-associated antigen 4 (CTLA4) on salivary gland tissue and haplotypes of CTLA4, alterations in the T-cell receptor (TCR) repertoire of infiltrating T cells [3, 4] and abnormal selection in editing Ig receptors on B cells [5], may also contribute to form the pathological lesion. ③ Perpetuation: production of cytokines by the injured gland that up-regulates chemokines and cell adhesive molecules on the high endothelial venules of the gland, a process that promotes the migration of lymphocytes and dendritic cells in the gland; Antigen presenting cells (APC) such as monocytes, macrophages and dendritic cells, secret cytokines including IL-1, IL-6, TNF-α, B-cell-activating factor (BAFF) and IFN-α. BAFF secreted by APC strongly influences the development of SS in both animal models and patients [6, 7]. IFN-α is produced during viral infection and is known to be a potent danger signal that up-regulates cell surface expression of HLA class I or II and of costimulatory molecules such as CD40L and B-7 [2]. Antibodies to Ro/SS-A antigen (a ribonucleoprotein particle composed of hY-RNAs and two proteins components of 60kDa and 52kDa confirming a ribonucleoprotein complex) are produced by HLA-DR-positive B lymphocytes under the influence of T-helper lymphocytes. Although the cellular function of SS-A is unknown, SS-B is an RNA polymerase cofactor and has been documented to bind viral RNA, suggesting that immuno-complexes containing anti-SS-A/anti-SS-B antibodies and ribonucleo-protein may stimulate Toll-like receptor through complex with double-stranded RNA [8]. ④ Epithelial damage: Production of IFN-α by the dendritic cells perpetuates the process of lymphocyte homing, activation and apoptosis

*Address correspondence to this author at the Department of Hematology and Immunology, Kanazawa Medical University, 1-1 Daigaku, Uchinada, Ishikawa, 920-0293, Japan; E-mail: umehara@kanazawa-med.ac.jp

1573-3955/07 $50.00+.00

tion and apoptosis of glandular cells. It has been reported that affected organs of SS produce increased IFN-α and carry a molecular signature characterized by the expression of IFN genes and IFN-dependent transcripts [9]. Subsequently, an increase in apoptotic protease activities together with an abnormal surface exposure of some cytoplasmic autoantigens such as SS-A/SS-B may be involved in the progression of self-protein proteolysis and tissue destruction. Thus, this vicious cycle that links the innate and acquired immune systems may occur in SS patients [10] (Fig. 1).

INCIDENCE OF LYMPHOMA DEVELOPMENT IN PSS PATIENTS

The most frightening complication of pSS is lymphoproliferative disease (LPD) such as B cell lymphoma, since patients with SS have a relatively increased risk for the development of LPD compared with other autoimmune rheumatic diseases. The high incidence of lymphoma in SS was first reported in 1963 by Bunim and Talal [11]. Kassan *et al.* have reported that among 136 patients with SS admitted to the National Institute of Health, seven patients were observed with lymphoma development, thus the relative risk of lymphoma development was found to be 43.8 for SS [12]. Thereafter, the lifetime risk of incidence of lymphoma development has been verified around 5%-10% in several studies [13-15]. However, estimations of incidence are generally based on a few lymphoma cases and/or a highly selected group of patients. Therefore, the magnitude of the average lymphoma risk varies considerably among studies. Recently, several large cohort studies and a meta-analysis effectively estimate the incidence of lymphoma risk. Kauppi, *et al.* reported that among hospitalized patients including 676 with primary and 709 with secondary SS lymphoma risk (standardized incident rates; SIRs) was 8.7 in association with pSS and 4.5 for secondary SS [16]. Another more recent cohort study including 507 incident patients with pSS revealed that the risk of developing lymphoma is about 16-fold higher in patients with SS fulfilling the diagnostic American-European Consensus Criteria (AECC) compared with those who did not fulfill them [17]. In their study, the risk was more pronounced with longer follow-up time (>10 years) among AECC patients. A meta-analysis of the 20 cohort studies including 6 for SLE, 9 for RA and 5 for pSS suggested that SIRs for non-Hodgkin lymphoma are 18.8, 7.4 and 3.9 for pSS, SLE and RA, respectively [18]. Moreover, some studies investigating lymphoma development in pSS reported that those patients who develop a lymphoma appear to have a greater risk of developing the second malignancy [13, 19]. The potential link between the development of lymphoma and the subsequent development of additional cancers suggests that there may be a common etiology. An alternative explanation might be that the lymphomas in

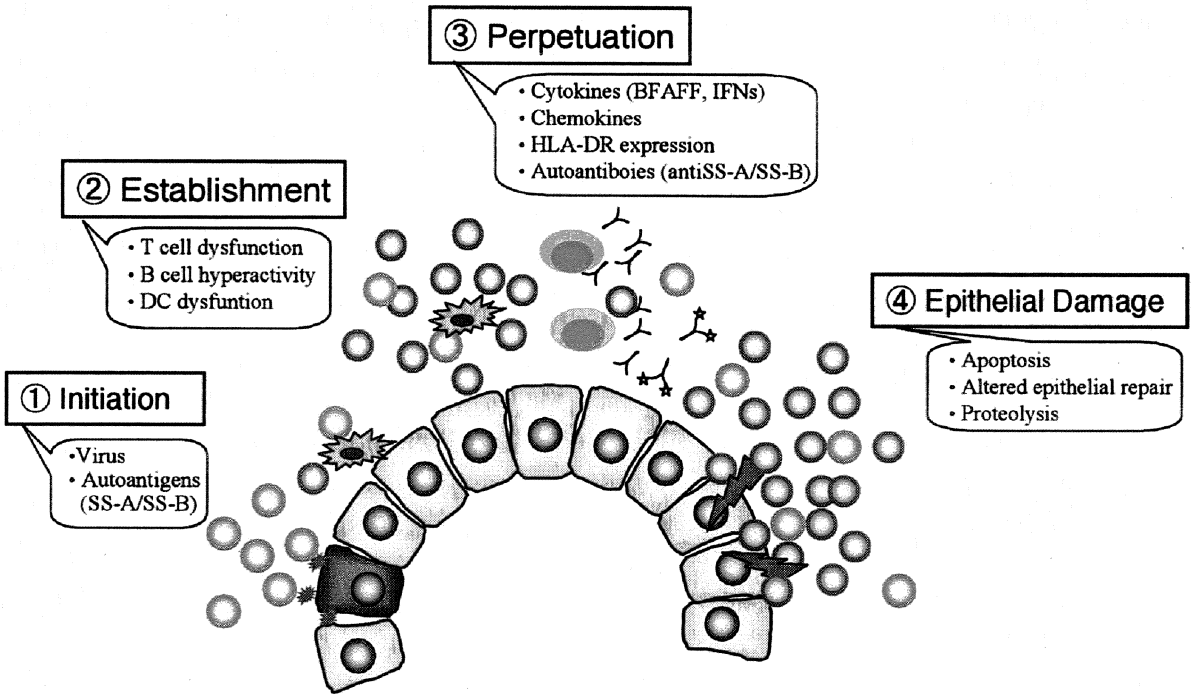

Fig. (1). Pathogenesis of primary SS. The pathogenesis of SS is multifactorial and includes several different steps. ① Initiation: An initial event (either viral or non-viral) induces cellular necrosis or apoptosis, subsequently expressing the SS-A and/or SS-B antigens on the glandular-cell surface. ② Establishment: T cell dysfunction, B cell hyperactivity and abnormal function of dendritic cell contribute to the establishment of the histopathological lesions. ③ Perpetuation: Production of cytokines (BAFF, IFNs, etc.) and chemokines by the injured gland promote the migration of lymphocytes and dendritic cells in the gland.. IFNs up-regulate cell surface expression of HLA class I or II and of costimulatory molecules such as CD40L and B-7.; production of antibodies to SS-A/SS-B antigens are produced by HLA-DR-positive B lymphocytes under the influence of a T-helper lymphocytes.; ④ Epithelial damage: Production of IFNs by the dendritic cells, which further perpetuates the process of lymphocyte homing, activation and apoptosis of glandular cells.. Thus, this vicious cycle that links the innate and acquired immune systems may occur in SS patients.

pSS are associated with suppressed immunity [20], thus making the patients more susceptible to the second malignancies.

Concerning lymphoma subtypes associated with pSS, various lymphoma subtypes have been described in literature. By case reports and case series, indolent lymphomas, such as mucosa associated lymphoid tissue (MALT) lymphoma, are more commonly reported in SS patients, especially those with the parotid gland involvement [21-23]. In contrast, two well-defined cohort studies of patients with SS indicate that the predominance of MALT lymphoma may not be as high as that described in initial reports and that diffused large B cell lymphoma was the most common subtype in SS patients [17, 24]. Therefore, besides the biologically well defined association between SS and parotid MALT lymphoma, there may also be a strong association with diffused large B cell lymphomas subtype, although the putative mechanisms underlying this association still remain unclear. Other histological subtypes of malignant lymphoma for patients with pSS, such as follicle center lymphoma [25], lymphoplasmacytoid [12] and angioimmuoblastic T cell lymphoma, a relatively common type of T cell lymphoma in SS [26] were also reported. The salivary glands are the most common site, but other extra-nodal sites are also involved such as stomach, nasopharynx, skin, liver, kidney and lungs. Lymph nodes and bone marrow are also identified as initial sites of transformation [27]. Gender differences in lymphoma development have not been evaluated due to the heavy predominance of female patients with SS. Although there have been case reports of the association of SS with infectious agents, such as *Helicobacter pylori*, human herpes virus 6, human T-lymphotropic virus type I and Epstein-Barr virus, no increased occurrence of lymphoma with such infectious agents has been reported in patients with SS [28].

PREDICTIVE RISK FACTORS FOR LYMPHOMA DEVELOPMENT

Up to the present, many predictors of lymphoma development have been identified. Clinical signs such as lymphadenopathy, swollen salivary glands, palpable purpura or skin vasculitis, peripheral involvement (i.e. peripheral neuropathy, such as trigeminal neuropathy, sensorineural deafness, mononeuritis multiplex and small fiber sensory neuropathy), leg ulcers, low grade fever, use of cytotoxic drugs, younger onset pSS and laboratory predictors such as anemia, lymphopenia, low levels of complement factor C3 and/or low C4 and cryoglobulinemia have been described. More recent and systematic assessments by Theander *et al.* documented that CD4+ T lymphocytopenia is an additional strong risk factor for developing lymphoma in SS [17]. They also indicated that the strongest predictor of lymphoma was a lowered CD4+/CD8+ T cell ratio. One possible explanation for this is that the traffic of CD4+ cells from the periphery into the tissues results in a decreased number of circulating CD4+ as well as a decrease in the CD4+/CD8 ratio. In Ioannidis's study, the presence of palpable purpura and low C4 levels at the first visit adequately distinguished high-risk patients (type I pSS) from patients with an uncomplicated disease course (type II low-risk primary SS) [29]. Low levels of complement factor C3 and/or low C4 could facilitate the survival of auto-reactive B cells, subsequently increasing the risk of unfavorable mutations, resulting in malignancy. CD27 expression has been shown in almost all types of B cell lymphoma, suggesting that significantly enhanced expression of CD27 might serve as an early indicator of the lymphoma development in pSS patients [30]. There are a few reports concerning specific associations between immunosuppressive treatment and lymphoma risk in SS patients [31]. Taken together, we need to learn more about the risk factors for development of B cell malignancies as well as the mechanisms underlying risk factors in SS and we should carefully identify individuals who are at substantially increased risk of lymphoma development.

POSSIBLE MECHANISM OF LYMPHOMA DEVELOPMENT

Primary SS has been described as an autoimmune exocrinopathy or epitheliitis with the major feature of lymphocytic infiltration in the grandular epithelial tissue, which consists of T cells (mostly CD4+ cells) and B cells. SS patients who have insufficient infiltration to meet the biopsy criterion might be less likely to have a chance of developing lymphoma suggesting the importance of interaction among T cells, B cells and epithelial cells [32]. Here we will discuss the recently proposed possible mechanisms underlying the development of B cell lymphomas, including defects in apoptosis and the mutageniecity of B cells, T cell modulation, persistent antigenic stimulation and the effects of various molecular such as BAFF (BlyS) [7] or type I interferons [33].

T Cell Modulation

The lymphocytes infiltrated in the minor salivary glands are predominantly T-cells with a bias towards CD4+ T cells rather than CD8+ T cell (CD4/CD8 ration > 2). Most CD4+ T-cells are of a primed memory phenotype (CD45RO+) and over 50% of all T cells express CD40/CD40L [34]. In SS, it is possible that regulatory T cells might inhibit protective polyclonal T cell lymphocytic infiltration in mucosal and exocrine tissues, allowing clonal B lymphoid cells to escape immunological surveillance and elimination [35]. Moreover, T cells can stimulate B cells through the CD40L-CD40 interaction in conjunction with the action of various cytokines and chemokines [36], or through the production of BAFF or other promoters of B cell proliferation, which in turn may enhance the tendency toward the development of lymphoma.

Abnormal B Cell Biology (Distribution, Mutgenesis and Clonal Expansion)

Analyses of the distribution of B cell subpopulations from patients with pSS revealed that the number of circulating CD27+ memory B cells was reduced. In contrast, accumulation of the CD27+ memory B cells in the inflamed salivary glands was inflated. Remarkably, SS patients with lymphoma uniquely exhibited an increase in CD27-expressing B cells, including CD27 (high) plasma blasts [37]. Extensive analyses of the mature B-cell subsets (Bm1-Bm5 classification of peripheral blood B cells in pSS) by Bohnhorst *et al.* showed further altered proportions of most mature B-cell subsets in pSS compared with a healthy donor and RA patients [38]. Although it is unclear whether these alterations reflect a disturbance in B cell trafficking and/or alteration in B cell differentiation, the biased repertoire may potentially contribute to lymphoma development [39]. In this regard,

[39]. In this regard, Groom *et al.* have reported the elevated levels of BAFF in sera and salivary tissues from pSS patients [7]. Since BAFF specifically regulates B lymphocyte proliferation and survival, altered B cell differentiation and tolerance induced by excess BAFF may be involved in lymphoma development.

Mutagenicity of B cell is another potential mechanism for lymphoma in SS [33, 40]. Hansen, *et al.* found that the proportion of B cells expressing mutated V(H) genes was significantly higher in B-cells isolated from the parotid gland compared with circulating B cells. Furthermore, V(L) gene analysis of B cells isolated from salivary glands revealed biased usage of the V(L) chain gene [41]. As we know, immunoglobulin generation occurs early in the development of B cells in the bone marrow. During later steps of B cell development, immunoglobulins undergo recombination, somatic mutation and isotype switching. These events require breaking and reconnecting DNA, subsequently increasing the risk of chromosome translocation of oncogenes such as Bcl-2 [42] and c-Myc to immunoglobulin loci (chromosome 14q32). Mutagenesis during these processes may result in generation of defective apoptosis and proliferation-enhanced B cells, which would tend to favor the development of lymphoma [33].

It has been demonstrated over the past few years that the transition from autoimmune state to lymphoma is a multi-step process and that chronic stimulation by exoantigen or autoantigen plays an important role in the development of these tumors by driving the proliferation of specific B cells and increasing the frequency of their transformation [27, 43]. In addition, immunoglobulin is proposed to be an important factor in stimulation rheumatoid factor-producing clones [44] and the development and expansion of MESA-associated clones. MALT lymphomas express a unique antibody repertoire with frequent rheumatoid factor reactivity [45]. Prolonged inflammation due to persistent antigenic stimulatory organisms such as *Helicobacter pylori* [46] may also be associated with the development of lymphoma. It has been reported that *Helicobacter pylori* stimulates tumor growth with the help of T cells in gastric MALT lymphomas [47] and that antibiotics regress MALT lymphoma. These evidences support the speculation that chronic antigenic stimulation by *Helicobacter pylori* may play a role in development of MALT-type B cell lymphoma [48].

Virus

A number of viruses have been suspected to launch pSS, including herpes virus 6, cytomegalovirus, Epstein-Barr virus, human T lymphotropic virus type 1, human immunodeficiency viruses, human intracisternal A-type retrovial particle, human retrovirus 5, recently identified coxsackie virus and so on. However, it remains unclear whether these viruses serve as antigen in antigen-driven clonal B cell proliferation [28]. Experimental, virological and clinical evidences have revealed a close association between Hepatitis C virus (HCV) and SS. However, a possible association between B cell lymphoma and HCV is still controversial. Some studies from Scandinavia and the US have found no association between SS and HCV [49, 50]. But recent studies have reported similarities in the etiopathogenical mechanism of lymphoma development in both patients with SS and those with HCV [51, 52]. Ramos-Casals *et al.* collected and characterized a large number of SS patients with HCV who developed B cell lymphoma, then described that SS patients with HCV and B cell lymphoma are characterized by a high frequency of parotid enlargement and vasculitis, an immunological pattern of the presence of RF and mixed type II cryoglobulins, a predominance of MALT lymphomas and an elevated frequency of primary extra-nodal involvement in organs in which HCV replicates (exocrine glands, liver, and stomach) [50]. One interpretation is that both SS and chronic HCV infection are characterized by an underlying B cell hyperactivity that is predisposed to monoclonal B cell selection, in some patients, to the development of an overt B cell lymphoma. Human herpes virus infection has also been reported to be linked with the development of MALT lymphoma in SS ptients [53]. In contrast, it has been reported that lymphomas in SS are not associated with viruses such as Epstein-Barr virus, human herpes virus 8, or human T lymphotropic virus-1 [21].

Oncogenic Molecules and Others

Together with persistent antigenic stimulation, additional oncogenic events such as inactivation of tumor suppression gene and/or activation of proto-oncogenes are undoubtedly required for lymphoma development. The role of tumor-suppressor genes such as P53 probably is probably important for lymphoma development in SS [54]. The presence of antibodies to p53 in sera from patients with SS and NHL [55], as well as novel mutations of the p53 gene in MSG from patients SS and NHL [54], undoubtedly implicated that dysregulation of this tumor suppressor gene as a possible mechanism for lymphoma development in SS. In addition, partial loss of P53 tumor-suppressor activity is associated with the development of low-grade MALT lymphoma, whereas complete loss of the function is related to high grade transformation [56]. Pisa, *et al.* found high frequency of t (14, 18) translocation in salivary gland lymphoma from SS patients [57]. One study has shown evidence of defective repair of a pro-mutagenic DNA base lesion, O6-methylguanine, in the lymphocytes of patients with pSS predisposed to lymphoma [58]. This raised the possibility that pSS patients predisposed to lymphoma may have defective DNA repair mechanisms. Other genetic events such as bcl-2 [42], c-Myc amplification or trisomy 3 may facilitate the progression of low-grade MALT lymphoma to a more malignant high-grade lymphoma [32, 33].

Cytokines

Cytokines as regulators of the immune system certainly contribute to pathogenesis of SS as well as lymphoma development in SS [32]. Th1 and Th2 cytokine profiles have been studied in blood and salivary gland tissues from patients with SS [39]. Analyses in humans showed that both types of cytokines are expressed by lymphocytes infiltrating the salivary glands of patients with SS. It has been suggested that Th-2 cytokines are predominant in the early phase of SS whereas a shift towards Th-1 cytokines is associated with advanced lymphocytic infiltration at a later stage of disease [59]. Most notably, recent studies have focused on the role of BAFF in pathogenesis of pSS. BAFF is a member of the TNF superfamily, also called the B lymphocyte stimulator (BLys), that specifically regulates B lymphocyte prolifera-

tion and survival. It has been reported that patients with pSS have marked increase in level of BAFF in the serum and target organs of the disease. Continuous B cell activation induced by increased BAFF production may lead to the development of B cell lymphoma [7]. Type I interferons can increase expression of BAFF, which in turn is postulated to tip the development of B cell lymphoma [9]. Taken together, the complicated interactions and various factors in microenvironment of SS play an indispensable role in the genesis of lymphoma (Fig. **2**).

CLONALITY ANALYSIS IN LYMPHOMA DEVELOPMENT

In contrast to the focal sialadenitis of the minor salivary glands observed commonly in pSS patients, the lymphocyte infiltration of the major salivary glands often forms secondary lymph follicles. B cells have been shown to infiltrate the glandular duct epithelium in pSS patients and thereby contribute to the characteristic pattern of chronic lymphocytic inflammation, the so called myoepithelial sialadenitis (MESA) or benign lymphoepithelial lesion. Patients with clonal expansion of B cells in their salivary glands have been suggested to be at high risk of developing lymphomas, and it was hypothesized that chronic exogenous or endogenous stimulation in MESA could play an important role in the lymphoproliferative process during the course of SS through restricted usage of immunoglobulin heavy chain complementarities determining region 3 (IgVH-CDR3) from MESA-associated clones [43, 60].

An evaluation of immunoglobulin heavy chain gene rearrangement has been used as a diagnostic assay to determine monoclonality in pSS patients with lymphoma over the past decade [61]. By this method, we examined B cell clonality in lymphoproliferative tissues from 6 primary SS patients associated with lymphoproliferative disorders or lymphoma. Three patients with sequential observation were showed progressional clonal expansion with the presence of the same subclone in different tissues during the course of disease. Among them, one patient developed mucosa-associated lymphoid tissue (MALT) lymphoma in glandular parotid. The other three SS patients concomitant with malignant B cells lymphomas showed different clonal expansion of B cells between nodal sites and salivary glands [62]. We summarized the literature regarding monoclonality and lymphoma development including 45 patients with SS in Table **1**. Forty-two patients showed evidence of monoclonal B cell expansion by PCR. Among them, however, only 16 patients developed lymphoma implying that the simple detection of B cell clonality by PCR cannot be used as a crite-

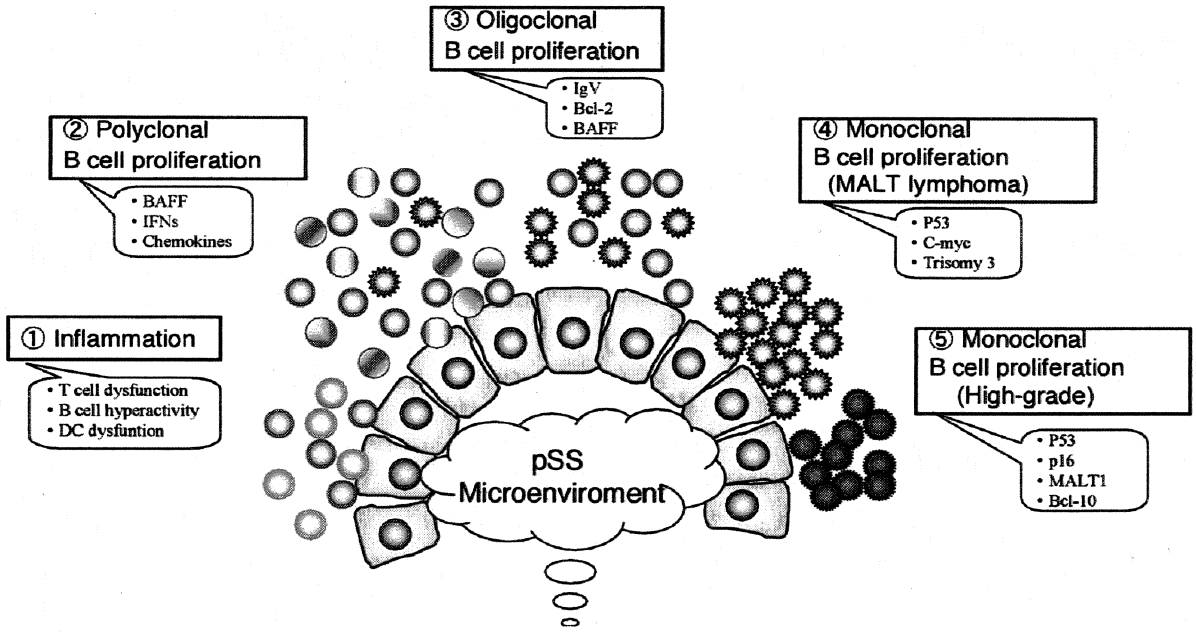

Fig. (2). Hypothetical model of lymphoma development in SS patients. The transition from autoimmune state to lymphoma is a multi-step process and chronic stimulation by exoantigen or autoantigen plays an important role in the development of lymphoma by driving the proliferation of specific B cells and increasing the frequency of their transformation. ① Inflammation: Infiltration of CD4+ T cells, memory B cells and dendritic cells in the minor salivary glands perpetuate chronic inflammation. ② Polyclonal B cell proliferation: Increased production of BAFF and IFNs in SS patients cause polyclonal B cell proliferation and thereby contribute to the characteristic pattern of myoepithelial sialadenitis (MESA) or benign lymphoepithelial lesion. ③ Oligoclonal B cell proliferation: BAFF specifically regulates B lymphocyte proliferation and survival, altered B cell differentiation. Chronic stimulation by exoantigen or autoantigen may drive the proliferation of specific B cells through restricted usage of immunoglobulin heavy chain complementarity determining region 3 (IgVH-CDR3) and increasing the frequency of their transformation. ④ Monoclonal B cell proliferation: During B cell development, immunoglobulins undergo recombination, somatic mutation and isotype switching. These events may increase the risk of translocation of oncogenes such as Bcl-2 and c-Myc to immunoglobulin loci (chromosome 14q32). ⑤ Transformation to high grade malignancy: Defect of P53 tumor-suppressor activity, high frequency of t(14,18) translocation, amplification of bcl-2 and/or c-Myc, and trisomy 3 may facilitate the progression of low-grade MALT lymphoma to more malignant high-grade lymphoma.

Table 1. The Literatures of Monoclonality and Lymphoma Development

Author	Year of Publication	Journal	Number of Cases	SS	Lymphoma	Same Clone†	Different Clone‡
Diss PC	1993	The New England Journal of Medicine	1	1SS→	MALToma	1	
Pablos JL	1994	Arthritis Rheum	14	1SS→	B cell neoplasm		1
Jordan R	1995	Oral Surgery Oral Medicine Oral Pathology	11	4SS→	lymphoma	4 §	
Lasota J	1997	Mod Pathol	1	1SS→	MALToma		1
De Vita S	1997	Arthritis Rheum	6	1SS→	Lymphoma (DLB)	1	
Bathler DW	1998	Blood	7	5SS→	lymphoma	4	1
Aiello A	1999	Blood	1	1SS→	MALToma→FL	1	
Gellrich S	1999	Arthritis Rheum	2	0	0	0	0
Gasparotto D	2003	Arthritis Rheum	1	1SS→	Lymphoma (MZB)	1	
Hansen A	2006	Arthritis Rheum	1	1SS→	Lymphoma (MZB)	1	
			45	**16**		**13**	**3**

†Same clone: malignant clone is from the initial lymphoproliferative glandular tissues by PCR and/or sequence, data to identify same monocloloanl or mutated monoclonal B cell expansion with conserved amino acids sequence motifs in their CDR3. ‡Different clone: different size of monoclonal bands by PCR or same size bands with distinct IgVH-CDR3 between initial lymphoproliferation and lymphoma. § Without sequence data, the result is from PCR. DLB, diffuse large B cell lymphoma; FL, follicular lymphoma; MZB, marginal zone B cell lymphoma.

rion for diagnosis of B cell lymphoma. The malignant lymphoma clones established from 13 SS patients were identified as being derived from the initial clones in lymphoproliferative glandular tissues, because both clones have the conserved amino acids sequence motifs in the CDR3 by sequence analysis [43, 60, 63-70]. Although these SS patients reported in the literature are not representative of all patients with SS, it is likely that patients with the same and persistent monoclonal B cell expansion in follow-up biopsy specimens are at higher risk of developing lymphoma and that malignant clones are derived from those in initial lymphoproliferative glandular tissues. In contrast, other investigations showed that the detection of monoclonality by immunoglobulin gene rearrangement has not proved to be a reliable predictor of clinical behavior in MESA, inasmuch as distinctly different B cell clones have been detected in different biopsy specimens and follow-up biopsies from the same patient [60]. Similar cases were also observed in our study [62]. Thus, it seems that the only molecular genetic analysis of monoclonality has only a litter practical value in the clinical diagnosis of salivary gland lymphoma in MESA. Therefore, clinicians should be diligent in examining patients with careful and correct evaluation for the evidence of lymphoma development.

THE MOST RECENT DISCOVERIES IN THE POTENTIAL ROLE ON THE TREATMENT OF LYMPHOMA IN PSS

SS is at the crossroads of autoimmune disease and lymphoma malignancy. Therefore, treatment of SS-associated lymphoma should target both the autoimmune and neoplastic nature of the disease. Several groups have observed that combined therapy with rituximab was well tolerated and proved to be effective on pSS-associated B cell aggressive lymphomas (four patients by Voulgarelis's group [71] and 4 of 5 by Seror's group [72]), indicating that targeting of B cells might be a promising treatment against pSS patients with lymphoma. Another clinical group reported the achievement of complete response in 3 of 4 patients with SS-associated B cell lymphoproliferation during 4 years of follow up after treatment with 2-chloro-2'-deoxyadenosine, a deoxyadenosine analog that acts independently on cell division. Therefore, a larger controlled trial is warranted to assess the effectiveness of these two regimens in such patients.

In addition, BAFF is likely to be an attractive and promising target for rheumatic diseases and B cell lymphoma by the reasomomh of its important roles in the pathogenesis of pSS and involvement of B cell lymphoma. Modulating the level and activity of BAFF may alleviate symptoms associated with the disease. Several potential therapeutic inhibitors targeting BAFF such as anti-BAFF antibody and receptor Fc fusion proteins are under investigation [73, 74].

SUMMARY

SS, at the crossroads of autoimmune disease and lymphoma malignancy, is a powerful model for the potential insight into the pathogenetic mechanisms responsible for lymphoma development. Moreover, the focus on pre-lymphomatous stages is crucial to better understanding the entire lymphomagenesis in SS. Monoclonal B cell proliferation in salivary gland is a frequent event in patients with pSS, but these cells are not necessarily malignant. It turned out that the prediction of lymphoma by PCR amplification of immunoglobulin heavy chain gene rearrangement was not reliable. DNA sequence may provide insight of clonal progression, although its predictive value of lymphoma is still controversial. Clinical symptoms and parameters such as parotid enlargement, palpable purpura, low C4 levels, especially CD4+ T lymphocytopenia, are valuable indicators for lymphoma development. The association between pSS and lymphoma is real. Thus, we need to examine SS patients carefully to determine the disease progression

and identify individuals who are at substantially increased risk of lymphoma development. Simultaneously, we need to learn how optimally to intervene against this risk, although the mechanisms underlying lymphoma development in pSS are complicated and mysterious.

ACKNOWLEDGEMENTS

We are thankful to all members of our department for their helpful cooperation in research and clinical works. This work was supported by grants from Japanese Ministry of Education, Culture, Sports, Science and Technology (13557160, 15024236, 15390313, 13877075, to H.U. and 17591060 to Y.M.), Uehara Memorial Foundation (to H.U.), and Kanazawa Medical University Research Foundation (C2006-1 to H.U. and S2004-16 to Y.M.).

ABBREVIATION

APC	=	Antigen presenting cells
BAFF	=	B-cell-activating factor
HCV	=	Hepatitis C virus
MALT	=	Mucosa associated lymphoid tissue
MESA	=	Myoepithelial sialadenitis
pSS	=	Primary Sjögren's syndrome
RA	=	Rheumatoid arthritis
SIRs	=	Standardized incident rates
SLE	=	Systemic lupus erythematosus
SS	=	Sjögren's syndrome

REFERENCES

[1] Dafni UG, Tzioufas AG, Staikos P, Skopouli FN, Moutsopoulos HM. Prevalence of Sjogren's syndrome in a closed rural community. Ann Rheum Dis 1997; 56: 521-5.

[2] Bredberg A, Henriksson G, Larsson A, Manthorpe R, Sallmyr A. Sjogren's syndrome and the danger model. Rheumatology (Oxford) 2005; 44: 965-70.

[3] Bolstad AI, Eiken HG, Rosenlund B, Alarcon-Riquelme ME, Jonsson R. Increased salivary gland tissue expression of Fas, Fas ligand, cytotoxic T lymphocyte-associated antigen 4, and programmed cell death 1 in primary Sjogren's syndrome. Arthritis Rheum 2003; 48: 174-85.

[4] Downie-Doyle S, Bayat N, Rischmueller M, Lester S. Influence of CTLA4 haplotypes on susceptibility and some extraglandular manifestations in primary Sjogren's syndrome. Arthritis Rheum 2006; 54: 2434-40.

[5] Kaschner S, Hansen A, Jacobi A, *et al.* Immunoglobulin Vlambda light chain gene usage in patients with Sjogren's syndrome. Arthritis Rheum 2001; 44: 2620-32.

[6] Rolink AG, Melchers F. BAFFled B cells survive and thrive: roles of BAFF in B-cell development. Curr Opin Immunol 2002; 14: 266-75.

[7] Groom J, Kalled SL, Cutler AH, *et al.* Association of BAFF/BLyS overexpression and altered B cell differentiation with Sjogren's syndrome. J Clin Invest 2002; 109: 59-68.

[8] von Muhlen CA, Tan EM. Autoantibodies in the diagnosis of systemic rheumatic diseases. Semin Arthritis Rheum 1995; 24: 323-58.

[9] Bave U, Nordmark G, Lovgren T, *et al.* Activation of the type I interferon system in primary Sjogren's syndrome: a possible etiopathogenic mechanism. Arthritis Rheum 2005; 52: 1185-95.

[10] Fox RI. Sjogren's syndrome. Lancet 2005; 366: 321-31.

[11] Talal N, Bunim JJ. The Development of Malignant Lymphoma in the Course of Sjoegren's Syndrome. Am J Med 1964; 36: 529-40.

[12] Kassan SS, Thomas TL, Moutsopoulos HM, *et al.* Increased risk of lymphoma in sicca syndrome. Ann Intern Med 1978; 89: 888-92.

[13] Lazarus MN, Robinson D, Mak V, Moller H, Isenberg DA. Incidence of cancer in a cohort of patients with primary Sjogren's syndrome. Rheumatology (Oxford) 2006; 45: 1012-5.

[14] Zufferey P, Meyer OC, Grossin M, Kahn MF. Primary Sjogren's syndrome (SS) and malignant lymphoma. A retrospective cohort study of 55 patients with SS. Scand J Rheumatol 1995; 24: 342-5.

[15] Valesini G, Priori R, Bavoillot D, *et al.* Differential risk of non-Hodgkin's lymphoma in Italian patients with primary Sjogren's syndrome. J Rheumatol 1997; 24: 2376-80.

[16] Kauppi M, Pukkala E, Isomaki H. Elevated incidence of hematologic malignancies in patients with Sjogren's syndrome compared with patients with rheumatoid arthritis (Finland). Cancer Causes Control 1997; 8: 201-4.

[17] Theander E, Henriksson G, Ljungberg O, Mandl T, Manthorpe R, Jacobsson LT. Lymphoma and other malignancies in primary Sjogren's syndrome: a cohort study on cancer incidence and lymphoma predictors. Ann Rheum Dis 2006; 65: 796-803.

[18] Zintzaras E, Voulgarelis M, Moutsopoulos HM. The risk of lymphoma development in autoimmune diseases: a meta-analysis. Arch Intern Med 2005; 165: 2337-44.

[19] Sutcliffe N, Inanc M, Speight P, Isenberg D. Predictors of lymphoma development in primary Sjogren's syndrome. Semin Arthritis Rheum 1998; 28: 80-7.

[20] Kamel OW, van de Rijn M, Hanasono MM, Warnke RA. Immunosuppression-associated lymphoproliferative disorders in rheumatic patients. Leuk Lymphoma 1995; 16: 363-8.

[21] Royer B, Cazals-Hatem D, Sibilia J, *et al.* Lymphomas in patients with Sjogren's syndrome are marginal zone B-cell neoplasms, arise in diverse extranodal and nodal sites, and are not associated with viruses. Blood 1997; 90: 766-75.

[22] Isaacson PG, Spencer J. Malignant lymphoma of mucosa-associated lymphoid tissue. Histopathology 1987; 11: 445-62.

[23] Voulgarelis M, Dafni UG, Isenberg DA, Moutsopoulos HM. Malignant lymphoma in primary Sjogren's syndrome: a multicenter, retrospective, clinical study by the European Concerted Action on Sjogren's Syndrome. Arthritis Rheum 1999; 42: 1765-72.

[24] Tonami H, Matoba M, Kuginuki Y, *et al.* Clinical and imaging findings of lymphoma in patients with Sjogren syndrome. J Comput Assist Tomogr 2003; 27: 517-24.

[25] Pavlidis NA, Drosos AA, Papadimitriou C, Talal N, Moutsopoulos HM. Lymphoma in Sjogren's syndrome. Med Pediatr Oncol 1992; 20: 279-83.

[26] Saito M, Fukuda T, Shiohara T, Homori M. Angioimmunoblastic T-cell lymphoma: a relatively common type of T-cell lymphoma in Sjogren's syndrome. Clin Exp Rheumatol 2005; 23: 888-90.

[27] Voulgarelis M, Moutsopoulos HM. Malignant lymphoma in primary Sjogren's syndrome. Isr Med Assoc J 2001; 3: 761-6.

[28] Youinou P, Pers JO, Saraux A, Pennec YL. Viruses contribute to the development of Sjogren's syndrome. Clin Exp Immunol 2005; 141: 19-20.

[29] Ioannidis JP, Vassiliou VA, Moutsopoulos HM. Long-term risk of mortality and lymphoproliferative disease and predictive classification of primary Sjogren's syndrome. Arthritis Rheum 2002; 46: 741-7.

[30] Dorner T, Lipsky PE. Abnormalities of B cell phenotype, immunoglobulin gene expression and the emergence of autoimmunity in Sjogren's syndrome. Arthritis Res 2002; 4: 360-71.

[31] Leandro MJ, Isenberg DA. Rheumatic diseases and malignancy--is there an association? Scand J Rheumatol 2001; 30: 185-8.

[32] Masaki Y, Sugai S. Lymphoproliferative disorders in Sjogren's syndrome. Autoimmun Rev 2004; 3: 175-82.

[33] Mackay IR, Rose NR. Autoimmunity and lymphoma: tribulations of B cells. Nat Immunol 2001; 2: 793-5.

[34] Nakamura H, Kawakami A, Tominaga M, *et al.* Expression of CD40/CD40 ligand and Bcl-2 family proteins in labial salivary glands of patients with Sjogren's syndrome. Lab Invest 1999; 79: 261-9.

[35] Gottenberg JE, Lavie F, Abbed K, *et al.* CD4 CD25high regulatory T cells are not impaired in patients with primary Sjogren's syndrome. J Autoimmun 2005; 24: 235-42.

[36] Ogawa N, Ping L, Zhenjun L, Takada Y, Sugai S. Involvement of the interferon-gamma-induced T cell-attracting chemokines, interferon-gamma-inducible 10-kd protein (CXCL10) and monokine induced by interferon-gamma (CXCL9), in the salivary gland lesions of patients with Sjogren's syndrome. Arthritis Rheum 2002; 46: 2730-41.

[37] Hansen A, Odendahl M, Reiter K, *et al.* Diminished peripheral blood memory B cells and accumulation of memory B cells in the salivary glands of patients with Sjogren's syndrome. Arthritis Rheum 2002; 46: 2160-71.

[38] Bohnhorst JO, Bjorgan MB, Thoen JE, Natvig JB, Thompson KM. Bm1-Bm5 classification of peripheral blood B cells reveals circulating germinal center founder cells in healthy individuals and disturbance in the B cell subpopulations in patients with primary Sjogren's syndrome. J Immunol 2001; 167: 3610-8.

[39] Delaleu N, Jonsson R, Koller MM. Sjogren's syndrome. Eur J Oral Sci 2005; 113: 101-13.

[40] Pillemer SR. Lymphoma and other malignancies in primary Sjogren's syndrome. Ann Rheum Dis 2006; 65: 704-6.

[41] Dorner T, Hansen A, Jacobi A, Lipsky PE. Immunglobulin repertoire analysis provides new insights into the immunopathogenesis of Sjogren's syndrome. Autoimmun Rev 2002; 1: 119-24.

[42] Sugai S, Saito I, Masaki Y, *et al.* Rearrangement of the rheumatoid factor-related germline gene Vg and bcl-2 expression in lymphoproliferative disorders in patients with Sjogren's syndrome. Clin Immunol Immunopathol 1994; 72: 181-6.

[43] Bahler DW, Swerdlow SH. Clonal salivary gland infiltrates associated with myoepithelial sialadenitis (Sjogren's syndrome) begin as nonmalignant antigen-selected expansions. Blood 1998; 91: 1864-72.

[44] Chen X, Sugai S, Nakasaki S, Ogawa Y, Takeshita S Rheumatoid factor idiotypes in patients with Sjogren's syndrome. Nihon Rinsho Meneki Gakkai Kaishi 1996; 19: 468-76.

[45] Bende RJ, Aarts WM, Riedl RG, de Jong D, Pals ST, van Noesel CJ. Among B cell non-Hodgkin's lymphomas, MALT lymphomas express a unique antibody repertoire with frequent rheumatoid factor reactivity. J Exp Med 2005; 201: 1229-41.

[46] Nishimura M, Miyajima S, Okada N. Salivary gland MALT lymphoma associated with Helicobacter pylori infection in a patient with Sjogren's Syndrome. J Dermatol 2000; 27: 450-2.

[47] Hussell T, Isaacson PG, Crabtree JE, Spencer J. The response of cells from low-grade B-cell gastric lymphomas of mucosa-associated lymphoid tissue to Helicobacter pylori. Lancet 1993; 342: 571-4.

[48] Savio A, Franzin G, Wotherspoon AC, *et al.* Diagnosis and post-treatment follow-up of Helicobacter pylori-positive gastric lymphoma of mucosa-associated lymphoid tissue: histology, polymerase chain reaction, or both? Blood 1996; 87: 1255-60.

[49] King PD, McMurray RW, Becherer PR. Sjogren's syndrome without mixed cryoglobulinemia is not associated with hepatitis C virus infection. Am J Gastroenterol 1994; 89: 1047-50.

[50] Ramos-Casals M, la Civita L, de Vita S, *et al.* Characterization of B cell lymphoma in patients with Sjogren's syndrome and hepatitis C virus infection. Arthritis Rheum 2007; 57: 161-70.

[51] Mariette X. Lymphomas complicating Sjogren's syndrome and hepatitis C virus infection may share a common pathogenesis: chronic stimulation of rheumatoid factor B cells. Ann Rheum Dis 2001; 60: 1007-10.

[52] De Re V, De Vita S, Gasparotto D, *et al.* Salivary gland B cell lymphoproliferative disorders in Sjogren's syndrome present a restricted use of antigen receptor gene segments similar to those used by hepatitis C virus-associated non-Hodgkins's lymphomas. Eur J Immunol 2002; 32: 903-10.

[53] Klussmann JP, Wagner M, Guntinas-Lichius O, Muller A. Detection of HHV-8 sequences and antigens in a MALT lymphoma associated with Sjogren's syndrome. J Oral Pathol Med 2003; 32: 243-5.

[54] Tapinos NI, Polihronis M, Moutsopoulos HM. Lymphoma development in Sjogren's syndrome: novel p53 mutations. Arthritis Rheum 1999; 42: 1466-72.

[55] Mariette X, Sibilia J, Delaforge C, Bengoufa D, Brouet JC, Soussi T. Anti-p53 antibodies are rarely detected in serum of patients with rheumatoid arthritis and Sjogren's syndrome. J Rheumatol 1999; 26: 1672-5.

[56] Du M, Peng H, Singh N, Isaacson PG, Pan L. The accumulation of p53 abnormalities is associated with progression of mucosa-associated lymphoid tissue lymphoma. Blood 1995; 86: 4587-93.

[57] Pisa EK, Pisa P, Kang HI, Fox RI. High frequency of t(14; 18) translocation in salivary gland lymphomas from Sjogren's syndrome patients. J Exp Med 1991; 174: 1245-50.

[58] Guo K, Major G, Foster H, *et al.* Defective repair of O6-methylguanine-DNA in primary Sjogren's syndrome patients predisposed to lymphoma. Ann Rheum Dis 1995; 54: 229-32.

[59] Mitsias DI, Tzioufas AG, Veiopoulou C, *et al.* The Th1/Th2 cytokine balance changes with the progress of the immunopathological lesion of Sjogren's syndrome. Clin Exp Immunol 2002; 128: 562-8.

[60] De Vita S, Boiocchi M, Sorrentino D, *et al.* Characterization of prelymphomatous stages of B cell lymphoproliferation in Sjogren's syndrome. Arthritis Rheum 1997; 40: 318-31.

[61] Schwartz RS. Shattuck lecture: Diversity of the immune repertoire and immunoregulation. N Engl J Med 2003; 348: 1017-26.

[62] Dong L, Masaki Y, Takegami T, *et al.* Clonality analysis of lymphoproliferative disorders in patients with Sjogren's syndrome. Clin Exp Immunol 2007; 150: 279-84.

[63] Diss TC, Peng H, Wotherspoon AC, Pan L, Speight PM, Isaacson PG. Brief report: a single neoplastic clone in sequential biopsy specimens from a patient with primary gastric-mucosa-associated lymphoid-tissue lymphoma and Sjogren's syndrome. N Engl J Med 1993; 329: 172-5.

[64] Pablos JL, Carreira PE, Morillas L, Montalvo G, Ballestin C, Gomez-Reino JJ. Clonally expanded lymphocytes in the minor salivary glands of Sjogren's syndrome patients without lymphoproliferative disease. Arthritis Rheum 1994; 37: 1441-4.

[65] Lasota J, Miettinen MM. Coexistence of different B-cell clones in consecutive lesions of low-grade MALT lymphoma of the salivary gland in Sjogren's disease. Mod Pathol 1997; 10: 872-8.

[66] Jordan R, Diss TC, Lench NJ, Isaacson PG, Speight PM. Immunoglobulin gene rearrangements in lymphoplasmacytic infiltrates of labial salivary glands in Sjogren's syndrome. A possible predictor of lymphoma development. Oral Surg Oral Med Oral Pathol Oral Radiol Endod 1995; 79: 723-9.

[67] Aiello A, Du MQ, Diss TC, *et al.* Simultaneous phenotypically distinct but clonally identical mucosa-associated lymphoid tissue and follicular lymphoma in a patient with Sjogren's syndrome. Blood 1999; 94: 2247-51.

[68] Gellrich S, Rutz S, Borkowski A, *et al.* Analysis of V(H)-D-J(H) gene transcripts in B cells infiltrating the salivary glands and lymph node tissues of patients with Sjogren's syndrome. Arthritis Rheum 1999; 42: 240-7.

[69] Gasparotto D, De Vita S, De Re V, *et al.* Extrasalivary lymphoma development in Sjogren's syndrome: clonal evolution from parotid gland lymphoproliferation and role of local triggering. Arthritis Rheum 2003; 48: 3181-6.

[70] Hansen A, Reiter K, Pruss A, *et al.* Dissemination of a Sjogren's syndrome-associated extranodal marginal-zone B cell lymphoma: circulating lymphoma cells and invariant mutation pattern of nodal Ig heavy- and light-chain variable-region gene rearrangements. Arthritis Rheum 2006; 54: 127-37.

[71] Voulgarelis M, Giannouli S, Anagnostou D, Tzioufas AG. Combined therapy with rituximab plus cyclophosphamide/doxorubicin/vincristine/prednisone (CHOP) for Sjogren's syndrome-associated B-cell aggressive non-Hodgkin's lymphomas. Rheumatology (Oxford) 2004; 43: 1050-3.

[72] Seror R, Sordet C, Guillevin L, *et al.* Tolerance and efficacy of rituximab and changes in serum B cell biomarkers in patients with systemic complications of primary Sjogren's syndrome. Ann Rheum Dis 2007; 66: 351-7.

[73] Mackay F, Sierro F, Grey ST, Gordon TP. The BAFF/APRIL system: an important player in systemic rheumatic diseases. Curr Dir Autoimmun 2005; 8: 243-65.

[74] Kalled SL, Ambrose C, Hsu YM. BAFF: B cell survival factor and emerging therapeutic target for autoimmune disorders. Expert Opin Ther Targets 2003; 7: 115-23.

Mod Rheumatol (2006) 16:124–130
DOI 10.1007/s10165-006-0471-9

REVIEW ARTICLE

**Hisanori Umehara · Masao Tanaka · Toshioki Sawaki
Zhe-Xiong Jin · Cheng-Ri Huang · Lingli Dong
Takafumi Kawanami · Hiromi Karasawa
Yasufumi Masaki · Toshihiro Fukushima · Yuko Hirose
Toshirou Okazaki**

Fractalkine in rheumatoid arthritis and allied conditions

Received: February 24, 2006 / Accepted: March 14, 2006

Abstract Leukocyte adhesion and trafficking at the endothelium requires both adhesion molecules and chemotactic factors. Fractalkine (CX3C) is a unique chemokine, and is expressed on tumor necrosis factor-α- and interleukin-1-activated endothelial cells (ECs). Fractalkine receptor, CX3CR1, is expressed on NK cells, monocytes, and some portion of CD4- and CD8-positive T cells. Interactions between fractalkine and CX3CR1 can mediate not only chemotaxis, but also cell adhesion in the absence of substrates for other adhesion molecules. Furthermore, fractalkine activates NK cells, leading to increased cytotoxicity and interferon-γ production. Recently, accumulating evidence has shown that fractalkine is involved in the pathogenesis of rheumatoid arthritis and allied conditions. This review examines new concepts underlying fractalkine-mediated leukocyte migration and tissue damage, focusing primarily on the pathophysiological roles of fractalkine in rheumatic diseases.

Key words Chemokines · Fractalkine (CX3C) · Inflammation · Rheumatic disease · Vascular biology

Introduction

The migration of leukocytes into extravascular tissues involves a cascade of molecular events including the elaboration of chemotactic factors, the response to these factors, the interaction of leukocytes with endothelial cells (ECs), and leukocyte transmigration through the blood vessel wall.[1,2] The endothelium plays an important role in the recruitment and emigration of circulating leukocytes into sites of inflammation and immune responses, and ECs can be the primary target of immunologic injury, which results in vasculopathy and organ dysfunction.[1–3]

Chemokines were first described as chemoattractant cytokines synthesized at sites of inflammation and are major regulatory proteins for leukocyte recruitment and trafficking.[4,5] More than 50 chemokines have been identified to date and are subdivided into four subfamilies, C-, CC-, CXC-, and CX3C-chemokine, based on the number and spacing of the first two cysteines in a conserved cysteine structural motif. Different chemokine classes tend to exhibit different ranges of leukocyte specificity, and the chemokines produced during the inflammatory process are expected to determine the extent, quality, and duration of the cellular infiltrate.[5–7] However, inappropriately elevated expression of inflammatory chemokines may result in extensive tissue damage caused by activated leukocytes.[8,9] Because fractalkine is expressed on ECs activated by proinflammatory cytokines[10] and has both chemoattractive and adhesive functions,[11–13] it is likely that fractalkine is involved in the extravasation of leukocytes into inflamed tissues in the inflammatory conditions such as rheumatic diseases.[13,14]

H. Umehara (✉) · M. Tanaka · T. Sawaki · Z.-X. Jin · C.-R. Huang · L. Dong · T. Kawanami · H. Karasawa · Y. Masaki · T. Fukushima · Y. Hirose
Division of Hematology and Immunology, Department of Internal Medicine, Kanazawa Medical University, Daigaku, Uchinada-machi, Kahoku-gun, Ishikawa 920-0293, Japan
Tel. +81-76-218-8158; Fax +81-76-286-9290
e-mail: umehara@kanazawa-med.ac.jp

M. Tanaka
Department of Rheumatology and Clinical Immunology, Kyoto University Graduate School of Medicine, Kyoto, Japan

T. Okazaki
Department of Clinical Laboratory, Medicine/Hematology, Faculty of Medicine, Tottori University, Tottori, Japan

Fractalkine (CX3C chemokine)

Unique structure and function

Fractalkine, a large protein of 373 amino acids containing multiple domains, is the first CX3C-chemokine to be described and is structurally distinct from other chemokines.[10,13–15] Importantly, fractalkine is a transmembrane molecule expressed on the cell surface. Beginning with its extracellular domain, the first 76 amino acids of

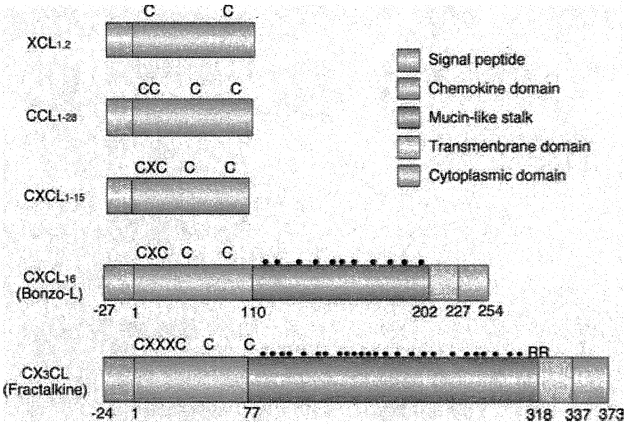

Fig. 1. Schematic structure of fractalkine.[13,14] CX3C-chemokine, fractalkine is a large protein of 373 amino acids containing multiple domains and structurally distinct from other chemokines, i.e., CXCLs, CCLs, and CLs. Beginning with the predicted signal peptide, it contains an N-terminal chemokine domain (residues 1–76) with the unique three-residue insertion between cysteines (CX3C), mucin-like stalk (residues 77–317) with predicted *O*-glycosylated serine and threonine (●), transmembrane domain (residues 318–336), and intracellular domain (residues 337–373). *RR* indicates a membrane-proximal dibasic motif similar to a dibasic cleavage site in syndecans. CXCL16 (Bonzo ligand) has a structure similar to that of of fractalkine

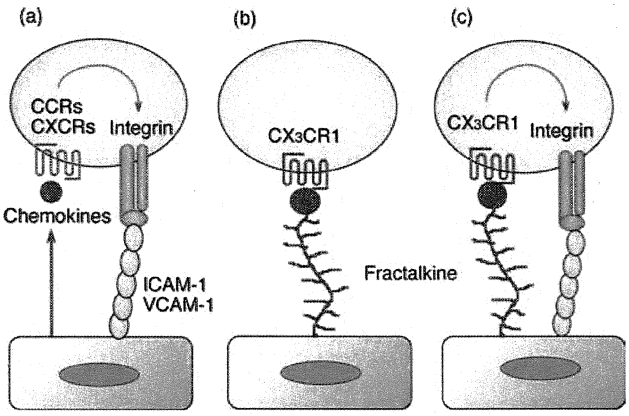

Fig. 2a–c. Dual functions of fractalkine as an adhesion molecule and chemokine.[13,14] **a** Soluble chemokines bind to specific receptors (CCRs or CXCRs) and trigger integrin activation. Integrins with high avidity bind to their ligands (ICAM-1 or VCAM-1) and support cell adhesion. **b** Fractalkine, consisting of chemokine domain and mucin-like stalk, are expressed as the membrane-bound form on activated endothelial cells. Interaction between fractalkine and CX3CR1 can suppose cell adhesion without involvement of integrins. **c** In addition to the intrinsic adhesion function of fractalkine, CX3CR1 can also transduce signals for integrin activation. Therefore, fractalkine and integrins cooperatively mediate cell adhesion. *ICAM-1*, intercellular adhesion molecule-1; *VCAM-1*, vascular cell adhesion molecule-1

fractalkine comprise a chemokine domain with a novel arrangement of cysteines (CXXXC: three amino acids separate the first two cysteines), an extended mucin-like stalk, a transmembrane domain, and an intracellular domain of 37 amino acids. Membrane-bound fractalkine can be markedly induced on primary ECs by inflammatory cytokines such as tumor necrosis factor (TNF)-α and interleukin (IL)-1, and soluble fractalkine can be released, presumably by proteolysis at a membrane-proximal dibasic cleavage site similar to those of syndecans, and exhibits an efficient chemotactic activity for monocytes and T cells (Fig. 1).[10]

Following the original report that fractalkine receptor (CX3CR1)-expressing cells adhered to immobilized fractalkine,[11] transfection studies with chimeric proteins revealed that the mucin domain provides a stalk which extends the chemokine domain away from the endothelial cell surface enabling presentation of the chemokine domain to leukocytes and supporting cell adhesion.[16,17] In addition to the intrinsic adhesion function of fractalkine, we found that soluble-fractalkine enhanced the binding of CX3CR1-expressing THP-1 cells to immobilized fibronectin and intercellular adhesion molecule-1 (ICAM-1). This enhancement was efficiently inhibited by a G_i inhibitor, pertussis toxin, suggesting that CX3CR1 transduces signals to increase integrin avidity through G protein activation (Fig. 2).[12] Furthermore, THP-1 cells adhered to a fractalkine transfected-ECV304 cells or TNF-α-activated human umbilical vein endothelial cells (HUVECs) more efficiently than to control cells.[12] Moreover, we observed that co-immobilization of fractalkine with integrin ligands, including either fibronectin or ICAM-1, enhanced cell adhesion compared with that observed for the fractalkine interaction with CX3CR1 or each integrin system alone.[18] Taken together, these findings suggest that fractalkine can function as an adhesion molecule between fractalkine-expressing ECs and CX3CR1-expressing cells rather than a chemotactic factor.[13]

Fractalkine receptor (CX3CR1) and leukocyte subset

$CD4^+$ helper T cells (Th) as well as $CD8^+$ cytotoxic T cells (Tc) are subdivided into two distinct populations based on the profile of cytokine production. Th1 and Tc1 cells secret interferon (IFN)-γ, TNF-β, and IL-2, mediate immune responses against intracellular pathogens, and are associated with pathological process such as organ-specific autoimmune diseases. Conversely, Th2 and Tc2 cells produce IL-4, IL-5, IL-6, and IL-13, mediate immune responses against extracellular pathogens, and are associated with allergic immune responses.[19,20] Recent studies have shown that various lymphocyte subsets with differential tissue tropism, in accordance with their particular developmental stages and/or functional properties, express specific chemokine receptors.[21,22] It has been reported that Th1 cells preferentially express CCR5 and CXCR3 (Th1-associated chemokine receptors), while Th2 cells preferentially express CCR4, possibly CCR3 and CCR8 (Th2-assocaited chemokine receptors). Helper T cells are further subdivided into two distinct subsets according to the expression of CCR7; $CCR7^+$ naïve cells, $CCR7^+$ lymph-node homing memory cells, and $CCR7^-$ tissue-homing effector memory cells. Memory T cells lacking CCR7 produce the effector cytokine IFN-γ with rapid kinetics (effector memory T cells:

T_{EM}), whereas T cells expressing CCR7 represent a pool of central memory T cells (T_{CM}).[22]

$CD8^+$ cytotoxic T cells start to express lytic mediators, perforin and granzymes, during differentiation to memory/effector stages after antigenic stimulation.[23] Terminally differentiated effector $CD8^+$ T cells do not express CD27, CD28 (costimulatory molecules), and CD62L (L-selectin), and possess high cytolytic activity producing IFN-γ and TNF-α.[24,25]

Imai et al. have identified CX3CR1 and have demonstrated that it is expressed on most $CD16^+$ NK cells, the majority of $CD14^+$ monocytes, and a substantial fraction of $CD3^+$ T cells.[11] Recently, we characterized the phenotypes of lymphoid cells expressing CX3CR1. The majority of CX3CR1-expressing $CD4^+$ and $CD8^+$ T cells co-express CCR5, but not CXCR3, suggesting that CX3CR1-expressing T cells partly overlap with Th1 and Tc1 cells, respectively.[26] In addition, CX3CR1-expressing cells including $CD4^+$ T cells, $CD8^+$ T cells, γδ T cells, and NK cells, express CD57 and CD11b (good markers for cytotoxic lymphocytes) and possess cytoplasmic granules containing perforin and granzyme B.[26] Collectively, these data suggest that CX3CR1 is a highly selective chemokine receptor and surface marker for cytotoxic effector lymphocytes including NK cells, cytotoxic T lymphocytes (CTLs), and γδ T cells.[13,14] Fractalkine is also known to exert an effect on monocytes. Bazan et al. reported that fractalkine induces the migration of monocytes,[10] and Imai et al. demonstrated that $CD14^+$ monocytes express CX3CR1.[11] Profiles of CX3CR1-expressing cells are summarized in Table 1.

Table 1. Profiles of CX3CR1+ cells

	Expression of CX3CR1	
CD4 T cell	5%	
CD8 T cell	40%	
γδ T cell	70%	
NK cell	90%	
Monocytes	80%	
B cell	<1%	
T cells (CD3+)		
Naive	Central memory	Cytotoxic effector
(CD45RA+/CD27+)	(CD45RA−/CD27−)	(CD45RA± /CD27±) CX3CR1+
	Perforin+ Granzyme+ CD57+	
	CCR4+	CD11b+
CCR7+	CCR7−	CCR7−
CD62L+	CD62L−	CD62L−
CD28+	CD28−	CD28−
NK cells (CD16+)		
CX3CR1+, CXCR1+, Perforin+, Granzyme+		
Macrophages (CD14+)		
Immature	Mature	
CX3CR1+	CX3CR1++	
CCR2+	CCR2−	
CD62L+	CD62L−	
Gr1+	Gr1−	

Unique roles in cell transmigration

In the classical pathway of leukocyte migration, the first step involves transient, selectin-mediated interactions between rolling leukocytes and the endothelium (rolling or tethering). Next, integrins on leukocytes are activated by chemokines that have been produced locally and presented on glycosaminoglycans (triggering), resulting in firm adhesion between leukocytes and endothelial cells (firm adhesion). Leukocytes then extravasate through the vascular wall and into the tissue (transmigration).[1,2,27] Prior to the identification and description of fractalkine, chemokines had been perceived to be secreted as the soluble molecule and associate with the tissue matrix such as glycosaminoglycan to retain themselves on the cell surface. Following this binding, the interaction between chemokines and their specific receptors on leukocytes triggers activation of members of the integrin family through a G protein-dependent mechanism.[27]

In the case of fractalkine, the chemokine domain is presented at the top of a cell-bound extended mucin-like stalk and fractalkine itself functions as an adhesion molecule,[10,15,11] thereby obviating the need for both the association with proteoglycans and other adhesion molecules. Indeed, CX3CR1-expressing cells bind rapidly and with high affinity to immobilized fractalkine or fractalkine-expressing cells in both static and physiologic flow conditions.[11,12,28] Video microscopy revealed that CX3CR1-expressing cells adhere more rapidly to immobilized fractalkine than to vascular cell adhesion molecule-1 (VCAM-1) without cell tethering and dislodging in flow conditions.[29] Thus, fractalkine may facilitate extravasation of circulating leukocytes by mediating cell adhesion through the initial tethering and the final transmigration steps (Fig. 3).[13] In addition, we found that engagement of both CX3CR1 and integrins through co-expression of fractalkine and integrin ligands, such as intercellular adhesion molecule-1 (ICAM-1) and VCAM-1, results in greatly enhanced cell adhesion compared with each system alone.[13,18]

Cytotoxic function

Natural killer (NK) cells, which express cytolytic activity without known prior antigenic stimulation, are thought to mediate immunity against viruses and surveillance for protection against neoplastic transformation.[30] NK cells are stimulated through NK activating receptors such as CD2, CD16 and NKG2D, and can mediate target cell lysis through several pathways including exocytosis of granules containing lytic mediators, such as perforin and granzymes, and CD95(Fas)–CD95L(FasL) interaction.[31,32]

Almost all NK cells express CX3CR1,[11,33] suggesting that they are important effectors of the biological functions of

fractalkine, i.e., chemotaxis and cellular activation. Certainly, soluble fractalkine can induce NK cell transmigration[11] and enhance granule exocytosis and cytolytic function of NK cells.[33] In addition, fractalkine-expressing ECV304 cells or HUVECs showed increased interaction with NK cells and susceptibility to NK cell-mediated cytolysis, indicating that fractalkine on ECs actually functions as a triggering molecule for NK cell activation.[33]

Similar to NK cells, CX3CR1-expressing $CD8^+$ and $CD4^+$ T cells, but not those without surface CX3CR1, showed terminally differentiated effector phenotypes with cytotoxic granules. We found that $CD8^+$ T cells sorted into CX3CR1-positive population indeed possess much greater cytotoxic activity than presorted or CX3CR1-negative $CD8^+$ T cells by CD3 monoclonal antibody-mediated redirected cytotoxicity assay.[26] These findings suggest that the expression of fractalkine at the site of inflammation can attract and activate NK cells through CX3CR1, and that NK cells, once activated under such conditions, can lyse neighboring ECs despite MHC class I expression.[13,33]

Roles in inflammation

Nishimura et al. have reported that transmigration of $CD8^+$ T cells ($CX3CR1^+/CCR5^+$) and NK cells ($CX3CR1^+/CXCR1^+$) to secondary chemokines, macrophage inflammatory protein (MIP)-1β or IL-8, was significantly increased in the presence of membrane-bound fractalkine.[26] Thus, fractalkine expressed on inflamed endothelium may play a role as vascular gateway for cytotoxic effector cells (CX3CR1-expressing cells) by rapidly capturing them from the blood, and by promoting their migration into tissue, where Th1 polarization may be occurring through IFN-γ production.

NK cells are important in innate immunity through production of cytokines, including IFN-γ, TNF-α, granulocyte-macrophage colony-stimulating factor (GM-CSF), IL-3, IL-5, IL-10, and IL-15.[34] Interferon-γ, produced by NK cells and γδ T cells as well as Th1 cells, has also been shown to be Th1 cell polarization.[35,36] Recently, Yoneda et al. reported that stimulation of NK cells with immobilized fractalkine, but not with soluble fractalkine, or coculture of NK cells with fractalkine-expressing cells, markedly induced IFN-γ production,[37] suggesting a role for fractalkine expressed on ECs in developing Th1 responses.[13,14] Interferon-γ also enhances expression of fractalkine on ECs,[10,11] indicating existence of a paracrine feedback loop system in which ECs may be activated to produce more fractalkine (Fig. 4).[14]

Fractalkine in rheumatoid arthritis and allied conditions

Inflammation is caused by proinflammatory cytokines produced by activated immune-potent cells. Inflammatory cytokines, such as TNF-α and IFN-γ, increase expression of adhesion molecules and production of chemokines including fractalkine, leading to leukocyte transmigration into tissues. Therefore, inappropriately elevated expression of inflammatory chemokines may result in extensive tissue damage and/or chronic inflammation. Since fractalkine promotes cell transmigration and activates CX3CR1-positive cells to produce IFN-γ, it is likely that fractalkine is involved in the immunopathogenesis of autoimmune diseases through chronic inflammation.[13,14]

Rheumatoid arthritis

Recently, several papers indicate that fractalkine may be involved in pathogenesis of rheumatoid arthritis. Ruth et al. have reported that increased expression of fractalkine and CX3CR1 on synovial tissue macrophages, fibroblasts, endothelial cells and dendritic cells in rheumatoid arthritis (RA) patients as well as in an adjuvant-induced arthritis model in rats.[38,39] Furthermore, they observed that expression of fractalkine on $CD14^+$ monocytes and CX3CR1 on $CD3^+$ T cells in synovial fluids correlated positively with morning stiffness and swollen joint count, respectively.[39] Nanki et al. have reported that CX3CR1 expression on $CD4^+$ and $CD8^+$ T cells was up-regulated in RA patients and that these T cells in RA patients produced IFN-γ and TNF-α.[40] Similar results have been reported by Sawai et al., namely that fractalkine expression on fibroblast-like synoviocytes co-stimulated T-cell-activating signals and amplified proliferation and IFN-γ production.[41] Volin et al. have reported that fractalkine in synovial fluid from RA patients promotes angiogenic activity in vitro.[42] It has been reported that antifractalkine monoclonal antibody ameliorates arthritis by inhibiting infiltration of inflammatory cells into the synovium in collagen-induced arthritis mouse model.[43]

Systemic lupus erythematosus

Systemic lupus erythematosus (SLE) is an autoimmune disease characterized by multiorgan damage with infiltration and sequestration of various immune potent cells. A variety of diffuse and focal neuropsychiatric symptoms often occur in SLE patients. Originally, fractalkine has been reported as neurotactin to be expressed in brain inflammation.[15] Yajima et al. have reported that serum fractalkine levels were significantly elevated in patients with SLE than in healthy controls and correlated well with the SLE damage index, titers of anti-DNA and anti-Sm antibodies, immune complex, and serum complement levels.[44] They also reported that fractalkine levels were significantly higher in cerebrospinal fluid from SLE patients with neuropsychiatric involvement that those without involvement.

Autoimmune diseases in MRL/lpr mice resemble human SLE and are characterized by the dysregulation of both cellular and humoral immunity. MRL/lpr mice spontaneously develop lethal glomerulonephritis in association with an increase in circulating immune complexes, autoantibody production, and abnormalities of cytokines and chemokines. There are a number of reports suggesting a

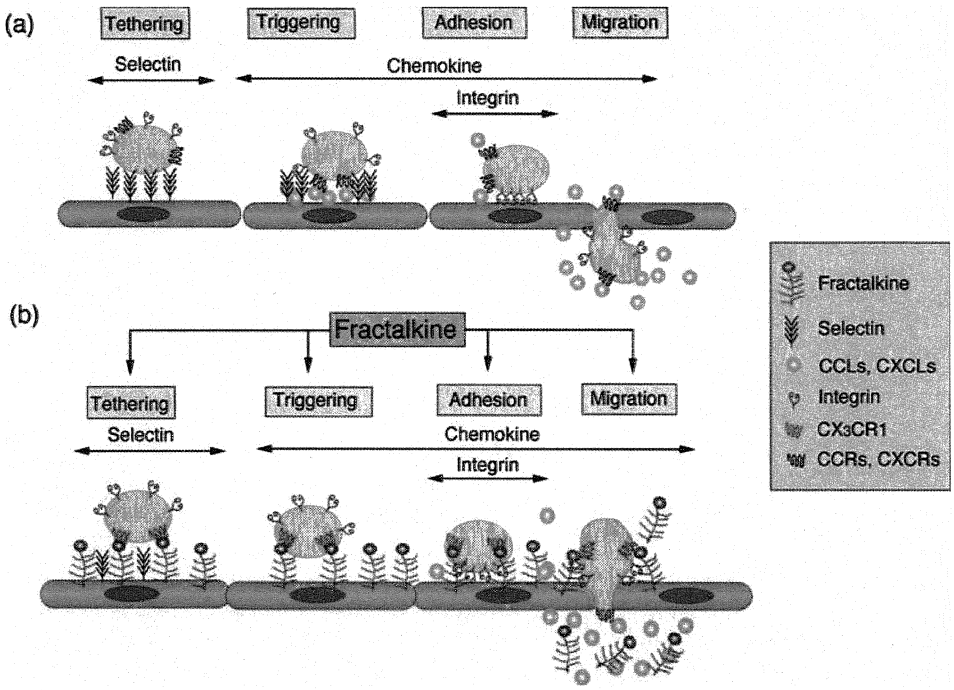

Fig. 3a,b. Schematic model of classical and fractalkine-mediated pathways in the adhesion cascade.[13,14] Leukocyte migration from the circulation into the peripheral tissue is a stepwise process. **a** The classical pathway. The first step involves transient, weak, selectin-mediated binding (*Tethering*). Next, integrins on leukocytes are activated by chemokines that have been presented on glycosaminoglycans (*Triggering*), resulting in firm adhesion between leukocytes and endothelial cells (*Adhesion*). Finally, leukocytes migrate through the endothelial layer in response to a chemokine gradient (*Migration*). **b** Fractalkine-mediated pathway. Fractalkine is expressed on endothelial cells as the membrane-bound form and captures leukocytes in a selectin- and integrin-independent manner. Interaction between fractalkine and CX3CR1 can also increase integrin avidity, resulting in firmer adhesion. Leukocytes then extravasate through the vascular wall and into the tissue to a chemokine gradient. Fractalkine may facilitate extravasation of circulating leukocytes by mediating cell adhesion through the initial tethering and the final transmigration steps

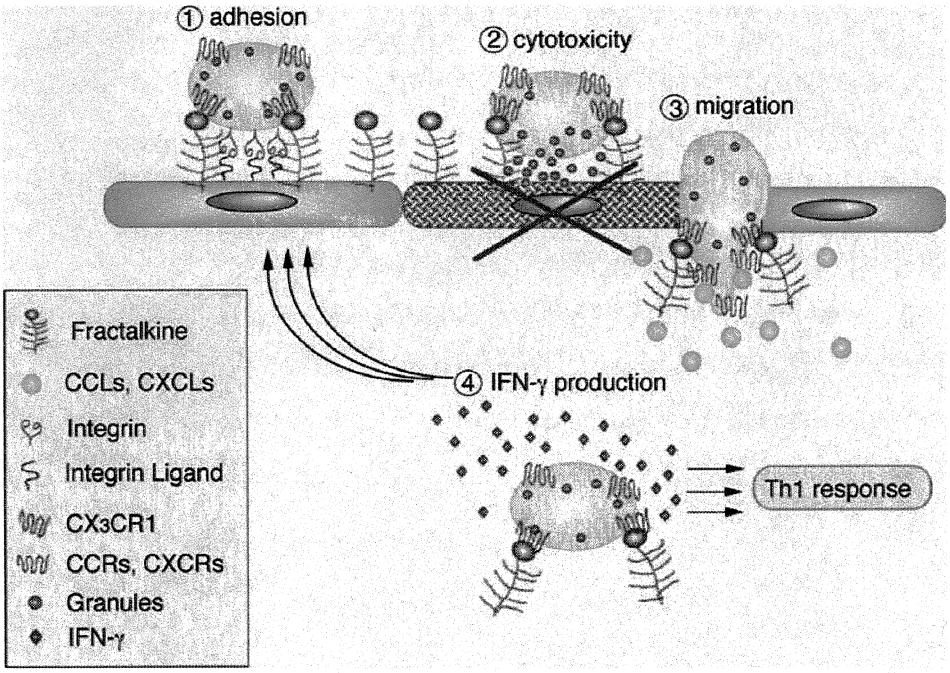

Fig. 4. Biological functions of fractalkine.[14] *1*, Engagement of CX3CR1 and integrins through coexpression of fractalkine and integrin ligands results in firm adhesion. *2*, CX3CR1-expressing cytotoxic effector cells including NK cells, $CD8^+$ T cells and γδ T cells containing cytoplasmic granules. When these cells are activated by membrane-bound fractalkine or activating receptors, they may damage neighboring endothelial cells. *3*, Membrane-bound fractalkine enhanced the effect of other chemokines on migration of CX3CR1-expressing cells into tissue. *4*, Transmigrated CX3CR1-expressing cells, activated by fractalkine, produce interferon-gamma (*IFN-γ*), leading to Th1 response. IFN-γ also enhances expression of fractalkine on endothelial cells, indicating a paracrine feedback loop system

role for fractalkine in human renal diseases (glomerulonephritis, renal tumor, and renal transplants) and in kidney disease in animal models. For example, viral chemokine similar to macrophage inflammatory protein II (vMIP-II), with antagonistic activity for CC-, CXC- and CX3C-chemokine receptors, reduced the infiltration of leukocytes significantly and attenuated proteinuria in the rat crescent glomerulonephritis model.[45] Feng et al. have reported that anti-CX3CR1 antibody treatment dramatically blocked leukocyte infiltration into the glomeruli, prevented crescent formation, and improved renal function.[46] In SLE model mice, Inoue et al. have reported that fractalkine antagonist (fractalkine analogs truncated by >4 amino acid residues from N-terminus) significantly reduced glomerular hypercellularity, glomerulosclerosis, crescent formation, and vasculitis compared with control mice.[47]

Systemic sclerosis

Systemic sclerosis (SSc) is an autoimmune disease with disorders of connective tissue characterized by excessive fibrosis and vascular abnormality in the skin and internal organs. Perivascular cellular infiltration is often observed in affected lesions, and may promote endothelial damage and fibrosis through the production of soluble mediators in patients with SSc. Hasegawa et al. have reported that expression of CX3CR1 on monocytes and T cells were increased in lesions of skin and lungs, and that levels of soluble fractalkine in SSc patients were higher than controls and correlated well with erythrocyte sedimentation rates, digital ischemia, and severity of pulmonary fibrosis.[48]

Myositis

Idiopathic inflammatory myopathy such as polymyositis or dermatomyositis is characterized by chronic inflammation of the voluntary muscles associated with infiltration of immune competent cells, including $CD4^+$ and $CD8^+$ T cells and monocytes, in the skeletal muscle. Infiltrated T cells express cytotoxic molecules, such as granzyme and perforin, and produce TNF-α and IFN-γ. Nanki et al. have reported fractalkine expression on mononuclear cells and endothelial cells, and CX3CR1 expression on the infiltrated $CD4^+$ and $CD8^+$ T cells in an experimental autoimmune myositis mouse model. They also reported that treatment of experimental mice with antifractalkine monoclonal antibody significantly reduced the histopathological myositis score, and infiltration of $CD4^+$ and $CD8^+$ T cells and macrophages.[49]

Pulmonary arterial hypertension

Pulmonary arterial hypertension (PAH) is a common complication of systemic inflammatory conditions, such as SLE and SSc, leading to progressive right heart failure and ultimately death. This disease results from chronic obstruction of small pulmonary arteries through endothelial and vascular smooth muscle cell dysfunction accompanied by infiltration of T and B lymphocytes and macrophages. Balabanian et al. have reported that CX3CR1 expression and function are upregulated in circulating T lymphocytes, mostly of the $CD4^+$ T cells, and soluble fractalkine concentrations are elevated in patients with PAH. They also reported that fractalkine mRNA and protein product are expressed in pulmonary artery endothelial cells.[50,51]

Conclusions

The unique chemokine, fractalkine, can fulfill the dual functions of an adhesion molecule and a chemoattractant. Fractalkine is expressed on activated ECs, and functions as a vascular gateway by attracting CX3CR1-expressing NK cells, CTLs, and macrophages with immediate cytolytic function. Inappropriate expression or function of fractalkine might well be involved in inflammatory conditions leading to vascular and tissue damage. Taken together, fractalkine may be expressed in many tissues and be involved in the accumulation of CX3CR1-positive T cells at inflammation sites in rheumatoid arthritis and allied conditions.

Acknowledgments. This work was supported by grants 13557160, 15024236, 15390313, 13877075, 15024236, 15390313 from the Japanese Ministry of Education and Science and Culture (to H.U.), Uehara Memorial Foundation (to H.U.), and the Kanazawa Medical University Research Foundation (to H.U.). J.Z.-X. was supported by JSPS Grant-in-Aid research funds and the Uehara Memorial Foundation.

References

1. Luscinskas FW, Gimbrone MA. Endothelial-dependent mechanisms in chronic inflammatory leukocyte recruitment. Annu Rev Med 1996;47:413–21.
2. Cines DB, Pollak ES, Buck CA, Loscalzo J, Zimmerman GA, McEver RP, et al. Endothelial cells in physiology and in the pathophysiology of vascular disorders. Blood 1998;91:3527–61.
3. Montovani A, Bussolino F, Introna M. Cytokine regulation of endothelial cell function: from molecular level to the bedside. Immunol Today 1997;18:231–40.
4. Taub DD, Oppenheim JJ. Chemokines, inflammation and the immune system. Ther Immunol 1994;1:229–46.
5. Rollins BJ. Chemokines. Blood 1997;90:909–28.
6. Baggiolini M, Dewald B, Moser B. Interleukin-8 and related chemokines-CXC and CC chemokines. Adv Immunol 1994;55:97–179.
7. Murphy PM. The molecular biology of leukocyte chemoattractant receptors. Annu Rev Immunol 1994;12:593–633.
8. Gerard C, Rollins BJ. Chemokine and disease. Nat Immunol 2001;2:108–15.
9. Proudfoot AEI. Chemokine receptors: Multifaceted therapeutic targets. Nat Rev Immunol 2002;2:106–15.
10. Bazan JF, Bacon KB, Hardiman G, Wang W, Soo K, Ross D, et al. A new class of membrane-bound chemokine with a CX3C motif. Nature 1997;385:640–4.
11. Imai T, Hieshima K, Haskell C, Baba M, Nagira M, Nishimura M, et al. Identification and molecular characterization of Fractalkine receptor CX3CR1, which mediates both leukocyte migration and adhesion. Cell 1997;91:521–30.

12. Goda S, Imai T, Yoshie O, Yoneda O, Inoue H, Nagano Y, et al. CX3C-chemokine, fractalkine enhanced adhesion of THP-1 cells to endothelial cells through integrin-dependent and independent mechanisms. J Immunol 2000;164:4313–20.
13. Umehara H, Bloom ET, Okazaki T, Domae N, Imai T. Fractalkine and vascular injury. Trends Immunol 2001;22:602–7.
14. Umehara H, Bloom ET, Okazaki T, Yoshie O, Imai T. Fractalkine and vascular biology: from basic research to clinical diseases (Review). Arterioscler Thromb Vasc Biol 2004;24:34–40.
15. Pan Y, Lioyd C, Zhou H, Dolich S, Deeds J, Gonzalo J-A, et al. Neurotactin, a membrane-anchored chemokine upregulated in brain inflammation. Nature 1997;387:611–7.
16. Fong AM, Erickson HP, Zachariah JP, Poon S, Schamberg NJ, Imai T, et al. Ultrastructure and function of the fractalkine mucin domain in CX3C chemokine domain presentation. J Biol Chem 2000;275:3781–6.
17. Haskell CA, Cleary MD, Charo IF. Unique role of the chemokine domain of fractalkine in cell capture. J Biol Chem 2000;275:34183–9.
18. Umehara H, Goda S, Imai T, Nagano Y, Minami Y, Tanaka Y, et al. Fractalkine, a CX3C-chemokine, functions predominantly as an adhesion molecule in monocytic cell line THP-1. Immunol Cell Biol 2001;79:298–302.
19. Kourilsky P, Truffa-Bachi P. Cytokine fields and the polarization of the immune response. Trends Immunol 2001;22:502–9.
20. Rhodes SG, Graham SP. Is 'timing' important for cytokine polarization? Trends Immunol 2002;23:246–9.
21. Yoshie O, Imai T, Nomiyama H. Related article chemokines in immunity. Adv Immunol 2001;78:57–110.
22. Sallusto F, Mackay CR, Lanzavecchia A. The role of chemokine receptors in primary, effector, and memory immune responses. Annu Rev Immunol 2000;18:593–620.
23. Shresta S, Pham CT, Thomas DA, Grauber TA, Ley TJ. How do cytotoxic lymphocytes kill their targets? Curr Opin Immunol 1998;10:581–7.
24. Hamann D, Roos MTL, van Lier RAW. Face and phases of human $CD8^+$ T-cell development. Immunol Today 1999;20:177–80.
25. Tomiyama H, Matsuda T, Takiguchi M. Differentiation of human CD8+ T cells from a memory to memory/effector phenotype. J Immunol 2002;168:5538–50.
26. Nishimura M, Umehara H, Nakayama T, Yoneda O, Hieshima K, Kakizaki M, et al. Dual functions of fractalkine/CX3CR1 in trafficking of circulating cytotoxic effector lymphocytes that are defined by CX3CR1 expression. J Immunol 2002;168:6173–80.
27. Tanaka Y, Adams DH, Hubscher S, Hirano H, Siebenlist U, Shaw S. T-cell adhesion induced by proteoglycan-immobilized cytokine MIP-1β. Nature 1993;361:79–82.
28. Fong AM, Robinson LA, Steeber DA, Tedder TF, Yoshie O, Imai T, et al. Fractalkine and CX3CR1 mediate a novel mechanism of leukocyte capture, firm adhesion, and activation under physiologic flow. J Exp Med 1998;188:1413–9.
29. Haskell CA, Cleary MD, Charo IF. Molecular uncoupling of fractalkine-mediated cell adhesion and signal transduction. Rapid flow arrest of CX3CR1-expressing cells is independent of G-protein activation. J Biol Chem 1999;274:10053–8.
30. Moretta L, Ciccone E, Mingari MC, Biassoni R, Moretta A. Human natural killer cells: Origin, clonality, specificity, and receptors. Adv Immunol 1993;55:341–80.
31. Umehara H, Huang J-Y, Kono T, Tabassam FH, Okazaki T, Bloom ET, et al. Involvement of protein tyrosine kinase $p72^{syk}$ and phosphatidylinositol 3-kinase in CD2-mediated granular exocytosis in natural killer cell line. J Immunol 1997;159:1200–7.
32. Lanier LL. On guard-activating NK cell receptors. Nat Immunol 2001;2:23–7.
33. Yoneda O, Imai T, Gouda S, Inoue H, Yamauchi A, Okazaki T, et al. NK cell-mediated vascular injury. J Immunol 2000;164:4055–62.
34. Seaman WE. Natural killer cells and natural killer T cells. Arthritis Rheum 2000;43:1204–17.
35. Rengarajan J, Szabo SJ, Glimcher LH. Transcriptional regulation of Th1/Th2 polarization. Immunol Today 2000;21:479–83.
36. Murphy KM, Reiner SL. The lineage decisions of helper T cells. Nat Rev Immunol 2002;2:933–44.
37. Yoneda O, Imai T, Inoue H, Nishimura M, Minami Y, Bloom ET, et al. Membrane bound form of fractalkine induces IFN-γ production by NK cells: a role for Th1 response. Eur J Immunol 2003;33:53–8.
38. Ruth JH, Rottman JB, Katschke KJ Jr, Qin S, Wu L, LaRosa G, et al. Selective lymphocytes chemokine receptor expression in the rheumatoid joint. Arthritis Rheum 2001;44:2750–60.
39. Ruth JH, Volin MV, Haines III GK, Woodruff DC, Katschke Jr KJ, Woods JM, et al. Fractalkine, a novel chemokine in rheumatoid arthritis and in rat adjuvant-induced arthritis. Arthritis Rheum. 2001;44:1568–81.
40. Nanki T, Imai T, Nagasaka K, Urasaki Y, Nonomura Y, Taniguchi K, et al. Migration of CX3CR1-positive T cells producing type 1 cytokines and cytotoxic molecules into synovium of patients with rheumatoid arthritis. Arthritis Rheum 2002;46:2878–83.
41. Sawai H, Park YW, Roberson J, Imai T, Goronzy JJ, Weyand CM. T cell costimulation by fractalkine-expressing synoviocytes in rheumatoid arthritis. Arthritis Rheum 2005;52:1392–401.
42. Volin MV, Woods JM, Amin MA, Connors MA, Harlow LA, Koch AE. Fractalkine: a novel angiogenic chemokine in rheumatoid arthritis. Am J Pathol 2001;159:1521–30.
43. Nanki T, Urasaki Y, Imai T, Nishimura M, Muramoto K, Kubota T, et al. Inhibition of fractalkine ameliorates murine collagen-induced arthritis. J Immunol 2004;173:7010–6.
44. Yajima N, Kasama T, Isozaki T, Odai T, Matsunawa M, Negishi M, et al. Elevated levels of soluble fractalkine in active systemic lupus erythematosus. Arthritis Rheum 2005;52:1670–5.
45. Chen S, Bacon KB, Li L, Garcia GE, Xia Y, Lo D, et al. In vivo inhibition of CC and CX3C chemokine-induced leukocyte infiltration and attenuation of glomerulonephritis in Wistar-Kyoto (WKY) rats by vMIP-II. J Exp Med 1998;188:193–8.
46. Feng L, Chen S, Garcia GE, Xia Y, Siani MA, Botti P, et al. Prevention of crescent glomerulonephritis by immunoneutralization of the fractalkine receptor CX3CR1. Kidney Int 1999;56:612–20.
47. Inoue A, Hasegawa H, Kohno M, Ito MR, Terada M, Imai T, et al. Antagonist of fractalkine (CX3CL1) delays the inhibition and ameliorates the progression of lupus nephritis in MRL/lpr mice. Arthritis Rheum 2005;52:1522–33.
48. Hasegawa M, Sato S, Echigo T, Ysui M, Takehara K. Up regulated expression of fractalkine/CX3CL1 and CX3CR1 in patients with systemic sclerosis. Ann Rheum Dis 2005;64:21–8.
49. Suzuki F, Nanki T, Imai T, Kikuchi H, Hirohata S, Kohsaka H, et al. Inhibition of CX3CL1 (fractalkine) improves experimental autoimmune myositis in SJL/J mice. J Immunol 2005;175:6987–96.
50. Balabanian K, Foussat A, Dormuller P, Durand-Gasselin I, Capel F, Bouchet-Delbos L, et al. CX3C chemokine fractalkine in pulmonary arterial hypertension. Am J Respir Crit Care Med 2002;165:1419–25.
51. Dorfmuller P, Perros F, Balabanian K, Humbert M. Inflammation in pulmonary arterial hypertension. Eur Respir J 2003;22:358–63.

１．研究課題名：分子生物学的手法による顎関節症の発症メカニズム解明と新規治療法開発
（研究番号　C2006-2）

２．キーワード：１）顎関節症（Temporomandibular joint disorders）
２）発症メカニズム（Pathogenesis）
３）生化学的解析（Biochemical analysis）
４）遺伝子学的解析（Genetic analysis）

３．研究代表者：瀬上　夏樹・医学部・教　授・顎口腔機能病態学　（口腔科学）
研究分担者：金山　景錫・医学部・講　師・顎口腔機能病態学　（口腔科学）
高橋　　克・京都大学・医学部・講　師・感覚運動系外科学講座口腔外科学分野
佐藤　　淳・北海道大学・歯学部・助　手・口腔病態学
出村　　昇・医学部・講　師・顎口腔機能病態学　（口腔科学）

４．研 究 目 的

近年、世界的規模で高齢化社会への移行が進んでおり、我国でも高齢化社会への移行につれてリウマチや変形性関節症などの老人性疾患の急増が社会的問題になりつつある。歯科領域でもウ蝕・歯周病と並んで三大疾患にあげられる変形性関節症に属する顎関節症は臨床的に関節疼痛と開口障害など日常生活に多大な影響を及ぼすことから、この疾患の発症機構の解明と治療薬の開発が社会的に強く要望されている。われわれもこれまで顎関節症における臨床的・基礎的研究によりその主病態が滑膜炎であることを明らかにするとともに、サイトカインや発痛物質がその病態に関与して関節疼痛と機能障害に関連していることを世界に先駆けて報告してきた。他方、昨今では遺伝子レベルでの病態解明と治療が非常に注目されているが、顎関節症においてはいまだ未開拓の分野となっている。今研究では遺伝子に着眼し、これまでの成果をさらに推し進め、世界に先駆けて遺伝子レベルで顎関節症の発症メカニズムを明らかにし、あわせて遺伝子組み換えなどによる抗サイトカイン療法など新規治療法の開発を行うことを目的とした。

５．研 究 計 画

（基礎的検討）①現在我々が開発中の顎関節症の動物モデル（ウサギ）に対して、ター ゲットとするサイトカインおよび受容体の抗体を注入し、経時的な病理組織学的効果を判定して、サイトカイン療法の臨床応用の発展への可能性を模索する。②ヒトおよびウサギの滑膜細胞の培養細胞株を樹立して、ター ゲットとする抗体の遺伝子のベクター を導入する。③ウサギの顎関節症モデルの顎関節部に同培養細胞を注入して病理組織学効果を判定して、遺伝子治療の臨床応用の可能性を検索する。④正常ウサギにおける薬剤による関節構造への影響を経時的に評価して、合併症の可能性への配慮を行う。

（臨床的検討）①顎関節症患者の滑膜組織中における炎症性サイトカインおよびその受容体のタンパク、mRNA の局在を組織学的、組織化学的染色手法により同定する。②患者の滑液中ならびに滑膜組織中の発痛物質（Bradykinin など）の定量的評価を行い、サイトカインとの関連を検討する。③顎関節症患者のなかで、通常の治療法で関節疼痛のコントロールが困難な症例を選択し、抗サイトカイン製剤（ヒト型の抗 TNF-α抗体、抗 IL-6 受容体抗体など）の関節腔内への局所注入を開始する。この際には、術前の患者管理、インフォームドコンセントの確立、術後の症状、画像所見の変化を記録すべくプロトコールを作製のうえ慎重に臨床応用する。

なお、臨床検体ならびに動物実験におけるゲノム解析、遺伝子検索に際しては、本学の倫理委員会における申請と承認を受けることが前提となる。

６．研 究 成 果

顎関節症、とくに最も発症頻度の高い顎関節症 III 型（顎関節内障）のより詳細な病態を明らかにするために以下の臨床的基礎的研究を遂行した。

（1）55 例の顎関節症患者と 5 名の無症状対照者の上関節腔から滑液を希釈採取して TNF-α、IL-6、IL-1β、可溶性 TNF-α receptor-1 および-II（sTNFR-I、sTNFR-II）、IL-6 可溶性 receptor（IL-6sR）、IL-1 可溶性 receptor II、IL-1 拮抗 receptor を ELISA 法で測定した。この結果、患者群の TNF-α、IL-6、IL-1β、sTNFR-I、sTNFR-II、IL-6sR 濃度が対照群よりも有意に高値であった [1]。これらのサイトカインならびに receptor は滑膜炎の up-regulate に作用し顎関節内障の発症過程で重要な役割を担うことが示された。

（2）家兎６羽６顎関節に対してスプリングを用いた外力を４週間負荷して作成した顎関節炎において、滑液を採取し総蛋白量を測定後、蛋白２μｇを SDS-PAGE に用いた。電気泳動で分離した各蛋白バンドをデンシトメトリック解析し、その強度を総バンド量に対する割合として数量化した。この結果、負荷群では非負荷群に比べて蛋白濃度が有為に高値を示した（1824μg vs. 398μg）。さらに泳動解析で負荷群では 140kd 以上のバンドが多く検出された [2]。外力付加による顎関節症モデルにおいても同様に患者と類似して滑液蛋白量は増加することが解明され、今後、本モデルを応用した病態解明および薬剤など新規治療法の開発に有用と考えられる。

（3）54 関節 54 例の顎関節内障患者と 8 例 10 関節の習慣性顎関節脱臼患者（対照群）について上腔鏡視下に滑膜組織をパンチ生検し Substance-P（SP）の免疫組織化学的染色を施行して両群を比較検討した。この結果、陽性細胞は滑膜表層細胞付近の血管内皮細胞に主に認められたが、患者群（陽性率 87%）では対照群（陽性 5/10 関節）よりも有意に陽性細胞数が多く認められた（P=.002）。しかしながら陽性細胞率と関節疼痛度あるいは鏡視下滑膜炎 score との関連はみられなかった [3]。以上より、SP は顎関節内障の病態形成に深く関与し、とくに疼痛発現との関連が示唆されるが、今後症例を追加して詳細な検討が必要と考えられる。

（4）46 関節 44 例の顎関節内障患者と 8 例 10 関節の習慣性顎関節脱臼患者（対照群）について上腔鏡視下に滑膜組織をパンチ生検し Interleukin-8（IL-8）の免疫組織化学的染色を施行して両群を比較検討した。この結果、陽性細胞は滑膜表層細胞付近の血管組織に主に認められたが、患者群（陽性率 80%）では対照群（陽性 2/10 関節）よりも有意に陽性細胞数が多く認められた（P=.004）。しかしながら陽性率と臨床所見との関連は明らかでなかった [4]。以上より、IL-8 は円板後方滑膜における炎症性変化を二次的に up-regulate し、病態形成に深く関与する可能性が示された。

（5）MR 画像において関節円板転位がなく正常円板位を示した 14 例 14 関節の顎関節内障クローズドロック症例についてその病態を検討した。全体の平均ロック期間は３か月で、その他、平均開口量は 28mm（15-32mm）、自覚的疼痛度（0-10）は平均 5（2-10）であった。全例で関節洗浄療法を施行したが、その際得られた上腔よりの滑液解析（9 関節）では平均蛋白量は 343μg/ml（36-791）と以前に行った非復位性転位を伴う同症例に比して低値を呈した。関節洗浄療法が無効であった５例に対しては関節鏡視下剥離授動術を施行したが、その際の鏡視下所見の定量的評価（0-10 点）では、滑膜炎が平均６点（2-7）、線維性癒着が平均７点（6-8）と通常のクローズドロック例と同等であった [5]。以上の検討により、典型的所見とされる関節円板前方転位を伴わないクローズドロック例が存在し典型例と類似した症状と病態を示すこと、また通法による治療法でコントロール可能なことが明らかとされた。

（6）一次治療として関節腔洗浄療法を施行した66例66関節の顎関節内障クローズドロック症例について、その際に希釈回収した上腔滑液の発痛物質すなわち Bradykinin (BK)、Leukotrien B4 (LTB4)、Prostaglandin E2 (PGE2)、Substance P (SP)について奏効群(51関節)と非奏効群(15関節)の両群で比較した。この結果、LTB4 の検出率は奏効群(47%)が非奏効群(16%)よりも有意に高かった(P<.05)。またBK の平均濃度は奏効群(425pg/ml)が非奏効群(144pg/ml)よりも有意に高値を示した(P<.0005)。さらにLTB4 とPGB4 の相互検出率は有意であった(P<.01) [6]。以上の結果により、本症の罹患関節では発痛物質の活性がup-regulate され治療奏効度に関与することを明らかにした。

（7）26例の顎関節症患者（顎関節内障16例、変形性顎関節症10例）および対照群：(無症候者7名)の上関節腔滑液を希釈回収して総蛋白量を測定後、蛋白２μｇをSDS-PAGE に用いた。電気泳動で分離した各蛋白バンドをデンシトメトリック解析し、その強度を総バンド量に対する割合として数量化した。この結果、滑液中の平均総蛋白量は患者群（変形性顎関節症：2485μg、顎関節内障：1353μg）が対照群（615μg）より有為に高値を示した。電気泳動解析では、22 種の分子量の異なる糖鎖バンド（14ー700kd）が検出されたが、患者群では140kd より大きな分子量の糖鎖が多く検出された [7]。以上より、罹病顎関節では炎症性変化の波及に伴い滑液蛋白の変化が惹起されることが明らかとなった。(本研究期間の掲載論文であるが謝辞記載欠落のため参考文献)

（8）30 例の顎関節内障患者について上腔鏡視下に滑膜組織をパンチ生検し receptor activator of nuclear factor-kappaB ligand (RANKL)の免疫組織化学的染色を施行し、陽性所見を定量評点化した鏡視所見（滑膜炎、癒着、退行変性：0-10 点）と対比検討した。この結果、陽性細胞は滑膜表層細胞、血管内皮細胞、線維芽細胞の細胞質に主に認められた。しかしながら陽性率と各鏡視所見との有意な相関は認めなかった [8]。蛋白成分であるRANKL は滑液中にも認められるが、関節包内でup-regulate したRANKL の産生細胞を特定するには至らなかった。

（9）27例28関節の顎関節症（IIIb型21関節、IV型7関節）から上腔穿刺により無菌的に採取した希釈滑液で、習慣性顎関節脱臼５例を対照とした。方法は、滑液からの抽出 DNA について 16S rRNA のPCR 増幅によるクローニング解析により細菌の塩基配列を同定した。この際には既に報告されているUniversal bacterial primer を用いた。得られた細菌情報は臨床所見、MR 画像所見と対比した。この結果、顎関節症群の 19 関節(68%)で以下の 11 種の細菌が検出された。*Granulicatella adiacen*(6検体)、*Pseudomonas sp.* (6検体)、*Methylobacterium sp.* (5検体)、*Beta proteobacterium* (4検体) *Acidovorax sp.*, *Bradyrhizobium sp.*, *Sphingomonas Streptococcus*, *Leptothrix sp. oral clone* (各２検体), *Thiobacillus denitrificans*, *Comamonadaceae bacterium* (各 1 検体) で 8 検体からは２ー４種の細菌が同定された。症型別検出率は、IIIb 型 57%、IV 型 100%であり、対照群では検出されなかった。また *Granulicatella abiacen* および複数菌種は45歳以上の高齢患者で認められる傾向があった。さらに滑液中平均蛋白濃度は、細菌陽性群(2.75±1.39 mg/ml)が陰性群(1.34±1.40 mg/ml)よりも有意に高値を示した [9]。以上より、これまでに本症で報告された１菌種（*Streptococcus*)ならびに未報告菌種であるが、顎関節症の局所での細菌存在がより明らかとなり、炎症反応の増幅に貢献する可能性がある。今後、細菌が顎関節症の病態形成に関わる役割の詳細についてはさらに検討が必要と考えられる。

７．研究の考察・反省

以上の当該研究期間に得られた結果ならびにこれまで当講座で報告した結果から、顎関節症 III 型（顎関節内障クローズドロック）では、関節円板の非復位性前方転位の発現に伴って開口障害と関節運動痛が出現するが、この際に関節内でみられる病的所見は滑膜炎、線維性癒着が主体である。

しかしながら滑膜炎の程度は組織学的には比較的経度であり、むしろ活性化された炎症性サイトカイン、発痛物質の up-regulation が顕著に認められたことから疼痛症状の大きな要因と考えられる。これらの種々の関節マーカーの活性化に伴う滑液中蛋白の増加が併せて特徴であるが、その発生起源は滑膜表層付近の血管内皮細胞であり円板の位置異常と機械的負荷に伴って増生した血管が反応性に炎症発現に貢献するものと考えられる。また、退行変性を伴う顎関節症 IV 型でみられる骨軟骨変形に関して、破骨細胞活性化因子である RANKL を組織学的に検討したが、内視鏡的に定量評価された各病態と相関は得られず、今後視点を変えた検討が必要とされた。一方、III 型、IV 型における滑液中の細菌存在に関する PCR 法による遺伝子学的検討では、68%で細菌陽性を呈し一部病態と関連することが示された。この結果は国際的にも新知見として評価されるべきもので、今後追試やさらなる検討など新しい展開へ門戸を開いたものといえる。

反省点として、

1）市販キットなどを応用した主な関節マーカーの濃度測定あるいは免疫組織化学的染色は比較的容易に遂行できたが、滑液の微小蛋白の解析が困難であり、より詳細な病因解明として今後の課題である。

2）臨床検体ならびに動物実験におけるゲノム解析、遺伝子検索について倫理委員会の承認は得られたが、とくに骨変形に関する遺伝子解析の遂行が遅れ結果が未だ得られていない。本検討について継続して行う必要がある。

3）関節内のマーカーの活性上昇の結果をもとに、とくに新たな薬剤治療法の開発が急務である。

4）関節構成体の退行変性のメカニズムに関わる検討が遅延傾向であり、さらに細菌学的検討の必要性が生じた。

８．研 究 発 表

1. Kaneyama K, Segami N, Sato J, Yoshimura H, Nishiura R.: Expression of receptor activator of nuclear factor-kappaB ligand in synovial tissue: comparison with degradation of articular cartilage in temporomandibular joint disorders. Oral Surg Oral Med Oral Pathol Oral Radiol Endod. 2007; 104(2): e12-17. (MLDB)
2. Sun W, Dong L, Kaneyama K, Takegami T, Segami N.: Bacterial diversity in synovial fluids of patients with TMD determined by cloning sequencing analysis of the 16S ribosomal RNA gene. Oral Surg Oral Med Oral Pathol Oral Radiol Endod. 2008; 105(5): 566-571. (MLDB)

Expression of receptor activator of nuclear factor-κb ligand in synovial tissue: Comparison with degradation of articular cartilage in temporomandibular joint disorders

Keiseki Kaneyama, DDS, PhD,[a] Natsuki Segami, DDS, PhD,[b] Jun Sato, DDS, PhD,[c] Hiroshi Yoshimura, DDS, PhD,[d] and Rie Nishiura, DDS,[e] Ishikawa and Hokkaido, Japan
KANAZAWA MEDICAL UNIVERSITY AND HOKKAIDO UNIVERSITY

Objective. The present study was performed to investigate the correlations between expression of the receptor activator of nuclear factor-κB ligand (RANKL) in synovial tissue and the degrees of synovitis, degeneration of articular cartilage, and adhesions in patients with internal derangement (ID) of the temporomandibular joint (TMJ).
Study design. Expression of RANKL, detected immunohistochemically, and the severity of arthroscopic features (synovitis, degenerative changes of articular eminence, and adhesion) in 30 patients with ID of the TMJ were assessed and the correlations between them were analyzed statistically.
Results. RANKL expression was detected in the cytoplasm of synovial lining cells, endothelial cells, and fibroblast cells. However, there were no correlations between RANKL expression in any cell type and the severity of arthroscopic features.
Conclusion. These observations indicated that the cellular source of osteoclastic differentiation exists in TMJ with ID and may provide insight into the mechanism of osteoclast differentiation. **(Oral Surg Oral Med Oral Pathol Oral Radiol Endod 2007;104:e12-e17)**

Arthroscopic investigations of patients with internal derangement (ID) of the temporomandibular joint (TMJ) have revealed a significantly high prevalence of degenerative changes in the fibrocartilage of the articular eminence.[1,2] The initial degenerative changes of the TMJ are degradation and softening of the proteoglycans in the fibrocartilage of the articular eminence.[1] These changes are followed by exposure of subchondral bone and bone resorption by osteoclasts. Thus, degenerative changes appear to be related to osteoclastogenesis,[3-5] but the etiology of these changes is not yet fully understood. Previously, we reported that in patients with ID of the TMJ, a reduction in level of the osteoclast genesis inhibitory factor, osteoprotegerin, may induce the development of degenerative changes of articular cartilage.[6] However, the mechanism by which the receptor activator of nuclear factor-κB ligand (RANKL) promotes osteoclastic differentiation is still unclear.

RANKL is a newly discovered member of the tumor necrosis factor ligand family and has been shown to be essential for osteoclastogenesis.[7,8] RANKL is usually a transmembrane protein that interacts with RANK expressed on osteoclast precursors of the monocyte/macrophage lineage. The osteoclastogenic effect of RANKL is strongly suppressed by osteoprotegerin, which is a soluble decoy receptor for RANKL. Moreover, there is strong evidence that osteoprotegerin inhibits bone resorption both in vivo and in vitro.[9-11] Although RANKL plays a role in bone resorption in other joints, the importance and role of RANKL in the TMJ have not yet been determined. Therefore, we investigated immunologically the expression of RANKL in the TMJ with ID and assessed the correlation between RANKL and arthroscopic intra-articular features of the TMJ, such as degenerative changes in articular cartilage.

MATERIAL AND METHODS

Subjects

In the present study, we examined 30 patients with ID of the TMJ (29 women and 1 man) who underwent

Supported by a Grant-in-Aid for Young Scientists (B-16791265 to K.K.), a Grant-Aid for Scientific Research (17592118 to N.S.) from the Ministry of Education, Culture, Sports, Science and Technology of Japan, and by a Grant for Collaborative Research from Kanazawa Medical University (C2005-5 to N.S.).
[a]Lecturer, Department of Oral and Maxillofacial Surgery, Kanazawa Medical University.
[b]Professor and Chairman, Department of Oral and Maxillofacial Surgery, Kanazawa Medical University.
[c]Assistant Professor, Oral Diagnosis and Oral Medicine, Department of Oral Pathobiological Science, Graduate School of Dental Medicine, Hokkaido University.
[d]Associate Professor, Department of Oral and Maxillofacial Surgery, Kanazawa Medical University.
[e]Assistant Professor, Department of Oral and Maxillofacial Surgery, Kanazawa Medical University.
Received for publication Aug 22, 2006; returned for revision Feb 1, 2007; accepted for publication Feb 23, 2007.
1079-2104/$ - see front matter

doi:10.1016/j.tripleo.2007.02.016

Table I. Details of patients and percentage of RANKL-stained cells

Case No.	Age/sex (y)	Duration of symptoms (mo)	Maximum interincisal opening (mm)	VAS score (0-10)	Morphology of the condyle	Degrees of arthroscopic features			Cells for stained for RANKL (%)		
						Synovitis	Degeneration of articular cartilage	Adhesions	Synovial cells	Endothelial cells	Fibroblast cells
1	52/F	3	25	5	N	2	7	8	80	80	60
2	22/F	12	30	4	N	6	0	4	31	31	29
3	34/F	1	35	8	N	5	0	5	90	93	89
4	25/F	4	30	3	N	6	4	7	41	56	60
5	73/F	7	29	5	N	5	8	8	69	51	71
6	22/F	2	28	5	N	8	3	8	89	95	12
7	50/F	5	31	5	N	6	1	6	69	75	11
8	13/F	3	32	5	N	9	0	5	5	88	51
9	36/F	9	38	8	N	5	4	7	79	87	55
10	40/F	1	30	4	N	9	2	7	93	93	89
11	55/F	3	30	8	N	9	1	7	8	10	9
12	32/F	5	30	7	N	4	1	9	89	91	83
13	23/F	15	36	5	N	5	2	5	70	87	67
14	39/M	2	33	2	N	9	1	7	89	95	94
15	17/F	2	38	9	N	4	0	7	78	91	81
16	24/F	2	36	9	N	8	1	5	90	71	42
17	56/F	5	32	3	N	5	0	7	89	90	90
18	18/F	2	30	8	N	2	0	5	84	70	20
19	24/F	4	33	6	N	5	2	6	10	36	25
20	52/F	2	32	1	N	3	7	7	88	80	40
21	38/F	13	24	7	N	3	7	10	65	95	61
22	40/F	2	28	8	N	5	0	7	88	93	81
23	17/F	4	33	6	F	5	0	7	33	91	87
24	38/F	1	31	8	F	5	0	4	91	81	9
25	24/F	1	30	8	F	8	0	0	8	94	77
26	76/F	7	30	5	F	2	4	5	10	45	5
27	40/F	6	38	7	F	8	0	6	77	83	68
28	58/F	3	30	6	F	4	3	7	60	61	21
29	28/F	24	37	6	F	6	0	5	15	80	40
30	23/F	6	27	4	F	8	0	7	88	91	89
Means	40/M1	5	32	6	N22	6	2	6	63	76	54
±SD	17/F29	5	4	2	F8	2	3	2	32	22	30

VAS, visual analog pain scale.

arthroscopic lysis and lavage. Magnetic resonance imaging (MRI) indicated anterior disk displacement without reduction in all of the patients. None of the 30 internally deranged joints showed bony changes or flattening of the condyle alone on MRI.[6] Table I summarizes the characteristics of the patients, their clinical symptoms (age, duration of illness, maximum interincisal opening, visual analog pain scale (VAS) score from 0 to 10), and the MRI findings.

Evaluation of arthroscopic findings

Conventional diagnostic arthroscopy of the whole area of the superior joint compartment was conducted and videotaped for periods of about 10 minutes, followed by arthroscopic lysis and lavage. The degrees of synovitis and degeneration of articular cartilage and adhesion were estimated by inspection and palpation with a probe, according to the criteria described in previous reports[12,13] (Tables II, III, and IV; i.e., the most pronounced degree of synovitis in the superior compartment was given a score on a scale of 0 to 10 by 2 oral surgeons, blinded to the patient's name and condition, while retrospectively viewing the videotapes).

Synovial tissues and immunohistochemical staining

Synovial biopsy specimens approximately 2 mm in diameter were obtained from the patients during arthroscopic lysis and lavage. Specifically, biopsies were performed on the most affected synovial area undergoing arthroscopy. Immediately after sampling, the specimens were fixed in 4% paraformaldehyde for 8 hours and embedded in paraffin. Consecutive sections were cut and stained immunohistochemically using the avidin-biotin-peroxidase complex technique. Endogenous

Table II. Arthroscopic degree of synovitis

Grade	Findings
0	Normal pale, almost translucent synovial lining with a fine network of anastomosing small blood vessels
1	Increased vascularity and capillary hyperaemia (mild)
2	Increased vascularity and capillary hyperaemia (moderate)
3	Increased vascularity and capillary hyperaemia (severe)
4	Capillary dilatation and increasing network (mild to moderate)
5	Capillary dilatation and increasing network (severe)
6	Contact bleeding occurs on probe palpation (mild to moderate)
7	Contact bleeding occurs on probe palpation (severe)
8	Microbleeding and effusion
9	Granulative change, effusion, and debris (mild to moderate)
10	Granulative change, effusion, and debris (severe)

Table III. Arthroscopic degree of degeneration of articular cartilage

Grade	Findings
0	Normal articular cartilage
1	Softening on probe palpation (mild)
2	Softening on probe palpation (moderate to severe)
3	Convex/concave surface
4	Fibrillation (mild)
5	Fibrillation (moderate)
6	Fibrillation (severe)
7	Exposure of bone (mild)
8	Exposure of bone (moderate)
9	Exposure of bone (severe)
10	Intracapsular fibrosis

Table IV. Arthroscopic degree of adhesions

Grade	Findings
0	No adhesion, no fibrous change
1	Filmy adhesion (mild)
2	Filmy adhesion (moderate to severe)
3	Fibrosynovial band (mild to moderate)
4	Fibrosynovial band (severe)
5	Fibrous band (mild to moderate)
6	Fibrous band (severe)
7	Pseudocapsular wall (mild to moderate)
8	Pseudocapsular wall (severe)
9	Capsular fibrosis (mild to moderate)
10	Capsular fibrosis (severe)

peroxidase activity was blocked by immersing the sections in 0.3% H_2O_2 in methanol for 10 minutes at room temperature. The sections were treated with 0.1% trypsin for 20 minutes at 37°C. After blocking nonspecific binding with 1.5% normal horse serum for 20 minutes at room temperature, the sections were treated with rabbit polyclonal antibody to RANKL (1:100 dilution; Cosmo Bioscience Co., La Jolla, CA) for 60 minutes at room temperature. The color was developed with diaminobenzidine. Negative controls in which the primary antibody was replaced with normal rabbit IgG were run with each specimen. The RANKL-stained cells were counted in all regions, and the percentage of RANKL-positive cells was calculated.

Statistical analysis

The correlations between the percentage of RANKL-positive cells and the degree of each arthroscopic feature were analyzed statistically using the Spearman rank correlation coefficient and the Mann-Whitney *U* test. The correlations between the percentage of RANKL-positive cells and the clinical symptoms were analyzed statistically using the Spearman rank correlation coefficient. Probabilities of less than .05 were considered significant.

RESULTS

Arthroscopic features and immunohistochemical detection of RANKL expression

The main arthroscopic features were synovitis and adhesion (Table I). RANKL immunoreactivity in the TMJ was observed in the cytoplasm of the synovial lining cells, endothelial cells of the blood vessels, and fibroblasts (Table I and Fig. 1, *A*). The negative control sections showed only background staining (Fig. 1, *B*).

Correlation between arthroscopic features and RANKL expression

Table V shows the correlation coefficients among each cell type for immunohistochemical expression of RANKL. There were no correlations between RANKL expression and the degrees of other arthroscopic features (Table V and Fig. 2). With respect to degeneration of the articular cartilage, all joints were classified into 2 groups according to whether degeneration of the articular cartilage was seen or not. That is, grade 0—which is normal of articular cartilage—was regarded as control and was compared with degeneration of the articular cartilage, which was grade 1 to 10. There are no correlations for immunohistochemical expression of RANKL in the synovial lining cells, endothelial cells, and fibroblasts between normal and degeneration of the articular cartilage (Table VI).

Correlation between clinical symptoms and RANKL expression

There were no correlations between the concentrations of any of the RANKL expression and the clinical symptoms (age, duration of symptoms, maximum in-

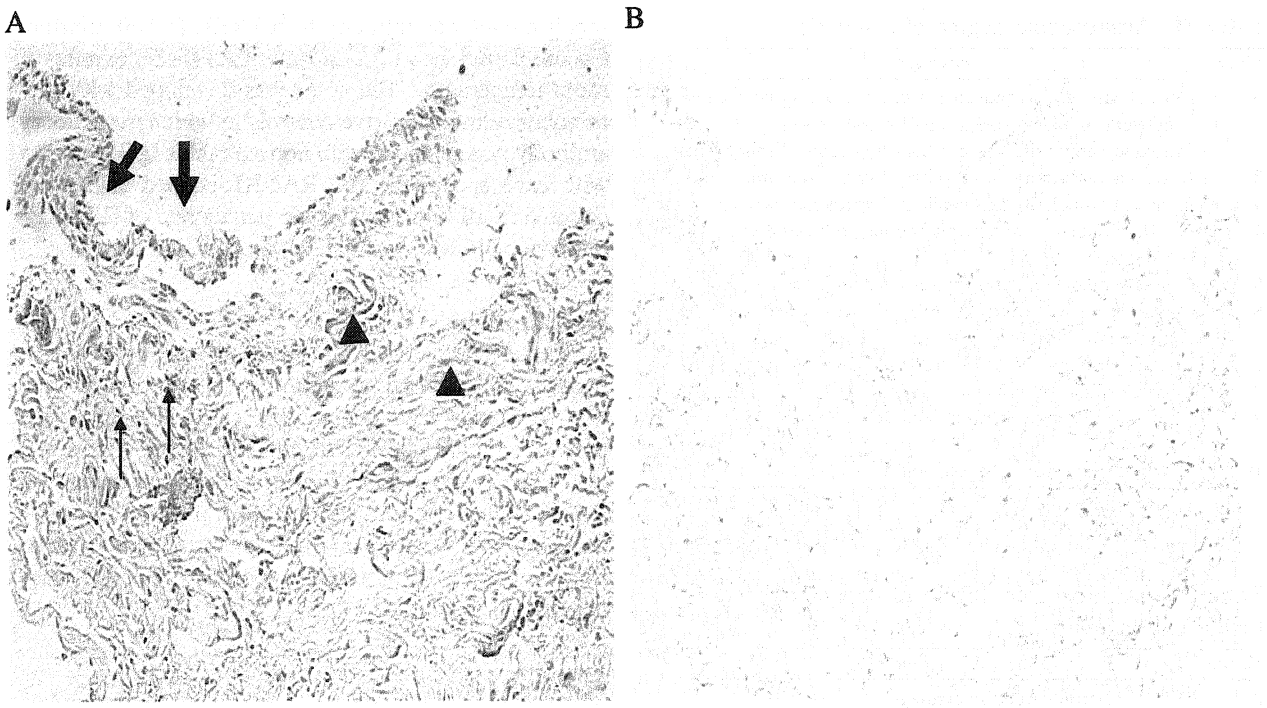

Fig 1. **A,** Receptor activator of nuclear factor-κB ligand (RANKL) immunoreactivity in specimens from internal derangement patients was observed in synovial lining cells (*large arrows*), endothelial cells of the blood vessels (*arrowheads*), and fibroblasts (*small arrows*) in the synovial tissues (magnification ×50). **B,** Negative controls using normal rabbit IgG in the same section showed only background staining (magnification ×50).

Table V. Correlation coefficients between arthroscopic features and immunohistochemical expression of RANKL

	Expression of RANKL		
	Synovial lining cells	*Endothelial cells*	*Fibroblasts*
Arthroscopic features			
Synovitis	−.13 (P = .85)	0.046 (P = .37)	0.17 (P = .41)
Degeneration of articular cartilage	0.093 (P = .85)	−.14 (P = .23)	−.12 (P = .20)
Adhesions	0.040 (P = .23)	0.035 (P = .12)	0.12 (P = .10)

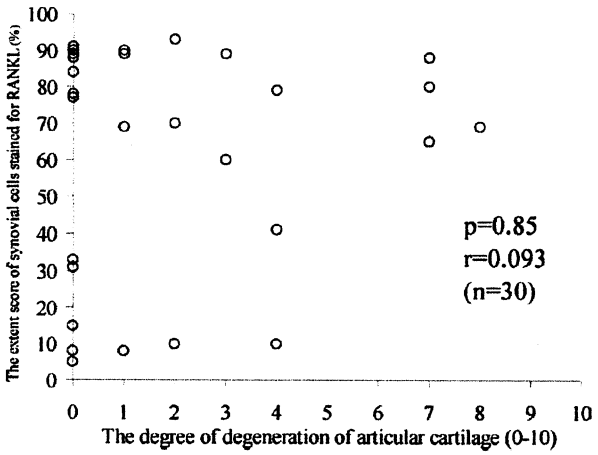

Fig 2. The extent score of synovial cells stained for RANKL and the degree of degeneration of articular cartilage are not correlated significantly (Spearman correlation coefficient; P = .85, r = 0.093).

terincisal opening, and visual analog pain scale score; Table VII).

DISCUSSION

The results of the present study demonstrated for the first time that RANKL is localized predominantly in the synovial tissue of the TMJ with ID. This observation indicated that the cellular source of osteoclastic differentiation exists in TMJ with ID, and that not only synovial lining cells, but also endothelial cells and fibroblasts may be important stimulators of osteoclastogenesis. This was supported by the findings of recent studies indicating the expression of RANKL in osteoarthritis of other joints.[14,15] RANKL is expressed on fibroblastlike synovial cells as well as on activated T

Table VI. Relationship between degeneration of articular cartilage and immunohistochemical expression of RANKL

Arthroscopic degree of degeneration of articular cartilage	*Expression of RANKL*					
	Synovial lining cells		*Endothelial cells*		*Fibroblasts*	
	Normal 0	*Degeneration 1-10*	*Normal 0*	*Degeneration 1-10*	*Normal 0*	*Degeneration 1-10*
Average (%)	60	65	83	71	62	47
SD	35	30	17	25	29	29
	$P = .87$		$P = .24$		$P = .17$	

Table VII. Correlation coefficients between clinical symptoms and immunohistochemical expression of RANKL

	Expression of RANKL		
	Synovial lining cells	*Endothelial cells*	*Fibroblasts*
Clinical symptoms			
Age	0.069 ($P = .59$)	−0.32 ($P = .19$)	−0.059 ($P = .62$)
Duration of symptoms	−0.092 ($P = .87$)	−0.082 ($P = .92$)	−0.068 ($P = .63$)
Maximum interincisal opening	−0.036 ($P = .98$)	0.014 ($P = .77$)	−0.10 ($P = .43$)
VAS score	0.014 ($P = .93$)	0.095 ($P = .84$)	0.11 ($P = .68$)

VAS,visual analog pain scale.

cells in the synovial tissue of osteoarthritis (OA) patients. These cells may also be important stimulators of osteoclastogenesis in OA, especially in erosive lesions in the affected joints. On the other hand, there have also been reports that RANKL expression was lacking or weak in OA compared with rheumatoid arthritis (RA), which is expressed at high levels in the synovial tissue.[9,16] The reasons for these discrepancies remain unclear, but they may be due to the differences in cell types, methods, or the severity of inflammation in OA joints between the studies. Thus, further studies are required to investigate which cells play the most important roles in the expression of RANKL in the TMJ with ID.

Degeneration of intra-articular cartilage based on chondromalacia is one of the main pathological characteristics of TMJ with ID.[1] The present study was also the first to compare the intensity of RANKL expression with degenerative changes in the articular cartilage on arthroscopy. However, no statistically significant correlations were found. This result suggests that investigation of RANKL expression in the rheumatoid synovium may allow a better understanding of the pathological conditions.[15,17,18] Osteoclasts were identified at the pannus-bone and pannus-subchondral bone junctions of RA joints, where they formed erosive pits in the bone. RANKL mRNA was also expressed at high levels in cells in the pannus, which are capable of developing into osteoclasts. On the other hand, although osteoclasts were formed within the intra-articular eminence and condyle of the TMJ, these osteoclasts were not in direct contact with synovial tissue of the TMJ. That is, the intra-articular eminence and condyle are only in contact with the anterior and posterior synovial portions of the TMJ.[3-5] Therefore, it remains unclear how the osteoclasts are formed in TMJ away from the sites of RANKL expression. It has been suggested that T lymphocytes and monocytes in the synovial fluid and tissue can differentiate into osteoclasts under certain conditions and may have important roles in osteoclastic bone degeneration.[10,11] In addition, despite the presence of severe inflammatory changes, whether degenerative changes in articular cartilage can occur is dependent on the presence and number of osteoclasts.[19,20] That is, degenerative changes of articular cartilage cannot develop in the absence of osteoclasts. Therefore, further studies are needed to define the timing of RANKL expression in relation to the development of synovitis and degradation of articular cartilage and to precisely identify the cell types that express RANKL in TMJ.

The main limitation of the present study was the lack of control samples in the normal joints. This problem is difficult to overcome, as it is impossible to obtain fresh samples of synovial tissue from healthy people. Therefore, with respect to degeneration of the articular cartilage, all joints were classified into 2 groups according to whether degeneration of the articular cartilage was seen or not. Although we think that those controls would be control subjects for the present study, there are no correlations between them. However, this does not exclude the possibility that RANKL may play a role in the pathogenesis of TMD. In the future, it will be

necessary to investigate the RANKL in normal joints to clarify the pathogenesis of the TMDs.

In conclusion, the expression of RANKL within cells of the TMJ provides insight into the mechanism of osteoclast differentiation and function at sites of degradation of articular cartilage. Our results suggest that RANKL expression in these cells may be a good therapeutic target in the prevention of osteoarthritic joint destruction. Further molecular and biochemical studies are needed to fully understand RANKL-induced bone metabolism of the TMD.

REFERENCES

1. Quinn JH. Arthroscopic and histologic evidence of chondromalacia in the temporomandibular joint. Oral Surg Oral Med Oral Pathol Oral Radiol Endod 1990;70:387-92.
2. Holmlund A, Hellising G. Arthroscopy of the temporomandibular joint: occurrence and location of osteoarthrosis and synovitis in a patient material. Int J Oral Maxillofac Surg 1988;17:36-40.
3. De Bont LGM, Boering G, Liem RSB, Eulderink F, Westesson PL. Osteoarthritis and internal derangement of the temporomandibular joint: a light microscopic study. J Oral Maxillofac Surg 1986;44:634-43.
4. Blackwood HJ. Arthritis of the mandibular joint. Br Dent J 1963;115:317-26.
5. Helmy E, Bays R, Sharawy M. Osteoarthrosis of the temporomandibular joint following experimental disc perforation in Macaca fascicularis. J Oral Maxillofac Surg 1988;46:979-90.
6. Kaneyama K, Segami N, Sato J, Nishimura M, Yoshimura H. Expression of osteoprotegerin in synovial tissue and degradation of articular cartilage: comparison with arthroscopic findings of the temporomandibular joint disorders. Oral Surg Oral Med Oral Pathol Oral Radiol Endod 2003;96:258-62.
7. Yasuda H, Shima N, Nakagawa N, Yamaguchi K, Kinosaki M, Mochizuki S, et al. Osteoclast differentiation factor is a ligand for osteoprotegerin/osteoclastogenesis-inhibitory factor and is identical to TRANCE/RANKL. Proc Natl Acad Sci U S A 1998;95:3597-602.
8. Lacey DL, Timms E, Tan HL, Kelley MJ, Dunstan CR, Burgess T, et al. Osteoprotegerin ligand is a cytokine that regulates osteoclast differentiation and activation. Cell 1998;93:165-76.
9. Takayanagi H, Iizuka H, Juji T, Nakagawa T, Yamamoto A, Miyazaki T, et al. Involvement of receptor activator of nuclear factor κB ligand/osteoclast differentiation factor in osteoclastogenesis from synoviocytes in rheumatoid arthritis. Arthritis Rheum 2000;43:259-69.
10. Kong YY, Feige U, Sarosi I, Bolon B, Tafuri A, Morony S, et al. Activated T cells regulate bone loss and joint destruction in adjuvant arthritis through osteoprotegerin ligand. Nature 1999; 402:304-9.
11. Kotake S, Udagawa N, Hakoda M, Mogi M, Yano K, Tsuda E, et al. Activated human T cells directly induce osteoclastogenesis from human monocytes: possible role of T cells in bone destruction in rheumatoid arthritis patients. Arthritis Rheum 2001;44: 1003-12.
12. Murakami K, Segami N, Moriya Y, Iizuka T. Correlation between pain and dysfunction and intra-articular adhesions in patients with internal derangement of the temporomandibular joint. J Oral Maxillofac Surg 1992;50:705-8.
13. Nishimura M, Segami N, Kaneyama K, Suzuki T, Miyamaru M. Proinflammatory cytokines and arthroscopic findings of patients with internal derangement and osteoarthritis of the temporomandibular joint. Br J Oral Maxillofac Surg 2002;40:68-71.
14. Komuro H, Olee T, Kuhn K, Quach J, Brinson DC, Shikhman A, et al. The osteoprotegerin/receptor activator of nuclear factor kappaB/receptor activator of nuclear factor kappaB ligand system in cartilage. Arthritis Rheum 2001;44:2768-76.
15. Nakano K, Okada Y, Saito K, Tanaka Y. Induction of RANKL expression and osteoclast maturation by the binding of fibroblast growth factor 2 to heparan sulfate proteoglycan on rheumatoid synovial fibroblasts. Arthritis Rheum 2004;50:2450-8.
16. Crotti TN, Smith MD, Weedon H, Ahern MJ, Findlay DM, Kraan M, et al. Receptor activator NF-kappaB ligand (RANKL) expression in synovial tissue from patients with rheumatoid arthritis, spondyloarthropathy, osteoarthritis, and from normal patients: semiquantitative and quantitative analysis. Ann Rheum Dis 2002;61:1047-54.
17. Gravallese EM, Manning C, Tsay A, Naito A, Pan C, Amento E, et al. Synovial tissue in rheumatoid arthritis is a source of osteoclast differentiation factor. Arthritis Rheum 2000;43:250-8.
18. Romas E, Bakharevski O, Hards DK, Kartsogiannis V, Quin JMW, Ryan PFJ, et al. Expression of osteoclast differentiation factor at sites of bone erosion in collagen-induced arthritis. Arthritis Rheum 2000;43:821-6.
19. Pettit AR Ji H, von Stechow D, Muller R, Goldring SR, Choi Y, Benoist C, et al. TRANCE/RANKL knockout mice are protected from bone erosion in a serum transfer model of arthritis. Am J Pathol 2001;159:1689-99.
20. Redlich K, Hayer S, Ricci R, David JP, Tohidast-Akrad M, Kollias G, et al. Osteoclasts are essential for TNF-α-mediated joint destruction. J Clin Invest 2002;110:1419-27.

Reprint requests:

Keiseki Kaneyama, DDS, PhD
1-1 Daigaku, Uchinada-machi
Kahoku-gun, Ishikawa-Pref.
920-0293 Japan
k-k@kanazawa-med.ac.jp

Bacterial diversity in synovial fluids of patients with TMD determined by cloning and sequencing analysis of the 16S ribosomal RNA gene

Wei Sun, DDS,[a] Lingli Dong, MD, PhD,[b] Keiseki Kaneyama, DDS, PhD,[c]
Tsutomu Takegami, PhD,[d] and Natsuki Segami, DDS, PhD,[e] Ishikawa, Japan; and Hubei, China
KANAZAWA MEDICAL UNIVERSITY AND HUAZHONG UNIVERSITY OF SCIENCE AND TECHNOLOGY

Objective. The purpose of this study was to examine the presence of bacterial in synovial fluids from patients with temporomandibular joint disorder (TMD) by polymerase chain reaction (PCR) targeting the 16S ribosomal RNA (rRNA) gene, followed by cloning and sequencing.
Study design. Universal bacterial primers were used to amplify 16S rRNA genes in 28 synovial fluid samples from 27 patients with TMD (TMD group) as well as control subjects: 5 patients with dislocation of TMJ (non-TMD group). Subsequently, PCR amplicons were purified and cloned. Partial 16S rRNA sequences of the cloned insert were used to determine the species identities or closest relative by comparison with known sequences using GeneBank.
Results. Nineteen (67.86%) of 28 samples from patients in the TMD group were identified with the presence of bacterial DNA by PCR. The 5 control samples from the nonTMD group were all negative in this study. After cloning and sequencing, a total of 11 bacterial species was detected, including *Granulicatella adiacen* (6 samples), *Pseudomonas sp.* (6 samples), *Methylobacterium sp.* (5 samples), and *Beta proteobacterium* (4 samples). Other species, such as *Acidovorax sp., Bradyrhizobium sp., Sphingomonas, Streptococcus, Leptothrix sp.* oral clone, *Thiobacillus denitrificans,* and *Comamonadaceae bacterium,* were also identified. Eight patients were found with mixed bacteria, with 2-4 bacteria per sample. The patients with fastidious bacteria such as *Granulicatella adiacen* and mixed bacteria were more likely to be older than 45 years ($P < .05$).
Conclusion. A wide variety of bacteria, including some not previously reported associated with TMD, were identified in the synovial fluids from patients with TMD. **(Oral Surg Oral Med Oral Pathol Oral Radiol Endod 2008;105:566-71)**

Temporomandibular joint (TMJ) disorder (TMD) is a complex disease which represents a group of painful and dysfunctional conditions involving the TMJ. Although the etiology of TMD has been reported as stress, trauma, hormonal imbalance, malocclusion, and so on, the detailed mechanisms underlying the development of TMD still remain largely unknown.[1] Recently, several studies had reported that the presence of bacteria is related to TMD; however, that was determined by polymerase chain reaction (PCR) targeting limited specific bacterial species.[2-4] which may have the possibility of missing the determination of some novel microorganisms.

Advances in molecular biology have permitted us to perform the study of microbial communities and obtain improved information of bacterial diversity from clinical synovial fluid samples. The 16S ribosomal RNA (rRNA) molecular is a basic constituent of bacterial ribosome, which is a highly conserved structure with an important function in protein synthesis. By designing PCR primers complementary to conserved regions of the rRNA gene and subsequent cloning and sequencing of the PCR products, the 16S rRNA gene sequences are compared with other known 16S rRNA sequences to identify the bacteria species. This approach has provided a useful way to identify fastidious, uncultivable, and novel microorganisms.[5,6]

In the present study, by PCR amplification of the bacterial 16S ribosomal rRNA gene using universal

This study was partially supported by a Grant-Aid for Scientific Research (18592207 and 19592324) from the Ministry of Education, Culture, Sports, Science and Technology of Japan and a Grant for Specially Promoted Research (C2005-5) from Kanazawa Medical University.
The first 2 authors contributed equally to this work.
[a]Graduate student, Department of Oral and Maxillofacial Surgery, Kanazawa Medical University; Assistant Professor, Department of Stomatology, Union Hospital, Tongji Medical college, Huazhong University of Science and Technology.
[b]Postdoctoral researcher, Department of Hematology and Immunology, Kanazawa Medical University; Assistant Professor, Department of Internal Medicine, Tongji Hospital, Tongji Medical college, Huazhong University of Science and Technology.
[c]Assistant Professor, Department of Oral and Maxillofacial Surgery, Kanazawa Medical University.
[d]Professor, Department of Molecular Oncology and Virology, Kanazawa Medical University.
[e]Professor and Chairman, Department of Oral and Maxillofacial Surgery, Kanazawa Medical University.
1079-2104/$ - see front matter

doi:10.1016/j.tripleo.2007.08.015

bacterial primers, we identified the presence of bacterial DNA in synovial fluids from patients with TMD. Subsequently, followed by cloning and sequencing of the PCR amplicons, we analyzed the bacterial diversity based on information of nucleic acids from PCR amplification of the bacterial 16S rRNA gene. Furthermore, the relation between the obtained bacteria information and clinical parameters was analyzed.

MATERIAL AND METHODS

Subjects and clinical sample collection

Thirty-one synovial fluid samples were collected under strictly aseptic conditions from 30 patients (26 women, 4 men; female-to-male ratio 6.5:1) with TMD who underwent arthrocentesis for therapeutic purposes at the Kanazawa Medical University Hospital from November 2005 to December 2006 after obtaining informed consent. These patients showed painful hypomobility of the TMJ, and magnetic resonance imaging (MRI) confirmed anterior disc displacement without reduction in all except 2 cases (Table I). Antisepsis of the operation field was conducted with providone-iodine by careful scrub to minimize contamination from skin and other potential sources. Arthrocentesis was performed as described previously.[7] In brief, after a local anesthesia (2% lidocaine), the synovial fluid was taken by puncture with a sterile 21-gauge needle inserted inferolaterally into the superior joint space. Then, samples were collected into sterile tubes and shipped to the laboratory immediately. After the removal of cells by centrifuging at 500*g* for 30 minutes at 4°C, DNA was extracted within 2 hours after collection. All steps were performed under strict sterile conditions. Three samples were excluded because of blood contamination. Five patients with dislocation of TMJ were used as control subjects. The MRI observation was as described previously.[8-10] No patients were being treated with antibiotics at the time of sample collection.

DNA preparation from the synovial fluid samples

The DNA was extracted using a commercial kit (DNAzol Reagent; Invitrogen, Carlsbad, CA) according to the manufacturer's instruction. Control synovial fluid samples including sterile water (Nacalai Tesque, Kyoto, Japan) were run in parallel to check the sterility of the solutions and buffer used in the DNA extraction method.

PCR amplification of 16S rRNA gene

The PCR amplification of 16S rRNA gene was undergone with previous published universal bacterial primers (5′-GAT TAG ATA CCC TGG TAG TCC AC-3′ and 5′-CCC GGG AAC GTA TTC ACC G-3′).[2] The PCR was performed in 50 μL reaction mixture containing 2.5 units Taq DNA polymerase (Takara Bio, Kyoto, Japan), 1× PCR buffer with 1.5 mmol/L $MgCl_2$, 200 μmol/L each deoxynucleotide, 0.2 μmol/L each primer, and 10 μL template DNA. Reaction were carried out in a thermal cycler (DNA Engine PTC-200; Bio-Rad, Hercules, CA) beginning with an initial denaturation of 98°C for 2 minutes preceding the addition of the DNA polymerase and terminated by an extension step of 72°C for 10 minutes. Thirty-five round cycles consisting of 96°C for 1 minute, 60°C for 1 minute, and 72°C for 1 minute were performed. Each set of experiments included negative controls with sterile distilled water instead of template DNA and positive controls containing purified DNA from *Escherichia coli*.[11] Use of the primers would be expected to generate a fragment of about 610 bp in length. The reaction products were analyzed by 1.5% agarose gel electrophoresis, stained with ethidium bromide, and viewed under ultraviolet light. Simultaneously, the presence of previous reported *Chlamydia trachomatis* and *Mycoplasma fermentans* in the synovial fluid of TMD was examined by PCR using its relative specific primers.[2]

Cloning and 16S rRNA gene sequencing

Amplicons were purified using Rapid PCR Purification System (Marligen Bioscience, Ljamsville, MD). Approximately 20 ng purified DNA was cloned using T-A Cloning Kit (Invitrogen, Tokyo, Japan) according to the instructions of the manufacturer. Up to 10 clones containing the insertion for each sample were picked up at random and cultured in 2 mL Luria-Bertani overnight at 37°C. Plasmid DNA was extracted using QIAprep Spin Minipre Kit (Qiagen, Tokyo, Japan) and sequenced using the ABI Bigdye Terminator 1.1 Cycle Sequencing Kit (Applied Biosystems, Foster City, CA). Sequencing reactions were performed with M13 primer on the ABI 310 Genetic Analyzer (Applied Biosystems). Precautions against contamination were taken at each step.

Analysis of 16S rRNA gene sequencing

The DNA sequences were analyzed by Genetyx-Win (version 3.2) software. The partial 16S rRNA gene sequences were used to determined identity or nearest phylogenetic position. For identification of closest relatives, the consensus sequences were compared with 16S rRNA gene sequence in GenBank databases using the National Center for Biotechnology Information Blast search tool (http://www.ncbi.nlm.nih.gov/BLAST/).

Statistics

The results were subjected to the independent-sample *t* test, χ^2 test, and bivariate analysis. A value of $P < .05$ was considered to be statistically significant. The

Table I. General characteristics of patients studied and bacteria species by PCR and cloning 16S rRNA gene sequence

						MRI			
No.	*Gender*	*Age*	*Diagnosis*	*Joint pain*	*MMO*	*Disk shape**	*Bone change†*	*Joint effusion‡*	*Bacteria species*
1	F	33	ID	+	40	2	3	−	*Streptococcus*
2	F	34	ID	+	45	1	3	±	*Pseudomonas* sp.
3	F	12	ID	+	30	1	4	±	—
4	F	22	ID	+	30	1	4	+	*Methylobacterium* sp.
5	F	34	OA	+	38	2	1	±	*Pseudomonas* sp.
6	F	18	ID	+	30	2	4	−	—
7	F	34	ID	++	30	1	4	+	—
8	F	28	ID	++	30	2	2	±	—
			OA	+	30	2	1	+	*Bradyrhizobium* sp.
9	F	60	OA	+	33	2	1	++	*Granulicatella adiacen* *Methylobacterium* sp.
10	M	71	ID	+	22	1	4	++	*Acidovorax* sp. *Granulicatella adiacen* *Pseudomonas* sp.
11	F	62	ID	++	35	1	2	++	*Granulicatella adiacen* *Methylobacterium* sp. *Leptothrix* sp. oral clone
12	F	42	ID	+	30	1	4	+	*Pseudomonas* sp.
13	F	53	OA	+	32	2	1	±	*Bradyrhizobium* sp *Pseudomonas* sp. *Sphingomonas*
14	F	56	OA	+	28	2	2	+	*Beta proteobacterium* *Granulicatella adiacen*
15§	M	34	ID	+	30	4	4	−	—
16	F	27	ID	+	32	2	4	±	—
17	F	50	ID	+	40	2	4	−	*Beta proteobacterium* *Granulicatella adiacen*
18	M	18	ID	+	37	2	3	±	—
19	F	36	ID	+	21	2	3	+	—
20	F	52	ID	+	30	2	4	±	*Granulicatella adiacen* *Thiobacillus denitrificans*
21	F	47	ID	+	23	2	4	±	*Beta proteobacterium* *Comamonadaceae bacterium* *Sphingomonas*
22	F	24	ID	+	34	2	4	±	*Methylobacterium* sp.
23§	M	21	ID	+	23	1	4	+	*Beta proteobacterium*
24	F	20	ID	+	36	1	4	±	*Methylobacterium* sp.
25	F	27	ID	+	42	1	4	±	—
26	F	41	OA	+	35	2	2	−	*Pseudomonas* sp.
27	F	58	OA	+	37	1	1	±	*Granulicatella adiacen* *Leptothrix* sp. oral clone *Pseudomonas* sp.

ID, internal derangement; *MMO*, maximum mouth opening; *MRI*, magnetic resonance imaging; *OA*, osteoarthrosis; *PCR*, polymerase chain reaction.

*Disk shape: 1, biconcave; 2, biconvex; 3, biplanar; 4, normal.

†Bone change: 1, ++ exosion; 2, + osteophyte; 3, flattening; 4, normal.

‡Joint effusion: −, high signal intensity is not visible in joint space; ±, high spot signals are indentified in anterior recesses; +, band shape high signals are indicated in anterior and posterior recesses; ++, high signal is depicted in wide area in joint space as pooling.

§MRI of the TMJ showed normal disc position.

difference of bacterial presence between the TMD group (27 studied TMD patients) and the non-TMD group (5 control patients with TMJ dislocation) was compared. The association between the presence of each bacteria and clinical parameters was analyzed.

RESULTS

The PCR amplification of 16S rRNA gene in determining the presence of bacterial DNA was examined using *Escherichia coli* as positive control. In 28 studied TMJs, 19 were identified with the presence of bacterial

Table II. Incidence of bacterial species in 19 bacteria-positive samples

Bacterial species	*No. of samples*	*%*
Granulicatella adiacens	6	31.6
Pseudomonas sp.	6	31.6
Methylobacterium sp.	5	26.3
Beta proteobacterium	4	21.1
Bradyrhizobium sp.	2	10.5
Streptococcus	2	10.5
Acidovorax sp.	2	10.5
Leptothrix sp. oral clone	2	10.5
Sphingomonas	2	10.5
Thiobacillus denitrificans	1	5.3
Comamonadaceae bacterium	1	5.3

Table III. Signs and symptoms in joints with mixed bacteria and single bacteria

	Absence of bacteria (9 joints)	*Presence of mixed bacteria (8 joints)*	*Presence of single bacterial (11 joints)*
Age (yrs)	25 ± 7	57 ± 7*	30 ± 8
Duration of illness (month)	33 ± 22	25 ± 41	37 ± 67
Opening degree (mm)	30 ± 7	31 ± 7	30 ± 8

Data are presented as mean ± SD.
*$P < .05$ compared with presence of single bacteria.

DNA. No bacteria DNA was found in all 5 control patients with dislocation of TMJ. The presence of bacterial DNA was significantly different between TMD group and the non-TMD group ($P < .01$). The 28 samples of synovial fluids included 2 samples from the bilateral TMJs of 1 patient. Sequencing was used to analyze a total of more than 200 clones from 19 samples with bacterial DNA. All 16S rRNA gene sequences showed >97% homology to sequences deposited in Genebank. A total of 11 bacteria species were identified, including *Granulicatella adiacen* (6 samples), *Pseudomonas sp.* (6 samples), *Methylobacterium sp.* (5 samples), and *Beta proteobacterium* (4 samples). Other species, such as *Acidovorax sp.*, *Bradyrhizobium sp.*, *Sphingomonas*, *Streptococcus*, *Leptothrix sp.* oral clone, *Thiobacillus denitrificans*. and *Comamonadaceae bacterium*, were also detected. Some important clinical parameters of the patients studied for the presence of bacteria are summarized in Table I. The incidence of bacterial diversity in 19 bacterial positive patients is shown in Table II. No bacteria DNA was found in all 5 control patients with dislocation of TMJ.

Eight patients were identified with mixed bacteria in synovial fluid of TMJ. Among them, 6 patients were found to contain *Granulicatella adiacen*, which is a fastidious bacteria and has been considered as a possible cause of endocarditis. Moreover, those TMD patients with mixed bacteria, in particular with the existence of *Granulicatella adiacen* in synovial fluid, were much more likely to be over 45 years old (Table III).

No significant association was found of bacteria presence and species with other clinical parameters, such as gender, TMJ pain, limitation of mouth opening, and MRI finding, including disk shape and bone change. Previously reported *Chlamydia trachomatis* and *Mycoplasma fermentans* in TMD tissue were not identified in any samples in the present study.

DISCUSSION

PCR assay of 16S rDNA has been widely used to detect bacterial infection in a variety of clinical samples[12,13]; however, it cannot be used to identify each pathogen, especially in case of mixed infection.[14] In the present study we used molecular biology based on a broad-range PCR followed by sequencing and cloning procedures. This approach provides us a complementary way to identify microorganisms from synovial fluid samples, as well as allows us to detect bacterial diversity, including previously unknown pathogens and potentially novel bacterial. First, the methodology should be discussed here. It should be emphasized that strict aseptic conditions were performed to avoid contamination in each step both during surgery and in the laboratory. Control samples from non-TMD patients in the present study were all negative. Furthermore, control samples that were used to test the sterility of solutions and buffer used during DNA preparation and PCR also gave negative results. In addition, no amplification of bacterial DNA was seen in the PCR using sterile water instead of template DNA, which also argued against contamination of PCR reagents. Therefore, our results on the presence of bacteria were very reliable. This study thus may provide insight for the identity of putative pathogens in TMD.

About 67.86% samples from patients with TMD were identified with the presence of bacterial DNA by PCR. Moreover, after cloning and sequencing, a total of 11 bacterial species were detected, and 8 out of 19 bacteria-positive samples contained multiple bacteria, suggesting that it is not a specific species that contributes to the development of TMD. *Granulicatella adiacen* was detected in 31% of the bacteria-positive samples, which was considered to be a high incidence of bacteria presence in the present study. It is a fastidious bacteria and has been regarded as a possible agent of bacteremia in neutropenic patients and can cause a variety of infections, primarily endocarditis.[15] Interestingly, most patients (6 of 8) with multiple bacteria were

identified with the presence of this pathogen in their synovial fluids; in addition, they were all over 45 years old. Clinical data did not show any history or sign of endocarditis. There are only several case reports concerning joint infection caused by *Granulicatella adiacen* in literature.[16,17] Take together, it is likely that *Granulicatella adiacen* may be a possible pathogen requiring the coexistence of other pathogens to contribute to the pathogenesis of TMD, particularly in the aged population. *Pseudomonas sp.*, which also have been previously identified as present in synovial fluid and tissue from patients with reactive arthritis,[18,19] was also isolated from our clinical samples, indicating that it may act as a pathogen in TMD. *Methylobacterium sp.* are a group of aerobic gram-negative rod-shaped bacteria which were isolated previously from various environments. These bacteria were isolated from various patient specimens, such as blood, cerebrospinal fluid, sputum, bronchoscopic material, and so on.[20] To our knowledge, this is the first description of *Methylobacterium sp.* isolated from synovial fluids. Some cases of human infections have been reported to be related to these bacteria, and in all cases an underlying immunosuppression, e.g., leukemia, tuberculosis, AIDS, or alcohol abuse. *Methylobacterium sp.* might be a potentially infectious agent in TMD, because they are opportunistic pathogens; they are difficult to cultivate and identify. Other species detected in this study, such as *Beta proteobacterium*, *Streptococcus* oralis strain, *Acidovorax sp.*, *Bradyrhizobium sp.*, *Sphingomonas*, *Leptothrix sp.* oral clone, *Thiobacillus denitrificans*, and *Comamonadaceae bacterium*, have been reported as either opportunistic or true pathogens in different human diseases.[14,21] We may therefore speculate that these unusual microorganisms are difficult to isolate in culture and that they may have low pathogenic potential. Previously reported *Chlamydia trachomatis* and *Mycoplasma fermentans* in TMD tissue were not identified in any samples in the present study, suggesting that these 2 bacteria may not be major pathogens in Japanese patients with TMD.

In conclusion, by PCR amplification of the bacterial 16S rRNA gene using universal bacterial primes, we identified the presence of bacterial DNA in synovial fluids from patients with TMD. Subsequently, followed by cloning and sequencing of the PCR amplicon, we analyzed the bacterial diversity based on information of nucleic acids from PCR amplification of the bacterial 16S rRNA gene. A wide variety of bacteria, including some not previously reported to be associated with TMD, were identified in the synovial fluids of patients with TMD. The presence of bacteria in TMJ, either single or concurrently with other bacteria, is related to TMD.

REFERENCES

1. Paegle DI, Holmlund AB, Ostlund MR, Grillner L. The occurrence of antibodies against *Chlamydia* species in patients with monoarthritis and chronic closed lock of the temporomandibular joint. J Oral Maxillofac Surg 2004;62:435-9.
2. Kim SJ, Park YH, Hong SP, Cho BO, Park JW, Kim SG. The presence of bacteria in the synovial fluid of the temporomandibular joint and clinical significance: preliminary study. J Oral Maxillofac Surg 2003;61:1156-61.
3. Henry CH, Hudson AP, Gerard HC, Franco PF, Wolford LM. Identification of *Chlamydia trachomatis* in the human temporomandibular joint. J Oral Maxillofac Surg 1999;57:683-8; discussion 689.
4. Henry CH, Hughes CV, Gerard HC, Hudson AP, Wolford LM. Reactive arthritis: preliminary microbiologic analysis of the human temporomandibular joint. J Oral Maxillofac Surg 2000;58: 1137-42; discussion 1143-34.
5. Johnson SM, Bruckner F, Collins D. Distribution of *Mycoplasma pneumoniae* and *Mycoplasma salivarium* in the synovial fluid of arthritis patients. J Clin Microbiol 2007;45:953-7.
6. Fenollar F, Roux V, Stein A, Drancourt M, Raoult D. Analysis of 525 samples to determine the usefulness of PCR amplification and sequencing of the 16S rRNA gene for diagnosis of bone and joint infections. J Clin Microbiol 2006;44:1018-28.
7. Kaneyama K, Segami N, Nishimura M, Sato J, Suzuki T, Fujimura K. Osteoclastogenesis inhibitory factor/osteoprotegerin in synovial fluid from patients with temporomandibular disorders. Int J Oral Maxillofac Surg 2003;32:404-7.
8. Segami N, Miyamaru M, Nishimura M, Suzuki T, Kaneyama K, Murakami K. Does joint effusion on T2 magnetic resonance images reflect synovitis? Part 2. Comparison of concentration levels of proinflammatory cytokines and total protein in synovial fluid of the temporomandibular joint with internal derangements and osteoarthrosis. Oral Surg Oral Med Oral Pathol Oral Radiol Endod 2002;94:515-21.
9. Segami N, Nishimura M, Kaneyama K, Miyamaru M, Sato J, Murakami KI. Does joint effusion on T2 magnetic resonance images reflect synovitis? Comparison of arthroscopic findings in internal derangements of the temporomandibular joint. Oral Surg Oral Med Oral Pathol Oral Radiol Endod 2001;92:341-5.
10. Segami N, Suzuki T, Sato J, Miyamaru M, Nishimura M, Yoshimura H. Does joint effusion on T2 magnetic resonance images reflect synovitis? Part 3. Comparison of histologic findings of arthroscopically obtained synovium in internal derangements of the temporomandibular joint. Oral Surg Oral Med Oral Pathol Oral Radiol Endod 2003;95:761-6.
11. Vernon SD, Shukla SK, Conradt J, Unger ER, Reeves WC. Analysis of 16S rRNA gene sequences and circulating cell-free DNA from plasma of chronic fatigue syndrome and nonfatigued subjects. BMC Microbiol 2002;2:39.
12. Tsai JC, Teng LJ, Hsueh PR. Direct detection of bacterial pathogens in brain abscesses by polymerase chain reaction amplification and sequencing of partial 16S ribosomal deoxyribonucleic acid fragments. Neurosurgery 2004;55:1154-62.
13. Schnarr S, Putschky N, Jendro MC, Zeidler H, Hammer M, Kuipers JG, Wollenhaupt J. *Chlamydia* and *Borrelia* DNA in synovial fluid of patients with early undifferentiated oligoarthritis: results of a prospective study. Arthritis Rheum 2001;44: 2679-85.
14. Rogers GB, Hart CA, Mason JR, Hughes M, Walshaw MJ, Bruce KD. Bacterial diversity in cases of lung infection in cystic fibrosis patients: 16S ribosomal DNA (rDNA) length heterogeneity PCR and 16S rDNA terminal restriction fragment length polymorphism profiling. J Clin Microbiol 2003;41:3548-58.
15. Senn L, Entenza JM, Greub G, Jaton K, Wenger A, Bille J, et al.

Bloodstream and endovascular infections due to *Abiotrophia defectiva* and *Granulicatella* species. BMC Infect Dis 2006;6:9.
16. Hepburn MJ, Fraser SL, Rennie TA, Singleton CM, Delgado B Jr. Septic arthritis caused by *Granulicatella adiacens:* diagnosis by inoculation of synovial fluid into blood culture bottles. Rheumatol Int 2003;23:255-7.
17. Riede U, Graber P, Ochsner PE. *Granulicatella* (*Abiotrophia*) *adiacens* infection associated with a total knee arthroplasty. Scand J Infect Dis 2004;36:761-4.
18. Cuchacovich R, Japa S, Huang WQ, Calvo A, Vega L, Vargas RB, et al. Detection of bacterial DNA in Latin American patients with reactive arthritis by polymerase chain reaction and sequencing analysis. J Rheumatol 2002;29:1426-9.
19. Gerard HC, Wang Z, Wang GF, El-Gabalawy H, Goldbach-Mansky R, Li Y, et al. Chromosomal DNA from a variety of bacterial species is present in synovial tissue from patients with various forms of arthritis. Arthritis Rheum 2001;44:1689-97.
20. Hornei B, Luneberg E, Schmidt-Rotte H, Maass M, Weber K, Heits F, et al. Systemic infection of an immunocompromised patient with *Methylobacterium zatmanii.* J Clin Microbiol 1999; 37:248-50.
21. Paster BJ, Falkler WA Jr, Enwonwu CO, Idigbe EO, Savage KO, Levanos VA, et al. Prevalent bacterial species and novel phylotypes in advanced noma lesions. J Clin Microbiol 2002;40: 2187-91.

Reprint requests:
Natsuki Segami, DDS, PhD
Professor and Chairman
Department of Oral and Maxillofacial Surgery
Kanazawa Medical University
1-1, Daigaku, Uchinada-machi, Kahoku-gun
Ishikawa 920-0293
Japan
n-segami@kanazawa-med.ac.jp

１．研究課題名：モデル動物を利用した肥満・高脂血症の発がんへの関与とその阻止に関する研究
（研究番号　C2006-3）

２．キーワード：１）大腸がん（colon cancer）
２）肥満（obesity）
３）高脂血症（hyperlipemia）
４）動物モデル（animal model）
５）脂肪肝（fatty liver）

３．研究代表者：杉江　茂幸・医学部・教　授・腫瘍病理学　（病理学Ⅰ）
研究分担者：甲野　裕之・医学部・准教授・腫瘍病理学　（病理学Ⅰ）
堤　　幹宏・奈良医科大学・医学部・教　授・医療情報学
吉谷新一郎・医学部・助　教・消化器外科治療学　（消化器外科学）
山田　泰広・岐阜大学・医学部・講　師・腫瘍病理学

４．研究目的

高脂肪食に代表される食事の欧米化や運動不足などが大腸などでの発がんに対して促進的に働くことが疫学や動物実験から示唆されている。同時に、これらライフスタイルの変化は昨今の肥満者の急増をもたらしており、さらに肥満はいわゆる生活習慣病の根底をなす病態とされている。肥満の発症に関与する遺伝子群(以下肥満関連遺伝子と称する)にはレプチンや peroxisome proliferator-activated receptor γ(PPARγ)などがあり、エネルギー倹約遺伝子とも称される。一般に大腸がんには生活習慣病に属するべき側面が多々あると思われるが、大腸発がんの危険因子としての肥満の重要性あるいは大腸発がんと肥満関連遺伝子との関係についての解析には乏しいのが現状である。一方、肝臓においては、肥満に伴う脂肪肝はよく知られるが、肥満、高脂血症からの非アルコール性脂肪性肝炎 nonalcoholic steatohepatitis (NASH)の増加が近年報告され、肝硬変、肝癌へ進行することやその発症は高率であるとの報告も見られる。従って、肥満者・高脂血症患者における肝がんの発生を阻止することは重要と考えられる。　そこで、本研究では、柑橘類化合物（auraptene、nobiletin）についてレプチン受容体欠損のため高レプチン血症を伴う db マウスや高脂血症を伴う Min マウス等を用いて、azoxymethane（AOM）誘発大腸発がん及び diethylnitrosamine(DEN)ないし 2-amino-3,8-dimethylimidazo[4,5-f]quinoxaline (MeIQx)誘発肝発がんに対する修飾効果を検討し、有意の結果を報告してきた。これにより、肥満阻止、大腸・肝発がん阻止のための基礎的資料を得、柑橘類化合物（auraptene、nobiletin）の肥満に係る発がん阻止物質としての可能性を示した。本年は、最終年でもあり、Target を絞り、主に、脂質低下作用をもつ HMG-CoA 還元酵素阻害薬 Pitavastatin の azoxymethane（AOM）誘発大腸発がんに対する修飾効果を検討し、これにより、肥満阻止、大腸・肝発がん阻止のための基礎的資料を得、HMG-CoA 還元酵素阻害薬 Pitavastatin の肥満に係る発がん阻止物質としての可能性を検討した。また、GSK-3beta の阻害剤であるリチウムクロライド処理により GFP 発現の増加が生体において beta-catenin/tcf 転写活性の検出が可能な 3 つの TOP-GFP マウスの異なるラインを確立し、このレポーターマウスを家族性大腸腺腫症のモデルマウスである Apc Min マウスに交配し、大腸腫瘍での beta-catenin/tcf 転写活性を検討した結果、大腸腫瘍では著しい転写活性の亢進が確認され、この pathway の活性化が大腸発がんに重要な役割を果たすことを報告してきた。本年、canonical

Wnt pathway を可視化するマウスを用いて、高脂肪食摂取による大腸粘膜における Wnt pathway への修飾を検討する。

5．研究計画

1）(Azoxymethane (AOM)、Dextran sodium sulfate (DSS)誘発マウス大腸がんモデルを用いて、脂質低下作用をもつHMG-CoA還元酵素阻害薬Pitavastatinによる大腸発がん修飾作用について検討した。

2）rasH2マウスを使用して、MeIQx誘発発がん及びPhIP誘発発がんへの影響を解析した。

3）Beta-catenin/tcf転写活性を可視化するために、Tcf binding elements (TBE)の下流にEGFPを結合したトランスジーンを持つマウス(TOP-GFPマウス)を作製し、高脂肪食投与によるその活性化を検討する。また、レポーター遺伝子としてGFPの代わりにluciferaseを有するトランスジェニックマウスを作製する。

6．研究成果

1）(Pitavastatinの投与による大腸腺がんの発生頻度に有意な差は認められなかったが、発生個数は有意に抑制された。また、Pitavastatin 未処理群で認められた血清総コレステロール値ならびに血清中性脂肪値の上昇が、Pitavastatin投与群において、未処理対照群レベルまで有意に低下していた。

2）MeIQxは、rasH2マウスに発がん性を示さなかった。PhIPは、rasH2マウス脾臓に血管肉腫の発生を認め、発がん性を示した。肝に対しては発癌性を見出せなかった。

3）TOP-GFP マウスは3つの異なるラインを確立した。このマウスでは、脾臓細胞の初代培養にて、GSK-3betaの阻害剤であるリチウムクロライド処理により、GFP発現の増加が確認され、生体においてbeta-catenin/tcf転写活性の検出が可能であることが分かった。さらに、このレポーターマウスを家族性大腸腺腫症のモデルマウスである Apc Min マウスに交配し、大腸腫瘍でのbeta-catenin/tcf 転写活性を検討した。その結果、大腸腫瘍では著しい転写活性の亢進が確認され、このpathwayの活性化が大腸発がんに重要な役割を果たすことが示唆された。TOP-luciferaseマウス作製は、ES細胞にレポーター遺伝子をランダムインテグレーションさせ、レポーターES細胞を作製後、その ES 細胞をマウスブラストシストにインジェクションした。キメラマウスから、germ line transmissionしたラインを確立した。

7．研究の考察・反省

1、2）マウス炎症性大腸発がんモデルにおける大腸腫瘍発生において、血中脂質成分濃度の変化が深く関わっていることが明らかとなり、同時に、高脂血症を改善することによる大腸がんの発生を予防できる可能性が示唆された。今後、これらの研究成果をもとに、大腸発がん過程における肥満、高脂血症などとの関係をより詳細に解析する必要がある。MeIQx誘発発がん及びPhIP誘発発がんのrasH2マウスへの発がん性は、さらなる改良が必要と考えられた。

3）TOP-GFPマウスは生体においてbeta-catenin/tcf転写活性を検出可能であり、個体レベルでの複雑な生体現象における Wnt pathway 活性化の意義を明らかにするために、非常に有用であると考えられる。期間内には実施できなかったが、今後はこのマウスモデルにおいて高脂肪食投与による、beta-catenin/tcf 転写活性への影響を検討し、大腸発がんへの関与を明らかにしたい。一方で GFP は生体臓器において高いバックグラウンドを示し、本来の転写活性との区別が場合によっ

ては困難であることが明らかとなった。

８．研究発表

１） Hayashi K, Suzuki R, Miyamoto S, Yoshitani S, Kohno H, Sugie S, Takashima S, Tanaka T. Citrus auraptene suppresses azoxymethane-induced colonic preneoplastic lesions in C57BL/KsJ-db/db mice. Nutr Cancer 2007; 58: 75-84.

２）Yasui Y, Suzuki R, Miyamoto S, Tsukamoto T, Sugie S, Kohno H, Tanaka T. A lipophilic statin, pitavastatin, suppresses inflammation-associated mouse colon carcinogenesis. Int J Cancer 2007; 121: 2331-2339.

３） Kohno H, Totsuka Y, Yasui Y, Suzuki R, Sugie S, Wakabayashi K, Tanaka T. Tumor-initiating potency of a novel heterocyclic amine, aminophenylnorharman in mouse colonic carcinogenesis model. Int J Cancer 2007; 121: 1659-1664.

NUTRITION AND CANCER, *58*(1), 75–84

Citrus Auraptene Suppresses Azoxymethane-Induced Colonic Preneoplastic Lesions in C57BL/KsJ-*db/db* Mice

Kei Hayashi, Rikako Suzuki, Shingo Miyamoto, Yoshitani Shin-ichiroh, Hiroyuki Kohno, Shigeyuki Sugie, Shigeki Takashima, and Takuji Tanaka

Abstract: *The current study was designed to investigate whether dietary citrus auraptene (AUR) suppresses the development of azoxymethane (AOM)-induced colorectal preneoplastic lesions in C57BL/KsJ-db/db (db/db) mice with obese and diabetic phenotypes. Female db/db and wild (+/+) mice were divided into the AOM + AUR, AOM alone, AUR alone, and the untreated groups in each phenotype. AOM was given 3 weekly intraperitoneal injections (10 mg/kg bw). AUR (250 ppm) was given in diet during the study (for 10 wk). Dietary AUR significantly reduced the number of aberrant crypt foci (ACF) and β-catenin-accumulated crypt (BCAC) in both phenotypes. The treatment also lowered cell proliferation activity and increased apoptotic cells in both lesions. Our findings indicate that dietary AUR is able to suppress the early phase of colon carcinogenesis in both phenotypes, suggesting possible application of AUR as a chemopreventive agent in both the high-risk and general populations for colorectal cancer.*

Introduction

Numerous epidemiological results suggest that obesity is a risk factor for colon cancer (1,2). There are several studies to investigate possible mechanism for this (3,4). Obesity is a complex, heterogeneous, and multi-factorial syndrome resulting from both genetic susceptibility and environmental factors (5). Besides obesity, it is well known that several factors, including a high fat and low-fiber diet (6), low physical activity (7), inflammatory bowel diseases (8), or hereditary disorders such as familial adenomatous polyposis and non-polyposis syndrome (9), increase the risk for development of colorectal cancer (CRC). For fighting this malignancy, we tried to find natural compounds that are capable to effectively inhibit colon carcinogenesis in a series of pre-clinical studies.

As one of the possible cancer chemopreventive agents, we proposed citrus auraptene (AUR) that is able to inhibit carcinogenesis in various tissues (10–13), including colon (14–17). A prenyloxycoumarin, AUR is a secondary metabolite, mainly found in plants belonging to the families of Rutaceae and Umbelellierae. Several coumarins, including AUR were shown to possess valuable pharmacological properties. These were reported to have anti-inflammatory activity (18). AUR significantly attenuated the lipopolysaccharide-induced protein expression of inducible nitric oxide synthase and cyclooxygenase-2, with decreases in production of nitric anion and prostaglandin E_2, and yet suppressed the release of tumor necrosis factor-α and IκB degradation (19,20). Furthermore, AUR possesses anti-oxidative activity and suppresses lipid peroxidation in rat colon exposed to a colonic carcinogen azoxymethane (AOM) (14,21). AUR is able to induce the activity of detoxifying enzymes without affecting phase I drug metabolizing enzymes in mouse liver (22). In addition, AUR can enhance immune system by affecting macrophage function and cytokine production in mice (23). AUR also suppress experimental lung metastasis of melanoma cells in mice (24). More recently we have found AUR suppresses *β-cetenine* gene mutations in chemically-induced hepatocarcinogenesis in rats (25) and inhibits the expression of matrix metalloproteinase-7 (matrilysin 1), which plays essential roles in cancer progression, in the human colorectal adenocarcinoma cell line HT-29 (26). A variety of biological activities of AUR can be thus responsible for its cancer chemopreventive ability. However, in our series of preclinical chemopreventive studies we used in vitro assays and an experimental animal model, in which colonic carcinogens, such as AOM, were applied to rodents, assuming general population.

C57BL/KsJ-*db/db* (*db/db*) mice are genetically altered models with phenotypes of obesity and diabetes mellitus (27). Disruption of the leptin receptor (Ob-R) gene in the *db/db* mice leads to over-expression of leptin in the adipose tissue and a concomitantly high concentration of leptin in the blood of the mice (28,29). It is widely accepted that leptin

Kei Hayashi, Yoshitani Shin-ichiroh, and Shigeki Takashimaare affiliated with Department of Surgical Oncology, Oncologic Pathology, Kanazawa Medical University, 1-1 Daigaku, Uchinada, Ishikawaa 920-0293. Rikako Suzuki, Shingo Miyamoto, Hiroyuki Kohno, Shigeyuki Sugie, and Takuji Tanaka are affiliated with Department of Oncologic Pathology, Kanazawa Medical University, 1-1 Daigaku, Uchinada, Ishikawaa 920-0293. Shingo Miyamoto is also affiliated with Division of Food Science and Biotechnology, Graduate School of Agriculture, Kyoto University, Kyoto 606-8502, Japan.

functions as a satiety factor through Ob-R, which is mainly expressed in the hypothalamus (29). Because of a deficiency of the leptin-mediated satiety signaling, abnormal dietary habits such as hyperphagia occur in homozygous *db/db* mice, resulting in complex phenotypes. It is now well-established that leptin not only interacts with pathways in the central nervous system, but also functions in the peripheral tissues as a mediator of energy expenditure, a permissive factor for puberty and a signal of metabolic status (30). Interestingly, some lines of evidence suggest that leptin in the periphery behaves as a growth factor in lung (31), breast (32), and colonic tissues (33). Although plausible role of leptin in tumorigenesis remains undetermined, there have been several studies suggesting the leptin-related pathway as a possible modulator in neoplastic development (34–36). We recently reported that the *db/db* mice are susceptible to colon carcinogenesis (3).

In the current study we conducted a short-term assay to examine whether dietary AUR can inhibits the occurrence of AOM-induced preneoplastic lesions, aberrant crypt foci (ACF) (37), and β-catenin-accumulated crypt (BCAC) (38) for CRC in genetically obese *db/db* mice, and compared the effects on +/+ female mice. We also examined the effects of AUR on clinical chemistry in both phenotypes, since certain serum chemistry is related to the occurrence of CRC (39,40). Since modification of cell proliferation activity and apoptosis in the non-lesional and lesional areas in the organ for cancer chemoprevention (41), the effects of AUR on cell proliferation activity and apoptotic index were analyzed immunohistochemically. The main goal of this study was to assess the involvement of obesity-related events such as hyper-leptinemia in colon carcinogenesis and to find promising cancer chemopreventive agents for such a high-risk group of CRC.

Materials and Methods

Animals, Diets, and Carcinogen

Thirty female *db/db* and 30 +/+ mice (4 wk of age) for the study were purchased from the Jackson Laboratories (Bar Harbor, ME). CRF-1 (Oriental Yeast Co., Tokyo, Japan) was used as a basal diet, which consists of 5.7% fat, 22.4% protein, 6.6% minerals, 3.1% fiber, and 62.3% carbohydrate and others (~3.59 kcal/g). The major fatty acids present in CRF-1 were linoleic acid, oleic acid and palmitic acid. AOM was obtained from Sigma (St. Louis, MO). They were housed in a holding room under controlled conditions of a 12 h light/dark cycle, 23 ± 2°C room temperature and 50 ±10% relative humidity. AUR (99.9% purity) was synthesized as described previously (12). Diet containing AUR at a dose level of 250 ppm was made by mixing AUR with powdered CRF-1 every week during the study and stored in the cold room (<4°C). Diets and water during an experimental period were freely available.

Experimental Procedures

Animals of each phenotype was divided into 4 groups: the AOM + AUR group (10 mice), AOM alone group (10 mice), AUR alone group (5 mice), and untreated group (5 mice). They were given 3 weekly intraperitoneal injections of AOM (10 mg/kg body weight). They also fed the AUR-containing diet for 10 wk (entire experimental period). At sacrifice (10 wk after the start of the study), we determined the frequency of ACF and BCAC in the colon. At autopsy, colons of all the mice were removed, cut open longitudinally and fixed in 10% buffered formalin. After removing the rectal sides (2.0 cm from the anus), the colons were cut into two portions (distal and proximal) and the distal colons were used in this study. BCAC was quantified in the rectal mucosa after immunohistochemical staining for β-catenin, and ACF were counted in the remaining parts of the colon that were stained with methylene blue. At autopsy, the weights for pancreas, liver, kidney, and peritoneal adipose tissue were measured.

Counting the Number of Colonic ACF and BCAC

The ACF and BCAC were determined according to the standard procedures that areroutinely used in our and other laboratories (15,38). At necropsy, the colons were flushed with saline, excised, cut open longitudinally along the main axis, and then washed with saline. They were cut, placed on the filter paper their mucosal surface up, and then fixed in 10% buffered formalin for at least 24 h. The fixed colons were stained with methylene blue (0.5% in distilled water) for 20 seconds, dipped in distilled water, and placed on a microscope slide to count the ACF. After counting the ACF, the distal parts (1 cm from the anus) of the colon were cut in order to count the number of BCAC. To identify BCAC intramucosal lesions, the colonic mucosa (mean area: 0.75 cm^2/colon) was embeddedin paraffin, and then a total of 20 serial sections (4 μm thick each) per mouse were made by an *en face* preparation (38). For each case, twoserial sections were used to analyze the BCAC.

Immunohistochemistry for β-Catenin, Cell Proliferation, and Apoptosis

Four serial sections (4 μm thickness) were made from paraffin-embedded blocks. One section was subjected to hematoxylin and eosin (H & E) staining for histopathology and the others for immunohistochemistry of β-catenin, proliferating cell nuclear antigen (PCNA), and apoptosis.

Immunohistochemistry for β-catenin was performed on 4-μm-thick paraffin-embedded sections from the distal segments of the colons, using the labeled streptavidin-biotin method (LSAB Kit; Dako, Glostrup, Denmark) with microwave accentuation. The paraffin-embedded sections were heated for 30 min at 65°C, deparaffinized in xylene, and rehydrated through graded alcohols at room temperature. A 0.05 M Tris-HCl buffer (pH 7.6) was used to prepare solutions and for washes between various steps. The sections were treated for 40 min at room temperature with 2% bovine serum albumin and incubated overnight at 4°C with a primary antibody against β-catenin protein (diluted 1:1000, catalog no. 610154, BD Transduction Laboratories, Lexington, KY). Horseradish peroxidase activity was visualized by treatment

with H_2O_2 and diaminobenzidine for 5 min. Negative control sections were immunostained without the primary antibody. Immunoreactivity was regarded as positive if apparent staining was detected in the cytoplasm and/or nuclei to determine the BCAC.

For PCNA immunohistochemistry, formalin-fixed, paraffin-embedded distal colon sections were subjected to deparaffinization and dehydration prior to quenching of endogenous peroxidase activity (1.5% H_2O_2 in methanol for 20 min). An antigen-unmasking step was done by placing the slides in a pressure cooker containing 0.01 M sodium citrate (pH 6.0) for 10 min. The sections were incubated for 60 min with the primary mouse anti-rat PCNA monoclonal antibody (Clone PC-10, DakoCytomation, Cat no. M0879) at a dilution of 1:1500 in 10% goat serum. Secondary antibody, biotinylated goat anti-mouse IgG (Cat no. BA-2000, Vector Laboratories, Burlingame, CA) was applied for 30 min in a 1:500 dilution. Slides were processed with the ABC reagent from Vectastain Elite (Vector Laboratories) using DAB as the substrate. Sections were counterstained with hematoxylin. In the distal colonic mucosa without lesions from 5 mice of each group, 20 fields, randomly selected from each slide, were analyzed at ×400 magnification. PCNA-positive cell nuclei were determined in 10 ACF each from the AOM + AUR and AOM alone groups of each phenotype. Also, PCNA-positive cell nuclei were analyzed in 5 BCAC from the AOM + AUR group and 12 BCAC from the AOM alone group from each phenotype. Cells staining positive for PCNA were scored as a percentage of total cells in each field or lesion.

Levels of apoptosis in distal colon tissue were determined by the TdT-mediated dUTP nick-end labeling (TUNEL) method. Four-μm formalin-fixed, paraffin-embedded tissue sections from the distal colons were processed according to manufacturer's instructions using Apoptosis in situ Detection Kit Wako (Cat. No. 298-60201, Wako Pure Chemical Industries, Ltd., Osaka, Japan). The kit is based on TUNEL procedure. Appropriate positive and negative controls for determining the specificity of staining were generated. Negative controls were processed in the absence of the terminal deoxynucleotidyl transferase (TdT) enzyme in the reaction buffer. Sections of colon tissue digested with nuclease enzyme and colon lymphoid nodules, which are known to exhibit high rates of apoptosis, were used as positive controls. Color was developed with the peroxidase substrate DAB, and sections were counterstained with hematoxylin. For each section, 20 fields of normal-appearing tissue were randomly selected and photographed at ×400 magnification. The numbers of apoptotic cells per field of normal mucosa from 5 mice of each group of both phenotypes were counted and recorded as a percentage of total cells in each field or lesion. Also, randomly chosen 10 ACF each from the AOM + AUR and AOM alone groups, 5 BCAC each from the AOM + AUR group of both phenotypes, and 12 BCAC each from the AOM group of both phenotypes were counted for apoptosis. The apoptotic index was calculated by dividing the total number of apoptotic cells by the number of atypical cells that consist of ACF or BCAC, and was expressed the percentage.

Measurement of Serum Glucose, Leptin, Total Cholesterol, and Triglycerides Levels

At sacrifice, blood to measure the serum concentrations of glucose, leptin, total cholesterol, and triglycerides was collected from all mice each of genotypes. They were starved overnight prior to blood collection for clinical chemistry. The serum glucose level was measured enzymatically using the hexokinase method. The serum triglycerides were assayed by enzymatic hydrolysis with lipase. Serum cholesterol was determined enzymatically using cholesterol esterase and cholesterol oxidase. Serum concentration of leptin was measured by an enzyme immunoassay according to the manufacturer's protocol (R&D Systems, Minneapolis, MN).

Statistical Analysis

Where applicable, data were analyzed using Tukey-Kramer multiple comparison test (GraphPad Instat version 3.05, GraphPad Software, San Diego, CA) with $P < 0.05$ as the criterion of significance.

Results

General Observation

Mean daily intakes of diet of mice of all groups in the *db/db* mice were about 1.30 times greater than those of the +/+ mice. Dietary feeding with AUR did not cause clinical symptoms including toxicity in each phenotype. The mean body, liver, kidney, and peritoneal adipose tissue weights in all groups of *db/db* mice were significantly greater than those of respective groups of +/+ mice, regardless of treatment ($P < 0.001$ for each comparison, data not shown). In the *db/db* mice, the mean body weight in the AOM + AUR group (39.6 ± 3.8 g, $P < 0.01$) was significantly lower than that of the AOM group (44.0 ± 1.7 g). The mean pancreas weights of the AOM + AUR, AOM alone, and untreated groups of *db/db* mice were relatively lower than +/+ mice without statistical significance. Interestingly, the pancreas ($P < 0.001$) weight in the AOM + AUR group (0.13 ± 0.02 g, $P < 0.001$) of the *db/db* mice were significantly lower than that of the AOM group (0.18 ± 0.03 g). The mean weights for liver, kidney, and peritoneal fat tissue did not significantly differ among the groups of the *db/db* mice. Dietary administration of AUR did not affect the weights of body, liver, kidney, pancreas, and peritoneal fat tissue in the +/+ mice.

Frequencies of ACF and BCAC

Data on ACF (Fig. 1A and B) counting are listed in Table 1. ACF developed in *db/db* and +/+ mice that received AOM injections, and the value of the AOM alone group was significantly greater in *db/db* mice when compared to that of +/+ mice ($P < 0.001$). Dietary feeding with AUR significantly lowered the numbers of total ACF and large ACF with 4 or more crypts in the *db/db* mice ($P < 0.001$) and +/+ mice ($P < 0.001$) when compared to those of the AOM

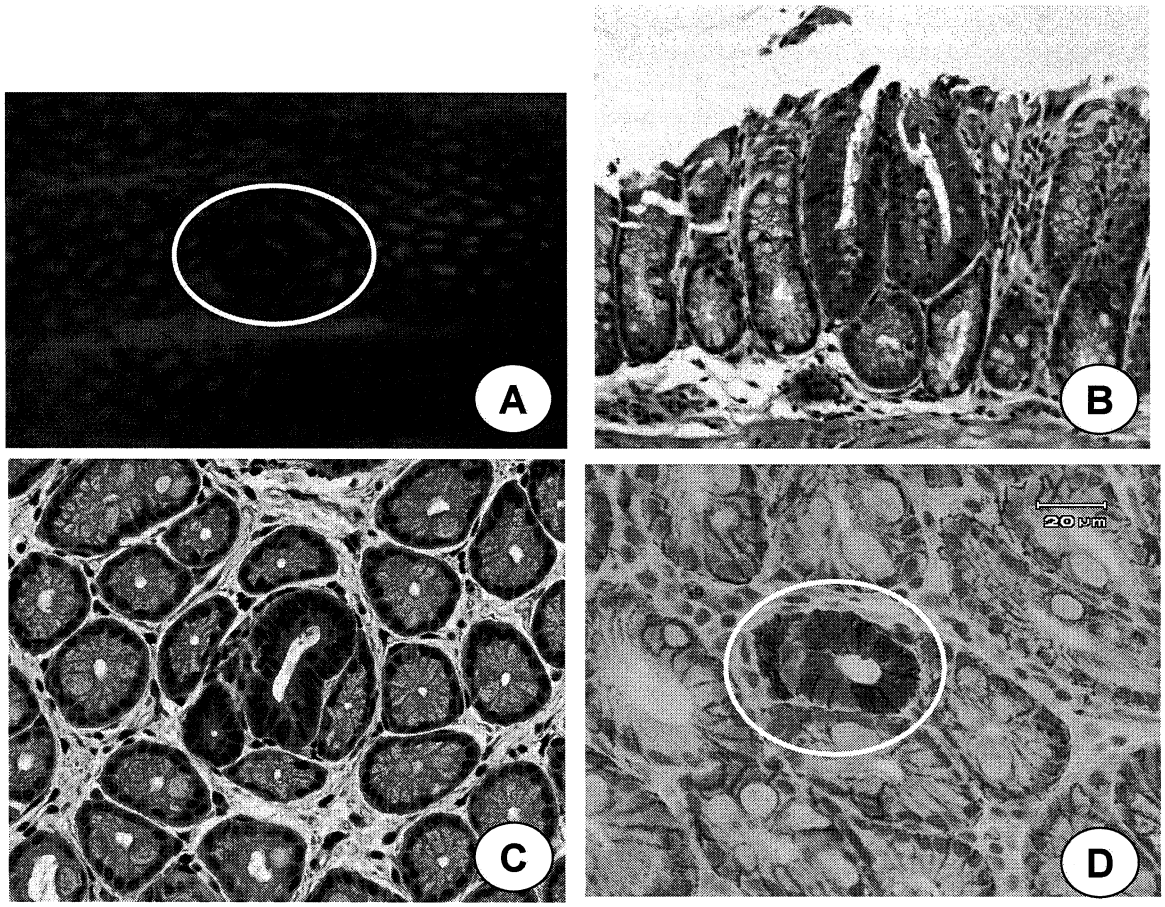

Figure 1. Morphology of preneoplastic lesions, ACF and BCAC, for CRC in the *db/db* mice that received AOM. (A) a large ACF (circled) consists of 4 aberrant crypts is observed methylene-blue stained colonic mucosa; (B) Histopathology of an ACF consists of 2 aberrant crypts in H& E-stained section; (C) a BCAC (circled) found in H & E-stained section. Cells in a BCAC have relatively large and hyperchromatic nuclei with mitoses; and (D) a BCAC found in the section of β-catenin immunohistochemistry. Cells in BCAC strongly express immunoreactivity for β-catenin in their cell membrane, cytoplasm, and some nuclei. Original magnification: (A) ×4; (B) ×10; (C) ×10; and (D) ×20.

alone group. Similarly the number of BCAC (Fig. 1C and D) in the AOM alone group of *db/db* mice was larger than that of the +/+ mice ($P < 0.05$), as shown in Fig. 2. The values of the AOM + AUR group of both phenotypes were significantly smaller than those of the AOM alone group ($P < 0.001$ for the *db/db* mice and $P < 0.01$ for the +/+ mice). ACF and BCAC were not present in the AUR alone and untreated groups of each phenotype.

PCNA-Labeling Index

As shown in Fig. 3A, PCNA-labeling index of non-lesional crypts in the *db/db* mice was greater than that of +/+ mice, regardless of the treatment: the labeling indices of the AOM alone and AOM + AUR groups were significantly larger than those in +/+ mice ($P < 0.001$ and $P < 0.01$, respectively). In the *db/db* mice, the index of the AOM + AUR group was significantly smaller than that of the AOM alone group ($P < 0.01$). The PCNA labeling index of ACF of the AOM alone group in the *db/db* mice was significantly larger than that of +/+ mice (Fig. 3B, $P < 0.05$). AUR feeding significantly lowered the index in the *db/db* mice ($P < 0.05$). As for the PCNA labeling index of BCAC, feeding with AUR significantly reduced the index in both the +/+ and *db/db* mice (Fig. 3C, $P < 0.001$).

Apoptotic Index

The data on the apoptotic index of non-lesional crypts, ACF, and BCAC are illustrated in Fig. 4. The apoptotic index of the non-lesional crypts of the AOM alone group in the *db/db* mice was significantly larger than that of +/+ mice (Fig. 4A, $P < 0.05$). In the AOM + AUR group of the *db/db* mice was significantly smaller than that of the AOM alone group (Fig. 4A, $P < 0.001$ each). AUR feeding significantly elevated the index of ACF that developed in both the phenotypes (Fig. 4B, $P < 0.001$). Also, the index of BCAC in the AOM + AUR group was significantly higher than that of the AOM alone group of both the phenotypes (Fig. 4C, $P < 0.001$ each).

Table 1. Effect of auraptene on the development of ACF induced by AOM.

Phenotype	Treatment (number of mouse examined)	Total ACF/colon	1 crypt	2 crypts	3 crypts	4 or more crypts	Total ACs/colon
db/db	AOM→250 ppm AUR (10)	30.6±8.7	7.5±2.7	7.4±2.6	8.4±2.4	7.3±2.3	84.3±24.2
		(p<0.001)	(p<0.001)		(p<0.001)	(p<0.001)	(p<0.001)
	AOM alone (10)	80.4±14.6	14.0±3.2	11.7±3.0	17.2±4.0	37.5±6.9	294.3±53.1
		(p<0.001)			(p<0.001)	(p<0.001)	(p<0.001)
	250 ppm AUR (5)	0	0	0	0	0	0
	None (5)	0	0	0	0	0	0
Wild	AOM→250 ppm AUR (10)	29.1±8.2	7.7±2.0	7.8±3.3	6.1±2.1	7.5±4.1	78.7±30.8
		(p<0.001)	(p<0.01)	(p<0.05)	(p<0.01)	(p<0.001)	(p<0.001)
	AOM alone (9)	58.8±6.8	12.6±2.2	13.3±5.1	11.0±2.6	21.9±2.5	193.2±24.0
	250 ppm AUR (4)	0	0	0	0	0	0
	None (5)	0	0	0	0	0	0

Statistical analysis was done by ANOVA, Tukey-Kramer multiple comparison test.

Serum Levels of Total Cholesterol, Triglycerides, Glucose, and Leptin

As illustrated in Fig. 5, all the measurements (total cholesterol, triglycerides, glucose, and leptin) were significantly larger in the *db/db* mice than in the +/+ mice ($P < 0.001$ or $P < 0.01$). Among the measurements in the *db/db* mice, serum concentration of triglycerides in the AOM + AUR group was significantly smaller than that of the AOM alone group ($P < 0.01$, Fig. 5B). Also, the value of the AUR alone group was significantly lower than that of the untreated group ($P < 0.001$, Fig. 5B). Dietary AUR did not affect the chemical profiles other than triglycerides measured in the *db/db* mice (Fig. 5A, C, and D). In the +/+ mice, there were no significant differences on all the measurements among the groups (Fig. 5A, B, C, and D).

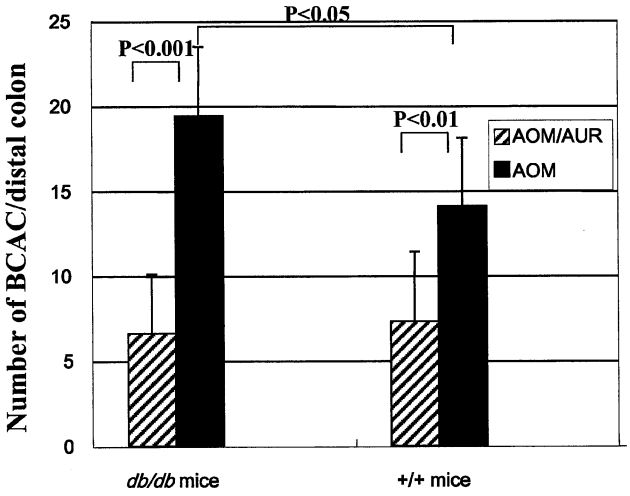

Figure 2. Frequencies of BCAC in the AOM + AUR and AOM alone groups in the *db/db* and +/+ mice. The frequency of the AOM group is significantly greater in the *db/db* mice than in the +/+ mice ($P < 0.05$). Dietary feeding with AUR significantly reduced the frequency in both phenotypes ($P < 0.001$ for the *db/db* mice and $P < 0.01$ for the +/+ mice).

Discussion

Our results in the current study clearly indicated that dietary AUR is able to suppress the development of precursor lesions, ACF and BCAC, for CRC in obese mice as well as wild type mice. The inhibition is considered to be cause by lowering serum triglycerides, inducing apoptosis, and/or reducing cell proliferation. In addition, the results of the current study confirmed the high susceptibility of the obese/diabetic *db/db* mice to AOM-induced colon carcinogenesis (3,42).

The high susceptibility in the *db/db* mice might be related to the increases in the high cell proliferation activity in the non-lesional crypts (Fig. 4A) that may be related obese and high levels of serum cholesterol, triglycerides, glucose, insulin, and leptin, thus suggesting a positive association

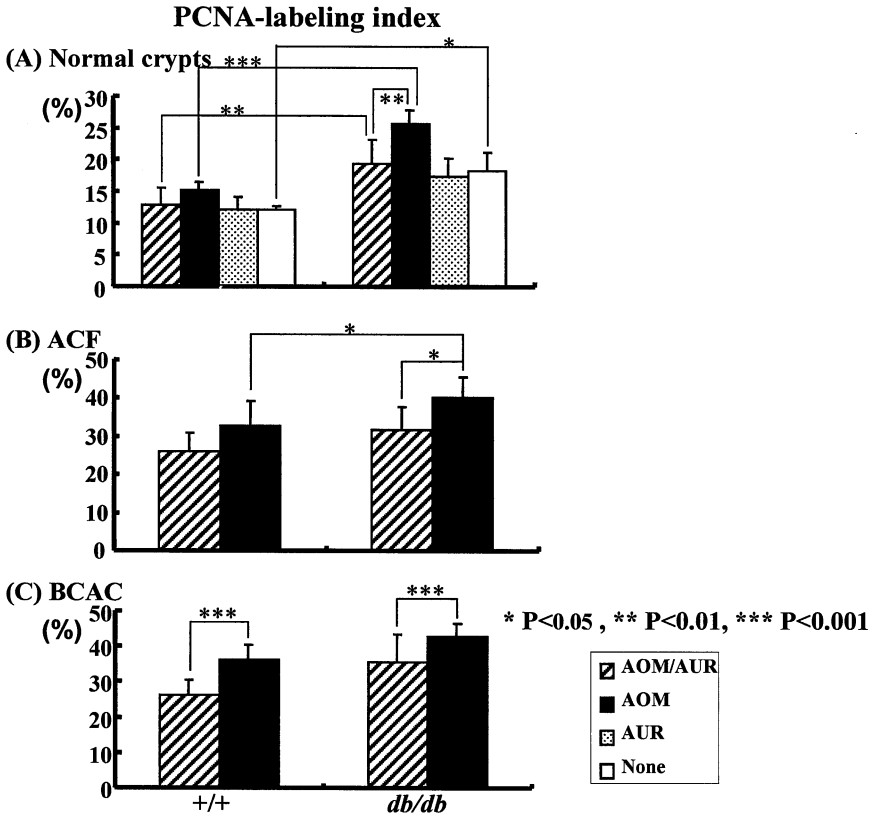

Figure 3. PCNA-labeling indices in the normal crypts, ACF, and BCAC in the colon of *db/db* and +/+ mice. (A) In the normal crypts, PCNA labeling indices of the AOM/AUR, AOM alone, and untreated groups of *db/db* mice were significantly greater than those of +/+ mice. While AUR feeding did not affect the PCNA-labeling index of the normal crypts of +/+ mice, the treatment significantly lowered the index in *db/db* mice. (B) The PCNA-labeling index of ACF of *db/db* mice was greater than that of +/+ mice, and feeding with AUR significantly decreased the index of each phenotype. (C) Feeding with AUR significantly lowered the PCNA-labeling index of BACA that developed in each phenotype. $*P < 0.05$, $**P < 0.01$, and $***P < 0.001$.

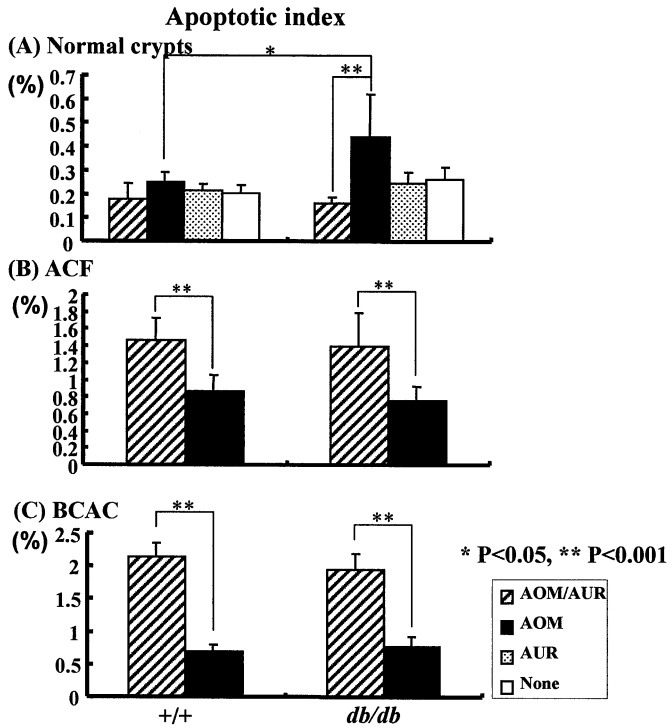

Figure 4. Apoptotic indices in the normal crypts, ACF, and BCAC in the colon of *db/db* and +/+ mice. (A) In the normal crypts, apoptotic index of the AOM alone group of *db/db* mice was significantly greater than that of +/+ mice. While AUR feeding did not affect the apoptotic index of the normal crypts of +/+ mice, the treatment significantly lowered the index in *db/db* mice. (B) AUR feeding significantly increased the apoptotic indices of ACF in +/+ and *db/db* mice. (C) The treatment with AUR also significantly increased the index of BCAC of mice with each phenotype. $*P < 0.05$ and $**P < 0.001$.

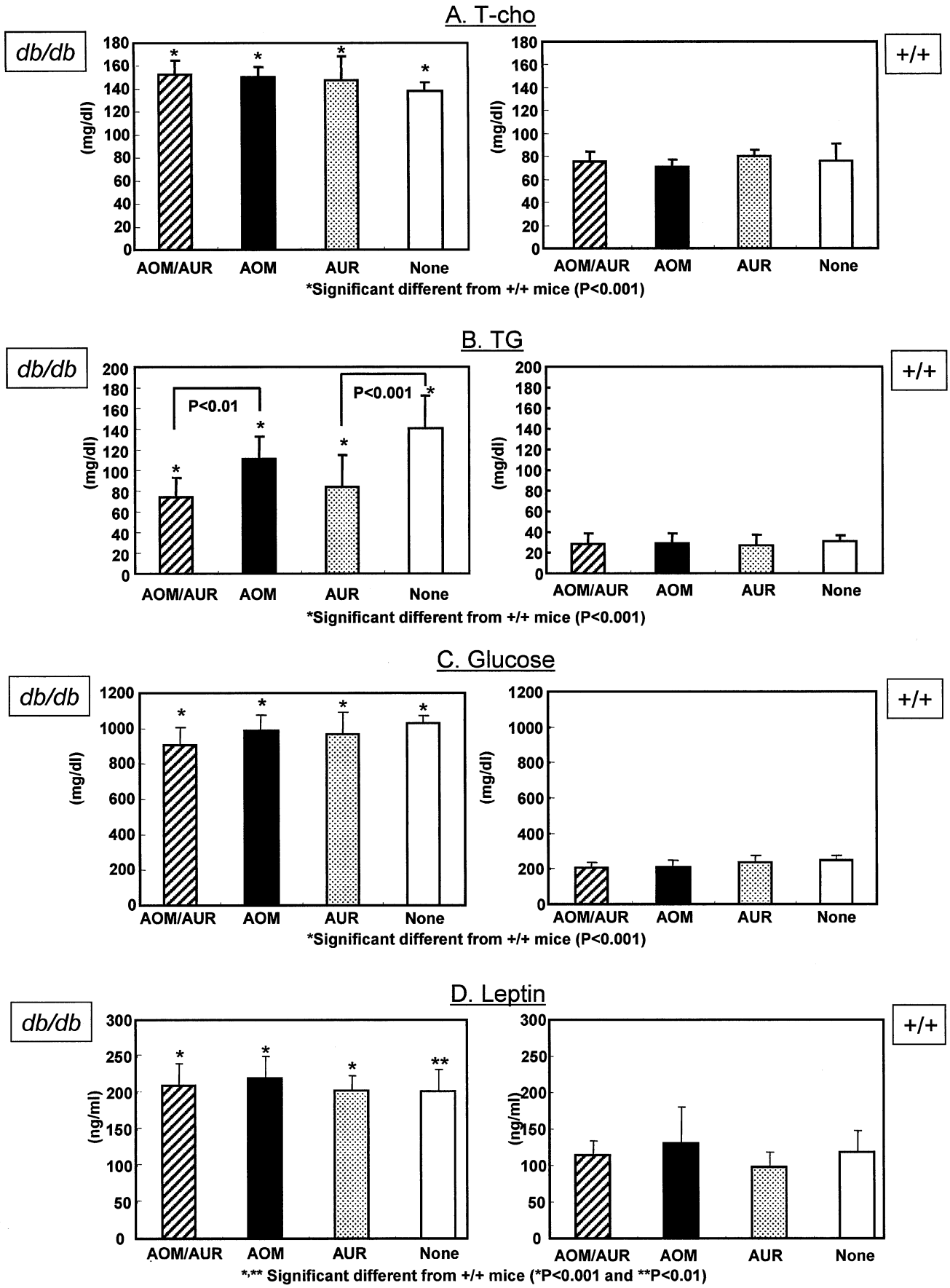

Figure 5. Clinical chemical profiles for (A) total cholesterol, (B) triglycerides, (C) glucose, and (D) leptin the serum of the *db/db* and +/+ mice. All the measurements were high in the *db/db* mice regardless of the treatments. AUR feeding significantly lowered the serum levels of triglycerides in the *db/db* mice.

between obesity/diabetes and colon tumorigenesis. Our findings also suggest that insulin resistance involves CRC development (43), although we were not able to determine serum insulin in this study because we did not get enough serum volumes to measure. The main purpose of the current study was to investigate the effect of AUR on the early phase of AOM-induced colon carcinogenesis in the *db/db* mice. Since ACF (37) and BCAC (38,44) are considered to be putative precursor lesions of colonic adenocarcinoma, the results described clearly indicate the inhibitory effects of the dietary administration of AUR on the early phase of colon carcinogenesis in the *db/db* mice as well as the +/+ mice.

In this study, all the serum measurements of total cholesterol, triglycerides, glucose, and leptin were greater in the *db/db* mice than those of +/+ mice, thus suggesting that these measurements may contribute to the high susceptibility of *db/db* mice to AOM-induced colon tumorigenesis. However, interestingly among the chemical profiles, only the triglycerides level lowered by feeding with AUR, and this was correlated with lower incidences of ACF and BACA in the *db/db* mice. These findings may suggest that a high level of serum triglycerides is the most important biological effect for developing colonic tumors in *db/db* mice, and a modification (lowering) of this measurement may thus lead the inhibition of colon tumorigenesis. In humans, a positive association between the serum triglycerides level and the risk of CRC development was reported (45). This association was also suspected by the findings in animal experiments (39,40,46), in which model animals for human familial adenomatous polyposis were used, Our recent study indicated that dietary citrus segment membrane (CUSM) is able to suppress the occurrence of BCAC in male *db/db* mice by lowering their serum triglycerides level (42).

Feeding a high fat diet, which is implicated to play a role in the stimulation of colonic cryptal cell proliferation while also promoting colon carcinogenesis (47), increases the circulating leptin level (48). In addition, dietary fiber that is known to suppress colon carcinogenesis (49) is reported to decrease serum leptin concentration and to lower the degree of cryptal cell proliferation (50). In this study, AUR feeding did not significantly affect serum leptin levels in the *db/db* mice, but the feeding reduced immunohistochemical expression of insulin-like growth factor-1 receptor (IGF-1R) in BCAC developed in the *db/db* mice (data not shown). Since insulin and IGF axis may be related to CRC development (51), IGF-1 may be able to influence both pre-malignant and cancer development. Insulin resistance is associated with hyper-insulinemia, increased levels of growth factors including IGF-1 (52).

In the current study, feeding with AUR reduced cell proliferation activity in the BCAC of +/+ mice and non-lesional crypts, ACF, and BCAC of *db/db* mice. In addition, AUR treatment induced apoptotic cells in the ACF and BCAC that developed in +/+ and *db/db* mice, suggesting that AUR is able to inhibit progression of precursor lesions for CRC, ACF, and BCAC, through inducing apoptosis and lowering cell proliferation. Many chemicals that are candidates for cancer chemopreventive agents are able to modulate apoptosis and cell proliferation activity in target tissues (14,41). Hence our findings on apoptosis and cell proliferation are important for clinical application of AUR as one of the cancer chemopreventive agents for obese.

In summary, our data provide further evidence that citrus AUR is able to inhibit the early phase of colon carcinogenesis in the genetically altered obese mice as well as the wild rodents. The effects may be caused by lowering lipid profiles in conjunction with modification of apoptosis and cell proliferation. Our finding also suggest that *db/db* mice are susceptible to AOM-induced carcinogenesis (3,42) and such *db/db* mice can thus be an appropriate animal model for the high risk group for CRC, such as obesity/diabetes (1,4). Since current study focused on the effects of obesity and AUR on the colonic pre-malignancies, further studies focusing the detailed mechanisms of inhibitory effects of AUR on the development of CRC in the *db/db* mice should be carried out for the prevention and treatment of the colonic malignancies associated with these conditions.

Acknowledgments and Notes

We express our thanks to the staff of the Research Animal Facility. This study was supported by the Grant-in-Aid for Cancer Research from the Ministry of Health, Labour and Welfare of Japan; the Grant-in-Aid for the 3rd Term for a Comprehensive 10-year Strategy for Cancer Control from the Ministry of Health, Labour and Welfare of Japan; the Grants-in-Aid for Scientific Research (nos. 00120029 and 18592076) from the Ministry of Education, Culture, Sports, Science and Technology of Japan; and the grants (H2006-6 and C2006-3) from Kanazawa Medical University. Address correspondence to Shingo Miyamoto, Department of Oncologic Pathology, Kanazawa Medical University, 1-1 Daigaku, Uchinada, Ishikawa 920-0293, Japan. E-mail: takutt@kanazawa-med.ac.jp.

References

1. Murphy TK, Calle EE, Rodriguez C, Kahn HS, and, Thun MJ: Body mass index and colon cancer mortality in a large prospective study. *Am J Epidemiol* **152,** 847–854, 2000.
2. Bergstrom A, Pisan P, Tenet V, Wolk A, and Adami H-O: Overweight as an avoidable cause of cancer in Europe. *Int J Cancer* **91,** 421–430, 2001.
3. Hirose Y, Hata K, Kuno T, Yoshida K, Sakata K, et al.: Enhancement of development of azoxymethane-induced colonic premalignant lesions in C57BL/KsJ-*db/db* mice. *Carcinogenesis* **25,** 821–825, 2004.
4. John BJ, Irukulla S, Abulafi AM, Kumar D, and Mendall MA: Systematic review: adipose tissue, obesity and gastrointestinal diseases. *Aliment Pharmacol Ther* **23,** 1511–1523, 2006.
5. Bray GA: The underlying basis for obesity: relationship to cancer. *J Nutr* **132,** 3451–3455, 2002.
6. Willett CW: Diet and cancer. *Oncologist* **5,** 393–404, 2000.
7. Friedenreich CM and Orenstein MR: Physical activity and cancer prevention: etiologic evidence and biological mechanisms. *J Nutr*, **132,** 3456S–3455S, 2002.
8. Campbell S and Ghosh S: Ulcerative colitis and colon cancer:strategies for cancer prevention. *Dig Dis* **20,** 38–48, 2002.
9. Jass JR: Familial colorectal cancer: pathology and molecular characteristics. *Lancet Oncol* **1,** 220–226, 2000.
10. Kawabata K, Tanaka T, Yamamoto T, Hara A, Murakami A, et al.: Suppression of N-nitrosomethylbenzylamine-induced rat esophageal

tumorigenesis by dietary feeding of auraptene. *J Exp Clin Cancer Res* **19,** 45–52, 2000.
11. Murakami A, Kuki W, Takahashi Y, Yonei H, Nakamura Y, et al.: Auraptene, a citrus coumarin, inhibits 12-*O*-tetradecanoylphorbol-13-acetate-induced tumor promotion in ICR mouse skin, possibly through suppression of superoxide generation in leukocytes. *Jpn J Cancer Res* **88,** 443–452, 1997.
12. Sakata K, Hara A, Hirose Y, Yamada Y, Kuno T, et al.: Dietary supplementation of the citrus antioxidant auraptene inhibits N,N-diethylnitrosamine-induced rat hepatocarcinogenesis. *Oncology* **66,** 244–252, 2004.
13. Tanaka T, Kawabata K, Kakumoto M, Matsunaga K, Mori H, et al.: Chemoprevention of 4-nitroquinoline 1-oxide-induced oral carcinogenesis by citrus auraptene in rats. *Carcinogenesis* **19,** 425–431, 1998.
14. Tanaka T, Kawabata K, Kakumoto M, Hara A, Murakami A, et al.: Citrus auraptene exerts dose-dependent chemopreventive activity in rat large bowel tumorigenesis: the inhibition correlates with suppression of cell proliferation and lipid peroxidation and with induction of phase II drug-metabolizing enzymes. *Cancer Res* **58,** 2550–2556, 1998.
15. Tanaka T, Kawabata K, Kakumoto M, Makita H, Hara A, et al.: Citrus auraptene inhibits chemically induced colonic aberrant crypt foci in male F344 rats. *Carcinogenesis* **11,** 2155–2161, 1997.
16. Tanaka T, Makita H, Kawabata K, Mori H, Kakumoto M, et al.: Chemoprevention of azoxymethane-induced rat colon carcinogenesis by naturally occurring flavonoids diosmin and hesperidin. *Carcinogenesis* **18,** 957–965, 1997.
17. Kohno H, Suzuki R, Curini M, Epifano F, Maltese F, et al.: Dietary administration with prenyloxycoumarins, auraptene and collinin, inhibits colitis-related colon carcinogenesis in mice. *Int J Cancer* **118,** 2936–2942, 2006.
18. Curini M, Epifano F, Maltese F, Marcotullio MC, Tubaro A, et al.: Synthesis and anti-inflammatory activity of natural and semisynthetic geranyloxycoumarins. *Bioorg Med Chem Lett* **14,** 2241–2243, 2004.
19. Murakami A, Matsumoto K, Koshimizu K, and Ohigashi H: Effects of selected food factors with chemopreventive properties on combined lipopolysaccharide- and interferon-gamma-induced IkappaB degradation in RAW264.7 macrophages. *Cancer Lett* **195,** 17–25, 2003.
20. Murakami A, Nakamura Y, Tanaka T, Kawabata K, Takahashi D, et al.: Suppression by citrus auraptene of phorbol ester- and endotoxin-induced inflammatory responses: role of attenuation of leukocyte activation. *Carcinogenesis* **21,** 1843–1850, 2000.
21. Murakami A and Ohigashi H: Cancer-preventive anti-oxidants that attenuate free radical generation by inflammatory cells. *Bio Chem* **387,** 387–392, 2006.
22. Murakami A, Wada K, Ueda N, Sasaki K, Haga M, et al.: In vitro absorption and metabolism of a citrus chemopreventive agent, auraptene, and its modifying effects on xenobiotic enzyme activities in mouse livers. *Nutr Cancer* **36,** 191–199, 2000.
23. Tanaka T, Sugiura H, Inaba R, Nishikawa A, Murakami A, et al.: Immunomodulatory action of citrus auraptene on macrophage functions and cytokine production of lymphocytes in female BALB/c mice. *Carcinogenesis* **20,** 1471–1476, 1999.
24. Tanaka T, Kohno H, Murakami M, Kagami S, and El-Bayoumy K: Suppressing effects of dietary supplementation of the organoselenium 1,4-phenylenebis(methylene)selenocyanate and the Citrus antioxidant auraptene on lung metastasis of melanoma cells in mice. *Cancer Res* **60,** 3713–3716, 2000.
25. Hara A, Sakata K, Yamada Y, Kuno T, Kitaori N, et al.: Suppression of beta-catenin mutation by dietary exposure of auraptene, a citrus antioxidant, in N,N-diethylnitrosamine-induced hepatocellular carcinomas in rats. *Oncol Rep* **14,** 345–351, 2005.
26. Kawabata K, Murakami A, and Ohigashi H: Citrus auraptene targets translation of MMP-7 (matrilysin) via ERK1/2-dependent and mTOR-independent mechanism. *FEBS Lett* **580,** 5288–5294, 2006.
27. Potter JD: Colorectal cancer: molecules and populations. *J Natl Cancer Inst* **91,** 916–932, 1999.
28. Fruhbeck G and Gomez-Ambrosi J: Rationale for the existence of additional adipostatic hormones. *FASEB J* **15,** 1996–2006, 2001.
29. Lee GH, Proenca R, Montez JM, Carroll KM, Darvishzadeh JG, et al.: Abnormal splicing of the leptin receptor in diabetic mice. *Nature* **379,** 632–635, 1996.
30. Margetic S, Gazzola C, Pegg GG, and Hill RA: Leptin: a review of its peripheral actions and interactions. *Int J Obes Relat Metab Disord* **26,** 1407–1433, 2002.
31. Tsuchiya T, Shimizu H, Horie T, and Mori M: Expression of leptin in lung: leptin as a growth factor. *Eur J Pharmacol* **365,** 273–279, 1999.
32. Dieudonne MN, Machinal-Quelin F, Serazin-Leroy V, Leneveu MC, Pecquery R, et al.: Leptin mediates a proliferative response in human MCF7 breast cancer cells. *Biochem Biophys Res Commun* **293,** 622–628, 2002.
33. Hardwick JCH, van den Brink GR, Offerhaus GJ, van Deventer JH, and Peppelenbosch MP: Leptin is a growth factor for colonic epithelial cells. *Gastroenterology* **121,** 79–90, 2001.
34. Mix H, Jandl O, Comberg M, Kaul A, Goke M, et al.: Expression of leptin and leptin receptor isoforms in the human stomach. *Gut* **47,** 481–486, 2000.
35. Nakao T, Hino M, Yamane T, Nishizawa Y, Morii H, et al.: Expression of the leptin receptor in human leukaemic blast cells. *Br J Haematol* **102,** 740–745, 1998.
36. O'Brien SN, Welter BH, and Price TM: Presence of leptin in breast cell lines and breast tumors. *Biochem Biophys Res Commun* **259,** 695–698, 1999.
37. Alrawi SJ, Schiff M, Carroll RE, Dayton M, Gibbs J, et al.: Aberrant crypt foci. *Anticancer Res* **26,** 107–119, 2006.
38. Yamada Y, and Mori H: Pre-cancerous lesions for colorectal cancers in rodents: a new concept. *Carcinogenesis* **24,** 1015–1019, 2003.
39. Niho N, Takahashi M, Kitamura T, Shoji Y, Itoh M, et al.: Concomitant suppression of hyperlipidemia and intestinal polyp formation in *Apc*-deficient mice by peroxisome proliferator-activated receptor ligands. *Cancer Res* **63,** 6090–6095, 2003.
40. Niho N, Takahashi M, Shoji Y, Takeuchi Y, Matsubara S, et al.: Dose-dependent suppression of hyperlipidemia and intestinal polyp formation in Min mice by pioglitazone, a PPAR gamma ligand. *Cancer Sci* **94,** 960–964, 2003.
41. Mori H, Yamada Y, Hirose Y, Kuno T, Katayama M, et al.: Chemoprevention of large bowel carcinogenesis; the role of control of cell proliferation and significance of beta-catenin-accumulated crypts as a new biomarker. *Eur J Cancer Prev* **11** (Suppl 2), S71–S75, 2002.
42. Suzuki R, Kohno H, Yasui Y, Hata K, Sugie S, et al.: Diet supplemented with citrus unshiu segment membrane suppresses chemically induced colonic preneoplastic lesions and fatty liver in male *db/db* mice. *Int J Cancer*, in press, 2006.
43. Bruce WR, Wolever TM, and Giacca A: Mechanisms linking diet and colorectal cancer: the possible role of insulin resistance. *Nutr Cancer* **37,** 19–26, 2000.
44. Mori H, Hata K, Yamada Y, Kuno T, and Hara A: Significance and role of early-lesions in experimental colorectal carcinogenesis. *Chem Biol Interact* **155,** 1–9, 2005.
45. Yamada K, Araki S, Tamura M, Sakai I, Takahashi Y, et al.: Relation of serum total cholesterol, serum triglycerides and fasting plasma glucose to colorectal carcinoma in situ. *Int J Epidemiol* **27,** 794–798, 1998.
46. Niho N, Mutoh M, Takahashi M, Tsutsumi K, Sugimura T, et al.: Concurrent suppression of hyperlipidemia and intestinal polyp formation by NO-1886, increasing lipoprotein lipase activity in Min mice. *Proc Natl Acad Sci USA* **102,** 2970–2974, 2005.
47. Reddy BS: The Fourth DeWitt S. Goodman lecture. Novel approaches to the prevention of colon cancer by nutritional manipulation and chemoprevention. *Cancer Epidemiol Biomarkers Prev* **9,** 239–247, 2000.
48. Lin X, Chavez MR, Bruch RC, Kilroy GE, Simmons LA, et al.: The effects of a high fat diet on leptin mRNA, serum leptin and the response

to leptin are not altered in a rat strain susceptible to high fat diet-induced obesity. *J Nutr* **128,** 1606–1613, 1998.
49. Reddy BS: Role of dietary fiber in colon cancer: an overview. *Am J Med* **106,** 16S–19S, 1999.
50. Agus MS, Swain JF, Larson CL, Eckert EA, and Ludwig DS: Dietary composition and physiologic adaptations to energy restriction. *Am J Clin Nutr* **71,** 901–907, 2000.
51. Giovannucci E: Insulin, insulin-like growth factors and colon cancer: a review of the evidence. *J Nutr* **131** (11 Suppl), 3109S–3120S, 2001.
52. Moore MA, Sobue T, Kuriki K, Tajima K, Tokudome S, et al.: Comparison of Japanese, American-Whites, and African-Americans—pointers to risk factors to underlying distribution of tumours in the colorectum. *Asian Pac J Cancer Prev* **6,** 412–419, 2005.

Int. J. Cancer: **121,** 2331–2339 (2007)

A lipophilic statin, pitavastatin, suppresses inflammation-associated mouse colon carcinogenesis

Yumiko Yasui[1], Rikako Suzuki[1], Shingo Miyamoto[2], Tetsuya Tsukamoto[3], Shigeyuki Sugie[1], Hiroyuki Kohno[1] and Takuji Tanaka[1]*

[1]*Department of Oncologic Pathology, Kanazawa Medical University, Uchinada, Ishikawa, Japan*
[2]*Division of Food Science and Biotechnology, Graduate School of Agriculture, Kyoto University, Kyoto, Japan*
[3]*Division of Oncological Pathology, Aichi Cancer Center Research Institute, Chikusa-ku, Nagoya, Japan*

3-Hydroxy-3-methylglutaryl coenzyme A (HMG-CoA) reductase inhibitors are known to modulate carcinogenesis. In this study, we investigated whether a lipophilic HMG-CoA reductase inhibitor pitavastatin suppresses inflammation-related mouse colon carcinogenesis. Male CD-1 (ICR) mice were initiated with a single intraperitoneal injection of azoxymethane (AOM, 10 mg/kg body weight) and promoted by 2% (w/v) dextran sodium sulfate (DSS) in drinking water for 7 days. The experimental diets containing pitavastatin at 2 dose levels (1 and 10 ppm) were fed to male CD-1 (ICR) mice for 17 weeks, staring 1 week after the cessation of DSS exposure. The effects of dietary pitavastatin on colonic tumor development were assessed at Weeks 5, 10 and 20. Feeding with pitavastatin at both doses significantly inhibited the multiplicity of colonic adenocarcinoma at Week 20. Furthermore, the treatment significantly lowered the positive rates of proliferating cell nuclear antigen and increased the apoptotic index in the colonic epithelial malignancies. The treatment also reduced nitrotyrosine-positivity in the colonic mucosa. Our findings thus show that pitavastatin is effective in inhibiting colitis-related colon carcinogenesis through modulation of mucosal inflammation, oxidative/nitrosative stress, and cell proliferation.

Key words: statin; chemoprevention; inflammation; colon carcinogenesis; mouse

Statins, which are 3-hydroxy-3-methylglutaryl coenzyme A (HMG-CoA) reductase inhibitors, are commonly-used drugs for the treatment of hypercholesterolemia.[1,2] They are able to decrease low-density lipoprotein (LDL) cholesterol levels by inhibiting HMG-CoA reductase. Furthermore, a triglyceride (TG)-lowering effect and a high-density lipoprotein (HDL) cholesterol-raising effect were observed in patients with hyperlipidemia, who take statins.[3,4] Statins have multibiological effects other than antilipidemia. Recently, it has been highlighted that statins are linked with several beneficial effects beyond their effect on cardiovascular disease. They include reduction in the risk of dementia,[5,6] fracture[7] and cancer.[8–10] Several recent preclinical studies indicated that statins may have chemopreventive potential against cancer at various sites,[10–12] including colon.[13–16] In addition, there is growing evidence that statins exert anti-inflammatory and antioxidative actions that are independent of their serum lipid lowering effects.[17]

Association between inflammation and cancer has long been suspected.[18,19] An example is that inflamed colon is a high risk for colorectal cancer (CRC) development.[20] CRC is thus one of the most serious complications of inflammatory bowel disease (IBD), including ulcerative colitis (UC)[20] and Crohn's disease (CD).[21] For understanding the pathogenesis of IBD and IBD-related CRC, we have developed a novel colitis-related and two-stage mouse CRC model, using a colon carcinogen azoxymethane (AOM) and a colitis-inducing agent dextran sodium sulfate (DSS).[22] In this animal model, numerous large bowel adenocarcinomas occur within a short-term period, and their histology and biological alterations resemble those found in human.[22] The model can be used for investigating and determining cancer chemopreventive agents against CRC[23] as well as initiating or modulating agents for CRC.[24]

A lipophilic statin pitavastatin, (+)-monocalcium bis{(3*R*.5*S*,6*E*)-7-[2-cyclopropyl-4-(4-fluorophenyl)-3-quinolyl]-3,5-dihydroxy-6-heptenoate} ($C_{50}H_{46}CaF_2N_2O_8$, MW 880.98, Fig. 1), that has been developed in Japan is highly effective for lowering serum cholesterol and TG levels.[25] The lowering effect of pitavastatin on serum LDL-cholesterol is more potent than that of pravastatin, simbastatin and atorvastatin.[26–28] The drug possessing a high oral bioavailability is only slightly metabolized, suggesting a longer duration of action and is less potent for drug interactions.[28] Therefore, the agent is currently undergoing Phase III trials in Europe, US and Japan.[25] Since pitavastatin possesses pleiotrophic biological effects, including anti-inflammatory actions,[29,30] we in the present study investigated the potential chemopreventive ability of colitis-related colon cancer development using our mouse model[22] to find desirable cancer chemopreventers against IBD-related CRC.[31] Since numerous evidence demonstrates that a high-fat diet is associated with the risk of CRC development and serum levels of TG and cholesterol are positively associated with colon carcinogenesis,[32] we monitored serum levels of TG and cholesterol during the study.

Material and methods

Animals, chemicals and diets

Male Crj: CD-1 (ICR) mice (Charles River Japan, Tokyo, Japan) aged 5 weeks were used in this study. They were maintained at Kanazawa Medical University Animal Facility according to the Institutional Animal Care Guideline. All animals were housed in plastic cages (4 or 5 mice/cages) with free access to drinking water and pelleted basal diet, CRF-1 (Oriental Yeast, Tokyo, Japan), under controlled conditions of humidity (50 ± 10%), light (12/12 hr light/dark cycle) and temperature (23 ± 2°C). After arrived, animals were quarantined for the first 7 days, and then randomized by their body weights into experimental and control groups. A colonic carcinogen AOM was purchased from Sigma Chemical (St. Louis, MO). DSS with a molecular weight of 36000–50000 (Cat. No. 160110) was purchased from MP Biomed-

Abbreviations: AOM, azoxymethane; CD, Crohn's disease; CRC, colorectal cancer; DSS, dextran sodium sulfate; H&E, hematoxylin and eosin; HMG-CoA, 3-hydroxy-3-methylglutaryl coenzyme A; IBD, inflammatory bowel disease; iNOS, inducible bitric oxide synthase; LDL, low-density lipoprotein; NF-κB, nuclear factor-kappa B; NO, nitric oxide; PCNA, proliferating cell nuclear antigen; PSC, primary sclerosing cholangitis; ssDNA, single-stranded DNA; TG, triglycerides; UC, ulcerative colitis; UDCA, ursodeoxycholic acid.

Grant sponsor: Ministry of Education, Culture, Sports, Science and Technology of Japan (Grants-in-Aid for Scientific Research); Grant numbers: 152052, 00120029, 18592076; Grant sponsor: Kanazawa Medical University; Grant numbers: H2006-6, C2006-3; Grant sponsor: Ministry of Health, Labour and Welfare of Japan (Grant-in-Aid for Cancer Research and a Grant-in-Aid for the 3rd Term for a Comprehensive 10-year Strategy for Cancer Control).

***Correspondence to:** Department of Oncologic Pathology, Kanazawa Medical University, 1-1 Daigaku, Uchinada, Ishikawa 920-0293, Japan. Fax: +81-76-286-6926. E-mail: takutt@kanazawa-med.ac.jp

Received 9 April 2007; Accepted after revision 6 June 2007
DOI 10.1002/ijc.22976
Published online 26 July 2007 in Wiley InterScience (www.interscience.wiley.com).

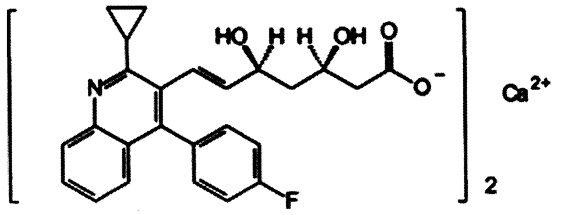

FIGURE 1 – Chemical structure of pitavastatin. (+)-Monocalcium bis{(3*R*.5*S*,6*E*)-7-[2-cyclopropyl-4-(4-fluorophenyl)-3-quinolyl]-3,5-dihydroxy-6-heptenoate}, $C_{50}H_{46}CaF_2N_2O_8$, MW 880.98.

icals, LLC (Aurora, OH). DSS for induction of colitis was dissolved in water at a concentration of 2% (w/v).

Experimental procedures

A total of 132 male ICR mice were divided into 7 experimental and control groups (Fig. 2). Mice in Groups 1–3 were given a single intraperitoneal injection of AOM (10 mg/kg body weight). Starting 1 week after the injection, animals received 2% DSS in the drinking water for 7 days. Subsequently, they were fed the diets containing 0, 1 and 10 ppm pitavastatin for 17 weeks, respectively, starting 1 week after the cessation of DSS exposure. Group 4 was fed the diet containing 10 ppm pitavastatin, and received no further treatments. Groups 5 and 6 were given AOM alone and DSS alone, respectively. Group 7 was an untreated control. Animals are sequentially sacrificed at Weeks 5, 10 and 20 by ether overdose to determine the effects of pitavastatin on colon tumorigenesis and biochemical profiles, including serum lipids measurements. Prior to sacrifice, animals were starved overnight for clinical chemistry. At sacrifice, the large bowels were flushed with saline, and excised. After measuring their length (from the ileocecal junction to the anal verge), large bowels were cut open longitudinally along the main axis, and gently washed with saline. The whole large bowel was macroscopically inspected for the presence of tumors, cut along a vertical axis and fixed in 10% buffered formalin for a least 24 hr. Histopathological examination was performed on paraffin-embedded sections after hematoxylin and eosin (H&E) staining. On H&E-stained sections, pathological lesions, such as mucosal ulceration, dysplasia and colonic tumors, were determined.

Clinical chemistry

At autopsy, whole blood anticoagulated with heparin lithium was taken from the inferior vena cava with a sterile syringe (Terumo, Tokyo, Japan) at each time point. The serum was obtained by centrifugation (3,000 rpm for 10 min), and stored at −80°C until measurement. Serum cholesterol was determined enzymatically using cholesterol esterase and cholesterol oxidase. The serum TG was assayed by enzymatic hydrolysis with lipase. These measurements were expressed as mg/dL.

Scoring of inflammation in the large bowel

Inflammation in the large bowel was scored on the H&E-stained sections. For scoring, large intestinal inflammation was graded according to the following morphological criteria described by Cooper *et al.*[33]: Grade 0, normal appearance; Grade 1, shortening and loss of the basal 1/3 of the actual crypts with mild inflammation in the mucosa; Grade 2, loss of the basal 2/3 of the crypts with moderate inflammation in the mucosa; Grade 3, loss of the entire crypts with severe inflammation in the mucosa and submucosa, but with retainment of the surface epithelium; Grade 4, presence of mucosal ulcer with severe inflammation (infiltration of neutrophils, lymphocytes, and plasma cells) in the mucosa, submucosa, muscularis propria and/or subserosa. The scoring was made on the entire colon with or without proliferative lesions and expressed as a mean average score/mouse.

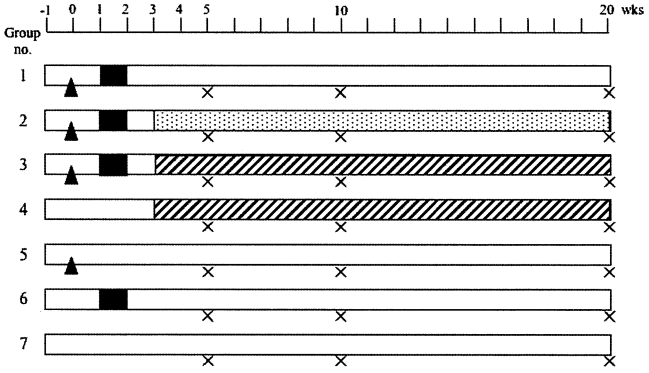

FIGURE 2 – Experimental protocol. ▲: AOM (10 mg/kg i.p.); ■: 2% DSS in drinking water; □: Basal diet and tap water; ▒: 1 ppm pitavastatin in diet; ▨: 10 ppm pitavastatin in diet; ×: Sacrifice.

Immunohistochemistry

Immunohistochemistry for proliferating cell nuclear antigen (PCNA)-positive nuclei, apoptotic nuclei, and nitrotyrosine-positive cells was performed on 4-μm-thick paraffin-embedded sections, from the colons of mice in each group by the labeled streptavidin biotin method, using a LSAB KIT (DAKO Japan, Kyoto, Japan), with microwave accentuation. The paraffin-embedded sections were heated for 30 min at 65°C, deparaffinized in xylene and rehydrate through grade ethanols at room temperature. A 0.05 M Tris HCl buffer (pH 7.6) was used to prepare solutions and for washes between various steps. Incubations were performed in a humidified chamber. For the determination of PCNA-incorporated nuclei, the PCNA-immunohistochemistry was performed. Apoptotic index was also evaluated by immunohistochemistry for single-stranded DNA (ssDNA). Sections were treated for 40 min at room temperature, with 2% BSA, and incubated overnight at 4°C with primary antibodies, anti-PCNA mouse monoclonal antibody (PC10, 1:50 dilution, DAKO Japan), anti-ssDNA rabbit polyclonal antibody (1:300 dilution, DAKO Japan) and anti-nitrotyrosine rabbit polyclonal antibody (1:500 dilution, Update Biotechnology, Lake Placid, NY). To reduce the nonspecific staining of mouse tissue by a mouse antibody (anti-PCNA), a Mouse On Mouse IgG blocking reagent (Vector Laboratories, Burlingame, CA) was applied for 1 hr. House-radish peroxidase activity was visualized by treatment with H_2O_2 and 3,3′-diaminobenzidine for 5 min. At the last step, the sections were weakly counterstained with Mayer's hematoxylin (Merck, Tokyo, Japan). For each case, negative controls were performed on serial sections. On the control sections, incubation with the primary antibodies was omitted.

Intensity and localization of immunoreactivity against all primary antibodies used were assessed using a microscope (Olympus BX41, Olympus Optical, Tokyo, Japan). The indices for PCNA and apoptosis were determined by counting the number of positive nuclei among at least 200 cells in 5 adenocarcinomas developed at Week 20 from each of Groups 1–3, and were indicated as percentages. The nitrotyrosine-positive cells were evaluated for their intensity of immunoreactivity on a 0 or 4+ scale. The overall intensity of the staining reaction was scored with 0 indicating no immunoreactivity and no positive cells, 1+ weak immunoreactivity and <10% of positive cells, 2+ mild immunoreactivity and 10–30% of positive cells, 3+ moderate immunoreactivity and 31–60% of positive cells and 4+ strong immunoreactivity and 61–100% of positive cells. This evaluation was done on the colonic mucosa with or without tumors from all the mice of each sacrifice time point (4 mice each from all groups at Week 5; 4 mice each from all groups at Week 10; and 9 mice each of Groups 1 and 3, 10 mice each of Groups 2 and 6, and 5 mice each of Groups 4, 5 and 7 at Week 20).

TABLE I – BODY, LIVER WEIGHT AND LENGTH OF LARGE BOWEL OF MICE AT WEEK 20

Group no.	Treatment (no. of mice examined)	Body weight (g)	Liver weight (g)	Relative liver weight (g/100 g body weight)	Length of colon (cm)
1	AOM/2% DSS (9)	44.02 ± 3.44[a]	2.45 ± 0.34	5.56 ± 0.44	11.63 ± 0.41
2	AOM/2% DSS/1 ppm pitavastatin (7)	43.09 ± 6.79	2.21 ± 0.26	5.15 ± 0.28	11.66 ± 0.61
3	AOM/2% DSS/10 ppm pitavastatin (9)	38.40 ± 2.61	2.28 ± 0.32	5.94 ± 0.64[b]	11.29 ± 0.86
4	10 ppm pitavastatin (5)	42.47 ± 4.17	2.28 ± 0.23	5.39 ± 0.27	11.70 ± 1.54
5	AOM (5)	53.26 ± 6.63[c]	2.50 ± 0.40	4.68 ± 0.38[d]	12.18 ± 0.47
6	2% DSS (7)	44.16 ± 5.12	2.45 ± 0.30	5.59 ± 0.76	11.13 ± 0.28
7	None (4)	42.84 ± 4.23	2.40 ± 0.32	5.58 ± 0.23	12.78 ± 0.17

[a]Mean ± SD.–[b]Significantly different from Group 2 by Tukey–Kramer multiple comparison post test ($p < 0.05$).–[c]Significantly different from Groups 1, 6, and 7 by Tukey–Kramer multiple comparison post test ($p < 0.05$).–[d]Significantly different from Group 1 by Tukey–Kramer multiple comparison post test ($p < 0.05$).

TABLE II – INCIDENCE OF COLONIC LESIONS AT WEEKS 5, 10 AND 20

Group no.	Treatment (no. of mice examined at wk 5/wk 10/wk 20)	Mucosal ulcer			Dysplasia		
		Wk 5	Wk 10	Wk 20	Wk 5	Wk 10	Wk 20
1	AOM/2% DSS (4/4/9)	4/4, 100%	4/4, 100%	6/9, 67%	4/4, 100%	4/4, 100%	9/9, 100%
2	AOM/2% DSS/1 ppm pitavastatin (4/4/10)	4/4, 100%	3/4, 75%	3/10, 30%	4/4, 100%	4/4, 100%	8/10, 80%
3	AOM/2% DSS/10 ppm pitavastatin (4/4/9)	2/4, 50%	3/4, 75%	0/9, 0%	3/4, 75%	4/4, 100%	9/9, 100%
4	10 ppm pitavastatin (4/4/5)	0/4, 0%	0/4, 0%	0/5, 0%	0/4, 0%	0/4, 0%	0/5, 0%
5	AOM (4/4/5)	0/4, 0%	1/4, 25%	0/5, 0%	1/4, 25%	0/4, 0%	0/5, 0%
6	2% DSS (4/4/10)	4/4, 100%	4/4, 100%	0/10, 0%	1/4, 25%	0/4, 0%	0/10, 0%
7	None (4/4/5)	0/4, 0%	0/4, 0%	0/5, 0%	0/4, 0%	0/4, 0%	0/5, 0%

Data were from histopathological analysis.

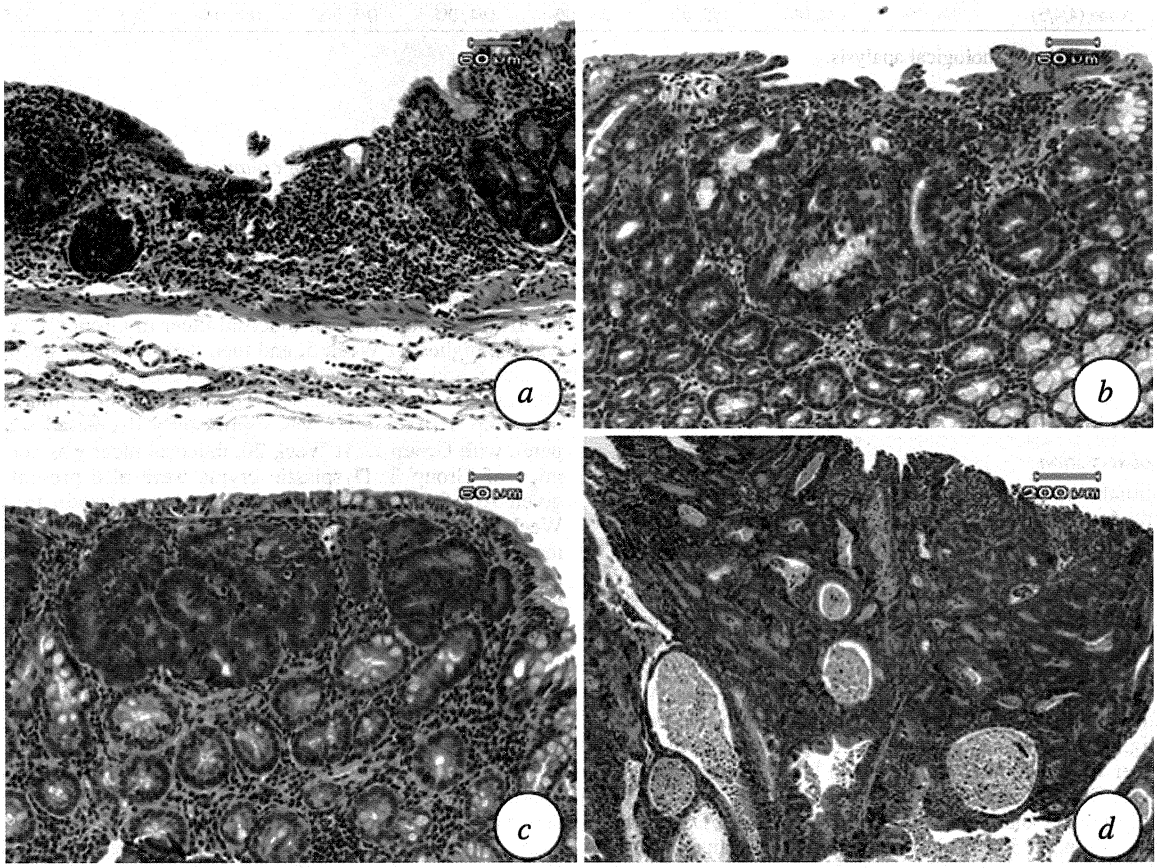

FIGURE 3 – Colonic lesions induced by AOM and 2% DSS. (*a*) A mucosal ulcer, (*b*) dysplastic crypts, (*c*) a tubular adenomas and (*d*) a tubular adenocarcinoma that developed in a mouse that received AOM and 2% DSS (Group 1). Bars inserted are (a) 60 μm, (b) 60 μm, (c) 60 μm and (d) 200 μm.

TABLE III – MULTIPLICITIES OF COLONIC LESIONS AT WEEKS 5, 10 AND 20

Group no.	Treatment (no. of mice examined at wk 5/wk 10/wk 20)	Mucosal ulcer			Dysplasia		
		Wk 5	Wk 10	Wk 20	Wk 5	Wk 10	Wk 20
1	AOM/2% DSS (4/4/9)	3.25 ± 1.71[a]	2.75 ± 0.96	0.82 ± 0.98	4.50 ± 1.30	4.00 ± 1.41	3.18 ± 1.66
2	AOM/2% DSS/1 ppm pitavastatin (4/4/10)	2.00 ± 0.82	1.25 ± 0.96	1.50 ± 2.46	3.25 ± 0.50	3.30 ± 1.30	2.20 ± 1.99
3	AOM/2% DSS/10 ppm pitavastatin (4/4/9)	1.25 ± 1.50	0.75 ± 0.50[b]	0	2.00 ± 1.83	3.75 ± 1.89	1.89 ± 0.93
4	10 ppm pitavastatin (4/4/5)	0	0	0	0	0	0
5	AOM (4/4/5)	0	0.25 ± 0.50	0	0.25 ± 0.50	0	0
6	2% DSS (4/4/10)	6.00 ± 2.16	3.75 ± 1.71	0	0.25 ± 0.50	0	0
7	None (4/4/5)	0	0	0	0	0	0

Data were from histopathological analysis.
[a]Mean ± SD.–[b]Significantly different from Group 1 by Tukey–Kramer multiple comparison post test ($p < 0.05$).

TABLE IV – INCIDENCE OF COLONIC TUMOR AT WEEKS 5, 10 AND 20

Group no.	Treatment	Adenoma			Adenocarcinoma			Total		
		Wk 5	Wk 10	Wk 20	Wk 5	Wk 10	Wk 20	Wk 5	Wk 10	Wk 20
1	AOM/2% DSS (4/4/9)	4/4, 100%	3/4, 75%	9/9, 100%	4/4, 100%	3/4, 75%	9/9, 100%	4/4, 100%	4/4, 100%	9/9, 100%
2	AOM/2% DSS/1 ppm pitavastatin (4/4/10)	4/4, 100%	4/4, 100%	9/10, 90%	3/4, 75%	3/4, 75%	9/10, 90%	4/4, 100%	4/4, 100%	9/10, 90%
3	AOM/2% DSS/10 ppm pitavastatin (4/4/9)	2/4, 50%	4/4, 100%	7/9, 78%	2/4, 50%	4/4, 100%	7/9, 78%	2/4, 50%	4/4, 100%	8/9, 89%
4	10 ppm pitavastatin (4/4/5)	0/4, 0%	0/4, 0%	0/5, 0%	0/4, 0%	0/4, 0%	0/5, 0%	0/4, 0%	0/4, 0%	0/5, 0%
5	AOM (4/4/5)	0/4, 0%	0/4, 0%	0/5, 0%	0/4, 0%	0/4, 0%	0/5, 0%	0/4, 0%	0/4, 0%	0/5, 0%
6	2% DSS (4/4/10)	0/4, 0%	0/4, 0%	0/10, 0%	0/4, 0%	0/4, 0%	0/10, 0%	0/4, 0%	0/4, 0%	0/10, 0%
7	None (4/4/5)	0/4, 0%	0/4, 0%	0/5, 0%	0/4, 0%	0/4, 0%	0/5, 0%	0/4, 0%	0/4, 0%	0/5, 0%

Data were from histopathological analysis.

Statistical analysis

The incidences among the groups were compared using χ^2 test or Fisher's extract probability test (GraphPad Instat version 3.05, GraphPad Software, San Diego, USA). Other measurements expressing mean ± SD were statistically analyzed using Tukey–Kramer multiple comparison post test (GraphPad Instat version 3.05, GraphPad Software). Differences were considered statistically significant at $p < 0.05$.

Results

General observation

The animals that received DSS in their drinking water (Groups 1, 2, 3 and 6) had bloody stool between Weeks 1–3. Also, some mice treated with AOM/DSS with or without pitavastatin (Groups 1, 2 and 3) had bloody stool, and tumors developed in their colon. However, other groups including Group 4 (the pitavastatin alone group) did not have such symptom. Body weights, liver weights, and relative liver weights in all groups at Week 20 are shown in Table I. With regard to the mean body weights, Group 5 (the AOM alone group, 53.3 ± 6.6 g) significantly increased when compared with all other groups. However, the mean liver weight did not significantly differ among the groups, whereas the mean relative liver weight (g liver weight/100 g body weight) of Group 3 (the AOM/DSS/10 ppm pitavastatin group, 5.94 ± 0.64) was significantly greater than that of Group 2 (the AOM/DSS/1 ppm pitavastatin group, 5.15 ± 0.28, $p < 0.05$), and the value of Group 5 (4.68 ± 0.38) was significantly lower than that of Groups 1 (the AOM/DSS group, 5.56 ± 0.44, $p < 0.05$) and 3 (5.94 ± 0.64, $p < 0.01$). As shown in Table I, the mean length of the colon did not significantly differ among the groups.

Incidence and multiplicity of colonic mucosal ulcer and dysplasia

Table II summarizes the incidence of colonic mucosal ulcer (Fig. 3*a*) and colonic dysplasia (Fig. 3*b*) at each time point. The incidence of mucosal ulcer gradually decreased as administration of pitavastatins doses increased at each time-point. On the other hand, the incidence of dysplasia were unaffected. As given in Table III, the multiplicity of mucosal ulcer in Groups 1, 2, 3 and 6 was the highest at Week 5, and then they gradually decreased. At Weeks 5 and 10, the value was decreased by administration of pitavastatin dose-dependently. The multiplicity of mucosal ulcer of Group 3 ($p < 0.05$) was significantly decreased when compared with Group 1. At Week 20, mucosal ulcer was not found in mice of Group 3. Dysplastic crypts were also present in mice given AOM and DSS with or without pitavastatin treatment at Week 5. Colonic dysplasia tended to decrease during the experiment, as did mucosal ulcer. The multiplicities of dysplasia in the mice of Groups 2 and 3 were lower than that of Group 1, but the differences among the groups did not reach statistical significance.

Incidence and multiplicity of large bowel neoplasms

Table IV shows the incidence of colonic tumor at each time-point. It was observed that adenoma (Fig. 3*c*) and adenocarcinoma (Fig. 3*d*) located in the middle and distal colon at each time point. However, treatment with pitavastatin unaffected the incidence of colonic tumor at Weeks 10 and 20. The multiplicities of colonic neoplasms at Weeks 5, 10 and 20 are given in Table V. Colonic adenoma and adenocarcinoma were observed even at Week 5. The multiplicities of adenoma in Groups 2 and 3 were smaller than that of Group 1 at weeks 5 and 20, but the differences were not statistically significant among the groups. As for the

TABLE V – MULTIPLICITIES OF COLONIC TUMOR AT WEEKS 5, 10 AND 20

Group no.	Treatment (no. of mice examined at wk 5/wk 10/wk 20)	Adenoma			Adenocarcinoma			Total		
		Wk 5	Wk 10	Wk 20	Wk 5	Wk 10	Wk 20	Wk 5	Wk 10	Wk 20
1	AOM/2% DSS (4/4/9)	4.00 ± 1.15[a]	2.25 ± 1.71	3.82 ± 1.78	3.00 ± 1.63	5.30 ± 1.30	5.27 ± 3.13	7.00 ± 1.15	7.50 ± 2.38	9.09 ± 3.86
2	AOM/2% DSS/1 ppm pitavastatin (4/4/10)	2.00 ± 0.82	2.25 ± 1.89	2.70 ± 1.42	2.30 ± 1.70	1.50 ± 1.29	1.50 ± 0.97[b]	4.25 ± 2.06	3.75 ± 2.75	4.20 ± 2.10[c]
3	AOM/2% DSS/10 ppm pitavastatin (4/4/9)	1.25 ± 1.50	3.75 ± 0.96	3.00 ± 1.87	1.50 ± 1.90	1.50 ± 1.00	2.00 ± 1.00[c]	2.75 ± 3.20	5.25 ± 1.89	5.00 ± 2.50[d]
4	10 ppm pitavastatin (4/4/5)	0	0	0	0	0	0	0	0	0
5	AOM (4/4/5)	0	0	0	0	0	0	0	0	0
6	2% DSS (4/4/10)	0	0	0	0	0	0	0	0	0
7	None (4/4/5)	0	0	0	0	0	0	0	0	0

All data were from histopathological analysis.
[a]Mean ± SD.–[b,c,d]Significantly different from Group 1 by Tukey–Kramer multiple comparison post test ([b]$p < 0.001$, [c]$p < 0.01$, and [d]$p < 0.05$).

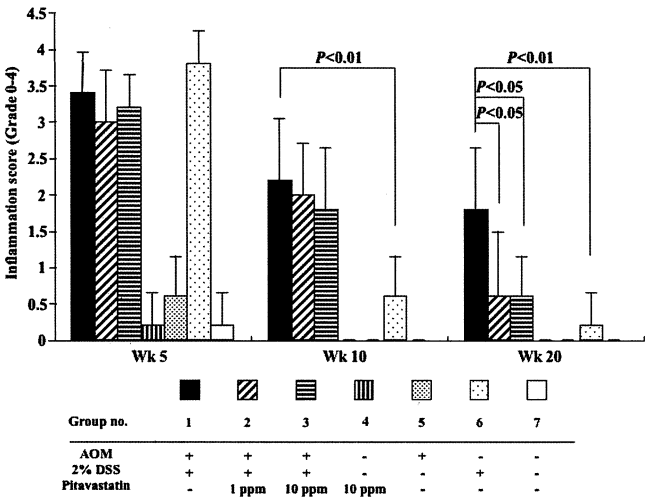

FIGURE 4 – Inflammatory scores in the large bowel of mice in all groups.

multiplicity of adenocarcinoma, the values of Groups 2 and 3 were low without statistical significance when compared to Group 1 at Weeks 5 and 10. However, the values of Groups 2 ($p < 0.001$) and 3 ($p < 0.01$) at Week 20 were significantly smaller than that of Group 1, although the inhibition was not dose-dependent.

Inflammation score in the large bowel

Figure 4 illustrates data on colonic inflammation scores at Weeks 5, 10 and 20. The inflammation scores of Groups 1, 2, 3 and 6 were the greatest at Week 5, and they gradually lowered with time. Colonic inflammation in the mice of Groups 4, 5 and 7, which were not given 2% DSS, were not observed at Weeks 10 and 20, while they had slight colitis at Week 5. At Weeks 5 and 10, the scores in Groups 2 and 3 that were given pitavastatin-containing diets were smaller than that of Group 1, but the differences did not reach the statistical significance. However, their scores were significantly lower than Group 1 at Week 20 (*vs.* Group 2, $p < 0.05$; Group 3, $p < 0.05$; and Group 6, $p < 0.01$).

Immunohistochemical scores for PCNA-, ssDNA- and nitrotyrosine-positive cells in the colonic adenocarcinomas

Scoring data on PCNA- (Fig. 5*a*) and ssDNA- (Fig. 5*b*) in adenocarcinoma cells and nitrotyrosine-positivity (Fig. 5*c*) in colonic mucosa with or without tumors are illustrated in Figure 6. As shown in Figure 6*a*, the mean PCNA-labeling indices of colonic adenocarcinomas developed in Groups 2 ($p < 0.001$) and 3 ($p < 0.001$) were significantly lower than that of Group 1. The mean apoptosis indices of Groups 2 ($p < 0.05$) and 3 ($p < 0.001$), which were measured by ssDNA immunohistochemistry, were significantly greater than that of Group 1, as shown in Figure 6*b*. Immunoreactivity of nitrotyrosine was noted in the adenocarcinoma cells (Fig. 5*c*). The reaction was also observed in the cryptal cells with or without disruption, infiltrated mononuclear inflammatory cells and endothelial cells of the small vessels in the mucosa and submucosa (Fig. 5*c*). The positive reaction was not detected in the colon of mice in Groups 4, 5 and 7. As illustrated in Figure 7, the scores of nitrotyrosine-positivity in Groups 1, 2, 3 and 6 were the greatest at Week 5, and decreased with time. At Week 5, the scores of Groups 2 ($p < 0.001$), 3 ($p < 0.001$) and 6 ($p < 0.05$) were significantly lower than that of Group 1. At Week 10, the scores of Groups 2 ($p < 0.01$), 3 ($p < 0.001$) and 6 ($p < 0.001$) were significantly lower than that of Group 1. Also, the scores of Groups 3 ($p < 0.05$) and 6 ($p < 0.01$) were significantly lower than that of Group 1 at Week 20.

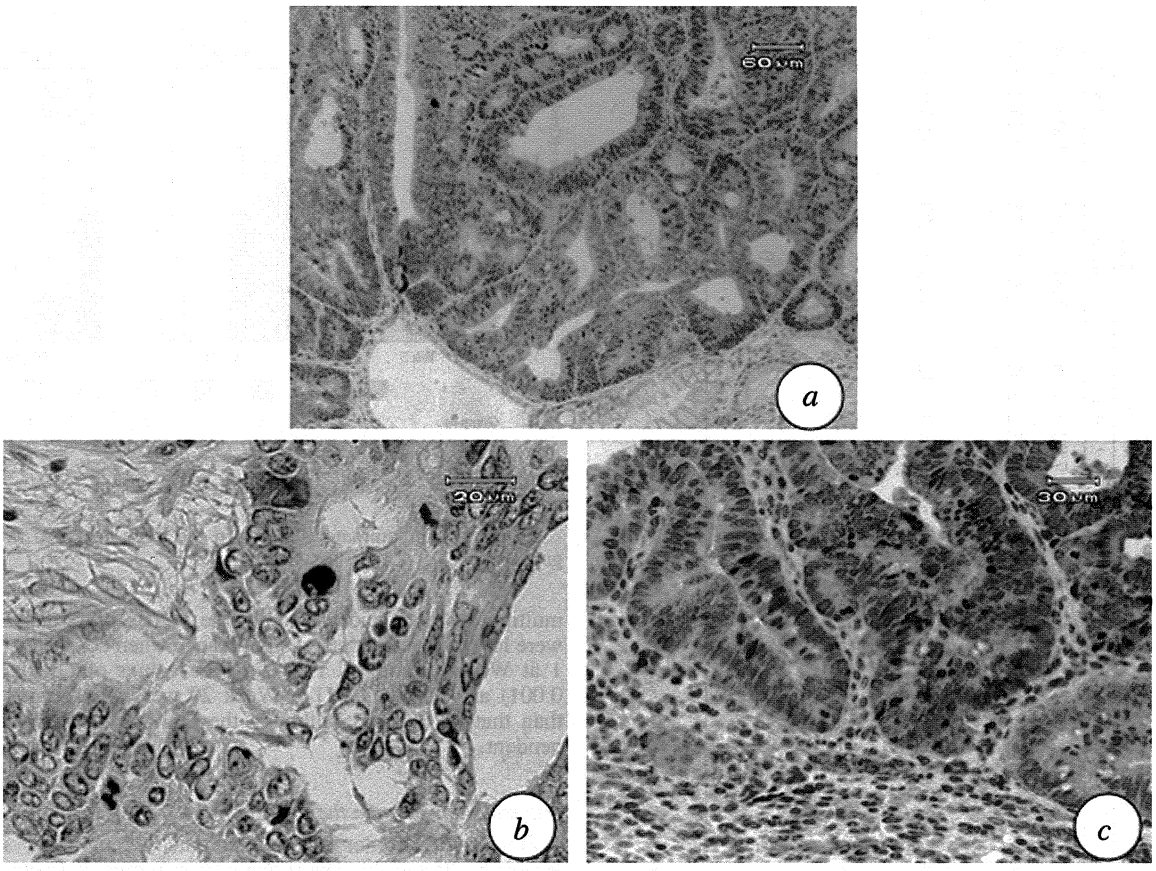

FIGURE 5 – Immunohistochemistry of (*a*) PCNA-labeled nuclei, (*b*) ssDNA-positive nuclei and (*c*) nitrotyrosine-positive cells in adenocarcinomas developed in the colon of a mouse from Group 1. Bars inserted are (a) 60 μm, (b) 20 μm and (c) 30 μm.

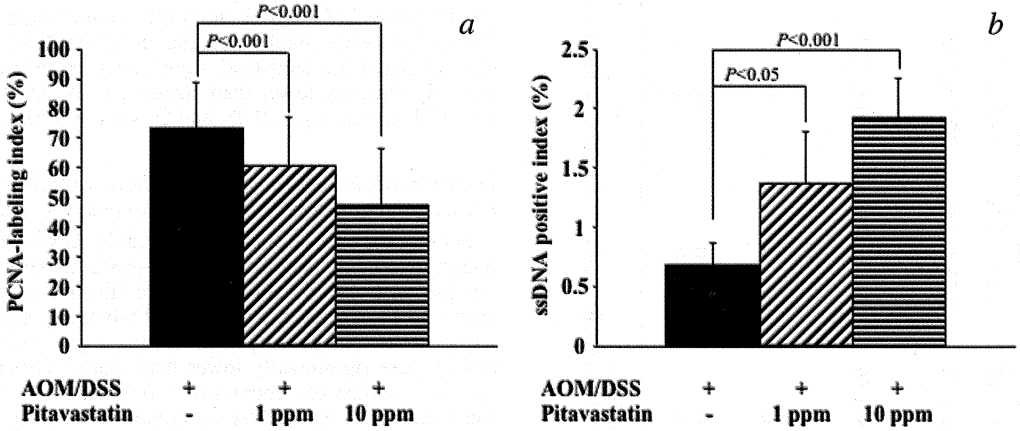

FIGURE 6 – Indices of (*a*) PCNA-labeled nuclei and (*b*) ssDNA-positive nuclei in 5 colonic adenocarcinomas each from Groups 1–3 at Week 20.

Serum levels of TG and total cholesterol

Table VI summarizes data on serum levels of TG and total cholesterol at each time point. The serum TG level of Group 1 (AOM/DSS group) was the greatest among the group at 3 time points. At Week 20, but not at Weeks 5 and 10, the values of Groups 2 ($p < 0.001$) and 3 ($p < 0.001$) were significantly lower than that of Group 1. Similarly, the serum level of total cholesterol of Group 3 ($p < 0.05$) was significantly smaller than that of Group 1, as listed in Table VII.

Discussion

In the current study, we first demonstrated cancer chemopreventive effects of pitavastatin on colitis-related mouse colon carcinogenesis induced by AOM/DSS. Suppressing effects of colitis-related colon carcinogenesis by pitavastatin may be due to reduction of cell proliferation, induction of apoptosis, inhibition of inflammation and suppression of oxidative/nitrosative stress in the colonic malignancy. In the current study, treatment with pitavastatin alone (Group 4) did not affect colonic morphology, including

induction of ulcer and neoplasms. This is important, since a recent case report described the development of UC in a patient who took simvastatin and was fatal.[34]

In the current study, we observed that dietary pitavastatin inhibits the multiplicity, but not the incidence, of colonic adenocarcinomas induced by AOM/DSS. This may be related to weak chemopreventive effects of a low dose of pitavastatin. Also, there was no dose-response of the inhibition, although data on the indices of PCNA and ssDNA may suggest that pitavastatin affects dose-dependently proliferation and apoptosis in adenocarcinoma cells. Since only 2 doses (1 and 10 ppm in diet) of pitavastatin were used for assessing chemopreventive ability of the drug against AOM/DSS-induced mouse colon carcinogenesis in this study, additional doses (>10 ppm in diet) must be investigated to determine the dose-dependent efficacy of pitavastatin in suppressing AOM/DSS-induced colon carcinogenesis. As for colonic adenoma, the incidence did not significantly alter at 3 time points (Weeks 5, 10 and 20). The multiplicity of Group 2 was increased with time, but the increase was insignificant. The findings may suggest that a high dose (10 ppm) of pitavastatin is able to inhibit progress from adenoma to adenocarcinoma.

While statins are primarily known as drugs for the treatment of hypercholesterolemia because of their potency of reduction in LDL-cholesterol level by competitively inhibiting HMG-CoA reductase that is a rate-limiting enzyme in the synthesis of mevalonate, they have pleiotropic distinct effects on process such as angiogenesis[35] and inflammation.[36,37] Thus, statins affect a number of novel molecular targets and complex signaling pathways. Certain statins (simvastatin and rosuvastatin) are able to exert anti-inflammatory action in DSS-induced acute or chronic murine colitis model.[38,39] A lipophilic statin pitavastain also possesses multiple biological function[25] and anti-inflammatory action.[29,30] Pitavastatin is recently reported to down-regulate chemokines[40] that are involved in IBD pathogenesis.[41] Also, a low dose of pitavastatin can affect PI3K-AKT pathway,[42] which plays a critical role in the balance between cell survival and apoptosis, the inflammatory response by activating chemokine receptors and promoting inflammatory cell migration and the human cancer development,[43–45] including colon cancer.[46] In the current study, the treatment with pitavastatin in diet significantly lowered colonic inflammation induced by DSS, as revealed by histopathology (number of mucosal ulcer and inflammation scores). As observed in the colonic mucosa of UC patients, where colonic mucosal damage is associated with increased production of nitric oxide (NO) through the inducible nitric oxide synthase (iNOS) pathway,[47] the numbers of cryptal, infiltrated inflammatory, endothelial and tumor cells positive for nitrotyrosine, being a good biomarker for nitrosative stress,[48] were increased in the inflamed colon induced by DSS in this study. Pitavastatin treatment significantly lowered the nitrotyrosine-positive immunohistochemical score in conjunction with reduction in the number of mucosal ulcer and inflammatory score. iNOS is reported to be over-expressed in colonic tumors of humans[49] and chemically induced colonic tumors.[50] Although there are no reports that pitavastatin affects iNOs expression in inflamed tissues and neoplasms, our findings may suggest the possible effects of pitavastatin on iNOS expression. Activated nuclear factor-kappa B (NF-κB), which is a key player in inflammatory processes in the tissues,[51,52] is observed in different cancer cell lines and primary malignant tissue samples.[53] Recently, Lee *et al.*[38] demonstrated that simvastatin inhibits proinflammatory gene expression by blocking NF-κB signaling in intestinal epithelial cells, and attenuates DSS-induced acute murine colitis. Wang *et al.*[54] have also found that pitavastatin inhibits NF-κB activation and decreases IL-6 production induced by tumor necrosis factor-α in human hepatocellular carcinoma cells. NF-κB activation also plays an important role in enhancing IL-6 and IL-8 in human colon cancer cells.[55] Although we did not examine mRNA expression of NF-κB and cytokines in this study, it is possible that paitavastatin affects the expression in the inflamed mouse colon. The anti-inflammatory and antioxidative/nitrosative potential of pitavastatin is possibly related to prenylation of certain proteins that are involved in inflammatory processes,[56,57] but not its effect on HMG-CoA enzyme, as is the case of other statins.[17,58] The findings reported by others and those described here, thus, may suggest the potential use of statins, including pitavastatin as an anti-inflammatory drug for the treatment of IBD.

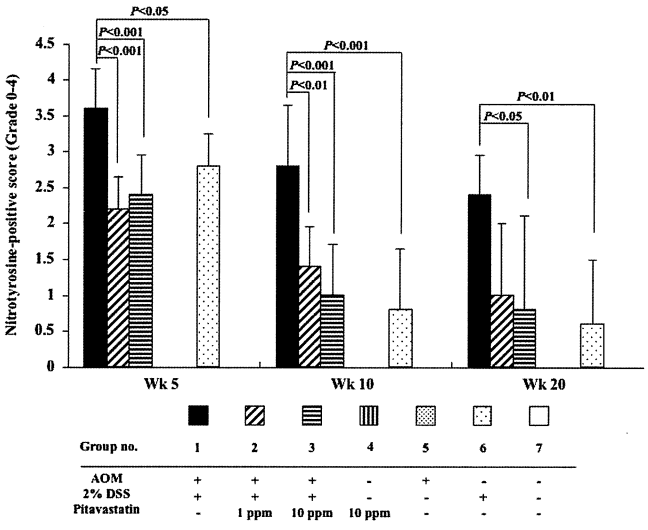

FIGURE 7 – Nitrotyrosine-positive indices in the colonic mucosa with or without tumors from all the mice of each sacrifice time point (4 mice each from all groups at Week 5; 4 mice each from all groups at Week 10; and 9 mice each of Groups 1 and 3, 10 mice each of Groups 2 and 6, and 5 mice each of Groups 4, 5 and 7 at Week 20).

Other interesting findings in the current study are that administration of pitavastatin induced apoptosis in the colonic epithelial malignancies. There are no reports describing apoptosis-inducing effects of pitavastatin on tumor cells, although certain statins possess proapoptotic properties in a variety of tumor cell lines.[59–62]

TABLE VI – SERUM TRIGLYCERIDE (MG/DL) AT WEEKS 5, 10 AND 20

Group no.	Treatment	Wk 5	Wk 10	Wk 20
1	AOM/2% DSS	134.8 ± 63.5[a] (5)	174.6 ± 96.7 (5)	159.0 ± 59.7 (9)
2	AOM/2% DSS/1 ppm pitavastatin	79.4 ± 27.5 (5)	117.4 ± 21.7 (5)	64.4 ± 16.8[b] (7)
3	AOM/2% DSS/10 ppm pitavastatin	67.2 ± 26.8 (5)	84.2 ± 28.0 (5)	61.0 ± 27.5[b] (7)
4	10 ppm pitavastatin	77.8 ± 36.8 (5)	67.2 ± 13.3 (5)	59.0 ± 23.4 (5)
5	AOM	126.0 ± 51.2 (5)	92.0 ± 35.9 (5)	94.8 ± 34.0 (5)
6	2% DSS	70.4 ± 33.4 (5)	105.2 ± 24.8 (5)	79.3 ± 37.9 (7)
7	None	105.2 ± 38.1 (5)	54.0 ± 15.3 (5)	54.5 ± 16.0 (4)

Numbers of parentheses are numbers of mice examined.
[a]Mean ± SD.–[b]Significantly different from Group 1 by Tukey–Kramer multiple comparison post test ($p < 0.001$).

TABLE VII – SERUM TOTAL CHOLESTEROL (MG/DL) AT WEEKS 5, 10 AND 20

Group no.	Treatment	Wk 5	Wk 10	Wk 20
1	AOM/2% DSS	137.2 ± 10.0[a] (5)	137.4 ± 22.7 (5)	152.8 ± 43.7 (9)
2	AOM/2% DSS/1 ppm pitavastatin	127.6 ± 14.8 (5)	119.1 ± 20.9 (5)	114.9 ± 18.2 (7)
3	AOM/2% DSS/10 ppm pitavastatin	156.4 ± 26.2 (5)	105.2 ± 10.5 (5)	105.1 ± 23.5[b] (7)
4	10 ppm pitavastatin	117.2 ± 19.1 (5)	109.0 ± 10.7 (5)	106.6 ± 7.6 (5)
5	AOM	134.8 ± 20.6 (5)	146.4 ± 29.2 (5)	161.4 ± 33.3 (5)
6	2% DSS	151.2 ± 28.2 (5)	137.6 ± 35.4 (5)	119.1 ± 20.3 (7)
7	None	151.8 ± 14.6 (5)	140.6 ± 18.4 (5)	137.5 ± 25.1 (4)

Numbers of parentheses are numbers of mice examined.
[a]Mean ± SD.–[b]Significantly different from Group 1 by Tukey–Kramer multiple comparison post test ($p < 0.05$).

Lipophilic statins are reported to induce apoptosis in malignant cells. For example, Agarwal *et al.*[59] reported that lovastatin induces apoptosis with differing sensitivity in a variety of colon cancer cell lines (SW480, HCT 116, LoVo and HT29). They also found that lovastatin treatment results in decreased expression of the antiapoptotic protein Bcl-2 and increased the expression of the proapoptotic protein Bax. There are some reports describing the comparison of apoptosis inducing ability between lipophilic and hydrophilic statins in tumor[60] and nontumor cells.[63,64] These reports suggested that lipophilic statins are more effective for inducing apoptosis when compared to hydrophilic statins. As to antiproliferative action of statins, the effect of lovastatin on prostate cancer cells is stronger than that of a hydrophilic statin, pravastatin.[65] Thus, the lipophilic property of pitavastatin may be related to the apoptosis induction and inhibition of proliferation in adenocarcinomas observed in this study.

Statins, including pitavastatin, are drugs that primarily affect LDL-cholesterol levels in plasma through the induction of the hepatic LDL receptor.[66] In this experiment, pitavastatin treatment effectively lowered serum total cholesterol level at Week 20. In addition, administration of pitavastatin significantly decreased serum TG level that was 3-fold increased by AOM/DSS exposure at Week 20. Hypertriglyceridemia is a risk for human CRC development.[67,68] Also, hyperlipidemia is a relatively frequent complication in patients with familial adenomatous polyposis patients.[69] In this context, a recent report[70] that lipoprotein lipase gene polymorphism influences lipid metabolism in UC patients and age of onset of UC is of interest.

A growing body of literature has emerged on the prevention of CRC in patients with long-standing CD and UC.[71,72] However, the data are not definitive and consist almost exclusively of retrospective case–control and cohort studies rather than the more rigorous prospective multiple randomized controlled trials.[31] Although the data on statins use are still too limited to endorse its use for the prevention of colitis-related CRC, further studies with statins need to be performed to develop an optimal strategy for the reduction of cancer risk in IBD patients. While most statins are metabolized in part by one or more hepatic cytochrome P450 enzymes (mainly CYP3A4), leading to an increased potential for drug interactions and problems with certain foods, such as grapefruit juice, pitavastatin appears to be metabolized by a substrate of CYP2C9.[25] This property may prove beneficial for the long-term use of the drug in clinic.

In conclusion, our current findings that a lipophilic statin pitavastatin was effective for inhibiting colitis-related mouse colon carcinogenesis through modulating the cell proliferation, mucosal inflammation and oxidative/nitrosative stress in the target tissue suggest possible application of pitavastatin in suppressing colon carcinogenesis in the inflamed colon of patients with IBD. Further studies on detailed mechanisms of the action involved are underway in our laboratory using microarray and proteomics techniques.

References

1. Shepherd J, Cobbe SM, Ford I, Isles CG, Lorimer AR, MacFarlane PW, McKillop JH, Packard CJ, for the West of Scotland Coronary Prevention Study Group. Prevention of coronary heart disease with pravastatin in men with hypercholesterolemia. N Engl J Med 1995;333:1301–7.
2. Collins R, Armitage J, Parish S, Sleigh P, Peto R. MRC/BHF Heart Protection Study of cholesterol-lowering with simvastatin in 5963 people with diabetes: a randomised placebo-controlled trial. Lancet 2003;361:2005–16.
3. Saito Y, Yamada N, Teramoto T, Itakura H, Hata Y, Nakaya N, Mabuchi H, Tushima M, Sasaki J, Goto Y, Ogawa N. Clinical efficacy of pitavastatin, a new 3-hydroxy-3-methylglutaryl coenzyme A reductase inhibitor, in patients with hyperlipidemia. Dose-finding study using the double-blind, three-group parallel comparison. Arzneimittelforschung 2002;52:251–5.
4. Streja L, Packard CJ, Shepherd J, Cobbe S, Ford I. Factors affecting low-density lipoprotein and high-density lipoprotein cholesterol response to pravastatin in the West of Scotland Coronary Prevention Study (WOSCOPS). Am J Cardiol 2002;90:731–6.
5. Jick H, Zornberg GL, Jick SS, Seshadri S, Drachman DA. Statins and the risk of dementia. Lancet 2000;356:1627–31.
6. Crisby M. The role of pleiotropic effects of statins in dementia. Acta Neurol Scand Suppl 2006;185:115–18.
7. Meier CR, Schlienger RG, Kraenzlin ME, Schlegel B, Jick H. HMG-CoA reductase inhibitors and the risk of fractures. JAMA 2000;283:3205–10.
8. Graaf MR, Richel DJ, van Noorden CJ, Guchelaar HJ. Effects of statins and farnesyltransferase inhibitors on the development and progression of cancer. Cancer Treat Rev 2004;30:609–41.
9. Chan KK, Oza AM, Siu LL. The statins as anticancer agents. Clin Cancer Res 2003;9:10–19.
10. Jakobisiak M, Golab J. Potential antitumor effects of statins. Int J Oncol 2003;23:1055–69.
11. Campbell MJ, Esserman LJ, Zhou Y, Shoemaker M, Lobo M, Borman E, Baehner F, Kumar AS, Adduci K, Marx C, Petricoin EF, Liotta LA, et al. Breast cancer growth prevention by statins. Cancer Res 2006;66:8707–14.
12. Demierre MF, Higgins PD, Gruber SB, Hawk E, Lippman SM. Statins and cancer prevention. Nat Rev Cancer 2005;5:930–42.
13. Narisawa T, Fukaura Y, Terada K, Umezawa A, Tanida N, Yazawa K, Ishikawa C. Prevention of 1,2-dimethylhydrazine-induced colon tumorigenesis by HMG-CoA reductase inhibitors, pravastatin and simvastatin, in ICR mice. Carcinogenesis 1994;15:2045–8.
14. Narisawa T, Morotomi M, Fukaura Y, Hasebe M, Ito M, Aizawa R. Chemoprevention by pravastatin, a 3-hydroxy-3-methylglutaryl-coenzyme A reductase inhibitor, of *N*-methyl-*N*-nitrosourea-induced colon carcinogenesis in F344 rats. Jpn J Cancer Res 1996;87:798–804.
15. Reddy BS, Wang CX, Kong AN, Khor TO, Zheng X, Steele VE, Kopelovich L, Rao CV. Prevention of azoxymethane-induced colon cancer by combination of low doses of atorvastatin, aspirin, and celecoxib in F 344 rats. Cancer Res 2006;66:4542–6.
16. Swamy MV, Patlolla JM, Steele VE, Kopelovich L, Reddy BS, Rao CV. Chemoprevention of familial adenomatous polyposis by low doses of atorvastatin and celecoxib given individually and in combination to APCMin mice. Cancer Res 2006;66:7370–7.
17. Pleiner J, Schaller G, Mittermayer F, Zorn S, Marsik C, Polterauer S, Kapiotis S, Wolzt M. Simvastatin prevents vascular hyporeactivity during inflammation. Circulation 2004;110:3349–54.
18. Balkwill F, Mantovani A. Inflammation and cancer: back to Virchow? Lancet 2001;357:539–45.
19. Coussens LM, Werb Z. Inflammation and cancer. Nature 2002;420:860–7.

20. Rutter M, Saunders B, Wilkinson K, Rumbles S, Schofield G, Kamm M, Williams C, Price A, Talbot I, Forbes A. Severity of inflammation is a risk factor for colorectal neoplasia in ulcerative colitis. Gastroenterology 2004;126:451–9.
21. Eaden JA, Abrams KR, Mayberry JF. The risk of colorectal cancer in ulcerative colitis: a meta-analysis. Gut 2001;48:526–35.
22. Tanaka T, Kohno H, Suzuki R, Yamada Y, Sugie S, Mori H. A novel inflammation-related mouse colon carcinogenesis model induced by azoxymethane and dextran sodium sulfate. Cancer Sci 2003;94:965–73.
23. Kohno H, Suzuki R, Curini M, Epifano F, Maltese F, Gonzales SP, Tanaka T. Dietary administration with prenyloxycoumarins, auraptene and collinin, inhibits colitis-related colon carcinogenesis in mice. Int J Cancer 2006;118:2936–42.
24. Hata K, Tanaka T, Kohno H, Suzuki R, Qiang SH, Kuno T, Hirose Y, Hara A, Mori H. Lack of enhancing effects of degraded λ-carrageenan on the development of β-catenin-accumulated crypts in male DBA/2J mice initiated with azoxymethane. Cancer Lett 2006;238:69–75.
25. Mukhtar RY, Reid J, Reckless JP. Pitavastatin. Int J Clin Pract 2005; 59:239–4.
26. Flores NA. Pitavastatin Nissan/Kowa Yakuhin/Novartis/Sankyo. Curr Opin Investig Drugs 2002;3:1334–41.
27. Saito Y, Yamada N, Teramoto T, Itakura H, Hata Y, Nakaya N, Mabuchi H, Tushima M, Sasaki J, Ogawa N, Goto Y. A randomized, double-blind trial comparing the efficacy and safety of pitavastatin versus pravastatin in patients with primary hypercholesterolemia. Atherosclerosis 2002;162:373–9.
28. Iglesias P, Diez JJ. New drugs for the treatment of hypercholesterolaemia. Expert Opin Investig Drugs 2003;12:1777–89.
29. Kajinami K, Takekoshi N, Saito Y. Pitavastatin: efficacy and safety profiles of a novel synthetic HMG-CoA reductase inhibitor. Cardiovasc Drug Rev 2003;21:199–215.
30. Morikawa S, Takabe W, Mataki C, Kanke T, Itoh T, Wada Y, Izumi A, Saito Y, Hamakubo T, Kodama T. The effect of statins on mRNA levels of genes related to inflammation, coagulation, and vascular constriction in HUVEC. Human umbilical vein endothelial cells. J Atheroscler Thromb 2002;9:178–3.
31. Chan EP, Lichtenstein GR. Chemoprevention: risk reduction with medical therapy of inflammatory bowel disease. Gastroenterol Clin North Am 2006;35:675–712.
32. Mutoh M, Niho N, Wakabayashi K. Concomitant suppression of hyperlipidemia and intestinal polyp formation by increasing lipoprotein lipase activity in Apc-deficient mice. Biol Chem 2006;387:381–5.
33. Cooper HS, Murthy SN, Shah RS, Sedergran DJ. Clinicopathologic study of dextran sulfate sodium experimental murine colitis. Lab Invest 1993;69:238–49.
34. Rea WE, Durrant DC, Boldy DA. Ulcerative colitis after statin treatment. Postgrad Med J 2002;78:286–7.
35. Skaletz-Rorowski A, Walsh K. Statin therapy and angiogenesis. Curr Opin Lipidol 2003;14:599–603.
36. Crisby M. Modulation of the inflammatory process by statins. Drugs Today (Barc) 2003;39:137–43.
37. Devaraj S, Rogers J, Jialal I. Statins and biomarkers of inflammation. Curr Atheroscler Rep 2007;9:33–41.
38. Lee JY, Kim JS, Kim JM, Kim N, Jung HC, Song IS. Simvastatin inhibits NF-κB signaling in intestinal epithelial cells and ameliorates acute murine colitis. Int Immunopharmacol 2007;7:241–8.
39. Naito Y, Katada K, Takagi T, Tsuboi H, Isozaki Y, Handa O, Kokura S, Yoshida N, Ichikawa H, Yoshikawa T. Rosuvastatin, a new HMG-CoA reductase inhibitor, reduces the colonic inflammatory response in dextran sulfate sodium-induced colitis in mice. Int J Mol Med 2006;17:997–1004.
40. Fujino M, Miura S, Matsuo Y, Tanigawa H, Kawamura A, Saku K. Pitavastatin-induced down-regulation of CCR2 and CCR5 in monocytes is associated with the arrest of cell-cycle in S phase. Atherosclerosis 2006;187:301–8.
41. Papadakis KA. Chemokines in inflammatory bowel disease. Curr Allergy Asthma Rep 2004;4:83–9.
42. Wang J, Tokoro T, Matsui K, Higa S, Kitajima I. Pitavastatin at low dose activates endothelial nitric oxide synthase through PI3K-AKT pathway in endothelial cells. Life Sci 2005;76:2257–68.
43. Procko E, McColl SR. Leukocytes on the move with phosphoinositide 3-kinase and its downstream effectors. Bioessays 2005;27:153–63.
44. Blume-Jensen P, Hunter T. Oncogenic kinase signalling. Nature 2001;411:355–65.
45. Luo J, Manning BD, Cantley LC. Targeting the PI3K-Akt pathway in human cancer: rationale and promise. Cancer Cell 2003;4:257–62.
46. Rychahou PG, Jackson LN, Silva SR, Rajaraman S, Evers BM. Targeted molecular therapy of the PI3K pathway: therapeutic significance of PI3K subunit targeting in colorectal carcinoma. Ann Surg 2006; 243:833–42.
47. Kankuri E, Hamalainen M, Hukkanen M, Salmenpera P, Kivilaakso E, Vapaatalo H, Moilanen E. Suppression of pro-inflammatory cytokine release by selective inhibition of inducible nitric oxide synthase in mucosal explants from patients with ulcerative colitis. Scand J Gastroenterol 2003;38:186–92.
48. Halliwell B. What nitrates tyrosine? Is nitrotyrosine specific as a biomarker of peroxynitrite formation in vivo? FEBS Lett 1997;411:157–60.
49. Ambs S, Merriam WG, Bennett WP, Felley-Bosco E, Ogunfusika MO, Oser SM, Klein S, Shields PG, Billiar TR, Harris CC. Frequent nitric oxide synthase-2 expression in human colon adenomas: implication for tumor angiogenesis and colon cancer progression. Cancer Res 1998;58:334–41.
50. Takahashi M, Mutoh M, Kawamori T, Sugimura T, Wakabayashi K. Altered expression of β-catenin, inducible nitric oxide synthase and cyclooxygenase-2 in azoxymethane-induced rat colon carcinogenesis. Carcinogenesis 2000;21:1319–27.
51. Barnes PJ, Karin M. Nuclear factor-κB: a pivotal transcription factor in chronic inflammatory diseases. N Engl J Med 1997;336:1066–71.
52. Chen C, Edelstein LC, Gelinas C. The Rel/NF-κB family directly activates expression of the apoptosis inhibitor Bcl-x(L). Mol Cell Biol 2000;20:2687–95.
53. Barkett M, Gilmore TD. Control of apoptosis by Rel/NF-κB transcription factors. Oncogene 1999;18:6910–24.
54. Wang J, Tokoro T, Higa S, Kitajima I. Anti-inflammatory effect of pitavastatin on NF-κB activated by TNF-α in hepatocellular carcinoma cells. Biol Pharm Bull 2006;29:634–9.
55. Garat C, Arend WP. Intracellular IL-1Ra type 1 inhibits IL-1-induced IL-6 and IL-8 production in Caco-2 intestinal epithelial cells through inhibition of p38 mitogen-activated protein kinase and NF-κB pathways. Cytokine 2003;23:31–40.
56. Kibayashi E, Urakaze M, Kobashi C, Kishida M, Takata M, Sato A, Yamazaki K, Kobayashi M. Inhibitory effect of pitavastatin (NK-104) on the C-reactive-protein-induced interleukin-8 production in human aortic endothelial cells. Clin Sci (Lond) 2005;108:515–21.
57. Masamura K, Oida K, Kanehara H, Suzuki J, Horie S, Ishii H, Miyamori I. Pitavastatin-induced thrombomodulin expression by endothelial cells acts via inhibition of small G proteins of the Rho family. Arterioscler Thromb Vasc Biol 2003;23:512–17.
58. Davignon J, Mabile L. Mechanisms of action of statins and their pleiotropic effects (in French). Ann Endocrinol (Paris) 2001;62 (Part 2):101–12.
59. Agarwal B, Bhendwal S, Halmos B, Moss SF, Ramey WG, Holt PR. Lovastatin augments apoptosis induced by chemotherapeutic agents in colon cancer cells. Clin Cancer Res 1999;5:2223–9.
60. Cafforio P, Dammacco F, Gernone A, Silvestris F. Statins activate the mitochondrial pathway of apoptosis in human lymphoblasts and myeloma cells. Carcinogenesis 2005;26:883–91.
61. Marcelli M, Cunningham GR, Haidacher SJ, Padayatty SJ, Sturgis L, Kagan C, Denner L. Caspase-7 is activated during lovastatin-induced apoptosis of the prostate cancer cell line LNCaP. Cancer Res 1998;58:76–83.
62. Wang IK, Lin-Shiau SY, Lin JK. Induction of apoptosis by lovastatin through activation of caspase-3 and DNase II in leukaemia HL-60 cells. Pharmacol Toxicol 2000;86:83–91.
63. Nagashima T, Okazaki H, Yudoh K, Matsuno H, Minota S. Apoptosis of rheumatoid synovial cells by statins through the blocking of protein geranylgeranylation: a potential therapeutic approach to rheumatoid arthritis. Arthritis Rheum 2006;54:579–86.
64. Tsujimoto A, Takemura G, Mikami A, Aoyama T, Ohno T, Maruyama R, Nakagawa M, Minatoguchi S, Fujiwara H. A therapeutic dose of the lipophilic statin pitavastatin enhances oxidant-induced apoptosis in human vascular smooth muscle cells. J Cardiovasc Pharmacol 2006;48:160–5.
65. Sivaprasad U, Abbas T, Dutta A. Differential efficacy of 3-hydroxy-3-methylglutaryl CoA reductase inhibitors on the cell cycle of prostate cancer cells. Mol Cancer Ther 2006;5:2310–16.
66. Maron DJ, Fazio S, Linton MF. Current perspectives on statins. Circulation 2000;101:207–13.
67. Tabuchi M, Kitayama J, Nagawa H. Hypertriglyceridemia is positively correlated with the development of colorectal tubular adenoma in Japanese men. World J Gastroenterol 2006;12:1261–4.
68. Yamada K, Araki S, Tamura M, Sakai I, Takahashi Y, Kashihara H, Kono S. Relation of serum total cholesterol, serum triglycerides and fasting plasma glucose to colorectal carcinoma in situ. Int J Epidemiol 1998;27:794–8.
69. Mutoh M, Akasu T, Takahashi M, Niho N, Yoshida T, Sugimura T, Wakabayashi K. Possible involvement of hyperlipidemia in increasing risk of colorectal tumor development in human familial adenomatous polyposis. Jpn J Clin Oncol 2006;36:166–71.
70. Kosaka T, Yoshino J, Inui K, Wakabayashi T, Okushima K, Kobayashi T, Miyoshi H, Nakamura Y, Hayashi S, Shiraishi T, Watanabe M, Yamamoto T et al. Impact of lipoprotein lipase gene polymorphisms on ulcerative colitis. World J Gastroenterol 2006;12:6325–30.
71. Itzkowitz SH. Cancer prevention in patients with inflammatory bowel disease. Gastroenterol Clin North Am 2002;31:1133–44.
72. Rubin DT, Parekh N. Colorectal cancer in inflammatory bowel disease: molecular and clinical considerations. Curr Treat Options Gastroenterol 2006;9:211–20.

Int. J. Cancer: **121,** 1659–1664 (2007)

Tumor-initiating potency of a novel heterocyclic amine, aminophenylnorharman in mouse colonic carcinogenesis model

Hiroyuki Kohno[1]*, Yukari Totsuka[2], Yumiko Yasui[1], Rikako Suzuki[1], Shigeyuki Sugie[1], Keiji Wakabayashi[2] and Takuji Tanaka[1]

[1]*Department of Oncologic Pathology, Kanazawa Medical University, 1-1 Daigaku, Uchinada, Ishikawa, Japan*
[2]*Cancer Prevention Basic Research Project, National Cancer Research Institute, 5-1-1 Tukiji, Chuo-ku, Tokyo, Japan*

A novel heterocyclic amine, 9-(4′-aminophenyl)-9*H*-pyrido[3,4-*b*]indole (aminophenylnorharman, APNH), which is formed from nonmutagenic 9*H*-pyrido[3,4-*b*]indole (norharman) and aniline, is mutagenic to bacteria and mammalian cells and potently carcinogenic in rats. APNH is detected in human urine samples, suggesting that humans are continuously exposed to APNH. In the present study, ^{32}P-postlabelin analysis revealed that the levels of APNH-DNA adduct 24 hr after the treatment with APNH (1, 5 and 20 mg/kg body weight) in male ICR mice were increased in a dose-dependent manner in the colon and liver. Based on these findings, we determined the tumor-initiating potency of APNH in an inflammation-related and two-stage mouse colon carcinogenesis model. Male Crj: CD-1 (ICR) mice were given a single intragastric administration (1, 2, 5 or 10 mg/kg body weight) of APNH and subsequent 1-week oral exposure to dextran sodium sulfate (DSS, 2% in drinking water). Treatment with APNH and DSS resulted in numerous colon tumor development: the incidence and multiplicity of the tumors were the highest in the mice received 10 mg/kg body weight of APNH and followed by DSS. Development of colon tumors was dose-dependent of APNH. Seven of 9 (77.8%) colonic adenocarcinomas developed in mice treated with APNH (10 mg/kg body weight) and DSS had β-*catenin* gene mutations at codons 32 and 37, being predominantly transversion. These findings indicate that APNH has an initiating activity in inflamed mouse colon and the APNH-DNA adduct formation correlates with its tumorigenic potential.

Key words: aminophenylnorharman; adenocarcinoma; β-catenin; colon; dextran sodium sulfate; DNA adduct; heterocyclic amines; initiation; mice

The development of most human cancer might be caused by carcinogenic agents in the diet and cigarette smoke.[1] Therefore, identification of mutagens and carcinogens in foods and cigarette smoke is very important for understanding the causal agents of human cancer. A series of mutagenic and carcinogenic heterocyclic amines (HCAs) have been identified in cooked foods and heating amino acids and proteins.[2] The β-carboline compound norharman (9*H*-pyrido[3,4-*b*]indole) is produced in the pyrolysis of tryptophan.[3] Norharman is present at much higher levels than 2-amino-1-methyl-6-phenylimidazo[4,5-*b*]pyridine (PhIP) and 2-amino-3,8-dimethylimidazo[4,5-*f*]quinoxaline (MeIQx) in human urine samples.[4] Although norharman is not mutagenic to *Salmonella* strains, it becomes mutagenic to *S. typhimurium* TA98 in the presence of S9 mix, when incubated with non-mutagenic aromatic amines, such as aniline.[5] A novel HCA, 9-(4′-aminophenyl)-9*H*-pyrido[3,4-*b*]indole (aminophenylnorharman, APNH) can be formed by this reaction, then converted to the *N*-hydroxyamino derivative which produces DNA adducts after esterification to induce mutations in *S. typhimurium* TA98 and YG1024.[6–8] APNH is able to induce sister chromatid exchanges and chromosome aberrations.[9] We have recently demonstrated that APNH forms DNA adducts at the C-8 position of guanine residues in the various tissues including liver and colon of F344 rats after administration of APNH.[10] Subsequently, it has been reported that the *gpt* mutant frequencies were elevated in the liver and colon of the *gpt* delta transgenic mouse treated with APNH.[11] Norharman is reported to be present at much higher levels than those of HCAs in cooked meat and fish and cigarette smoke condensate.[12] Aniline is also present in cigarette smoke condensate and certain vegetables.[13] In addition, APNH was detected in 24 hr urine samples collected from F344 rats that received norharman and aniline.[14] Moreover, we have detected APNH in human urine samples from both healthy volunteers and patients in the hospital,[15] suggesting thus that humans are continuously exposed to APNH.

To understand the effects of APNH on human health, it is important to elucidate its carcinogenicity in rodents. It has been demonstrated that dietary feeding with APNH induces preneoplastic hepatocellular lesions, glutathione *S*-transferase placental form-positive foci, in the liver of male F344 rats.[16] Moreover, it has been already reported that the feeding with APNH for 85 weeks resulted in the development of hepatocellular carcinomas (HCCs, 10–79% incidence), and the colonic adenocarcinomas with low incidences (3–13% incidence) in male and female F344 rats.[17] These findings suggest a weak tumor-initiating capability of APNH in the colon.

We recently developed a novel mouse model for inflammation-related colon carcinogenesis[18] and this can be used for detecting the HCAs with colonic carcinogenicity in mice within a short-term period.[19] Also, we have evaluated tumor-promoting activity of chemicals utilizing this inflammation-related and two-stage mouse model.[20]

In the present study, we examined the APNH-DNA adduct formation in the colon and liver of mice that received APNH using the ^{32}P-postlabeling method. Additionally, we investigated tumor-initiating activity of APNH in mice by gavage with various doses of APNH in the inflamed colon induced by dextran sodium sulfate (DSS). The β-*catenin* gene mutations in colonic adenocarcinomas developed were also analyzed by the single strand conformation polymorphism (SSCP) method and direct sequencing.

Material and methods

Animals, chemicals and diet

Male Crlj: CD-1 (ICR) mice (Charles River Japan, Tokyo, Japan) aged 5 weeks were used. They were maintained at Kanazawa Medical University Animal Facility according to the Institutional Animal Care Guidelines. All animals were housed in plastic cages

Abbreviations: APNH, aminophenylnorharman (9-(4′-amino-3′-aminophenyl)-9*H*-pyrido[3,4-*b*]indole); DSS, dextran sodium sulfate; HCA, heterocyclic amine; H&E, hematoxylin and eosin; i.g., intragastric; MeIQx, 2-amino-3,8-dimethylimidazo[4,5-*f*]quinoxaline; PCR, polymerase chain reaction; PhIP, 2-amino-1-methyl-6-phenylimidazo[4,5-*b*]pyridine; RAL, relative adduct labeling; SSCP, single strand conformation polymorphism.

Grant sponsors: Ministry of Health, Labour and Welfare of Japan, Ministry of Education, Culture, Sports, Science and Technology of Japan, Kanazawa Medical University; Grant numbers: H2006-6, C2006-3.

***Correspondence to:** Department of Oncologic Pathology, Kanazawa Medical University, 1-1 Daigaku, Uchinada, Ishikawa 920-0293, Japan. Fax: +81-76-286-6926. E-mail: h-kohno@kanazawa-med.ac.jp

Received 22 March 2007; Accepted after revision 24 April 2007
DOI 10.1002/ijc.22864
Published online 7 June 2007 in Wiley InterScience (www.interscience.wiley.com).

(4 or 5 mice/cage) with free access to drinking water and a pelleted basal diet, CRF-1 (Oriental Yeast, Tokyo, Japan), under controlled conditions of humidity (50% ± 10%), light (12/12 hr light/dark cycle) and temperature (23°C ± 2°C). After 7-days-quarantine, they were randomized by body weight into experimental and control groups. APNH was purchased from the Nard Institute (Osaka, Japan) and its purity was confirmed to be > 99% by HPLC. DSS with a molecular weight of 36,000–50,000 (Cat No. 160110) was purchased from MP Biochemicals, LLC (Aurora, OH).

Formation of APNH-DNA adducts

To analyze APNH-DNA adduct formation, nine male ICR mice were provided. At 6 weeks of age, they were given a single intragastric intubation (i.g.) of APNH at doses of 1, 5 and 20 mg/kg body weight and sacrificed after 24 hr. The liver and colon were excised and store at −80°C until DNA extraction by standard procedure involving enzymatic digestion of protein and RNA followed by extraction with phenol and chloroform/isoamyl alcohol (24:1, v/v).

DNA obtained from the experiment was digested with micrococcal nuclease and phosphodiesterase II, and the digest was ^{32}P-postlabeled under modified-standard and adduct-intensification conditions as reported previously.[10,21,22] Adducts were detected with a Bio-Image Analyzer (BAS 2000; Fuji Photo Film, Tokyo, Japan) after exposing the TLC sheets to Fuji imaging plates. Relative adduct labeling (RAL) was determined by the method of Randerath *et al.*,[23] and the values were calculated as averages of 3 assays.

Experimental procedure for tumor-initiating activity

A total of 53 male ICR mice were divided into 7 experimental and solvent control groups. Groups 1 through 4 were given a single i.g. of APNH at a dose of 1, 2, 5 or 10 mg/kg body weight. Starting one week after the APNH administration, animals in Groups 1 through 4 were given 2% (w/v) DSS in drinking water for 7 days, and then followed without any further treatment for 17 weeks. Groups 5 and 6 were given APNH (10 mg/kg body weight) alone and 2% DSS alone, respectively. Group 7 was untreated. All animals were sacrificed at week 20. The colon were flushed with saline, excised, measured their length (from ileocecal junction to the anal verge), cut open longitudinally along the main axis and then washed with saline. After careful macroscopic inspection on the colon, they were cut and fixed in 10% buffered formalin for at least 24 hr. Histological examination was performed on paraffin-embedded sections after hematoxylin and eosin (H&E) staining. Some tumors were stored in a deep-freezer at −80°C for analysis of β-*catenin* mutation. On the H&E-stained sections, histological alterations, such as mucosal ulceration, dysplasia and colonic neoplasms were examined. Colonic neoplasms were diagnosed according to the description by Ward.[24] A histopathological examination was also done in other organs. Mucosal inflammation with or without ulceration in the colon was analyzed on the H&E-stained sections. Colonic inflammation was graded according to the following morphological criteria described by Cooper *et al.*[25]: Grade 0, normal appearance; Grade 1, shortening and loss of the basal one-third of the actual crypts with mild inflammation in the mucosa; Grade 2, loss of the basal two-thirds of the crypts with moderate inflammation in the mucosa; Grade 3, loss of the entire crypts with severe inflammation in the mucosa and submucosa, but with retainment of the surface epithelium; and Grade 4, presence of mucosal ulcer with severe inflammation (neutrophil, lymphocyte and plasma cell infiltration) in the mucosa, submucosa, muscularis propria and/or subserosa. The scoring was made on the entire intestine with or without proliferative lesions and expressed as a mean average score/mouse.

DNA extraction

For analysis of β-*catenin* mutations, 9 colonic adenocarcinomas (frozen materials) developed in APNH (10 mg/kg body weight)/DSS-treated mice were used. DNA was extracted from frozen tissue using Wizard® Genomic DNA Purification Kit (Promega, Madison, WI).

Polymerase chain reaction (PCR)-SSCP analysis and direct sequencing

DNA from colonic adenocarcinomas was PCR-amplified with primers (5′-primer, GCTGACCTGATGGAGTTGGA; 3′-primer, GCTACTTGCTCTTGCGTGAA), which were designed to amplify exon 3 of the β-*catenin* gene containing the consensus sequence for glycogen synthase kinase-3β phosphorylation.[26] The length of the PCR product with these primers is 227 bp. The primers were synthesized with a 394 DNA/RNA synthesizer (Applied Biosystems, Foster City, CA) and purified with an OPC cartridge (Applied Biosystems). PCR for non-radioisotopic SSCP was performed in 50 μl of reaction mixture consisting of 0.5 μM of each primer, 1 × PCR buffer (Perkin Elmer, Applied Biosystems Division, Foster City, CA), 200 μM each dNTP, 2.5 U AmpliTaq Gold™ (Perkin Elmer) and 0.5–5 μl of template DNA. The mixture was heated at 94°C for 9 min and subjected to 40 or 35 cycles of denaturation (94°C, 1 min), annealing (55°C, 2 min) and extension (72°C, 3 min) using a using a Perkin Elmer-Cetus thermal cycler. The PCR products were purified and concentrated to 20 μl using Microcon 100 (Amicon, Beverley, MA). Ten volumes of 95% formamide, 20 mM EDTA, 0.05% bromophenol blue, 0.05% xylene cyanol were added to 0.5 μl of purified PCR products, heated to 90°C for 3 min and applied to 10% polyacrylamide gels containing 5% glycerol. Electrophoresis was carried out at 300 V for 2 hr at 20°C and the gels were soaked in 10% trichloroacetic acid and in 50% methanol for 10 min each. DNA bands were detected by silver staining using 2D Silver Staining Solution II (Daiichi Chemical DNA, Tokyo, Japan). When mutated shifted band were observed in the gels, mutation analysis was performed by direct sequencing of PCR products using on ALF express™ DNA sequencer (Pharmacia Biotech).

Statistical analysis

All measurements were compared by one-way ANOVA with either Tukey's correction or Fisher's exact probability test (GraphPad Instat version 3.05, GraphPad Software, San Diego, CA), with $p < 0.05$ as the criterion of significance.

Results

DNA adduct formation by APNH

Administration of APNH had no macroscopic lesions in any organs. APNH-DNA adduct formation was analyzed in colon and liver of male ICR mice treated with APNH at doses of 1, 5 and 20 mg/kg body weight for 24 hr. When the DNA samples from the colon of APNH-treated mice were analyzed by ^{32}P-postlabeling analysis, 2 major adduct spots corresponding to dG-C8-APNH were observed, and this TLC pattern was similar to that of DNA samples obtained from various tissues of rat received 40 ppm of APNH for 4 weeks.[10] Also, the TLC pattern of liver DNA samples were the similar to those of colon DNA samples. As shown in Table I, the adduct levels of the colon and liver were increased in a dose-dependent manner. Furthermore, the RAL values for colon were higher than those for liver.

TABLE I – LEVELS OF APNH-DNA ADDUCTS IN THE LIVER AND COLON ON MICE GIVEN APNH

Treatment (no of mice examined)	Adduct levels (adducts/10^7 nucleotides)	
	Liver	Colon
APNH 1 mg/kg (3)	0.39 ± 0.13[1]	5.9 ± 2.6
APNH 5 mg/kg (3)	3.82 ± 2.30	45.2 ± 10.3
APNH 20 mg/kg (3)	41.0 ± 15.3	141.9 ± 45.8

[1]Means ± SD.

TABLE II – BODY WEIGHTS, LIVER WEIGHTS, AND LENGTHS OF COLON IN EACH GROUP

Group no.	Treatment (no of mice examined)	Body weight (g)	Liver weight (g)	Length of colon 7(cm)
1	APNH 1 mg/kg→2%DSS (10)	44.9 ± 4.9[1]	2.99 ± 0.46[2]	14.6 ± 0.8
2	APNH 2 mg/kg→2%DSS (9)	42.8 ± 3.2	2.74 ± 0.32	14.3 ± 0.7
3	APNH 5 mg/kg→2%DSS (8)	43.0 ± 6.1	2.75 ± 0.57	13.9 ± 1.0
4	APNH 10 mg/kg→2%DSS (9)	42.1 ± 3.8	2.56 ± 0.47	12.3 ± 0.9[3]
5	APNH 10 mg/kg (5)	42.8 ± 3.6	2.31 ± 0.47	12.3 ± 0.9[3]
6	2%DSS (7)	42.3 ± 2.7	2.19 ± 0.22	13.3 ± 1.2
7	Untreated (5)	41.6 ± 2.8	2.45 ± 0.17	15.1 ± 0.5

[1]Mean ± SD.–[2]Significantly different from group 6 by Tukey's multiple comparison post test ([2]$p < 0.01$).–[3]Significantly different from group 7 by Tukey's multiple comparison post test ([3]$p < 0.001$).

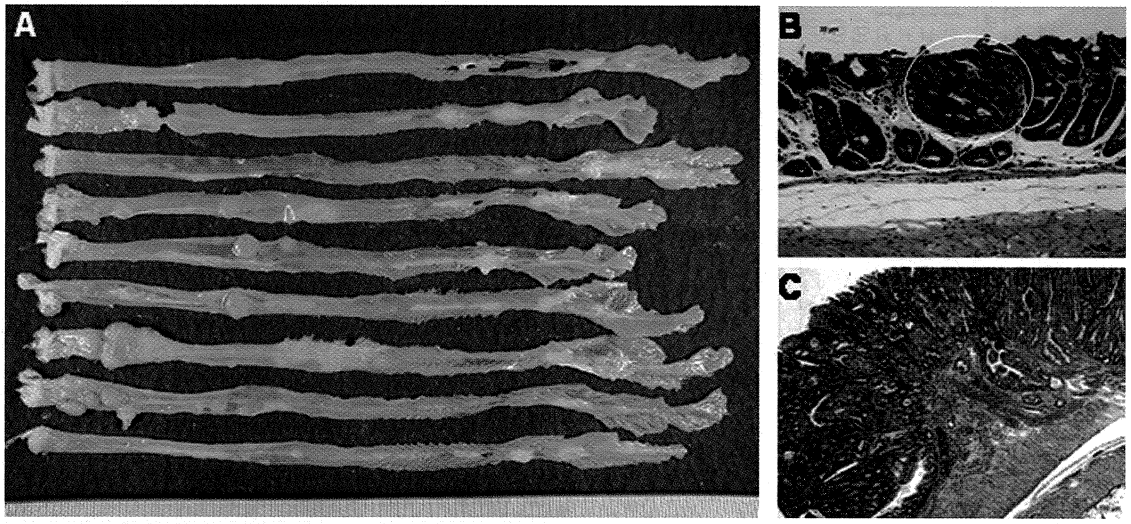

FIGURE 1 – Macroscopic view of the large bowel (*a*) and histopathology of the colonic lesions (*b*, *c*) of ICR mice treated with APNH 10 mg/kg body weight → 2% DSS. (*a*) A number of colonic tumors are seen in mice given APNH 10 mg/kg body weight → 2% DSS. (*b*) A tumor (white circle) is diagnosed as tubular adenoma. (*c*) A tumor is histologically well differentiated tubular adenocarcinomas. H&E stain, original magnification: (*b*), (*c*), × 100.

TABLE III – INCIDENCE OF VOLONIC NEOPLASMS IN MICE TREATED WITH APNH AND DSS

Group no.	Treatment (no of mice examined)	No. of mice with colonic neoplasms		
		Total (multiplicity)	Adenoma (multiplicity)	Adenocarcinoma (multiplicity)
1	APNH 1 mg/kg→2%DSS (10)	0% (0)	0% (0)	0% (0)
2	APNH 2 mg/kg→2%DSS (9)	11% (0.11 ± 0.33)	11% (0.11 ± 0.33)	0% (0)
3	APNH 5 mg/kg→2%DSS (8)	13% (0.38 ± 1.06)	13% (0.13 ± 0.35)	13% (0.25 ± 0.71)
4	APNH 10 mg/kg→2%DSS (9)	56%* (1.89 ± 2.09[1,2])	33% (0.78 ± 1.39)	56%* (1.11 ± 1.26[1,2])
5	APNH 10 mg/kg (5)	0	0	0
6	2%DSS (7)	0	0	0
7	Untreated (5)	0	0	0

Numbers in parentheses are mean ± SD.
Significantly different from group 6 by Fisher's exact probability test ($p = 0.033$).
[1]Significantly different from group 1 by Tukey's multiple comparison post test ([1]$p < 0.01$).–[2]Significantly different from group 2 by Tukey's multiple comparison post test ([2]$p < 0.05$).

General observation in the inflamed colon induced by DSS tumor-initiating activity

Bloody stool was found during and soon after of DSS exposure (Day 12–21) in a few mice that received 2% DSS and their body weight gains were slightly decreased (data not shown). The body and liver weights and lengths of colon of mice in all groups at the end of the study (week 20) are listed in Table II. The mean body weights showed no significant differences among the groups. The means liver weights of Group 1 (APNH 1 mg/kg (2% DSS) was significantly larger than that of Group 6 (2% DSS alone, $p < 0.01$). The mean length of colon of mice in Group 4 (APNH 10 mg/kg → 2% DSS, $p < 0.001$) were significantly lower than that of Group 7 (untreated).

Pathological findings in the inflamed colon induced by DSS tumor-initiating activity

Macroscopically, nodular, polypoid or flat-type colonic tumors were observed in the middle and distal colon of mice in Groups 2 through 4 (Fig. 1*a*, Table III). Their histopathology was well- or moderately differentiated tubular adenocarcinoma (Fig. 1*b*) or tubular adenoma (Fig. 1*c*). There were no tumors in any organs other than colon in these groups. The mice in Group 1 (APNH 1 mg/kg → 2% DSS) had no tumors in the colon and other organs, including liver. The incidences of total colonic neoplasms and adenocarcinoma in Groups 4 (APNH 10 mg/kg → 2% DSS; $p < 0.05$) were significantly greater than Group 6 (2% DSS alone). Also, the multiplicity of colonic neoplasms and colonic adenocar-

TABLE IV – INCIDENCE OF COLON ULCERATION AND DYSPLASIA IN MICE TREATED WITH APNH AND DSS

Group no.	Treatment (no of mice examined)	Inflammation score	Incidence of mucosal ulcer (multiplicity)	Incidence of colonic dysplasia		
				Total (multiplicity)	Low-grade (multiplicity)	High-grade (multiplicity)
1	APNH 1 mg/kg→2%DSS (10)	2.00 ± 0.94	100% (3.30 ± 1.70)	100%* (4.70 ± 1.57)	100%* (3.90 ± 1.45)	100%* (1.10 ± 4.70)
2	APNH 2 mg/kg→2%DSS (9)	2.22 ± 0.97	100% (3.78 ± 1.92)	100%* (6.22 ± 3.46)	100%* (3.89 ± 1.45)	100%* (2.33 ± 2.50)
3	APNH 5 mg/kg→2%DSS (8)	2.13 ± 0.83	100% (3.88 ± 1.46)	100%* (7.13 ± 2.80)	100%* (3.75 ± 1.39)	100%* (3.38 ± 2.13)
4	APNH 10 mg/kg→2%DSS (9)	1.78 ± 0.44	100% (3.11 ± 1.05)	100%* (9.11 ± 2.62[1])	100%* (4.44 ± 1.42)	100%* (4.67 ± 2.12[1])
5	APNH 10 mg/kg (5)	0	0% (0)	0% (0)	0% (0)	0% (0)
6	2%DSS (7)	1.86 ± 0.69	100% (3.00 ± 1.00)	0% (0)	0% (0)	0% (0)
7	Untreated (5)		0% (0)	0% (0)	0% (0)	0% (0)

Numbers in parentheses are mean ± SD.
Significantly different from group 6 by Fisher's exact probability test ($p < 0.001$).
[1]Significantly different from group 1 by Tukey's multiple comparison post test ([1]$p < 0.05$).

cinoma in Group 4 (APNH 10 mg/kg → 2% DSS) were significantly greater than Groups 2 (APNH 2 mg/kg → 2% DSS; $p < 0.01$). The squared correlation coefficients for the multiplicities of total colonic neoplasms (adenoma plus adenocarcinoma), adenoma and adenocarcinoma obtained by the regression were 0.97 ($p < 0.01$), 0.95 ($p < 0.05$) and 0.98 ($p < 0.01$), respectively. These values suggested a dose-response tumor-initiating potency of APNH on development of colonic tumors. In mice of Groups 5–7, no neoplasms developed in any organs including colon.

As indicated in Table IV, colonic dysplasia also developed in Groups 1 through 4. Their multiplicities of the total dysplasia and high-grade dysplasia were significantly increased when the dose of APNH increased in Groups 1–4. The correlation coefficients for the multiplicities of total dysplasia and high-grade-dysplasia were 0.97 ($p < 0.01$) and 0.96 ($p < 0.01$), respectively. These values suggested a dose-response effect on the development of colonic dysplasia. There were no dysplatic lesions in mice of Groups 5 through 7. In addition, colonic mucosal ulceration was found in the distal colon of mice that received DSS (Table IV). Table IV summarizes data on colonic inflammation scores in the colon. No significant differences on the degrees of colonic mucosal inflammation were noted among the groups treated with DSS (Groups 1–4 and 6).

Mutation in β-Catenin gene

In the current experiment, mutations of exon 3 of the β-*catenin* gene were investigated in the colonic adenocarcinomas developed in mice of Group 4 (APNH 10 mg/kg (2% DSS) by the PCR-SSCP method and direct sequencing. Seven of 9 (77.8%) colonic adenocarcinomas developed had β-*catenin* gene mutations that were restricted to codons 32 and 37 (Table V). The mutations were GAT (Asp) to TAT (Tyr) and GAT (Asp) to AAT (Asn) at the codon 32 and TCT (Ser) to TGT (Cys) and TCT (Ser) to TAT (Tyr) at the codon 37. The majority of these mutations were transversions.

Discussion

The results of the present study using an inflammation-related two-stage mouse colon carcinogenesis model indicate that one of the HCAs, APNH, has a strong tumor-initiation activity in the inflamed colon. This activity was dose-dependent and related with APNH-DNA adducts formation levels in the colon. The adenocarcinomas developed in mice initiated with APNH and promoted by DSS possessed β-*catenin* mutations. This is the first report demonstrating tumor-initiating ability of APNH in the colon. In this study, we also investigated the initiation activity of 20 mg/kg body weight of APNH. Although approximately half of the mice that received APNH (20 mg/kg body weight) followed by 2% DSS died due to hepatotoxicity of APNH 3–4 days after i.g. administration, the survivors had colonic tumors (50% incidence of adenocarcinoma with 0.73 ± 0.90 multiplicity and 33% incidence of adenomas with 0.55 ± 0.82 multiplicity).

DNA adduct formation by chemical carcinogens is important because the active dose of chemical carcinogen reaching its target site should exert their initiating events in chemical carcinogene-

TABLE V – MUTATIONS IN EXON 3 OF THE β-*CATENIN* GENE IN APNH/DSS-INDUCED MOUSE COLONIC ADENOCARCINOMAS

Sample	β-catenin status		Amino acid substitution
APNH /DSS-1	Codon 37	TCT→TGT	Ser→Cys
APNH /DSS-2	Codon 37	TCT→TGT	Ser→Cys
APNH /DSS-3	Codon 32	GAT→TAT	Asp→Tyr
APNH /DSS-4	Codon 37	TCT→TAT	Ser→Tyr
APNH /DSS-5		Wild type	
APNH /DSS-6	Codon 32	GAT→AAT	Asp→Asn
APNH /DSS-7	Codon 32	GAT→TAT	Asp→Tyr
APNH /DSS-8		Wild type	
APNH /DSS-9	Codon 32	GAT→TAT	Asp→Tyr

sis.[27] The HCAs form tissue DNA adducts in humans and rodents.[28] MeIQx induces HCCs[29] and produces relatively high hepatic DNA adduct levels in rats.[30] In contrast, PhIP that is not hepatocarcinogenic, forms relatively low hepatic PhIP-DNA adduct levels in comparison with other tissues in rats.[31] APNH-DNA adducts were detected in various organs of rats given APNH, with levels higher in the liver and colon than in other organs.[10] In the current study, we observed the APNH-DNA adduct formation in the colon and liver, as found in rats,[10] and the levels in colon were greater than in liver. Furthermore, there was a clear dose-dependency in the APNH-DNA adduct formations in both organs. Thus, APNH-DNA adducts should be involved in the induction of colonic neoplasia in mice. APNH formed DNA adducts in the liver and induced HCC in F344 rats.[17] However, the mice received with APNH/DSS had no liver tumors in this study. These differences in the liver carcinogenicity of APNH may be due to the differences in the experimental protocol. As reported previously in rats,[10] the major APNH-DNA adduct was dG-C8-APNH in this study, it is suggested that dG-C8-APNH was formed in the target genes, such as β-*catenin*, and these adducts might cause the mutations. In fact, the mutations detected in the APNH-induced tumors were mainly at G:C base pairs.

HCAs, such as PhIP and MeIQx are able to induce multi-site tumors in rodents and monkeys.[32,33] When given high doses of PhIP for a long-term period, colonic tumors developed in rats.[34] Although dietary APNH at a dose of 20 or 40 ppm for 85 weeks induced colonic tumors in F344 rats, the incidence of colonic tumors was low, being 3 or 9% in males and 4 or 13% in females, respectively,[17] suggesting a weak tumor-initiating ability of APNH in the rat colon. In the current study, colonic neoplasms developed in the mice given APNH at all doses except for 1 mg/kg b.w., when followed by DSS. The tumor-initiating ability of APNH in this model was greater than that of PhIP and MeIQx when used the same experimental protocol.[19] These findings suggest the importance of inflammation in colon carcinogenesis. For further understanding the role of APNH in human colon cancer development, studies for APNH-DNA adduct levels in human colon samples and *in vivo* rat experiments with the protocol used in this study will be required.

Recent evidence demonstrates that the β-catenin signaling pathway is closely associated with the development of colon cancer.[35,36] The β-*catenin* gene is frequently mutated in human colon cancers without *APC* mutations[37] and carcinogens induced colorectal cancer in rodents.[26,38] In the present study, we detected β-*catenin* gene mutations of mouse colon adenocarcinomas induced by APNH/DSS, at codons 32 and 37, being transversions (G:C to T:A and G:C to C:G) and transition (G:C to A:T), and all gene mutations detected in APNH/DSS-induced colon adenocarcinomas in the present study involved G:C base pairs. In contrast, the location and mutation pattern were slightly different from a report documenting that the β-*catenin* gene mutations of rat colon tumors induced by APNH; G:C to A:T transition at codon 34 was predominant.[17] Masumura *et al.* has also reported that PhIP[39]- and APNH[11]-induced *gpt* mutations in the liver and colon of the *gpt* delta transgenic mice were dominated by G:C to T:A transversions.[40] The difference of APNH-induced mutation sites and patterns in rats and mice might reflect differences in DNA repair or translesion DNA synthesis between these 2 species. Moreover, the colonic inflammation observed in DSS mouse model could influence mutation patterns and hotspots induced by APNH. Recently, we detected the β-*catenin* mutations of mouse colon adenocarcinomas, induced by azoxymethane/DSS, at codons 32, 33 and 34, being G:C to A:T transitions.[19] In 1,2-dimethylhydrazine/DSS-induced mouse colon adenocarcinomas, mutations of the β-*catenin* gene were present in codons 32, 34, 37 and 41, being G:C to A:T transitions.[41] In contrast, mutations of the β-*catenin* were observed at codons 32 and 34, mainly being transversions (G:C to T:A and G:C to C:G) in PhIP/DSS-induced colon adenocarcinomas.[19] We could not detect β-*catenin* mutations in 2 adenocarcinomas in the current study, but there is a possibility that they have mutations in the genes other than β-*catenin*. Additionally, in human colorectal cancer, the β-*catenin* mutations were dominated by transitions.[37,42] Although reason for differences of β-*catenin* mutation patterns between colorectal cancers of human and mice remains unclear, the differences might be related to the low occurrence of β-*catenin* mutations in human colorectal cancers when compared with *APC* mutations[43] or the different pathways of tumorigenesis between sporadic cancer and inflammation-associated cancer.

In conclusion, the results in the current study indicate that a potential tumor-initiating activity of APNH in the inflamed colon. β-*Catenin* mutations in adenocarcinomas induced by APNH and DSS were different from those other colonic carcinogens including HCAs, possibly due to the adduct (dG-C8-APNH) formation. Norharman and aniline are abundantly present in our environment and continuous exposure to both compounds during daily life is conceivable. We recently detected APNH in human urine samples from both healthy volunteers and inpatients.[15] Although their APNH levels were independent of dietary intake or cigarette smoking,[15] APNH could be a novel type of endogenous mutagen/carcinogen, as shown in this study and a previous investigation.[17] The APNH level in human urine samples was much lower than the MeIQx level and PhIP level, but the level is comparable to that for 3-amino-1,4-dimethyl-5*H*-pyrido[4,3-*b*]indole (Trp-P-1).[4,15] However, the carcinogenicity of APNH is thus considered to be more potent than that of PhIP and MeIQx in this animal model.[19] Our findings may provide scientific basis for further study on the involvement of APNH in human health.

References

1. Doll R. Nature and nurture: possibilities for cancer control. Carcinogenesis 1996;17:177–84.
2. Sugimura T, Wakabayashi K, Nakagama H, Nagao M. Heterocyclic amines: mutagens/carcinogens produced during cooking of meat and fish. Cancer Sci 2004;95:290–9.
3. Sugimura T, Kawachi T, Nagao M, Yahagi T, Seino Y, Okamoto T, Shudo K, Kosuge T, Tsuji K, Wakabayashi K, Iitaka Y. Mutagenic principle(s) in tryptophan and phenylalanine pyrolysis products. Proc Jpn Acad 1977;53:58–61.
4. Ushiyama H, Wakabayashi K, Hirose M, Itoh H, Sugimura T, Nagao M. Presence of carcinogenic heterocyclic amines in urine of healthy volunteers eating normal diet, but not of inpatients receiving parenteral alimentation. Carcinogenesis 1991;12:1417–22.
5. Nagao M, Yahagi T, Honda M, Seino Y, Matsushima T, Sugimura T. Demonstration of mutagenicity of aniline and *o*-toluidine by norharman. Proc Jpn Acad 1997;53B:34–7.
6. Totsuka Y, Hada N, Matsumoto K, Kawahara N, Murakami Y, Yokoyama Y, Sugimura T, Wakabayashi K. Structural determination of a mutagenic aminophenylnorharman produced by the comutagen norharman with aniline. Carcinogenesis 1998;19:1995–2000.
7. Sugimura T. A new concept of co-mutagenicity from a phenomenon forgotten for the past two decades: is it more important than previously expected? Environ Health Perspect 1998;106:A522–3.
8. Totsuka Y, Takamura-Enya T, Nishigaki R, Sugimura T, Wakabayashi K. Mutagens formed from β-carbolines with aromatic amines. J Chromatogr B 2004;802:135–41.
9. Ohe T, Takata T, Maedam Y, Totsuka Y, Hada N, Matsuoka A, Tanaka N, Wakabayashi K. Induction of sister chromatid exchanges and chromosome aberrations in cultured mammalian cells treated with aminophenylnorharman formed by norharman with aniline. Mutat Res 2002;515:181–8.
10. Totsuka Y, Takamura-Enya T, Kawahara N, Nishigaki R, Sugimura T, Wakabayashi K. Structure of DNA adduct formed with aminophenylnorharman, being responsible for the comutagenic action of norharman with aniline. Chem Res Toxicol 2002;15:1288–94.
11. Masumura K, Totsuka Y, Wakabayashi K, Nohmi T. Potent genotoxicity of aminophenylnorharman, formed from non-mutagenic norharman and aniline, in the liver of *gpt* delta transgenic mouse. Carcinogenesis 2003;24:1985–93.
12. Totsuka Y, Ushiyama H, Ishihara J, Sinha R, Goto S, Sugimura T, Wakabayashi K. Quantification of the co-mutagenic β-carbolines,

norharman and harman, in cigarette smoke condensates and cooked foods. Cancer Lett 1999;143:139–43.
13. IARC. Aniline and aniline hydrochloride, vol. 27. Lyon: IARC Scientific Publication, 1982.
14. Totsuka Y, Kataoka H, Takamura-Enya T, Sugimura T, Wakabayashi K. *In vitro* and *in vivo* formation of aminophenylnorharman from norharman and aniline. Mutat Res 2002;506/507:49–54.
15. Nishigaki R, Totsuka Y, Kataoka H, Ushiyama H, Goto S, Akasu T, Watanabe T, Sugimura T, Wakabayashi K. Detection of aminophenylnorharman, a possible endogenous mutagenic and carcinogenic compound, in human urine samples. Cancer Epidemiol Biomarkers Prev 2007;16:151–6.
16. Kawamori T, Totsuka Y, Ishihara J, Uchiya N, Sugimura T, Wakabayashi K. Induction of liver preneoplastic lesions by aminophenylnorharman, formed from norharman and aniline, in male F344 rats. Cancer Lett 2001;163:157–61.
17. Kawamori T, Totsuka Y, Uchiya N, Kitamura T, Shibata H, Sugimura T, Wakabayashi K. Carcinogenicity of aminophenylnorharman, a possible novel endogenous mutagen, formed from norharman and aniline, in F344 rats. Carcinogenesis 2004;25:1967–72.
18. Tanaka T, Kohno H, Suzuki R, Yamada Y, Sugie S, Mori H. A novel inflammation-related mouse colon carcinogenesis model induced by azoxymethane and dextran sodium sulfate. Cancer Sci 2003;94: 965–73.
19. Tanaka T, Suzuki R, Kohno H, Sugie S, Takahashi M, Wakabayashi K. Colonic adenocarcinomas rapidly induced by the combined treatment with 2-amino-1-methyl-6-phenylimidazo[4,5-*b*]pyridine and dextran sodium sulfate in male ICR mice possess β-*catenin* gene mutations and increases immunoreactivity for β-catenin, cyclooxygenase-2 and inducible nitric oxide synthase. Carcinogenesis 2005;26:229–38.
20. Hata K, Tanaka T, Kohno H, Suzuki R, Qiang SH, Kuno T, Hirose Y, Hara A, Mori H. Lack of enhancing effects of degraded λ-carrageenan on the development of β-catenin-accumulated crypts in male DBA/2J mice initiated with azoxymethane. Cancer Lett 2006;238:69–75.
21. Iidaka T, Tsukamoto T, Totsuka Y, Hirata A, Sakai H, Shirai N, Yamamoto M, Wakabayashi K, Yanai T, Masegi T, Donehower LA, Tatematsu M. Lack of elevated liver carcinogenicity of aminophenylnorharman in p53-deficient mice. Cancer Lett 2005;217:149–59.
22. Mori M, Totsuka Y, Fukutome K, Yoshida T, Sugimura T, Wakabayashi K. Formation of DNA adducts by the co-mutagen norharman with aromatic amines. Carcinogenesis 1996;17:1499–503.
23. Randerath E, Agrawal HP, Weaver JA, Bordelon CB, Randerath K. ^{32}P-postlabeling analysis of DNA adducts persisting for up to 42 weeks in the skin, epidermis and dermis of mice treated topically with 7,12-dimethylbenz[*a*]anthracene. Carcinogenesis 1985;6:1117–26.
24. Ward JM. Morphogenesis of chemically induced neoplasms of the colon and small intestine in rats. Lab Invest 1974;30:505–13.
25. Cooper HS, Murthy SN, Shah RS, Sedergran DJ. Clinicopathologic study of dextran sulfate sodium experimental murine colitis. Lab Invest 1993;69:238–49.
26. Takahashi M, Fukuda K, Sugimura T, Wakabayashi K. β-Catenin is frequently mutated and demonstrates altered cellular location in azoxymethane-induced rat colon tumors. Cancer Res 1998;58:42–6.
27. Hemminki K. DNA adducts, mutations and cancer. Carcinogenesis 1993;14:2007–12.
28. Schut HA, Snyderwine EG. DNA adducts of heterocyclic amine food mutagens: implications for mutagenesis and carcinogenesis. Carcinogenesis 1999;20:353–68.
29. Kato T, Ohgaki H, Hasegawa H, Sato S, Takayama S, Sugimura T. Carcinogenicity in rats of a mutagenic compound, 2-amino-3,8-dimethylimidazo[4,5-*f*]quinoxaline. Carcinogenesis 1988;9:71–3.
30. Yamashita K, Adachi M, Kato S, Nakagama H, Ochiai M, Wakabayashi K, Sato S, Nagao M, Sugimura T. DNA adducts formed by 2-amino-3,8-dimethylimidazo[4,5-*f*]quinoxaline in rat liver: dose-response on chronic administration. Jpn J Cancer Res 1990;81:470–6.
31. Ochiai M, Nakagama H, Watanabe M, Ishiguro Y, Sugimura T, Nagao M. Efficient method for rapid induction of aberrant crypt foci in rats with 2-amino-1-methyl-6-phenylimidazo[4,5-*b*]pyridine. Jpn J Cancer Res 1996;87:1029–33.
32. Wakabayashi K, Nagao M, Esumi H, Sugimura T. Food-derived mutagens and carcinogens. Cancer Res 1992;52 (Suppl):2092s–2098s.
33. Dashwood RH. Modulation of heterocyclic amine-induced mutagenicity and carcinogenicity: an 'A-to-Z' guide to chemopreventive agents, promoters, and transgenic models. Mutat Res 2002;511:89–112.
34. Ito N, Hasegawa R, Sano M, Tamano S, Esumi H, Takayama S, Sugimura T. A new colon and mammary carcinogen in cooked food, 2-amino-1-methyl-6-phenylimidazo[4,5-*b*]pyridine (PhIP). Carcinogenesis 1991;12:1503–6.
35. Korinek V, Barker N, Morin PJ, van Wichen D, de Weger R, Kinzler KW, Vogelstein B, Clevers H. Constitutive transcriptional activation by a β-catenin-Tcf complex in APC$^{-/-}$ colon carcinoma. Science 1997;275:1784–7.
36. Yamada Y, Mori H. Pre-cancerous lesions for colorectal cancers in rodents: a new concept. Carcinogenesis 2003;24:1015–9.
37. Sparks AB, Morin PJ, Vogelstein B, Kinzler KW. Mutational analysis of the APC/β-catenin/Tcf pathway in colorectal cancer. Cancer Res 1998;58:1130–4.
38. Dashwood RH, Suzui M, Nakagama H, Sugimura T, Nagao M. High frequency of β-*catenin* (ctnnb1) mutations in the colon tumors induced by two heterocyclic amines in the F344 rat. Cancer Res 1998;58:1127–9.
39. Masumura K, Matsui K, Yamada M, Horiguchi M, Ishida K, Watanabe M, Wakabayashi K, Nohmi T. Characterization of mutations induced by 2-amino-1-methyl-6-phenylimidazo[4,5-*b*]pyridine in the colon of *gpt* delta transgenic mouse: novel G:C deletions beside runs of identical bases. Carcinogenesis 2000;21:2049–56.
40. Nohmi T, Masumura K. Molecular nature of intrachromosomal deletions and base substitutions induced by environmental mutagens. Environ Mol Mutagen 2005;45:150–61.
41. Kohno H, Suzuki R, Sugie S, Tanaka T. β-*Catenin* mutations in a mouse model of inflammation-related colon carcinogenesis induced by 1,2-dimethylhydrazine and dextran sodium sulfate. Cancer Sci 2005;96:69–76.
42. Jass JR, Barker M, Fraser L, Walsh MD, Whitehall VL, Gabrielli B, Young J, Leggett BA. APC mutation and tumour budding in colorectal cancer. J Clin Pathol 2003;56:69–73.
43. Luchtenborg M, Weijenberg MP, Wark PA, Saritas AM, Roemen GM, van Muijen GN, de Bruine AP, van den Brandt PA, de Goeij F. Mutations in *APC, CTNNB1* and *K-ras* genes and expression of hMLH1 in sporadic colorectal carcinomas from the Netherlands Cohort Study. BMC Cancer 2005;5:160.

１．研究課題名：神経－血管連関からの血管および神経細胞機能の新しい調節メカニズムの解明（研究番号　C2006-4）

２．キーワード：１）神経－血管相互作用（neuro-vascular interaction）
２）血管ネットワーク形成（vascular network formation）
３）血管内皮細胞（vascular endothelial cells）
４）ミクロ RNA（microRNA）
５）可溶型 RAGE（esRAGE）

３．研究代表者：米倉　秀人・医学部・教　授・ゲノム医科学（生化学）
研究分担者：吉竹　佳の・医学部・准教授・ゲノム医科学（生化学）
鶴岡　直樹・医学部・助　教・ゲノム医科学（生化学）
渡辺　琢夫・金沢大学・医学系研究科・准教授・循環医科学専攻
山本　靖彦・金沢大学・医学系研究科・講　師・循環医科学専攻

４．研 究 目 的

本研究の目的は、血管と神経の関連性・相互作用に着目して、医学上の 2 大課題である血管系と神経系の機能を制御する新しい分子メカニズムを明らかにすることである。血管系と神経系は、情報を遠隔に送達するために全身ネットワークを形成するという類似性を有しており、発生やリモデリングの場で共通の分子やシグナル経路が用いられていることが最近示されつつある。また多くの場合血管と神経は併走しており、発生や病態の場でのクロストークの存在が強く考えられる。しかしながら、血管と神経の相互作用の場で働く分子メカニズムを系統的に探ろうという試みは、これまでほとんど行われていない。本研究の成果は、神経系と血管系で働く新たな調節機構と両者間の相互作用の解明に寄与するとともに、それらを利用・標的とする血管および神経疾患のリスク予知・診断・予防・治療法開発への応用へつながると期待される。

５．研 究 計 画

本研究では、血管系と神経系の関連性・相互作用に着目して、これまで見出されていない両者の細胞機能の調節メカニズムを以下のように明らかにする。

(1) 血管-神経相互作用による血管管腔ネットワーク形成時に働く遺伝子を同定し、それらの機能を明らかにする。
(2) 血管および神経細胞で働くミクロ RNA 種を同定し、ネットワーク形成におけるそれらの機能を明らかにする。
(3) 申請者が血管で見出した血管細胞保護作用を持つ分泌性タンパク質 esRAGE (可溶型 RAGE) (Biochem. J. 370, 1097-1109, 2003)の神経系での機能を明らかにする。
(4) 申請者の海外共同研究者が見出した新規神経細胞接着因子 AMIGO (J. Cell

Biol. 160, 963-973, 2003)の血管系での機能を明らかにする。

(5) 上記の成果を基盤として、上記遺伝子・ミクロ RNA を血管および神経疾患の診断・予防・治療法開発の分子標的として利用する可能性を検討する。

６．研 究 成 果

(1) 血管-神経相互作用による血管管腔ネットワーク形成時に働く遺伝子を同定し機能を明らかにする。(米倉、鶴岡分担)

ｉ) ラットおよびマウスの後根神経節(DRG)の初代培養による神経突起伸長系を確立した。

ii) マウス DRG とヒト初代培養微小血管内皮細胞(HMVEC)の接触共存培養を行なったところ、DRG が HMVEC の生存と増殖をサポートする因子を産生していることが示唆された。セルカルチャーインサートを用いた分離共存培養系でも HMVEC の生存と増殖がサポートされたことから、分泌性の因子が少なくとも一部関与していると推測された。

iii) マウス DRG と HMVEC を 6 時間接触共存培養した後 RNA を分離し、Affymetrix DNA マイクロアレイシステムで遺伝子発現の変化を解析し、単独で培養した HMVEC と比較した。その結果、両者の相互作用により HMVEC で再現性を持って 1.9 倍以上の発現誘導を受けた遺伝子を、機能未知の遺伝子を含め 9 個同定した。神経との相互作用により血管で発現変化する遺伝子が明らかになったのは初めてである。

(2) 血管および神経細胞で働くミクロ RNA 種を同定し機能を明らかにする。(吉竹分担)

ｉ) ヒト初代培養微小血管内皮細胞(HMVEC)を用いたラージスケールでの in vitro 血管新生モデルと管腔を形成した HMVEC から RNA を分離する条件を確立した。

ii) 管腔を形成した HMVEC と単層で培養した HMVEC からそれぞれ分離した RNA より、ミクロ RNA をクローニングし塩基配列を決定した。

iii) 以上の解析より、ミクロ RNA-21(miR-21)を筆頭として約 20 種のミクロ RNA が血管内皮細胞で発現していることが示された。また、いくつかのミクロ RNA 種が血管管腔形成の過程で変動することが示された。

(3) 申請者が血管で見出した血管細胞保護作用を持つ分泌性タンパク質 esRAGE (可溶型 RAGE)の神経系での機能を明らかにする。(山本分担)

ｉ) 免疫組織化学的解析により esRAGE 蛋白が神経細胞でも発現していることを見出している(Mod. Pathol. 18, 1385-1396, 2005)ので、抗ヒト esRAGE 特異抗体を用いてヒト脳組織抽出物のウエスタンブロット分析を行なった。その結果、ヒト esRAGE に相当する 50 kDa と 42kDa のバンドが検出され、免疫組織化学的解析で陽性の物質は esRAGE であると考えられた。

ii) アルツハイマー病(AD)の脳神経細胞で esRAGE の発現がどう変化するかを免疫組織化学的に解析した。AD (n=19)およびコントロール (n=21)の海馬組織を抗ヒト esRAGE 特異抗体で染色し、ニューロンの esRAGE 染色をスコア化し

て定量的解析を行った。その結果、海馬神経細胞の染色性が有意に低下していることが示された。アストロサイトの染色性は AD とコントロールで差が認められなかった。

ⅲ） 上記の成果の応用につき、特許を出願した（アルツハイマー病の診断方法，出願者：金沢大学，出願番号：特願 2006-155378)。また上記の成果が論文として受理された（研究発表欄参照)。

(4) 申請者の海外共同研究者が見出した新規神経細胞接着因子 AMIGO の血管系での機能を明らかにする。(渡辺分担)

ⅰ）HMVEC での AMIGO 遺伝子ファミリー(AMIGO1～3)の発現を RT-PCR で解析した結果、HMVEC では AMIGO2 が主に発現していることが明らかとなった。また、主要な血管新生刺激である低酸素状態で、AMIGO2 の発現が大きく低下することが示された。

ⅱ）AMIGO2 に対する RNAi を開発し HMVEC に導入したところ、AMIGO2 siRNA 発現ベクターが導入された培養は細胞数が大きく低下した。活性酸素(H_2O_2)による HMVEC 細胞死を解析したところ、AMIGO2 発現ベクターを導入した培養では細胞数の低下が抑えられ、AMIGO2 が HMVEC の生存に関わっている可能性が示唆された。

７．研究の考察・反省

(1) 今回 Affymetrix DNA マイクロアレイシステムで神経との相互作用により血管で発現変化する遺伝子を同定したが、リアルタイム PCR での再現性の確認が必要である。

(2) クローニング法で検出した in vitro 血管新生前後でのミクロ RNA の発現変動を、RNA プロテクション法・ノーザン法・ミクロ RNA アレイ法により総合的に確認する必要がある。

８．研 究 発 表

Nozaki I, Watanabe T, Kawaguchi M, Akatsu H, Tsuneyama K, Yamamoto Y, Ohe K, Yonekura H, Yamada M, Yamamoto H. Reduced expression of endogenous secretory receptor for advanced glycation endproducts in hippocampal neurons of Alzheimer's disease brains. Arch. Histol. Cytol. 2008; 70(5): 279-290.（MLDB）

米倉秀人，鶴岡直樹，吉竹佳の．血管内皮細胞自身による血管新生の制御・調節メカニズム．金医大誌 2007; 32(1): 8-15.

Arch Histol Cytol, 70 (5): 279-290 (2007)

Reduced expression of endogenous secretory receptor for advanced glycation endproducts in hippocampal neurons of Alzheimer's disease brains*

Ichiro Nozaki[1,2], Takuo Watanabe[1], Makoto Kawaguchi[3], Hiroyasu Akatsu[4], Koichi Tsuneyama[5], Yasuhiko Yamamoto[1], Kazuyo Ohe[1], Hideto Yonekura[6], Masahito Yamada[2], and Hiroshi Yamamoto[1]

[1]Department of Biochemistry and Molecular Vascular Biology, and [2]Department of Neurology and Neurobiology of Aging, Kanazawa University Graduate School of Medical Science, Kanazawa; [3]Department of Pathology, Niigata Rousai Hospital, Joetsu; [4]Choju Medical Institute, Fukushimura Hospital, Toyohashi; [5]First Department of Pathology, School of Medicine, University of Toyama, Toyama; and [6]Department of Biochemistry, Kanazawa Medical University, School of Medicine, Uchinada, Japan

Summary. The receptor for advanced glycation endproducts (RAGE) is a cell-surface multiligand receptor, which interacts with amyloid β (Aβ), a key protein in Alzheimer's disease (AD). RAGE-Aβ interaction is thought to be associated with pathological progression in AD. A splice variant of RAGE, endogenous secretory RAGE (esRAGE) can act as a decoy receptor for RAGE ligands that would prevent the progression of some pathologic conditions. In this study, the expression of esRAGE in the hippocampal tissues from AD brains compared with control (non-AD) was examined by immunohistochemistry and Western blot analysis. Semiquantitative immunohistochemical analysis of hippocampal tissues using esRAGE-specific antibody revealed significantly decreased immunoreactivities in pyramidal cells in CA1 and CA3 regions of AD compared with non-AD. On the other hand, immunoreactivities of astrocytes for esRAGE significantly increased in those regions. Dentate granule cells and astrocytes showed essentially invariant immunoreactivities between AD and non-AD. Changes in esRAGE immunoreactivity in CA3 neurons and astrocytes were observed from the early pathological stages. Moreover, the esRAGE-immunoreactive bands of AD samples were weaker than those of non-AD samples in Western blot analysis. The results indicate that low expression of esRAGE in the hippocampus would be associated with the development of AD.

Received December 13, 2007

* This work was supported in part by grants-in-aid from the Japan Society for the Promotion of Sciences (nos.18590260 and 19390085); grants (C2006-4 and C2007-1) for Collaborative Research from Kanazawa Medical University and a grant (H2007-10) for Project Research from the High-Technology Center of Kanazawa Medical University (to H. Yonekura).

Address for correspondence: Takuo Watanabe, M.D., Ph.D., Associate Professor, Department of Biochemistry and Molecular Vascular Biology, Kanazawa University Graduate School of Medical Science, 13-1 Takara-machi, Kanazawa, 920-8640, Japan
Tel.: +81-76-265-2181, Fax: +81-76-234-4217
E-mail: takuo@med.kanazawa-u.ac.jp

Introduction

The receptor for advanced glycation endproducts (RAGE) is a member of the immunoglobulin superfamily of cell surface receptors (Schmidt *et al.*, 1992; Yonekura *et al.*, 2005). Human RAGE has a 322-amino acid extracellular portion which is composed of one V-type immunoglobulin domain and two C-type immunoglobulin domains, a single 19-amino acid hydrophobic transmembrane-spanning

domain and a 41-amino acid, highly-charged cytoplasmic tail: V-domain is critical for ligand binding, and the cytoplasmic domain is essential for intracellular signaling (Huttunen *et al.*, 1999). RAGE is a multiligand receptor and endogenous ligands other than advanced glycation endproducts (AGE), such as amphoterin/high mobility group box 1 (HMGB-1) (Hori *et al.*, 1995), S100/calgranulin (Hofmann *et al.*, 1999), transthyretin (Sousa *et al.*, 2000), and amyloid β (Aβ) (Yan *et al.*, 1996; Mackic *et al.*, 1998) have been identified. The RAGE-signaling cascade is not yet fully understood, but ligand binding to RAGE has been reported to induce cellular oxidant stress to activate the transcription factor nuclear factor-κB (NF-κB) through a cascade of intracellular signaling that involves mitogen-activated protein kinase activation (Lander *et al.*, 1997; Stern *et al.*, 2002).

AD is a progressive neurodegenerative disease with amyloid burden (i.e. senile plaques), tau pathology (i.e. neurofibrillary tangles), and chronic inflammation. RAGE is also a receptor for Aβ, the major component of senile plaques, and RAGE-Aβ interaction is considered to be associated with neurotoxicity in AD brain. The neural dysfunction mediated by RAGE would be caused by the following mechanisms: induction of neuronal oxidative stress (Yan *et al.*, 1996); activated microglial inflammatory responses (Lue *et al.*, 2001); and increased Aβ influx into the brain across the blood-brain barrier (Deane *et al.*, 2003).

We recently identified a naturally occurring secreted soluble form of RAGE in human and in mouse RAGE, and this is expressed in multiple organs including the central nervous system (Yonekura *et al.*, 2003; Cheng *et al.*, 2005; Harashima *et al.*, 2006). This variant is generated by alternative splicing, and is called endogenous secretory RAGE (esRAGE); esRAGE is composed of the extracellular domain and unique C-terminal sequence that lacks both the transmembrane and intracellular domains, and has been shown to act as a decoy receptor that inhibits RAGE signaling (Yonekura *et al.*, 2003). It is thought that esRAGE suppresses the progression of diseases or pathological conditions by the inhibition of signaling via membrane-type RAGE (Yonekura *et al.*, 2005). Plasma esRAGE levels are significantly decreased compared with the control group in some diseases such as atherosclerosis and diabetic retinopathy (Koyama *et al.*, 2005; Sakurai *et al.*, 2006). Low levels of circulating esRAGE would cause vulnerability to those diseases. We hypothesized that low expression of esRAGE in the hippocampal neurons could be associated with susceptibility to AD in which hippocampal degeneration would be most critical. In the present study, this hypothesis was studied for human AD brains compared with control non-AD samples by using immunohistochemical methods and Western blot analysis that uses esRAGE-specific and membrane-type RAGE-specific antibodies.

Materials and Methods

Subjects and tissues

Included in this study were 19 patients with AD (6 men and 13 women, mean age: 85.3 ± 6.4 years), 21 patients with normal physiological aging or neurological diseases other than AD (called "non-AD"; 8 men and 13 women, mean age: 83.5 ± 8.0 years). The non-AD group involved cases in which AD was excluded by histopathological examination, including normal physiological aging (n=4), cerebral infarction (n=15), brain metastatic tumor (n=1), and Parkinson disease (n=1). Informed consent as regards participation was provided by all AD patients and control subjects or their legal guardians and the approval of the local ethical committee was obtained. All tissue specimens and corresponding clinical data were provided by Choju Medical Institute Brain Bank (Akatsu *et al.*, 2002), and all examinations were performed according to the principles expressed in the Declaration of Helsinki. Their clinical characteristics are summarized in Table 1.

Neuropathology

For this study, formalin-fixed, paraffin-embedded tissue blocks of AD or non-AD brains were randomly selected from autopsy specimens registered in Choju Medical Institute Brain Bank (Akatsu *et al.*, 2002). The tissue sections were stained with hematoxylin-eosin and with the Gallyas-Braak method. Each brain was examined and diagnosed by two neuropathologists. The neuropathological diagnosis of AD followed the Consortium to Establish A Registry for Alzheimer's Disease (CERAD) guidelines (Mirra *et al.*, 1991). Gallyas-Braak stains were used to determine Braak neurofibrillary scores (Braak and Braak, 1991).

Antibodies

Rabbit esRAGE-specific polyclonal antibody was raised against the unique C-terminal 16-amino-acid peptide (amino acids 332-347; EGFDKVREAEDSPQHM)-keyhole limpet hemocyanin conjugate, and immunoaffinity-purified with an antigen peptide-conjugated column as previously described (Yonekura *et al.*, 2003). The specificity of the immunostaining has been proven by the absorption test (Cheng *et al.*, 2005).

A rabbit polyclonal antibody raised against the C-terminal intracellular domain of membrane-type RAGE (C-terminal 20 amino acids) was purchased from Santa Cruz Biotechnology, CA, USA.

Immunohistochemistry and semiquantitative analyses

Immunostaining procedures were based on a new microwave technique as described previously (Kumada *et al.*, 2004). In brief, the section were deparaffinized, dehydrated, and treated for antigen retrieval with Target Retrieval Solution (DAKO, Carpinteria, CA, USA) in a wet chamber in a microwave oven (Type RE-11; Sharp, Tokyo; maximum 500 W) for 15 min. The sections were allowed to cool at room temperature for 30 min, rinsed under running water for 1 min, and then treated with 3% H_2O_2 for 5 min to exhaust endogenous peroxidase. After washing with Tris-buffered saline (TBS) containing 0.1% Tween-20 (TBS-T) and blocking with 5% normal bovine serum albumin (BSA) (Sigma-Aldrich, St. Louis, MO, USA) for 1 min, the sections were incubated with primary antibodies (5 μg/m*l* for esRAGE-specific antibody; 2 μg/m*l* for membrane-type RAGE-specific antibody) in a wet chamber, with intermittent microwave irradiation (MI-77; Azumaya, Tokyo) for 10 min. After washing with TBS-T, the peroxidase-labeled polymer for rabbit polyclonal antibody (EnVison; DAKO) was applied for 10 min in a wet chamber with intermittent microwave irradiation. After washing with TBS, color was developed with 3-3'- diaminobenzidine (Sigma-Aldrich). The sections were then counterstained with Meyer's hematoxylin, and cover-slipped for microscopic observation. The conditions of immunostaining and digital imaging were carefully controlled to assure the uniformity of evaluation of immunoreactivity. The intensity of immunoreactivity (color; brown) in cells at hippocampus was scored on an arbitrary scale as follows: 0 = no staining; 1 = weak staining; 2 = intermediate staining; and 3 = strong staining. The proportion of cells in which the intensity of immunoreactivity is 0, 1, 2, and 3 is defined as p_0, p_1, p_2, and p_3, respectively. The scoring was done by plural analysts. The immunoreactivity index (IRI) for specific cell type was calculated with the following formula: $0 \times p_0 + 1 \times p_1 + 2 \times p_2 + 3 \times p_3$. The following three hippocampal subdivisions were analyzed; CA1, CA3, and dentate granule cell layer. The neuron/astrocyte esRAGE index was calculated for each case using the following formula: esRAGE IRI for neurons/esRAGE IRI for astrocytes. The identification of neurons and astrocytes were based on their histological characteristics in Meyer's hematoxylin stain as follows: pyramidal cells in CA1 and CA3 have a relatively large (10–50 μm in diameter) triangularly shaped cell body and multiple dendrites; granule cells in dentate gyrus are tiny neurons that are around 10 μm in diameter found in granular layer; astrocytes typically have a characteristic star-shaped cell body that is smaller than pyramidal cells, and round nuclei; oligodendrocytes that are recognizable by their small, rounded, lymphocyte-like nuclei and perinuclear halo were discriminated from astrocytes. Identification criteria for astrocytes and oligodendrocytes were confirmed by immunostaining for their specific makers, glial fibrillary acidic protein and olig2, respectively (data not shown).

Western blot analysis

Frozen blocks of hippocampal tissues were homogenized in SDS lysis buffer [62.5 mM Tris·HCl (pH 6.8), 2%(w/v) SDS, 10% glycerol] using Polytron homogenizer (KINEMATICA, Littau-Lucerne, Switzerland) and boiled at 95℃ for 5 min. The lysates were centrifuged at 15,000 g for 5 min and the supernatants were

Table 1. Clinical characteristics of subjects

Diagnosis	Number of patients (male/female)	Age (years)	Clinical duration (years)	CERAD score (number of cases)	Braak stage (number of cases)	FBS (mg/d*l*)
AD	19 (6/13)	85.3 ± 6.4	7.3 ± 3.7	B (3), C (16)	III (5), IV (3), V (4), VI (7)	133 ± 67
Non-AD	21 (8/13)	83.5 ± 8.0		A	I	123 ± 46

AD: Alzheimer's disease, CERAD: Consortium of Establish a Registry for Alzheimer's Disease, FBS: fasting blood glucose

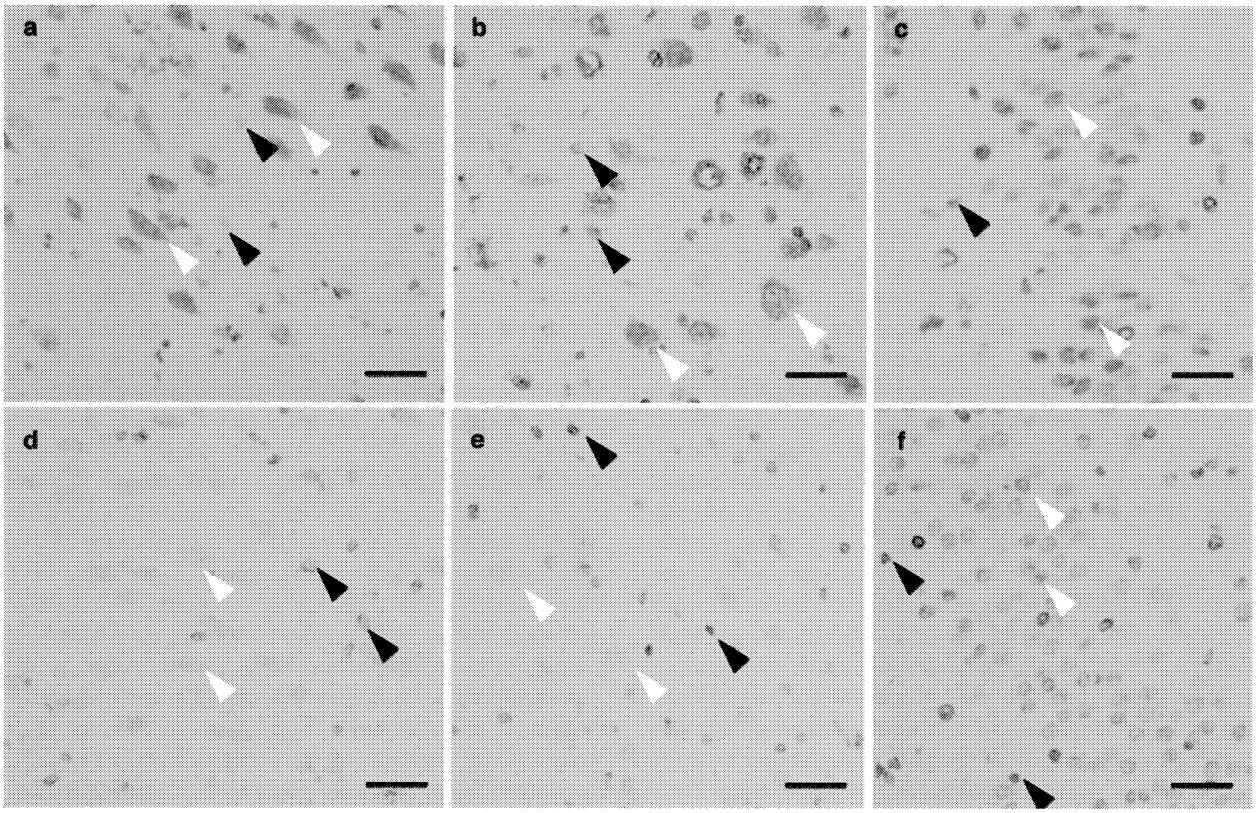

Fig. 1. Immunohistochemistry for endogenous secretory receptor for advanced glycation endproducts (esRAGE) in the hippocampus in non-Alzheimer's disease (non-AD) (**a**–**c**) and Alzheimer's disease (AD) (**d**–**f**). In AD, CA1 (**d**) and CA3 (**e**) pyramidal cells demonstrated low esRAGE immunoreactivities compared with CA1 (**a**) and CA3 (**b**) pyramidal cells in non-AD; however, the immunoreactivities of dentate granule cells in AD (**f**) appeared comparable with those in non-AD (**c**). In CA1 (**d**) and CA3 (**e**), the esRAGE immunoreactivities in astrocytes appeared to be preserved or increased in AD. Typical pyramidal cells (**a**, **b**, **d**, and **e**) and granule cells (**c** and **f**) are indicated by white arrowheads, and astrocytes are indicated by black arrowheads. Scale bars: 20 μm

collected for Western blot analysis. After determination of protein concentrations by BCA protein assay kit (Pierce, Rockford, IL, USA) using BSA as a standard, dithiothreitol and bromphenol blue were added to the final concentration of 100 mM and 0.001% (w/v), respectively. Fifty microgram of protein were resolved by SDS-PAGE, and then transferred onto an Immobilon-FL membrane (Millipore, Bedford, MA, USA). The membrane was incubated with 0.5 μg/ml esRAGE-specific polyclonal antibody in Can Get Signal solution 1 (Toyobo, Osaka) and then incubated with 1:10,000 diluted infrared fluorescent dye-labeled anti-rabbit IgG antibody (LI-COR Bioscience, Lincoln, NE, USA) in Can Get Signal solution 2 (Toyobo). The immunoreactive bands were visualized and quantified by Odyssey infrared fluorescence imaging system (LI-COR Bioscience).

Statistic analysis

Differences among groups were tested using parametric tests [if normally distributed, Student's t test or ANOVA combined with a multiple comparison test (Scheffe's type)] or non-parametric test [if not normally distributed, a Mann-Whitney U test]. *P* values under 5% were considered to indicate statistical significance. All analyses were performed with the use of StatView software (SAS institute).

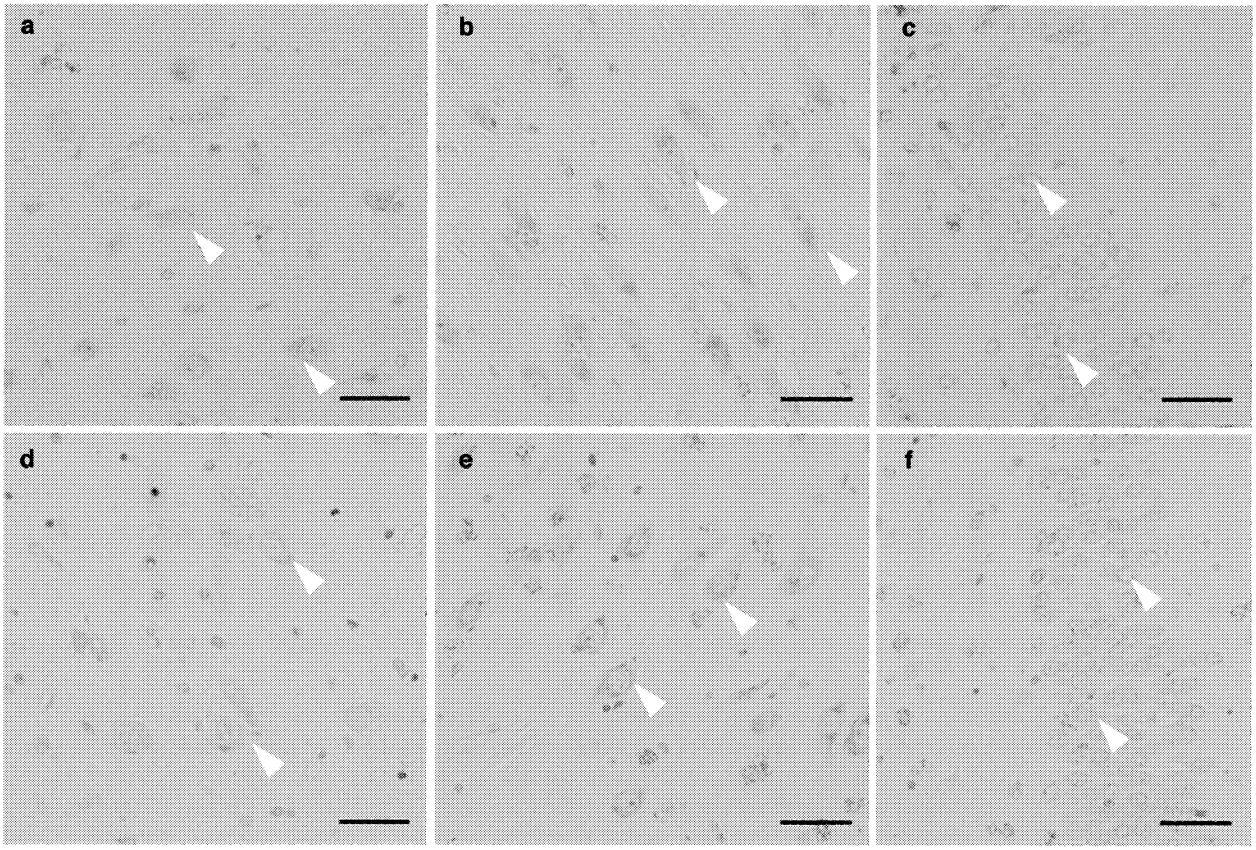

Fig. 2. Immunohistochemistry for membrane-type RAGE in the hippocampus in non-AD (**a**–**c**) and in AD (**d**–**f**). The expression of membrane-type RAGE in neurons and astrocytes in CA1 (**a** and **d**) and CA3 (**b** and **e**) was observed. In AD, CA1 (**d**) and CA3 (**e**) pyramidal cells demonstrated almost the same membrane-type RAGE immunoreactivities as CA1 (**a**) and CA3 (**b**) pyramidal cells in non-AD, respectively. The immunoreactivities in dentate granule cells were weak both in AD (**f**) and non-AD (**c**). Typical pyramidal cells (**a**, **b**, **d**, and **e**) and granule cells (**c** and **f**) are indicated by white arrowheads. Scale bars: 20 μm

Results

Cases

Table 1 summarizes age, sex, clinical duration, neuropathological findings and other information. There were no significant differences in age and the fasting blood glucose level between the AD and non-AD group. In the AD group, the CERAD score was B (n=3) or C (n=16), and the Braak stage was III (n=5), IV (n=3), V (n=4), or VI (n=7). In the non-AD group, the CERAD score was all A, and the Braak stage was all I.

Neuropathology and immunohistochemistry

In the hippocampus of AD, loss of the pyramidal cells in CA1 region was apparent in contrast to preservation of the pyramidal cells in CA3 region and the granule cells in dentate gyrus as reported previously (West *et al.*, 2004).

In the immunostaining for esRAGE, diffuse or dot-like cytoplasmic staining was observed in pyramidal cells, coarse cytoplasmic staining was observed in dentate granule cells, and diffuse cytoplasmic staining was observed in astrocytes. The immunoreactivities of esRAGE were varied in different regions of the hippocampal formation. In the non-AD group, strong immunoreactivities of esRAGE were observed in the pyramidal cells at CA1 and CA3, and in the

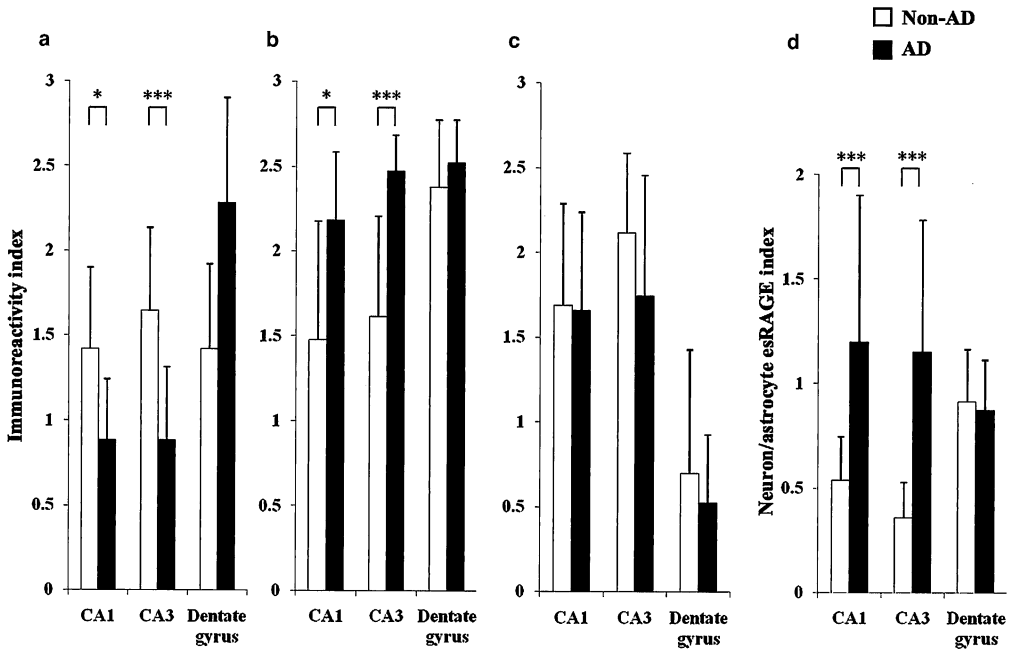

Fig. 3. Semiquantitative evaluation of immunoreactivity for esRAGE (**a**, **b**) and membrane-type RAGE (**c**) in each hippocampal subdivision. Neurons (**a**, **c**) and astrocytes (**b**) were separately evaluated, and neuron/astrocytes esRAGE index was calculated as described in the text (**d**). **a:** The esRAGE-immunoreactivity indexes (IRI) in pyramidal cells significantly decreased in CA1 region ($^{*}p < 0.05$) and CA3 region ($^{***}p < 0.001$) of AD compared with non-AD, and there was no significant statistical difference in dentate granule cells between AD and non-AD. **b:** esRAGE IRI in astrocytes were significantly increased in CA1 region ($^{*}p < 0.05$) and in CA3 region ($^{***}p < 0.001$) of AD compared with non-AD, and there was no significant statistical difference in dentate gyri between AD and non-AD. **c:** The IRI of membrane-type RAGE in pyramidal cells in CA1 and CA3 regions, and in dentate granular cells were not significantly different between AD and non-AD. **d:** The neuron/astrocyte esRAGE indexes significantly decreased in CA1 region ($^{***}p < 0.001$) and in CA3 region ($^{***}p < 0.001$) of AD compared with non-AD, and showed no difference in dentate granule cells between AD and non-AD. Open bars and closed bars indicate means of the immunoreactivity index of non-AD group and AD group, respectively. Error bars indicate standard deviation.

dentate granule cells. In the AD group, the esRAGE immunoreactivities decreased in surviving CA1 pyramidal cells and in CA3 pyramidal cells, but those in dentate granule cells appeared comparable with the non-AD group. In CA1 and CA3 regions, the esRAGE immunoreactivities in astrocytes appeared to be preserved or increased contrary to the decreased immunoreactivities in pyramidal cells in AD (Fig. 1).

In the immunostaining for membrane-type RAGE, diffuse or coarse cytoplasmic staining was observed in pyramidal cells, dentate granule cells and astrocytes; immunoreactivities of dentate granule cells were weak. Membrane-type RAGE immunoreactivities in the CA1 and CA3 pyramidal cells and dentate granule cells were not apparently different between the AD and the non-AD group (Fig. 2).

The neuronal IRI of esRAGE significantly decreased at CA1 region (Fig. 3a; $p < 0.05$) and CA3 region of AD (Fig. 3a; $p < 0.001$), and there was no significant statistical difference in dentate gyri between AD and non-AD (Fig. 3a). However, in the astrocytes, those were significantly increased at CA1 region (Fig. 3b; $p < 0.05$) and CA3 region of AD (Fig. 3b; $p < 0.001$), and showed no difference in dentate gyri between AD and non-AD (Fig. 3b). In the AD group, a significant decrease of esRAGE immunoreactivity in pyramidal cells was accompanied

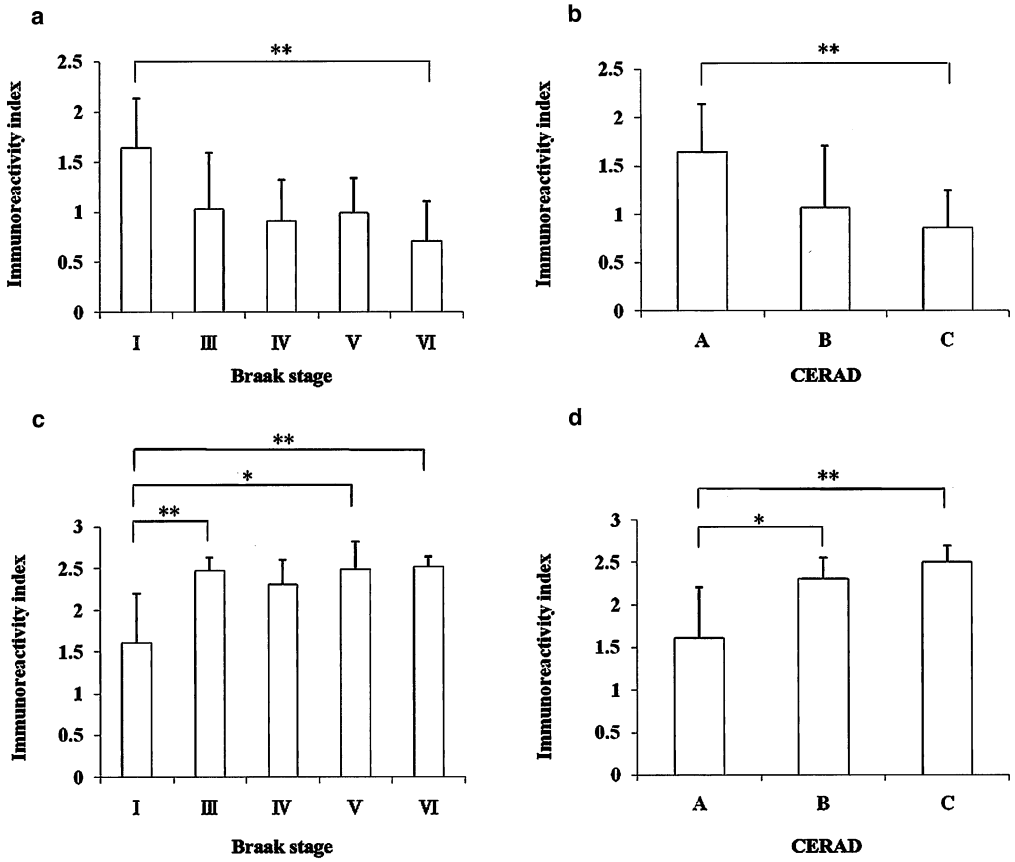

Fig. 4. Semiquantitative evaluation of immunoreactivity for esRAGE in CA3 region classified by pathological staging, Braak staging (**a**, **c**) and CERAD criteria (**b**, **d**). The cases of Stage I in Braak staging and stage A in CERAD criteria correspond to non-AD specimens. Tendencies of the decrease of immunoreactivity in the pyramidal cells (**a**, **b**) and the increase in astrocytes (**c**, **d**) were observed from the early stages in AD. Error bars indicate standard deviation. $^{*}p < 0.05$, $^{**}p < 0.01$

by a significant increase of the immunoreactivity in astrocytes compared with non-AD group. In contrast to esRAGE, the IRI of membrane-type RAGE in neurons were not significantly different at CA1, CA3 and dentate gyri between AD and non-AD (Fig. 3c). For esRAGE, to evaluate the decreased immunoreactivity in neurons and increased immunoreactivity in astrocytes simultaneously, the neuron/astrocyte esRAGE index (esRAGE IRI for neuron/esRAGE IRI for astrocyte) was calculated. As in the case of esRAGE IRI for neuron, the neuron/astrocyte esRAGE indexes significantly decreased at CA1 region ($p < 0.001$) and CA3 region of AD ($p < 0.001$), and showed no difference in dentate gyri between AD and non-AD (Fig. 3d). When the immunoreactivity of esRAGE in CA3 region was classified according to the pathological staging, CERAD criteria based on semiquantification of senile plaques and Braak staging based on distribution of neurofibrillary tangles, the tendencies of the decrease of esRAGE in neurons and its increase in astrocytes were observed from the early stages in both CERAD and Braak staging (Fig. 4, 5). The tendencies of esRAGE were equivocal in CA1 region (data not shown). No such apparent tendencies were observed for membrane-type RAGE immunoreactivity (data not shown).

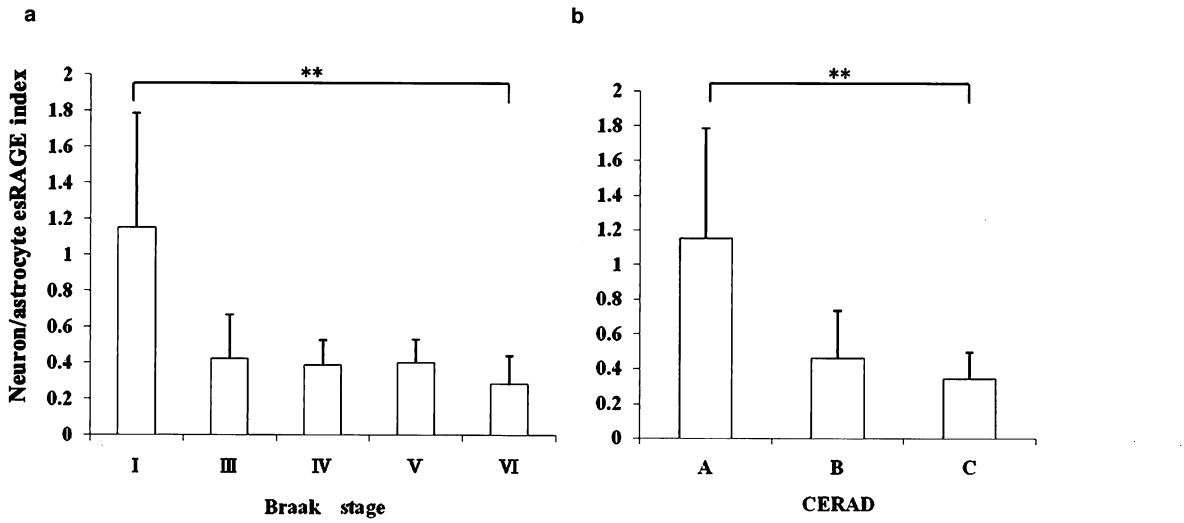

Fig. 5. Neuron/astrocytes esRAGE index classified by histological staging of AD. The neuron/astrocytes esRAGE index was classified by Braak staging (**a**) or CERAD criteria (**b**). The index showed a tendency to decrease as pathological changes progress. Error bars indicate standard deviation. $^{**}p < 0.01$

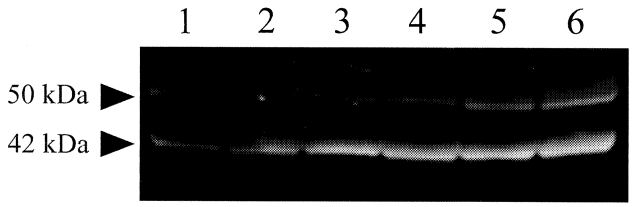

Fig. 6. Western blot analysis of hippocampus homogenates using esRAGE-specific antibody. Fifty microgram protein was loaded on each lane. Detection of immunoreactive bands was carried out using Odyssey infrared fluorescence imaging system. Three independent AD samples (*lanes* 1–3) and three independent normal aging samples (*lanes* 4–6) were analyzed. Two major immunoreactive bands at approx. 50 kDa and at approx. 42 kDa (arrowheads) were detected, and the intensities of the bands in AD samples were lower than those of normal aging samples.

Western blot analysis

In hippocampus homogenates, two major immunoreactive bands were identified at approx. 50 kDa and at approx. 42 kDa in Western blot analysis using the esRAGE-specific antibody. Three AD samples, whose esRAGE immunoreactivities in pyramidal cells were weak, and three normal aging samples, whose esRAGE immunoreactivities in pyramidal cells were strong, were analyzed, and the intensities of esRAGE bands in AD samples were relatively lower (~35% decrease on an average) compared with normal aging samples (Fig. 6). This result indicated that the immunoreactivity of esRAGE in neurons in immunostaining correlated with the total amount of esRAGE in the brain tissue.

Discussion

esRAGE has a protective effect as a decoy receptor, while membrane-bound, full-length RAGE transmits cytotoxic signals (Yonekura *et al.*, 2005). esRAGE is a different entity from sRAGE (soluble RAGE) that includes proteinase-cleaved form of membrane-type RAGE or esRAGE (Schmidt *et al.*, 1994; Hanford *et al.*, 2004) and genetically engineered (C-terminal truncated) recombinant soluble RAGE protein (Renard *et al.*, 1997; Park *et al.*, 1998); esRAGE is unique in that it is endogenously generated secretory isoform of RAGE. The esRAGE-specific antibody used in this study recognizes the unique C-terminal region of esRAGE, and does not crossreact with proteinase-cleaved form of RAGE. We have recently reported the expression of esRAGE in neurons in human and mouse brain (Cheng

et al., 2005; Harashima *et al.*, 2006). The administration of purified sRAGE was reported to inhibit membrane-type RAGE-mediated transport of Aβ across blood-brain barrier and to suppress Aβ accumulation in mouse brain parenchyma (Dean *et al.*, 2003). In AD brains, esRAGE would capture Aβ and reduce cytotoxicity induced by Aβ, and the levels of esRAGE expression may be associated with the vulnerability of neurons. AGE that has been reported to localize in the neurons in the hippocampus and parahippocampal gyrus in AD brain may also be RAGE ligand responsible for AD pathogenesis (Sato *et al.*, 2006).

The immunohistochemistry for esRAGE in the present study demonstrated that esRAGE-positive neurons and astrocytes were detectable in hippocampus in both AD and non-AD brains (Fig. 1, 2). Semiquantitative evaluation of immunoreactivity of neurons in AD hippocampus showed a significant decrease of esRAGE immunoreactivities in the pyramidal cells in CA1 and CA3 regions compared with non-AD although the dentate granule cells showed no difference of esRAGE immunoreactivity between AD and non-AD (Fig. 3). In AD, there is selective neuronal loss that is critical for cognitive function. The pyramidal cells in the CA1 region of hippocampus are vulnerable to degeneration, whereas the CA3 pyramidal cells and dentate granule cells are resistant to degeneration (West *et al.*, 2004). The decrease of esRAGE immunoreactivity of CA3 pyramidal cells, which are relatively preserved in AD, indicates that the decrease of esRAGE immunoreactivity in neurons is not simply a reflection of neuronal cell death. The selective loss of CA1 pyramidal cells may be a consequence of reduced protection by esRAGE and CA1-specific neuronal vulnerability.

Immunohistochemistry in AD brains demonstrated an increase of esRAGE immunoreactivity in astrocytes compared with non-AD contrary to the decrease of immunoreactivity in pyramidal cells. The induction of the esRAGE expression in astrocytes may reflect the inflammatory process in AD brains (Akiyama *et al.*, 2000).

In CA3 region, the above mentioned tendencies, that is, the decrease of esRAGE in the pyramidal cells and it's increase in the astrocytes, were apparent in the early stages of pathological classifications of AD (*i.e.* CERAD criteria and Braak staging) (Fig. 4). It is noteworthy that the tendencies were apparent in the limbic stages (stages III and IV) of Braak staging, the stages that do not directly correlate with clinical dementia. Those tendencies were equivocal in CA1 region, which may be due to modification by neuronal loss at later stages in CA1 region (data not shown). No apparent tendencies were observed for membrane-type RAGE immunoreactivity (data not shown).

To evaluate decreased immunoreactivity in neurons and increased immunoreactivity in astrocytes simultaneously, the neuron/astrocyte esRAGE index (esRAGE IRI for neuron/esRAGE IRI for astrocyte) was calculated. Since the statistical significance of the difference of the neuron/astrocyte esRAGE index between the AD and non-AD group was more than esRAGE IRI for neurons or esRAGE IRI for astrocytes (Fig. 3), the decrease of the neuron/astrocyte esRAGE index may be more sensitive and useful than simply using these IRI as a diagnostic index for AD. The decrease of neuron/astrocyte esRAGE index was observed from the early pathological stages classified by CERAD or Braak staging (Fig. 5). Although the neuron/astrocyte esRAGE index did not show statistically significant differences in the early stages of pathological changes, in which the esRAGE IRI for astrocyte showed statistically significant differences (Fig. 4c, d), the neuron/astrocyte esRAGE index would be more specific for AD than esRAGE IRI for astrocytes that could increase in any inflammatory disease.

Western blot analysis of hippocampus homogenates using the esRAGE-specific antibody revealed two major immunoreactive bands at approx. 50 kDa and at approx. 42 kDa. In our previous Western blot analysis on lysate of COS-7 cells transfected with human-esRAGE cDNA-expression vector, N-glycosylated 50-kDa esRAGE and unmodified 46-kDa esRAGE were identified (Yonekura *et al.*, 2003). The 50-kDa immunoreactive band in hippocampus homogenates corresponds to the N-glycosylated form of esRAGE. The 42-kDa immunoreactive band might be a partially proteolytic form of esRAGE. The intensities of the immunoreactive bands in the homogenates of AD hippocampus were relatively lower than those of the normal aging samples, and this might reflect the decrease of esRAGE expression in neurons and/or a decrease in the number of neurons.

Since the neuronal expression levels of membrane-type RAGE in AD were almost same as in non-AD (Fig. 2), the selective reduction of neuronal esRAGE expression may be involved in AD. The balance of production between esRAGE and membrane-type RAGE is regulated by alternative 5'-splice site selection of intron 9 in human RAGE mRNA (Yonekura *et al.*, 2003), and some nuclear factors appeared to be involved in the regulatory mechanism (K.O., T.W., and H.Y., unpublished data). In the process of AD pathology, the expression or functions of these factors may be altered.

Donahue *et al.* reported the decrease of immunoreactivity of RAGE in hippocampal neurons of AD using immunohistochemical methods (Donahue *et al.*, 2006). Since the antibody used in their study was raised

against the extracellular domain of RAGE and was supposed to recognize both membrane-type RAGE and esRAGE, their results were consistent with the decreased esRAGE and the unchanged membrane-type RAGE immunoreactivity in our results. However, the Western blot analysis in their study indicated an increase of total RAGE protein in hippocampal tissue of AD. Because different antibodies were used and because of the small number of samples (three AD and three controls in our study; one AD and one control in their study), there is room for further investigation using isoform-specific antibodies for more samples.

esRAGE detected in neurons appeared to be intracellular storage of esRAGE and/or esRAGE on the secretory pathway. Although the immunoreactivity of esRAGE in extracellular space was not apparent in this study, the amount of secreted esRAGE is supposed to correspond to its expression level, which is indicated by esRAGE immunoreactivity in the cell. Since it was suggested that sRAGE and esRAGE bind heparan sulfate on the cell membranes or in the extracellular matrix (Hanford *et al.*, 2004), it is probable that the secreted esRAGE does not diffuse out but localizes and captures the ligands on the cell surface and/or in the vicinity of the cell. This may explain the observation that the increase of esRAGE expression in astrocytes did not appear to be effective for protection of neurons.

In conclusion, esRAGE appeared to be involved in AD pathology in the subdivision specific manner in hippocampus. Decreased neuronal expression of esRAGE in CA1 and CA3 regions is correlated with elevated glial expression of esRAGE in AD brains. The onset and/or progression of AD might be associated with reduction of esRAGE in the pyramidal cells. The neuronal expression of esRAGE should thus be a novel diagnostic marker of AD and could have a therapeutic potential in the treatment of AD.

Acknowledgments

We thank, Kenji Kosaka and Yoshio Hashizume for neuropathological examinations, Yuji Fujinawa and Osamu Yamamoto for their excellent technique and Shin-ichi Matsudaira and Reiko Kitamura for assistance.

References

Akatsu H, Takahashi M, Matsukawa N, Ishikawa Y, Kondo N, Sato T, Nakazawa H, Yamada T, Okada H, Yamamoto T, Kosaka K: Subtype analysis of neuropathologically diagnosed patients in a Japanese geriatric hospital. *J Neurol Sci* 196: 63-69 (2002).

Akiyama H, Barger S, Barnum S, Bradt B, Bauer J, Cole GM, Cooper NR, Eikelenboom P, Emmerling M, Fiebich BL, Finch CE, Frautschy S, Griffin WS, Hampel H, Hull M, Landreth G, Lue L, Mrak R, Mackenzie IR, McGeer PL, O'Banion MK, Pachter J, Pasinetti G, Plata-Salaman C, Rogers J, Rydel R, Shen Y, Streit W, Strohmeyer R, Tooyoma I, Van Muiswinkel FL, Veerhuis R, Walker D, Webster S, Wegrzyniak B, Wenk G, Wyss-Coray T: Inflammation and Alzheimer's disease. *Neurobiol Aging* 21: 383-421 (2000).

Braak H, Braak E: Neuropathological stageing of Alzheimer-related changes. *Acta Neuropathol* 82: 239-259 (1991).

Cheng C, Tsuneyama K, Kominami R, Shinohara H, Sakurai S, Yonekura H, Watanabe T, Takano Y, Yamamoto H, Yamamoto Y: Expression profiling of endogenous secretory receptor for advanced glycation end products in human organs. *Mod Pathol* 18: 1385-1396 (2005).

Deane R, Du Yan S, Submamaryan RK, LaRue B, Jovanovic S, Hogg E, Welch D, Manness L, Lin C, Yu J, Zhu H, Ghiso J, Frangione B, Stern A, Schmidt AM, Armstrong DL, Arnold B, Liliensiek B, Nawroth P, Hofman F, Kindy M, Stern D, Zlokovic B: RAGE mediates amyloid-beta peptide transport across the blood-brain barrier and accumulation in brain. *Nat Med* 9: 907-913 (2003).

Donahue JE, Flaherty SL, Johanson CE, Duncan JA 3rd, Silverberg GD, Miller MC, Tavares R, Yang W, Wu Q, Sabo E, Hovanesian V, Stopa EG: RAGE, LRP-1, and amyloid-beta protein in Alzheimer's disease. *Acta Neuropathol* 112: 405-415 (2006).

Hanford LE, Enghild JJ, Valnickova Z, Petersen SV, Schaefer LM, Schaefer TM, Reinhart TA, Oury TD: Purification and characterization of mouse soluble receptor for advanced glycation end products (sRAGE). *J Biol Chem* 279: 50019-50024 (2004).

Harashima A, Yamamoto Y, Cheng C, Tsuneyama K, Myint KM, Takeuchi A, Yoshimura K, Li H, Watanabe T, Takasawa S, Okamoto H, Yonekura H, Yamamoto H: Identification of mouse orthologue of endogenous secretory receptor for advanced glycation end-products: structure, function and expression. *Biochem J* 396: 109-

115 (2006).
Hofmann MA, Drury S, Fu C, Qu W, Taguchi A, Lu Y, Avila C, Kambham N, Bierhaus A, Nawroth P, Neurath MF, Slattery T, Beach D, McClary J, Nagashima M, Morser J, Stern D, Schmidt AM: RAGE mediates a novel proinflammatory axis: a central cell surface receptor for S100/calgranulin polypeptides. *Cell* 97: 889-901 (1999).
Hori O, Brett J, Slattery T, Cao R, Zhang J, Chen JX, Nagashima M, Lundh ER, Vijay S, Nitecki D, Morser J, Stern D, Schmidt AM: The receptor for advanced glycation end products (RAGE) is a cellular binding site for amphoterin. *J Biol Chem* 270: 25752-25761 (1995).
Huttunen HJ, Fages C, Rauvala H: Receptor for advanced glycation end products (RAGE)-mediated neurite outgrowth and activation of NF-κB require the cytoplasmic domain of the receptor but different downstream signaling pathways. *J Biol Chem* 274: 19919-19924 (1999).
Koyama H, Shoji T, Yokoyama H, Motoyama K, Mori K, Fukumoto S, Emoto M, Shoji T, Tamei H, Matsuki H, Sakurai S, Yamamoto Y, Yonekura H, Watanabe T, Yamamoto H, Nishizawa Y: Plasma level of endogenous secretory RAGE is associated with components of the metabolic syndrome and atherosclerosis. *Arterioscler Thromb Vasc Biol* 25: 2587-2593 (2005).
Kumada T, Tsuneyama K, Hatta H, Ishizawa S, Takano Y: Improved 1-h rapid immunostaining method using intermittent microwave irradiation: practicability based on 5 years application in Toyama Medical and Pharmaceutical University Hospital. *Mod Pathol* 17: 1141-1149 (2004).
Lander HM, Tauras JM, Ogiste JS, Hori O, Moss RA, Schmidt AM: Activation of the receptor for advanced glycation end products triggers a p21(ras)-dependent mitogen-activated protein kinase pathway regulated by oxidant stress. *J Biol Chem* 272: 17810-17814 (1997).
Lue LF, Walker DG, Rogers J: Modeling microglial activation in Alzheimer's disease with human postmortem microglial cultures. *Neurobiol Aging* 22: 945-956 (2001).
Mackic JB, Stins M, McComb JG, Calero M, Ghiso J, Kim KS, Yan SD, Stern D, Schmidt AM, Frangione, B, Zlokovic BV: Human blood-brain barrier receptors for Alzheimer's amyloid-beta 1-40. Asymmetrical binding, endocytosis, and transcytosis at the apical side of brain microvascular endothelial cell monolayer. *J Clin Invest* 102: 734-743 (1998).
Mirra SS, Heyman A, McKeel D, Sumi SM, Crain BJ, Brownlee LM, Vogel FS, Hughes JP, van Belle G, Berg L: The Consortium to Establish a Registry for Alzheimer's Disease (CERAD). Part II. Standardization of the neuropathologic assessment of Alzheimer's disease. *Neurology* 41: 479-486 (1991).
Park L, Raman KG, Lee KJ, Lu Y, Ferran LJ Jr, Chow WS, Stern D, Schmidt AM: Suppression of accelerated diabetic atherosclerosis by the soluble receptor for advanced glycation endproducts. *Nat Med* 4: 1025-1031 (1998).
Renard C, Chappey O, Wautier MP, Nagashima M, Lundh E, Morser J, Zhao L, Schmidt AM, Scherrmann JM, Wautier JL: Recombinant advanced glycation end product receptor pharmacokinetics in normal and diabetic rats. *Mol Pharmacol* 52: 54-62 (1997).
Sakurai S, Yamamoto Y, Tamei H, Matsuki H, Obata KI, Hui L, Miura J, Osawa M, Uchigata Y, Iwamoto Y, Watanabe T, Yonekura H, Yamamoto H: Development of an ELISA for esRAGE and its application to type 1 diabetic patients. *Diabetes Res Clin Pract* 73: 158-165 (2006).
Sato T, Shimogaito N, Wu X, Kikuchi S, Yamagishi S, Takeuchi M: Toxic advanced glycation end products (TAGE) theory in Alzheimer's disease. *Am J Alzheimers Dis Other Demen* 21: 197-208 (2006).
Schmidt AM, Vianna M, Gerlach M, Brett J, Ryan J, Kao J, Esposito C, Hegarty H, Hurley W, Clauss M, Wang F, Pan YCE, Tsang TC, Stern D: Isolation and characterization of two binding proteins for advanced glycosylation end products from bovine lung which are present on the endothelial cell surface. *J Biol Chem* 267: 14987-14997 (1992).
Schmidt AM, Hori O, Brett J, Yan SD, Wautier JL, Stern D: Cellular receptors for advanced glycation end products. Implications for induction of oxidant stress and cellular dysfunction in the pathogenesis of vascular lesions *Arterioscler Thromb* 14: 1521-1528 (1994).
Sousa MM, Yan SD, Stern D, Saraiva MJ: Interaction of the receptor for advanced glycation end products (RAGE) with transthyretin triggers nuclear transcription factor κB (NF-κB) activation. *Lab Invest* 80: 1101-1110 (2000).
Stren DM, Schmidt AM, Yan SD, Yan SF : Receptor for advanced glycation endproducts (RAGE) and the complications of diabetes. *Ageing Res Rev* 1: 1-15(2002).
West MJ, Kawas CH, Stewart WF, Rudow GL, Troncoso JC: Hippocampal neurons in pre-clinical Alzheimer's disease. *Neurobiol Aging* 25: 1205-1212 (2004).

Yan SD, Chen X, Fu J, Chen M, Zhu H, Roher A, Slattery T, Zhao L, Nagashima M, Morser J, Migheli A, Nawroth P, Stern D, Schmidt AM: RAGE and amyloid-β peptide neurotoxicity in Alzheimer's disease. *Nature* 382: 685-691 (1996).

Yonekura H, Yamamoto Y, Sakurai S, Petrova RG, Abedin Md J, Li H, Yasui K, Takeuchi M, Makita Z, Takasawa S, Okamoto H, Watanabe T, Yamamoto H: Novel splice variants of the receptor for advanced glycation end-products expressed in human vascular endothelial cells and pericytes, and their putative roles in diabetes-induced vascular injury. *Biochem J* 370: 1097-1109 (2003).

Yonekura H, Yamamoto Y, Sakurai S, Watanabe T, Yamamoto H: Roles of the receptor for advanced glycation endproducts in diabetes-induced vascular injury. *J Pharmacol Sci* 97: 305-311 (2005).

金医大誌（J Kanazawa Med Univ）32：8－15, 2007

血管内皮細胞自身による血管新生の制御・調節メカニズム

米倉秀人，鶴岡直樹，吉竹佳の

血管新生(angiogenesis)は既存の毛細(微小)血管から新しい血管が増生される現象で，発生，成長といった生理的過程に必須であるのみならず，癌の増殖・転移，糖尿病網膜症といった病的状態の発生・進展に深く関与する。したがって，血管新生を制御する仕組みを解明することは，医学的，生物学的に極めて重要である。血管新生はこれまでの研究から促進因子(angiogenic factor)と抑制因子(angiostatic factor)のバランスで厳密にコントロールされていることが明らかになっている。血管新生を行なう微小血管の内皮細胞は，これまでもっぱら，癌細胞などの周りの組織からの働きかけを受けて血管新生を行なう受動的な立場としてとらえられてきた。筆者らは，血管内皮細胞がVEGF(vascular endothelial growth factor)遺伝子ファミリーのメンバーと複数の血管新生抑制因子を同時に発現し，血管内皮細胞自身が血管新生を制御する仕組みを持っていることを明らかにした。また，血管新生制御に働く血管内皮細胞遺伝子の探索を行い，可溶型VEGF受容体mRNAの選択的3'端プロセシングの制御を介して血管新生制御を調節するというこれまで知られていなかったRNAレベルでの制御機構の存在を見出した。

キーワード：　血管新生, 血管内皮細胞, 血管内皮増殖因子 (VEGF), 可溶型VEGF受容体, 選択的mRNAプロセシング

はじめに

血管新生(angiogenesis)は，既存の毛細(微小)血管から新しい血管が増生される現象で，発生，成長，創傷治癒といった生理的過程に必須であるのに加え，癌の増殖・転移，糖尿病網膜症，リウマチ性関節炎といった病的状態の発生・進展に深く関与している(1)。したがって，血管新生を制御する仕組みを解明することは，上記の生理過程を理解するためだけでなく，各種病態の成因，さらにはそれらの予防・治療手段を明らかにする上で極めて重要である。血管新生を行なう微小血管の内皮細胞は，これまでもっぱら癌細胞などの周りの組織からの働きかけをうけて血管新生を行なう受動的な立場としてとらえられてきたが，近年血管内皮細胞自身が血管新生を積極的に制御しうる仕組みを持っていることが明らかになってきた。本稿では，筆者らの研究結果を中心に，近年の知見を紹介したい。

1. 血管新生促進因子による内皮細胞オートクリン制御

血管新生の場となる微小血管は，一層の内皮細胞とそれを取り巻く周皮細胞から構成されている。血管新生は図1Aのような過程を経て進行するが，これまでの研究から血管新生は生理的には促進因子(angiogenic factor)と抑制因子(angiostatic factor)のバランスで厳密にコントロールされていることが明らかにされてきた(2)。低酸素状態や癌細胞の存在などでこのバランスが促進方向へずれると，血管新生が引き起こされる(angiogenic switch)(図1B)。血管新生を誘導する主要な生理的要因は低酸素状態と考えられるが，以前は低酸素状態に陥った組織で血管新生が誘導されるのは周囲の組織が低酸素に応答して血管新生誘導因子を産生・分泌するためで，血管内皮細胞自身はそれを受けて反応するだけの受動的な立場としてのみとらえられていた。また，低酸素状態に対して血管内皮細胞自身がどう反応するのかという点に関してもほとんど明らかにされていなかった。1995年にNomuraらは，周囲の組織だけでなく，血管内皮細胞自身が内皮細胞の主要な増殖因子であるvascular endothelial growth factor (VEGF)を発現し，低酸素状態ではその発現が亢進して自身の増殖を促進することを見出した(3)。VEGFは1989年に発見された血管内皮細胞の主要な増殖因子(4)で，これまでの研究で複数の遺伝子からなる遺伝子ファミリー(VEGFファミリー)を形成し，それぞれが複数のVEGF受容体を共有していることが明らかになっている(図2)(5)。VEGFファミリーは選択的mRNAスプライシングにより産生されるバリアントを持つものが多い(図2)。また，受容体も後述のようにmRNAの選択的3'端プロセシングにより可溶型の受容体を生じ，このフォームは血管新生抑制に働く(図2)。

金沢医科大学医学部ゲノム医科学（生化学Ⅱ）
石川県河北郡内灘町大学1-1
平成19年7月17日受理

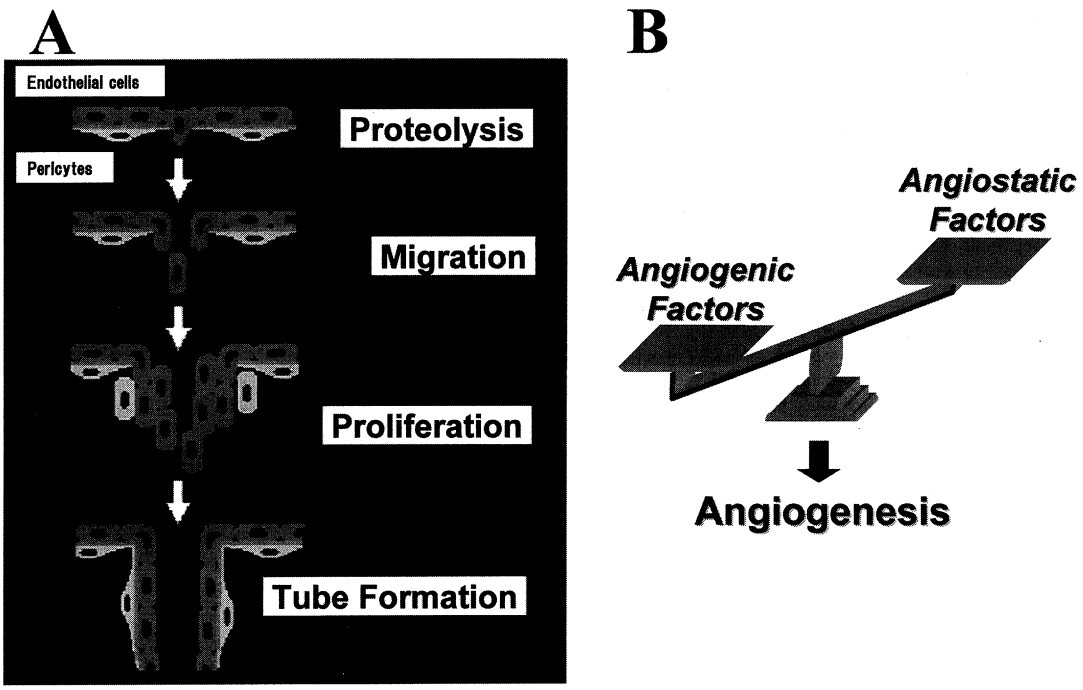

図１．(A)血管新生のステップと(B)促進因子と抑制因子のバランスによる血管新生制御。

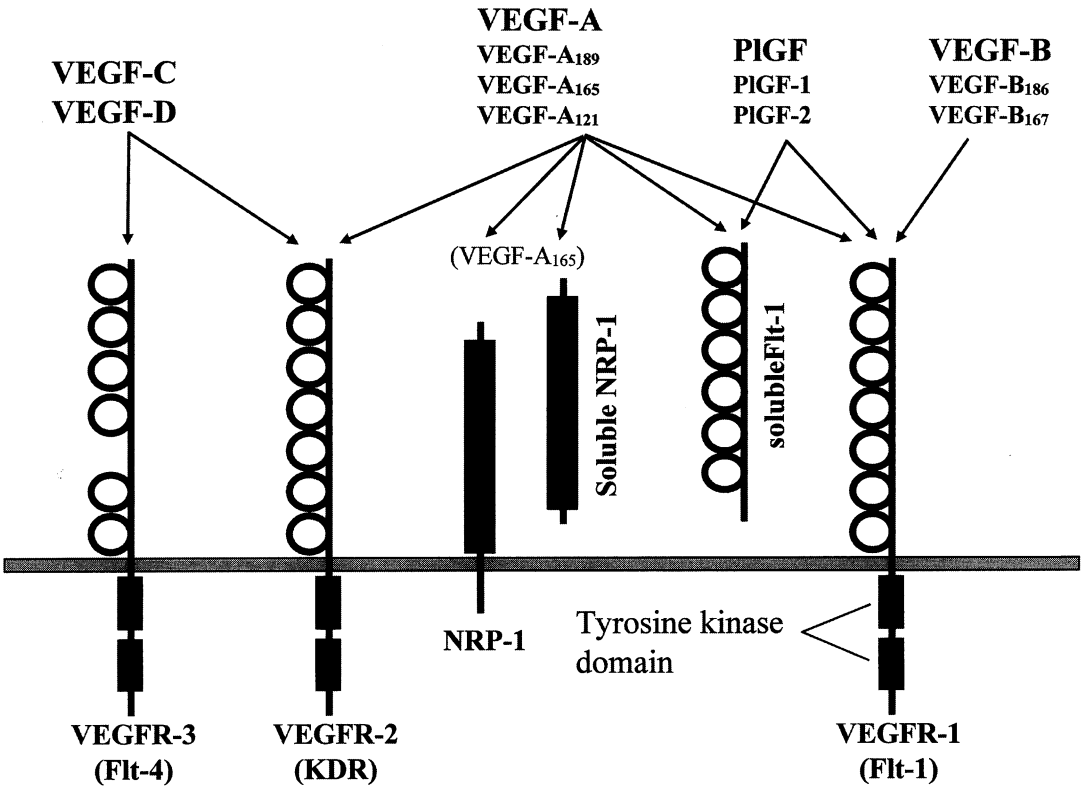

図２．VEGFファミリーのメンバーと受容体との対応。VEGF, vascular endothelial growth factor; VEGFR, VEGF receptor; NRP-1, neuropilin-1; Flt-1, fms-like tyrosine kinase-1; KDR, kinase domain receptor; PlGF, placenta growth factor.

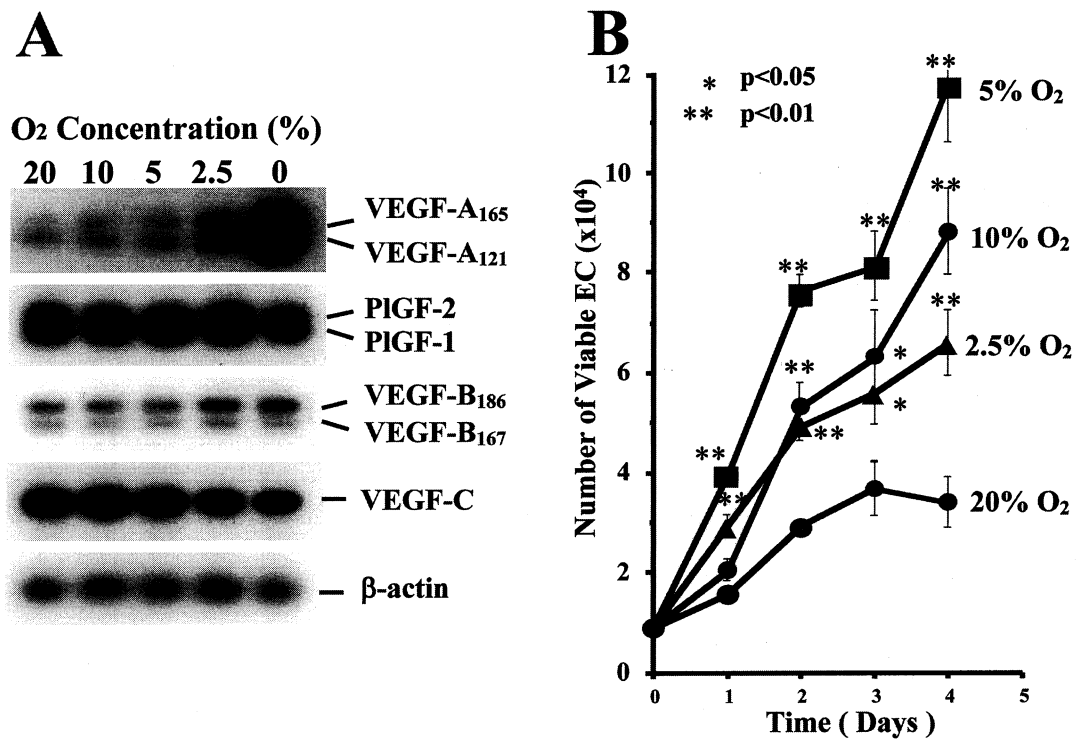

図３．(A) 初代培養ヒト血管内皮細胞でのVEGFファミリー遺伝子の発現。各種酸素濃度化で24時間培養したヒト皮膚微小血管内皮細胞よりRNAを分離し，RT-PCR法により解析した。(B) 各種酸素濃度化でのヒト皮膚微小血管内皮細胞の増殖。図に示した日数の培養後，細胞をトリプシン処理して回収し生細胞をカウントした。EC, endothelial cells.

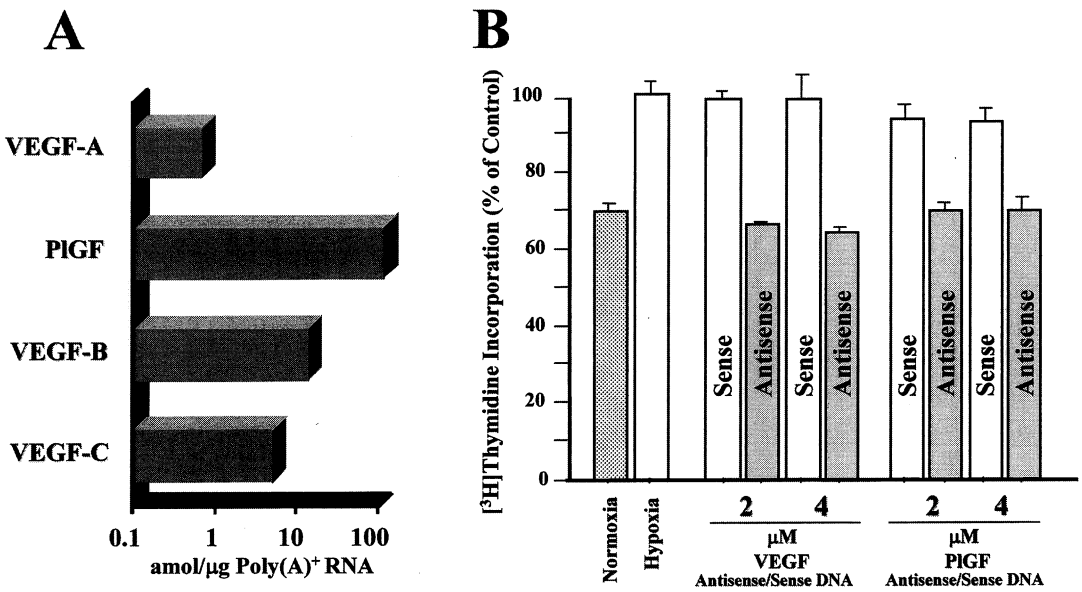

図４．(A) 初代培養ヒト血管内皮細胞に存在するVEGFファミリーのmRNA量。ヒト皮膚微小血管内皮細胞より分離したRNAを用い，competitive RT-PCR法により定量を行なった。(B)低酸素誘導性内皮細胞増殖へのVEGF-A mRNAとPlGF mRNAに対するアンチセンスDNAの影響。ヒト皮膚微小血管内皮細胞を，示した濃度のアンチセンスオリゴヌクレオチド(Antisense)あるいはコントロールのセンスオリゴヌクレオチド(Sense)の存在下で培養し，[³H]Thymidineの取り込みによりDNA合成(増殖速度)を解析した。低酸素状態(5% O_2)での[³H]Thymidineの取り込み量を100%として示した。

VEGFファミリーの中で最も重要と考えられているのが，最初に発見されたVEGF-Aである。ヒト皮膚由来の初代培養血管内皮細胞を低酸素状態で培養すると，VEGF-AのmRNA量が増大し(図3A)，内皮細胞の増殖が促進される(図3B)(3,6)。ほぼ同時期にNamikiらも同様の結果を報告している(7)。さらに筆者ら(8)は，血管内皮細胞がVEGF遺伝子ファミリーに属する他のメンバーであるVEGF-B, VEGF-C, placenta growth factor(PlGF)も発現していることを見出した(図3A, 図4A)。そのうちPlGF mRNAは，モル比でVEGF-A mRNAの100倍近く発現し(図4A)，低酸素での発現増加は見られないが，PlGF mRNAに対するアンチセンスDNAはVEGF-A mRNAに対するアンチセンスDNAと同様に低酸素による内皮細胞の増殖促進を抑制した(図4B)(8)。以上の結果は，低酸素状態で，PlGF共存の下，VEGF-Aにより内皮細胞の増殖を促進させるオートクリン調節機構が存在することを示している。このオートクリン血管新生促進機構は，組織が低酸素状態に陥ったとき，周りの組織からの十分な増殖因子が届くまで内皮細胞の生存を維持し，そして増殖のエンジンをかけておくという重要な機構であると考えられる。VEGF-B, VEGF-Cの役割の詳細についてはいまだ明らかではないが，モル比でVEGF-A mRNAよりも多量に発現し，それぞれが受容体を共有していることから，内皮細胞の増殖や血管ネットワークの形成の調節にやはり何らかの役割を担っているものと予想される。

これまでのin vitro, in vivoの研究結果から，VEGFが血管新生の場で大きな役割を果たしていることが明らかにされているが，血管新生を促進するのはVEGFのみではない。Fibroblast growth factor (FGF)もその強力な血管新生活性と癌細胞での発現亢進などから重要な因子である(9)。FGFは，その作用が内皮細胞のVEGF発現亢進を伴うことが報告されている(10)。さらに，tumor necrosis factor-α (TNF-α)も血管新生促進作用が報告されているが，これもその作用がVEGFなどのオートクリン因子を介することが見出されている(11)。また，angiopoietinファミリー(1)も血管構造の安定化に非常に重要である。

表1．初代培養ヒト血管内皮細胞と周皮細胞で発現する血管新生抑制因子

血管内皮細胞	
	Angiomotin
	Angiopoietin 2
	Endostatin (collagen XVIII)
	Pigment epithelium-derived factor (PEDF)
	Soluble Flt-1
	Soluble NRP-1
	Thrombospondin-1
血管周皮細胞	
	Angiomotin
	Endostatin (collagen XVIII)
	Pigment epithelium-derived factor (PEDF)
	Soluble NRP-1
	Thrombospondin-1

各因子の文献は以下のとおり：angiomotin (24), angiopoietin 2 (1), endostatin (14), pigment epithelium-derived factor (25), soluble Flt-1 (19), soluble neuropilin-1 (20), thrombospondin-1 (26).

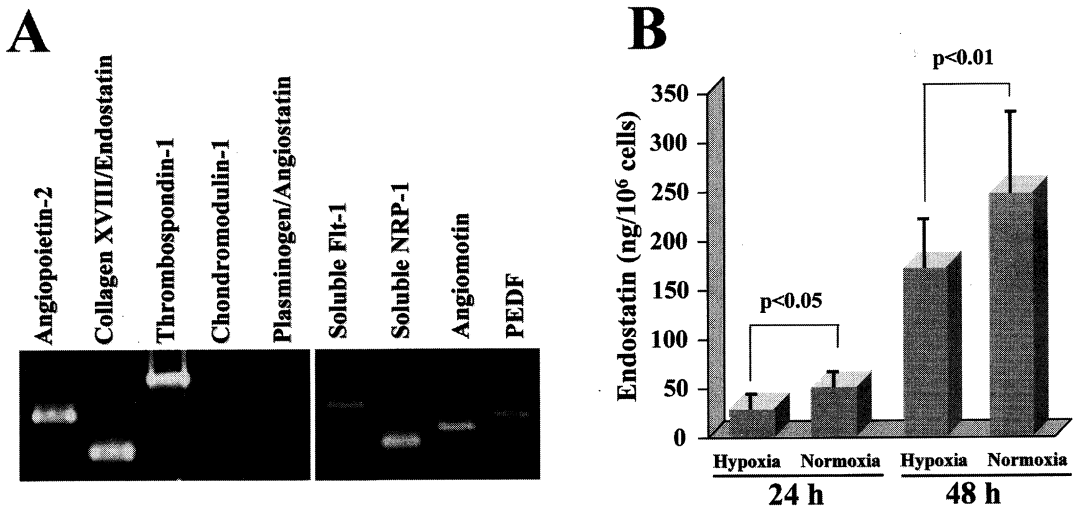

図5．(A) 初代培養ヒト血管内皮細胞での各種血管新生抑制遺伝子の発現。ヒト皮膚微小血管内皮細胞よりRNAを分離し，RT-PCR法により解析した。Angiopoietin 2, endostatin, thrombospondin-1, soluble Flt-1, soluble NRP-1, angiomotin, PEDF(pigment epithelium-derived factor)の発現が検出された。(B) ヒト皮膚微小血管内皮細胞が産生するendostatin量の低酸素状態での変化。細胞を正常酸素濃度あるいは低酸素(5% O2)で24時間培養後，培養液を回収し，endostatin定量用ELISAにて定量した。

2. 血管新生抑制因子による内皮細胞オートクリン制御

上述のように血管新生の制御は促進因子のみではなく，抑制因子の働きも非常に重要である。最近まで，血管内皮細胞自身が血管新生抑制因子を発現しているのか，発現しているとしたら実際にそれらが働いているのかについて，ほとんど明らかにされていなかった。内皮細胞での血管新生抑制因子の発現は，癌組織など周囲から血管新生促進刺激が血管内皮細胞に到達した際に，内皮細胞がどう挙動するかを決める大きな要因となりうるため，たいへん重要な課題であると考えられる。そこで筆者らは，まず血管内皮細胞と血管周皮細胞での主要な血管新生抑制因子の発現をRT-PCR法により検討した(12,13)。その結果，表1に示すように複数の血管新生抑制因子が血管内皮細胞(図5A)と周皮細胞で発現されていることが明らかとなった。

そこでこの中からまず，抗腫瘍血管新生薬剤として制癌への応用に向けて研究が進められているendostatinの産生を解析した(12)。Endostatinは18型コラーゲンのC末端部位が切断されて遊離されたもので，血管内皮細胞の増殖と遊走を強く阻害する(14)。まず，初代培養ヒト血管内皮細胞とヒト血管周皮細胞の培養液をendostatin特異抗体を用いてウエスタンブロット解析をおこなったところ，20 kDaのendostatin蛋白質が検出された(12)。ついで両者の細胞を通常酸素濃度下と低酸素(5% O_2)下で培養し，培養液中に遊離されたendostatin蛋白質をELISA法を用いて測定した(12)。その結果，endostatin産生量が低酸素状態で有意に低下することが明らかとなった(図5B)。以上より，低酸素により血管新生抑制因子であるendostatinの産生量が低下し，上記のVEGF-Aの発現上昇と相まって，血管新生制御因子のバランスを血管新生促進の方向へ変化させていることが明らかとなった。以上の知見は，血管内皮細胞が，血管新生促進因子とともに血管新生抑制因子も加えた，血管新生制御機構を持っていることを示している。さらに以下に示すように，血管新生抑制因子として可溶型VEGF受容体[可溶型fms-like tyrosine kinase-1(可溶型Flt-1)と可溶型neuropilin-1(可溶型NRP-1)]が重要な役割を担っていることが明らかとなってきた(13)。

3. 新しい血管新生制御遺伝子の探索

筆者らは，血管内皮細胞自身による血管新生制御機構をさらに解明するため，機能面から遺伝子を同定する遺伝子スクリーニング法(Antisense display法)を独自に開発し，血管新生制御に働く血管内皮細胞遺伝子の探索を行なった(13,15,16)。Antisense display法の原理は，概ね全てのmRNA分子種をカバ

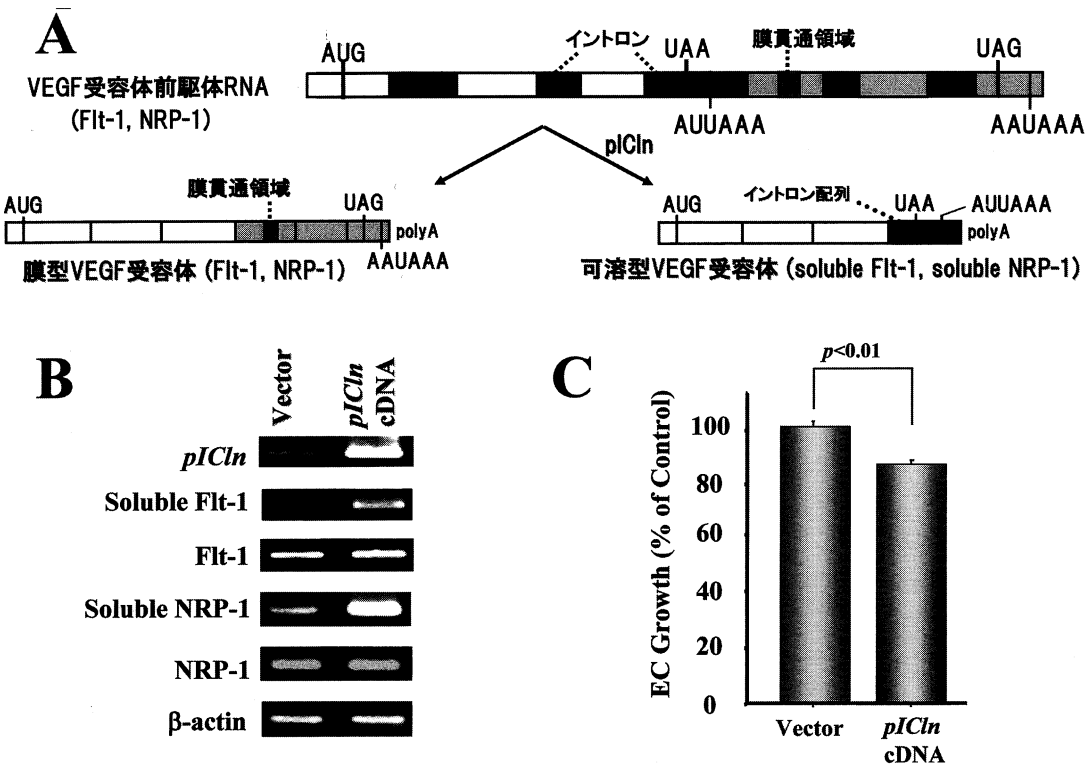

図6．(A) 可溶型Flt-1 mRNAと可溶型NRP-1 mRNAの選択的3'端プロセシング。(B) pIClnを過剰発現したヒト皮膚微小血管内皮細胞での各種血管新生関連遺伝子の発現。ヒトpIClnを持つ発現ベクターをヒト皮膚微小血管内皮細胞に導入して(pIClnと標記)，24時間培養後，RNAを分離しRT-CPCR法で解析した。コントロールとしてcDNAを持たない発現ベクターを細胞に導入した(Vectorと標記)。(C) pIClnを過剰発現したときのヒト皮膚微小血管内皮細胞の増殖。細胞増殖はMTT法で解析した。EC, endothelial cell.

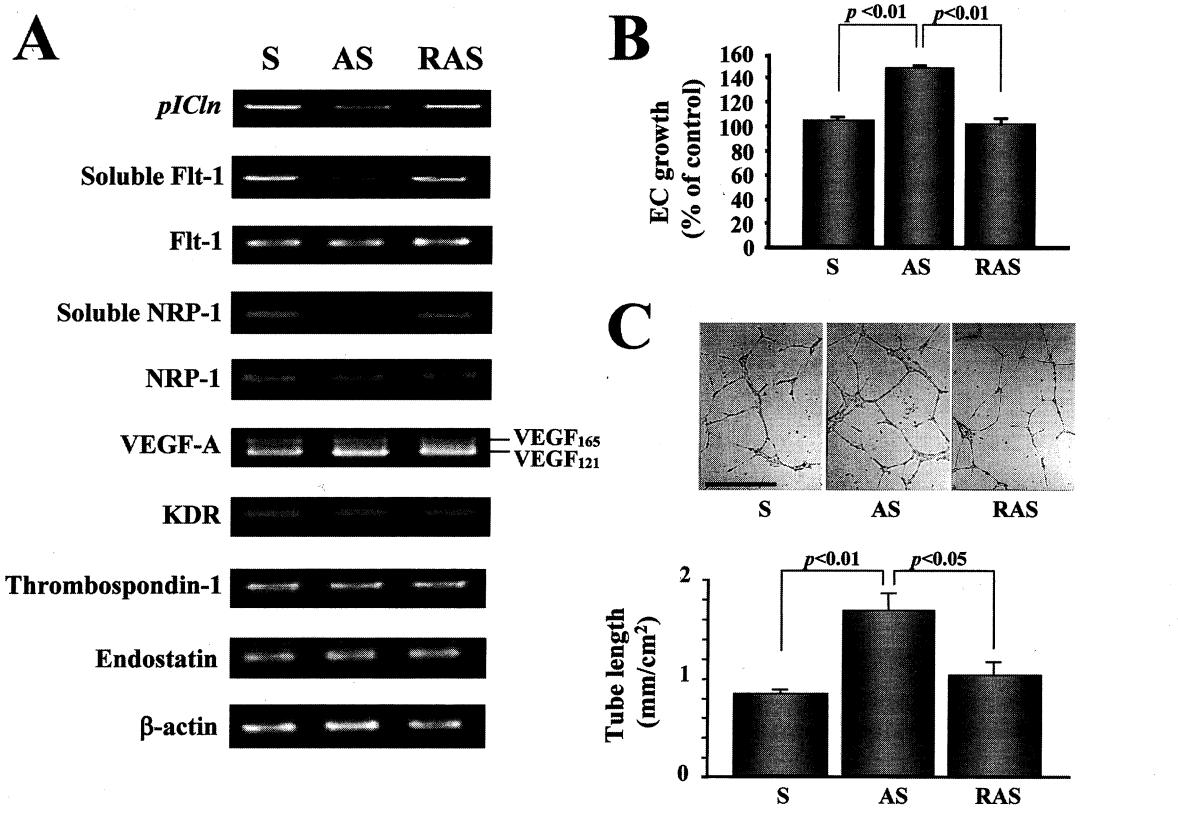

図７．pICln発現を抑制したときの各種血管新生関連遺伝子の発現(A)，細胞増殖(B)およびin vitro血管管腔形成(C)。(A) pICln mRNAに対するアンチセンスオリゴヌクレオチド存在下で培養したヒト皮膚微小血管内皮細胞(ASと標記)よりRNAを分離し，RT-PCR法で発現を検討した。コントロールとしてセンス配列(Sと標記)および逆センス配列(RASと標記)を持つオリゴヌクレオチドを用いた。(B) pIClnアンチセンスオリゴヌクレオチド(AS)存在下で培養したヒト皮膚微小血管内皮細胞の増殖。細胞増殖はMTT法で解析した。コントロールのセンスオリゴヌクレオチド(S) 存在下で培養した血管内皮細胞の値を100%として示した。(C) pIClnアンチセンス(AS)存在下で培養したヒト皮膚微小血管内皮細胞をMatrigel上に播種し，in vitro血管新生を解析した。顕微鏡下で写真撮影し，形成された管腔の長さを測定した。

ーしうるアンチセンスオリゴヌクレオチド(アンチセンスDNA)のレパートリーを調整し，これらのアンチセンス配列の中から血管新生の変化を引き起こす配列を同定し，その配列を基にその原因遺伝子を分離するというものである(15,16)。初代培養ヒト血管内皮細胞の増殖促進を指標としてAntisense displayスクリーニングを行い，アンチセンスDNAで発現を抑制したときに有意に内皮細胞の増殖が促進される遺伝子pICln [protein ICln(chloride channel, nucleotide sensitive)]を同定した(13)。すなわちこの遺伝子は，内皮細胞増殖を抑制する活性をもつ遺伝子ということになる。pIClnは，当初細胞膜クロライドチャンネルの候補としてクローニングされた(17)が，その後は疑問視され，最近ではmRNAスプライシングを行なうスプライソソームの形成に関与しているという報告がある(18)。

pIClnが実際にどのような機構で血管内皮細胞の増殖を抑制しているかについて解析を行ったところ，血管新生抑制因子である可溶型Flt-1(19)と可溶型NRP-1(20)の産生を介していることが明らかとなった(12)。可溶型Flt-1と可溶型NRP-1(図２)は，

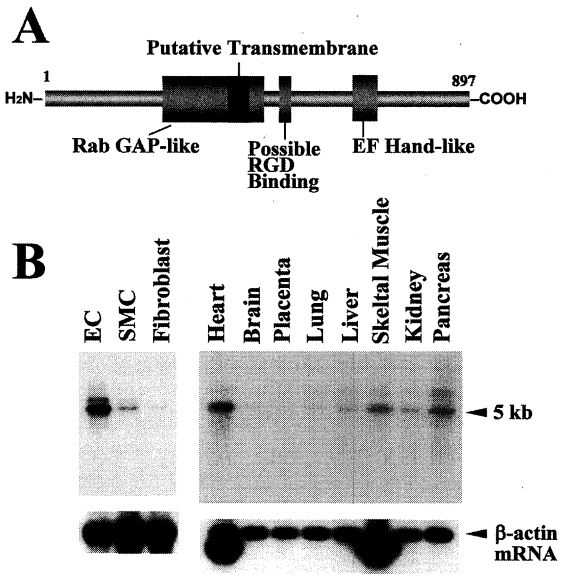

図８．(A)Vascular RabGAP-containing Protein, VRP (TBC1D8)の構造と(B)各種細胞・組織での発現。発現解析はノーザンブロット法で行った。EC, endothelial cells; SMC, smooth muscle cells.

膜貫通型の細胞表面受容体を産生するのと同じ遺伝子からmRNAの選択的3'端プロセシングで生成される。すなわち可溶型受容体mRNAは，膜貫通型受容体をコードする遺伝子途中のイントロン中にある選択的なポリA付加シグナルを利用してプロセシングを受け，細胞膜貫通領域を持たない分泌性可溶型蛋白質として産生され，細胞外へ分泌される(図6A)。細胞外へ分泌された可溶型Flt-1と可溶型NRP-1は，VEGFとの結合能はそのまま保持しているため，周囲の組織や内皮細胞自身が分泌したVEGFを細胞外でトラップして内皮細胞表面の受容体への結合を阻害し，強力な血管新生抑制因子として働く(図2)。これら可溶型VEGF受容体は，癌細胞の増殖，転移を強く抑制することが報告されている(21)。また眼の角膜に血管網が形成されないのは，可溶型Flt-1が角膜で大量に産生されているからである(22)。

pIClnを血管内皮細胞で過剰発現させると，可溶型Flt-1と可溶型NRP-1をコードするmRNAが特異的に上昇し(図6B)，それに伴い内皮細胞の増殖が有意に抑制された(図6C)(13)。逆に，アンチセンスDNAで血管内皮細胞のpIClnの発現を抑制すると，可溶型Flt-1 mRNAと可溶型NRP-1 mRNAが特異的に低下し(図7A)，内皮細胞増殖が促進され(図7B)，さらにin vitroでの血管新生(管腔形成)も促進された(図7C)(13)。以上の結果は，今回同定された遺伝子pIClnがmRNAの選択的3'端プロセシングを介して血管新生制御を制御するというこれまで知られていなかった機能を持つこと，可溶型Flt-1と可溶型NRP-1が血管内皮細胞が持つオートクリン血管新生制御機構の中で主要な役割を持っていることを示している。

筆者らはまた，初代培養ヒト血管内皮細胞の増殖抑制を指標としたAntisense displayスクリーニングで，血管内皮細胞に特異的に発現し，増殖促進に働くと考えられる新しい遺伝子vascular RabGAP-containing protein, VRP (現在の統一名称：TBC1D8)の分離に成功している(図8)(15,16)。VRP (TBC1D8)の詳細な機能はいまだ明らかではないが，最近の筆者らの予備的な実験で，血管内皮細胞が神経細胞と相互作用した際にこの遺伝子の発現が増大することが見出された(未発表データ)。VRP (TBC1D8)が神経-血管相互作用による全身血管ネットワーク形成に何らかの役割を持っている可能性が考えられ，注目している。

おわりに

以上述べてきた筆者らの研究により，血管内皮細胞自身が血管新生促進因子と抑制因子を産生・分泌し，それらのバランスで自らの血管新生を制御する，オートクリン血管新生制御機構が存在することが明らかになった。この機構ではまた，これまでほとんど注目されていなかったRNAのレベルでの制御で，実際に細胞外で働く因子の産生量が調節されていることも明らかとなってきた。現在筆者らは，この可溶型VEGF受容体mRNAを産生するmRNAの選択的3'端プロセシングの制御機構の解明を行なっている。またRNA段階での血管新生制御因子の調節という観点では，最近その機能の重要性が認識されつつあるミクロRNA(microRNA) (23)の関与が注目される。ミクロRNAは，上述の血管新生促進因子とその受容体や血管新生抑制遺伝子のmRNAを標的として，やはりRNAレベルで血管新生の調節を行なっている可能性が強く考えられる。筆者らは現在，mRNA選択的3'端プロセシング制御機構の解明とともに，血管内皮細胞に存在し血管新生・血管ネットワークの形成に働くミクロRNAの解析を進めている。これら研究の進展により，血管内皮細胞の内外で働いている血管新生の調節機構の詳細がさらに明らかになってくると期待している。そしてその成果は，このオートクリン機構を人工的に制御することにより，抗腫瘍血管新生による制癌や血管新生が関わる疾患のコントロールあるいは虚血性疾患での血管形成促進などに応用できるのではないかと期待している。

本研究の多くは金沢大学医学系研究科血管分子生物学研究分野での共同研究の成果である。また最近の知見は，金沢医科大学共同研究(C2006-4 and C2007-1)，金沢医科大学奨励研究(S2006-6 and S2007-10)，金沢医科大学ハイテクリサーチセンタープロジェクト研究(H2007-10)の助成を受けたものである。

文献

1. Carmeliet P: Angiogenesis in health and disease. Nature Medicine 2003; **9:** 653-60.
2. Hanahan D. and Folkman J: Patterns and emerging mechanisms of the angiogenic switch during tumorigenesis. Cell 1996; **86:** 353-64.
3. Nomura M, Yamagishi S, Harada S et al: Possible participation of autocrine and paracrine vascular endothelial growth factors in hypoxia-induced proliferation of endothelial cells and pericytes. J Biol Chem 1995; **270:** 28316-24.
4. Leung DW, Cachianes G, Kuang WJ et al: Vascular endothelial growth factor is a secreted angiogenic mitogen. Science 1989; **246:** 1306-9.
5. Shibuya M, Claesson-Welsh L: Signal transduction by VEGF receptors in regulation of angiogenesis and lymphangiogenesis. Exp Cell Res 2006; **312**(5): 549-60.
6. Yamagishi S, Kawakami T, Fujimori H et al: Insulin stimulates the growth and tube formation of human microvascular endothelial cells through autocrine vascular endothelial growth factor. Microvasc Res 1999; **57:** 329-39.
7. Namiki A, Brogi E, Kearney M et al: Hypoxia induces vascular endothelial growth factor in cultured human endothelial cells. J Biol Chem 1995; **270:** 31189-95.
8. Yonekura H, Sakurai S, Liu X et al: Placenta growth factor and vascular endothelial growth factor B and C expression in microvascular endothelial cells and pericytes: implication in autocrine and paracrine regulation of angiogenesis. J Biol Chem 1999; **274:** 35172-8.
9. Presta M, Dell'Era P, Mitola S et al: Fibroblast growth factor/fibroblast growth factor receptor system in angiogenesis. Cytokine Growth Factor Rev 2005; **16:** 159-78.
10. Seghezzi G, Patel S, Ren CJ et al: Fibroblast growth factor-2 (FGF-2) induces vascular endothelial growth factor (VEGF) expression in the endothelial cells of forming capillaries: an autocrine mechanism contributing to angiogenesis. J Cell Biol 1998; **141:** 1659-73.
11. Yoshida S, Ono M, Shono T et al: Involvement of interleukin-8, vascular endothelial growth factor, and basic fibroblast growth factor in tumor necrosis factor alpha-dependent angiogenesis. Mol Cell Biol 1997; **17:** 4015-23.
12. Wu P, Yonekura H, Li H et al: Hypoxia down-regulates endostatin production by human microvascular endothelial cells and pericytes. Biochem Biophys Res Commun 2001; **288:** 1149-54.

13. Li H, Yonekura H, Kim CH et al: Possible participation of pICln in the regulation of angiogenesis through alternative splicing of vascular endothelial growth factor receptor mRNAs. Endothelium 2004; **11:** 293-300.
14. O'Reilly MS, Boehm T, Shing Y et al: Endostatin: an endogenous inhibitor of angiogenesis and tumor growth 1997; Cell **88:** 277-85.
15. Yonekura H, Migita H, Sakurai S et al: Antisense display - a method for functional gene screening: evaluation in a cell-free system and isolation of angiogenesis-related genes. Nucleic Acids Research 1999; **27:** 2591-600.
16. Yonekura H, Yasui K, Sakurai S et al: Antisense display - a new method for functional gene screen and its application to angiogenesis-related gene isolation. Ann N Y Acad Sci. 2001; **947:** 382-6.
17. Paulmichl M, Li Y, Wickman K et al: New mammalian chloride channel identified by expression cloning. Nature 1992; **356:** 238-41.
18. Pu WT, Krapivinsky GB, Krapivinsky L et al: pICln inhibits snRNP biogenesis by binding core splicsomal proteins. Mol Cell Biol 1999; **19:** 4113-20.
19. Kendall RL, Thomas KA: Inhibition of vascular endothelial cell growth factor activity by an endogenously encoded soluble receptor. Proc Natl Acad Sci U S A 1993; **90:** 10705-9.
20. Gagnon ML, Bielenberg DR, Gechtman Z: Identification of a natural soluble neuropilin-1 that binds vascular endothelial growth factor: In vitro expression and antitumor activity. Proc Natl Acad Sci U S A 2000; **97:** 2573-8.
21. Goldman CK, Kendall RL, Cabrera G et al: Paracrine expression of a native soluble vascular endothelial growth factor receptor inhibits tumor growth, metastasis, and mortality rate. Proc Natl Acad Sci U S A 1998; **95:** 8795-800.
22. Ambati BK, Nozaki M, Singh N et al: Corneal avascularity is due to soluble VEGF receptor-1. Nature 2006; **443:** 993-7.
23. Ambros V: The functions of animal microRNAs. Nature 2004; **431:** 350-5.
24. Troyanovsky B, Levchenko T, Mansson G et al: Angiomotin: an angiostatin binding protein that regulates endothelial cell migration and tube formation. J Cell Biol 2001; **152:** 1247-54.
25. Dawson DW, Volpert OV, Gillis P et al: Pigment epithelium-derived factor: a potent inhibitor of angiogenesis. Science 1999; **285:** 245-8.
26. Good DJ, Polverini PJ, Rastinejad F et al: A tumor suppressor-dependent inhibitor of angiogenesis is immunologically and functionally indistinguishable from a fragment of thrombospondin. Proc Natl Acad Sci U S A 1990; **87:** 6624-8.

Autocrine Regulation of Angiogenesis.

Hideto Yonekura, Naoki Tsuruoka and Yoshino Yoshitake

Department of Biochemistry II, School of Medicine, Kanazawa Medical University, Uchinada, Kahoku-gun, Ishikawa 920-0293, Japan

Angiogenesis is essential not only for various physiological events such as development, growth, and reproduction, but also for the progression of various pathological conditions including cancer growth and metastasis. Recent studies have demonstrated that angiogenesis is controlled by a balance between angiogenic and angiostatic factors. It is well known that, among angiogenic factors, vascular endothelial growth factor (VEGF) has emerged as a central regulator of the angiogenic process in both physiological and pathological conditions. We have shown that the VEGF family genes are expressed in vascular endothelial cells and pericytes and that the autocrine VEGF-A promoted EC growth and angiogenesis in combination with another VEGF family member, PlGF (placenta growth factor). We have also demonstrated that EC and pericytes express plural angiostatic factors including endostatin, soluble Flt-1 and soluble neuropilin-1(NRP-1). On the other hand, with an antisense-oriented method for functional gene screening, we have identified a novel type of angiostatic gene, pICln, which regulates alternative 3'-end processing of soluble Flt-1 and soluble NRP-1 pre-mRNAs. Soluble Flt-1 and soluble NRP-1 can trap extracellular VEGF-A, thereby acting as a potent angiostatic factor. These results indicated that vascular endothelial cells have an autocrine regulation mechanism of angiogenesis with a balance of angiogenic and angiostatic factors. The results also indicated that this autocrine mechanism can be regulated at the RNA processing level.

Key Words: Angiogenesis, Vascular endothelial cell, Vascular endothelial growth factor (VEGF), Soluble VEGF receptor, Alternative mRNA processing

１．研究課題名：治療的電撃けいれん(ECS)の神経生理学的機序（研究番号　C2006-5）

２．キーワード：１）治療的電撃けいれん　（Electroconvulsive therapy）
２）ニューロン興奮性　（Neuronal exitability）
３）シナプス可塑性　（Synaptic plasticity）
４）カルシウムチャンネル　（Calcium channel）
５）うつ病モデル　（Animal model for mood disorder）

３．研究代表者：加藤　伸郎・医学部・教　授・生理機能制御学（生理学）
研究分担者：須貝外喜夫・医学部・准教授・生理機能制御学（生理学）
吉村　　弘・医学部・准教授・顎口腔機能病態学（口腔科学）
杉浦　重樹・奈良県立医科大学・先端医学研究機構・准教授
井ノ口　馨・三菱化学生命科学研究所・記憶形成・精神疾患研究
グループ・グループディレクター
小島　正己・(独)産業技術総合研究所・セルエンジニアリング研究部門
主任研究員

４．研 究 目 的

治療的電撃けいれん（ECS）は、うつ病や統合失調症の治療において、絶大な治療効果を持つ。しかし、その大脳生理学的な作用機序は不明である。ECS によって発現が高まる分子群については、分子生物学的研究が進められ、（１）神経栄養因子 BDNF に関連した分子群、（２）アラキドン酸代謝に関連した分子群、（３）足場タンパクである Homer1a/Vesl-1S、の３つの分子群が強く発現してくることがコンセンサスとなっている。ところが、これらの分子群が、実際の脳内でどのように働き、個々のニューロンにどのように作用するか、という生理学的側面についてはほとんど知られてこなかった。本研究では、「なぜ ECS が不安障害・うつ病に治療効果を発揮するのか？」を統合的に解明するために、分子・生理・行動学的解析を実行する。最近、うつ病者の発生が高止まりしており、社会的にも国民経済的にも大きな問題となっている。本研究により、うつ病治療法の改良や、うつ病病態生理の解明が進展することが期待される。また、うつ病における脳機能失調の本態の解明に資することが期待される。

５．研 究 計 画

本研究計画では、治療的電撃けいれん（ECS）によって発現増加することの知られている 3 分子群のうち、Homer1a/Vesl-1S と BDNF 関連の 2 分子群に絞って生理学的解析を行うことをめざした。Homer1a/Vesl-1S に関しては、これまでに過分極作用やカルシウムチャンネル促進作用のあることを確認した。そこで、これを発展させて様々なシナプス可塑性に対する作用を調べることを計画した。BDNF 関連分子群に関しても、生理解析をすすめることを計画した。共同研究者・小島らは、ヒト BDNF（脳由来神経栄養因子）の SNP 研究（細胞生物学的研究と SNP マウスライブラリーの研究）を通して精神疾患の発症に関係する BDNF のサブタイプ（精神疾患関連 BDNF）を見

出しているので、この精神疾患関連 BDNF およびそのノックインマウスを使うことを予定した。まず野生型マウスからスライスを作製し、正常 BDNF と精神疾患関連 BDNF 間で、生理作用の対比を行うことを計画した。

6．研 究 成 果

① Homer1a/Vesl-1S によるシナプス可塑性への影響に関して、一定の成果があった。シナプス伝達長期抑圧（LTD）は、大きく分けて NMDA 型グルタミン酸受容体（NMDAR）依存性のタイプと代謝型グルタミン酸受容体（mGluR）依存性のタイプに２分出来る。まず、ラット視覚皮質から作製したスライス標本を用いて、視覚皮質内の種々のシナプスにおける LTD を、NMDAR 依存型と mGluR 依存型とに分類した。皮質を構成する６層構造のうち最下層の第６層に位置する細胞へのシナプスでの LTD は mGluR 依存的であり、他の層においては NMDAR 依存的であることが判明した。これら２種の受容体依存性と Homer1a/Vesl-1S による修飾作用との関連を調べたところ、LTD が mGluR 依存性であるシナプスにおいては、Homer1a/Vesl-1S 発現によって LTD が阻害され、NMDAR 依存型 LTD では影響を受けないことがわかった。電撃けいれん刺激（ECS）によって発現させた Homer1a/Vesl-1S も、蛋白質の形で細胞内投与した場合と同様、第６層シナプスにおける LTD を阻害した。第６層は、大脳皮質への視覚入力の最終中継地となっている視床に対して、フィードバック調整をかける役割をしている。ECS によって大脳皮質が興奮することによって、そのフィードバックが強化されることが示唆される。この結果、視床と大脳皮質の間に形成される反響的な興奮伝播が是正され、これが ECS による高次神経活動への効果を一部説明する可能性を提案した（Ueta et al., 2008）。

② うつ病や統合失調症の症状の責任部位としては、主に大脳新皮質と大脳辺縁系の二つが挙げられる。大脳辺縁系の中でも、扁桃核は不安条件付けに必須の部位であることが知られ、うつ病との関連性が高いと考えられる。この部位におけるニューロン興奮性が、精神疾患治療薬のターゲットのひとつとなっているドパミン受容体によって、どのように修飾されるかを調べた。ドパミン受容体の活性化によって、神経細胞の興奮が正フィードバック的に高まる新規メカニズムを発見した。この過程で、ニューロン活動依存的なカリウムチャンネルの閉鎖の起こることを明らかにした。この実験によって、うつ病モデル動物における細胞レベルまたは回路網レベルでの興奮性変化、あるいはそれに対する ECS の効果を、扁桃核とその周辺の神経回路を用いて評価する可能性が示唆された（Yamamoto et al., 2007）。実際に、これが評価システムとして使用可能なことが確認できた。

③ Homer1a/Vesl-1S の注入にカルシウムチャンネル促進作用のあることが以前の研究で明確化していた。また、ECS 施行後のラットから作成したスライス標本においても、Homer1a 依存的に同様のカルシウムチャンネル促進作用が確認されていた。このチャンネルが促進された場合に生ずるシナプス可塑性への影響については、シナプス増強の場合にはすでに調べて報告していたが（Isomura and Kato, 1999）、シナプス抑圧（LTD）との関連については未知であったので、カルシウムイメージングなどを使って調べた。その結果、L 型カルシウムチャンネルには活動性の低いシナプスの恒常性を維持する作用のあることが判明し、論文報告した（Udagawa et al., 2006）。この結

果は、成果①として記したECSのシナプス抑圧ブロッキング作用の解釈に有用である。一般的に、シナプス増強もシナプス抑圧も細胞内カルシウム上昇によって引き起こされるが、細胞内濃度が大きく上昇するとシナプス増強が起こり、小規模であるとシナプス抑圧が招来し、中間段階の増加においてはどちらも起こらないような中立域となると理解されている。ECSによるカルシウムチャンネルの促進によって、小規模となるべきカルシウム上昇が中立域にまで上昇幅を高めたと考えると成果①の結果がうまく解釈できることが判明した。

④　ECS作用の行動レベルでの解析の研究に関しても進展があった。うつ病の動物モデルとして広く採用されている強制水泳試験を使って ECS 効果の評価を行えるよう準備を進めた。行動解析のための実験室を整備した。解析用のプールを作成し、ディジタルカメラならびにビデオファイルから動物行動の特徴を抽出するための汎用ソフトウエアを導入した。強制水泳パラダイムを用いて、総水泳距離や不動時間などのパラメーターによって表現できる抑うつ状態を定量評価し、ECSの作用を調べ始めた。また、同じ実験システムを Homer1a ノックアウトマウスに適用し、ECS 作用のうちHomer1aが媒介するのはどの部分であるか同定することを試み始めた。これらはまだ発表には至らないが端緒的成果としては有望であり、今後の一層の展開を予定している。

⑤　スライスによる分子細胞レベルの成果と行動解析の結果を有機的に統合するためには、全動物標本からニューロン活動を計測することが望ましい。このような諸レベルの研究を統合することは生理学的手法の本領でもあり、また、うつ病の病態生理を解明するためには避けることの出来ない通過点でもある。このような解析のために必要な準備としては、まず成果④として記した行動レベルの実験と成果①②③に記した分子・細胞レベルの実験があげられるが、これらだけでは大まかな対応関係が理解できるに過ぎない。両レベルの間をつなぐ実験として、全動物標本において個々の神経細胞や局所神経回路の活動を評価する実験が不可欠である。うつ病者においては、大脳皮質内における抑制機構が減退し、またこれと相容れることには抑制性神経伝達物質のGABAが濃度低下していること、そして治療的電撃けいれん（ECT）の施行によってこれが改善されることが知られており、これに基づいて「うつ病成因のGABA仮説」が提唱されている。細胞レベルの実験によって、我々はECSが細胞の興奮性を抑制することを報告しており、これは「うつ病成因のGABA仮説」を支持している。抑制の弱まることが実際に強制水泳における総移動距離短縮などの抑うつ行動につながり、また逆にECTによって抑制が強まれば抑うつ行動の改善につながることが証明できれば、病態生理の一段深い理解と、それに基づく創薬ターゲットの絞込みが可能となる。このような展望の下で、抑うつモデル動物における抑制を評価する方法の確立に努めてきた。その方法の第一は、内因性電位シグナルまたは電位感受性色素を使った回路網レベルでの抑制性評価であり、これまでに脳スライスにおいて抑制や興奮の程度を評価する方法を開発し学会報告した。第二の方法は、全動物標本から神経細胞の活動を細胞外ユニットとして記録し、活動の自己相関を解析する方法である。この場合にどのようにニューロン興奮性を評価するかについて、スパイク自己相関ソーティングと呼ぶ新規の手法を論文報告することができた　(Murata and Kato, 2007)。

７．研究の考察・反省

「うつ病成因の GABA 仮説」の証明とそれに基づく新しい創薬ターゲットの発見に向けて、一定の前進があった。この仮説の証明に至るストラテジーについては、金沢医科大雑誌に 2 編の総説として報告している通りである（加藤伸郎,2007a と b)。強制水泳を使ったモデルうつ病の作製に関しては、従来この手技に慣れ親しんでいなかったために着手が遅れた。近隣大学の研究者から手法を学ぶなどして、急速に実験装置をセットアップすることが出来た。スタンダードな実験プロトコールによる強制水泳の施行に対して再現性のある結果が得られており、実験セットアップの信頼性は確保できたと考えている。うつ病モデルにおけるＧＡＢＡ神経系の関与については、研究の進め方が確立できたが、あと２つの当面の課題であるカルシウムチャンネルの関与とシナプス抑圧の関与について未確立であるのは反省点のひとつである。反省すべきもうひとつのポイントは、主に Homer1a との関連という切り口から研究を推進した結果、BDNF 関連の研究が進展しなかったことである。しかし、行動実験の手技、回路網における抑制の評価システム、さらには遺伝子改変動物のジェノタイピングなど、Homer1a 関連の研究におけるプラットフォームは BDNF 関連の研究でも共有できるものであり、これまでの研究成果を生かして急速に進展させることが出来ると見込んでいる。このように研究内容の網羅性には問題点を残したが、研究代表者の本学着任直後にはじまった本助成により活発な研究活動のスタートと 2 年間に及ぶ維持が保証されることになった。

８．研 究 発 表

Udagawa R, Nakano M, Kato N. Blocking L-type calcium channels enhances long-term depression induced by low frequency stimulation at hippocampal CA1 synapses. Brain Res 2006; 1124: 28-36.（MLDB）

Yamamoto R, Ueta Y, Kato N.　Dopamine induces a slow afterdepolarization in lateral amygdale neurons. J Neurophysiol 2007; 98: 984-992.　（MLDB）

Murata M, Kato N. Autocorrelogram sorting: a novel method for evaluating negative-feedback　regulation of spike firing.　Brain Res 2007; 1133: 27-33.（MLDB）

加藤伸郎　電撃けいれん療法の神経生物学的基盤－うつ病成因の GABA 仮説との接点－. 金医大誌 2007a; 32: 73-81.

加藤伸郎　電撃けいれん療法の神経生物学的基盤（続編）－シナプス可塑性の関与－. 金医大誌 2007b; 32: 82-88.

Ueta Y, Yamamoto R, Sugiura S, Inokuchi K, Kato N. Homer 1a suppresses neocortex long-term depression in a cortical layer-specific manner. J Neurophysiol 2008; 99: 950-957.　（MLDB）

BRAIN RESEARCH 1124 (2006) 28–36

available at www.sciencedirect.com

ScienceDirect

www.elsevier.com/locate/brainres

BRAIN RESEARCH

Research Report

Blocking L-type calcium channels enhances long-term depression induced by low-frequency stimulation at hippocampal CA1 synapses

Rie Udagawa[a], *Makoto Nakano*[a], *Nobuo Kato*[a,b,*]

[a]*Department of Integrative Brain Science, Kyoto University Graduate School of Medicine, Kyoto 606-8501, Japan*
[b]*Department of Physiology, Kanazawa Medical University, Ishikawa 920-0293, Japan*

ARTICLE INFO

Article history:
Accepted 17 September 2006
Available online 7 November 2006

Keywords:
Long-term depression
Calcium
Rat
Hippocampus CA1
Voltage-dependent calcium channel

Abbreviations:
APV, D(−)-2-amino-5-phosphonovaleric acid
ER, endoplasmic reticulum
fEPSP, filed excitatory postsynaptic potential
LTD, long-term depression
VDCC, voltage-dependent calcium channel
mGluR, metabotropic glutamate receptor
NMDA, N-methyl-D-aspartate
NMDAR, N-methyl-D-aspartate receptor
RyR, ryanodine receptor

ABSTRACT

Specific contributions of voltage-dependent calcium channels (VDCCs) to induction of long-term depression (LTD) have not been thoroughly elucidated. The present study examined roles of T- and L-type VDCCs in N-methyl-D-aspartate (NMDA) receptor-dependent LTD induced at several different levels of synaptic activation (0.5- to 10-Hz presynaptic stimulations) at Schaffer collateral-CA1 synapses in rat hippocampal slices. Blockade of T-type VDCCs with nickel ions failed to change LTD magnitude at all levels of stimulation. However, blockade of L-type VDCCs reduced LTD in response to stimulation at 1 and 2 Hz and, conversely, enhanced LTD at a lower frequency (0.5 Hz). The enhancement of 0.5-Hz LTD under L-type VDCC blockade was shown pharmacologically to depend on NMDA receptors (NMDARs) and intracellular Ca^{2+} release. Calcium imaging revealed that contribution of L-type VDCC-mediated calcium influx to the total calcium increase was greater during 0.5-Hz stimulation than during 1.0-Hz stimulation. This finding, combined with the reported suppression of NMDARs mediated by L-type VDCCs, may be relevant to the present enhancement of 0.5-Hz LTD due to L-type VDCC blockade.

* *Corresponding author.* Department of Physiology, Kanazawa Medical University, Ishikawa 920-0293, Japan. Fax: +81 76 286 3523.
E-mail address: kato@kanazawa-med.ac.jp (N. Kato).

0006-8993/$ – see front matter © 2006 Elsevier B.V. All rights reserved.
doi:10.1016/j.brainres.2006.09.051

1. Introduction

Long-term depression (LTD) is a form of synaptic plasticity and, together with its counterpart long-term potentiation (LTP), is regarded as cellular substrate for learning and memory (Bear and Abraham, 1996; Bliss and Collingridge, 1993; Linden, 1994; Malenka and Bear, 2004; Malenka and Nicoll, 1999). It has been established that induction of LTD at hippocampus CA1 synapses requires postsynaptic calcium increases (Cummings et al., 1996; Mulkey and Malenka, 1992). A number of studies further revealed that, in addition to the quantity of Ca^{2+} that enters the postsynaptic cell upon synaptic activation, the source of Ca^{2+} can be an important determinant of the polarity of synaptic plasticity (Kato, 1993; Kato et al., 2000; Nishiyama et al., 2000; Oliet et al., 1997). We reported one of the first studies on this subject matter, which demonstrated that intracellular calcium release facilitates LTD induction in the visual cortex (Kato, 1993; Kato et al., 2000). Voltage-dependent calcium channels (VDCCs) have been investigated in the light of a specific supply source of calcium ions required for LTD (Bolshakov and Siegelbaum, 1994; Christie et al., 1997; Cummings et al., 1996). However, to our knowledge, roles of VDCCs in LTD induced by low frequency stimulation (0.5 Hz) have not been clarified to date. Recently we have reported a particular NMDAR-independent LTD induced by 0.5 Hz, suggesting that 0.5-Hz LTD may have more characteristic features that are lacking in 1.0-Hz LTD (Nakano et al., 2004). The present study therefore focused on looking for roles of VDCCs in induction of 0.5-Hz LTD.

2. Results

2.1. *Magnitude of LTD depended on stimulus frequencies*

Synaptic depression was induced at hippocampal CA1 synapses in normal ACSF using four protocols differing in stimulus frequency (a train of 900 pulses delivered to Schaffer collateral fibers at 0.5, 1, 2, or 10 Hz). A modest LTD was induced by 0.5- and 2-Hz stimulations, and a larger LTD was evoked by 1-Hz stimulation (0.5 Hz, −12.4±0.9%, n=22; 1 Hz, −19.3±0.7%, n=23; 2 Hz, −10.5±2.1%, n=13; Fig. 1). On the other hand, 10-Hz stimulation failed to induce LTD (2.1±2.8%, n=6, Fig. 1). These data that were obtained using drug-free normal medium served as the control hereafter. The frequency–response curve thus obtained (Fig. 1) supported theoretical predictions (Artola and Singer, 1993; Bienenstock et al., 1982): these theoretical considerations postulate that there are a set of upper and lower thresholds to postsynaptic activity, within which LTD can be induced. LTD induction failed with NMDARs antagonized by APV (0.5 Hz, −1.1±4.8, n=5; 1 Hz, 5.2±8.9, n=5; 2 Hz, −1.4±1.2, n=5; Fig. 1), confirming the dependence of LTD induction on NMDARs at these frequencies examined (Nakano et al., 2004; Oliet et al., 1997).

2.2. *Blockade of T-type VDCC left LTD unchanged*

Next we examined whether another major source of calcium entry, the VDCC, is involved in LTD induction over the whole range of stimulation frequency that we tested. Although LTD induction is generally known to require activation of T- and L-type VDCCs (Christie et al., 1997), LTD induced by 0.5 Hz has not been examined in this light to date. We first bath-applied nickel ions at a concentration that exclusively blocks T-type VDCCs (50 μM; Avery and Johnston, 1996; Fox et al., 1987). Application of Ni^{2+} had no effect on the magnitude of LTD evoked by any of the stimuli we used (0.5Hz, −13.7±3.2%, n=6; 1 Hz, −18.0±1.8%, n=5; 2 Hz, −12.5±3.0%, n=6; Figs. 2A–C, E). These results suggest that T-type VDCCs do not contribute to LTD induction. Application of Ni^{2+} was shown to suppress the transient component of low threshold VDCC currents: the net suppression (−22.2±8.1pA at the peak, n=3) was approximately to the same extent as reported by other groups (Avery and Johnston, 1997; Su et al., 2002).

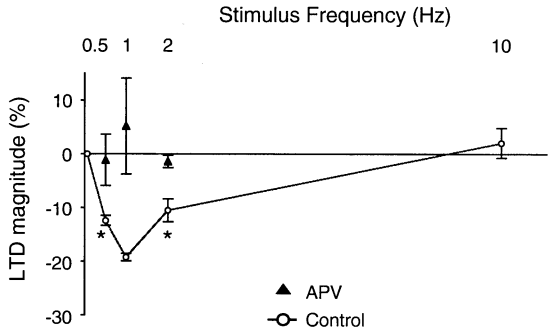

Fig. 1 – Frequency–response function of LTD at hippocampal CA1 synapses. LTD magnitude varied depending on stimulus frequency (Control: 0.5 Hz, n=22; 1 Hz, n=23; 2 Hz, n=13; 10 Hz, n=6). LTD induced by 0.5-, 1-, and 2-Hz stimulation required NMDA receptor activation (APV: 0.5 Hz, n=5; 1 Hz, n=5; 2 Hz, n=5). Each data point represents mean±SEM. The asterisk indicates significant difference (P<0.05) from LTD magnitude evoked by 1-Hz stimulation. The plot is based on data pools that contained observations reported previously (Nakano et al., 2004) in addition to the present data.

The present results disagree with the previous study about the effect on LTD induced by 1- and 2-Hz stimulations (Christie et al., 1997; Wang et al., 1997). One possibility is that the stimuli used in the present study may have been relatively strong. Such strong stimuli would allow high threshold VDCCs to participate in intracellular calcium increases during the LTD induction protocol to a greater extent, thereby reducing the relative contribution of T-type VDCCs.

2.3. *Blockade of L-type VDCC enhanced LTD induced by 0.5-Hz stimulation*

We then tried blocking L-type VDCC by the antagonist nifedipine. Neither with 1- nor 2-Hz stimulation, did nifedipine modify LTD magnitude (1 Hz, 19.1±1.2%, n=9, Fig. 3B; 2 Hz, 13.2±1.1, n=5, Figs. 3A,C). These results were in agreement with the previous reports (Oliet et al., 1997). With 0.5-Hz stimulation, however, LTD was significantly enhanced (P<0.05): nifedipine (−22.7±3.7%, n=6) vs. control (−12.4±0.9%, n=22). Since we encountered a report that nifedipine facilitates presynaptic release (Hirasawa and Pittman, 2003), we attempted to exclude the possibility that the present

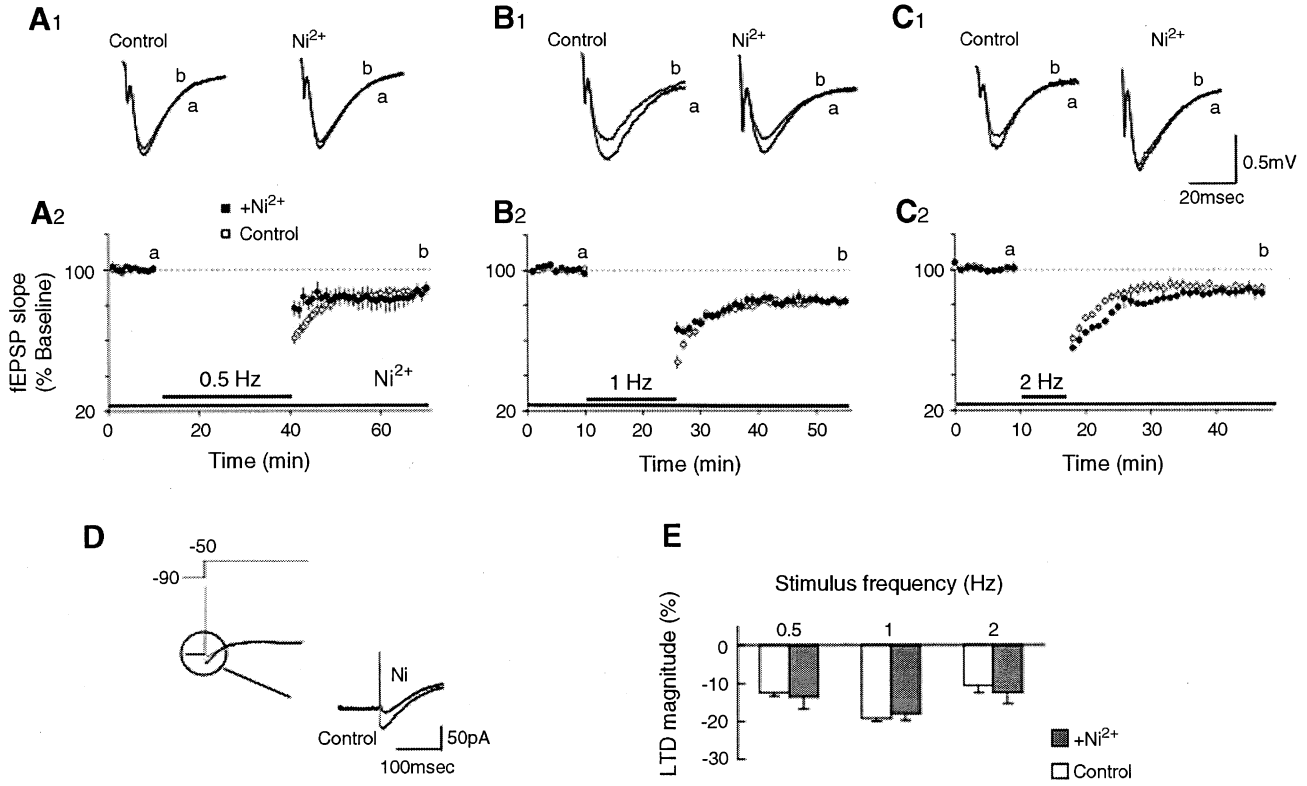

Fig. 2 – Magnitude of LTD under blockade of T-type VDCCs. $A_{1,2}$, $B_{1,2}$, $C_{1,2}$, Changes of fEPSP slope after low-frequency stimulations. LTD is induced in the presence of nickel ions (50 μM) by stimulation at 0.5 Hz ($A_{1,2}$), 1 Hz ($B_{1,2}$), or 2 Hz ($C_{1,2}$). The duration of Ni^{2+} application and that of induction stimulus are indicated by the horizontal bars (A_2, B_2, C_2). Representative fEPSP traces (A_1, B_1, C_1) are obtained at the time points indicated in A_2, B_2, and C_2. Each data point (mean ± SEM) represents an average of four consecutive traces measured in normal medium (○) or in medium containing Ni^{2+} (●). (D) Voltage-clamp recording showing blockade of low threshold VDCC current by Ni^{2+}: top, voltage command; middle and bottom, representative current traces shown in two scales. (E) Summary diagram for LTD magnitudes obtained from experiments shown in A_1, B_1, and C_1.

nifedipine-induced enhancement of LTD in response to 0.5-Hz stimulation is due to its presynaptic action. For this purpose, we utilized another L-type VDCC blocker nimodipine, which has not been reported to have presynaptic action. Blockade of L-type VDCC by nimodipine, as well as that by nifedipine, increased the magnitude of LTD evoked by 0.5-Hz stimulation (nimodipine, −23.9±2.0%, n=7; Fig. 4A) and left 2-Hz LTD unchanged (−7.3±3.7%, n=9; Fig. 4C). Moreover, LTD induced by 10-Hz stimulation was also unaffected (control, 2.1±2.8%, n=6; nimodipine, 1.6±3.5%, n=4; Figs. 4D). However, with 1-Hz simulation only, results were conflicting (nifedipine, 1 Hz, 19.1±1.2%, n=9, Fig. 3B; nimodipine, 1Hz, −3.0± 2.8%, n=7, Fig. 4B): nimodipine but not nifedipine suppressed LTD induction at 1 Hz. This discrepancy might be attributed to the reported presynaptic action of nifedipine (Hirasawa and Pittman, 2003), though decisive explanation has yet to be looked for. At the very least, however, the enhancement of LTD at 0.5 Hz was observed both in nifedipine- and nimodipine-containing media, supporting the conclusion that this enhancement of LTD is attributed to blockade of L-type VDCCs.

If blockade of L-type VDCCs enhanced 0.5-Hz LTD, their facilitation should then suppress 0.5-Hz LTD. To test this assumption, the L-type VDCC activator Bay-K8644 (10 μM) was applied and LTD was attempted. Qualitatively, 0.5-Hz LTD tended to be decreased in magnitude by application of BayK-8644 (control, 0.5 Hz, −12.4±0.9%, n=22; Bay-K8644, 0.5 Hz, −8.2±6.8, n=5; Fig. 5). Though the difference was not significant, the activator Bay-K8644 indeed showed tendency opposite to that of the blockers of L-type VDCCs.

2.4. *Involvement of NMDARs and internal Ca^{2+} release to the enhancement of LTD induced by L-type VDCC blockade*

We showed that another type of enhancement of 0.5-Hz LTD under caffeine application, in which calcium release is crucially involved but NMDARs are unnecessary (Nakano et al., 2004). We have now tested involvement of calcium release and NMDARs in the present enhancement of 0.5-Hz LTD induced by blockade of L-type VDCCs. First, we applied the calcium store depletor thapsigargin (5 μM) in addition to nimodipine, and delivered 0.5-Hz stimulation. This treatment significantly reduced LTD magnitude: nimodipine and thapsigargin (−10.4±4.7%, n=6) vs. nimodipine alone (−23.9± 2.0%, n=7; Fig. 6A). Nifedipine, another blocker that may have presynaptic action, also significantly reduced LTD magnitude: nifedipine and thapsigargin (−12.7±1.8%, n=6) vs. nifedipine

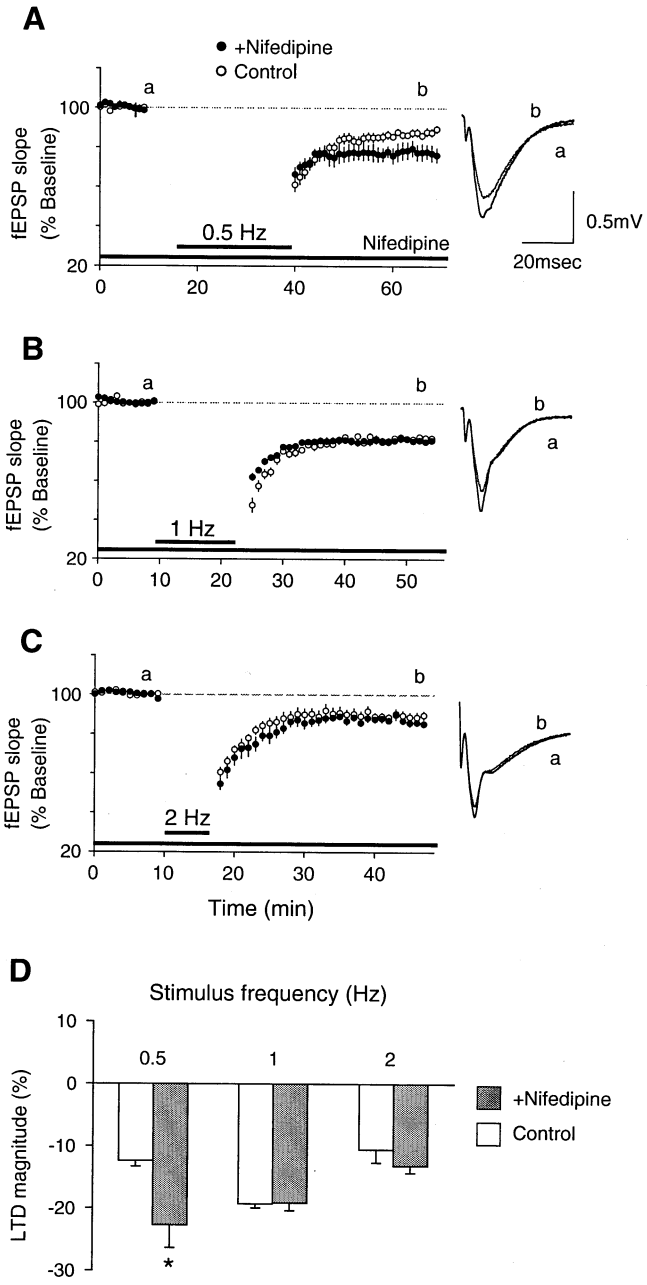

Fig. 3 – Enhancement of 0.5-Hz LTD under blockade of L-type VDCCs. (A, B, C) Time course of fEPSP slope before and after 0.5-Hz (A), 1-Hz (B) and 2-Hz stimulation (C). Insets, representative fEPSP traces obtained from nifedipine-treated slices at time points indicated alphabetically. (D) Summary diagram for LTD magnitudes obtained from experiments shown in panels A–C. The asterisk indicates significant change as compared with control. Nifedipine application (10 μM) enhanced LTD magnitude evoked by 0.5-Hz stimulation (A, D). Induction of 1.0-Hz LTD was unaffected (B, D). Magnitude of LTD evoked by 2-Hz stimulation was similarly modest with or without nifedipine (C, D).

alone (−22.7±3.6%, n=6; Fig. 6B). Application of thapsigargin alone did not significantly alter 0.5-Hz LTD: thapsigargin alone (−5.9±6.1%, n=5) vs. control (−12.4±0.9%, n=22, Fig. 6D).

Secondly, effects of NMDAR blockade were examined. Nimodipine and the NMDAR blocker APV were co-applied, and LTD induction was attempted at 0.5 Hz. Under this condition, LTD induction failed: nimodipine and APV (−4.2± 2.4%, n=3) vs. nimodipine alone (−23.9±2.0%, n=7; Fig. 6C). The enhancement of 0.5-Hz LTD induced by blockade of L-type VDCCs was thus shown to depend on NMDAR activation, which is in contrast with the caffeine-induced enhancement of 0.5-Hz LTD (Nakano et al., 2004). In our previous report (Nakano et al., 2004), the caffeine-induced enhancement, which is NMDAR-independent, was interpreted as a supplementary LTD induction mechanism that would become in operation in case NMDARs functioning failed. The present enhancement was NMDAR-dependent and, therefore, a totally different role should be assigned. Thus, the enhancement of 0.5-Hz LTD by L-type VDCC blockade was shown to depend both on calcium release and NMDARs.

2.5. *Calcium fluorimetry during spike trains at 0.5-Hz stimulation*

To better understand why 0.5-Hz LTD, but not 1-Hz LTD, is enhanced by blockade of L-type VDCCs, we measured calcium increases during spike trains of these two frequencies with or without L-type VDCC blockade by nifedipine. Average calcium increases during the 1-Hz train were 0.135±0.008 (n=11) in the unit of $-\Delta F_{380}/F_{360}$ in control medium, and was 0.113±0.011 (n=12) in nifedipine-containing medium, which were not significantly different. During the 0.5-Hz train, by contrast, the average increase was 0.080±0.006 (n=11) in control medium, and was significantly larger than that induced in nifedipine-containing medium (0.061±0.007; n=12; P<0.02).

Thus, it was at least shown that the VDCC blockade affects spike-induced calcium increases at the 0.5-Hz but not 1-Hz train, with the other experimental conditions completely the same. The calcium increase we measured here was spike-induced calcium rise, and was therefore attributable to calcium channels, but not to NMDA receptors. Also, our calcium fluorimetry set-up is not as sensitive as to detect synaptically driven calcium increases, suggesting that spike-induced calcium rise is considerably larger than synaptically driven calcium rise (Isomura and Kato, 1999). Since the stimulus intensity we used for the present LTD induction was well above the threshold for population spikes, the majority of calcium increases during the present LTD protocol are thought to stem from calcium channel-mediated calcium entry. Therefore, it is presumed that spike-induced calcium increase measured here may well provide a sufficiently reliable approximation of calcium increases during LTD induction. We have thus suggested that L-type VDCC blockade affects calcium increases differentially during 0.5-Hz and 1-Hz stimulation, which might be relevant to the frequency-specific enhancement of LTD.

3. Discussion

VDCCs have been reported to be critically involved in the hippocampal CA1 LTD (Bolshakov and Siegelbaum, 1994; Christie et al., 1997; Cummings et al., 1996). In the present

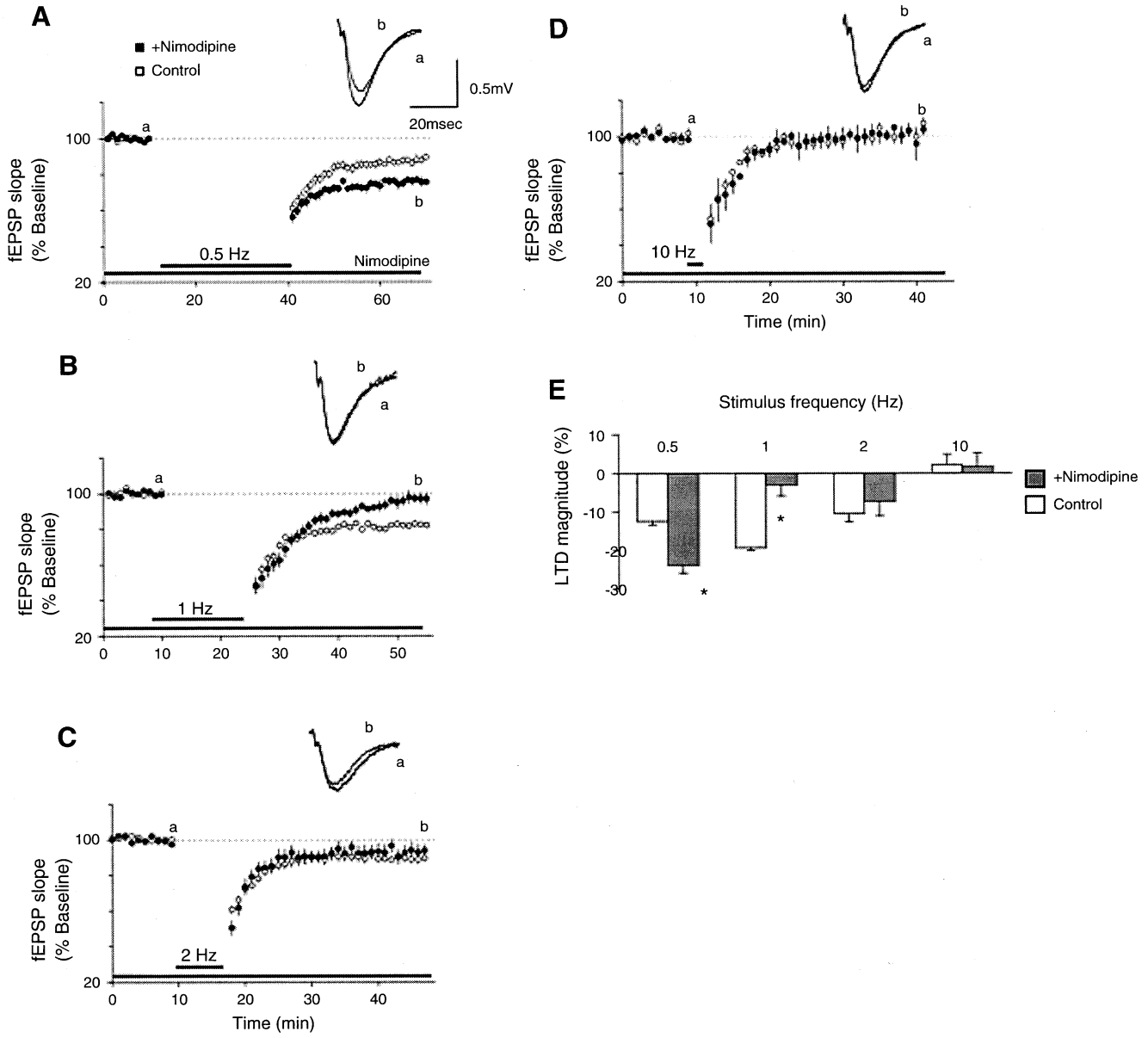

Fig. 4 – Reevaluation of enhanced 0.5-Hz LTD with another blocker of L-type VDCCs. (A) In the presence of an L-type VDCC antagonist, nimodipine (20 μM), LTD magnitude in response to 0.5-Hz stimulation was enhanced. Inset, representative fEPSP traces obtained from nimodipine-treated slices at the indicated points of time, and the same is applicable to the following diagrams as well. (B–D) Nimodipine application prevented 1-Hz LTD (B). LTD induction with 2- (C) or 10-Hz stimulation (D) was not significantly affected by nimodipine. (E) Summary diagram for LTD magnitudes obtained from experiments shown in panels A–D. The asterisks indicate significant change as compared with control.

report, we attempted to induce the CA1 LTD at different synaptic activation levels under VDCC blockade. Three stimulation frequencies were chosen so that the postsynaptic activation range could cover the theoretically predicted window within which LTD is induced (Bienenstock et al., 1982; Dudek and Bear, 1992). The results suggest that T-type VDCCs contribute little to LTD induction throughout the theoretical LTD window, and that blockade of L-type VDCC enhanced the magnitude of 0.5-Hz LTD.

There have been reports that T-type VDCCs are required for LTD induction in the hippocampus (Magee et al., 1995; Christie et al., 1997; Oliet et al., 1997). However, the present observation and another report (Sui et al., 2000) suggest that involvement of T-type VDCC was not necessary. Moreover, the same authors (Oliet et al., 1997) claimed that metabotropic glutamate receptor (mGluR)-dependent LTD is also dependent on T-type VDCCs, whereas NMDAR-dependent LTD is not. This discrepancy might be due to possible variety in stimulation strength adopted in different experiments. Synaptic potentials most likely activate T-type VDCCs only, whereas, during action potential trains, R-type and L-type VDCCs should participate as well. In particular, NMDAR blockade, but not mGluR blockade, may reduce amplitude of synaptic potentials so much as to preclude activation of high threshold VDCCs. Also if

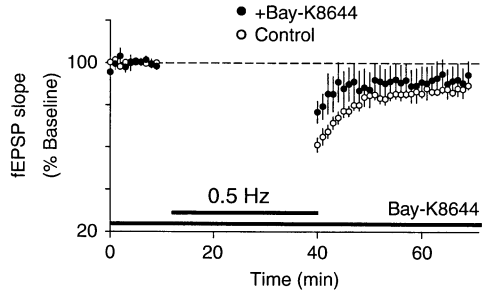

Fig. 5 – Effect of the L-type VDCC agonist Bay-K8644 on 0.5-Hz LTD. Time course of the fEPSP slope is plotted with (Bay-K8644) or without the drug (Control).

postsynaptic neurons are activated strongly and repetitively, inactivation of the T-type VDCC would be prolonged, which would further decrease relative contribution of T-type VDCCs during LTD induction.

In agreement with the previous report (Bolshakov and Siegelbaum, 1994; Christie et al., 1997), the present experiments suggested that LTD induced by 1-Hz stimulation depended on L-type VDCCs, on condition that the present nifedipine data largely represented its presynaptic action. However, there has been a report that T-type but not L-type VDCCs are required for dentate gyrus LTD (Wang et al., 1997). The reason for this discrepancy may be again due to difference in the relative contribution to calcium entry between T-type and L-type VDCCs. In their stimulation paradigm (Wang et al., 1997), calcium entry through T-type VDCC may predominate over entry through L-type VDCCs.

Among the present findings on involvement of VDCCs in LTD induction, the most interesting is that blockade of L-type VDCCs enhanced 0.5-Hz LTD. The present enhancement depended both on calcium release and NMDARs. L-type VDCCs is well known to undergo calcium-dependent inactivation with the calcium ions that the channels themselves let through (Hille, 2001). Molecular mechanisms for this inactivation have been partly elucidated (Cens et al., 2006). As for down-regulation of NMDARs, another class of calcium channels, Ca^{2+} influx through L-type VDCCs is suggested to suppress NMDARs (Froemke et al., 2005). Blockade of L-type VDCCs might then prevent such calcium-dependent suppression of NMDARs, thereby enhancing LTD at the low postsynaptic activation range. In support of this interpretation, enhancement of 0.5-Hz LTD has been observed in slices obtained from dark-reared rats, which is likely due to experience-dependent increase in NMDAR functioning (Philpot et al., 2003).

The present enhancement of 0.5-Hz LTD depended also on calcium release. If NMDARs escaped from calcium-dependent down-regulation by blockade of L-type VDCCs (Froemke et al., 2005) as discussed above, calcium entering through NMDARs might cause a more robust Ca^{2+}-induced Ca^{2+} release, which may play a role similar to upregulation of ryanodine receptors in our previous caffeine-induced enhancement of 0.5-Hz LTD (Nakano et al., 2004). Based on the present calcium fluorimetry, we may be able to propose another interpretation. The fluorimetry data indicated that contribution of Ca^{2+} influx to the total Ca^{2+} increases is greater during 0.5-Hz stimulation than during 1.0-Hz stimulation. In other words, this suggests that a lesser contribution of other Ca^{2+} sources, most notably Ca^{2+} release from the store, during 0.5-Hz stimulation. If the balance between Ca^{2+} release and Ca^{2+} influx were in order during 1-Hz stimulation, by which LTD could be induced in normal medium, such a delicate balance may be disrupted during 0.5-Hz stimulation and Ca^{2+} influx may predominate over Ca^{2+} release. Blockade of calcium channels might serve to rectify this imbalance. In fact, the present enhancement of 0.5-Hz LTD was disputed by reducing Ca^{2+} release with thapsigargin treatment. In this latter finding, thapsigargin may have restored the predominance of Ca^{2+} influx, so that the delicate balance may be disrupted again.

In summary, the present study revealed a unique role of L-type VDCCs, by which 0.5-Hz LTD was interfered. We have so far shown that L-type VDCCs are developmentally (Isomura and Kato, 1999; Norris et al., 1998) and activity dependently regulated (Yamamoto et al., 2005), and their activation are correlated intimately with fine-tuning of synaptic plasticity and neural excitability. Taken together, L-type VDCCs might be involved in neural regulation at a scale larger than hitherto imagined.

4. Experimental procedures

4.1. *Slice preparation*

All experiments were performed in accordance with the guiding principle of the Physiological Society of Japan and with the approval of the Animal Care Committee of Kyoto University Graduate School of Medicine. Slices were prepared from Wistar rats (18–24 days old, males and females) as previously described (Isomura and Kato, 1999). In brief, rats were anesthetized with ether and decapitated. Hippocampi were dissected out in cold artificial cerebrospinal fluid (ACSF) containing (in mM) NaCl, 124; KCl, 3.0; $CaCl_2$, 2.0; $MgSO_4$, 2.0; NaH_2PO_4, 1.3; $NaHCO_3$, 26; and glucose 10–20 saturated with 95% O_2, 5% CO_2. Slices were made transversely (400 μm thick) with a slicer (D.S.K. EM Co., Ltd., Kyoto, Japan). Slices were allowed to recover for at least 60 min in ACSF that was maintained at 30 °C.

4.2. *Electrophysiology*

Individual slices were transferred to a submerge-type recording chamber and were continuously perfused with 30 °C ACSF saturated with 95% O_2, 5% CO_2. Field excitatory postsynaptic potentials (fEPSPs) were recorded from the stratum radiatum of the CA1 region with glass microelectrodes (1–3 MΩ) containing ACSF. fEPSPs were evoked by electrical stimulation on Schaffer collateral fibers with a pair of tungsten wires. Test stimuli were delivered at 0.067 Hz with stimulus intensity that evoked 30–40% of the maximal fEPSP. The stratum radiatum and Schaffer collateral fibers were visually identified under an upright microscope (Axioskop, Zeiss, Germany). To induce LTD, a train of 900 pulses were continuously given to Schaffer

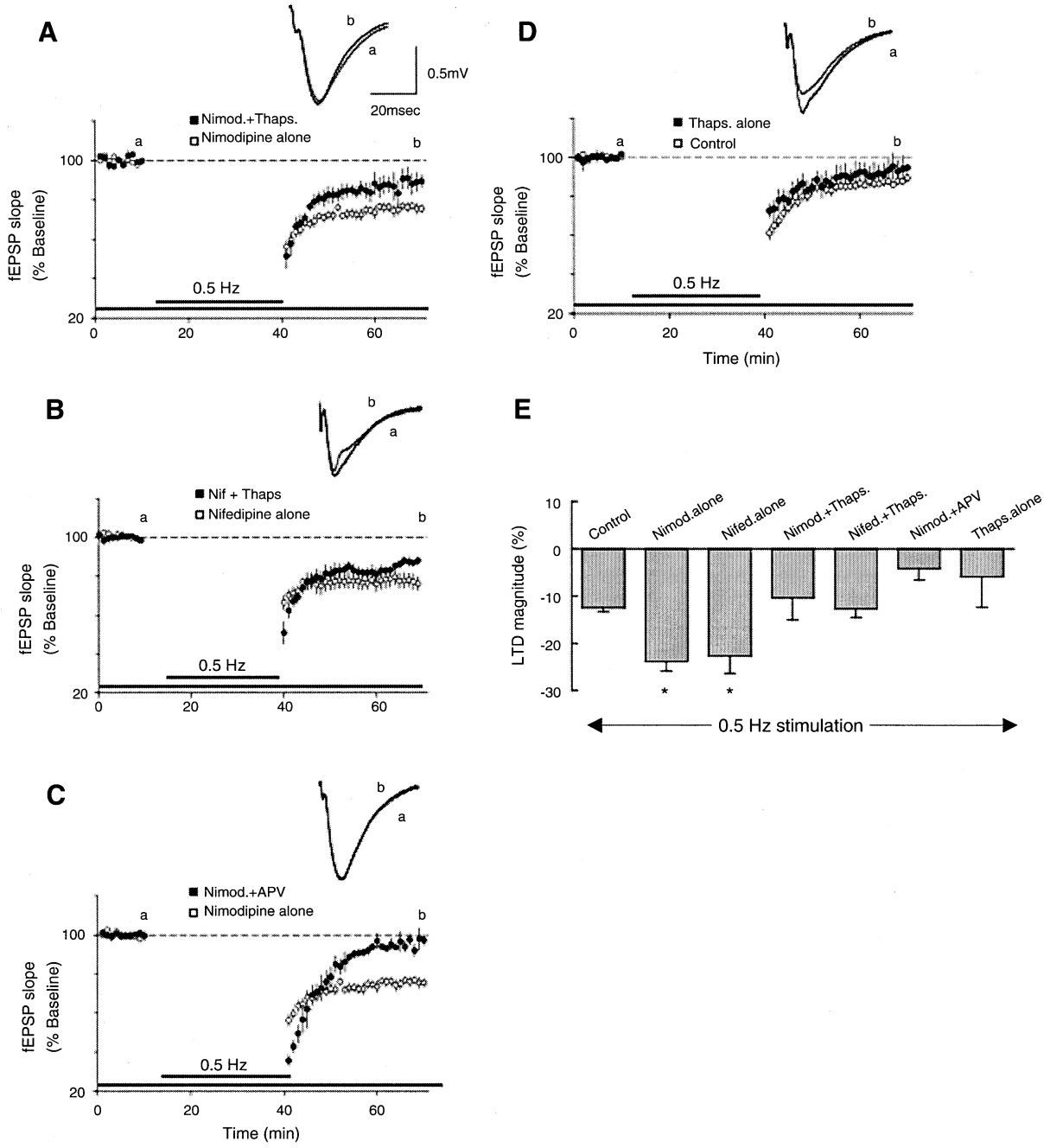

Fig. 6 – Dependence of the enhanced 0.5-Hz LTD on NMDAR blockade and Ca^{2+} store depletion. (A) Effect of co-application of the calcium store depletor thapsigargin (5 μM) and nimodipine (20 μM). LTD was smaller than evoked in the presence of nimodipine alone. Insets, fEPSP traces under the dual drug treatment, obtained at the indicated time points, and this is applicable to the following diagrams as well. (B) Effect of co-application of nifedipine and thapsigargin. LTD was again smaller than was evoked with nifedipine alone. (C) Co-application of nimodipine (20 μM) and APV (50 μM) prevented LTD induction. (D) Thapsigargin alone (•) did not significantly alter LTD magnitude (○; Control). (E) Summary diagram showing the effects of various drugs on 0.5-Hz LTD. The asterisks indicate significant enhancement of LTD.

collateral fibers at 0.5, 1.0, 2.0, or 10.0 Hz depending on the purpose of the experiment. The induction stimulus was delivered after fEPSPs had reached their stabilization (usually in 30–60 min).

For calcium current measurement, whole-cell recording was attempted in ACSF with Ca^{2+} concentration elevated to 5 mM to improve sealing (Fox et al., 1987; Hamill et al., 1981). After sealing, the medium was gradually replaced with ACSF containing (in mM) NaCl, 100; KCl, 3.0; 4-aminopyridine, 0.5; $CaCl_2$, 2.5; $MgCl_2$, 1.5; $NaHCO_3$, 26; tetraethylammonium chloride, 20; tetrodotoxin 0.001; and glucose 10 saturated with 95% O_2, 5% CO_2. Also, nimodipine (20 μM) was added to block L-type VDCC current. Glass pipettes (3–6 MΩ) contained (in mM) cesium chloride, 130; tetraethylammonium chloride,

10; EGTA, 0.5; 5′-ATP Na_2, 2; GTP-Na_2, 0.1; $MgCl_2$, 2.0; HEPES, 10; QX314, 5. With cesium hydroxide, pH was adjusted to 7.35. T-type calcium current was evoked by a step depolarization from a −90 mV (holding potential) to −50 mV for 300 ms. The initial transient component of the current was measured at the peak with and without Ni^{2+} extracellularly applied.

4.3. *Calcium imaging*

Calcium imaging with the calcium indicator fura-2 were performed as previously descried (Isomura and Kato, 1999). Briefly, by using the RatioVision and RatioArc imaging systems (Attofluor, Maryland, USA), fura-2 was excited by 360 or 380 nm illuminations and images with 380 nm excitation were recorded at the video-rate (30 Hz). The fluorescence images were captured by an intensified charge-coupled device (I-CCD) camera placed on an upright microscope (Axioskop FS, Zeiss, Germany) with a 63× water immersion objective. To estimate absolute changes of the calcium concentration, we defined $-\Delta F_{380}/F_{360}$ as the index, in which F_{360} is the 360 nm excited fluorescence intensity at the beginning of each trial, and ΔF_{380} is the difference between the 380 nm excited fluorescence intensity (F_{380}) at the resting state and the fluorescence intensity at a given time during repetitive stimulation (15 pulses at 0.5 or 1.0 Hz). Positive values of this index reflect the level of increase in concentration of free calcium ions.

4.4. *Drugs used*

The following drugs were bath applied at concentrations as indicated; D-2-amino-5-phosphonovaleric acid (APV; 50 μM, Sigma, St. Louis, USA), thapsigargin (5 μM, Alomone Laboratories, Jerusalem, Israel), nickel chloride (50 μM, Nakalai, Kyoto, Japan), nifedipine (10 μM, Nakalai), nimodipine (20 μM, Nakalai) and Bay-K8644 (10 μM, Sigma). Bath application of these drugs started 30–40 min prior to LTD induction and continued throughout the recording period. Treating slices with the drugs did not significantly change baseline synaptic transmission. For control purposes, we checked stability of recording during application of some of the blockers. The baseline fEPSP slope during a 10-min period within 50–80 min after the application, as expressed in percent of the slope averaged over the initial 10-min period after the application, was as follows: Ni^{2+}, 101.9±0.1%, $n=3$; nimodipine, 97.6±3.5%, $n=4$. Baseline drifts due to the drug application itself were largely negligible.

4.5. *Data analysis*

All data were collected with an amplifier (Axoclamp-2A, Axon Instruments, Foster City, CA), filtered at 5 kHz and digitized at 10 kHz with an A/D converter (Digi Data 1200 Series, Axon Instruments). The recording and analysis of the digitized data were performed with pClamp7 (Axon Instruments). Initial slopes of the fEPSPs were measured as the percentage change from the baseline level, where baseline was calculated as the average of fEPSP slopes during the last 10 min of the pre-conditioning period. Four consecutive fEPSP slopes were averaged to represent each data point. The data presented as LTD magnitude in the text and figures were averages of fEPSP slopes over a 5-min period (26 to 30 post-conditioning). Data were statistically analyzed by using paired or unpaired *t*-tests with the significance level set at $P<0.05$. Data were excluded from analysis when the average fiber volley amplitude during the 10-min pre-stimulus period changed by more than ±10% in the 5-min post-stimulus period.

Acknowledgments

We thank Professor K. Kawano for support, Drs. K. Yamamoto, N. Inaba, I. Kanchiku and H. Takechi for helpful advice, and Ms. M. Kano for improving the language. This work was supported partly by a Grant for Collaborative Research (C2006-5) from Kanazawa Medical University.

REFERENCES

Artola, A., Singer, W., 1993. Long-term depression of excitatory synaptic transmission and its relationship to long-term potentiation. Trends Neurosci. 16, 480–487.

Avery, R.B., Johnston, D., 1996. Multiple channel types contribute to the low-voltage-activated calcium current in hippocampal CA3 pyramidal neurons. J. Neurosci. 16, 5567–5582.

Avery, R.B., Johnston, D., 1997. Ca^{2+} channel antagonist U-92032 inhibits both T-type Ca^{2+} channels and Na^{+} channels in hippocampal CA1 pyramidal neurons. J. Neurophysiol. 77, 1023–1028.

Bear, M.F., Abraham, W.C., 1996. Long-term depression in hippocampus. Annu. Rev. Neurosci. 19, 437–462.

Bienenstock, E.L., Cooper, L.N., Munro, P.W., 1982. Theory for the development of neuron selectivity: orientation specificity and binocular interaction in visual cortex. J. Neurosci. 2, 32–48.

Bliss, T.V., Collingridge, G.L., 1993. A synaptic model of memory: long-term potentiation in the hippocampus. Nature. 361, 31–39.

Bolshakov, V.Y., Siegelbaum, S.A., 1994. Postsynaptic induction and presynaptic expression of hippocampal long-term depression. Science 264, 1148–1152.

Cens, L., Rousset, M., Leyris, J.P., Fesquet, P., Charnet, P., 2006. Voltage- and calcium-dependent inactivation in high voltage-gated Ca(2+) channels. Prog. Biophys. Mol. Biol. 90, 104–117.

Christie, B.R., Schexnayder, L.K., Johnston, D., 1997. Contribution of voltage-gated Ca^{2+} channels to homosynaptic long-term depression in the CA1 region in vitro. J. Neurophysiol. 77, 1651–1655.

Cummings, J.A., Mulkey, R.M., Nicoll, R.A., Malenka, R.C., 1996. Ca^{2+} signaling requirements for long-term depression in the hippocampus. Neuron 16, 825–833.

Dudek, S.M., Bear, M.F., 1992. Homosynaptic long-term depression in area CA1 of hippocampus and effects of N-methyl-D-aspartate receptor blockade. Proc. Natl. Acad. Sci. U. S. A. 89, 4363–4367.

Fox, A.P., Nowycky, M.C., Tsien, R.W., 1987. Kinetic and pharmacological properties distinguishing three types of calcium currents in chick sensory neurones. J. Physiol. 394, 149–172.

Froemke, R.C., Poo, M.M., Dan, Y., 2005. Spike-timing-dependent synaptic plasticity depends on dendritic location. Nature 434, 221–225.

Hille, B., 2001. Ion channels of excitable membranes, 3rd ed. Sinauer, Sunderland, MA, pp. 124–126.

Hirasawa, M., Pittman, Q.J., 2003. Nifedipine facilitates neurotransmitter release independently of calcium channels. Proc. Natl. Acad Sci. U. S. A. 100, 6139–6144.

Isomura, Y., Kato, N., 1999. Action potential-induced dendritic calcium dynamics correlated with synaptic plasticity in developing hippocampal pyramidal cells. J. Neurophysiol. 82, 1993–1999.

Kato, N., 1993. Dependence of long-term depression on postsynaptic metabotropic glutamate receptors in visual cortex. Proc. Natl. Acad Sci. U. S. A. 90, 3650–3654.

Kato, N., Isomura, Y., Tanaka, T., 2000. Intracellular calcium releases facilitate induction of long-term depression. Neuropharmacology 39, 1107–1110.

Linden, D.J., 1994. Long-term synaptic depression in the mammalian brain. Neuron 12, 457–472.

Magee, J.C., Christofi, G., Miyakawa, H., Christie, B., Lasser-Ross, N., Johnston, D., 1995. Subthreshold synaptic activation of voltage-gated Ca^{2+} channels mediates a localized Ca^{2+} influx into the dendrites of hippocampal pyramidal neurons. J. Neurophysiol. 74, 1335–1342.

Malenka, R.C., Bear, M.F., 2004. LTP and LTD: an embarrassment of riches. Neuron 44, 5–21.

Malenka, R.C., Nicoll, R.A., 1999. Long-term potentiation—A decade of progress? Science 285, 1870–1874.

Mulkey, R.M., Malenka, R.C., 1992. Mechanisms underlying induction of homosynaptic long-term depression in area CA1 of the hippocampus. Neuron 9, 967–975.

Nakano, M., Yamada, S., Udagawa, R., Kato, N., 2004. Frequency-dependent requirement for calcium store-operated mechanisms in induction of homosynaptic long-term depression at hippocampus CA1 synapses. Eur. J. Neurosci. 19, 2881–2887.

Nishiyama, M., Hong, K., Mikoshiba, K., Poo, M.M., Kato, K., 2000. Calcium stores regulate the polarity and input specificity of synaptic modification. Nature 408, 584–588.

Norris, C.M., Halpain, S., Foster, T.C., 1998. Reversal of age-related alterations in synaptic plasticity by blockade of L-type Ca^{2+} channels. J. Neurosci. 18, 3171–3179.

Oliet, S.H., Malenka, R.C., Nicoll, R.A., 1997. Two distinct forms of long-term depression coexist in CA1 hippocampal pyramidal cells. Neuron 18, 969–982.

Philpot, B.D., Espinosa, J.S., Bear, M.F., 2003. Evidence for altered NMDA receptor function as a basis for metaplasticity in visual cortex. J. Neurosci. 23, 5583–5588.

Su, H., Sochivko, D., Becker, A., Chen, J., Jiang, Y., Yaari, Y., Beck, H., 2002. Upregulation of a T-type Ca^{2+} channel causes a long-lasting modification of neuronal firing mode after status epilepticus. J. Neurosci. 22, 3645–3655.

Sui, L., Ruan, D.Y., Ge, S.Y., Meng, X.M., 2000. Two components of long-term depression are impaired by chronic lead exposure in area CA1 and dentate gyrus of rat hippocampus in vitro. Neurotoxicol. Teratol. 22, 741–749.

Wang, Y., Rowan, M.J., Anwyl, R., 1997. Induction of LTD in the dentate gyrus in vitro is NMDA receptor independent, but dependent on Ca^{2+} influx via low-voltage-activated Ca^{2+} channels and release of Ca^{2+} from intracellular stores. J. Neurophysiol. 77, 812–825.

Yamamoto, K., Sakagami, Y., Sugiura, S., Inokuchi, K., Shimohama, S., Kato, N., 2005. Homer 1a enhances spike-induced calcium influx via L-type calcium channels in neocortex pyramidal cells. Eur. J. Neurosci. 22, 1338–1348.

J Neurophysiol 98: 984–992, 2007.
First published June 6, 2007; doi:10.1152/jn.00204.2007.

Dopamine Induces a Slow Afterdepolarization in Lateral Amygdala Neurons

Ryo Yamamoto,[1,2] Yoshifumi Ueta,[1,2] and Nobuo Kato[1]

[1]*Department of Physiology, Kanazawa Medical University, Ishikawa; and* [2]*Department of Integrative Brain Science, Kyoto University Graduate School of Medicine, Kyoto, Japan*

Submitted 26 February 2007; accepted in final form 1 June 2007

Yamamoto R, Ueta Y, Kato N. Dopamine induces a slow afterdepolarization in lateral amygdala neurons. *J Neurophysiol* 98: 984–992, 2007. First published June 6, 2007; doi:10.1152/jn.00204.2007. The amygdala and dopaminergic innervation thereunto are considered to cooperatively regulate emotional states and behaviors. The present experiments examined effects of dopamine on lateral amygdala (LA) neuron excitability by whole cell recordings. Bath application of dopamine induced slow afterdepolarization (sADP). This sADP lasted for >5 s, and its magnitude varied in a concentration-dependent manner. Co-application of the D1 receptor antagonist SKF83566 reduced its amplitude. The D1 receptor agonist SKF38393, applied alone, induced sADP of a smaller amplitude. Induction of the full sADP required 5-HT_2 and noradrenalin α_1 receptor activation as well. D2 receptor activation or blockade did not affect sADP induction. The calcium channel blocker cadmium or intracellular calcium chelator bis-(*o*-aminophenoxy)-*N,N,N′,N′* tetraacetic acid (BAPTA) blocked induction of the sADP, which was suggested to be triggered by calcium influx. Under voltage clamp, membrane conductance decreased at the peak of sADP current (I_{sADP}). I_{sADP} was suppressed by cesium included in pipettes. The *I-V* curve of the net I_{sADP} was shifted as the external concentration of potassium was raised, and the reversal potential was identical to that of potassium, suggesting that dopamine decreases potassium conductance to induce the sADP. The present sADP may serve as a positive-feedback regulator of excitability in LA neurons.

INTRODUCTION

The amygdala plays significant roles in affective learning (Fenselow and Gale 2003; LeDoux 2000; Maren and Quirk 2004). A moderate dopaminergic innervation onto the amygdala has been well known (Asan 1997, 1998). The cooperative activity of amygdala neurons and dopaminergic input thereunto is important to acquire fear memory and to express affective responses appropriately. This is revealed by studies done with systemic administration of dopamine (DA) receptor antagonists (Rosenkranz and Grace 2002) and their direct injection into the lateral amygdala (Greba and Kokkinidis 2000; Greba et al. 2001; Lamont and Kokkinidis 1998; Nader and Ledoux 1999). It was also reported that, in affective learning and memory retrieval, the concentration of dopamine in the lateral amygdala (LA) is raised (Harmer and Phillips 1999; Inglis and Moghaddam 1999; Yokoyama et al. 2005). These results suggest pivotal roles played by dopamine in regulating the neuronal activity in the amygdala. In fact, it has been reported that dopamine enhances excitatory transmission (Pickel et al. 2006), suppresses inhibitory transmission (Bissiere et al. 2003; Rosenkranz and Grace 1999, 2001), and alters the activity of interneurons (Kroner et al. 2005; Marowsky et al. 2005).

With all these reports, direct effects of dopamine on the LA principal neurons have not been elucidated extensively. Although a recent report has shown that dopamine enhances membrane excitability of LA neurons by inhibiting D-type potassium current (Kroner et al. 2005), it would be unlikely that this provides the sole mechanism by which dopamine regulates excitability of LA principal neurons given that effects of dopamine on various other ion channels have been reported in the cortex (Gorelova and Yang 2000; Seamans and Yang 2004; Yang and Seamans 1996; Young and Yang 2004).

Spike afterpotentials, consisting of afterhyperpolarization and -depolarization (AHP and ADP), result from spike-induced changes in ion channel conductance (Constanti and Bagetta 1991; Faber and Sah 2002; Madison and Nicoll 1984; Schwindt et al. 1988). Typically, AHP represents a spike-induced opening of specific classes of potassium channels (Sah 1996). Making use of AHP as the index with which to assess neocortex pyramidal cell excitability, we have recently investigated cholinergically operated feedback regulation of spike firing (Yamamoto et al. 2000, 2002a,b), and then have pinned down the channel involved (Yamada et al. 2004). Spike afterpotentials thus seem to be useful for initial survey of neuromodulator-based regulation of neuron excitability. We attempted to apply this strategy for studying dopamine-operated regulation of amygdala neuron excitability in the present study, and started assessing dopamine effects on spike afterpotentials in these neurons. Although we have not yet specified the channel involved, several characteristics of dopamine-operated ADP in amygdala principal neurons were clarified in the present report.

METHODS

All experiments were performed in accordance with the guiding principle of the Physiological Society of Japan and with the approval of the Animal Care Committee of Kanazawa Medical University.

Slice preparation

Brain slices containing the lateral nucleus of the amygdala were prepared from Wistar rats (16–20 days old). Rats were decapitated under ether anesthesia. The brain was removed and sectioned with a microslicer at 300 μm (Pro7; Dosaka, Kyoto, Japan) in ice-cold artificial cerebrospinal fluid (ACSF) composed (in mM) of 234 sucrose, 2.5 KCl, 1.25 NaH_2PO_4, 10 $MgSO_4$, 0.5 $CaCl_2$, 26 $NaHCO_3$ and 20 glucose. Slices were kept at 30°C for 15 min and then at room temperature for ≥45 min before experiments. Recordings were done in normal ACSF composed (in mM) of 124 NaCl, 3.0 KCl, 2.5 $CaCl_2$, 2.0 $MgSO_4$, 1.3 NaH_2PO_4, 26 NaHCO3, and 20 glucose. Also,

Address for reprint requests and other correspondence: N. Kato, Dept. of Physiology, Kanazawa Medical University, 920-0293 Ishikawa, Japan (E-mail: kato@kanazawa-med.ac.jp).

The costs of publication of this article were defrayed in part by the payment of page charges. The article must therefore be hereby marked "*advertisement*" in accordance with 18 U.S.C. Section 1734 solely to indicate this fact.

ascorbate (0.02 mM) was used to prevent dopaminergic agents from oxidation in all experiments. The slices were placed in a recording chamber on the stage of an upright microscope (BX51WI, Olympus) with a ×60 water-immersion objective (LUMPlanFI/IR). Recordings were made from slices submerged in normal ACSF at 30°C. In experiments in which cadmium was added to the purfusate to block voltage-gated calcium channels, $MgSO_4$ was replaced with $MgCl_2$, and NaH_2PO_4 was omitted. All solutions were aerated with 95% O_2-5% CO_2.

Electrophysiology

Whole cell recordings were made from the soma of visually identified pyramidal like neurons located in the nucleus of the LA. Recordings were continued only in cells that had resting membrane potential below −55 mV. In current- and voltage-clamp recordings, glass pipette electrodes were filled with a solution containing (in mM) 140 K-gluconate, 10 KCl, 2 $MgCl_2$, 2 Na_2-ATP, 0.4 Na_2-GTP, 0.2 EGTA, and 10 HEPES, with pH adjusted to 7.2–7.3 with KOH. In some current-clamp recordings, 10 mM BAPTA was added in the pipette solution to chelate intracellular free calcium. In some voltage-clamp recordings, glass pipettes were filled with a solution containing (in mM) 120 Cs-methansulfonate, 10 CsCl, 2 $MgCl_2$, 2 Na-ATP, 0.4 Na-GTP, 0.2 EGTA, 10 HEPES, 10 TEA-Cl, and 5 QX314-Cl, with pH adjusted to 7.2–7.3 by adding CsOH. Liquid junction potentials of the K-gluconate-based internal solution and Cs-methanesulfonate-based internal solution were about 10 and 5 mV, respectively. These potentials were not corrected. To induce slow ADP (sADP) in current-clamp mode, we used current injection (200 pA, 500 ms) through the patch electrode. To induce sADP current (I_{sADP}) in voltage-clamp mode, we used various voltage steps (for 500 ms, to 0 mV from the holding potentials of −40, −50, −60, −70, and −80 mV). To quantify the amplitude of sADP or I_{sADP}, we calculated integration of the amplitude for a 5-s period beginning from 300 ms postdepolarization, which is hereafter called the area sADP (or area I_{sADP}). Recordings were obtained with a Multiclamp 700A amplifier (Axon Instruments) and digitized at 10 kHz (Digidata1322A and pClamp9; Axon Instruments).

Drugs used

Depending on the purpose of experiments, we bath-applied one or more of the following drugs: cyclopiazonic acid (CPA, 30 μM; Wako, Osaka, Japan), dopamine (1–50 μM; Nacalai, Kyoto, Japan), ketanserin (1 μM; Wako), prazosin (1 μM; Wako), quinpirole (10 μM; Tocris, Bristol, UK), SKF38393 (30 μM; Tocris), SKF81297 (20 μM; Tocris), SKF83566 (10 μM; Tocris), sulpiride (10 μM; Tocris), and TTX (0.5 μM; Wako).

Data analysis

Data are expressed as means ± SE. Paired or unpaired *t*-test and ANOVA were used for statistics with the significance level set at $P < 0.05$.

RESULTS

Recordings were obtained from visually identified pyramidal-like neurons (Faber et al. 2001; Kroner et al. 2005; Washburn and Moises 1992) in the lateral nucleus of the amygdala (LA). The vast majority of the recorded neurons showed regular spike firing patterns. Depolarizing current injection (200 pA, 500 ms) evoked repetitive firing with frequency adaptation to various extents, and the present report describes neurons exhibiting this firing pattern. This feature is consistent with one of the firing patterns characteristic to principal neurons in the basolateral amygdala complex (BLA) (Faber et al. 2001; Kroner et al. 2005; Washburn and Moises 1992). We refer to these neurons as the principal neurons. Some other neurons showed a fast spiking pattern, which is characteristic to interneurons in the LA (Kroner et al. 2005; Washburn and Moises 1992). These interneurons were not taken into account in this paper.

Dopamine induced sADP

Principal neurons in the LA responded to a depolarizing current injection (200 pA, 500 ms), exhibiting a burst of spikes followed by an AHP (Fig. 1*A*, control). With bath application of dopamine (50 μM), this AHP was eliminated and instead a sADP was induced (Fig. 1*A*, dopamine). The sADP lasted for >5 s. To quantify the amplitude of sADP, we calculated integration of sADP from 300 ms for a 5-s period after the termination of current injection. We refer to this integration as the area sADP. The area sADP was increased from −4.00 ± 1.58 to 15.70 ± 4.49 mV·S ($n = 7$, $P < 0.005$) within 3–5 min by bath application of dopamine and was decreased to 5.70 ± 3.09 mV·S by washing out dopamine (Fig. 1, *A*, washout, and *B*). This sADP was induced in a concentration-dependent manner (Fig. 1*C*). The area sADPs induced by dopamine (1, 5, 10, and 50 μM) were 0.10 ± 0.76 mV·S ($n = 7$), 2.64 ± 1.15 mV·S ($n = 12$), 8.57 ± 2.20 mV·S ($n = 10$), and 17.08 ± 2.50 mV·S ($n = 13$), respectively. With bath application of dopamine, principal neurons showed a small membrane depolarization in agreement with previous reports (Kroner et al. 2005; Shi et al. 1997). Hereafter we use dopamine at the concentration of 50 μM.

Dopamine induced sADP current

Recordings were then performed in the voltage-clamp mode. An AHP current (I_{AHP}) was induced in principal neurons in the LA by a voltage step (+50 mV for 500 ms from the holding potential of −50 mV; Fig. 1*A*, control). This is consistent with a feature of the principal neurons in the LA previously reported (Faber and Sah 2002). With bath application of dopamine (50 μM), this I_{AHP} was replaced by a sADP current (I_{sADP}; Fig. 1*D*, dopamine). We calculated the area I_{sADP} by integrating I_{sADP} for a 5-s period starting from 300 ms after the termination of a voltage step. The area I_{sADP} was initially positive and became negative within 2–3 min after bath application of dopamine (50 μM; Fig. 1*E;* from 35.21 ± 19.24 to −52.09 ± 6.08 pA·S, $n = 8$, $P < 0.001$). The present findings obtained under the voltage- and current-clamp modes agree with each other.

D1 but not D2 receptors are involved in sADP

To determine which group of dopamine receptors was involved in generating this sADP, we examined effects of dopaminergic agents on this sADP. When a D1-like receptor agonist (SKF38393, 30 μM) was bath-applied, the area sADP was increased within 4–6 min (Fig. 2, *A* and *C;* from −1.13 ± 1.04 to 7.02 ± 1.99 mV·S, $n = 6$, $P < 0.001$). However, the amplitude of area sADP induced by SKF38393 was smaller than that induced by dopamine. We tested another selective D1-like receptor agonist SKF81297. SKF81297 (20 μM) failed to induce sADP and only reduced the AHP (from −3.78 ±

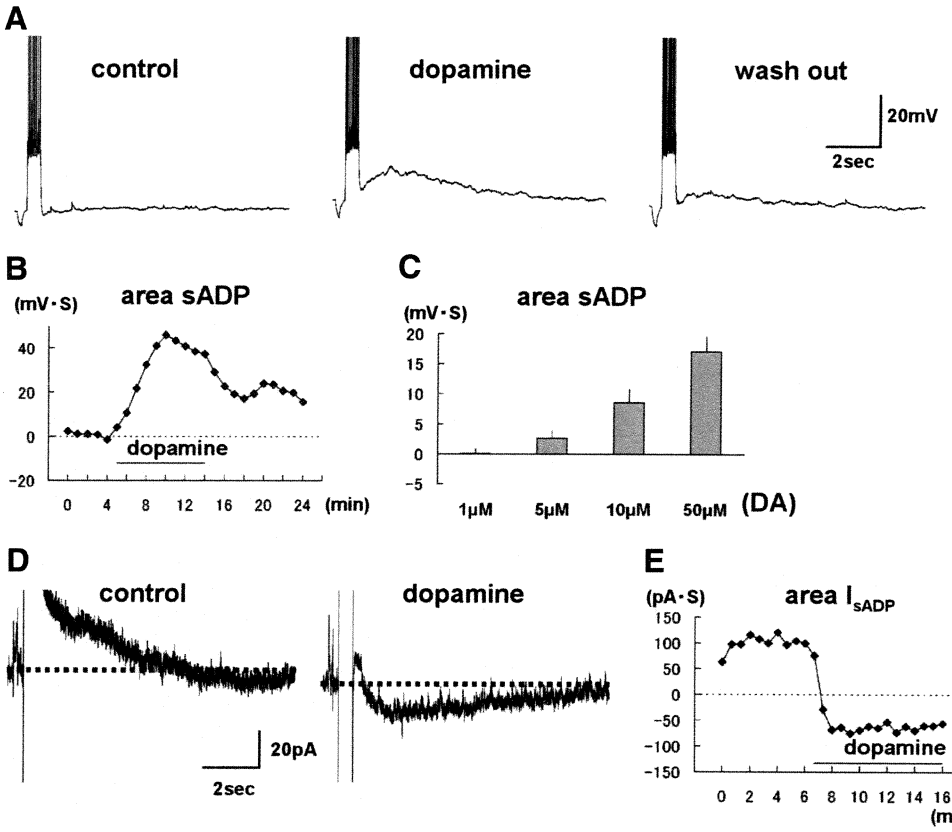

FIG. 1. Dopamine- induced slow afterdepolarization (sADP). *A*, *left*: response of a lateral amygdala neuron to current injection (200 pA, 500 ms) under control condition (control). *A*, *middle*: after bath application of dopamine (50 μM), sADP was induced (dopamine). *A*, *right*: after dopamine washout, the amplitude of sADP was decreased (washout). *B*: time course of the dopamine effects on the area sADP. In this and following figures, dopamine and the other drugs were bath-applied during the time spans indicated by the horizontal bars. *C*: dopamine induced sADP in a concentration-dependent manner. *D*: dopamine induced sADP current (I_{sADP}) under voltage-clamp condition. *Left*: response induced by a 500-ms-long voltage step (to 0 mV from the holding potential of −50 mV) under control condition. An outward afterhyperpolarization current was observed (control). *Right*: after bath application of dopamine (50 μM), the outward current was replaced by an inward I_{sADP} (dopamine). *E*: time course of the dopamine effects on the area I_{sADP}.

1.17 to 0.35 ± 1.23 mV·S, n = 4). Bath application of a D2-like receptor agonist (quinpirole, 10 μM) failed to induce sADP (Fig. 2, *B* and *C;* from −3.35 ± 1.37 to −1.12 ± 1.40 mV·S, n = 6). Next we tested effects of antagonists of D1- and D2-like receptors. Bath application of a D1-like receptor antagonist (SKF83566, 10 μM) reduced the amplitude of sADP induced by dopamine (50 μM; Fig. 2, *D* and *F;* from −1.22 ± 1.08 to 4.89 ± 2.03 mV·S, n = 4). The area sADP induced in the presence of SKF83566 was significantly smaller than that induced without SKF83566 (Fig. 2*F;* 4.89 ± 2.03 vs. 17.08 ± 2.50 mV·S, $P < 0.002$). On the other hand, even in the presence of a D2-like receptor antagonist (sulpiride, 10 μM), bath application of dopamine (50 μM) induced the full sADP (Fig. 2, *E* and *F;* from −3.80 ± 1.58 to 17.50 ± 4.07 mV·S, n = 6, $P < 0.005$). These results indicate that induction of the present dopamine (DA)-induced sADP requires activation of D1-like, but not D2-like, receptors and that even activation of D1-like receptors still fails to induce the full DA-induced sADP, suggesting that dopamine may activate receptors other than those for dopamine.

More than one classes of monoamine receptors is involved in this sADP

We observed that selective D1 receptor agonists induced only a small sADP. It has been reported that dopamine activates other monoamine receptors (Bhattacharyya et al. 2006; Cornil et al. 2002; Malenka and Nicoll 1986; Woodward et al. 1992) and that sADPs were induced by activating noradrenalin α_1 receptors or 5-HT_2 receptors in other structures (Araneda and Andrade 1991; Spain 1994; Zhang and Arsenault 2005). To test the possibility that the present DA-induced sADP may result from activating these monoamine receptors, we examined involvement of noradrenalin and serotonin receptors. With the noradrenalin α_1 receptor antagonist prazosin (1 μM) and the 5-HT_2 receptor antagonist ketanserin (1 μM) applied together, DA-induced sADP was reduced its amplitude (Fig. 2, *G* and *H;* 3.86 ± 1.78 mV·S, n = 8, vs. 17.08 ± 2.50 mV·S, $P < 0.001$). With either prazosin or ketanserin applied alone, DA-induced sADP also reduced its amplitude (Fig. 2*H;* with prazosin 5.49 ± 1.96 mV·S, n = 7, with ketanserin 5.51 ± 1.29 mV·S, n = 7). These results suggest that the present DA-induced sADP involves not only D1 receptors but also noradrenalin α_1 and 5-HT_2 receptors.

Calcium influx triggered sADP

Similar sADPs induced by stimulation of muscarinic acetylcholine receptors or metabotropic glutamate receptors were reported in layer V neocortex neurons (Greene et al. 1994; Haj-Dahmane and Andrade 1998), layer II–III olfactory cortex neurons (Constanti et al.1993) and hippocampal CA1 pyramidal neurons (Fraser and MacVicar 1996). All these studies unanimously revealed that sADP is triggered by calcium influx. We therefore assumed that the present sADP induced by dopamine in LA neurons were also triggered by calcium influx. First, to check whether action potentials are necessary for the sADP or not, we used TTX (0.5 μM) to block sodium channels. Even in the presence of TTX, DA-induced sADP was observed (Fig. 3, *A* and *D;* from −2.70 ± 1.22 to 20.47 ± 5.64 mV·S, n = 6, $P < 0.005$). Next we tested effects of calcium channel blockade on the sADP. After bath application of dopamine, the sADP

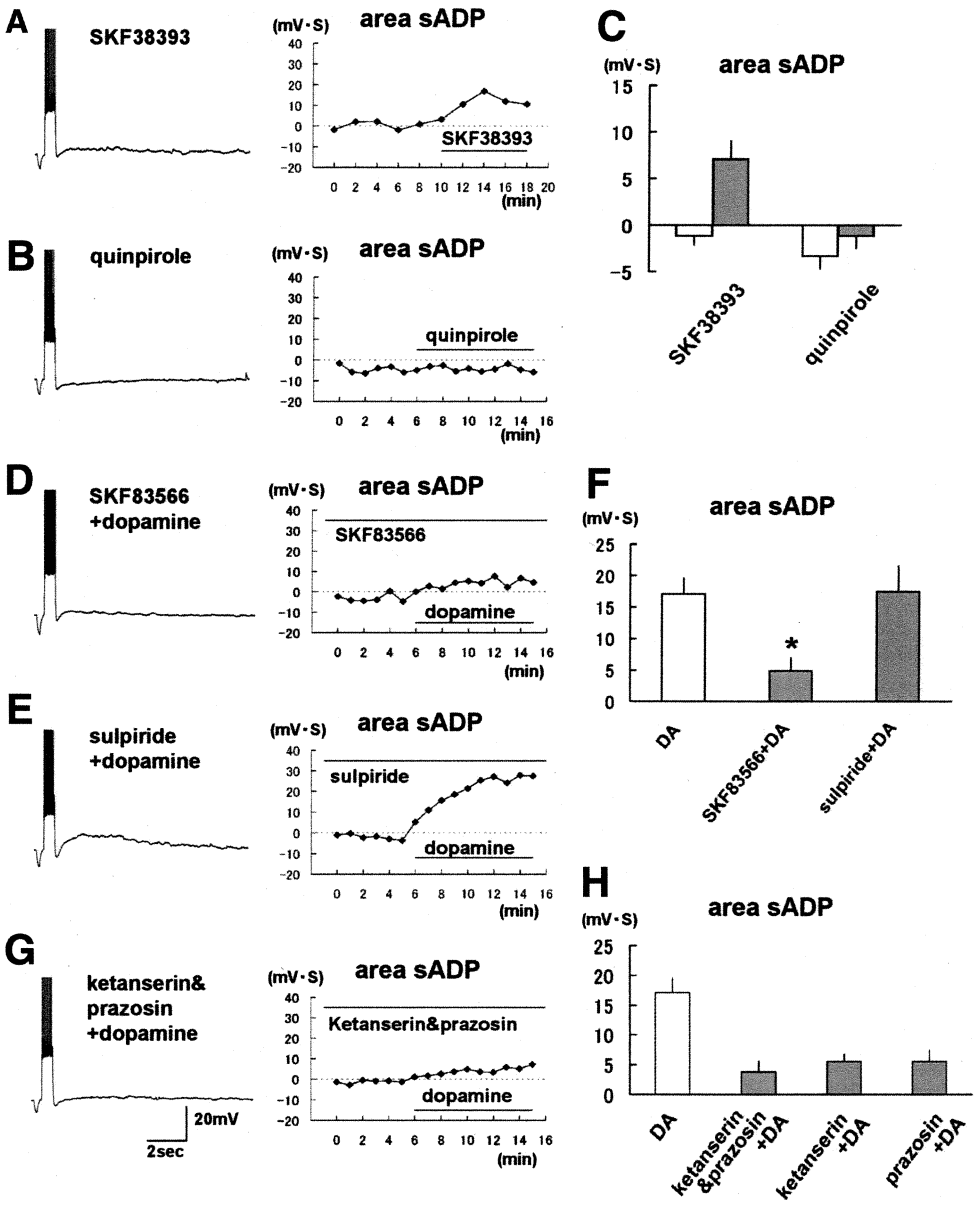

FIG. 2. D1 receptors mediate a small sADP. *A*: bath application of SKF38393 (30 μM) induced a small sADP. *Right*: change in the area sADP. *B*: quinpirole (10 μM) failed to induce sADP. *Right*: time course of the area sADP. *C*: comparison of the effects of SKF38393 and quinpirole. *D*: D2 receptors do not mediate dopamine (DA)-induced sADP. With SKF83566 (10 μM), dopamine (50 μM) failed to induce the full sADP. *Right*: time course of the dopamine effects on the area sADP. SKF83566 was always present in the external solution in this experiment. *E*: with sulpiride (10 μM), dopamine induced the full sADP. Sulpiride was always present in the external solution in this experiment. *F*: summary diagram showing that SKF83566 significantly reduced the area sADP. *G*: monoamine receptors other than those for dopamine are also required in this sADP. With ketanserin (1 μM) and/or prazosin (1 μM), dopamine failed to induce the full sADP. *Right*: time course of the dopamine effects on the area sADP. *H*: summary diagram showing that ketanserin and prazosin significantly reduced the area sADP.

was induced within 3-5min. Bath application of the voltage-dependent calcium channel (VDCC) blocker cadmium (250 μM) abolished sADP induced by dopamine (Fig. 3, *B* and *D;* control, −2.31 ± 1.27 mV·S; dopamine, 19.10 ± 3.69 mV·S; cadmium, 2.54 ± 3.53 mV·S; $n = 4$, $P < 0.05$). To further confirm the necessity of calcium influx for sADP, we chelated intracellular calcium by adding BAPTA (10 mM) to the internal solution. With BAPTA (10 mM), bath application of dopamine failed to induce sADP (Fig. 3, *C* and *D;* from −7.81 ± 1.56 to 1.09 ± 1.03 mV·S, $n = 7$). To test involvement of calcium release from internal stores in the present sADP, we used the calcium store depletor CPA (30 μM). Bath application of CPA still allowed induction of the DA-induced sADP (Fig. 3*D;* from −1.96 ± 2.16 to 16.47 ± 7.22 mV·S, $n = 3$), ruling out an essential involvement of calcium stores. These results showed that the present DA-induced sADP is triggered by calcium influx, and is generated by membrane depolarization irrespective of whether action potentials are fired or not.

Voltage dependency of DA-induced I_{sADP}

We have thus shown that calcium influx triggered induction of the DA-induced sADP. A next question would be what kind of currents mediate expression of the sADP. It was previously shown that both calcium-activated currents and decrease of potassium currents could be responsible for sADP as follows. Constanti et al. (1993) reported that, in the olfactory cortex, sADP was induced by decrease of potassium current. According to Greene et al. (1994), sADP was induced by both calcium-activated current and decrease of potassium current in the prefrontal cortex. In the neocortex and hippocampal CA1 neuron, it was reported that sADP was induced by calcium-activated current alone (Fraser and MacVicar 1996; Haj-Dahmane and Andrade 1998). To elucidate what class of currents are responsible for the present sADP, we first examined voltage dependency of the DA-induced I_{sADP}. Voltage steps (500 ms, to 0 mV from holding potentials −80, −70, −60, −50, and −40 mV) were applied to neurons in the presence of TTX

(0.5 μM). The currents induced were compared before and 5 min after bath application of dopamine (50 μM). Before the application, each voltage step induced outward currents (Fig. 4*A*, control). After the application, by contrast, the voltage steps induced inward currents (I_{sADP}) at the holding potentials of −50 and −40 mV (Fig. 4*A*, dopamine). At −80, −70, and −60 mV, although I_{sADP} was not apparent, reduction of outward currents was observed. By subtracting the currents induced in control condition from the currents induced with dopamine, the net increase in I_{sADP} induced by dopamine was obtained. The net increase thus obtained became stronger at more depolarized membrane potentials (Fig. 4*A*, subtract). The currents reached the peak at ~1.5 s after the termination of the voltage step. The amplitudes of the currents at this timing were plotted in Fig. 4*B* (−4.64 ± 0.61 pA at −80 mV, −4.45 ± 1.06 pA at −70 mV, −10.96 ± 1.79 pA at −60 mV, −19.07 ± 4.06 pA at −50 mV, −20.45 ±4.57 pA at −40 mV, n = 7).

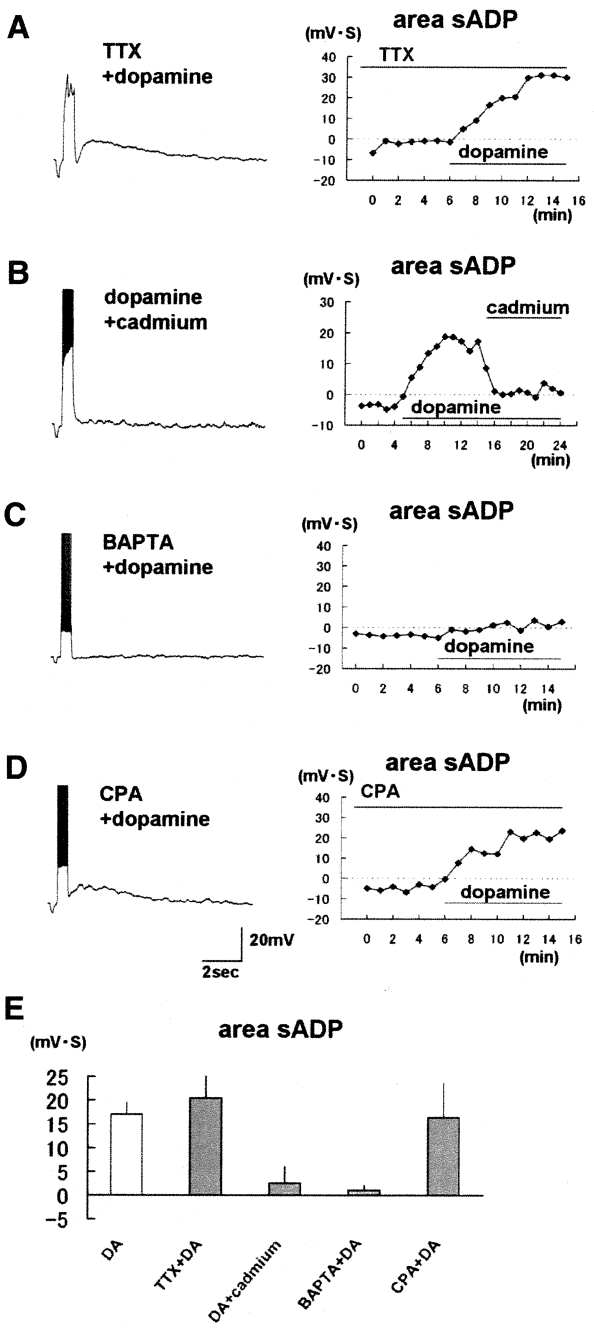

FIG. 3. Calcium influx required for generating sADP. *A*: after bath application of dopamine (50 μM), sADP was induced by a depolarizing current (200 pA, 500 ms), even in the presence of TTX (0.5 μM). TTX was always present in the external solution in this experiment. *B*: with bath application of cadmium (250 μM), the amplitude of the sADP induced by dopamine was reduced. *C*: dopamine failed to induce sADP with 10 mM bis-(*o*-aminophenoxy)-*N,N,N′,N′* tetraacetic acid (BAPTA). *Right*: time course of the dopamine effects on the area sADP with BAPTA (10 mM). *D*: calcium store depletor cyclopiazonic acid (CPA, 30 μM) left the sADP unchanged. *Right*: time course of the dopamine effects on the area sADP with CPA. *E*: across group comparison of the area sADP. Dopamine increased the area sADP even in the presence of TTX or CPA. Cadmium significantly reduced the area sADP induced by dopamine. With BAPTA, the area sADP induced by dopamine was significantly smaller.

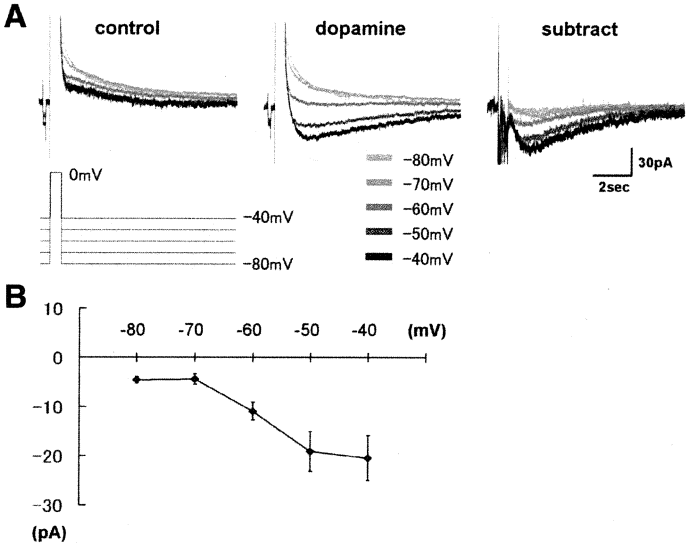

FIG. 4. Voltage dependency of DA-induced I_{sADP} *A*, *left*: currents induced by the voltage steps (to 0 mV from the holding potentials of either −80, −70, −60, −50, or −40 mV, 500 ms) were superimposed (control). *A*, *middle*: after bath application of dopamine (50 μM). *A*, *right*: by subtracting the currents induced under control condition from the currents induced after bath application of dopamine, the net current (subtracted I_{sADP}) induced by dopamine were obtained. Each trace represents the average of 2 trials (subtract). *B*: amplitudes of the subtracted I_{sADP} recorded at 1.5 s after the termination of the voltage steps were plotted.

Membrane conductance was decreased at the peak of I_{sADP}

To clarify whether the event underlying I_{sADP} is current activation or decrease of current, we measured change in membrane conductance during the I_{sADP}. We applied a voltage step (+10 or −10 mV) and compared the amplitude of currents induced at rest and during the I_{sADP}. The outward currents induced by the +10-mV voltage step commands were decreased in synchrony with I_{sADP} (Fig. 5*A*) and the inward currents induced by the −10-mV voltage step were also decreased (Fig. 5*B*). This is consistent with the previous descriptions although based on recordings from different classes of neurons (Constanti et al. 1993; Haj-Dahmane and Andrade 1998). These previous reports and the present experiments alike indicate that, during the I_{sADP}, the membrane conductance was decreased, suggesting that the I_{sADP} resulted from decrease of currents.

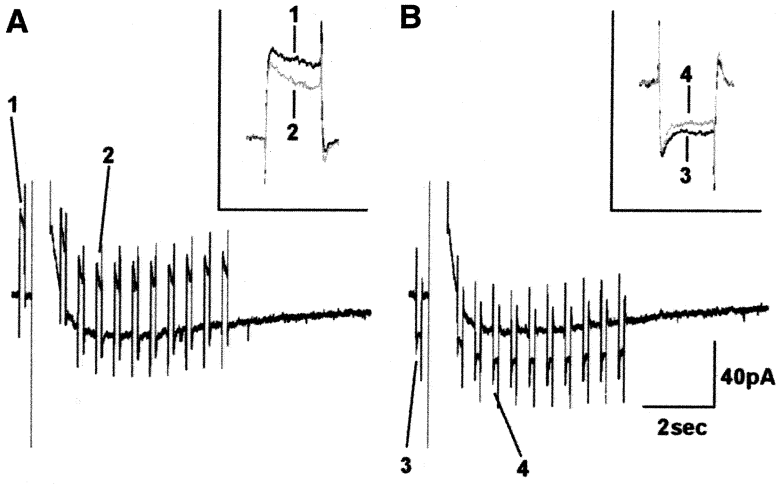

FIG. 5. Decrease in membrane conductance at the peak of I_{sADP}. *A*: outward currents induced by the +10-mV voltage step commands were decreased in synchrony with I_{sADP}. *Insets*: currents induced at rest (black, 1) and at the peak of I_{sADP} (gray, 2). *B*: inward currents induced by the −10-mV voltage step commands were also decreased in synchrony with I_{sADP}. *Insets*: currents induced at rest (black, 3) and at the peak of I_{sADP} (*gray*, 4).

Involvement of a potassium current in the DA-induced I_{sADP}

The *I-V* relationship of subtracted I_{sADP} (Fig. 4) and the reduction of membrane conductance during the I_{sADP} (Fig. 5) imply that this I_{sADP} resulted from decrease of potassium current. To test this possibility, we examined *I-V* relationship of subtracted I_{sADP} at different concentration of potassium (5 and 10 mM) in the external solution. The *I-V* curve was shifted upward significantly as the external concentration of potassium ($[K^+]_o$) was raised to 10 mM (Fig. 6, *A*, 10 mM KCl, and *B;* 3.69 ± 1.43 pA at −70 mV, 1.49 ± 1.51 pA at −60 mV, −13.61 ± 2.07 pA at −50 mV; $n = 7$; $P < 0.001$ ANOVA). The *I-V* curve was shifted upward when $[K^+]_o$ was raised to 5 mM (Fig. 6, *A*, 5 mM KCl, and *B;* −2.24 ± 2.31 pA at −70 mV, −4.29 ± 2.28 pA at −60 mV, −15.42 ± 3.28 pA at −50 mV; $n = 7$).

In the light of the reversal potential (E_{rev}), as well, the involvement of potassium currents was confirmed. DA-induced net I_{sADP}, which was inward at −50 mV, was almost undetectable at −60 mV, and was outward at −70 mV. These findings obviously point to a potassium reversal potential of about −60 mV, which is consistent with the prediction on the basis of the Goldman-Hodgkin-Katz equation (−61.4 mV with $[K^+]_o$ 10 mM, including the liquid junction potential).

To confirm the involvement of potassium conductance further, we examined effects of potassium channel blockade on this I_{sADP}. To block potassium channels, we made patch-clamp recording with cesium-based internal solution containing TEA (10 mM). With cesium, bath application of dopamine failed to induce I_{sADP} (Fig. 6, *C* and *D;* area I_{sADP};

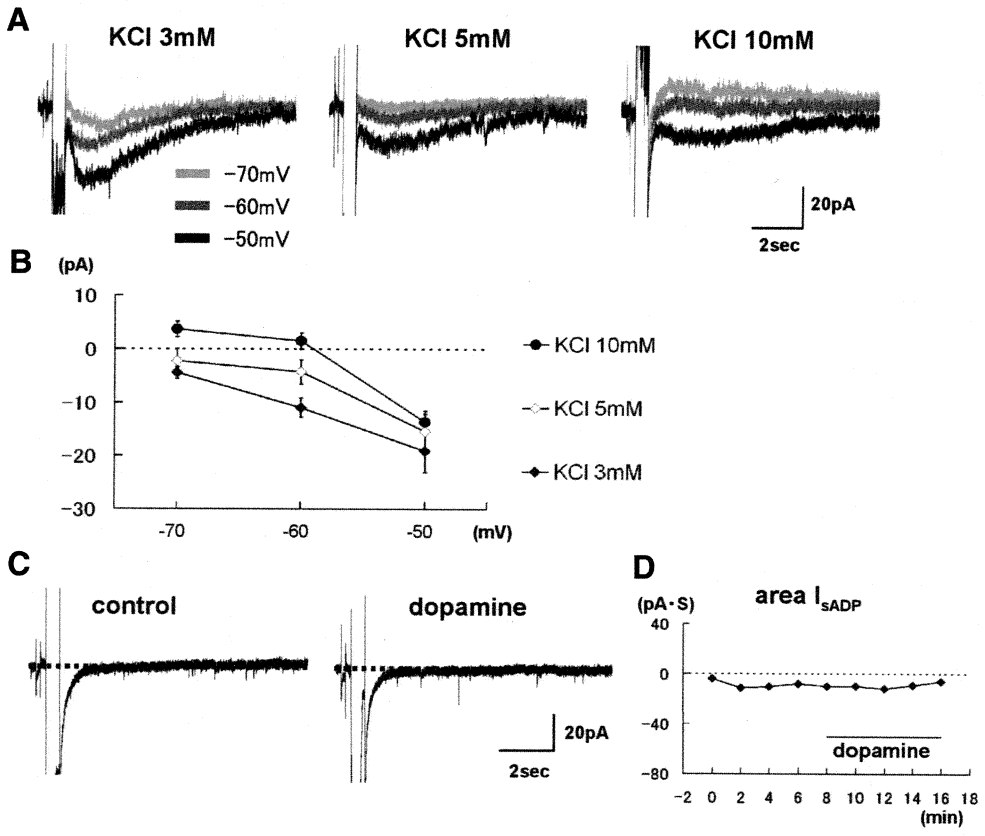

FIG. 6. Involvement of potassium current in the sADP. *A, left*: subtracted I_{sADP} induced by 500-ms-long voltage steps (to 0 mV from the holding potentials of −70, −60, and −50 mV) were superimposed. *A, middle*: subtracted I_{sADP} induced with $[K^+]_o$ 5 mM. *A, right*: subtracted I_{sADP} induced with $[K^+]_o$10 mM. Each trace represents the average of 2 trials. *B*: amplitudes of the currents recorded at 1.5 s after the termination of the voltage steps were plotted. *C*: effects of potassium channel blockade on DA-induced I_{sADP}. *Left*: currents were induced by a 500-ms-long voltage step (to −5 mV from the holding potential of −55 mV) with cesium methane sulfonate-based internal solution including 10 mM TEA (control). *Right*: under potassium channel blockade, dopamine (50 μM) did not alter the amplitude of the area I_{sADP}. *D*: time course of the dopamine effects on the area I_{sADP}. TTX was always added to the external solution in these experiments.

from -17.75 ± 3.22 to -14.75 ± 7.07 pA·S, $n = 8$, not significant). These results clearly indicate involvement of potassium conductance in this I_{sADP}.

DISCUSSION

Although simple DA-induced depolarization and changes in membrane resistance have been reported in LA neurons (Kroner et al. 2005), the present study is the first to demonstrate a DA-induced sADP, which is regarded as a positive feedback regulation of membrane excitability in LA neurons. We have shown that *1*) this sADP was mediated by D1- rather than D2-like receptors, *2*) was triggered by calcium influx, and *3*) was underlain by decrease in potassium conductance. However, involvement of receptors for other monoamines has also been suggested. The present sADP with decreasing potassium conductance would enhance the excitability of LA neurons activity-dependently.

Role of D1-like receptors in the present sADP

In the present experiments, activation of D1-like receptors by SKF38393 only partially mimicked the effect of dopamine itself, and blockade of D1-like receptors failed to abolish the DA-induced sADP completely. The present experiments indeed showed that the full expression of DA-induced sADP requires activation of noradrenalin α_1 receptors and 5-HT_2 receptors. There are two possibilities as to how dopamine activates these two classes of receptors. One possibility is that dopamine directly activates not only D1-like receptors but also these two classes of monoamine receptors as if effects of these three receptors are additive and in parallel. Another possibility is that dopamine activates presynaptic D1-like receptors at noradrenergic and serotonergic terminals, which might elicit release of these monoamines. However, this possibility is unlikely because specific activation of D1-like receptors failed to reproduce the dopamine effect. At the very least, the present study excluded involvement of D2-like receptors. The present findings therefore points to collaboration participated by D1-like, noradrenalin α_1 and 5-HT_2 receptors in inducing the present DA-induced sADP. What different roles are played by these receptors in this collaboration has yet to be clarified.

The present experiments also showed that DA increases the number of action potentials induced by injecting depolarizing current and depolarizes the resting membrane potential slightly. These are in agreement with the previous report (Kroner et al. 2005).

Similarity to other sADPs induced in various neurons

There is no other report on sADP in LA neurons although similar sADPs have been reported in other types of neurons. In the olfactory cortex, sADP is induced by activation of muscarinic acetylcholine receptors or metabotropic glutamate receptors (Constanti and Bagetta 1991; Constanti and Libri 1992; Constanti et al. 1993). In the neocortex, sADP is also induced by activation of muscarinic acetylcholine receptors (Haj-Dahmane and Andrade 1998; Schwindt et al. 1988), group I metabotropic glutamate receptors (Greene et al. 1992, 1994), α_1-noradrenalin receptors (Araneda and Andrade 1991) and 5-HT_2 receptors (Araneda and Andrade 1991; Spain 1994; Zhang and Arsenault 2005). In the hippocampal CA1, sADP was induced by activating muscarinic acetylcholine receptors (Fraser and MacVicar 1996; McQuiston and Madison 1999).

The present sADP and those sADPs reported previously are all triggered by calcium influx and have similar voltage dependency. These similarities of sADPs suggest that appearance of sADP by activating G-protein-coupled receptors is a common mechanism with which to modulate neuronal excitability.

Involvement of potassium current

Even though sADPs induced in various neurons resemble one another in many features, the currents underlying sADPs are diverse. Three types of sADPs were reported; sADP induced by decreasing potassium current (Constanti and Bagetta 1991; Constanti et al. 1993), that induced by activation of cation current and decreasing potassium current (Greene et al. 1994), and that induced by activation of calcium activated nonselective cation current (Haj-Dahmane and Andrade 1998).

In the present experiments, we revealed involvement of potassium current in the DA-induced sADP based on the following grounds: membrane conductance was reduced during I_{sADP}; the *I-V* relation curve of the net DA-induced I_{sADP} was shifted upward as $[K^+]_o$ was raised; the reversal potential of the net I_{sADP} was identical to that of potassium; and with cesium and TEA, dopamine failed to induce this I_{sADP}. These results clearly indicate that decrease in potassium conductance underlies the present DA-induced I_{sADP}.

Physiological role of the DA-induced sADP in LA

We showed that dopamine not only reduces AHP but also induces sADP in LA neurons. This sADP may be a part of a positive-feedback regulation of neuronal excitability in the following sense. Once a neuron is excited by an excitatory synaptic input, sADP is induced, during which the same neuron would be excited more easily than before. Such a positive-feedback enhancement of excitability will occur not only by consecutively incoming homosynaptic inputs but also by any combination of homo- and heterosynaptic inputs. It is thus suggested that sADP offers a platform on which various synaptic inputs are associatively integrated.

Also, because sADP lasts for seconds, two incoming volleys with time delay shorter than seconds could as well be associatively integrated. Such heterosynaptic integration with time delay, especially that with delay of subsecond order, may be important in delayed fear learning, given that the time sequence of conditioned and unconditioned stimuli is especially critical in the associative conditioning. The later phase of the sADP, which spans a few second after spikes, may be too late to be relevant to delayed fear conditioning obtained by specific pairs of conditioned and unconditioned stimuli. However, in a more generalized sense, once neuron circuits in the amygdala are activated, the late phase of sADP would render the amygdala circuit more sensitive to the next input in a positive feedback manner. Such a highly sensitized amygdala might be subject to context-*in*dependent activation, which could possibly underlie "fear of unrealistic danger."

The DA-induced sADP may also modulate long-term synaptic plasticity. Reduction of AHP is reported to facilitate LTP (Cohen et al. 1999; Disterhoft and Oh 2006; Kramar et al. 2004; Sah and Bekkers 1996), and both membrane depolariza-

tion and decrease in potassium conductance are advantageous to occurrence of LTP (Johnston et al. 2000; Lisman and Spruston 2005). LTP occurs in the amygdala during fear learning, and this LTP has been shown to be necessary for fear leaning (Blair et al. 2001; Maren and Quirk 2004; Rodrigues et al. 2004). Concentration of dopamine in the amygdala is reported to increase during fear conditioning (Harmer and Phillips 1999; Inglis and Moghaddam 1999; Yokoyama et al. 2005), suggesting a critical role of dopamine in fear learning. In fact, the blockade of dopamine receptors impairs acquisition of fear memory (Greba and Kokkinidis 2001; Greba et al. 2000; Lamont and Kokkinidis 1998; Nader and LeDoux 1999). All these combined together, the present DA-induced sADP may serve to facilitate LTP in LA principal neurons, thereby enabling amygdala-dependent fear learning.

ACKNOWLEDGMENTS

The authors thank Prof. K. Kawano for encouragement, Dr. M. Murata for helpful discussion, and H. Adachi and S. Muramoto for technical assistance.

This work was supported partly by a Grant for Collaborative Research (C2006-5) from Kanazawa Medical University.

REFERENCES

Araneda R, Andrade R. 5-Hydroxytryptamine2 and 5-hydroxytryptamine 1A receptors mediate opposing responses on membrane excitability in rat association cortex. *Neuroscience* 40: 399–412, 1991.

Asan E. Ultrastructural features of tyrosine-hydroxylase-immunoreactive afferents and their targets in the rat amygdala. *Cell Tissue Res* 288: 449–469, 1997.

Asan E. The catecholaminergic innervation of the rat amygdala. *Adv Anat Embryol Cell Biol* 142: 1–118, 1998.

Bhattacharyya S, Raote I, Bhattacharya A, Miledi R, Panicker MM. Activation, internalization, and recycling of the serotonin 2A receptor by dopamine. *Proc Natl Acad Sci USA* 103: 15248–15253, 2006.

Bissiere S, Humeau Y, Luthi A. Dopamine gates LTP induction in lateral amygdala by suppressing feedforward inhibition. *Nat Neurosci* 6: 587–92, 2003.

Blair HT, Schafe GE, Bauer EP, Rodrigues SM, LeDoux JE. Synaptic plasticity in the lateral amygdala: a cellular hypothesis of fear conditioning. *Learn Mem* 8: 229–242, 2001.

Cohen AS, Coussens CM, Raymond CR, Abraham WC. Long-lasting increase in cellular excitability associated with the priming of LTP induction in rat hippocampus. *J Neurophysiol* 82: 3139–3148, 1999.

Constanti A, Bagetta G. Muscarinic receptor activation induces a prolonged post-stimulus afterdepolarization with a conductance decrease in guinea-pig olfactory cortex neurons in vitro. *Neurosci Lett* 131: 27–32, 1991.

Constanti A, Bagetta G, Libri V. Persistent muscarinic excitation in guinea-pig olfactory cortex neurons: involvement of a slow post-stimulus afterdepolarizing current. *Neuroscience* 56: 887–904, 1993.

Constanti A, Libri V. Trans-ACPD induces a slow post-stimulus inward tail current (IADP) in guinea-pig olfactory cortex neurons in vitro. *Eur J Pharmacol* 216: 463–464, 1992.

Cornil CA, Balthazart J, Motte P, Massotte L, Seutin V. Dopamine activates noradrenergic receptors in the preoptic area. *J Neurosci* 22: 9320–9330, 2002.

Disterhoft JF, Oh MM. Learning, aging and intrinsic neuronal plasticity. *Trends Neurosci* 29: 587–599, 2006.

Faber ES, Callister RJ, Sah P. Morphological and electrophysiological properties of principal neurons in the rat lateral amygdala in vitro. *J Neurophysiol* 85: 714–723, 2001.

Faber ES, Sah P. Physiological role of calcium-activated potassium currents in the rat lateral amygdala. *J Neurosci* 22: 1618–1628, 2002.

Fanselow MS, Gale GD. The amygdala, fear, and memory. *Ann NY Acad Sci* 985: 125–134, 2003.

Fraser DD, MacVicar BA. Cholinergic-dependent plateau potential in hippocampal CA1 pyramidal neurons. *J Neurosci* 16: 4113–4128, 1996.

Gorelova NA, Yang CR. Dopamine D1/D5 receptor activation modulates a persistent sodium current in rat prefrontal cortical neurons in vitro. *J Neurophysiol* 84: 75–87, 2000.

Greba Q, Gifkins A, Kokkinidis L. Inhibition of amygdaloid dopamine D2 receptors impairs emotional learning measured with fear-potentiated startle. *Brain Res* 899: 218–226, 2001.

Greba Q, Kokkinidis L. Peripheral and intraamygdalar administration of the dopamine D1 receptor antagonist SCH 23390 blocks fear-potentiated startle but not shock reactivity or the shock sensitization of acoustic startle. *Behav Neurosci* 114: 262–272, 2000.

Greene C, Schwindt P, Crill W. Metabotropic receptor mediated afterdepolarization in neocortical neurons. *Eur J Pharmacol* 226: 279–280, 1992.

Greene CC, Schwindt PC, Crill WE. Properties and ionic mechanisms of a metabotropic glutamate receptor-mediated slow afterdepolarization in neocortical neurons. *J Neurophysiol* 72: 693–704, 1994.

Haj-Dahmane S, Andrade R. Ionic mechanism of the slow afterdepolarization induced by muscarinic receptor activation in rat prefrontal cortex. *J Neurophysiol* 80: 1197–1210, 1998.

Harmer CJ, Phillips GD. Enhanced dopamine efflux in the amygdala by a predictive, but not a non-predictive, stimulus: facilitation by prior repeated D-amphetamine. *Neuroscience* 90: 119–130, 1999.

Inglis FM, Moghaddam B. Dopaminergic innervation of the amygdala is highly responsive to stress. *J Neurochem* 72: 1088–1094, 1999.

Johnston D, Hoffman DA, Magee JC, Poolos NP, Watanabe S, Colbert CM, Migliore M. Dendritic potassium channels in hippocampal pyramidal neurons. *J Physiol* 525: 75–81, 2000.

Kramar EA, Lin B, Lin CY, Arai AC, Gall CM, Lynch G. A novel mechanism for the facilitation of theta-induced long-term potentiation by brain-derived neurotrophic factor. *J Neurosci* 24: 5151–5161, 2004.

Kroner S, Rosenkranz JA, Grace AA, Barrionuevo G. Dopamine modulates excitability of basolateral amygdala neurons in vitro. *J Neurophysiol* 93: 1598–1610, 2005.

Lamont EW, Kokkinidis L. Infusion of the dopamine D1 receptor antagonist SCH 23390 into the amygdala blocks fear expression in a potentiated startle paradigm. *Brain Res* 795: 128–136, 1998.

LeDoux JE. Emotion circuits in the brain. *Annu Rev Neurosci* 23: 155–184, 2000.

Lisman J, Spruston N. Postsynaptic depolarization requirements for LTP and LTD: a critique of spike timing-dependent plasticity. *Nat Neurosci* 8: 839–841, 2005.

Madison DV, Nicoll RA. Control of the repetitive discharge of rat CA 1 pyramidal neurons in vitro. *J Physiol* 354: 319–331, 1984.

Malenka RC, Nicoll RA. Dopamine decreases the calcium-activated afterhyperpolarization in hippocampal CA1 pyramidal cells. *Brain Res* 379: 210–215, 1986.

Maren S, Quirk GJ. Neuronal signalling of fear memory. *Nat Rev Neurosci* 5: 844–852, 2004.

Marowsky A, Yanagawa Y, Obata K, Vogt KE. A specialized subclass of interneurons mediates dopaminergic facilitation of amygdala function. *Neuron* 48: 1025–1037, 2005.

McQuiston AR, Madison DV. Muscarinic receptor activity induces an afterdepolarization in a subpopulation of hippocampal CA1 interneurons. *J Neurosci* 19: 5703–5710, 1999.

Nader K, LeDoux JE. Inhibition of the mesoamygdala dopaminergic pathway impairs the retrieval of conditioned fear associations. *Behav Neurosci* 113: 891–901, 1999.

Pickel VM, Colago EE, Mania I, Molosh AI, Rainnie DG. Dopamine D1 receptors co-distribute with *N*-methyl-D-aspartic acid type-1 subunits and modulate synaptically-evoked *N*-methyl-D-aspartic acid currents in rat basolateral amygdala. *Neuroscience* 142: 671–690, 2006.

Rodrigues SM, Schafe GE, LeDoux JE. Molecular mechanisms underlying emotional learning and memory in the lateral amygdala. *Neuron* 44: 75–91, 2004.

Rosenkranz JA, Grace AA. Modulation of basolateral amygdala neuronal firing and afferent drive by dopamine receptor activation in vivo. *J Neurosci* 19: 11027–11039, 1999.

Rosenkranz JA, Grace AA. Dopamine attenuates prefrontal cortical suppression of sensory inputs to the basolateral amygdala of rats. *J Neurosci* 21: 4090–4103, 2001.

Rosenkranz JA, Grace AA. Dopamine-mediated modulation of odour-evoked amygdala potentials during pavlovian conditioning. *Nature* 417: 282–287, 2002.

Sah P. Ca(2+)-activated K+ currents in neurons: types, physiological roles and modulation. *Trends Neurosci* 19: 150–154, 1996.

Sah P, Bekkers JM. Apical dendritic location of slow afterhyperpolarization current in hippocampal pyramidal neurons: implications for the integration of long-term potentiation. *J Neurosci* 16: 4537–4542, 1996.

Schwindt PC, Spain WJ, Foehring RC, Chubb MC, Crill WE. Slow conductances in neurons from cat sensorimotor cortex in vitro and their role in slow excitability changes. *J Neurophysiol* 59: 450–467, 1988.

Seamans JK, Yang CR. The principal features and mechanisms of dopamine modulation in the prefrontal cortex. *Prog Neurobiol* 74(1): 1–58, 2004.

Shi WX, Zheng P, Liang XF, Bunney BS. Characterization of dopamine-induced depolarization of prefrontal cortical neurons. *Synapse* 26: 415–422, 1997.

Spain WJ. Serotonin has different effects on two classes of Betz cells from the cat. *J Neurophysiol* 72: 1925–1937, 1994.

Washburn MS, Moises HC. Electrophysiological and morphological properties of rat basolateral amygdaloid neurons in vitro. *J Neurosci* 12: 4066–4079, 1992.

Woodward RM, Panicker MM, Miledi R. Actions of dopamine and dopaminergic drugs on cloned serotonin receptors expressed in *Xenopus* oocytes. *Proc Natl Acad Sci USA* 89: 4708–4712, 1992.

Yamada S, Takechi H, Kanchiku I, Kita T, Kato N. Small-conductance Ca^{2+}-dependent K^+ channels are the target of spike-induced Ca^{2+} release in a feedback regulation of pyramidal cell excitability. *J Neurophysiol* 91: 2322–2329, 2004.

Yamamoto K, Hashimoto K, Isomura Y, Shimohama S, Kato N. An IP3-assisted form of Ca^{2+}-induced Ca^{2+} release in neocortical neurons. *Neuroreport* 11: 535–539, 2000.

Yamamoto K, Hashimoto K, Nakano M, Shimohama S, Kato N. A distinct form of calcium release down-regulates membrane excitability in neocortical pyramidal cells. *Neuroscience* 109: 665–676, 2002a.

Yamamoto K, Nakano M, Hashimoto K, Shimohama S, Kato N. Emergence of a functional coupling between inositol-1,4,5-trisphosphate receptors and calcium channels in developing neocortical neurons. *Neuroscience* 109: 677–685, 2002b.

Yang CR, Seamans JK. Dopamine D1 receptor actions in layers V-VI rat prefrontal cortex neurons in vitro: modulation of dendritic-somatic signal integration. *J Neurosci* 16: 1922–35, 1996.

Yokoyama M, Suzuki E, Sato T, Maruta S, Watanabe S, Miyaoka H. Amygdalic levels of dopamine and serotonin rise upon exposure to conditioned fear stress without elevation of glutamate. *Neurosci Lett* 379: 37–41, 2005.

Young CE, Yang CR. Dopamine D1/D5 receptor modulates state-dependent switching of soma-dendritic Ca^{2+} potentials via differential protein kinase A and C activation in rat prefrontal cortical neurons. *J Neurosci* 24: 8–23, 2004.

Zhang ZW, Arsenault D. Gain modulation by serotonin in pyramidal neurones of the rat prefrontal cortex. *J Physiol* 566: 379–394, 2005.

BRAIN RESEARCH 1133 (2007) 27–33

available at www.sciencedirect.com

ScienceDirect

www.elsevier.com/locate/brainres

BRAIN RESEARCH

Research Report

Autocorrelogram sorting: A novel method for evaluating negative-feedback regulation of spike firing

Miyahiko Murata[a], *Nobuo Kato*[a,b,*]

[a]*Department of Integrative Brain Science, Kyoto University Graduate School of Medicine, Kyoto 606-8501, Japan*
[b]*Department of Physiology, Kanazawa Medical University, Ishikawa 920-0293, Japan*

ARTICLE INFO

Article history:
Accepted 16 November 2006
Available online 20 December 2006

Keywords:
Acetylcholine
Extracellular recording
Hippocampal neuron
Inhibition
Spike train

ABSTRACT

Spontaneously firing units were recorded extracellularly from the hippocampus of anesthetized rats, and autocorrelograms were conventionally constructed. These conventional autocorrelograms were sorted into frequency-specific autocorrelograms according to the instantaneous firing frequency of the spike at $\Delta t=0$, which was calculated based on the interval between the spike at $\Delta t=0$ and the preceding spike. In this fashion, we found that autocorrelogram values were negatively correlated with instantaneous firing frequency during the 4–12 ms post-spike time period. The negative correlation during the 4–6 ms post-spike period could not have been due to the refractory period or GABAergic inhibition, and thus represented a third type of feedback regulation of spike firing completed within single neurons. Application of acetylcholine significantly enhanced this feedback regulation. Our 'autocorrelogram sorting' method thus proved to be successful in detecting cholinergically enhanced feedback regulation of spike firing intrinsic to single neurons.

1. Introduction

GABAergic feedback inhibition and neuronal refractoriness play critical roles in homeostatic regulation of neural excitability (Eccles, 1953; Dayan and Abbott, 2001; Hille, 2001). However, by GABAergic mechanisms alone, a spike can prevent subsequent firing of the same neuron only after a certain delay, because of the synaptic transmission involved. On the other hand, refractoriness can explain feedback regulation within only a few ms after a spike. The question arises whether between these two time periods, during which these two mechanisms work separately, a time period exists during which feedback mechanisms are entirely lacking. The presence of such a period seems counter-intuitive. Anticipated feedback mechanisms, if any exist, should be switched on after termination of the refractory period and switched off early enough not to be affected by synaptic transmission. To answer this question, we checked for the occurrence of feedback regulation during this particular time window. For this purpose, we devised a method of 'autocorrelogram sorting', by which the dependence of unit firing on instantaneous firing frequency can be determined, and then applied this method to

* *Corresponding author*. Department of Physiology, Kanazawa Medical University, Ishikawa 920-0293, Japan. Fax: +81 76 286 3523.
E-mail address: kato@kanazawa-med.ac.jp (N. Kato).

Abbreviations: Ach, acetylcholine; AchR, acetylcholine receptor; ACSF, artificial cerebrospinal fluid; CICR, calcium-induced calcium release; IP_3, inositol-1,4,5-trisphosphate; IP_3R, inositol-1,4,5-trisphosphate receptor; mAchR, muscarinic acetylcholine receptor; MK channel, K channel that generates the M currents; PTZ, pentylenetetrazole; SFA, spike frequency adaptation; SK channel, small conductance calcium activated K^+ channel

0006-8993/$ – see front matter © 2006 Elsevier B.V. All rights reserved.
doi:10.1016/j.brainres.2006.11.050

extracellular unit recordings obtained from the hippocampus of anesthetized rats.

2. Results

2.1. *Construction of autocorrelograms based on hippocampal unit recordings*

In total, we obtained 129 spontaneously firing units from the hippocampus. Based on histological examination and reading of electrode depths, these neurons were shown to be located in CA1. Those situated in other structures were excluded from the present study. For 15 units, the convulsant pentylenetetrazole (PTZ) was injected during the recording sessions, so that the average firing frequency changed while recording continued. In this fashion, we attempted to determine the dependence of the autocorrelation function of spike trains on average firing frequency. For 73 other units, such activity-dependence of unit firing was analyzed without PTZ injection, and instead with the 'autocorrelogram sorting' method described below. The other 41 units were used for pharmacological analysis of activity-dependent unit firing.

2.2. *Changes in average firing frequency and the autocorrelogram induced by pentylenetetrazole injection*

We initially recorded spontaneously firing units in CA1 of the hippocampus. Since injections of PTZ were performed during recording, recorded units were often lost due to the maneuvers associated with injection. When a unit was lost in this fashion, recording from another unit was attempted, in successive fashion. In this manner, one to four unit recordings were successfully performed per animal, with varying time periods starting 400 s before PTZ injection up to 1600 s after it. Because the experiments were performed under chloral hydrate anesthesia, the rats never exhibited seizure behaviorally, and the firing pattern was usually not bursting. Instead, the frequency of firing varied. Episodes of burst firing were excluded from the present analysis. A total of fifteen unit recordings were collected in this fashion. A typical example of increase in firing rate averaged for each 100-s period is shown in Fig. 1. In this case, a single unit recording could be maintained from 300 to 1200 s after injection. This period was divided into 9 sections of 100-s duration each. After the PTZ injection, the frequency of firing began to increase, and, in several minutes, reached the peak range (8–12 Hz). In this fashion, this and the other units were allowed to fire at widely varying frequencies. Based on recording during each of the 9 sections, autocorrelograms were constructed, with a bin size of 1 ms. The right halves (the areas representing $\Delta t>0$ only) of the autocorrelograms thus constructed are displayed for a

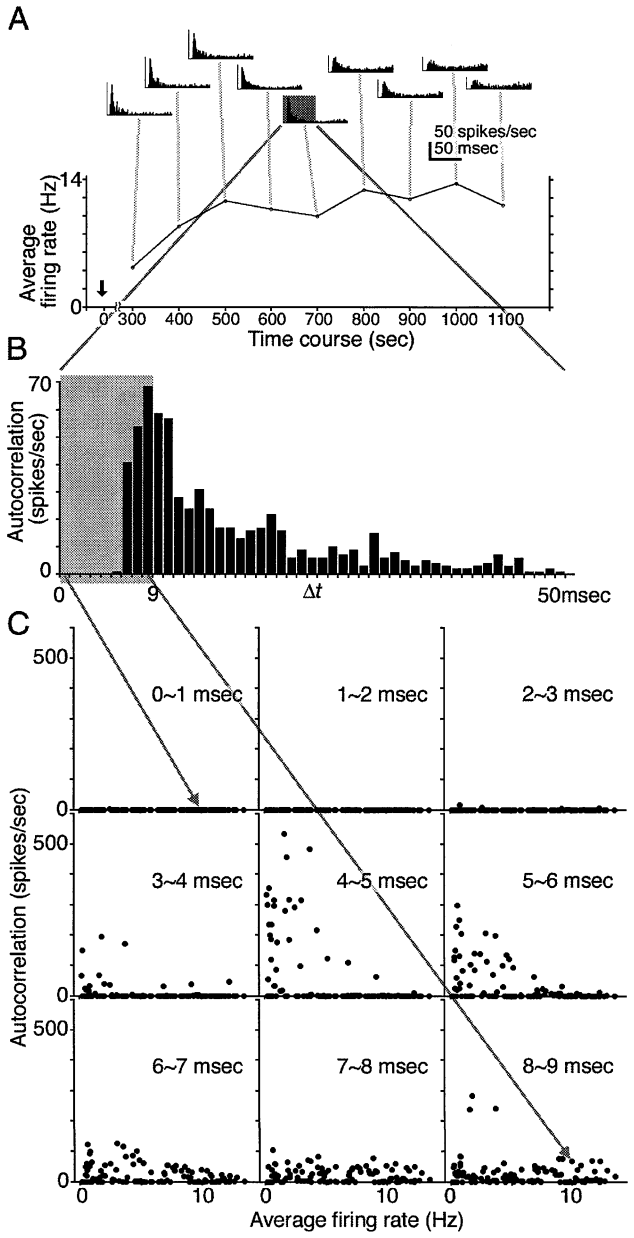

Fig. 1 – Time-dependent changes in firing frequency and frequency-dependent changes in the autocorrelogram for a representative, spontaneously firing unit. (A) Change in mean firing frequency plotted against time after injection of the epileptogenic drug PTZ (indicated by the arrow). Time-dependent changes in the autocorrelogram are also shown for the same unit. The time period from 300 to 1200 s after injection was divided into 9 sections of 100 s each. Based on unit recordings during each of the 9 sections, autocorrelograms were constructed, and the right halves of the autocorrelograms (the areas representing $\Delta t>0$ only; a half-autocorrelogram) are displayed here. (B) A half-autocorrelogram for the unit shown in A, calculated based on firing recorded at 700–800 s after PTZ injection. The autocorrelations for the initial 9 bins representing the 0–9 ms post-spike period (shaded in gray) were of interest. (C) Relationship between spike autocorrelogram and firing frequency. For 15 units, we constructed autocorrelograms, as shown in B. The autocorrelation represented by the first 9 bins, i.e., those for 0–9 ms post-spike, were scatter-plotted against the average firing frequency separately for each bin, in cumulative fashion so that data from all 110 autocorrelograms were combined bin by bin. For example, two autocorrelation values in B were represented as two dots in C, indicated by respective arrows.

representative unit in Fig. 1. As the firing rate increased, the autocorrelation averaged over 0–100 ms post-spike increased as well.

For each of the 15 units recorded with PTZ injection, we constructed a series of autocorrelograms based on firing for 100-s periods, as illustrated for the single representative unit in Fig. 1A. Based on recording for each section of 100-s duration, we obtained one autocorrelogram chart, with a bin size of 1 ms (Fig. 1B): the example shown was obtained from recording between 700 to 800 s after PTZ injection. Among these autocorrelograms, the autocorrelations for the initial 9 bins representing the 0–9 ms post-spike period (shaded in gray in Fig. 1B) were of interest in the present experiments, since the latency of GABAergic feedback inhibition in the hippocampus can reasonably be regarded as 8–9 ms on average (Karnup and Stelzer, 1999), and since our interest was in the time period prior to this feedback inhibition.

For the other 14 units, as well, we constructed autocorrelograms like that shown in Fig. 1B. Due to variation in duration of recording time, 110 autocorrelograms were obtained in total. Since the firing frequencies of units were altered by PTZ injection (Fig. 1A), these 110 autocorrelograms were based on spike trains exhibiting a wide variety of average frequencies. The autocorrelations represented by the first 9 bins, i.e., those for 0–9 ms post-spike, were scatter-plotted against the average firing rate bin by bin, in cumulative fashion with data from all the 110 autocorrelograms (Fig. 1C). Of the 9 bins represented by these 9 scatter plots, the first 3 bins (<3 ms post-spike) exhibited no autocorrelation, reflecting the refractory period of the excitable membrane. In the next 3 bins (3–6 ms post-spike), the autocorrelation values decreased with growth of firing frequency up to 10 Hz, and were thus negatively correlated with firing frequency (Kendall's τ=−0.124, −0.343, −0.187, respectively). The correlation was significantly negative for 4–6 ms post-spike ($P<0.01$). In the last 3 bins (6–9 ms post-spike), frequency dependence was no longer significant. Thus, a negative correlation between autocorrelation and frequency, although qualitative, was observed in the time-window between termination of the refractory period and initiation of GABAergic feedback inhibition, which should take 8–9 ms on average (Karnup and Stelzer, 1999) because of synaptic transmission.

This negative correlation between 4 and 6 ms post-spike probably represents feedback regulation of spike firing that is independent of GABAergic interneurons. Since it is also clear that refractoriness due to simple mechanisms intrinsic to sodium channels cannot be the explanation for this negative correlation, the feedback regulation we observed is probably attributable to intracellular mechanisms involving two or more classes of molecules, and not to sodium channels alone. A quantitative study of this negative correlation is described in the next section.

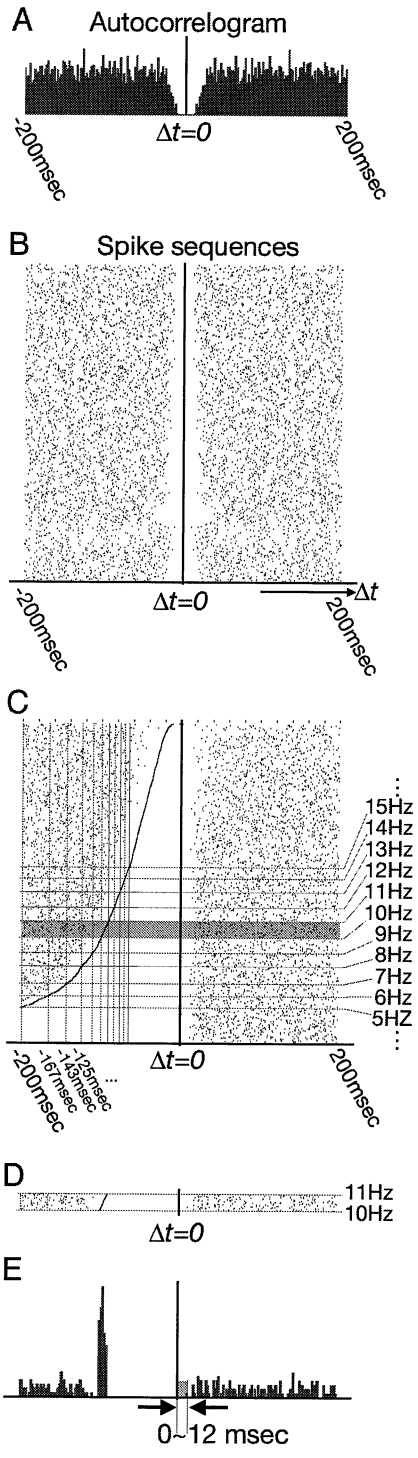

Fig. 2 – Procedures for 'autocorrelogram sorting'. (A) A spike autocorrelogram was conventionally constructed. Details are shown only for interspike intervals between −200 and +200 ms, in this and the following autocorrelograms. (B) The autocorrelogram in A was expressed in raster fashion, with each dot representing a spike firing. (C) Sorting of the raster autocorrelogram with instantaneous firing frequency at $\Delta t=0$ as the sorting key. The dot rows were re-arranged, so that rows with lower instantaneous firing rates at $\Delta t=0$ are located at lower positions. (D, E) Construction of frequency-specific autocorrelogram. The dot rows were grouped by instantaneous firing frequency at $\Delta t=0$, with the frequency range for the *n*th group (11th, for the example here) from *n*−1 Hz to *n* Hz (10 to 11 Hz; D). For each frequency group (that representing 10–11 Hz, for the example here), the conventional autocorrelogram was reconstructed (E). These frequency-specific autocorrelograms were used for the plots in Fig. 3.

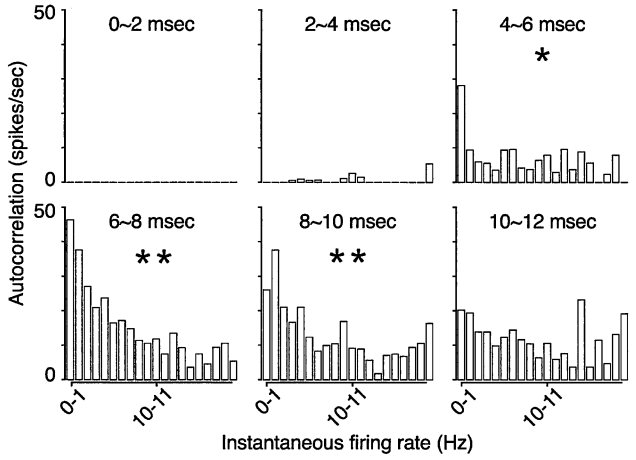

Fig. 3 – Dependence of autocorrelation on the immediately preceding history of firing. Frequency-specific autocorrelograms, like that shown in Fig. 2E, were constructed based on combined data obtained from 73 spontaneously firing hippocampal units. The post-spike portion (right half) of the autocorrelogram was divided into bins of 2 ms duration each. For each of the first 6 bins covering the first 12 ms post-spike, the autocorrelogram value was calculated, and the same procedure was repeated for the other frequency ranges. In this fashion, a bar graph was obtained for each of the 6 post-spike bins of 2 ms duration, plotting the frequency-specific autocorrelogram values for the bin against the instantaneous firing frequency. The correlation was significantly negative in bins representing 4–10 ms post-spike. *$P<0.05$; **$P<0.01$ (Kendall's τ tests).

2.3. *Dependence of the autocorrelogram on instantaneous firing frequency as revealed by 'autocorrelogram sorting'*

The negative correlation detected in PTZ-injected rats was examined in quantitative fashion and under more physiological conditions without use of PTZ. To obtain recording data with comparable variation in frequencies without PTZ, we introduced the 'autocorrelogram sorting' method, which utilizes instantaneous firing frequency (Fig. 2). For this purpose, we first conventionally constructed the spike autocorrelogram based on a sequence of spike firings (Fig. 2A). The usual columnar pattern of an autocorrelogram was then expressed in raster fashion (Fig. 2B). The dot rows constituting the raster autocorrelogram were sorted with the instantaneous firing frequency at $\Delta=0$ as the sorting key in the following manner. In each horizontal row of dots, the interspike interval was measured between the reference spike at $\Delta=0$ and the spike immediately preceding it. Then, from this interspike interval, the instantaneous firing frequency at $\Delta=0$ was calculated and used as the key for sorting the dot rows along the y-axis. After sorting, the dot rows were re-arranged, so that rows with lower instantaneous firing rates at $\Delta=0$ are located at the lower positions in the diagram obtained after sorting (Fig. 2C). The dot rows were grouped according to the instantaneous firing frequency at $\Delta=0$, in such a way that the frequency for the nth group could range from $n-1$ Hz to n Hz (Fig. 2D). For each frequency group, the conventional autocorrelogram was reconstructed (Fig. 2E), thus yielding a frequency-specific autocorrelogram.

The post-spike portion (Fig. 2E, right half) of the frequency-specific autocorrelogram was then divided into bins of 2 ms duration each. For each of the first 6 bins covering the initial 12 ms post-spike, the autocorrelogram value corresponding to a specific instantaneous frequency was calculated. Then, for each bin, the same procedure was applied to the autocorrelogram values that represented the other frequency ranges. Separately for each of the 6 bins, frequency-specific autocorrelogram values based on one unit were obtained for all the frequency ranges examined (instantaneous firing rate between 0 and 20 Hz; Fig. 3). The results obtained from 73 units in total were combined and plotted (Fig. 3).

Using this 'autocorrelogram sorting' method, we attempted to determine the dependence of autocorrelation on the immediately preceding history of firing. For each post-spike bin, the frequency-specific autocorrelogram values were plotted against frequency in a bar graph (Fig. 3). A significant

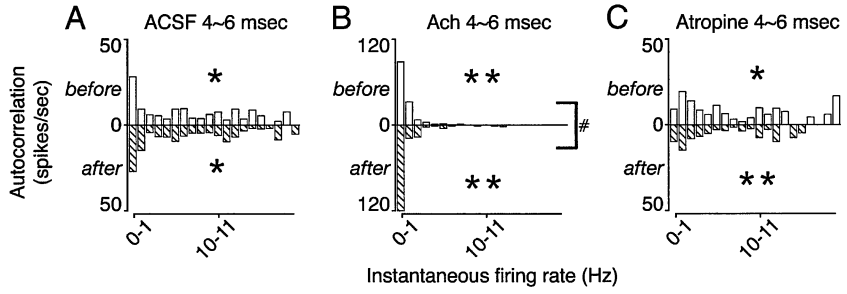

Fig. 4 – Cholinergic modulation of the activity dependence of the autocorrelogram. The autocorrelogram sorting methods were applied to unit recordings before and after administration of ACSF (A, $N=73$), acetylcholine (B, $N=19$), or atropine (C, $N=22$). Diagrams were drawn in the same fashion as for Fig. 3, but for the 4–6 ms post-spike period only. The data based on recording for 50 sec shortly before the injection, or on 500 firings recorded during the same time period, were plotted upward (*before*; white bars). The corresponding data obtained after injection were plotted downward (*after*; hatched bars). Acetylcholine injection enhanced activity dependence. On the other hand, there was a tendency for degree of activity dependence to decrease with atropine injection, though not to a significant extent. *$P<0.05$; **$P<0.01$ (Kendall's τ tests). #$P<0.05$ (Sen and Adichie's asymptotically distribution free tests for parallelism).

negative correlation was found between autocorrelogram value and firing frequency for the time period after 4 ms post-spike, with Kendall's τ values of −0.349 ($P<0.05$), −0.737 ($P<0.01$), and −0.453 ($P<0.01$) for 4–6, 6–8, and 8–10 ms post-spike, respectively. For the time period after 10 ms post-spike, a negative correlation was still detected (Kendall's $\tau=-0.316$), although it was no longer significant. The correlation was most strongly negative from 6 to 8 ms post-spike. Autocorrelogram values were exactly or nearly zero before 4 ms post-spike, reflecting the refractory period.

2.4. *Cholinergic effects on the activity dependence of autocorrelation*

Using autocorrelogram sorting, we examined pharmacological effects on the negative correlation between the autocorrelogram and instantaneous firing frequency. For control purposes, comparison was made between the correlations before and after ACSF microinjection (Fig. 4A). Bar graphs were constructed based on 41 unit recordings obtained before (Fig. 4A, top) and after the microinjection (Fig. 4, bottom). We focused on the time period between 4 and 6 ms post-spike, which undoubtedly represents the time window after termination of the refractory period but prior to initiation of GABAergic feedback inhibition. ACSF microinjection did not induce a significant difference in the correlation coefficient for this time period (Sen and Adichie's tests; Hollander and Wolfe, 1999). On the other hand, acetylcholine (Ach) injection made the correlation coefficient significantly more negative ($P<0.05$, Sen and Adichie's method; $N=19$; Fig. 4B). Injection of atropine tended to have the opposite effect, though it did not significantly change the correlation coefficient ($N=22$; Fig. 4C).

3. Discussion

The present study demonstrated the presence of a feedback mechanism intrinsic to hippocampal single neurons that suppresses spike firing in activity-dependent fashion. This mechanism appears to be independent of membrane refractoriness and the synaptically based feedback inhibition that involves GABAergic neurons. Experiments with the convulsant PTZ and analysis with our autocorrelogram sorting method suggested that spike suppression by this mechanism becomes stronger when instantaneous firing frequency is increased. It was also found that this mechanism is reinforced by muscarinic activation.

This feedback mechanism is intrinsic to single cells, in that no transsynaptic feedback circuits are involved in it. Its occurrence is too late to be attributed to the absolute refractory period or channel inactivation, and too early to be explained by transsynaptic mechanisms including GABAergic feedback inhibition. Hippocampal pyramidal neurons are known to receive feed-forward inhibition via inhibitory GABAergic interneurons that are excited by the same afferents as innervate the pyramidal neurons (Freund and Buzsaki, 1996). Schaffer's collateral stimuli are known to elicit a sequence of excitatory postsynaptic current followed by inhibitory postsynaptic current, with an approximately 2 ms delay (Pouille and Scanziani, 2001), representing feed-forward inhibition. This inhibition is evoked by incoming afferent volleys, and it occurs independently of the firing of neurons that are subject to it. Therefore, as far as feedback regulation of spike firing is concerned, the effects of feed-forward inhibition appear to be statistically random and to constitute a time-independent, background.

The underlying mechanism that appears to be responsible for the present feedback mechanism is spike-frequency adaptation (SFA). SFA yields activity-dependent suppression of spike firing, in which calcium channels serve as detectors of neural activity and allow calcium ions to flow in. The calcium increase caused by calcium channels activates the small conductance calcium-activated K (SK) channels, thereby reducing neural excitability (Sah, 1996). Activity-dependent opening of SK channels is observable after each spike in the form of spike after-hyperpolarization. There thus appears to be no reason to exclude SFA as a candidate for the mechanism underlying the present feedback regulation.

However, a question of considerable importance here is how the cholinergic reinforcement of this feedback regulation can be explained. Most of the known types of cholinergic regulation of membrane excitability favor up-regulation of excitability, rather than down-regulation, as follows. First, blockade of K channels that generate the M currents (MK channels) by mAchR activation is known to increase spike firing (Marrion, 1997). However, this effect is independent of firing frequency, and will increase excitability. The present findings thus cannot be attributed to MK channels. Second, it has been reported that muscarinic activation reduces SFA, and that spike after-hyperpolarization is converted to spike after-depolarization. This conversion of polarity is thought to be due to AchR-mediated activation of calcium-activated cation channels, which predominates over the hyperpolarizing bias of SK channel activation in forebrain neurons (Haj-Dahmane and Andrade, 1996, 1998; Fransen et al., 2002). Here again, AchR-mediated mechanisms work in favor of increase in excitability rather than decrease. Third, activation of some subtypes of mAchRs (M2 and M4) is known to increase cAMP concentration, which in turn is known to reduce spike after-hyperpolarization in hippocampal pyramidal cells and thereby spike-frequency adaptation as well (Madison and Nicoll, 1986). This is again a mAchR-mediated elevation, instead of reduction, of membrane excitability, and cannot explain the intrinsic suppression we observed.

Notably, we have recently documented muscarinic receptor-mediated reduction of membrane excitability in neocortical pyramidal cells (Yamamoto et al., 2002a,b). In these experiments, inositol-1,4,5-trisphosphate (IP_3) receptors (IP_3Rs) were primed first by AchR-mediated increases in IP_3 concentration. Calcium sites of IP_3Rs were then occupied by calcium due to spike-induced calcium influx, thus finally activating IP_3Rs. This IP_3R activation triggered calcium release from IP_3Rs, leading to supra-linear enhancement of spike-induced calcium increase. We call this type of calcium release IP_3-assisted calcium-induced calcium release (IP_3-assisted CICR; Yamamoto et al., 2000). The spike-induced calcium influx and IP_3-assisted CICR, when combined, open SK channels to a greater extent than does calcium influx alone (Yamada et al., 2004). The result of this is a supra-linear increase in SK channel opening, which reinforces SFA. This mechanism clearly offers a

reasonable explanation for cholinergic reinforcement of the feedback regulation we observed. However, determination of whether this mechanism actually underlies the suppression we observed will require further in vivo study.

The cholinergic effects on the present feedback regulation appear to be complicated, since atropine did not significantly change the correlation coefficient in the present experiments. However, the present results clearly offer the following two interpretations. First, some mechanisms of negative feedback regulation of spike firing, which are effected non-synaptically and completed solely by machinery within single cells, can exist without muscarinic cholinergic activation. Second, cholinergic mechanisms are nevertheless able to reinforce such negative feedback regulation mechanisms when agonists are applied or cholinergic inputs are activated.

The sudden development of abnormally high, uncontrollable excitability is a feature of some neurological disorders such as epilepsy. Although pharmaceutical manipulation of neural excitability appears to be a powerful means of treating such disorders, normal brain function may also be affected by non-specific treatment that continuously suppresses neural activity. If neural excitability is suppressed exclusively in neurons that discharge abnormally, baseline brain function would remain unaffected. Ideal treatment of this type may be implemented by cholinergic reinforcement of the feedback mechanism we observed. Given its independence of GABAergic inhibition, this mechanism could be exploited in pharmaceutical treatment of patients with intractable epilepsy, in which GABAergic neurons are decreased in number (Savic et al., 1988; Coulter, 2001; Richardson et al., 2001; Bouilleret et al., 2002; Szelies et al., 2002) or may become excitatory with a positive shift of reversal potential (Khalilov et al., 2003; Fujiwara-Tsukamoto et al., 2003).

4. Experimental procedures

4.1. *Animals and surgery*

All the experiments were performed under approval of the Animal Welfare Committee of the Kyoto University Graduate School of Medicine, and in accordance with the Guiding Principles for the Care and Use of Animals of the Physiological Society of Japan. Thirty male adult Wistar rats weighing 200–250 g were obtained from our in-house colony. Under chloral hydrate anesthesia (360 mg/kg i.p., supplemented as needed), the rats were placed in a stereotaxic frame (Narishige, Japan). After incision of the scalp, the parietal region of the skull was exposed and a small hole was made with a dental drill. The dura was then cut with needles to expose the pia. The pial surface was kept moist with artificial cerebrospinal fluid (ACSF) throughout electrophysiological experiments.

4.2. *Electrophysiological recordings*

Single or multi-barrel glass microelectrodes were used. The multi-barrel microelectrodes were hand-made by bending and gluing straight glass pipettes with internal fibrils (GC-1, Narishige, Tokyo; external diameter, 1 mm). Microelectrodes were set to a microdrive (Narishige, MO-81). ACSF consisted of the following (in mM): NaCl, 124; KCl, 3; $NaHCO_3$, 26; NaH_2PO_4, 1.3; $CaCl_2$, 2.5; $MgSO_4$, 2; glucose, 20. The three electrode barrels were each filled with ACSF, a pontamine sky blue solution (2%, v/v, in 0.5 M Na-citrate), and one of the following drugs: sodium glutamate (0.1 M), acetylcholine chloride (Ach, 1 M), or atropine (0.5 M) dissolved in ACSF. The drugs were microinjected using a Picospritzer II (General Valve Corp.). The parameters used for microinjection were determined and repeatedly confirmed by evident increase in firing rate, by applying glutamate (0.1 M) to units that were separately recorded during intermission periods in every experiment. For some experiments, the convulsant pentylenetetrazole (PTZ) was administered (i.p., 100 mg/kg body weight) to increase firing rates. In some animals, repetitive administration was performed at 1-h intervals. For data acquisition, a Spike II recording system (Cambridge Electronic Design) was used. All drugs were purchased from Nakalai Ltd. (Kyoto, Japan). After the experiments, the rats were perfused with a 4% paraformaldehyde solution and the brain was removed and histologically examined for electrode tracks and recording locations.

4.3. *Data analysis*

To reduce the number of units recorded, high (~60 MΩ)-impedance glass electrodes were used. Furthermore, separation of spikes to a single unit was performed by Spike II software. Spike trains were analyzed by standard autocorrelation techniques (e.g., Abeles, 1991). Moreover, a special variation of autocorrelographic analysis ('autocorrelogram sorting') was applied to firing data obtained for 50 s or periods containing 500 spikes. Details of this method are described in the Results, making use of a unit recording as a typical example. Statistical analyses were performed using nonparametric methods (Hollander and Wolfe, 1999).

Acknowledgments

The authors thank Professor Kenji Kawano for encouragement. This work was supported partly by a Grant for Collaborative Research (C2006-5) from Kanazawa Medical University.

REFERENCES

Abeles, M., 1991. Corticonics. Neural Circuit of the Cerebral Cortex. Cambridge University Press, Cambridge.

Bouilleret, V., Dupont, S., Spelle, L., Baulac, M., Samson, Y., Semah, F., 2002. Insular cortex involvement in mesiotemporal lobe epilepsy: a positron emission tomography study. Ann. Neurol. 51, 202–208.

Coulter, D.A., 2001. Epilepsy-associated plasticity in gamma-aminobutyric acid receptor expression, function, and inhibitory synaptic properties. Int. Rev. Neurobiol. 45, 237–252.

Dayan, P., Abbott, L.F., 2001. Theoretical Neuroscience. Computational and Mathematical Modeling of Neural Systems. The MIT Press, Cambridge, MA.

Eccles, J.C., 1953. The Neurophysiological Basis of Mind: The Principles of Neurophysiology. Clarendon Press, Oxford, UK.

Fransen, E., Alonso, A.A., Hasselmo, M.E., 2002. Simulations of the role of the muscarinic-activated calcium-sensitive nonspecific cation current INCM in entorhinal neuronal activity during delayed matching tasks. J. Neurosci. 22, 1081–1097.

Freund, T.F., Buzsaki, G., 1996. Interneurons of the hippocampus. Hippocampus 6, 347–470.
Fujiwara-Tsukamoto, Y., Isomura, Y., Nambu, A., Takada, M., 2003. Excitatory GABA input directly drives seizure-like rhythmic synchronization in mature hippocampal CA1 pyramidal cells. Neuroscience 119, 265–275.
Haj-Dahmane, S., Andrade, R., 1996. Muscarinic activation of a voltage-dependent cation nonselective current in rat association cortex. J. Neurosci. 16, 3848–3861.
Haj-Dahmane, S., Andrade, R., 1998. Ionic mechanism of the slow afterdepolarization induced by muscarinic receptor activation in rat prefrontal cortex. J. Neurophysiol. 80, 1197–1210.
Hille, B., 2001. Ion Channels of Excitable Membranes, 3rd ed. Sinauer Associates, Sunderland, MA.
Hollander, M., Wolfe, D.A., 1999. Nonparametric Statistical Methods, 2nd edition. Wiley-Interscience, New York.
Karnup, S., Stelzer, A., 1999. Temporal overlap of excitatory and inhibitory afferent input in guinea-pig CA1 pyramidal cells. J. Physiol. 516, 485–504.
Khalilov, I., Holmes, G.L., Ben-Ari, Y., 2003. In vitro formation of a secondary epileptogenic mirror focus by interhippocampal propagation of seizures. Nat. Neurosci. 6, 1079–1085.
Madison, D.V., Nicoll, R.A., 1986. Cyclic adenosine 3′,5′-monophosphate mediates β-receptor actions of noradrenaline in rat hippocampal pyramidal cells. J. Physiol. (Lond.) 372, 245–259.
Marrion, N.V., 1997. Control of M-current. Annu. Rev. Physiol. 59, 483–504.
Pouille, F., Scanziani, M., 2001. Enforcement of temporal fidelity in pyramidal cells by somatic feed-forward inhibition. Science 293, 1159–1163.
Richardson, M.P., Hammers, A., Brooks, D.J., Duncan, J.S., 2001. Benzodiazepine–GABA(A) receptor binding is very low in dysembryoplastic neuroepithelial tumor: a PET study. Epilepsia 42, 1327–1334.
Sah, P., 1996. Ca(2+)-activated K^+ currents in neurones: types, physiological roles and modulation. Trends Neurosci. 19, 150–154.
Savic, I., Persson, A., Roland, P., Pauli, S., Sedvall, G., Widen, L., 1988. In-vivo demonstration of reduced benzodiazepine receptor binding in human epileptic foci. Lancet 2, 863–866.
Szelies, B., Sobesky, J., Pawlik, G., Mielke, R., Bauer, B., Herholz, K., Heiss, W.D., 2002. Impaired benzodiazepine receptor binding in peri-lesional cortex of patients with symptomatic epilepsies studied by [(11)C]-flumazenil PET. Eur. J. Neurol. 9, 137–142.
Yamada, S., Takechi, H., Kanchiku, I., Kita, T., Kato, N., 2004. Small-conductance Ca^{2+}-dependent K^+ channels are the target of spike-induced Ca^{2+} release in a feedback regulation of pyramidal cell excitability. J. Neurophysiol. 91, 2322–2329.
Yamamoto, K., Hashimoto, K., Isomura, Y., Shimohama, S., Kato, N., 2000. An IP_3-assisted form of Ca^{2+}-induced Ca^{2+} release in neocortical neurons. NeuroReport 11, 535–539.
Yamamoto, K., Hashimoto, K., Nakano, M., Shimohama, S., Kato, N., 2002a. A distinct form of calcium release down-regulates membrane excitability in neocortical pyramidal cells. Neuroscience 109, 665–676.
Yamamoto, K., Nakano, M., Hashimoto, K., Shimohama, S., Kato, N., 2002b. Emergence of a functional coupling between inositol-1,4,5-trisphosphate receptors and calcium channels in developing neocortical neurons. Neuroscience 109, 677–685.

金医大誌（J Kanazawa Med Univ）32：73－81, 2007

電撃けいれん療法の神経生物学的基盤
－うつ病成因のGABA仮説との接点－

加　藤　伸　郎

要　約：うつ病治療において，電撃けいれん療法（ECT；Electroconvulsive Therapy）への期待は大きい。ECTの生物学的根拠を明確化することにより，ECTの改良や新規薬物治療コンセプトへとつながる可能性がある。ECTの後に発現が高まる分子は多数報告されているが，それらの機能解析はほとんど進められていない。そのひとつHomer1aは最初期遺伝子の産物である。私共はHomer1aの機能解析を行い，ニューロンへの興奮抑制作用を見出した。さらに，ECTの効果のひとつが興奮抑制であって，その際Homer1aがECTのメディエーターとなっていることも解かった。臨床データに基づく研究から，うつ病者の大脳皮質では抑制性神経伝達物質GABAの濃度が低下し，興奮抑制の損なわれていることが知られている。うつ病成因のGABA仮説によれば，これがうつ病の成因であり，ECTなどの抗うつ治療はこれを是正するとされる。私共の神経生物学的研究は，ECTが単一ニューロンレベルにて興奮抑制をもたらすことを明らかにし，このGABA仮説を支持する結果となった。

キーワード：　うつ病，電撃けいれん療法，GABA仮説，興奮抑制，Homer

1　はじめに　―ECTとは何か―

自殺の背景にはうつ病がある(1)。うつ病の治療アルゴリズムの中で，電撃けいれん療法（ECT；Electroconvulsive Therapy）は重要な位置を占めている(2,3)。一方，この治療法には歴史的にネガティブなイメージも形成されてきた。これを払拭できれば，うつ病治療にECTをより一層役立て，高い自殺死亡率の低減化という国民的課題に貢献させることができる。この面から，3点の改善が考えられる。第一にはECTの方法面での改良であり，これは麻酔や筋弛緩の併用による修正型ECTとして，すでに実現されつつある。第二には，装置面の改良が考えられ，電源として交流波を使う1930年代来の原初型の治療器から，パルス波を使うパルス波治療器への転換が始まっている。これらに加えて，第三にとりくむべき改善点として私共が希求するのは，ECTの生物学的根拠の明確化である。何故ECTには絶大な治療効果があるのか，という疑問はこれまで放置されてきたと言って過言ではない。今日に至るまで，神経生物学的説明は欠落している。この解明により，ECTの生物学的本質を抽出できれば，より低侵襲で相同な効果が得られるようにECTを改良することや，従来とは全く異なる薬物治療コンセプトを提案することも可能となろう。また，より深い理解と得心に裏打ちされたインフォームドコンセントの実現が期待できる。

ECTの歴史はルネッサンスに遡る。パラケルススは錬金術師でありながら，近代医学の父とも称される二面性を持ち，樟脳(カンフル)によって精神病者にけいれんを起させることで治療を試みたと伝えられている。ECTの近代的な試みは，1934年にフォン・メドゥーナが同じ樟脳によるけいれん療法を報告したところからである。その後，樟脳のほかペンチレンテトラゾール（PTZ）もけいれん誘発剤として使用された。PTZは今日でも動物実験に用いられるけいれん誘発薬であり，私共も最近これをラット腹腔へ投与してけいれんを発生させ，その際のニューロン活動の高揚を確認し，これを利用してニューロン興奮性のフィードバック調節機構を研究した(4)。ケルレッティは薬物ではなく通電によってけいれんを起すことを試み，まず犬で成功した。1938年には統合失調症患者に通電によるけいれん療法を行い，定圧通電80V・0.2秒では臨床効果なく，110Vに電圧を高めて奏功したと報告している。翌1939年には日本でもECTが開始された。その後，優れた薬物が発明されて薬物療法が台頭したため，電撃けいれん療法は下火となった。しかし，その間にも改良の努力は続けられ，治療方法の改善として，ペントバルビタールと筋弛緩剤サクシニルコリンを投与して行う修正型ECTが1950年代に導入された。1980年代になるとパルス波治療器が導入され，実施機器の改善が進み，この治療器は日本でも

金沢医科大学医学部生理機能制御学
石川県河北郡内灘町大学1-1
平成19年10月16日受理

2002年に厚生労働省の認可を受けた。パルス波にてニューロンを興奮させるほうが，サイン波（通常の交流）を使うよりもエネルギー効率の高いことは，興奮性膜に関する電気生理学的研究から数十年来明らかとなっており，これは哺乳類の中枢ニューロンにおいても確認されている(5)。1990年前後から，薬物療法の限界が指摘されるようになり，ECTもリバイバルを迎えることとなる。現在も，修正型ECTとパルス波治療器の普及を軸とする改善努力が進められている。

2　ECTの分子生物学

ECTの生物学根拠は未解明であるが，端緒的な研究が全く無いわけではない。分子生物学的研究だけは一歩先行しており，ECTの後に発現が高まる分子が多数報告されている。脳由来神経栄養因子（BDNF; Brain-derived neurotophic factor）は，ECTによって発現の高まることが最も初期に確認された分子のひとつであり，また抗うつ剤によっても発現してくることが知られている(6,7)。BDNFはそもそも，脳の正常発達や損傷後の代償性変化において，神経細胞の増殖・分化を促す物質として広く知られている。一方でうつ病の成因論として神経生育不全説が広く流布して来ており，うつ病治療におけるBDNFも含めた成長因子の果たす役割が注目されることになった。神経生育不全説とは，神経細胞が発達期に形成不全のために量的に充分ではなかったり，あるいは一旦は充分に生育しても成熟後にストレスによって失われたりして，それが海馬の容積縮小などとして表面化し，細胞の形成不全や脱落に基づく機能的ロスが本質的な背景として存在するところへ，さらなるストレスなどが切っ掛けとなって，うつ病など精神疾患発症への引き金が引かれるとする仮説である(6,8-12)。

神経生育不全説では，BDNFなどの成長因子は，神経細胞新生を促したり細胞死を阻止したりすることを通じて，ストレスによるニューロン喪失を補償し，精神疾患の治癒へ導くとされる。ECTによってBDNF発現が高まったり，恐らくはその結果として，歯状回からの出力線維である苔状線維の分枝や，歯状回のニューロンそのものが増殖したりすることも報告されている(13-18)。これはすなわち，この仮説で提示された発病への経過を，ECTが逆回転させて治療へ導くことを示唆する。薬物治療の面でも，抗うつ薬投与による成長因子の機能強化や神経新生が知られている(19-21)。また，ECTによるBDNF発現強化の分子的仕組みを調べる研究も報告されており，BDNFプロモーターのヒストンによる修飾の重要性が指摘されている(22)。ECTによって発現（転写）強化された蛋白質が別な転写機構を強化し，その結果発現したタンパク質がさらに別の転写機構を強化するというネットワークが複雑に形成されるならば，ECTの効果の持続性をうまく説明してくれるかもしれない。すなわち，BDNFなどの一過性発現で説明できるよりもはるかに長期間，ECT効果の持続する仕組みが，転写調節ネットワークの強化によって説明できるかもしれない(23,24)。

ターゲットを成長因子だけに絞ったマイクロアレイチップを用いた実験により，海馬における新規遺伝子グループの発現変化が調べられ，VEGF(Vascular endothelial growth factor)，VGF，線維芽細胞増殖因子などをはじめBDNF同様に神経新生や増殖を促す働きを持つ分子の発現強化が見出され，これらのいくつかは血管増殖作用も持つ因子であった(25)。ECTによる発現が既知である分子のなかでは，BDNF・Cox-2・転写因子（EGR3など）の発現増加が目立っている。加えて彼らは，脈絡膜叢での発現も調べ，成長因子のいくつかが発現強化されているのを見出した。このように神経組織と血管組織で血管増殖に関わる成長因子が発現してくることから，ECTには血管増殖作用があって，これが新生してくる神経細胞による組織増大を血流面からサポートしているのかもしれないとも考えられる。すなわち，ECTは一方では神経組織を増大させ，他方でそれを支えるために血管も増殖させているとする考え方である。Newton et al.(26)は血管増殖に関わるメディエーターが上昇するだけでなく，実際に血管が増殖することまで見出した。こうして神経生育不全説を支持する分子的所見が蓄積されつつある。

Neuroprotectionに関連する遺伝子の発現増大も知られている(27)。PloskiらはBDNFなど従来知られていた遺伝子群と並んで，新規にNuclear factor of activated T-cells 5やNeuropeptide Yの大量発現，およびTRHや海馬歯状回限定的な興奮性アミノ酸トランスポーター(EAAC1)の発現などを見出した。EAAC1には神経保護作用があり，他にECTで発現増加するアンチアポトーシス因子のGadd45betaと相まって，アポトーシスからのレスキュー効果を示唆する。これらの結果はうつ病成因の神経形成不全仮説と相容れ，なかでも歯状回における細胞保護作用は，この仮説の核心を支持するものである。

従来の精神疾患成因論としてのモノアミン仮説と，ECT関連分子とのつながりはどうだろうか。相容れる所見として，治療後に比較的速やかに効果が発揮されると期待できるECTではカテコルアミン伝達系が増強されるように作用し，遅発効果を持つ抗うつ薬であるフルオキセチンはセロトニン伝達系を強化するという結果が，ラット脳においてゲノムマイクロアレイを適用した実験から見出されている(28)。しかし，彼らはBDNFやHomerなどの発現増加も追認し，神経生育不全説も支持する結果となっている。一方，Algarら(29)ではBDNF・Homer・COX-2の発現強化は強調されているものの，モノアミン伝達系関連分子群の転写における大きなは変化は記載されていない。サルのECTモデルでセロトニン5HT 2 受容体へのバインディングが低下するという結果が出ているが，これが何らかの分子発現と関係あるかどうかは不明である。Svenningssonら(30)によると，p11というタンパク質はうつ病モデル動物でもうつ病患者でも低下し，逆にECTまたは薬物によって増加してセロトニン5HT1B受容体の機能を強化する。このように，ECTで発現強化される蛋白質の働きは，神経新生を促すことなど神経発育不全学説の枠組みで理解できる場合もあれば，モノアミン伝達

系の強化など従来のモノアミン仮説と整合することもある。GDNF (グリア細胞由来神経栄養因子) はモノアミン伝達系に含まれるドパミン作動性ニューロンにとっての成長因子としても知られているが，これがECTで発現増大するという報告(14) は興味深い。なぜなら，この結果は，ECTによって発現する成長因子が神経細胞一般の新生を促すという神経生育不全説に整合するだけではなく，モノアミン系特異的な細胞新生や細胞維持が図られることも示唆しているからである。これはすなわち，神経生育不全仮説のモノアミン伝達系特異的な具現であり，精神疾患の神経発育不全仮説とモノアミン仮説の統合を意味するとも解せる。

ここまで紹介してきたように，ECTによる分子発現の報告は多様である。また，特定の仮説との適合性を目的として研究するなどの際には，初めから意図して，ターゲットとなる分子の範囲を限定している場合もある。また，探索分子の範囲を限定しないような手法を用いた実験においても，サンプルの採取範囲が適切であるかどうかは重要である。特定の神経核に限局して高い発現が見られる場合には，その神経核を含めた広い範囲の脳組織からサンプルを得ている場合，発現量は平均化されて過小評価されることになる。逆に，脳の至る所で軽度の発現が見られるような分子群では，過大評価されることになる。そのような場合には，マイクロダイセクションによって特定の神経核からだけサンプルを得ることも必要であることが指摘されている(27)。さらには，たとえ同じ神経核内といえども，抑制性と興奮性ニューロンは隣接している。抑制性など特定の性質を持つニューロンにのみ特異的な発現がある場合には，神経核全体における発現量に注目していたのでは重要な知見を見落とすことになる。これを避ける究極の手段は，たとえば注目するmRNAの発現をcDNAプローブで組織学的に同定しつつ，他のマーカーで個々のニューロンの性質を確認することなどである。このように様々な理由により，ECTによって発現強化が報告されている分子のレパートリーは，研究グループごとに多かれ少なかれ異なる。しかし大きく眺めれば，多くの研究グループが共通して発現強化を報告している分子群があり，その代表例としてBDNFを筆頭とする成長因子群とHomer1aやCOX-2を含めた最初期遺伝子群の2グループを挙げることができると思われる。

3　ECT関連分子の機能解析

ECTによって発現する分子群は前節に記したように多彩であるが，発現強化される分子の中に，精神疾患の成因に関する伝統的仮説や最新の成因論と接点をもつものが含まれていることは重要である。また，接点を持たない分子の存在は新たな理論的枠組み形成を促しているとも考えられ，新規治療法の可能性を示唆するものでもある。しかし発現強化されるという事実だけでは，精神疾患の生物学的病態生理やECTの作用メカニズムの分子からのボトムアップな説明とはならない。そのためには，これらの分子生物学的研究によって探索されたECT関連分子が個々のニューロンやシナプスさらに神経回路にどのように働くかを知る必要がある。そして，ニューロンや神経回路への作用がわかっても，抑うつ感の醸成や解消の説明までのギャップは大きく，どんなに単純化したとしても精神疾患モデル動物を使った行動レベルでの解析を併用せねばならないだろう。

そのようなボトムアップ的研究に向けて一歩踏み出すにあたり，まずは一個のECT関連分子にしぼって，そのニューロン作用を調べるという最も単純な試みを私共は始めた。いっそうの単純化のために，まずは慢性ECTではなく急性ECTをラットに施すというモデル化を行い，ECT施行後24時間以内の作用を調べた。数あるECT関連分子の中で比較的発現増大の程度が大きく，知見が多くのグループによって固く追認されているような分子群は，成長因子 (特にBDNF) と最初期遺伝子にコードされた蛋白質であるが，急性ECT作用と関連の深いと考えられるのは最初期遺伝子産物である。その中でも神経細胞内で作用し，普段の脳活動においても神経細胞内での発現が増減することの知られているHomerにターゲットを絞った。Homerグループのなかで最初期遺伝子産物はHomer1aであり，他のほとんどは常時発現している。一般に最初期遺伝子の発現は活動依存的であり，Homer1aも例外ではない。そして，ここでの活動依存とはすなわち，ECTによる神経細胞の電気活動に依存していることであると理解できる。まずHomer1aを蛋白質として別途に作製して，ラット大脳皮質にある単一ニューロンの内側へ投与し，そのニューロンの反応を調べることから始めた(31,32)。このようにHomer1aから始めたのは，最も重要と思われたからではなく，これによって実験を最も単純にすることができるからである。

Homer1aを最初に細胞内注入して私共が見出したのは，ニューロンの興奮抑制である。注入後，数分の時間経過で静止膜電位が深くなっていった (図1C)。すなわちニューロンの興奮性が低下していった。これと呼応して，一定強度の電流を細胞内へ流してニューロンの反応を見た場合，Homer1a注入例では反応が低下していた(31)。しかし，この実験結果だけからECTとの関連を論ずるのは性急である。いくつもの懸念が浮かぶ。たとえば，ここで見出された作用は数あるHomer1aの作用のうちのひとつであり，これ以外の作用こそがECTの効果を媒介しているかもしれない。これと関連して，ここで注入した濃度はECTで発現するHomer1aよりもはるかに高濃度である可能性もあり，その場合にはECTとは関連のない作用を見ていることになってしまう。そこで，Homer1aとECTの関連を明確化するために，次に述べるような実験を行った。

私共の目標は，Homer1aが確かにECTのメディエーターであることを確かめ，どの側面をメディエートするかを知ることである。そのために，まず，モデルECTを施行したラットからスライスを作製して，Homer1aと同等の過分極が得られるかを調べた。その結果，Homer1aを注入しなくとも，Homer1a注入例

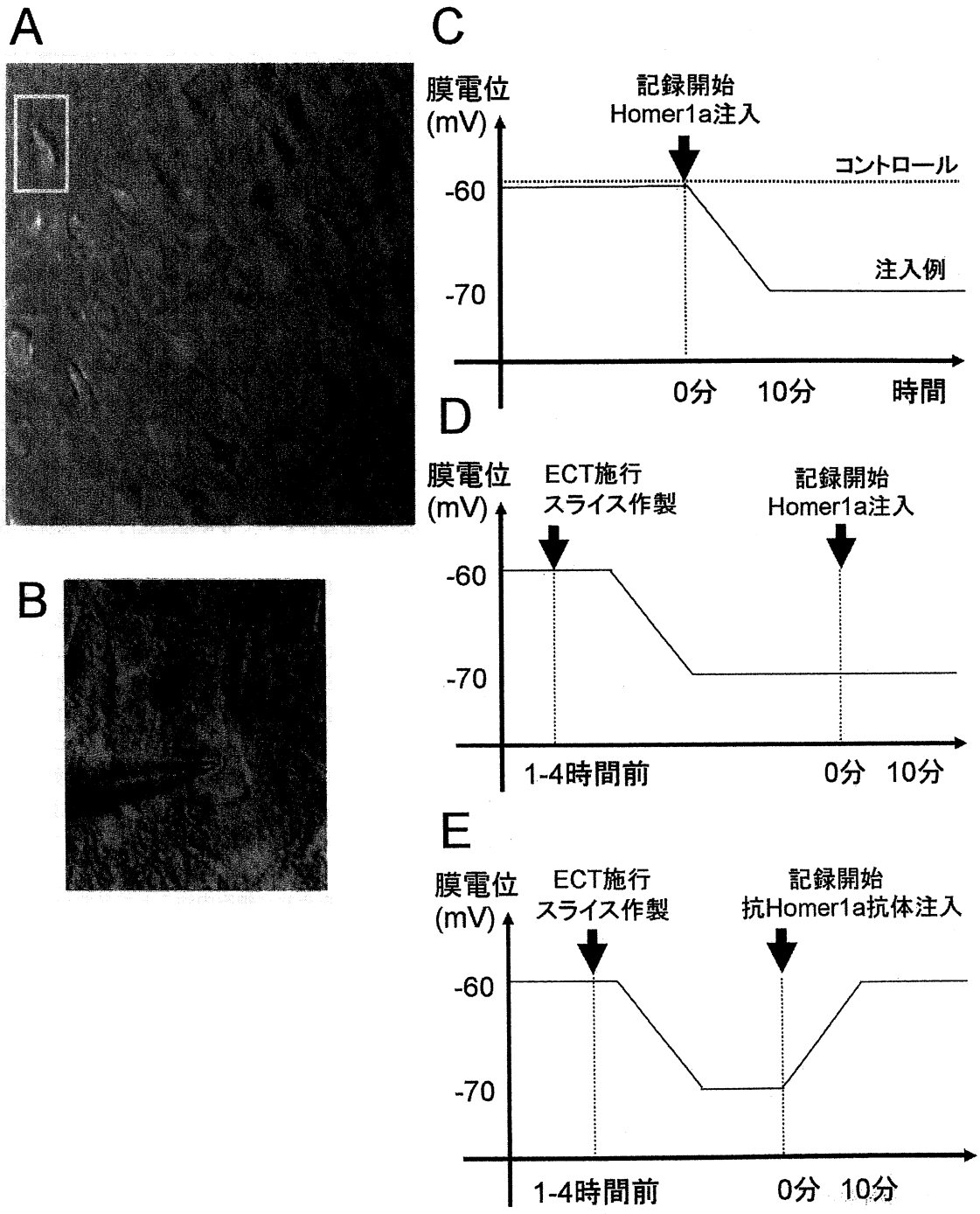

図1．ECTによって発現したHomer1aタンパク質が引き起こす過分極。
実験はラット大脳皮質視覚野から得たスライスを用いてvitroで行った。方法は別稿(31,32) に記述したが，ここでも簡潔に記す。まずスライスを顕微鏡下で観察し，記録すべきニューロンを1個選ぶ (A,白長方形内)。記録に用いたパッチクランプ法では，先端が直径1ミクロン程度まで細くなったガラス管を選んだニューロンに押し当て，吸引してシールした後，ガラス管先端部分を覆う細胞膜を破断し，電流や電圧を計測する (B)。こうすることによって，細胞膜全体を流れる電流，あるいはその電流によって形成される電位差が計測できる。この方法をパッチクランプ法の中でも特にホールセル法と呼ぶ。また，このガラス管に予め特定のタンパク質を充填しておくと，拡散によって細胞内へ注入される。Homer1aをラット大脳皮質錐体細胞へ細胞内注入すると過分極が起こったが，その経過を模式的に提示する (C)。ただし，記録開始前の膜電位に関しては，実測に基づくものではなく，推測で遡って外挿した。ECT施行後のラットからスライスを作成して得た記録では，記録前から既に過分極していたと考えられ，Homer1aを注入しても，さらなる過分極は起こらない (D)。一方，アンチHomer1a抗体を注入すると，過分極がキャンセルされて，正常の静止膜電位が記録される (E)。

と同等の過分極が得られた(図1D)。またHomer1aを注入した場合でも，さらに過分極が進展することはなく，ECTによる過分極とHomer1a注入による過分極がメカニズムを共有していることがわかった(図1D)。すなわち，ECTがHomer1aを発現させ，そのHomer1aが過分極を起したという解釈の蓋然性が高まった。最後に，ECT例から作製したスライスにて細胞内に抗Homer1a抗体を注入すると，過分極は打ち消された(図1E)。この実験結果は，Homer1aがECT効果のメディエーターのひとつであることを意味する。そして，Homer1aはECTによって神経細胞に引き起こされる様々な事象のうち，特に興奮抑制を媒介するメディエーターとなっていることがわかる。

次の問題は，ECTが引き起こす諸事象のひとつが興奮抑制であったとしても，それがECTの抗うつ効果の構成要素となっているかどうかは必ずしも保障されないという点である。つまり興奮抑制作用とは全く関係ないところで，ECTが他の作用によって抗うつ効果を発揮しているかもしれない。この点をクリアすることは今後の課題であるが，うつ病モデル動物を使った行動実験との組み合わせが欠かせないと思われる。

4　うつ病成因のGABA仮説

私共の実験結果は，「ECTの抗うつ効果は興奮抑制の強化による」とする仮説を支持するか，または，少なくともこの仮説と矛盾しない。これまでのところ，この仮説は私共のテストをパスしている，と言い換えても良い。興味深いことに，次に述べるように，この仮説は臨床の場でのテストにも耐えている。以下の記述では，単にうつ病と記した場合には，単極性気分障害のなかの大うつ病 (DSM-IV) と見なして差し支えない。また，抑制強化が抗うつ効果を持つことは，一見，自家撞着に思えるかもしれないが，これを解く生理学的キーを本節の最後に記した。

うつ病者では大脳皮質の興奮性が亢進していることが報告されている。これは経皮質磁気刺激TMS (transcortical magnetic stimulation) を使って，脳外科手術をすることなく病者の脳を刺激し，大脳皮質運動野の興奮性または易刺激性を評価する手法に基づいている。この方法の基盤は，磁場が頭皮や頭蓋を容易に透過し，その時間変化は脳内で電流を発生させるという物理学的事実に尽きる。この方法を用いれば，私共生理学者がパッチ電極からニューロンに直接通電するのと等価の刺激を，臨床医も生きている人の脳で非観血的に実行できるのである。ただし，1個のニューロンではなくニューロン集団が対象となり，しかもどのあたりを刺激しているかという局在性のコントロール精度の低い点は異なる。皮質興奮性評価法としての使用は，例えば次のようなものである。まず，第一背側骨間筋から筋電図を取りながら，大脳皮質運動野の手の領域を狙って磁気刺激を与えるようにしておく。数ミリ秒のインターバルで2発刺激を与えるが，1発目は筋電図にかろうじて記録が現れるかどうかという強度 (閾値) よりも弱くしておき，これを条件刺激とする。2発目は閾値以上の刺激として筋電図を実際に発生させてその大きさを測定する。そして，条件刺激を先行させない場合を基準として，先行させた時にどれくらいの大きさに変化するかをパーセント表示する。これが100%以下であれば何らかの抑制が皮質内であった可能性がある。また，Kujiraiら(33) なども含めたMarsdenらのグループによる報告では，動物実験との対比から，この測定法で抑制性神経回路の強さを評価できると見なしている。抑制系はγアミン酪酸 (GABA) を伝達物質とし，GABA作動性抑制にはGABA-A受容体とGABA-B受容体に媒介される2つの抑制があるが，両者を区別して評価することができるとまで論じられている(34)。このような大脳皮質における興奮抑制の評価法を使って，うつ病者では抑制が低下していること，および運動に至る刺激閾値が低下していることが報告されている(35)。

うつ病者では抑制が低下しているのに対して，ECTで抗うつ治療を行った場合には逆過程が働く。すなわち治療によって抑制が強化されることが報告されている(36-38)。ECTを電流ではなく磁場の賦課によって実行する方法もあり，これはrTMS (repetitive transcranial magnetic stimulation) と呼ばれるが，この方法で治療した時にも，抑制の回復が見られる(34)。

うつ病における大脳皮質での抑制低下と合致する臨床所見として，うつ病者の脳内におけるGABA濃度低下が指摘されている。うつ病者の脳脊髄液におけるGABA濃度の低下は以前から知られていた(39)。GABAは抑制性の神経伝達物質であるから，この濃度が脳で低下しておれば，抑制システムにおける異常すなわち機能低下が示唆される。実際，うつ病患者の大脳皮質(後頭葉) でGABA濃度が有意に低下していることが報告されている(40)。これは，MR機器のひとつであるプロトン磁気共鳴スペクトロスコピー (H^+－MRS) を使って非観血的に計測された。彼らは同じH^+－MRSを使って，治療経過に伴って後頭葉にてGABA濃度の上昇の起こることを，ECT(41) とセロトニン再取り込み阻害剤 (SSRI) による薬物治療(42) の両方の場合で明らかにした。しかし，薬剤もECTも使わずに認知行動的な療法で治療効果を得た場合には，GABA濃度の上昇は無かった(43)。これは治癒効果全般と皮質内GABA濃度との関係を否定するわけでは必ずしもなく，GABA濃度が変化無くとも他の要因によって補償される場合もあり得ることを示唆しているとも考えられる。違った角度からの知見として，うつ病者の死後脳では，前頭葉にてGABA作動性ニューロンの減数が報告されている(44)。

GABA伝達系の動態に関連する動物実験として，GreenとVincentは繰り返してラットにモデルECTを施行した場合，脳スライスでのGABA放出は大脳皮質・海馬・基底核線条体で増加し，GABA生成速度や生成酵素GAD (Glutamic acid decarboxylase) 活性は大脳皮質では不変であるが，低下する部位もあるという結果を得ている(45)。部位差がある所見であり，しかも手法もかなり異なるので一概に比較できないが，少なくとも大脳皮質に限ってはECTによるGABA伝達系の強化が示

唆され，この点ではうつ病患者でのECT治療後のGABA濃度上昇(41) と一致している。このように，うつ病では大脳皮質におけるGABA濃度が低下していて，脳組織に直接働きかけるタイプの治療によってそれが反転するという所見は，皮質における抑制機構がうつ病者で低下していて，治療によってそれがやはり反転して抑制強化がおこるという所見とうまく合致している。Inghilleri et al(46) はGABA抑制を回復させる手段として，ベンゾジアゼパンによるGABA－A受容体メカニズムの強化が有効であることを示唆している。

このように抑制強化はうつ病治療として有効とされているが，抑制強化とは即ち興奮性を下げることであり，興奮性の過剰を特徴とするてんかんの治療とうつ病治療が共通である可能性が示唆される。この観点からSackeimら(47,48) は，ECTには抗けいれんが作用あり，それはけいれん誘発閾値の上昇や，脳血流(CBF) の脳全体での低下から窺えることを指摘し，さらに踏み込んで，抗けいれん作用と抗うつ作用の本質的連関性に言及している。Krystalら(49) は，GABA作用低下そのものよりも，グルタミン酸伝達系との相対的な力関係が成因として重要であると考えている。彼らは，単極性の大うつ病ではGABAの低下によって，双極性障害である躁うつ病ではグルタミン酸伝達系の過剰によって，どちらも相対的にGABA伝達系が劣勢となり，これが病態をもたらすとしている。そして，治療ではGABA伝達系を助けて，グルタミン酸系をくじく方略が奏功すると言うわけである。興味深いことに，躁うつ病に対して用いられているバルプロ酸とカルバマゼピンは，抗てんかん薬としても有用である。バルプロ酸はシナプスにおけるGABA濃度を増加させる作用を持っており，これはGABA伝達系の相対的優位へと導くことになり，抗躁うつ治療および抗うつ治療としてのGABA増強という考え方と整合する。「うつ病成因のGABA仮説」は，「GABA伝達系劣化仮説」および「グルタミン酸伝達系優勢によるGABA伝達系の相対的劣化仮説」という2つの表現型を持っていると考えるならば，単極性大うつ病と双極性躁うつ病の両者を含めた気分障害へと，より一層適用範囲が広まることになる。つまり，「うつ病成因のGABA仮説」を「気分障害成因の相対的GABA劣化仮説」へとアップグレードできる可能性もある。

ここで紹介した臨床的所見は，私共のラットモデルにおける結果(31) とよく整合する。私共はGABA伝達系の機能低下を見たのではなくて，ECTによる膜電位の深化を見たのであって，さらに分子的に正確に指摘すると，それはBKタイプKチャンネルの機能強化によるものだった。しかし，Kチャンネルが強化されれば，NMDA受容体に媒介される機能は低下することが期待され，Krystalら(49) によるGABA伝達系とグルタミン酸系のバランス崩壊とその修復が，うつ病と躁うつ病の発病と治癒に関連しているという考えに沿うことになる。また，Kチャンネル強化は興奮性低下をもたらし，Sanacoraらによる一連の臨床所見と合致する。運動皮質における脳内抑制がうつ病者で低下し，ECTによって強化される，というBajboujらの所見とも一致する。私共の実験はラットの後頭葉から得た脳スライスで行っているが，Sanacoraらもまた後頭葉からH^+－MRSの結果を得ているのは興味深い。

うつ病者における脳賦活を，SPECTなどによる脳局所血流(rCBF) の測定を用いて評価した研究もある。ただし，方法の原理に付随する問題として，rCBFは興奮または抑制ニューロンのどちらかだけの活動を反映するのではなく，両方のニューロンの寄与を含むことが挙げられる。すなわち，rCBFは両者の絶対的な活動の総和を反映してしまう。ところが，両者の活動の総和ではなく，相対的優劣あるいは対比こそが，局所脳賦活の強弱を決めるのである。よって，脳内抑制の評価という観点からは，rCBFは相当に間接的な手段となってしまう。実際の測定結果においても，うつ病者におけるrCBFの測定結果は測定者と測定条件によって，または測定された脳内部位によって偏差がある。Segawaら(50) はうつ病の程度が強くなればrCBFも増大するとしており，脳内部位差を指摘する報告(51) においても，大脳皮質においてはrCBFが増加するとしている。これらは抑制が弱くなってニューロン活動全般が強まった結果であると解釈すれば，うつ病成因のGABA仮説とよく整合する。また，難治性うつ病では辺縁系に属する皮質である25野における代謝亢進が報告されており，さらには25野をECTでなくて，深部電極による直接刺激で治療すると，rCBTが低下することも報告されている(52)。これは，うつ病者では，皮質興奮抑制の低下によってニューロン活動が全般的に亢進して，代謝や血流も増加し，そして治療により反転低下すると解すれば，うつ病成因のGABA仮説と良く整合する。一方，うつ病者でrCBFが低下するとする報告もある(53，および51における扁桃核などの所見)。これらの結果は，抑制系機能は低下しているが，それとは独立に興奮性ニューロンの活動がそもそも弱いと解するならば，GABA仮説と矛盾するものではない。いづれにしても，rCBTの所見は抑制と興奮ニューロンの活動を分解して評価するものではなく，うつ病成因のGABA仮説に対して是非を論ずる決定的な根拠たりえないと思われる。

大脳皮質でのGABA抑制を強化することが，症状としての抑うつの改善につながるという命題は，一見矛盾しているように思えるかもしれない。しかし，ニューロンレベルの抑制と，気分という高次なレベルでの抑うつ感とは直接に対応しているのではない。ニューロン活動が，神経回路網の活動を作り出し，それが気分も含めた行動レベルでの現象へとボトムアップ的に結実していく間に，この見かけの矛盾を解き明かすキーがいくつか隠されている。たとえば，ニューロン興奮の本態ともいえるナトリウムチャンネルの開口について考えてみよう。ナトリウムチャンネルは一旦開くと，数ミリ秒後には必ず閉じるという性質を持っていて，これを不活性化(inactivation)と呼ぶ。神経回路網における興奮性が高くなった後では，その回路網に属するニューロンにおいて不活性化に陥っているナトリウムチャ

ンネルの割合は高いと見なせる。その際，その回路網を新たに活動させようとしても，ナトリウムチャンネルが十分に開口しないために，期待通りに行かないこともある。新たな活性化のためには，ナトリウムチャンネルの不活性化を取り除かねばならない。これを脱不活性化(deinactivation)と呼ぶ。ニューロンに抑制をかけて過分極させることは，ナトリウムチャンネルの脱不活性化につながり，今想定しているような場合には，回路網全体の興奮性を回復させることになる。言うなれば，興奮性が高まった後にデッドロックに陥って脳機能が不活発となった時，一旦GABA作動性ニューロンが働いてリセットがかかれば，デッドロックから開放されて，再び脳に活性がよみがえるような話である。つまりGABA作動性ニューロンの活動強化によって，脳は活性化されやすくなることもある。これは矛盾を解くキーの一例に過ぎない。抑制をかけることによって回路網が活性化するという一見矛盾した出来事も，ニューロンレベル，回路網レベル，そして行動レベルでの「抑制」を区別し，その相互関係をいくつかのキーを使って考慮するならば，あながち不可思議な現象でもない。

5　おわりに

うつ病成因論としての皮質内GABA伝達系機能低下説は，多くの臨床知見から支持されている。私共のラットモデルを用いた実験も，ECT効果のひとつは興奮抑制であることを示唆し，この成因仮説を細胞レベルで支持している。しかし，私共の別な実験では，ECTにはカルシウムチャンネルに対する促進(32)作用もあり，これもHomer1aに媒介されていた。これは，カルシウムチャンネル機能の低下がうつ病成因と関連することを示唆するのかもしれない。Homer1aのECTメディエーターとしての作用のうち本稿では触れなかった部分が，うつ病成因論のなかでどのように位置づけられるかについては，また稿を改めたい。

山本亮助教と山田清美氏の原稿作製への助力に感謝する。本稿に記載された研究の一部および本稿作成は金沢医科大学共同研究費 (C2006-5，C2007-2) の援助による。

1. 自殺総合対策の在り方検討会編：報告書「総合的な自殺対策の推進に関する提言」2007; 5-6.
2. 本橋伸高：ECTマニュアル－科学的精神医学をめざして，東京，医学書院, 2000.
3. Abraham R: Electroconvulsive therapy 4th Ed. Oxford University Press 2002.
4. Murata M, Kato N: Autocorrelogram sorting: a novel method for evaluating negative-feedback regulation of spike firing. Brain Res. 2007; **1133:** 27-33.
5. Sasaki K, Otani N: Accommodation in spinal motoneurons of the cat. Jpn J Physiol 1961; **11:** 443-56.
6. Angelucci F, Mathe AA, Aloe L: Neurotrophic factors and CNS disorders: findings in rodent models of depression and schizophrenia. Prog Brain Res 2004; **146:** 151-65.
7. Nibuya M, Morinobu S, Duman RS: Regulation of BDNF and trkB mRNA in rat brain by chronic electroconvulsive seizure and antidepressant drug treatments. J Neurosci 1995; **15:** 7539-47.
8. Gould E, McEwen BS, Tanapat P et al: Neurogenesis in the dentate gyrus of the adult tree shrew is regulated by psychosocial stress and NMDA receptor activation. J Neurosci 1997; **17:** 2492-8.
9. Pham K, McEwen BS, LeDoux JE et al: Fear learning transiently impairs hippocampal cell proliferation. Neuroscience 2005; **130:** 17-24.
10. Sheline YI, Wang PW, Gado MH et al: Hippocampal atrophy in recurrent major depression. Proc Natl Acad Sci USA 1996; **93:** 3908-13.
11. Manji HK, Duman RS: Impairments of neuroplasticity and cellular resilience in severe mood disorders: implications for the development of novel therapeutics. Psychopharmacol Bull 2001; **35:** 5-49.
12. Nestler EJ, Gould E, Manji H et al: Preclinical models: status of basic research in depression. Biol Psychiatry 2002; **52:** 503-28.
13. Bocchio-Chiavetto L, Zanardini R, Bortolomasi M et al: Electroconvulsive Therapy (ECT) increases serum Brain Derived Neurotrophic Factor (BDNF) in drug resistant depressed patients. Eur Neuropsychopharmacol 2006; **16:** 620-4.
14. Chen AC, Shin KH, Duman RS et al: ECS-Induced mossy fiber sprouting and BDNF expression are attenuated by ketamine pretreatment. J ECT 2001; **17:** 27-32.
15. Lamont SR, Stanwell BJ, Hill R et al: Ketamine pre-treatment dissociates the effects of electroconvulsive stimulation on mossy fibre sprouting and cellular proliferation in the dentate gyrus. Brain Res 2005; **1053:** 27-32.
16. Li B, Suemaru K, Cui R et al: Repeated electroconvulsive stimuli increase brain-derived neurotrophic factor in ACTH-treated rats. Eur J Pharmacol 2006; **529:** 114-21.
17. Madsen TM, Treschow A, Bengzon J et al: Increased neurogenesis in a model of electroconvulsive therapy. Biol Psychiatry 2000 ; **47:** 1043-9.
18. Scott BW, Wojtowicz JM, Burnham WM: Neurogenesis in the dentate gyrus of the rat following electroconvulsive shock seizures. Exp Neurol 2000; **165:** 231-6.
19. Malberg JE, Eisch AJ, Nestler EJ et al: Chronic antidepressant treatment increases neurogenesis in adult rat hippocampus. J Neurosci 2000; **20:** 9104-10.
20. Tanis KQ, Newton SS, Duman RS: Targeting neurotrophic/growth factor expression and signaling for antidepressant drug development. CNS Neurol Disord Drug Targets 2007; **6:** 151-60.
21. Santarelli L, Saxe M, Gross C et al: Requirement of hippocampal neurogenesis for the behavioral effects of antidepressants. Science 2003; **301:** 805-9.
22. Tsankova NM, Kumar A, Nestler EJ: Histone modifications at gene promoter regions in rat hippocampus after acute and chronic electroconvulsive seizures. J Neurosci 2004; **24:** 5603-10.
23. Sun W, Choi SH, Park SK et al: Identification and characterization of novel activity-dependent transcription factors in rat cortical neurons. J Neurochem 2007; **100:** 269-78.
24. Sun W, Park KW, Choe J et al: Identification of novel electroconvulsive shock-induced and activity-dependent genes in the rat brain. Biochem Biophys Res Commun 2005; **327:** 848-56.
25. Newton SS, Collier EF, Hunsberger J et al: Gene profile of electroconvulsive seizures: induction of neurotrophic and angiogenic factors. J Neurosci 2003; **23:** 10841-51.
26. Newton SS, Girgenti MJ, Collier EF et al: Electroconvulsive seizure increases adult hippocampal angiogenesis in rats. Eur J Neurosci 2006; **24:** 819-28.
27. Ploski JE, Newton SS, Duman RS: Electroconvulsive seizure-induced gene expression profile of the hippocampus dentate gyrus granule cell layer. J Neurochem 2006; **99:** 1122-32.
28. Conti B, Maier R, Barr AM et al: Region-specific transcriptional changes following the three antidepressant treatments electro convulsive therapy, sleep deprivation and fluoxetine. Mol Psychiatry 2007; **12:** 167-89.
29. Altar CA, Laeng P, Jurata LW et al: Electroconvulsive seizures regulate gene expression of distinct neurotrophic signaling pathways. J Neurosci 2004; **24:** 2667-77.
30. Svenningsson P, Chergui K, Rachleff I et al: Alterations in 5-HT1B receptor function by p11 in depression-like states. Science 2006; **311:** 77-80.
31. Sakagami Y, Yamamoto K, Sugiura S et al: Essential roles of Homer-1a in homeostatic regulation of pyramidal cell excitability: a possible link to clinical benefits of electroconvulsive shock. Eur J Neurosci. 2005; **21:** 3229-39.
32. Yamamoto K, Sakagami Y, Sugiura S et al: Homer 1a enhances spike-induced calcium influx via L-type calcium channels in neocortex pyramidal cells. Eur J Neurosci. 2005; **22:** 1338-48.
33. Kujirai T, Caramia MD, Rothwell JC et al: Corticocortical inhibition in

human motor cortex. J Physiol 1993; **471:** 501-19.
34. Bajbouj M, Brakemeier EL, Schubert F et al: Repetitive transcranial magnetic stimulation of the dorsolateral prefrontal cortex and cortical excitability in patients with major depressive disorder. Exp Neurol 2005; **196:** 332-8.
35. Bajbouj M, Lisanby SH, Lang UE et al: Evidence for impaired cortical inhibition in patients with unipolar major depression. Biol Psychiatry 2006; **59:** 395-400.
36. Bajbouj M, Lang UE, Neu P et al: Therapeutic brain stimulation and cortical excitability in depressed patients. Am J Psychiatry 2005; **162**: 2192-3.
37. Chistyakov AV, Kaplan B, Rubichek O et al: Effect of electroconvulsive therapy on cortical excitability in patients with major depression: a transcranial magnetic stimulation study. Clin Neurophysiol 2005; **116:** 386-92.
38. Bajbouj M, Lang UE, Niehaus L et al: Effects of right unilateral electroconvulsive therapy on motor cortical excitability in depressive patients. J Psychiatr Res 2006; **40:** 322-7.
39. Petty F : GABA and mood disorders: a brief review and hypothesis. J Affect Disord 1995; **34:** 275-81.
40. Sanacora G, Mason GF, Rothman DL et al: Reduced cortical gamma-aminobutyric acid levels in depressed patients determined by proton magnetic resonance spectroscopy. Arch Gen Psychiatry 1999; **56:** 1043-7.
41. Sanacora G, Mason GF, Rothman DL et al: Increased cortical GABA concentrations in depressed patients receiving ECT. Am J Psychiatry 2003; **160:** 577-9.
42. Sanacora G, Mason GF, Rothman DL et al: Increased occipital cortex GABA concentrations in depressed patients after therapy with selective serotonin reuptake inhibitors. Am J Psychiatry 2002; **159:** 663-5.
43. Sanacora G, Fenton LR, Fasula MK et al: Cortical gamma-aminobutyric acid concentrations in depressed patients receiving cognitive behavioral therapy. Biol Psychiatry 2006; **59:** 284-6.
44. Rajkowska G, Miguel-Hidalgo JJ, Wei J et al: Morphometric evidence for neuronal and glial prefrontal cell pathology in major depression. Biol Psychiatry 1999; **45:** 1085-98.
45. Green AR, Vincent ND: The effect of repeated electroconvulsive shock on GABA synthesis and release in regions of rat brain. Br J Pharmacol 1987; **92:** 19-24.
46. Inghilleri M, Berardelli A, Marchetti P et al: Effects of diazepam, baclofen and thiopental on the silent period evoked by transcranial magnetic stimulation in humans. Exp Brain Res 1996; **109:** 467-72.
47. Sackeim HA, Decina P, Prohovnik I et al: Anticonvulsant and antidepressant properties of electroconvulsive therapy: a proposed mechanism of action. Biol Psychiatry 1983; **18:** 1301-10.
48. Sackeim HA: The anticonvulsant hypothesis of the mechanisms of action of ECT: current status. J ECT 1999; **15:** 5-26.
49. Krystal JH, Sanacora G, Blumberg H et al: Glutamate and GABA systems as targets for novel antidepressant and mood-stabilizing treatments. Mol Psychiatry 2002; **7:** S71-80.
50. Segawa K, Azuma H, Sato K et al: Regional cerebral blood flow changes in depression after electroconvulsive therapy. Psychiatry Res 2006; **147:** 135-43.
51. Périco CA, Skaf CR, Yamada A et al: Relationship between regional cerebral blood flow and separate symptom clusters of major depression: a single photon emission computed tomography study using statistical parametric mapping. Neurosci Lett 2005; **384:** 265-70.
52. Mayberg HS, Lozano AM, Voon V et al: Deep brain stimulation for treatment-resistant depression. Neuron 2005; **45:** 651-60.
53. Takano H, Kato M, Inagaki A et al: Time course of cerebral blood flow changes following electroconvulsive therapy in depressive patients--measured at 3 time points using single photon emission computed tomography. Keio J Med 2006; **55:** 153-60.

Neurobiological Basis of Electroconvulsive Therapy (ECT): Consistency with the GABAergic Deterioration Hypothesis for Pathogenesis of Major Depression

Nobuo Kato

Department of Physiology, Kanazawa Medical University, Ishikawa 920-0293, Japan

Electroconvulsive therapy is regarded as an extremely powerful measure to treat depression. Why ECT works remains obscure. To elucidate its neurobiological basis might contribute to further amelioration of ECT methods and development of alternative effective measure. A large array of molecules have been reported to be highly expressed by ECT, but have not been analyzed to date in the light of their effects on ion channels, neurons, neuron circuits, and whole brain function. Among those molecules up-regulated by ECT, of which representatives appear to be classified into growth factors and immediate early genes, the scaffold protein Homer has been studied in our recent project. We have shown by electrophysiological methods that intracellular injection of the immediate early gene product Homer 1a, an activity-dependently expressed member of the Homer family, hyperpolarized rat neocortex pyramidal cells, thus reducing neural excitability. In rat brain tissue obtained after ECT, the same hyperpolarization was observed and was abolished by injection of anti-Homer1a antibody, suggesting that Homer 1a is one of the mediators of ECT effects. A number of lines of clinical investigation have revealed that intracortical inhibition and GABA concentration are decreased in depressed humans and that ECT reverses this pathology. These clinical observations and our neurobiological findings can all be understood consistently in the framework of the GABAergic deterioration hypothesis for the pathogenesis of major depression.

Key Words: Major depression, Electroconvulsive therapy, GABAergic deterioration hypothesis, Intracortical inhibition, Homer

金医大誌（J Kanazawa Med Univ）32：82－88，2007

電撃けいれん療法の神経生物学的基盤 (続編)
－シナプス可塑性の関与－

加　藤　伸　郎

要　約：ECTはうつ病治療において重要な位置を占めている。ECTの生物学的根拠は今日まで不明である。本稿ではECTのシナプス伝達やシナプス可塑性への影響について述べ，先稿を補ってECTの生物学的背景をさらに考察したい。シナプスの伝達効率は可変であり (シナプス可塑性)，その長期的変化の維持されることが記憶や学習の細胞レベルでの基本過程と想定されている。ECTの副作用のひとつは健忘症であり，この観点からECTとの関連が注目された。ECT後にシナプス伝達効率の上昇が見られること，同時にそれ以降に上昇余地の減少することが共通して報告されてきたが，これらは現象的記載に終始している。分子生物学的には，成長因子と最初期遺伝子群を中心とする分子群が，ECTによって発現上昇することが知られている。こうして発現してくる分子の機能解析は充分なされていない。これらの分子がシナプス可塑性を誘導する分子機構へどのような作用を及ぼすかを解析して行けば，ECTのシナプス可塑性への影響の研究を，現象的記載から分子メカニズムの探求へと深化させ，それによりECTの生物学的根拠をより明確化できると期待する。私共は，ECTによって発現の高まる最初期遺伝子のひとつであるHomer1aを取り上げ，シナプス可塑性への作用を調べ始めた。

キーワード：　うつ病，電撃けいれん療法，シナプス可塑性，LTP(long-term potentiation)，Homer

1．はじめに

電撃けいれん治療 (ECT) はうつ病治療において顕著な効果を発揮する。それは，精神科臨床では治療手段としての「最後の切り札」とまで呼ばれるような位置づけを得ていることからも伺える。しかし病態生理学的には，ECTの生物学的根拠は今日まで不明である。ECTに関する基礎的研究は皆無というわけではないが，散発的であり，近い将来に急速な発展が見込まれるほど系統的となっていない。そのなかでは，分子生物学的研究は比較的多く報告がなされ，神経成長因子などの分子発現の起こることがコンセンサスとなっている。この点は先稿で述べた(1)。神経生理学的側面からは，ECTによるシナプス伝達およびその可塑的変化への影響についての報告が1980年代から始まっている。本稿では，ECTのシナプス伝達やシナプス可塑性への作用について述べる。先稿(1)を補って，ECTの生物学的背景を探索する上での示唆をさらに抽出したい。

金沢医科大学医学部生理機能制御学
石川県河北郡内灘町大学1-1
平成19年11月30日受理

2．記憶とシナプス可塑性

ECTのシナプス可塑性への作用について述べる準備として，シナプスの可塑的変化とは何かを概説しておきたい。シナプスは2つのニューロン間でのシグナル伝達の場であるが，ここでの伝達効率は可変である。シナプス伝達は，よく脳スライスを用いて研究される (図1A)。シナプスでシグナルの送り手側のニューロンが電気活動を起すと，伝達物質が受け手に向けて放出され，それが受け手側のシナプス下膜にある受容体に結合して，受け手側ニューロンでシナプス電位 (より正確には，興奮性シナプス後電位: excitatory postsynaptic potential; EPSP) を発生させる (図1B)。シナプス前の電気活動が一定であって，シナプス後細胞でのシナプス電位が増大した場合には，シナプス伝達の効率が上昇したことになる (図1C)。シナプス前の神経軸索を高頻度で刺激すると，伝達効率が上昇する。この現象は少なくとも数十分は続くので，長期増強 (Long-term potentiation; LTP) と呼ばれる(2)。シナプス伝達効率が活動依存的に可変であるだけでなく，効率変化がすぐには元に戻らずに持続する性質も含めてシナプス可塑性と呼ばれる。シナプス可塑性の誘導に際しては，過去に受けた高頻度刺激の結果としてのシナプス伝達効率の上昇が，未来の数十分ないし数時間に渡って保持され続

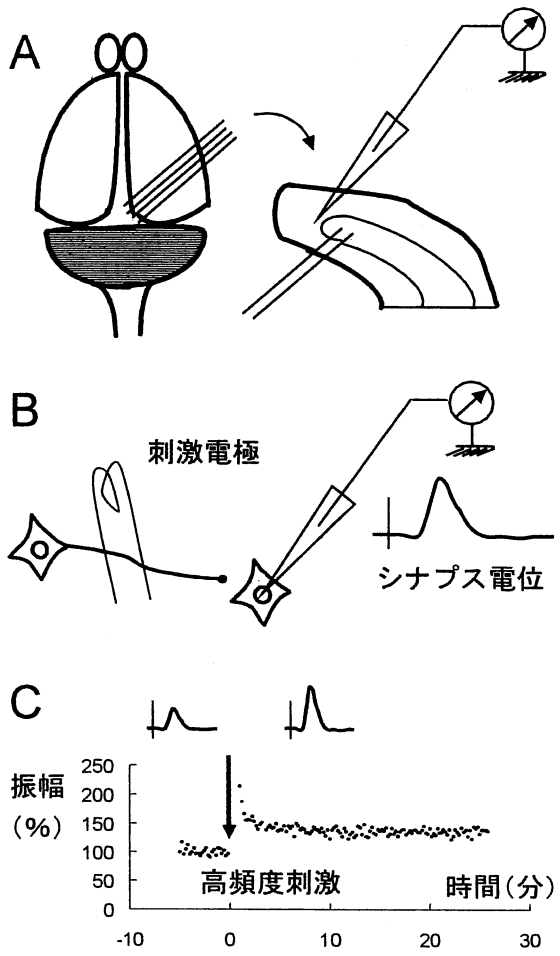

図1．シナプス可塑性とLTPの誘導
A：ラットやマウスの頭部を離断した後，脳を取り出し，マイクロスライサーで数百ミクロン厚の薄切片 (脳スライス) を作製する。ここでは，例としてラット視覚皮質からスライスを作成する手順を描いている。脳スライスを灌流槽に移し，記録電極および刺激電極を設置する。これはin vitroでの記録方法であるが，脳スライスを作成せずに，麻酔下や覚醒中の動物の脳から記録することもできる。B:刺激電極を通じて電気刺激をシナプス前線維に与える。シナプス後細胞からは，記録に応じてシナプス電位 (EPSP) が記録される。これは，数ミリ秒の時間経過にて数ミリボルトから20ミリボルト程度までのピーク値に達し，数十ミリ秒を経てまた元の電位に戻る。C:高頻度刺激はEPSPの振幅を持続的に増大させる。時間0にで高頻度刺激を与えた (矢印)。例えば海馬から得たスライスの場合には，時間0にて同じ強さの刺激を高頻度 (100Hz) で1秒間与える。高頻度刺激以前の振幅は安定しており，これを100%ととってコントロールにする。コントロールEPSPは再現性をもって誘起されている。高頻度刺激の後，それ以前と同じ強さの電気刺激を与えているにもかかわらず，EPSPの振幅は約150%にまで増大し，この状態が30分続く。これはシナプス伝達効率が増大し，かつ長期に維持されていると解釈される。この現象をシナプス伝達長期増強 (Long-term potentiation; LTP) と呼ぶ。逆に振幅が減少して維持される場合もあって，これは伝達効率の減少を意味し，シナプス伝達長期抑圧 (Long-term depression; LTD) と呼ばれる。あるシナプスがLTPやLTDを起すことのできる性質を持っている場合，その性質のことをシナプス可塑性といい，そのシナプスは可塑的であると呼ばれる。

ける。よってシナプス可塑性は記憶のモデルとしては格好であり，マクロ的な行動概念である記憶が細胞レベルで拠って立つミクロ的基本過程 (素過程) である，との仮説が広く流布しており，これは代表的な生理学または神経科学の教科書にも記載されている通りである(3,4)。LTPは1973年に始めて報告されたが，これは抗うつ薬物治療の限界が指摘されて，ECTが再び脚光を浴び始めた丁度その頃でもあった(5)。その数年後からLTPへのECTの影響を調べる実験は始められていた(6)。なお，ECTの歴史については先稿(1)で簡単にふれた。

LTPでは高頻度刺激によってシナプス伝達効率が増大するが，その逆過程も知られている。これは低頻度刺激などにより伝達効率低下を来たす場合で，長期抑圧 (Long-term depression; LTD) と呼ばれる(7)。ECTがLTDにおよぼす影響についても報告がある。たとえば，線条体スライスのニューロン (中型スパイニーニューロン) においては，通常LTDを誘導することができるが，ECTの後には1週間にわたってこのLTDが阻止されることが動物実験で報告されている(8)。双極性気分障害では線条体が関与するとも考えられており，この組織におけるLTD阻害は，ECTが双極性障害に治療効果をもつことと何らかの関連性を持つ可能性もある。LTDもLTPとならんで記憶の基本過程と考えられている。記憶の逆としての忘却や，記憶に伴う抽象化プロセスに必要な一次情報の棄却などが，LTDと関連しているのかもしれない。

ECTの副作用のなかで大きなもののひとつとして健忘症が挙げられる(9)。LTPは細胞レベルでの記憶の基本過程と目されてきたので，この観点からECTとの関連が注目された。すなわち，ECTがLTPやLTDに与える影響を調べることによって，副作用である健忘症を克服する可能性が期待された。LTPは高頻度刺激によって引き起こされるので，交流やパルス波電流によるECTは，LTPの誘導刺激と類似しているとも言える。異なる点は，LTPではシナプス前の神経線維を出来るだけ局所的に電気刺激するのに対して，ECTでは脳の外側から脳の広い領域を刺激するところである。

ECTの副作用としての健忘症も含めて，記憶に及ぼされるECTの影響を論ずる場合には，記憶の多義性に注意せねばならない。まず，記憶は記憶コンテンツ (内容ないし内実) の観点から少なくとも2つに分けられる。叙述記憶と手続き記憶である。叙述記憶の内容は，物事や現象あるいは個人的体験などに関する知識であって，言語を介した説明や了解が可能である。一方，手続き記憶は言語を介することなく習得され，行動によって提示できるようなタイプの記憶であり，手仕事や道具使いにおけるスキルの上達などが含まれる。ECTによる健忘に関連するのは，手続き記憶ではなく，叙述記憶である。叙述記憶はさらに，時間経過の観点から2つに分解される。短期記憶と長期記憶である。短期記憶は電話番号を数分覚えているような場合に該当し，翌日には記憶としては消滅している。ただし，これが自ら新規に加入した電話番号であるならば，覚えこんで消滅させないよ

うにするであろう。この覚え込みの作業を地固め(consolidation)と呼ぶ。地固めされて記憶が長期化することを,「長期記憶を獲得した」と表現する。さらに注意すべきは,長期記憶と言っても,「長期記憶の新規獲得」と「既存の長期記憶の想起」とは区別されなければならない。なぜなら,新規獲得は海馬に依存するが,想起は依存しないことが知られており,両者を実現する神経回路は部分的に異なっているからである。ECTで問題となるのは健忘であり,これは長期記憶と関連する。その際,新規獲得と過去に獲得された記憶の消滅という2つの側面に及ぶECTの影響を,それぞれ考慮する必要がある。これに対応するかのように,記憶モデルとしてのLTPでも,新規LTPの誘導不能と,誘導されたLTPの打ち消しとが区別されている。

3．ECTの副作用としての健忘とシナプス可塑性

記憶のモデルであるLTPは,主にラットやウサギなどの海馬を使って研究されてきた。海馬を構成する基本神経回路におけるシナプス結合の場は3箇所あり,それぞれ歯状回,CA1野,およびCA3野と呼ばれる。LTPは1973年に初めて報告され,その実験ではウサギの歯状回が使われた(2)。早くもその3年後,HessとTeyler(6)はラットCA1野を使って,ECTがLTPに及ぼす影響を調べている。そこでは,一旦LTPを誘導した後にECTを施して,その影響を調べた。その結果,一旦獲得されたLTPのサイズが減少し,2回目のECTによってLTPは完全に消失したと報告している。LTPは誘導された後に消滅させることができ,これは1990年代以降,脱LTP (depotentiation) と呼ばれている(10)。LTDはLTPの消滅ではなくて,デフォールトの状態からの伝達効率低下であって,分子機構の細部は異なるとされている(11)。HessとTeyler(6)が見たのはdepotentiationであるが,70年代当時はまだ,この呼称は使われていなかった。さらに彼らはECTによるdepotentiationの後で,LTPを再誘導することにも成功している(6)。ただしECTを繰り返した場合には,再誘導されるLTPサイズが小さくなっていくとも報告している。すなわち,ECTはLTPを消去するが,その獲得は妨げないと結論している。ECTによるdepotentiationは最近にも報告があり,ここではLTP誘導後1時間後ではdepotentiateされたが,6時間後にECTを行っても影響なかったと述べられている(12)。

HessとTeyler(6)は,ECTを施行した後にLTPへの影響を調べており,これは急性ECTのモデル化と言える。これに対して,20日間に渡って10回のECTを施すような形で慢性ECTのモデル化を行い,その後に脳スライスを作製してLTP誘導性を調べた報告もある(13)。ここでもLTPサイズが顕著に縮小したと述べられている。StewartとReid(14) は,モデル化慢性ECT後のLTPサイズ縮小や誘導不能化を報告している。この結果の解釈として,ECTを繰り返すことでシナプス前の神経線維に高頻度刺激を与えたことになるため,この段階ですでにLTPが起こって,それ以上にLTPの起こる余地がなくなったのでないか,すなわちLTP機構がECTにて飽和したのではないかと考えられている。この考え方を裏付ける結果として,ECT後にLTPのようなシナプス伝達効率上昇が見られること,すなわちECTが契機となってLTPが誘導されると解釈できることも報告された(15)。

うつ病成因のGABA仮説(1) もまた,ECTによるLTP減弱化をうまく説明できる。この仮説では,うつ病者やうつ病モデル動物においては,脳内のGABA作動性抑制が減退しており,ECTによって神経回路の抑制が強化されると観る。実際,ECTによる皮質での抑制強化やGABA濃度上昇がヒトで知られており(16-24),ラット大脳皮質での実験でも,モデルECTによる興奮性抑止を我々は見出している。LTP誘導はGABA作動性ニューロンによる調整下にあり,抑制を強化すればLTPは起こり難くなるとされている(25)。よって,ECTで抑制が強化されることは,LTP誘導をより困難にするであろうと推察できる。

LTPは記憶のモデルであり,LTPに対するECTの影響を調べても,記憶への影響を間接的に見ているに過ぎない。ラットに空間情報を記憶させて,この記憶へのECTの作用を直接調べる試みもなされている。空間記憶の研究パラダイムの典型例はモリス水迷路である(26)。これは直径2mくらいのプールで水を白濁させて底が見えない状態にし,ラットを泳がせて水中に隠された浅瀬プラットフォームを探させるものである。空間記憶の獲得はECTによって妨げられたが,抗うつ薬である選択的セロトニン再取り込み阻害剤 (SSRI) では影響がなかったという報告がある(27)。抗うつ効果はSSRIとECTの作用の共通部分であるが,ECTにはこれに加えて,ECT特有の副作用としての記憶障害作用もあわせ持つ,と解釈することのできる報告である。

4．NMDA受容体のLTPへの関与とECT

LTPの分子機構は年々詳細が解明されていくが,この点での初期のブレークスルーは1986年にあった。それはLTPのNMDA受容体依存性の発見である(28)。NMDA受容体はグルタミン酸受容体のなかで一つのサブグループを形成しており,その動作特性が,工学および心理学的背景から派生してきた数理モデルによる学習理論とよく整合していることがわかっている(29,30)。一時は記憶分子ともてはやされたが,これはLTPを起すための必要条件のひとつであって全てではない。ましてや十分条件ではない。さらには,NMDA受容体に依存しないLTPも知られている(31)。とはいえ,NMDA受容体依存性はLTPの最重要な性質の一つであり,ECTとLTPの関連を調べるに際しても,NMDA受容体の関与を考慮することには道理がある。

Watkins et al(32)は分子生物学的な研究に基づいて,ECTがNMDA受容体サブユニットの発現を増加させる一方,代謝型グルタミン酸受容体の発現は減少させることを報告している。どちらの受容体もLTPに関与するが,だからと言って,この結果がECTのLTPへの影響を直ちに明快に説明するわけではない。StewartとReid(15) はNMDA受容体阻害剤であり麻酔薬のひとつでもあるケタミンKetaminが,ECTのLTPへの影響をどのように変容させるかを調べた。ECTによるLTP様のシナプス伝達

効率増加(33) とLTPサイズの減少を(14) 彼らはすでに見ていたわけであるが，これをコントロールとし，ケタミン麻酔下でECTを施行した場合をテスト例として比較した(15)。その結果，ケタミンがLTPの縮小も，LTP様伝達効率増大もブロックすることを見いだした。これは，うつ病者にECTを施行する際にもケタミン麻酔を施せば，健忘の副作用が軽減できる可能性を意味する。

ECTによるシナプス伝達強化とLTP縮小は，ECTの主作用としての抗うつ効果と関連性がないのであろうか。この観点から，ラットに投与された抗うつ薬のSSRIが，歯状回におけるシナプス伝達効率を高めるという報告(27) は興味深い。シナプスの伝達効率は，さらなる増強の余地がない上限と抑圧の余地がない下限の間のどこかに設定され，通常はこのベースラインの効率を維持している。そして何か特別なパターンの入力があって適切に応答が行われた場合には，LTPやLTDが起こって伝達効率が上下することになる。それゆえ，ベースラインが上限近くに設定されているシナプスではLTPの余地は小さいと考えられる。SSRIを使った実験(27) でもLTP低減が報告されており，シナプス近傍で高濃度化したセロトニンが，シナプス伝達の強化とLTPの低減に寄与した可能性が示唆される。これは，手段がECTであれSSRIであれ，ベースラインのシナプス伝達を高めることが抗うつ治療の本質である，と示唆しているのかもしれない。

ECTによるシナプス伝達上昇を抑えるケタミンは，また，歯状回における神経新生や軸索分枝増殖などの形態的変化も抑制することが知られている(34; ただしLamont et al (35)では分子増殖だけが抑制されている)。うつ病成因の神経形成不全仮説によると，歯状回でのニューロンの形態的繁茂や増殖が発達期から抑制されて来たというヒストリーが，成人におけるうつ病発症と連関しており，その抑制を解除することによる形態的増殖の促進こそが治療の根幹であるとされている(36)。この考え方と一致して，ECTは実際に形態的増殖を促すことがモデル動物で明らかになっている(37,38)。ケタミンがシナプス伝達上昇と形態的増殖の両方を阻止すること(34) は，機能的なシナプス伝達強化とシナプスの形態的変化とが連関しているという考え方を支持しているのかもしれない。すなわち，シナプス伝達強化が個々の既存のシナプスの枠内で充分になされた後には，アクソン分枝の繁茂 (sprouting) や新規スパイン突出などの形態的変化が起こってシナプスの数が増え，伝達がさらに増強されていく，とする古典的な考え方である(39)。

5．BDNFのシナプス可塑性への作用とECT

ECTはどのようなメカニズムで，LTPとLTDも含めたシナプスの可塑的変化を阻害するのであろうか。ひとつは，ECTが高頻度刺激を先回りして代替的にLTPを起してしまって，それ以上に誘導される余地をなくすというもので，この可能性については本稿でもすでに指摘した。第二には，LTP・LTD誘導に寄与するメカニズムをECTが何らかの形で促進している可能性である。そのメカニズムに関与する分子としては，種々のレセプター・チャンネル・足場タンパク質・転写因子など数多く知られている(40)。NMDA受容体サブユニットの分子発現がECTで影響を受けることも知られている(32)。しかし，ECTによって発現増加する分子の代表格は，最初期遺伝子群 (IEG; immediate early gene) と成長因子であることが多くの分子生物学的研究でのコンセンサスとなっている(41-49)。IEGと成長因子に属する分子のいくつかも，シナプス可塑性との関与がよく知られている。以下では，その代表的分子を取り上げて解説する。

成長因子の中でもBDNFは，海馬や視覚皮質でのLTPやLTDに，さらに，視覚皮質における眼優位性に関する可塑性に関与することが詳しく調べられている(50-53)。眼優位性とは，視覚皮質の細胞は右目と左目からの視覚入力に等しく応答するとは限らず，どちらかにより強く反応するという性質である。左右それぞれによく応答する細胞群は，視覚皮質内で混在しているのではなく，円柱状に集まって存在しており，これを眼優位コラムと呼ぶ。左右の目に対応するコラムが交互に並んでいる。眼優位性は遺伝的に決定されているものではなく，発達途上のある一時期 (感受期と呼ばれる) に片目を閉じると，その反対側の眼に対応するコラムが拡大し，眼優位性が偏ってしまう。この眼優位の偏りやその修正にBDNFが関与するとされている。また，感受期を過ぎて眼優位性の変化が通常は起こらない成熟動物において，BDNFを視覚皮質内に注入することによって変化が起こるようになること，つまり片目閉鎖による眼優位性偏移への感受性が感受期終了後に復活することも知られている。眼優位性の解剖学的背景としては，外側膝状体から一次視覚野への投射線維が高密度化して繁茂することが挙げられる。このような解剖学的変化は，うつ病治療を行うと海馬歯状回の顆粒細胞からの神経投射が高密度化し，この過程でBDNFが関与する，とするうつ病の神経形成不全説とよく符合する。すなわち，BDNFが神経回路網を密にすることが脳の局所的な再構築を促し，一方では視覚機能を修飾し，他方，海馬では気分障害の改善につながると考えられる。

6．最初期遺伝子タンパク質Homer1aによるLTD修飾とECT

最初期遺伝子タンパク質のひとつであるHomer1aはECTによって発現が高まる(48)。Homer1aはアダプター蛋白質や足場蛋白質と呼ばれる分子群に属するが，それについては本誌別稿(1)にて簡単に説明している。Homer1aのシナプス可塑性への関与の探索は，そもそもHomerグループが最初に報告された時に遡る(54,55)。Homer1aはLTPを誘導するような高頻度刺激によって発現してくる分子の一つとして記載された。LTPの中には新規タンパク質合成が必要なLTPがある (タンパク質合成依存性LTP; 56)。これを引き起こす際の高頻度刺激は，通常のLTPのように一回だけではなく，繰り返し与えることが必要である。この結果ニューロンの核で転写されることになるmRNAからタ

ンパク質が合成され，これが刺激を受けた部分へ作用し，樹状突起におけるスパインの数を増やすことなどを通じて，シナプス伝達を強化するために使われる。LTPにおけるシナプス伝達の増強はニューロン全体で起こるのではないため，ここで理論的な難題が生ずる。LTPには入力特異性があって，高頻度刺激を受けたシナプスではLTPが起こるが，そこから距離を隔てたところに位置するシナプスでは，たとえ同じニューロン上であってもLTPが起きない。錐体細胞の樹状突起は1mmを超えて張られているので，特定地点で起した高頻度刺激があるシナプスには入力し，1mm隔たった別のシナプスでは入力しないことは当然起こりうる。タンパク質合成依存性LTPを入力特異的に起すためには，合成されたタンパク質がどのシナプスで作用するかを指示する目印が必要なことになる。新規タンパク質の合成は核での転写に始まるわけであるから，もし目印がなければ，新規合成されたタンパク質はニューロン全体に無差別に作用することになって入力特異性は保証されない。実際には目印があって，入力特異性を維持していると考えられている。この目印のことはシナプス・タグと呼ばれ，たとえばカルモディリンキナーゼなどがシナプス・タグとして働いていると提唱されている(57-59)。また，Homer1aはシナプス・タグと密接に関連する分子ではないかと想定されている。

さらに，Homer1aは代謝型グルタミン酸受容体（その中でもグループⅠ）を，細胞外のグルタミン酸に頼ることなく細胞内部から活性化することが，培養細胞で知られている(60)。私共は視覚皮質の錐体細胞でこれを確認し，こうして活性化された代謝型グルタミン酸受容体が，Homer1aによるニューロンの興奮抑制へとつながっていくことを明らかにした(61)。あわせて，ECTもまたニューロンの興奮を抑制し，その際にはHomer1aがメディエーターとなっていることも報告し(61)，本誌別稿(1)でも解説した。グループI代謝型グルタミン酸受容体が，海馬や視覚皮質でのLTPやLTDに不可欠の関与をしていることについては多くの報告があり，Homer1aの発現はこの受容体を介する道筋に干渉することによってシナプス可塑性に決定的な影響を与えることが示唆される。この点を明らかにすべく，私共は次に述べるような実験でLTDへの影響を調べた(62)。

Homer1aのラット視覚皮質におけるLTDへの影響を調べるにあたって，ニューロンがどの皮質層に位置するかによってLTDの受容体依存性が異なること(63)に，私共は注目した。ラット視覚皮質でのLTDでは，対象とする細胞が皮質第6層（最深層）に位置する場合にはグループⅠ代謝型グルタミン酸受容体に依存し，その他の層に存在する場合にはNMDA型グルタミン酸受容体に依存することが，Dawらによって報告されている。私共はまずそれを確認した。次いで細胞内にHomer1aを注入して，LTDのHomer1aによる修飾を調べた。ある種のLTDはグループI代謝型グルタミン酸受容体に依存しているので，Homer1aがこの受容体を活性化するのであれば，この種のLTDもまた干渉されるのではないか，と考えた。すなわち，このタイプの代謝型グルタミン酸受容体はHomer1aによって細胞内から活性化されるため，先立って注入されたHomer1aがこの受容体を活性化して，その後の細胞内プロセスを駆動してしまうと，それ以降のシナプス活動によってさらに駆動される余地が減少し（すなわち閉塞occlusionが起こり），この受容体活性化に依存するLTDもまた縮小すると予想した。これは実際に実験で確かめられた(62)。さらに，私共はモデルECT施行後のラットから脳スライスを作製し，グループⅠ代謝型グルタミン酸受容体に依存するLTDが縮小し，この際にHomer1aがメディエーターとなっていることを見出した(62)。

このような方法により，ECTがシナプス可塑性のひとつであるLTDに与える影響を調べ，その誘導のための分子機構の一翼をHomer1aが担っている可能性を検討している。シナプス可塑性へのECTの作用のうち，このアプローチで解明できるのはごく一部かもしれない。しかし，ECTが臨床効果を発揮するメカニズムを一部でも解明できれば，うつ病成因や新規治療法に関する重要な端緒となる可能性がある。うつ病には対象を欠いた不安や恐怖が悪循環に陥って自己増幅する側面があるように思われる。不安がさらに不安を強化する循環にはシナプス伝達のフィードバック的強化や減弱が関与している可能性があるが，これを遮断するならば不安の軽減へ向うことが予想できる。ECTのシナプス可塑性への効果がそのようなところで治療に結びついていても不思議ではない。

7．おわりに

前項に引き続いてECTの生物学的根拠をめぐる研究について解説したが，本稿では，特にシナプス可塑性との関連について述べた。シナプス可塑性は記憶・学習の細胞レベルでの基本過程と目されて，その分子機構の研究が進められている。シナプス可塑性は2つの側面からECTとつながりがあると考えられる。ひとつは，ECTの副作用のひとつである健忘症とシナプス可塑性との関連を明らかにすることによって，この副作用を軽減する方策を見出せる可能性がある点である。もうひとつは，分子生物学的に解明されてきたECT関連分子のいくつかが，従来知られていたシナプス可塑性関連分子と共通している点である。こちらの観点からは，ECTで発現する分子が，どのような作用をニューロン，神経回路網，そして行動に及ぼすかを解明し，それを通じて，うつ病患者やモデル動物の脳活動や行動をECTがどのように変容させるかを追究するというボトムアップ的な研究ストラテジーが展望できる。それは，ECTがなぜうつ病治療に有効なのか，そして，そもそもうつ病者の脳内では何が起きているのか，を理解するに至る道程の第一関門でもあるだろう。

山田清美氏の原稿作成への助力に感謝する。本稿に記載された研究の一部および本稿作成は金沢医科大学共同研究費（C2006-5, C2007-2）の援助による。

文　　献

1. 加藤伸郎：電撃けいれん療法の神経生物学的基盤－うつ病成因のGABA仮説との接点－．金医大誌 2007 印刷中.
2. Bliss TV, Lomo T: Long-lasting potentiation of synaptic transmission in the dentate area of the anaesthetized rabbit following stimulation of the perforant path. J Physiol 1973; **232:** 331-56.
3. 小澤瀞司：中枢神経シナプス伝達の可塑性. 小澤瀞司, 福田康一郎他(編), 標準生理学(第 6 版), 東京, 医学書院, 2005; 168-70.
4. Kandel E: Cellular Mechanisms of learning and the biological basis of individuality. Kandel E, Schwartz JH, Jessell TM (Eds), Principles of Neural Science (4th ed), New York, McGraw-Hill, 1991; 1247-77.
5. 本橋伸高：ECTマニュアル－科学的精神医学をめざして，医学書院，東京，2000.
6. Hesse GW, Teyler TJ: Reversible loss of hippocampal long term potentiation following electronconvulsive seizures. Nature 1976; 264: 562-4.
7. Linden DJ, Connor JA: Long-term synaptic depression. Annu Rev Neurosci 1995; **18:** 319-57.
8. De Murtas M, Tatarelli R, Girardi P et al: Repeated electroconvulsive stimulation impairs long-term depression in the neostriatum. Biol Psychiatry 2004; **55:** 472-6.
9. Abraham R: Electroconvulsive therapy 4th Ed. Oxford, Oxford University Press, 2002.
10. Fujii S, Saito K, Miyakawa H et al: Reversal of long-term potentiation (depotentiation) induced by tetanus stimulation of the input to CA1 neurons of guinea pig hippocampal slices. Brain Res 1991; 26; **555:** 112-22.
11. Lee HK, Barbarosie M, Kameyama K et al: Regulation of distinct AMPA receptor phosphorylation sites during bidirectional synaptic plasticity. Nature 2000; **405:** 955-9.
12. Trepel C, Racine RJ: Blockade and disruption of neocortical long-term potentiation following electroconvulsive shock in the adult, freely moving rat. Cereb Cortex 1999; **9:** 300-5.
13. Anwyl R, Walshe J, Roman M: Electroconvulsive treatment reduces long-term potentiation in rat hippocampus. Brain Res 1987; **435:** 377-9.
14. Stewart C, Reid I: Electroconvulsive stimulation and synaptic plasticity in the rat. Brain Res 1993; **620:** 139-41.
15. Stewart CA, Reid IC: Ketamine prevents ECS-induced synaptic enhancement in rat hippocampus. Neurosci Lett 1994; **178:** 11-4.
16. Bajbouj M, Brakemeier EL, Schubert F et al: Repetitive transcranial magnetic stimulation of the dorsolateral prefrontal cortex and cortical excitability in patients with major depressive disorder. Exp Neurol 2005; **196:** 332-8.
17. Bajbouj M, Lang UE, Neu P et al: Therapeutic brain stimulation and cortical excitability in depressed patients. Am J Psychiatry 2005; **162:** 2192-3.
18. Bajbouj M, Lang UE, Niehaus L et al: Effects of right unilateral electroconvulsive therapy on motor cortical excitability in depressive patients. J Psychiatr Res 2006; **40:** 322-7.
19. Bajbouj M, Lisanby SH, Lang UE et al: Evidence for impaired cortical inhibition in patients with unipolar major depression. Biol Psychiatry 2006; **59:** 395-400.
20. Sackeim HA: The anticonvulsant hypothesis of the mechanisms of action of ECT: current status. J ECT 1999; **15:** 5-26.
21. Sanacora G, Fenton LR, Fasula MK et al: Cortical gamma-aminobutyric acid concentrations in depressed patients receiving cognitive behavioral therapy. Biol Psychiatry 2006; **59:** 284-6.
22. Snacora G, Mason GF, Rothman DL et al: Reduced cortical gamma-aminobutyric acid levels in depressed patients determined by proton magnetic resonance spectroscopy. Arch Gen Psychiatry 1999; **56:** 1043-7.
23. Sanacora G, Mason GF, Rothman DL et al: Increased cortical GABA concentrations in depressed patients receiving ECT. Am J Psychiatry 2003; **160:** 577-9.
24. Sanacora G, Mason GF, Rothman DL et al: Increased occipital cortex GABA concentrations in depressed patients after therapy with selective serotonin reuptake inhibitors. Am J Psychiatry 2002; **159:** 663-5.
25. Artola A, Singer W: Long-term depression of excitatory synaptic transmission and its relationship to long-term potentiation. Trends Neurosci 1993; **16:** 480-7.
26. Morris RG: Synaptic plasticity and learning: selective impairment of learning rats and blockade of long-term potentiation in vivo by the N-methyl-D-aspartate receptor antagonist AP5. J Neurosci 1989; **9:** 3040-57.
27. Stewart CA, Reid IC: Repeated ECS and fluoxetine administration have equivalent effects on hippocampal synaptic plasticity. Psychopharmacology 2000; **148:** 217-23.
28. Herron CE, Lester RA, Coan EJ: Frequency-dependent involvement of NMDA receptors in the hippocampus: a novel synaptic mechanism. Nature 1986; **322:** 265-8.
29. Brown TH, Kairiss EW, Keenan CL: Hebbian synapses: biophysical mechanisms and algorithms. Annu Rev Neurosci 1990; **13:** 475-511.
30. Nakanishi S: Molecular diversity of glutamate receptors and implications for brain function. Science 1992; **258:** 597-603.
31. Johnston D, Williams S, Jaffe D et al: NMDA-receptor-independent long-term potentiation. Annu Rev Physiol 1992; **54:** 489-505.
32. Watkins CJ, Pei Q, Newberry NR: Differential effects of electroconvulsive shock on the glutamate receptor mRNAs for NR2A, NR2B and mGluR5b. Brain Res Mol Brain Res 1998; **61:** 108-13.
33. Stewart C, Jeffery K, Reid I: LTP-like synaptic efficacy changes following electroconvulsive stimulation. Neuroreport 1994; **5:** 1041-4.
34. Chen AC, Shin KH, Duman RS et al: ECS-Induced mossy fiber sprouting and BDNF expression are attenuated by ketamine pretreatment. J ECT 2001; **17:** 27-32.
35. Lamont SR, Stanwell BJ, Hill R et al: Ketamine pre-treatment dissociates the effects of electroconvulsive stimulation on mossy fibre sprouting and cellular proliferation in the dentate gyrus. Brain Res 2005; **1053:** 27-32.
36. Manji HK, Duman RS: Impairments of neuroplasticity and cellular resilience in severe mood disorders: implications for the development of novel therapeutics. Psychopharmacol Bull 2001; **35:** 5-49.
37. Madsen TM, Treschow A, Bengzon J et al: Increased neurogenesis in a model of electroconvulsive therapy. Biol Psychiatry 2000 ; **47:** 1043-9.
38. Scott BW, Wojtowicz JM, Burnham WM: Neurogenesis in the dentate gyrus of the rat following electroconvulsive shock seizures. Exp Neurol 2000; **165:** 231-6.
39. Eccles JC: The Understanding of the Brain 2nd Ed. McGraw-Hill Book Campany, New York, 1977; 177-87.
40. Malenka RC, Bear MF: LTP and LTD: an embarrassment of riches. Neuron 2004; **44:** 5-21.
41. Bocchio-Chiavetto L, Zanardini R, Bortolomasi M et al: Electroconvulsive Therapy (ECT) increases serum Brain Derived Neurotrophic Factor (BDNF) in drug resistant depressed patients. Eur Neuropsychopharmacol 2006; **16:** 620-4.
42. Busnello JV, Leke R, Oses JP et al: Acute and chronic electroconvulsive shock in rats: effects on peripheral markers of neuronal injury and glial activity. Life Sci 2006; **78:** 3013-7.
43. Newton SS, Collier EF, Hunsberger J et al: Gene profile of electroconvulsive seizures: induction of neurotrophic and angiogenic factors. J Neurosci 2003; **23:** 10841-51.
44. Ploski JE, Newton SS, Duman RS: Electroconvulsive seizure-induced gene expression profile of the hippocampus dentate gyrus granule cell layer. J Neurochem 2006; **99:** 1122-32.
45. Sun W, Choi SH, Park SK et al: Identification and characterization of novel activity-dependent transcription factors in rat cortical neurons. J Neurochem 2007; **100:** 269-78.
46. Sun W, Park KW, Choe J et al: Identification of novel electroconvulsive shock-induced and activity-dependent genes in the rat brain. Biochem Biophys Res Commun 2005; **327:** 848-56.
47. Nibuya M, Morinobu S, Duman RS: Regulation of BDNF and trkB mRNA in rat brain by chronic electroconvulsive seizure and antidepressant drug treatments. J Neurosci 1995; **15:** 7539-47.
48. Altar CA, Laeng P, Jurata LW et al: Electroconvulsive seizures regulate gene expression of distinct neurotrophic signaling pathways. J Neurosci 2004; **24:** 2667-77.
49. Schmidt HD, Duman RS: The role of neurotrophic factors in adult hippocampal neurogenesis, antidepressant treatments and animal models of depressive-like behavior. Behav Pharmacol 2007; **18:** 391-418.
50. Berardi N, Pizzorusso T, Maffei L: Critical periods during sensory development. Curr Opin Neurobiol 2000; **10:** 138-45.
51. Cabelli RJ, Hohn A, Shatz CJ: Inhibition of ocular dominance column formation by infusion of NT-4/5 or BDNF. Science 1995; **267:** 1662-6.
52. Akaneya Y, Tsumoto T, Kinosita S et al: Brain-derived neurotrophic factor enhances long-term potentiation in rat visual cortex. J Neurosci 1997; **17:** 6707-16.

53. Korte M, Bonhoeffer T: Activity-dependent synaptic plasticity: a new face of action for neurotrophins. Mol Psychiatry 1997; **2:** 197-9.
54. Kato A, Ozawa F, Saitoh Y et al: vesl, a gene encoding VASP/Ena family related protein, is upregulated during seizure, long-term potentiation and synaptogenesis. FEBS Lett 1997; **412:** 183-9.
55. Brakeman PR, Lanahan AA, O'Brien R et al: Homer: a protein that selectively binds metabotropic glutamate receptors. Nature 1997; **386:** 284-8.
56. Reymann KG, Frey JU: The late maintenance of hippocampal LTP: requirements, phases, 'synaptic tagging', 'late-associativity' and implications. Neuropharmacology 2007; **52:** 24-40.
57. Steward O, Worley PF: A cellular mechanism for targeting newly synthesized mRNAs to synaptic sites on dendrites. Proc Natl Acad Sci U S A. 2001; **98:** 7062-8.
58. Turrigiano G: A competitive game of synaptic tag. Neuron 2004; **44:** 903-4.
59. Sajikumar S, Navakkode S, Frey JU: Identification of compartment- and process-specific molecules required for "synaptic tagging" during long-term potentiation and long-term depression in hippocampal CA1. J Neurosci 2007; **27:** 5068-80.
60. Ango F, Prézeau L, Muller T et al: Agonist-independent activation of metabotropic glutamate receptors by the intracellular protein Homer. Nature 2001; **411:** 962-5.
61. Sakagami Y, Yamamoto K, Sugiura S et al: Essential roles of Homer-1a in homeostatic regulation of pyramidal cell excitability: a possible link to clinical benefits of electroconvulsive shock. Eur J Neurosci 2005; **21:** 3229-39.
62. Ueta Y, Yamamoto R, Sugiura S et al: Homer 1a suppresses neocortex long-term depression in a cortical layer-specific manner. J Neurophysiol 2008; **99:** 950-7
63. Rao Y, Daw NW: Layer variations of long-term depression in rat visual cortex. J Neurophysiol 2004; **92:** 2652-8.

Neurobiological Basis of Electroconvulsive Therapy (ECT): Effects on Synaptic Plasticity

Nobuo Kato

Department of Physiology, Kanazawa Medical University, Ishikawa 920-0293, Japan

Drug-resistant depression is often subjected to electroconvulsive therapy (ECT), which is highly relied upon in the psychiatry clinic. However, its neurobiological basis is not clear. The present article discusses its relation with synaptic plasticity, thereby describing one strategy for studying the neurobiology of ECT. The efficiency of synaptic transmission in the CNS is modifiable, and this malleability has been recognized as a cellular basis of memory and learning. Since one of the adverse effects of ECT is amnesia, it would be interesting to investigate how ECT interferes with synaptic plasticity. The view has been prevailing that ECT enhances synaptic transmission and reduces room for further enhancement of synaptic efficiency. While this view offers one explanation of ECT effects on synaptic plasticity, how altered synaptic plasticity could in turn contribute to the therapeutic effects of ECT is left unclear. To this point, a combined molecular and neurophysiological approach might be fruitful. Molecular biological studies have shown that large arrays of molecules are upregulated after ECT, representatives of which are growth factors and immediate early gene products. Homer1a, an immediate early gene product, is among those molecules highly expressed after ECT. We have been studying the cellular effects of Homer1a induced by ECT at the single neuron level, and are currently investigating its effects on synaptic plasticity in the neocortex. We hope that such neurophysiological analyses of functions of individual ECT-related molecules will lead to solid knowledge of why ECT works.

Key Words: Major depression, Electroconvulsive therapy, Synaptic plasticity, Long-term potentiation, Homer

J Neurophysiol 99: 950–957, 2008.
First published December 12, 2007; doi:10.1152/jn.01101.2007.

Homer 1a Suppresses Neocortex Long-Term Depression in a Cortical Layer-Specific Manner

Yoshifumi Ueta,[1,2] Ryo Yamamoto,[1] Shigeki Sugiura,[3] Kaoru Inokuchi,[4] and Nobuo Kato[1]

[1]*Department of Physiology, Kanazawa Medical University, Ishikawa;* [2]*Department of Integrative Brain Science, Kyoto University Graduate School of Medicine, Kyoto;* [3]*Medical Genetics Research Center, Nara Medical University, Nara; and* [4]*Mitsubishi Kagaku Institute of Life Sciences (MITILS), Tokyo, Japan*

Submitted 3 October 2007; accepted in final form 5 December 2007

Ueta Y, Yamamoto R, Sugiura S, Inokuchi K, Kato N. Homer 1a suppresses neocortex long-term depression in a cortical layer-specific manner. *J Neurophysiol* 99: 950–957, 2008. First published December 12, 2007; doi:10.1152/jn.01101.2007. Homer1a/Vesl-1S is an activity-dependently induced member of the scaffold protein family Homer/Vesl, which is known to link group I metabotropic glutamate receptors (mGluRs) to endoplasmic calcium release channels and to regulate them. Here we studied roles of Homer 1a in inducing long-term depression (LTD) in rat visual cortex slices. Homer 1a protein was injected by diffusion from whole cell patch pipettes. In layer VI pyramidal cells, LTD was reduced in magnitude with Homer 1a. LTD in layer VI was suppressed by applying antagonists of mGluR5, a subtype of group I mGluRs expressed with higher density than mGluR1 in neocortex pyramidal cells, or inositol-1,4,5-triphosphate receptors (IP3Rs) but not that against *N*-methyl-D-aspartate receptors (NMDARs). In layer II/III or layer V, Homer 1a injection was unable to affect LTD, which is mostly dependent on NMDARs and not on group I mGluRs in these layers. To examine the effects of endogenous Homer 1a, electroconvulsive shock (ECS) was applied. Homer 1a thereby induced, as did Homer 1a injection, reduced LTD magnitude in layer VI pyramidal cells and failed to do so in layer II/III or layer V pyramidal cells. These results indicate that both exo- and endogenous Homer 1a suppressed LTD in a cortical layer-specific manner, and its layer-specificity may be explained by the high affinity of Homer 1a to group I mGluRs.

INTRODUCTION

Elevation of intracellular calcium, which is well known to trigger induction of long-term synaptic plasticity, is regulated by an array of calcium channels inserted either in the postsynaptic membrane or endoplasmic reticulum (Anwyl 2006; Berridge 1998; Verkhratsky 2005). These channels are often linked by scaffold proteins (Fagni et al. 2002; Kim and Sheng 2004) and function in such organized manners that opening of one class of channels causes sequential activation of another class of channels (Emptage et al. 1999; Isaacson and Murphy 2001; Nakamura et al. 1999; Yamada et al. 2004; Yamamoto et al. 2000, 2002a,b). However, it is not clear whether particular scaffold proteins actually organize such functional channel couplings.

A scaffold protein Homer/Vesl family is capable of binding to group I metabotropic glutamate receptors (mGluRs) (Brakeman et al. 1997), inositol-1,4,5-triphosphate receptors (IP3Rs) (Tu et al. 1998), ryanodine receptors (RyRs) (Feng et al. 2002; Westhoff et al. 2003), and transient receptor potential channels (TRPs) (Yuan et al. 2003) directly, and *N*-methyl-D-aspartate receptors (NMDARs) indirectly through Shank, another scaffolding protein (Sheng and Kim 2000). All those Homer-attachable channels or proteins are critically involved in synaptic plasticity. Since the first report that activation of group I mGluRs is required for LTD induction in rat visual cortex slices (Kato 1993), there have been numerous studies that have implicated the role of group I mGluRs in long-term synaptic plasticity. IP3Rs are reported to determine the magnitude and polarity of long-term potentiation (LTP) or long-term depression (LTD) (Kato et al. 2000; Nishiyama et al. 2000). RyRs seem to modulate the magnitude of LTD (Nakano et al. 2004) or LTP (Balschun et al. 1999; Futatsugi et al. 1999; Shimuta et al. 2001). Functional coupling between mGluRs and TRPs is reported to be critical in LTP induction (Topolnik et al. 2006). Thus the Homer proteins seem to be in a strategic position to orchestrate these channels and to regulate long-term synaptic plasticity.

Homer1a/Vesl-1S is a unique member of Homer family because it misses the dimerization motif required for linking two or more channels (Brakeman et al. 1997; Kato et al. 1997) and, for this reason, is thought to be a dominant-negative regulator of the other members of Homer, the long Homer proteins. Homer 1a is also shown to serve as an intracellular ligand for group I mGluRs (Ango et al. 2001). More interestingly, Homer 1a is activity-dependently expressed, whereas expression of long Homer proteins is constitutive. Homer 1a may therefore be expressed by plasticity-prone synaptic stimulation and involved in synaptic modification in diverse manners. In fact, both up- and downregulation of synaptic transmission by Homer 1a have been reported (Hennou et al. 2003; Kammermeier and Worley 2007; Sala et al. 2003; van Keuren-Jensen and Cline 2006). Furthermore, it has been recently reported that genetically overexpressed Homer 1a impaired hippocampal LTP (Celikel et al. 2007). On the other hand, roles played by Homer 1a in LTD, induced by synaptic stimulation, have not been well studied. The present experiments examined the effects of Homer 1a, injected and induced by electroconvulsive shock (ECS), on LTD in visual cortex slices, because LTD in this structure is regulated at least partly by the mGluR-IP3 signaling (Kato 1993; Kato et al. 2000).

METHODS

Slice preparation

All experiments were performed in accordance with the guiding principle of the Physiological Society of Japan and with the approval

Address for reprint requests and other correspondence: N. Kato, Dept. of Physiology, Kanazawa Medical University, 920-0293 Ishikawa, Japan (E-mail: kato@kanazawa-med.ac.jp).

The costs of publication of this article were defrayed in part by the payment of page charges. The article must therefore be hereby marked "*advertisement*" in accordance with 18 U.S.C. Section 1734 solely to indicate this fact.

of the Animal Care Committee of Kanazawa Medical University. In brief, Wistar rats (15–19 days old) were decapitated under ether anesthesia. The brain was dissected out and soaked into high-sucrose containing medium composed of (in mM) 234 sucrose, 26 $NaHCO_3$, 10 $MgSO_4$, 2.5 KCl, 1.25 NaH_2PO_4, 0.5 $CaCl_2$, and 11 glucose, bubbled with a mixture of 95% O_2-5% CO_2. Slices (250 μm thick) of the primary visual cortex were prepared with a Linearslicer PRO-7 or microslicer Zero-1 (Dosaka, Kyoto, Japan). Slices were kept at 30°C for ≥60 min before experiments in normal artificial cerebrospinal fluid (ACSF) composed of (in mM) 124 NaCl, 3 KCl, 2.5 $CaCl_2$, 2 $MgSO_4$, 1.3 NaH_2PO_4, 26 $NaHCO_3$, and 20 glucose, bubbled with a mixture of 95% O_2-5% CO_2.

Electroconvulsive shock (ECS)

Electrical stimulations were carried out basically as described previously (Sakagami et al. 2005; Yamamoto et al. 2005) with minor modifications. Brief single electrical shock (60 V, 1 s) was applied to the head through two electrodes placed on the ears, one on each side, and then the rats were returned to the cage. Seizure thereby elicited lasted for a minute, during which the whole body became spastic with the eyelids closed and the extremities rigidly flexed. Then the rats stayed immobile for minutes in a fixed position in the cage with the eyelids opened and the extremities relaxed. Ten minutes after the electrical shock, the rats looked normal. The rats were killed at 30 min after the shock, and the brains were removed immediately for slice cutting. Excitatory postsynaptic currents (EPSCs) were recorded from pyramidal cells within 5 h because expression level of Homer 1a protein was gradually increased during this period (Brakeman et al. 1997). In some experiments, stimulation of a lower intensity subthreshold to seizure (30 V, 1 s) was applied. A single electrical shock (sub-ECS; 30 V, 1 s) was applied. Rats were jumped and vocalization occurred, but seizure was not elicited. Soon after the electrical shock, the rats looked normal. The rats were killed at 30 min after the shock. EPSCs were recorded from pyramidal cells at 2–5 h after sub-ECS.

Electrophysiology

Slices were placed in a recording chamber on the stage of an upright microscope (Axioskop FS2, Zeiss, Germany) with a ×63 water-immersion objective (Achroplan-63/0.9W, Zeiss). The chamber was continuously perfused with ACSF (30°C) bubbled with a mixture of 95% O_2-5% CO_2. For voltage-clamp experiments, we used patch pipettes (5–9 MΩ) filled with the internal solution containing (in mM) 130 Cs-methanesulfonate, 10 tetraethylammonium chloride, 0.2 EGTA, 5 QX-314 chloride, 10 HEPES, 2 Na_2ATP, 0.4 Na_2GTP, 2 $MgCl_2$, and 10 CsCl, adjusted to pH 7.2–7.3 with CsOH. In some experiments, Homer proteins or anti-Homer antibodies were included in the pipette solution. Whole cell recording was made from layer II/III, V, or VI pyramidal cells of the primary visual cortex. Membrane potential was voltage-clamped at −70 mV (Axopatch 700A, Axon Instruments), and EPSCs were evoked by stimulation at 0.05 Hz using a bipolar tungsten electrode. A stimulation electrode was inserted into layer IV for recording from layer II/III and into layer II/III for recording from layer V or VI. Experiments were begun only after series resistance had stabilized (typically 15–35 MΩ). Throughout the recording, series resistance was monitored continuously, and the recording was excluded from the data analysis if it varied by >20%. After a stable control level of EPSC was recorded for ≥5 min, LTD was induced by using a pairing protocol: 600 stimuli at 1 Hz were delivered under voltage-clamp at −40 mV.

Recombinant protein and antibody

Purified Homer1a/Vesl-1S protein (1 mg/ml) and rabbit polyclonal anti-Homer1a/Vesl-1S antibody were characterized as described previously (Kato et al. 1997, 1998, 2001).

Drugs used

Depending on the purpose of the experiments, D-2-amino-5- phosphonovaleric acid (D-APV, 50 μM; Tocris, Bristol, UK) or 2-methyl-6-(phenylethynyl)-pyridine (MPEP, 10 μM; Tocris) was bath-applied. Homer 1a protein (1 or 3 μg/ml), anti-Homer 1a antibody (0.4 μg/ml), or heparin (1 mg/ml; Nacalai, Kyoto, Japan) was contained in the pipette solution and distributed into the cell by diffusion.

Data analysis

Electrophysiological data were filtered at 5 kHz and digitized at 10 kHz (Digidata 1322A and pClamp8, Axon Instruments). For data analysis, pClamp9 (Axon Instruments) was used for calculating the amplitude of EPSCs, and three samples were averaged for each data point. EPSC amplitudes were normalized to baseline and expressed as averages ± SE. The magnitude of LTD was assessed by comparing the average amplitude of responses, obtained between 31 and 35 min after conditioning stimulation, with the preconditioning control. Paired or unpaired *t*-test were used for statistics with the significance level set at $P < 0.05$.

RESULTS

Group I mGluR-dependent LTD in layer VI pyramidal cells was suppressed by Homer 1a injection

EPSCs were recorded from layer VI pyramidal cells bathed in normal medium with or without Homer 1a protein injected. The presynaptic stimulation electrode was placed between layer II and III. In agreement with the previous data (Rao and Daw 2004), LTD was induced in control experiments without Homer 1a (61.1 ± 5.2%, $n = 7$; Fig. 1*A*). With Homer 1a injected by diffusion from patch pipettes (1 μg/ml), LTD magnitude at the late phase (≥22 min postpairing) was significantly reduced (79.4 ± 6.1%, $n = 9$; $P < 0.03$, 22 min postpairing; Fig. 1*B*). On the other hand, the baseline transmission was not changed even with Homer 1a injected (97.5 ± 12.6%, $n = 4$). We have previously reported that injection of Homer 1a protein elicited hyperpolarization of rat visual cortex pyramidal cells in layer II/III under current-clamp condition by using potassium-based internal solution. In that case, hyperpolarization progressed gradually and reached the steady state within 10 min after break-in (Sakagami et al. 2005), indicating that diffusion of Homer 1a must be completed within 10 min. We therefore started LTD induction ≥10 min after the whole cell break-in in the present study.

LTD is often classified into mGluR- and NMDAR-dependent groups (Oliet et al. 1997). Recently, it has been reported that LTD induced by 1-Hz presynaptic simulation of layer II/III paired with postsynaptic depolarization to −40 mV in layer VI of the rat visual cortex was dependent on group I mGluRs but not on NMDARs (Daw et al. 2004; Rao and Daw 2004). This finding was first confirmed in the present experiments. With the NMDAR antagonist D-APV bath-applied (50 μM), LTD was still induced (70.8 ± 4.6%, $n = 6$; Fig. 1*C*). On the other hand, bath application of MPEP (10 μM), a noncompetitive group I mGluR (mGluR5) antagonist, significantly suppressed LTD (83.8 ± 7.7%, $n = 7$; $P < 0.03$; Fig. 1*D*). Both subtypes of group I mGluRs, mGluR1 and mGluR5, are involved in group I mGluR-dependent long-term synaptic plasticity (Volk et al. 2006; Wang and Daw 2003). However, in pyramidal cells of the rat neocortex, the expression of mGluR5 is much more prominent than that of mGluR1 (Shigemoto et al. 1993).

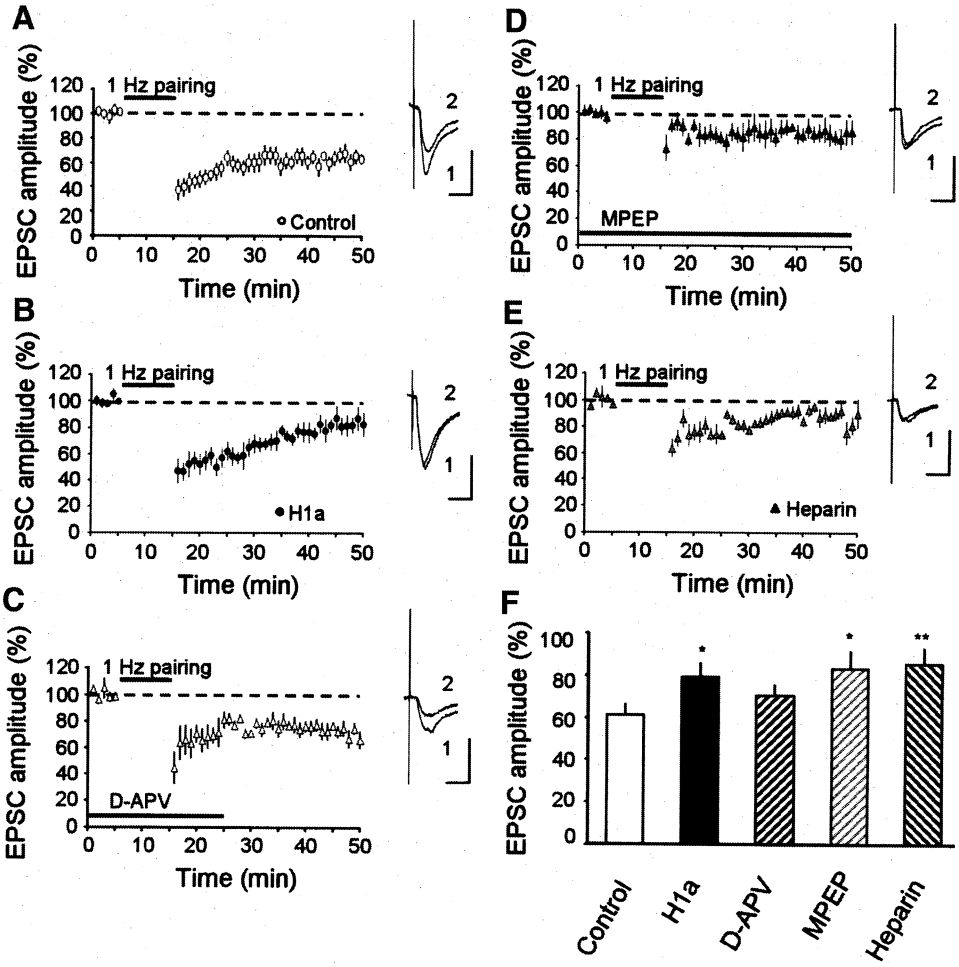

FIG. 1. Group I metabotropic glutamate receptor (mGluR)-dependent long-term depression (LTD) in layer VI pyramidal cells. *A*: in layer VI, LTD was induced by a 1-Hz pairing protocol. In specimen recordings shown in this and following figs, comparison was made between representative traces obtained before (1) and after (2) LTD induction. *B*: Homer 1a (1 μg/ml) injected by diffusion from patch pipettes suppressed LTD. *C*: LTD was resistant to *N*-methyl-D-aspartate receptor (NMDAR) blockade with D-2-amino-5-phosphonovaleric acid (D-APV, 50 μM). *D*: LTD was suppressed by bath application of the mGluR5 antagonist 2-methyl-6-(phenylethynyl)-pyridine (MPEP, 10 μM). *E*: with the inositol-1,4,5-triphosphate receptor (IP3R) blocker heparin (1 mg/ml) intracellularly injected, LTD magnitude was decreased. *F*: summary diagram describing averages of excitatory postsynaptic current (EPSC) amplitudes expressed as percent of the preconditioning baseline in various experimental conditions. In the control, EPSC amplitude was reduced to 61.1%; hence LTD was clearly induced. Error bars represent SE. $*P < 0.03$, $**P < 0.02$. Scale bars, 20 ms and 100 pA.

Furthermore, mGluR5 rather than mGluR1 seems to be preferentially associated with Homer-mediated signaling in the rat visual cortex (Yamamoto et al. 2005). We therefore used the mGluR5 antagonist MPEP as a representative group I mGluR antagonist. To check involvement of the IP3 signaling downstream of group I mGluRs, we examined the effect of IP3R blocker heparin on LTD in layer VI pyramidal cells. With heparin (1 mg/ml) injected by diffusion from patch pipettes, LTD was significantly suppressed (85.8 ± 6.8%, $n = 7$; $P < 0.02$; Fig. 1*E*). The dependence of layer VI LTD on the mGluR-IP3 signaling is consistent with its Homer 1a sensitivity because Homer 1a is known to modulate the mGluR-IP3 signaling by agonist-independent activation of mGluR (Ango et al. 2001; Yamamoto et al. 2005) or its dominant-negative effect on constitutive Homers (Fagni et al. 2002).

LTD was insensitive to Homer 1a in layer II/III and layer V pyramidal cells

EPSCs were recorded from layer II/III pyramidal cells with or without Homer 1a injected. The presynaptic stimulation electrode was placed in layer IV. Without Homer 1a, LTD was induced in normal medium (60.9 ± 5.0%, $n = 7$; Fig. 2*A*). In contrast to the findings obtained from layer VI neurons, Homer 1a injection allowed induction of a comparable LTD (1 μg/ml, 56.1 ± 3.6%, $n = 8$; Fig. 2*B*). LTD of much the same amplitude was observed again with the triple concentration of Homer 1a (3 μg/ml, 55.8 ± 4.2%, $n = 6$; Fig. 2*B*), suggesting that the lack of Homer 1a effect was not due to low concentration. In layer II/III, LTD was significantly suppressed with bath application of D-APV (50 μM, 82.4 ± 5%, $n = 9$; $P < 0.01$; Fig. 2*C*). Bath application of MPEP (10 μM), on the other hand, failed to block LTD (54.0 ± 5.1%, $n = 4$; Fig. 2*D*).

LTD was also induced in layer V pyramidal cells in normal medium (56.9 ± 5%, $n = 8$; Fig. 3*A*) with layer II/III stimulated. Similarly to the finding obtained by recording from layer II/III pyramidal cells, Homer 1a injection failed to suppress LTD (1 μg/ml, 55.2 ± 5.4%, $n = 7$; Fig. 3*B*). LTD magnitude was unchanged even when Homer 1a concentration was increased threefold (3 μg/ml, 65.6 ± 5.8%, $n = 4$; Fig. 3*B*). This layer V LTD was completely inhibited by applying D-APV (50 μM, 102 ± 10%, $n = 5$; $P < 0.005$; Fig. 3*C*), whereas the group I mGluR antagonist MPEP (10 μM) allowed induction of significant LTD (59 ± 10.4%, $n = 5$; Fig. 3*D*).

ECS inhibited LTD in layer VI, but not in layer II/III or V, pyramidal cells

The experiments so far suggest that Homer 1a could modulate mGluR-mediated LTD in layer VI. Although the mGluR antagonist MPEP or IP3R blocker heparin strongly suppressed LTD immediately after the induction protocol, the suppressing effect of injected Homer 1a slowly emerged and was not apparent at the earliest phase of LTD. Because intracellular

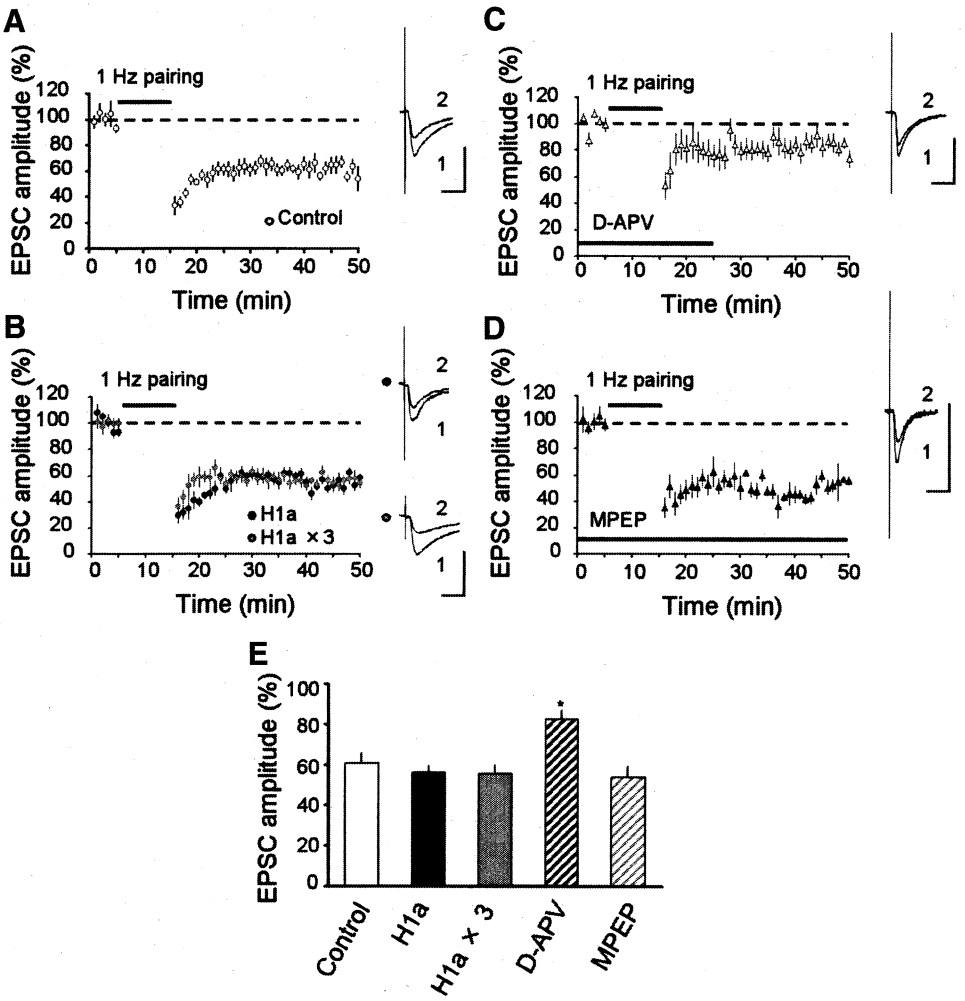

FIG. 2. Group I mGluR-independent LTD in layer II/III pyramidal cells. *A*: in layer II/III also, LTD was induced by a 1-Hz pairing protocol. *B*: Homer 1a (1 μg/ml, ●; 3 μg/ml, ⊜) was unable to affect LTD. *C*: LTD was suppressed by bath-application of NMDAR antagonist D-APV (50 μM). *D*: LTD magnitude was unchanged in the presence of MPEP (10 μM). *E*: summary diagram describing averages of EPSC amplitudes in various experimental conditions. Error bars represent SE. $*P < 0.01$. Scale bars, 20 ms and 100 pA.

distribution of injected Homer 1a protein was not visualized in our present study, we could not exclude the possibility that only a limited amount of Homer 1a was localized at synaptic sites at the earliest phase of LTD. To assure intracellular distribution of Homer 1a, we made use of ECS, a powerful experimental tool that has been confirmed to induce endogenous Homer 1a (Altar et al. 2004; Brakeman et al. 1997). Previous studies showed that activity-induced endogenous Homer 1a protein was accumulated in postsynaptic region (Kato et al. 2001). We thus examined whether ECS-induced Homer 1a, as well as Homer 1a injected from the pipette, alters neocortical LTD.

In slices obtained from ECS-subjected rats, LTD was significantly suppressed soon after pairing protocol in layer VI (90.2 ± 3.7%, $n = 9$; $P < 0.001$ as compared with the no-ECS control; Fig. 4*A*), although baseline transmission was not changed (86.5 ± 4.3%, $n = 4$). ECS triggers expression of not only Homer 1a, but a large number of gene products, some of which are thought to be involved in long-term synaptic plasticity (Altar et al. 2004). Previously, we reported that Homer 1a induced by ECS hyperpolarizes rat visual cortex pyramidal cells and upregulates L-type calcium channel currents under current-clamp mode with potassium-based internal solution and that both of these two Homer 1a effects were disrupted by co-application of anti-Homer 1a antibody (Sakagami et al. 2005; Yamamoto et al. 2005). We therefore checked the involvement of Homer 1a by using anti-Homer 1a antibody (0.4 μg/ml). In ECS-subjected tissue, the antibody injected through patch pipettes restored LTD (61.9 ± 8.3%, $n = 5$, not statistically different from the no-ECS control; Fig. 4*B*). However, rabbit IgG (0.4 μg/ml) injection failed to restore LTD (90.9 ± 9.5%, $n = 4$, not statistically different from just ECS cases), indicating that the effect of anti-Homer 1a antibody is not nonspecific. It was thus shown that the suppressing effect of ECS on LTD in layer VI was mediated at least partly by Homer 1a.

For a control purpose, we further carried out sub-ECS treatment, which is an electrical shock of a reduced intensity subthreshold to seizure. Sub-ECS was incapable of producing sufficient amounts of endogenous Homer 1a protein (our own unpublished observation), in agreement with the report that Homer 1a induction requires convulsion (Brakeman et al. 1997; Potschka et al. 2002). In slices from the sub-ECS group, significant LTD was still induced in layer VI pyramidal cells (66.9 ± 4.3%, $n = 5$, not statistically different from the no-ECS control; Fig. 4*C*). However, in contrast to the findings obtained from ECS group, the earliest phase of LTD appeared to be reduced.

As we showed, LTD in layer II/III (Fig. 2*B*) or layer V pyramidal cells (Fig. 3*B*) was still induced with Homer 1a injection. Here we examined whether ECS could modify LTD in these layers. However, LTD was still induced in layer II/III

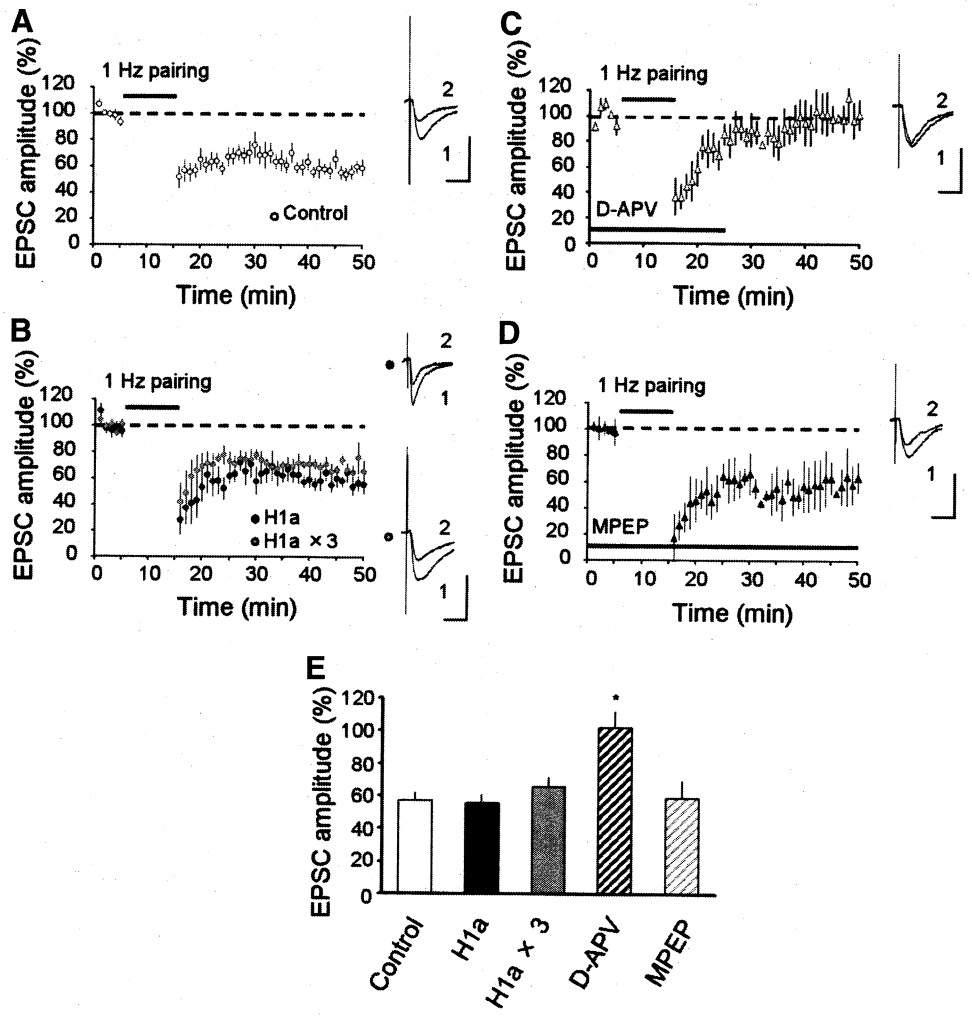

FIG. 3. Group I mGluR-independent LTD in layer V pyramidal cells. *A*: LTD was induced by a 1-Hz pairing protocol in layer V. *B*: Homer 1a (1 μg/ml, ●; 3 μg/ml, ◎) failed to suppress LTD. *C*: LTD was blocked by bath-application of D-APV (50 μM). *D*: LTD was still induced in the presence of MPEP (10 μM). *E*: summary diagram describing averages of EPSC amplitudes in various experimental conditions. Error bars represent SE. $*P < 0.005$. Scale bars, 20 ms and 100 pA.

(62.2 ± 4.2%, $n = 4$; Fig. 5*A*) and layer V pyramidal cells (66.9 ± 7.4%, $n = 5$; Fig. 5*B*) following ECS.

DISCUSSION

The present experiments revealed that intracellular application of Homer 1a protein suppressed LTD in layer VI pyramidal cells, which is dependent on group I mGluRs and IP3Rs but not on NMDARs. However, Homer 1a allowed LTD in layer II/III or layer V pyramidal cells, which is dependent mainly on NMDARs but not on group I mGluRs. We also made use of ECS as a method for inducing Homer 1a at a broadly physiological concentration range. ECS-induced Homer 1a also suppressed LTD in layer VI but not in layer II/III or layer V pyramidal cells. This ECS-elicited suppression of LTD in layer VI was restored by intracellular application of anti-Homer 1a antibody, which is supposed to neutralize endogenous Homer 1a expressed by ECS. Thus the present study clearly demonstrated for the first time the suppressing effect of Homer 1a on LTD at a population of cortical synapses.

Roles of Homer 1a on basal synaptic transmission

Homer 1a was initially characterized as a gene upregulated by tetanization leading to LTP (Kato et al. 1997). Subsequent studies have reported that Homer 1a both up- and downregulates glutamatergic synaptic responses in various preparations: suppression of AMPAR- and NMDAR-mediated synaptic transmission in rat hippocampal neurons through its protein-binding ability (Sala et al. 2003); facilitation of AMPAR-mediated synaptic transmission and clustering of synaptic AMPAR in rat hippocampal neurons (Hennou et al. 2003); reversal of group I mGluR-mediated up-regulation of AMPAR transmission in dark-reared tadpole tectal neurons (van Keuren-Jensen and Cline 2006); and restoration of group I mGluR-mediated EPSC decrease at hippocampal autaptic synapses (Kammermeier and Worley 2007). According to these results as well as a recently published review (Shiraishi-Yamaguchi and Furuichi 2007), AMPAR responses are considered to be both up- and downregulated by Homers interacting with mGluRs or other proteins, depending on experimental conditions such as activity states of recorded neurons or variation of extent in gene expression. In our present study, we used both protein injection and ECS application to induce Homer 1a expression. In both cases, we did not observe any marked changes in basal transmission in layer VI pyramidal cells, although LTD was modulated. Recently, it has reported that overexpression of Homer 1a inhibited LTP in the hippocampus (Celikel et al. 2007). Consistent with our study, they showed that basal transmission was unaffected by overexpression of Homer 1a. We cannot rule out short-term changes in

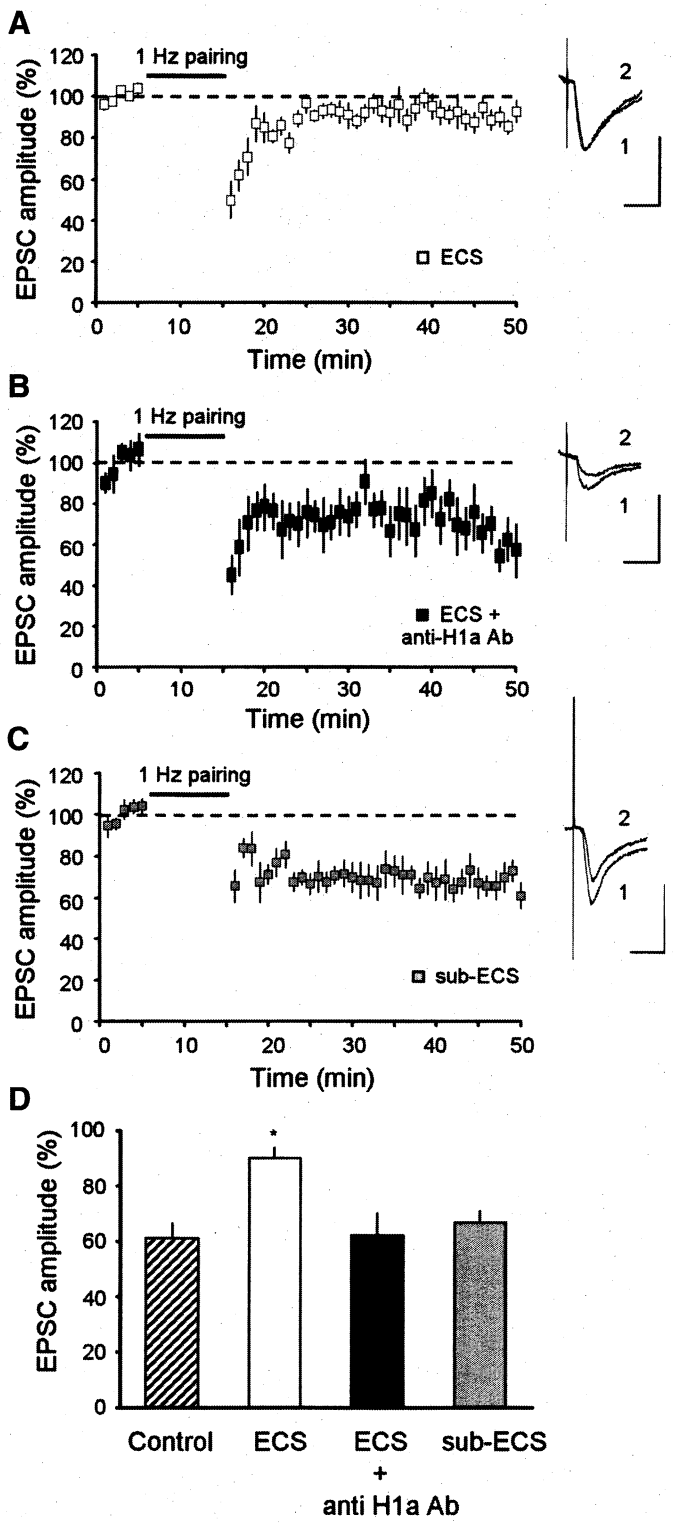

FIG. 4. Blockade of layer VI LTD by electroconvulsive shock (ECS). *A*: recordings obtained at 2–5 h after ECS (60 V, 1 s). In layer VI, LTD was suppressed. *B*: when anti-Homer 1a antibody (rabbit polyclonal antibody; 0.4 μg/ml) was injected through patch pipettes, LTD was induced in slices obtained from ECS-subjected rats. *C*: stimulation of a lower intensity (sub-ECS; 30 V, 1 s), subthreshold to seizure, allowed LTD. *D*: summary diagram describing averages of EPSC amplitudes in various experimental conditions. Data for Control was taken from Fig. 1*A*. Error bars represent SE. $*P < 0.001$. Scale bars, 20 ms and 100 pA.

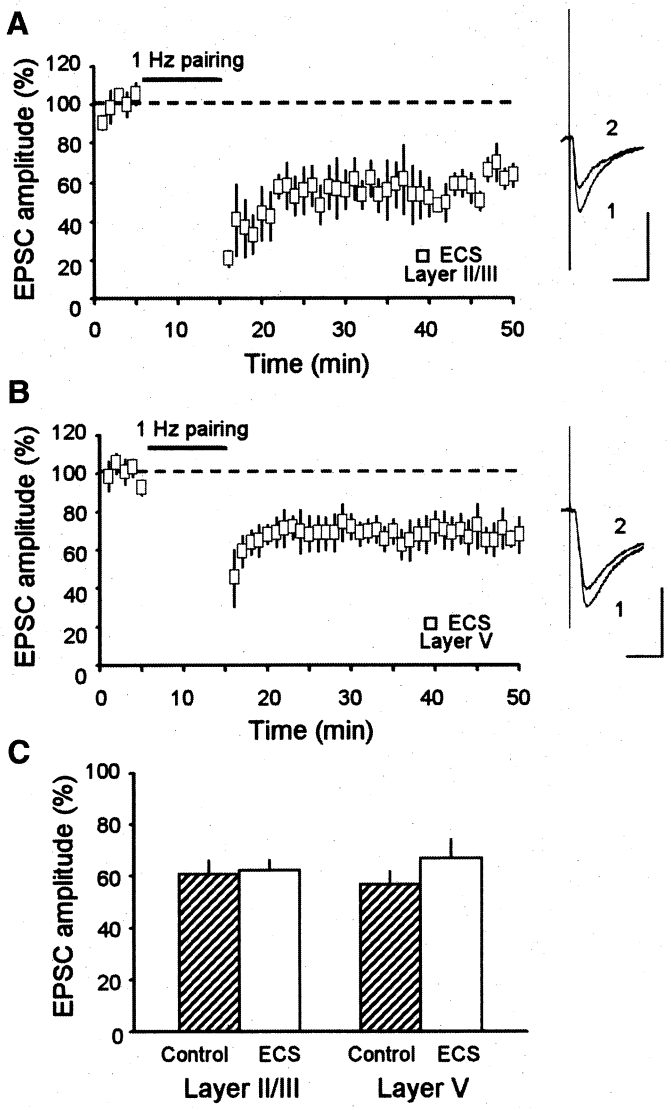

FIG. 5. Failure of ECS to affect layer II/III and V LTD. *A* and *B*: LTD in layer II/III (*A*) and layer V (*B*) was still induced after ECS. *C*: summary diagram describing averages of EPSC amplitudes in various experimental conditions. Error bars represent SE. Data for Control were taken from Figs. 2*A* and 3*A*. Scale bars, 20 ms and 100 pA.

synaptic transmission after Homer 1a expression because we began recording ≥5 to 10 min after break-in for diffusion of injected Homer 1a protein (Sakagami et al. 2005). Several recent studies have described effects of activity-induced Homer 1a in more physiological contexts: nociception (Tappe et al. 2006), visual experience (van Keuren-Jensen and Cline 2006), and seizure activity induced by ECS (Sakagami et al. 2005; Yamamoto et al. 2005; present study). These lines of investigation would provide further insights into mechanisms of Homer 1a action on basal synaptic responses.

Roles of Homer 1a on long-term synaptic modification

In contrast to action of Homer 1a on basal transmission, that on long-term synaptic modification remains unclear. Previous studies have reported involvement of constitutively expressed Homer, but not Homer 1a, proteins in LTD. First, impairment of mGluR-dependent LTD after status epilepticus was associ-

ated with decrease in expression levels of constitutive Homer and mGluR5 in the rat hippocampus but not that of Homer 1a (Kirschstein et al. 2007). Second, impairment of endocannabinoid-mediated LTD after cocaine administration was associated with increase in the expression level of constitutive Homer and decrease in surface expression of mGluR5 in the mouse nucleus accumbens (Fourgeaud et al. 2004). In both studies, changes in LTD or Homer expression were observed in chronic or subchronic conditions, in which just constitutive Homers would be in function or detectable. In contrast to constitutively expressed Homers, expression of the activity-induced Homer 1a was transient (Brakeman et al. 1997) and can last for only a few hours (Sakagami et al. 2005; Yamamoto et al. 2005). Our present experiments were done rather in acute conditions and demonstrated roles of injected and acute ECS-induced Homer 1a in LTD, thus shedding new light on roles of Homers in synaptic plasticity.

In the present study, the suppressing effect of Homer 1a on LTD was significant at the late phase of LTD (≥22 min postpairing). Similarly, a recent study has reported that overexpression of Homer 1a suppressed LTP at the late phase (20–25 min postpairing) in hippocampal CA1 neurons (Celikel et al. 2007). It is thus suggested that Homer 1a affects only a late phase of long-term modification of synaptic efficiency. On the other hand, effects of ECS on LTD were observed at both the early and late phases of LTD in the present experiments, suggesting that ECS interferes with the early phase of LTD by means of other mediators than Homer 1a. Indeed, after anti-Homer 1a antibody injection into pyramidal neurons in slices from ECS-subjected rats, LTD was restored only at the late phase. It would be interesting to look for the molecular identity of this early phase mediator. In this light, the present sub-ECS experiments may be suggestive, since sub-ECS suppressed only the early phase of LTD and left the late phase intact. Comparison between the two arrays of molecules expressed by ECS and sub-ECS might provide some cue for such a mediator or mediators.

Homer 1a as a feedback regulator of neural excitability

As we show in this paper, exogenously injected or ECS-induced Homer 1a significantly suppressed LTD in layer VI but not in layer II/III or layer V pyramidal cells. Homer 1a was detected in the pyramidal cells of all layers after ECS (Brakeman et al. 1997). Also, group I mGluRs are distributed throughout the cortical layers (Shigemoto et al. 1993). These observations and the present experiments, taken together, suggest that layer-specific effects of Homer 1a on group I mGluR-dependent LTD are not due to layer-specific expression of Homer 1a or group I mGluRs in the visual cortex. According to both anatomical and electrophysiological studies, corticothalamic efferents from the visual cortex to the lateral geniculate body originate exclusively from layer VI pyramidal cells (Kato et al. 1983, 1984). These corticothalamic feedback projections have been reported to sharpen receptive fields or increase filtering properties of visual thalamic neurons (Alitto and Usrey 2003; Cudeiro and Sillito 2006). According to the present results, Homer 1a induced by incoming visual activity would allow LTD induction in layers II/III and V but prevent it in layer VI, the output layer back to the lateral geniculate body. We propose that activity-dependently induced Homer 1a may downregulate cortical activities without drastically reducing corticothalamic feedback outputs and that such differential regulation may effectively fine tune the balance among thalamic, cortical, and thalamocortical activities.

Noninvasive strategy for the treatment of depressive disorders

For inducing endogenous Homer 1a expression, we carried out ECS as an experimental tool in this paper. It is well known that ECS is an experimental model of electroconvulsive therapy (ECT), which is a clinically efficient and trustworthy treatment for drug-resistant depressive disorders. However, convulsion necessitates anesthesiological care, and ECS could cause adverse effects such as memory loss (Squire et al. 1975). If neurobiological mechanisms of ECT effects became well understood, we could extract and exploit the essence of ECT for other forms of therapy that are based on neurobiological understanding of ECT but achieved by much less invasive methods. A recent microarray analysis has revealed that ~20 genes including Homer 1a are highly expressed by ECS (Altar et al. 2004). To date, Homer proteins have been implicated in memory, neuropsychiatric disorders and long-term synaptic plasticity (Celikel et al. 2007; Giuffrida et al. 2005; Szumlinski et al. 2006). We believe that to investigate physiological effects of Homers on neural behaviors including synaptic plasticity should contribute to understanding and extracting the neurobiological essence of ECT.

ACKNOWLEDGMENTS

The authors thank H. Adachi and S. Muramoto for technical assistance, Drs. T. Sugai, K. Yamamoto, and H. Yoshimura for valuable discussion, and Drs. M. Murata and K. Kawano for encouragement.

GRANTS

This work was supported partly by a Grant for Collaborative Research (C2006-5 and C2007-2) from Kanazawa Medical University.

REFERENCES

Alitto HJ, Usrey WM. Corticothalamic feedback and sensory processing. *Curr Opin Neurobiol* 13: 440–445, 2003.

Altar CA, Laeng P, Jurata LW, Brockman JA, Lemire A, Bullard J, Bukhman YV, Young TA, Charles V, Palfreyman MG. Electroconvulsive seizures regulate gene expression of distinct neurotrophic signaling pathways. *J Neurosci* 24: 2667–2677, 2004.

Ango F, Prezeau L, Muller T, Tu JC, Xiao B, Worley PF, Pin JP, Bockaert J, Fagni L. Agonist-independent activation of metabotropic glutamate receptors by the intracellular protein Homer. *Nature* 411: 962–965, 2001.

Anwyl R. Induction and expression mechanisms of postsynaptic NMDA receptor-independent homosynaptic long-term depression. *Prog Neurobiol* 78: 17–37, 2006.

Balschun D, Wolfer DP, Bertocchini F, Barone V, Conti A, Zuschratter W, Missiaen L, Lipp HP, Frey JU, Sorrentino V. Deletion of the ryanodine receptor type 3 (RyR3) impairs forms of synaptic plasticity and spatial learning. *EMBO J* 18: 5264–5273, 1999.

Berridge MJ. Neuronal calcium signaling. *Neuron* 21: 13–26, 1998.

Brakeman PR, Lanahan AA, O'Brien R, Roche K, Barnes CA, Huganir RL, Worley PF. Homer: a protein that selectively binds metabotropic glutamate receptors. *Nature* 386: 284–288, 1997.

Celikel T, Marx V, Freudenberg F, Zivkovic A, Resnik E, Hasan MT, Licznerski P, Osten P, Rozov A, Seeburg PH, Schwarz MK. Select overexpression of Homer1a in dorsal hippocampus impairs spatial working memory. *Front Neurosci* 1: 97–110, 2007.

Cudeiro J, Sillito AM. Looking back: corticothalamic feedback and early visual processing. *Trends Neurosci* 29: 298–306, 2006.

Daw N, Rao Y, Wang XF, Fischer Q, Yang Y. LTP and LTD vary with layer in rodent visual cortex. *Vision Res* 44: 3377–3380, 2004.

Emptage N, Bliss TV, Fine A. Single synaptic events evoke NMDA receptor-mediated release of calcium from internal stores in hippocampal dendritic spines. *Neuron* 22: 115–124, 1999.

Fagni L, Worley PF, Ango F. Homer as both a scaffold and transduction molecule. *Sci STKE* 137: RE8, 2002.

Feng W, Tu J, Yang T, Vernon PS, Allen PD, Worley PF, Pessah IN. Homer regulates gain of ryanodine receptor type 1 channel complex. *J Biol Chem* 277: 44722–44730, 2002.

Fourgeaud L, Mato S, Bouchet D, Hemar A, Worley PF, Manzoni OJ. A single in vivo exposure to cocaine abolishes endocannabinoid-mediated long-term depression in the nucleus accumbens. *J Neurosci* 24: 6939–6945, 2004.

Futatsugi A, Kato K, Ogura H, Li ST, Nagata E, Kuwajima G, Tanaka K, Itohara S, Mikoshiba K. Facilitation of NMDAR-independent LTP and spatial learning in mutant mice lacking ryanodine receptor type 3. *Neuron* 24: 701–713, 1999.

Giuffrida R, Musumeci S, D'Antoni S, Bonaccorso CM, Giuffrida-Stella AM, Oostra BA, Catania MV. A reduced number of metabotropic glutamate subtype 5 receptors are associated with constitutive homer proteins in a mouse model of fragile X syndrome. *J Neurosci* 25: 8908–8916, 2005.

Hennou S, Kato A, Schneider EM, Lundstrom K, Gahwiler BH, Inokuchi K, Gerber U, Ehrengruber MU. Homer-1a/Vesl-1S enhances hippocampal synaptic transmission. *Eur J Neurosci* 18: 811–819, 2003.

Isaacson JS, Murphy GJ. Glutamate-mediated extrasynaptic inhibition: direct coupling of NMDA receptors to Ca^{2+}-activated K^+ channels. *Neuron* 31: 1027–1034, 2001.

Kammermeier PJ, Worley PF. Homer 1a uncouples metabotropic glutamate receptor 5 from postsynaptic effectors. *Proc Natl Acad Sci USA* 104: 6055–6060, 2007.

Kato A, Fukuda T, Fukazawa Y, Isojima Y, Fujitani K, Inokuchi K, Sugiyama H. Phorbol esters promote postsynaptic accumulation of Vesl-1S/Homer-1a protein. *Eur J Neurosci* 13: 1292–1302, 2001.

Kato A, Ozawa F, Saitoh Y, Hirai K, Inokuchi K. vesl, a gene encoding VASP/Ena family related protein, is upregulated during seizure, long-term potentiation and synaptogenesis. *FEBS Lett* 412: 183–189, 1997.

Kato A, Ozawa F, Saitoh Y, Fukazawa Y, Sugiyama H, Inokuchi K. Nobel members of the vesl/Homer family of PDZ proteins that bind metabotropic glutamate receptors. *J Biol Chem* 273: 23969–23975, 1998.

Kato N. Dependence of long-term depression on postsynaptic metabotropic glutamate receptors in visual cortex. *Proc Natl Acad Sci USA* 90: 3650–3654, 1993.

Kato N, Kawaguchi S, Miyata H. Geniculocortical projection to layer I of area 17 in kittens: orthograde and retrograde HRP studies. *J Comp Neurol* 225: 441–447, 1984.

Kato N, Kawaguchi S, Yamamoto T, Samejima A, Miyata H. Postnatal development of the geniculocortical projection in the cat: electrophysiological and morphological studies. *Exp Brain Res* 51: 65–72, 1983.

Kato N, Isomura Y, Tanaka T. Intracellular calcium releases facilitate induction of long-term depression. *Neuropharmacology* 39: 1107–1110, 2000.

Kim E, Sheng M. PDZ domain proteins of synapses. *Nat Rev Neurosci* 5: 771–781, 2004.

Kirschstein T, Bauer M, Muller L, Ruschenschmidt C, Reitze M, Becker AJ, Schoch S, Beck H. Loss of metabotropic glutamate receptor-dependent long-term depression via downregulation of mGluR5 after status epilepticus. *J Neurosci* 27: 7696–7704, 2007.

Nakamura T, Barbara JG, Nakamura K, Ross WN. Synergistic release of Ca^{2+} from IP3-sensitive stores evoked by synaptic activation of mGluRs paired with backpropagating action potentials. *Neuron* 24: 727–737, 1999.

Nakano M, Yamada S, Udagawa R, Kato N. Frequency-dependent requirement for calcium store-operated mechanisms in induction of homosynaptic long-term depression at hippocampus CA1 synapses. *Eur J Neurosci* 19: 2881–2887, 2004.

Nishiyama M, Hong K, Mikoshiba K, Poo MM, Kato K. Calcium stores regulate the polarity and input specificity of synaptic modification. *Nature* 408: 584–588, 2000.

Oliet SH, Malenka RC, Nicoll RA. Two distinct forms of long-term depression coexist in CA1 hippocampal pyramidal cells. *Neuron* 18: 969–982, 1997.

Potschka H, Krupp E, Ebert U, Gumbel C, Leichtlein C, Lorch B, Pickert A, Kramps S, Young K, Grune U, Keller A, Welschof M, Vogt G, Xiao B, Worley PF, Loscher W, Hiemisch H. Kindling-induced overexpression of Homer 1A and its functional implications for epileptogenesis. *Eur J Neurosci* 16: 2157–2165, 2002.

Rao Y, Daw NW. Layer variations of long-term depression in rat visual cortex. *J Neurophysiol* 92: 2652–2658, 2004.

Sakagami Y, Yamamoto K, Sugiura S, Inokuchi K, Hayashi T, Kato N. Essential roles of Homer-1a in homeostatic regulation of pyramidal cell excitability: a possible link to clinical benefits of electroconvulsive shock. *Eur J Neurosci* 21: 3229–3239, 2005.

Sala C, Futai K, Yamamoto K, Worley PF, Hayashi Y, Sheng M. Inhibition of dendritic spine morphogenesis and synaptic transmission by activity-inducible protein Homer1a. *J Neurosci* 23: 6327–6337, 2003.

Sheng M, Kim E. The Shank family of scaffold proteins. *J Cell Sci* 113: 1851–1856, 2000.

Shigemoto R, Nomura S, Ohishi H, Sugihara H, Nakanishi S, Mizuno N. Immunohistochemical localization of a metabotropic glutamate receptor, mGluR5, in the rat brain. *Neurosci Lett* 163: 53–57, 1993.

Shimuta M, Yoshikawa M, Fukaya M, Watanabe M, Takeshima H, Manabe T. Postsynaptic modulation of AMPA receptor-mediated synaptic responses and LTP by the type 3 ryanodine receptor. *Mol Cell Neurosci* 17: 921–930, 2001.

Shiraishi-Yamaguchi Y, Furuichi T. The Homer family proteins. *Genome Biol* 8: 206, 2007.

Squire LR, Slater PC, Chace PM. Retrograde amnesia: temporal gradient in very long term memory following electroconvulsive therapy. *Science* 187: 77–79, 1975.

Szumlinski KK, Kalivas PW, Worley PF. Homer proteins: implications for neuropsychiatric disorders. *Curr Opin Neurobiol* 16: 251–257, 2006.

Tappe A, Klugmann M, Luo C, Hirlinger D, Agarwal N, Benrath J, Ehrengruber MU, During MJ, Kuner R. Synaptic scaffolding protein Homer1a protects against chronic inflammatory pain. *Nat Med* 12: 677–681, 2006.

Topolnik L, Azzi M, Morin F, Kougioumoutzakis A, Lacaille JC. mGluR1/5 subtype-specific calcium signaling and induction of long-term potentiation in rat hippocampal oriens/alveus interneurons. *J Physiol* 575: 115–131, 2006.

Tu JC, Xiao B, Yuan JP, Lanahan AA, Leoffert K, Li M, Linden DJ, Worley PF. Homer binds a novel proline-rich motif and links group 1 metabotropic glutamate receptors with IP3 receptors. *Neuron* 21: 717–726, 1998.

van Keuren-Jensen K, Cline HT. Visual experience regulates metabotropic glutamate receptor-mediated plasticity of AMPA receptor synaptic transmission by Homer1a induction. *J Neurosci* 26: 7575–7580, 2006.

Verkhratsky A. Physiology and pathophysiology of the calcium store in the endoplasmic reticulum of neurons. *Physiol Rev* 85: 201–279, 2005.

Volk LJ, Daly CA, Huber KM. Differential roles for group 1 mGluR subtypes in induction and expression of chemically induced hippocampal long-term depression. *J Neurophysiol* 95: 2427–2438, 2006.

Wang XF, Daw NW. Long term potentiation varies with layer in rat visual cortex. *Brain Res* 989: 26–34, 2003.

Westhoff JH, Hwang SY, Duncan RS, Ozawa F, Volpe P, Inokuchi K, Koulen P. Vesl/Homer proteins regulate ryanodine receptor type 2 function and intracellular calcium signaling. *Cell Calcium* 34: 261–269, 2003.

Yamada S, Takechi H, Kanchiku I, Kita T, Kato N. Small-conductance Ca^{2+}-dependent K^+ channels are the target of spike-induced Ca^{2+} release in a feedback regulation of pyramidal cell excitability. *J Neurophysiol* 91: 2322–2329, 2004.

Yamamoto K, Hashimoto K, Isomura Y, Shimohama S, Kato N. An IP3-assisted form of Ca^{2+}-induced Ca^{2+} release in neocortical neurons. *Neuroreport* 11: 535–539, 2000.

Yamamoto K, Hashimoto K, Nakano M, Shimohama S, Kato N. A distinct form of calcium release down-regulates membrane excitability in neocortical pyramidal cells. *Neuroscience* 109: 665–676, 2002a.

Yamamoto K, Nakano M, Hashimoto K, Shimohama S, Kato N. Emergence of a functional coupling between inositol-1,4,5-triphosphate receptors and calcium channels in developing neocortical neurons. *Neuroscience* 109: 677–685, 2002b.

Yamamoto K, Sakagami Y, Sugiura S, Inokuchi K, Shimohama S, Kato N. Homer 1a enhances spike-induced calcium influx via L-type calcium channels in neocortex pyramidal cells. *Eur J Neurosci* 22: 1338–1348, 2005.

Yuan JP, Kiselyov K, Shin DM, Chen J, Shcheynikov N, Kang SH, Dehoff MH, Schwarz MK, Seeburg PH, Muallem S, Worley PF. Homer binds TRPC family channels and is required for gating of TRPC1 by IP3 receptors. *Cell* 114: 777–789, 2003.

１．研究課題名：糖尿病腎症の発症・進展に関わる新規診断法の確立
（研究番号　C2006-6）

２．キーワード：１）糖尿病腎症（diabetic nephropathy）
２）診断法（diagnostic procedure）
３）プロテオーム解析（proteome analysis）
４）サポシンＢ（saposin B）
５）トランスサイレチン（transthyretin）

３．研究代表者：古家　大祐・医学部・教　授・内分泌代謝制御学（内分泌内科学）
研究分担者：木越　俊和・医学部・特任教授・内分泌代謝制御学（内分泌内科学）
柏木　厚典・滋賀医科大学付属病院・病院長
楢木　　徹・エーザイ株式会社・研究所・室長

４．研 究 目 的

現在、糖尿病腎症（腎症）患者数の増加は顕著であり、透析療法導入原疾患の第 1 位を占め年々増加の一途を辿っている。したがって、腎症の発症・進展機構の全貌解明、すなわち腎症標的分子の同定とそれに基づく診断と治療法の開発が急務である。このような観点から、糖尿病患者の腎症進展過程の尿蛋白質を網羅的に解析することにより腎組織における病的反応を非侵襲的に捕捉することに着目した。既に、糖尿病患者の尿サンプルを用いたプロテオーム解析による腎症の発症・進展に関わる標的分子の同定がなされており、その成果を基盤として「**新たな糖尿病腎症の診断法を開発する**」ことを本研究の主目的とする。

本研究成果により、腎症の進展ハイリスク群を特異的に診断することによって、厳格な治療介入を行うことが可能となり、腎症から透析導入数の減少と医療費の抑制に繋がる。

５．研 究 計 画

１）尿中サポシンＢおよびトランスサイレチンの免疫学的測定法の確立
サポシン B、またはトランスサイレチンのアミノ酸配列情報から 10 個～20 個のアミノ酸合成ペプチドを人工合成し、抗体作製用の免疫原として、それぞれ特異的抗体を作成する。その後、サポシン B およびトランスサイレチンの免疫測定法（ECL 法）を確立する。
２）金沢医科大学　糖尿病患者の合併症、特に腎症に関するデータベースの構築
３）尿中サポシンＢの臨床的意義の確立

６．研 究 成 果

１）尿中サポシンＢの免疫学的測定法の確立

サポニン B のアミノ酸配列をもとに、抗原性が高いと考えられる下記の４種類の peptide 配列を選択し合成した。さらに、carrier として KLH (Key hole limpet hemocyanin) を各 peptide に結合し免疫用抗原とした。　SaB-1 : aa7-aa21

(CRRRIQMVTDIQTAVRTN)(R を３つ付加)、SaB-2：aa21-aa36　(STFVQALVEHVKEEC)、SaB-3：aa47-aa61　(CKNYISQYSEIAIQM)、SaB-4：aa57-aa71　(IAIQMMMHMQPKEIC)。その後、各群２羽のウサギ（計８羽）に免疫（0.3mg／羽)、本採血後に採取した血清の抗体価の測定により、下記の如く抗体価の高い血清が得られ、ELISA 法を確立した。

２）金沢医科大学　糖尿病患者　糖尿病腎症１期（正常アルブミン尿）21 例、２期（微量アルブミン尿）14 例、３期（マクロアルブミン尿）27 例の血清 Cr およびシスタチン C 値の測定と臨床分類をお行い、来院時尿を文書による同意のもと採取した。さらに、共同研究者であるエーザイ株式会社　社員健診にて非糖尿病である健常者 21 例の尿を共同研究者　エーザイ株式会社の社則に則り採取した。

３）尿中サポシン B の臨床的意義の確立

プロテオーム解析により糖尿病腎症の進展とともに減少するサポシン B に関して、金沢医科大学糖尿病患者 62 例および健常者 21 例から採取した尿を用い、確立したサポシン B　ELISA 法にて定量した。図左に示すように、サポシン B の定量値は、健常者に比べ、糖尿病腎症 1 期、2 期、および 3 期にて有意に低下していた。さらに、排泄された蛋白分画におけるサポシン B の定量を行い、図右に示すように、健常者に比べ、糖尿病腎症 1 期、2 期、および 3 期にて有意に低下するとともに、腎症の病期の進展とともにさらに低下する結果が得られた。

図．サポシン B の定量（ng/ml）および尿蛋白量補正後のサポシン B 定量（ng/mg Cr）

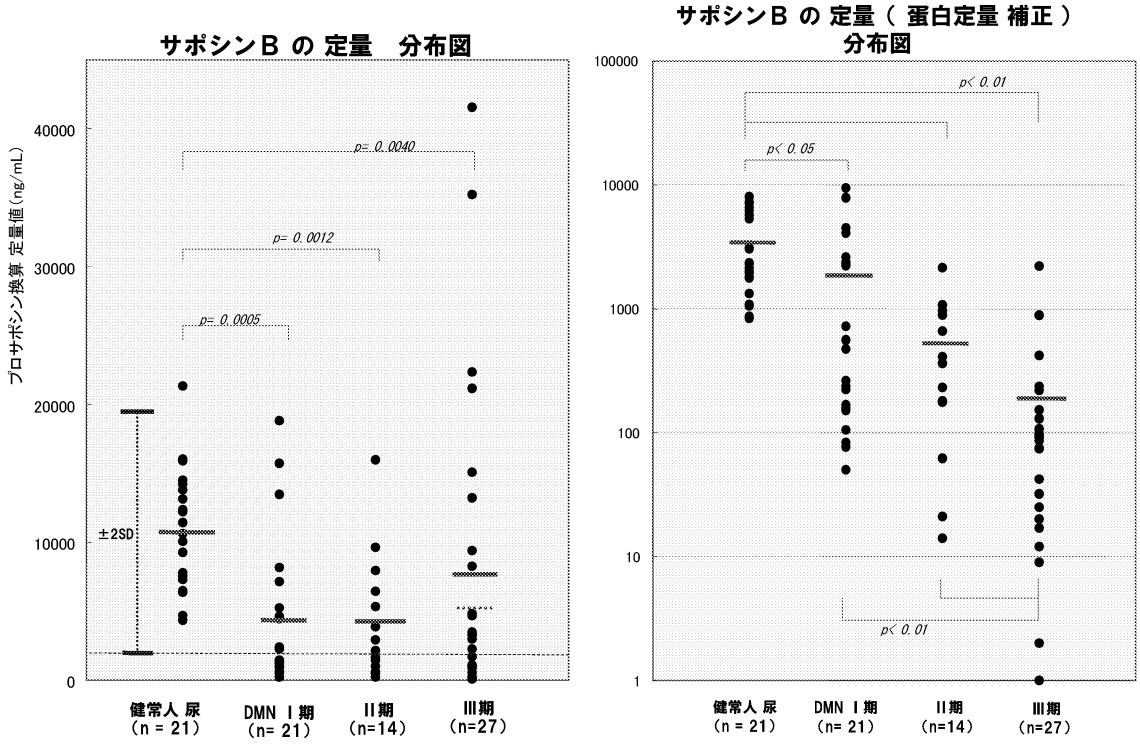

７．研究の考察・反省

糖尿病腎症の進行に伴い減少する新たな尿中蛋白サポシン B をプロテオーム解析により見出し、その ELISA 法の確立を行った。上記に示す如く、濃度表示および排泄された尿蛋白分画における定量から、プロテオーム解析と同様の結果が得られた。サ

ポシンは、セラミドの代謝に関わるスフィンゴ脂質代謝酵素の活性を大きく亢進させるタンパクとして見出され、現在ではサポシンＡ～Ｄの４種と、それと遺伝的に独立なサポシン３の存在が明らかにされている。それらは分子量 12-15 kDa の糖タンパク質であり、各分子中に存在する 6 個のすべてのシステイン残基、1 カ所の *N*-グリコシレーションサイトを有する。従って、我々は糖尿病腎症の進展とともに減少することを見出したことから、糖尿病腎症に対して保護的に機能している可能性が示唆される。今後、プロサポシン過剰発現マウスおよびサポシン産生促進薬による糖尿病腎症における意義を明らかにしていくことが望まれる。さらに、１）糖尿病状態における酸化ストレスはサポシン分子内に存在するシステイン残基の酸化を介してそれら活性を低下させている、２）糖尿病状態における過剰なブドウ糖の取り込みを介してヘキソサミン経路の亢進を介して *N*-グリコシレーションが増強されている可能性もあり、セラミドの代謝の変異が糖尿病腎障害に関わっている可能性も示唆される、これら課題を今後の研究テーマとしたい。

本研究において、糖尿病腎症の進展とともに増加する、つまり腎障害にたいして促進的に働いている可能性のあるトランスサイレチンの免疫学的測定法の関わりを検討することができなかった点が反省点であり、今後も研究を進めて行きたい。

８．研 究 発 表

（氏名）古家大祐

特許出願　2006 年 12 月　P-C60441　（非公開）

欧文論文

特許出願中につき、該当論文なし

和文論文

特許出願中につき、該当論文なし

平成１８年度

奨励研究成果報告書

１．研究課題名：ヒト成人Ｔ細胞白血病ウイルス１型（HTLV-1）関連脊髄症（HAM）
発症機構の解明（研究番号　S2006-1）

２．キーワード：１）ヒトＴ細胞白血病ウイルス（Human T lymphotropic virus type 1: HTLV-1）
２）HTLV-1 関連脊髄症（HTLV-1 associated myelopathy: HAM）
３）HTLV-1 特異的免疫応答（HTLV-1 specific immune response）
４）疾患関連遺伝子（disease associated genes）

３．研究代表者：　齊藤　峰輝・医学部・准教授・生体感染防御学（微生物学）

４．研 究 目 的

ヒトＴ細胞白血病ウイルス（Human T lymphotropic virus type 1: HTLV-1）は、世界ではじめて発見されたヒトレトロウイルスであり、HTLV-1 関連脊髄症（HTLV-1 associated myelopathy/tropical spastic paraparesis: HAM）および成人Ｔ細胞白血病（Adult T cell leukemia: ATL）の原因ウイルスである。単一のウイルスによる感染で自己免疫疾患類似の臓器特異的炎症性疾患と、がん双方の原因となるため、HTLV-1 感染症はヒトの自己免疫疾患や、がん研究のモデルとして優れている。HTLV-1 感染においては、ほとんどの感染者が生涯にわたって未発症の無症候性キャリアー（HC）として経過し、HAM や ATL を発症するのは感染者全体のわずかに 2-3%である。そこで、一部の感染者にのみ疾患が発症するメカニズムを解明することは、HTLV-1 関連疾患の発症予測と早期治療に寄与するのみならず、臓器特異的自己免疫疾患やがんの発症メカニズムについても有用な情報を提供できることが期待される。
我々は、これまでに HAM 発症リスクの高いウイルス型を見いだし、さらに、HAM 発症抑制・促進に関連する HLA が HTLV-1 の dominant epitope を拘束し、効率よく HTLV-1 特異的Ｔ細胞を誘導すること、発症に関連する非 HLA 遺伝子の一部が HTLV-1 の転写制御因子 Tax によって活性化され、その遺伝子多型が転写効率に影響することを明らかにして報告してきた。これらの結果は、ウイルス遺伝子型と遺伝的に規定された HTLV-1 感染に対する宿主遺伝子の応答効率の双方が疾患感受性に深くかかわっていることのみならず、抗 HTLV-1 免疫応答の制御による HAM 発症予防・治療の可能性をも示唆するものである。そこで、本研究では、HAM 発症にかかわる宿主免疫応答の選択的抑制による免疫療法の開発を最終目標に、HAM 患者および HC から末梢血単核球を分離し、HC と HAM 患者における HTLV-1 特異的免疫応答の相違と発症との関連を検討した。

５．研 究 計 画

我々の過去の研究から、HLA クラスⅠの HLA-A*02 と HLA-Cw*08 が HAM 発症抑制に、HLA クラスⅠの HLA-B*54 と HLA クラス II の HLA-DRB1*0101 が HAM 発症促進に関与していることが明らかになっている。HTLV-1 特異的 CTL およびヘルパーＴ細胞の immunodominant epitope がそれぞれ HLA-A*02 と

HLA-DRB1*0101 に拘束されることから、HAM 抑制 HLA アリルは効率のよい CTL による感染細胞の認識・排除の機構により HTLV-1 抗原量の低下をもたらすことで、HAM 促進 HLA アリルは、HTLV-1 に対する過剰な免疫応答を誘導することで、それぞれ HAM 発症感受性に関与する可能性が考えられる。今回はまず、CTL に比べて研究が進んでいない HLA-DRB1*0101 拘束性 HTLV-1 env gp21 特異的 CD4+ T 細胞の HAM 発症における意義を明らかにするため、以下の検討を行った。

① HAM 患者および HC から末梢血単核球を分離し、Ex vivo における HTLV-1 特異的ヘルパーT 細胞の頻度、フェノタイプの差を、各種細胞表面マーカーに対する抗体や、HAM 発症関連 HLA と標的抗原エピトープを用いて作成した DRB1*0101/env gp21 380-394 tetramer を用いて検出し、頻度、フェノタイプ、サイトカイン産生能を解析した。

② HAM 発症感受性クラス II アリルである HLA-DRB1*0101 を持つ HAM 患者 2 例の末梢血を env gp21 ペプチド（env gp21 380-394： RGLDLLFWEQGGLCK）で刺激して T 細胞株を樹立し、T 細胞受容体（TCR）β鎖の相補性決定領域 3（CDR3）の塩基配列を決定した。

さらに、「CTL による HTLV-1 感染細胞の認識、排除の効率が HAM 発症に関連している」という作業仮説の検証のため、以下の実験を行った。

① 年齢をあわせた HAM 患者、HC、非感染正常人の末梢血単核球中における CD28,CD27, CD80, CD86, CD152 陽性細胞の頻度、フェノタイプ、パーフォリン発現、CTL 機能の差を比較検討した。

② 活性化血管内皮細胞上に発現し免疫細胞の遊走に関与することが報告されているフラクタルカイン/CX3CL1 の受容体 CX3CR1 の、HAM 患者および HC の末梢血単核球における発現の差について検討した。

６．研 究 成 果

HAM 患者では、末梢血単核球中の HTLV-1 特異的 CD4 陽性ヘルパーT 細胞は HC に比較して有意に高頻度であった。特に、HAM ではプロウイルス量が同じ HC と比較して DRB1*0101/env gp21 380-394 tetramer 陽性 CD4+ T 細胞が高頻度に検出され、これらは HTLV-1 に効率よく感染し、Th1 type のサイトカインを発現した。また、env gp21 反応性 T 細胞の TCRβ鎖 CDR3 領域に HAM 患者間に共通する特定のアミノ酸モチーフを認めた。一方、HTLV-1 感染者では CD8 陽性 T 細胞における共刺激分子、パーフォリンの発現頻度が非感染正常コントロールより有意に低下しており、特に CD8+CD28-細胞の頻度は HAM 患者で HC より有意に低く、HC においてはプロウイルス量と逆相関を示したが、HAM 患者ではこの相関は認められなかった。HTLV-1 特異的 CD8+CD28-細胞におけるパーフォリンの発現頻度は、同一患者のサイトメガロウイルス（CMV）特異的 CD8+CD28-細胞より有意に低く、抗 CD27、CD28 抗体染色の結果、CMV tetramer 陽性 CD8 細胞のフェノタイプは HAM 患者群と HC 群で同じであるが HTLV-1 tetramer 陽性細胞では両群間で異なっていた。さらに、CD107a mobilization assay による解析結果から、HAM 患者では HC と比較して CTL

機能が低下している可能性が示唆された。一方、HAM 患者末梢血では、HC と比較して CX3CR1 陽性 CD4 陽性 T 細胞の頻度が有意に高かったが、これは HTLV-1 の転写制御因子 Tax によって誘導されるものではないことが明らかになった。

7．研究の考察・反省

HAMではプロウイルス量が同じHCと比較してDRB1*0101/env gp21 380-394 tetramer陽性CD4+T細胞が高頻度に検出され、これらはHTLV-1に効率よく感染し、Th1 typeのサイトカインを発現したことから、HLA-DRB1*0101はHTLV-1特異的CD4+ヘルパーT細胞を効率よく誘導することでHAM発症に関与するものと考えられる。また、env gp21反応性Ｔ細胞のTCRβ鎖CDR3領域にHAM患者間に共通する特定のアミノ酸モチーフが認められたことから、HAM患者末梢血単核球中のHTLV-1特異的CD4陽性ヘルパーT細胞は、HAM発症関連HLAとエピトープペプチドによる刺激により活性化することでin vivoにおいて選択された可能性が示唆された。一方、HTLV-1感染者末梢血T細胞における共刺激分子、パーフォリン発現の解析から、HTLV-1特異的CD8陽性CTLはHAM患者ではHCに比較して有意に高頻度であるという過去の報告とあわせ、生体内での長期にわたるHTLV-1による持続的な抗原刺激の結果、共刺激分子の発現が減弱することでT細胞の機能に影響を与え、CTL機能が低下することでプロウイルス量の増加を通じてHAM発症に関与する可能性が示唆された。本研究によりHTLV-1に対する過剰な免疫応答の選択的抑制による治療応用に向けた重要な基礎データが得られた。

8．研 究 発 表

Nose H, Kubota R, Seth NP, Goon PK, Tanaka Y, Izumo S, Usuku K, Ohara Y, Wucherpfennig KW, Bangham CR, Osame M, Saito M. Ex vivo analysis of human T cell lymphotropic virus type-1 (HTLV-1) specific CD4+ cells using MHC class II tetramer composed of neurological disease susceptive allele and its immunodominant peptide. J Infect Dis 2007; 196: 1761-1772.（MLDB）

Saito M, Usuku K, Arimura K, Izumo S, Osame M, Ohara Y. Increased frequency of CD4+T cells expressing fractalkine receptor CX3CR1 in patients with HTLV-1 associated myelopathy/tropical spastic paraparesis (HAM), but its AIDS susceptible polymorphisms are not associated with the disease. J Neurol Sci 2008; 266: 13-19.（MLDB）

Sabouri AH, Usuku K, Hayashi D, Izumo S, Ohara Y, Osame M, Saito M. Impaired function of human T lymphotropic virus type 1 (HTLV-1) specific CD8+ T cells in HTLV-1–associated neurological disease. Blood. 2008; 112: 2411-2420.（MLDB）

Ex Vivo Analysis of Human T Lymphotropic Virus Type 1–Specific CD4+ Cells by Use of a Major Histocompatibility Complex Class II Tetramer Composed of a Neurological Disease–Susceptibility Allele and Its Immunodominant Peptide

Hirohisa Nose,[1,a] Ryuji Kubota,[2] Nilufer P. Seth,[6] Peter K. Goon,[7,a] Yuetsu Tanaka,[3] Shuji Izumo,[2] Koichiro Usuku,[4] Yoshiro Ohara,[5] Kai W. Wucherpfennig,[6] Charles R. M. Bangham,[7] Mitsuhiro Osame,[1] and Mineki Saito[5]

[1]Department of Neurology and Geriatrics and [2]Center for Chronic Viral Diseases, Kagoshima University Graduate School of Medical and Dental Sciences, Kagoshima, [3]Department of Immunology, Graduate School of Medicine, University of the Ryukyus, [4]Department of Medical Information Technology and Administration Planning, Kumamoto University Hospital, Kumamoto, and [5]Department of Microbiology, Kanazawa Medical University, Ishikawa, Japan; [6]Department of Cancer Immunology and AIDS, Dana-Farber Cancer Institute and Harvard Medical School, Boston, Massachusetts; [7]Department of Immunology, Wright Fleming Institute, Imperial College London, London, United Kingdom

HLA-DRB1*0101 is associated with susceptibility to human T lymphotropic virus type 1 (HTLV-1)–associated myelopathy/tropical spastic paraparesis (HAM/TSP). Here, we used a synthetic tetramer of DRB1*0101 and its epitope peptide to analyze HTLV-1–specific CD4+ T cells ex vivo. The frequency of tetramer+CD4+ T cells was significantly greater in patients with HAM/TSP than in healthy HTLV-1 carriers (HCs) at a given proviral load and correlated with HTLV-1 *tax* messenger RNA expression in HCs but not in patients with HAM/TSP. These cells displayed an early to intermediate effector memory phenotype and were preferentially infected by HTLV-1. T cell receptor gene analyses of 2 unrelated DRB1*0101-positive patients with HAM/TSP showed similar Vβ repertoires and amino acid motifs in complementarity-determining region 3. Our data suggest that efficient clonal expansion of virus-specific CD4+ T cells in patients with HAM/TSP does not simply reflect higher viral burden but rather reflects a rapid turnover caused by preferential infection and/or in vivo stimulation by major histocompatibility complex–peptide complexes.

Human T lymphotropic virus type 1 (HTLV-1)–associated myelopathy/tropical spastic paraparesis (HAM/TSP) [1–4] is a chronic, progressive myelopathy characterized by spastic paraparesis, sphincter dysfunction, and mild sensory disturbance in the lower extremities and is observed only in a minority of infected individuals. Most previous investigations of the specific cellular immune response during HTLV-1 infection have focused on CD8+ cytotoxic T lymphocytes (CTLs), which are typically abundant, chronically activated [5, 6], and mainly targeted to the viral transactivator protein Tax [7–9]. HTLV-1–specific CD8+ T cells have the potential to produce proinflammatory cytokines [10]. However, possession of the HLA-A2 allele, which efficiently presents epitopes of HTLV-1 Tax protein, has been associated with protection against HAM/TSP as well as with a lower proviral load [11]. Thus, there is debate concerning the role played by HTLV-1–specific CD8+ T cells—namely, whether these cells contribute to the inflammatory and demyelinating processes of HAM/TSP or whether the dominant effect of such cells in vivo is pro-

Received 9 March 2007; accepted 4 June 2007; electronically published 14 November 2007.

Potential conflicts of interest: none reported.

Financial support: Ministry of Health, Labor, and Welfare, Japan (grant in aid for research on brain science to M.O. and M.S. and Neuroimmunological Disease Research Committee grant to M.O. and Y.O.); Ministry of Education, Science, Sports, and Culture, Japan (grant 17590886 to M.S.); Kanazawa Medical University (grant S2006-1 to M.S.).

[a] Present affiliations: Department of Immunology, Wright Fleming Institute, Imperial College London, London (H.N.), and Department of Genitourinary Medicine, Addenbrooke's Hospital, Cambridge (P.K.G.), United Kingdom.

Reprints or correspondence: Dr. Mineki Saito, Dept. of Microbiology, Kanazawa Medical University, 1-1 Daigaku, Uchinada-machi, Ishikawa 920-0293, Japan (mineki@kanazawa-med.ac.jp).

The Journal of Infectious Diseases 2007; 196:1761–72

0022-1899/2007/19612-0009$15.00
DOI: 10.1086/522966

tective against disease (although these 2 mechanisms are not mutually exclusive).

Because $CD4^+$ T cell help is necessary for optimal CTL and antibody responses, the $CD4^+$ T cell response against HTLV-1 must also be important. We have previously reported that an HTLV-1 envelope (Env) gp21 immunodominant epitope was restricted by HLA-DRB1*0101 [12, 13] and that HLA-DRB1*0101 was associated with susceptibility to HAM/TSP in independent HTLV-1–infected populations in southern Japan [11, 14] and northeastern Iran [15], indicating the reproducibility of the effect at the population level. Also, $CD4^+$ T cells are the main reservoir of HTLV-1 [16] in vivo and predominate in the mononuclear-cell infiltrate that is found in early active inflammatory spinal cord lesions in HAM/TSP [17] with spontaneous secretion of proinflammatory cytokines [18]. These data suggest that HLA-DRB1*0101 might be associated with susceptibility to HAM/TSP via an effect on $CD4^+$ T cell activation and subsequent bystander damage in the central nervous system (CNS) [5, 19]. Major histocompatibility complex (MHC) class II tetramers have been used for direct ex vivo characterization studies of HIV-1–specific $CD4^+$ T cell populations [20, 21], but such reagents have never been used for HTLV-1–specific $CD4^+$ T cells.

In the present study, we have used an MHC class II tetramer formed between the disease susceptibility–associated allele HLA-DRB1*0101 and its immunodominant epitope to analyze the frequency, phenotype, and T cell receptor (TCR) specificities directly ex vivo in HTLV-1–infected individuals without in vitro cultivation.

PATIENTS, MATERIALS, AND METHODS

Patients and cells. This research was approved by the institutional review boards of the authors' institutions, and written informed consent was obtained from all individuals. Peripheral blood was studied from 20 patients with HAM/TSP (diagnosed by World Health Organization criteria [22]) and from 19 healthy HTLV-1 carriers (HCs) from Kagoshima, an area in southern Japan where HTLV-1 infection is endemic. Characteristics of patients with HAM/TSP and HCs are shown in table 1. All individuals possessed HLA-DRB1*0101, determined by polymerase chain reaction (PCR) with sequence-specific primers, as described elsewhere [23]. Fresh peripheral blood mononuclear cells (PBMCs) were isolated by Histopaque-1077 (Sigma) density gradient centrifugation, washed, and stored in liquid nitrogen until use.

Quantification of HTLV-1 proviral load, tax mRNA expression, and anti–HTLV-1 antibody titers. We performed real-time quantitative PCR using an ABI Prism 7700 device (PE Applied Biosystems) to examine HTLV-1 proviral load and *tax* mRNA expression in PBMCs, as described elsewhere [24, 25]. The amount of HTLV-1 proviral DNA was calculated using β-actin as an internal control by the following formula: copy number of HTLV-1 (pX) per 1×10^4 PBMCs = [(copy number of pX)/(copy number of β-actin/2)] $\times 10^4$. For mRNA quantification, serially diluted cDNA from HTLV-1–infected MT-2 cells was used for generating standard curves for the value of HTLV-1 *tax* mRNA and hypoxanthine ribosyl transferase *(HPRT)* mRNA, and the relative HTLV-1 *tax* mRNA load was calculated by the following formula: HTLV-1 *tax* mRNA load = (value of *tax*)/(value of *HPRT*) $\times$ 10,000. All assays were performed in triplicate. We used aliquots of the same standard MT-2 cDNA preparation for all assays, and the correlation values of standard curves were always >99%. Serum HTLV-1 antibody titers were determined by the particle agglutination method.

Table 1. Characteristics of patients with human T lymphotropic virus type 1 (HTLV-1)–associated myelopathy/tropical spastic paraparesis (HAM/TSP) and of healthy HTLV-1 carriers (HCs).

Characteristic	HAM/TSP (n = 20)	HCs (n = 19)
Age, mean ± SD, years	59.1 ± 8.2	48.0 ± 15.2
Sex, no.		
Male	10	7
Female	10	12
Serum anti–HTLV-1 antibody titer[a]		
Mean ± SD	43,300 ± 48,400	1770 ± 2390
Median	16,384	1024
HTLV-1 proviral load in PBMCs[b]		
Mean ± SD	438 ± 322	245 ± 234
Median	354	151

[a] Anti–HTLV-1 antibodies were titrated by the particle agglutination method.
[b] HTLV-1 Tax copy no./1 $\times 10^4$ peripheral blood mononuclear cells (PBMCs).

Monoclonal antibodies and DRB1*0101/HTLV-1 Env380–394 tetramer. The following mouse anti–human monoclonal antibodies (MAbs) were used for flow cytometry: CD4–phycoerythrin (PE)–cyanine 5–succinimidylester (PC5), CD8–energy-coupled dye, CD28-PC5 (Beckman Coulter), CD45RA-PC5, CD27–fluorescein isothiocyanate (FITC), interferon (IFN)–γ–FITC (BD Pharmingen), and CCR7-FITC (R&D Systems). The PE-conjugated DRB1*0101/HTLV-1 Env380–394 (RGLDLLFWEQGGLCK) tetramer (DR1/Env tetramer) and control HLA-DRB1*0101/CLIP (PVSKMRMATPLLMQA) tetramer (DR1/CLIP tetramer) were generated by peptide exchange using DRB1*0101/CLIP complexes produced in CHO cells, as described elsewhere [26].

Flow cytometry. PBMCs first were surface stained with the DR1/Env tetramer or the control DR1/CLIP tetramer for 2 h at room temperature (RT). Various MAbs for costaining were added for the last 20 min of incubation. After cell-surface labeling, cells were washed with PBS and fixed in PBS containing 2% paraformaldehyde (Sigma) for 20 min and then resuspended in PBS. Isotype-matched mouse immunoglobulins were used as a control. Intracellular IFN-γ staining was done as described elsewhere [27], using freshly isolated PBMCs cultivated for 6 h at

37°C with 0.1 ng/mL phorbol myristate acetate (Sigma) and 0.5 μg/mL A23187 (Sigma), with brefeldin A (Sigma) at a final concentration of 10 μg/mL included for the last 5 h to inhibit secretion of cytokines from the cells. For intracellular Tax staining, PBMCs were incubated with PE-conjugated DR1/Env tetramer for 2 h at RT or with each MAb to cell-surface molecules for 15 min at RT. Then, cells were fixed and subjected to intracellular Tax staining with anti-Tax MAb (Lt-4; IgG3) [28] or with isotype control MAb, as described elsewhere [29]. Finally, the cells were washed and analyzed by use of an EPICS XL flow cytometer and EXPO32 analysis software (Beckman Coulter) in the lymphocyte gate, on the basis of forward versus side scatter. At least 500 DR1/Env tetramer$^+$CD4$^+$ cells were analyzed for each sample. The frequency of DR1/Env tetramer$^+$CD4$^+$ T cells denotes the frequency of tetramer$^+$ cells among total CD4$^+$ cells.

Enrichment of DR1/Env tetramer$^+$ cells. Cells from 2 Japanese HLA-DRB1*0101–positive patients with HAM/TSP who had relatively high frequencies of DR1/Env tetramer$^+$CD4$^+$ T cells were subjected to enrichment. First, CD4$^+$ T cells were negatively selected by use of the CD4$^+$ T Cell Isolation Kit II (Miltenyi Biotec) in accordance with the manufacturer's instructions, with purity determined to be >95% by flow cytometry (data not shown). Anti-PE MACS beads were incubated with purified CD4$^+$ T cells for 15 min at 4°C following PE-conjugated DR1/Env tetramer staining for 2 h at RT. After incubation with MACS beads, the cells were passed over a separation column, in accordance with the manufacturer's instructions.

Reverse-transcriptase PCR (RT-PCR) analysis and sequencing of TCR-Vβ transcripts. RT-PCR and sequencing analyses of TCR-Vβ transcripts were done as described elsewhere [30]. Briefly, cDNA was generated from 5×10^4 (for each) whole PBMCs and ex vivo–isolated DR1/Env tetramer$^+$CD4$^+$ T cells. Then, RT-PCR was performed with a panel of 26 TCR-Vβ–specific primers [31] and a reverse primer specific for the TCR-Vβ constant region (CB-R) that was end-labeled with 6-FAM (Applied Biosystems). The fluorescent intensity of each band was quantified using GeneScan software (version 3.1; Applied Biosystems). Finally, each purified PCR product was subcloned and sequenced [30].

Statistical analysis. The Mann-Whitney *U* test was used for comparing the differences in the frequencies of DR1/Env tetramer$^+$CD4$^+$ T cells and Tax-expressing cells between patients with HAM/TSP and HCs. Correlations between variables were examined by Spearman's rank correlation analysis. The results represent mean ± SD values, where applicable. $P < .05$ was considered to indicate statistical significance.

RESULTS

Direct ex vivo detection and enrichment of HTLV-1 Env gp21–specific CD4$^+$ T cells by an HLA class II tetramer. Specific binding of the DR1/Env tetramer is shown in figure 1. We confirmed the absence of detectable staining of PBMCs for 20 DRB1*0101-positive patients with HAM/TSP by use of the control DR1/CLIP tetramer (figure 1*A*, *left panel*), for 10 HTLV-1–seronegative subjects (5 DRB1*0101 positive and 5 negative) (data not shown) by use of the DR1/Env tetramer, and for 5 DRB1*0101-negative patients with HAM/TSP by use of the DR1/Env tetramer (figure 1*A*, *center panel*). In contrast, clear and distinct staining was observed for DRB1*0101-positive patients with HAM/TSP and HCs by use of the DR1/Env tetramer (figure 1*A*, *right panel*). All DR1/Env tetramer$^+$ cells were CD4$^+$. Enrichment of PE-labeled DR1/Env tetramer$^+$ cells from 2 patients with HAM/TSP (HAM1 and HAM2)—the 2 who had the highest frequencies of DR1/Env tetramer$^+$CD4$^+$ T cells (0.13% and 0.08% of PBMCs in HAM1 and HAM2, respectively) of 20 DRB1*0101-positive patients with HAM/TSP tested—was done by positive selection using anti-PE microbeads. After enrichment, we observed that 42.4% (HAM1) and 57.7% (HAM2) of CD4$^+$ T cells were DR1/Env tetramer$^+$ (figure 1*B*).

Significantly greater in vivo frequency of HTLV-1 Env gp21–specific CD4$^+$ T cells in patients with HAM/TSP than in HCs at a given proviral load. The mean frequency of DR1/Env tetramer$^+$ cells among the CD4$^+$ T cells from 20 patients with HAM/TSP (mean ± SD, 0.304% ± 0.287%) was significantly higher than that for 19 HCs (mean ± SD, 0.099% ± 0.189%; $P = .0002$, Mann–Whitney *U* test) (figure 2*A*). Because the mean HTLV-1 proviral load for the HAM/TSP group was significantly higher than that for the HCs (mean ± SD, 437.8 ± 322.0 for the HAM/TSP group vs. 245.1 ± 238.6 for the HC group; $P = .043$, Mann-Whitney *U* test), we compared the frequencies of DR1/Env tetramer$^+$CD4$^+$ T cells between the patients with HAM/TSP and the HCs who had a similar proviral load (mean ± SD, 397.9 ± 200.3 for patients with HAM/TSP [$n = 14$] and 381.1 ± 231.1 for HCs [$n = 11$]). The mean frequency of DR1/Env tetramer$^+$CD4$^+$ T cells was still significantly higher in patients with HAM/TSP (mean ± SD, 0.308% ± 0.318% [$n = 14$]) than in HCs (mean ± SD, 0.125% ± 0.238% [$n = 11$]) ($P = .0007$, Mann-Whitney *U* test) (figure 2*B*). In accordance with this observation, the frequency of DR1/Env tetramer$^+$CD4$^+$ T cells was not significantly correlated with HTLV-1 proviral load in patients with HAM/TSP alone, in HCs alone, or in both groups combined (data not shown). In contrast, the frequency of DR1/Env tetramer$^+$CD4$^+$ T cells was significantly correlated with HTLV-1 *tax* mRNA expression in the peripheral blood of HCs alone and in both groups combined but not in patients with HAM/TSP alone (figure 2*C*).

Preferential infection of HTLV-1 Env380–399–specific CD4$^+$ T cells by HTLV-1 in patients with HAM/TSP. Intracellular detection of HTLV-1 Tax in DR1/Env tetramer$^+$CD4$^+$ T cells after 6 h of in vitro cultivation of PBMCs

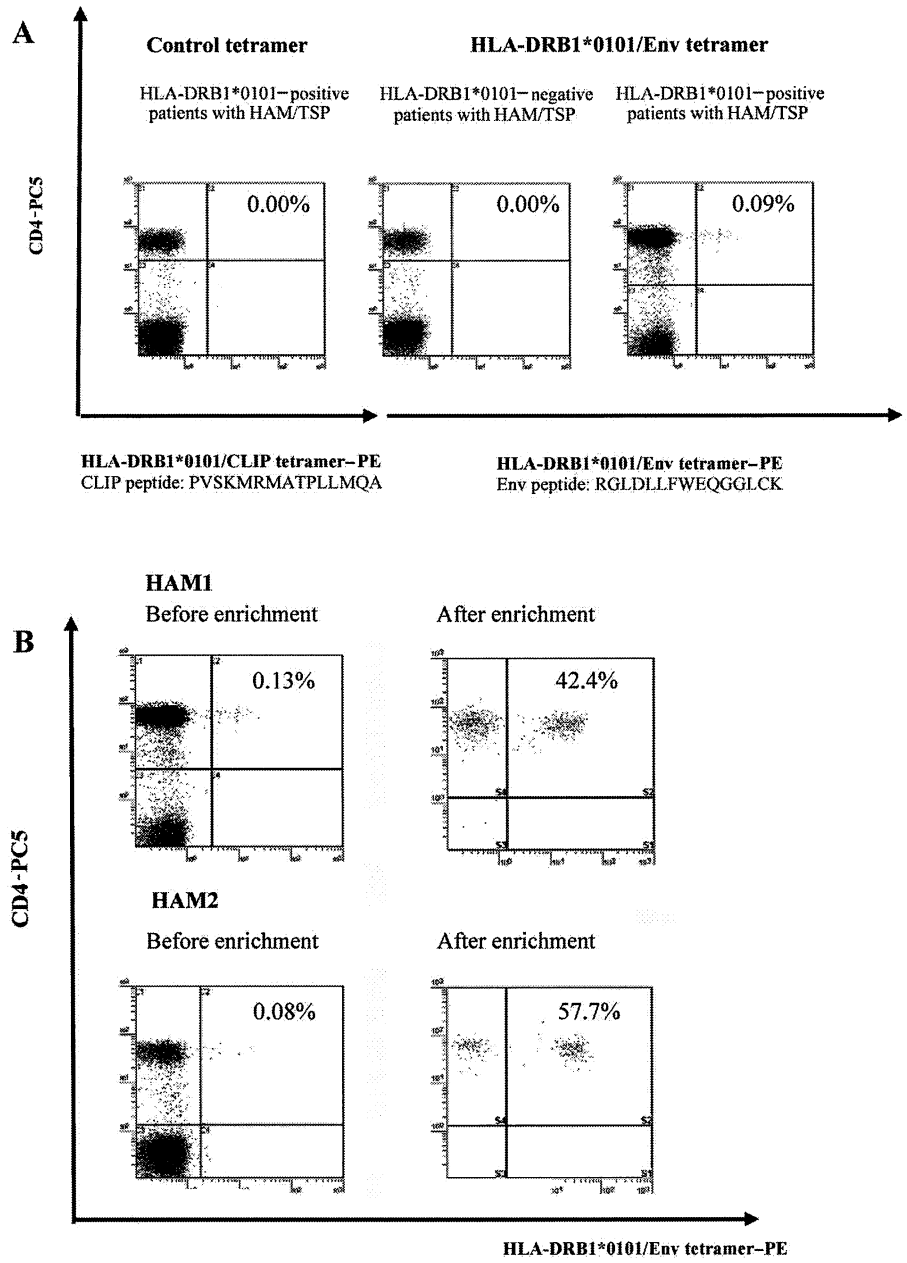

Figure 1. Direct ex vivo detection and enrichment of human T lymphotropic virus type 1 (HTLV-1) Env gp21–specific $CD4^+$ T cells by the DRB1*0101/Env380-394 (DR1/Env) tetramer. *A*, No detectable staining of tetramer$^+$ peripheral blood mononuclear cells in DRB1*0101-positive patients with HTLV-1–associated myelopathy/tropical spastic paraparesis (HAM/TSP) by the control HLA-DRB1*0101/CLIP tetramer *(left panel)* or in DRB1*0101-negative patients with HAM/TSP by the DR1/Env tetramer *(center panel)*. In contrast, clear and distinct staining was observed in DRB1*0101-positive patients with HAM/TSP by the DR1/Env tetramer *(right panel)*. All DR1/Env tetramer$^+$ cells were $CD4^+$. The percentages of cells in each quadrant are given in the upper right corner. *B*, Ex vivo major histocompatibility complex class II tetramer staining of HTLV-1 Env380-394–specific $CD4^+$ T cells *(left panels)*. DR1/Env tetramer$^+$ T cells were positively selected from negatively selected $CD4^+$ T cells by use of anti-phycoerythrin (PE) MACS beads and a magnetic separation column *(right panels)*. The purity was checked by flow cytometry with anti-CD4 monoclonal antibody staining. PC5, cyanine 5–succinimidylester.

revealed that the frequency of HTLV-1 Tax–expressing cells among DR1/Env tetramer$^+$$CD4^+$ T cells was always higher than that of Tax-expressing cells among $CD4^+$ cells in 5 patients with HAM/TSP tested (for the number of Tax^+ DR1/Env tetramer$^+$$CD4^+$ cells divided by total DR1/Env tetramer$^+$$CD4^+$ cells times 100, mean ± SD of 25.04% ± 8.99%; for the number of Tax^+CD4^+ cells divided by total $CD4^+$ cells times 100, mean ± SD of 5.34% ± 3.61%; $P = .009$, Mann-Whitney U test), indicating that DR1/Env tetramer$^+$$CD4^+$ T cells were preferentially infected by HTLV-1 (figure 3). A significant correla-

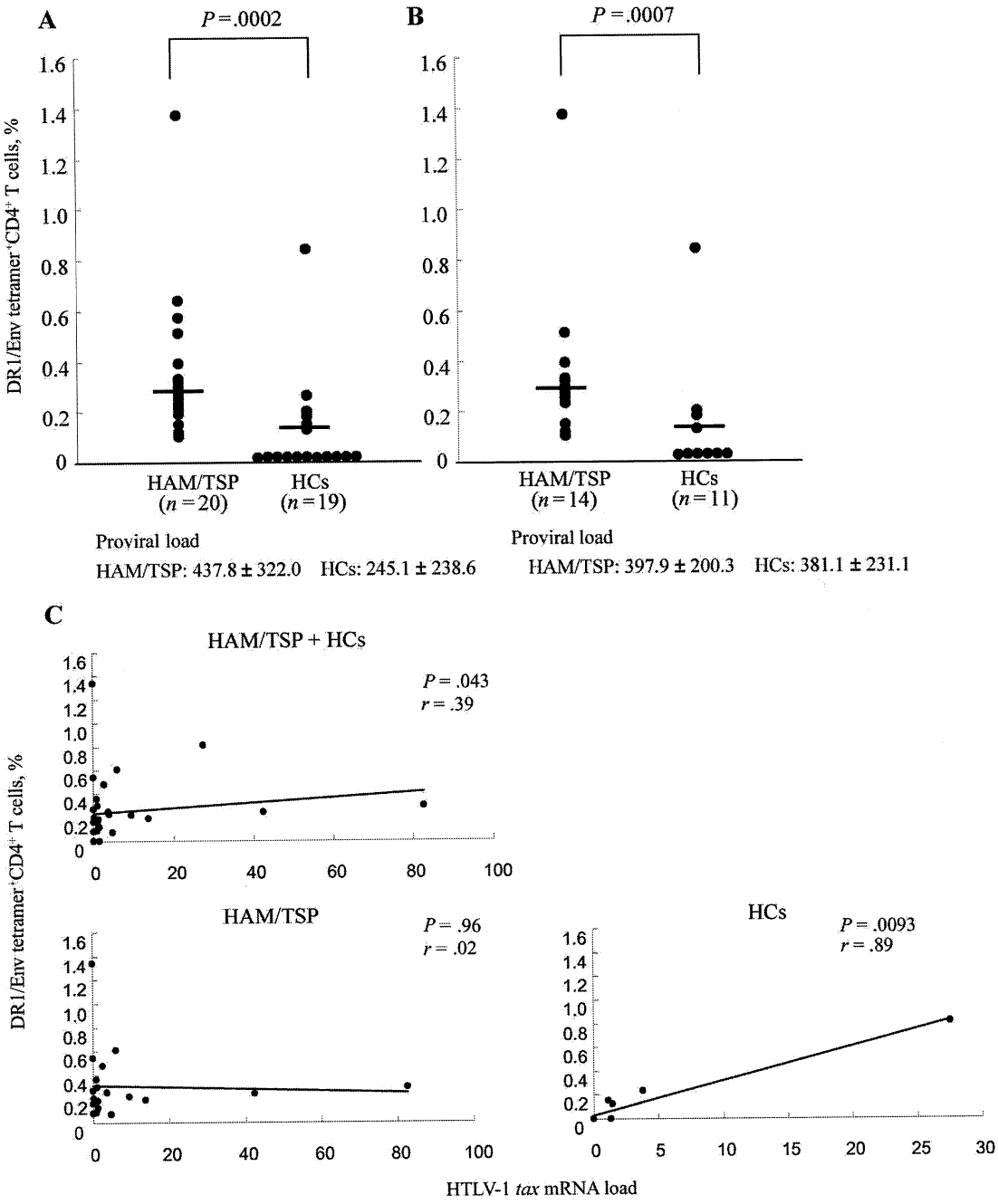

Figure 2. Ex vivo frequencies of DRB1*0101/Env380-394 (DR1/Env) tetramer$^+$ cells among peripheral blood mononuclear cells (PBMCs) from patients with human T lymphotropic virus type 1 (HTLV-1)–associated myelopathy/tropical spastic paraparesis (HAM/TSP) and from healthy HTLV-1 carriers (HCs). *A*, Frequency of DR1/Env tetramer$^+$CD4$^+$ T cells in 20 patients with HAM/TSP and in 19 HCs. The mean frequency of DR1/Env tetramer$^+$CD4$^+$ T cells among PBMCs from 20 patients with HAM/TSP was significantly higher than that of 19 HCs (mean ± SD, 0.304% ± 0.287% vs. 0.099% ± 0.189%; $P = .0002$, Mann-Whitney *U* test). HTLV-1 proviral load was also significantly higher in patients with HAM/TSP than in HCs (mean ± SD, 437.8 ± 322.0 vs. 245.1 ± 238.6; $P = .043$, Mann-Whitney *U* test). The percentage represents the frequency of the tetramer$^+$ cells among total CD4$^+$ T cells. Means are represented by horizontal lines. *B*, Frequency of DR1/Env tetramer$^+$CD4$^+$ T cells in 14 patients with HAM/TSP and in 11 HCs. Although there was no significant difference in HTLV-1 proviral load between these patients with HAM/TSP and HCs (mean ± SD, 397.9 ± 200.3 vs. 381.1 ± 231.1), the mean frequency of tetramer$^+$CD4$^+$ T cells was still significantly higher in the patients with HAM/TSP than in the HCs (mean ± SD, 0.308% ± 0.318% vs. 0.125% ± 0.238%; $P = .0007$, Mann-Whitney *U* test). The percentage represents the frequency of tetramer$^+$ cells among total CD4$^+$ cells. Means are represented by horizontal lines. *C*, Significant correlation between the frequency of tetramer$^+$CD4$^+$ T cells and HTLV-1 *tax* mRNA expression in the peripheral blood of HCs alone or both groups combined but not in patients with HAM/TSP alone. Data were analyzed by Spearman rank correlation. The solid line is the least-squares regression line. The relative HTLV-1 *tax* mRNA load was calculated by the following formula: HTLV-1 *tax* mRNA load = (value of *tax*)/(value of *HPRT*) × 10,000.

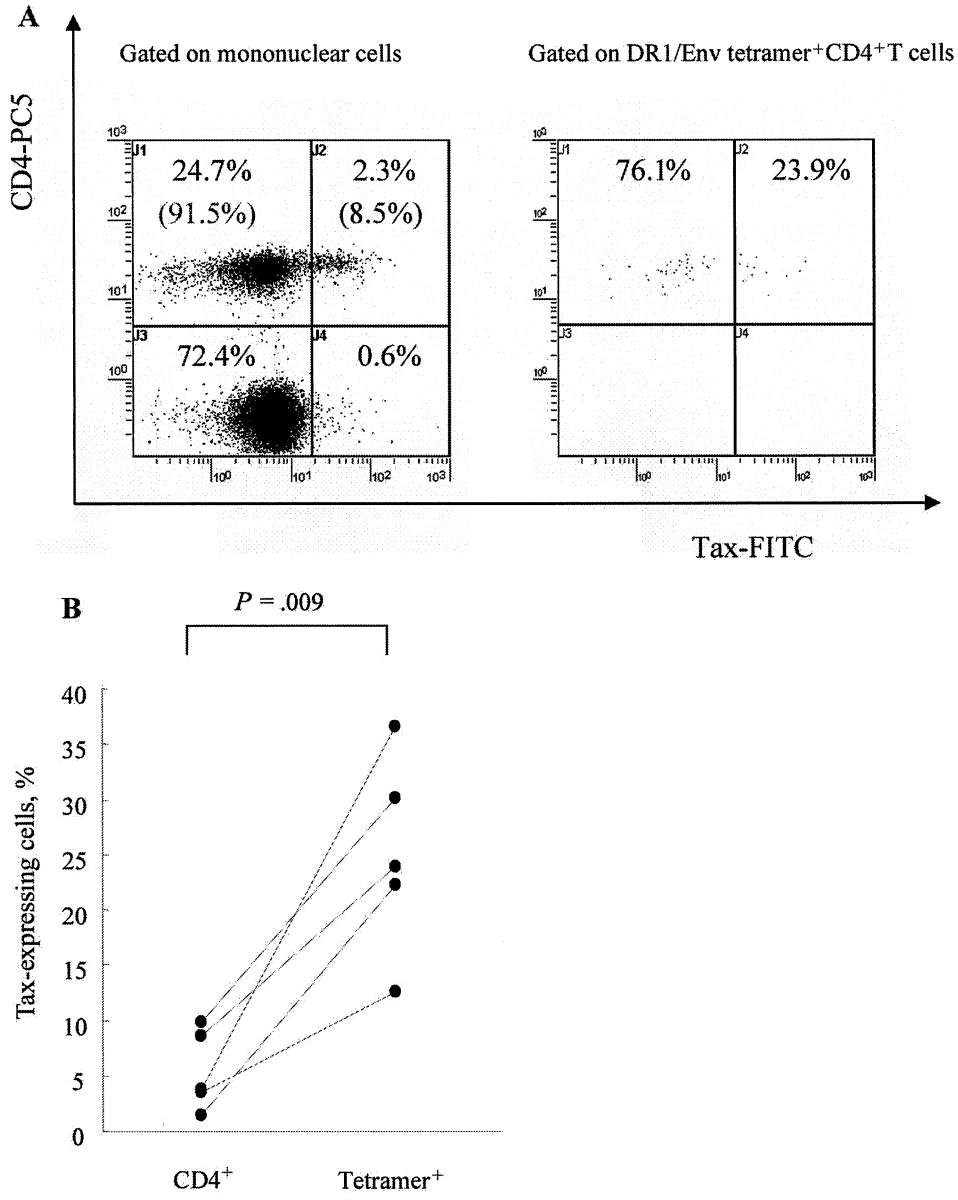

Figure 3. Increased frequency of Tax expression in human T lymphotropic virus type 1 (HTLV-1) Env380–399–specific $CD4^+$ T cells compared with that in total $CD4^+$ T cells, in patients with HTLV-1–associated myelopathy/tropical spastic paraparesis (HAM/TSP). *A*, Intracellular detection of HTLV-1 Tax in DRB1*0101/Env380-394 (DR1/Env) tetramer$^+$$CD4^+$ T cells after 6 h of in vitro cultivation of peripheral blood mononuclear cells. One representative result from those for 5 patients with HAM/TSP is shown. The frequency of HTLV-1 Tax–expressing cells among DR1/Env tetramer$^+$$CD4^+$ T cells (23.9%) was higher than that of Tax-expressing cells among $CD4^+$ T cells (8.5%). *B*, Data on all 5 patients with HAM/TSP tested. The frequency of HTLV-1 Tax–expressing cells among DR1/Env tetramer$^+$$CD4^+$ T cells was always higher than that of Tax-expressing cells among $CD4^+$ T cells (for the no. of Tax$^+$DR1/Env tetramer$^+$$CD4^+$ cells divided by total DR1/Env tetramer$^+$$CD4^+$ cells times 100, mean ± SD of 25.04% ± 8.99%; for the no. of Tax$^+$$CD4^+$ cells divided by total $CD4^+$ cells times 100, mean ± SD of 5.34% ± 3.61%; $P = .009$, Mann-Whitney *U* test). Lines link 2 data points for each patient. At least 500 DR1/Env tetramer$^+$$CD4^+$ cells were analyzed for each sample. FITC, fluorescein isothiocyanate; PC5, cyanine 5–succinimidylester.

tion was observed between the percentage of Tax$^+$$CD4^+$ cells and proviral load but not between the percentage of Tax$^+$DR1/Env tetramer$^+$$CD4^+$ cells and proviral load (data not shown).

Ex vivo phenotypic and functional analysis of Env380–399–specific $CD4^+$ T cells. We could directly determine the phenotype of DR1/Env tetramer$^+$$CD4^+$ T cells in 7 patients with HAM/TSP by costaining for cell-surface markers of memory (CD45RA), lymph node homing (CCR7), and costimulation (CD27 and CD28) without in vitro cultivation (figure 4*A*). The expression of CCR7 and CD45RA in DR1/Env tetramer$^+$$CD4^+$ T cells showed that the vast majority of DR1/Env tetramer$^+$$CD4^+$ T cells were effector memory ($CCR7^-CD45RA^-$) cells (mean ± SD, 90.56% ± 6.06%; median, 90.54%) (figure 4*B*). The maturational phenotype of memory $CD4^+$ T cells was determined by

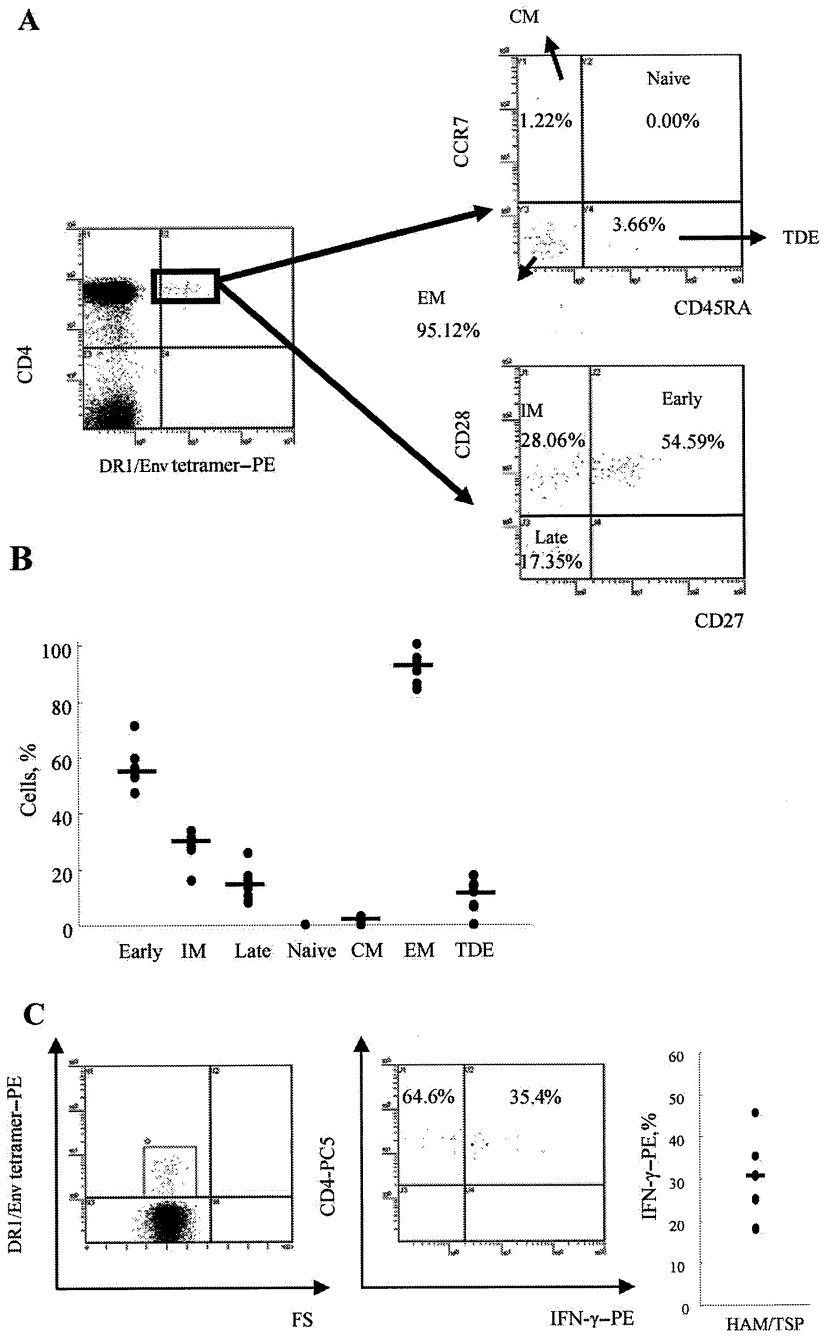

Figure 4. Phenotypic analysis of human T lymphotropic virus type 1 (HTLV-1) Env380–399–specific $CD4^+$ T cells by HLA class II tetramer staining. *A*, Peripheral blood mononuclear cells from 7 patients with HTLV-1–associated myelopathy/tropical spastic paraparesis (HAM/TSP) were stained with cell-surface markers of memory (CD45RA), lymph node homing (CCR7), and costimulation (CD27 and CD28). One representative result is shown. The expression of CCR7 and CD45RA in DRB1*0101/Env380-394 (DR1/Env) $tetramer^+CD4^+$ T cells indicates that the vast majority of DR1/Env $tetramer^+CD4^+$ T cells were effector memory (EM; $CCR7^-CD45RA^-$) cells. The expression of CD27 and CD28 in DR1/Env $tetramer^+CD4^+$ T cells indicated that the majority of HTLV-1–specific $CD4^+$ T cells were skewed to an early (54.59%) to intermediate (IM; 28.06%) memory phenotype. *B*, Ex vivo phenotypic profile of HTLV-1 Env380–399–specific $CD4^+$ T cells in 7 patients with HAM/TSP. Each dot represents the percentage of DR1/Env $tetramer^+CD4^+$ T cells that showed the indicated phenotype (early, $CD28^+CD27^+$; IM, $CD28^+CD27^-$; late, $CD28^-CD27^-$; central memory [CM], $CCR7^+CD45RA^-$; EM, $CCR7^-CD45RA^-$; and terminary differentiated effector [TDE], $CCR7^-CD45RA^+$). Means are represented by horizontal lines. *C*, Interferon (IFN)–γ expression in DRB1*0101/Env380-394 $tetramer^+$ cells. IFN-γ was detected in $tetramer^+$ cells in all 5 patients with HAM/TSP tested. More than half of DR1/Env $tetramer^+CD4^+$ T cells did not express IFN-γ (for IFN-$\gamma^+tetramer^+$ cells, mean ± SD of 32.47% ± 12.76% and median of 31.03%). At least 500 DR1/Env $tetramer^+CD4^+$ cells were analyzed for each sample.

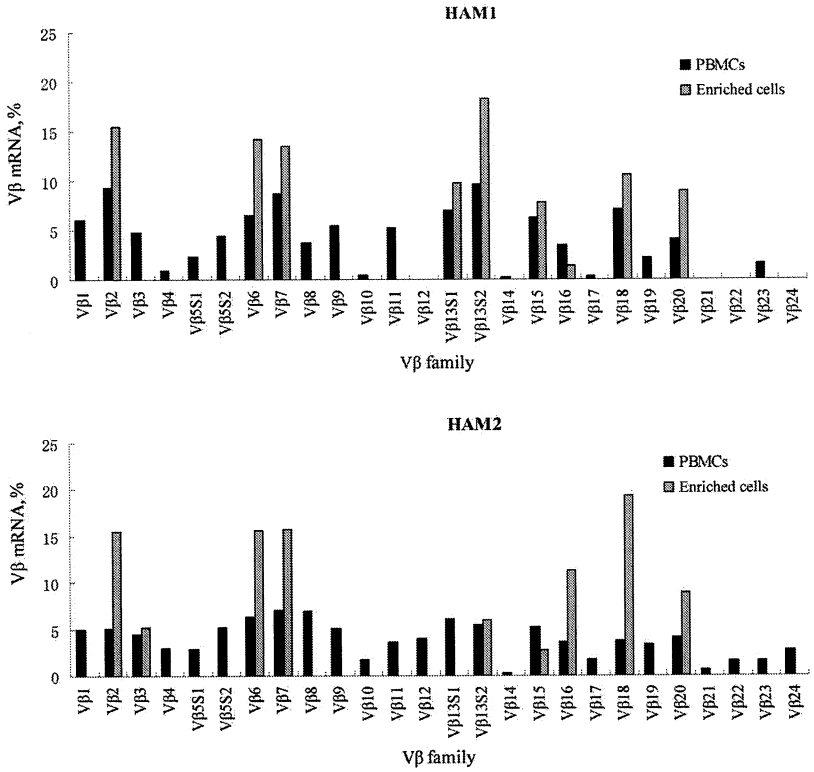

Figure 5. Expression of T cell receptor (TCR)–Vβ transcripts in enriched DRB1*0101/Env380-394 tetramer$^+$ cells and in whole peripheral blood mononuclear cells (PBMCs) from patients with human T lymphotropic virus type 1–associated myelopathy/tropical spastic paraparesis (HAM/TSP). Expression of TCR-Vβ transcripts in enriched DRB1*0101/Env380-394 (DR1/Env) tetramer$^+$CD4$^+$ T cells and whole PBMCs from 2 patients with HAM/TSP (HAM1 and HAM2) were analyzed by reverse-transcriptase polymerase chain reaction (RT-PCR). Two microliters of the final TCR-Vβ RT-PCR product mixture were subjected to electrophoresis on a 5% polyacrylamide sequencing gel, and the resulting bands were detected on an automated sequencer. The relative amounts of Vβ transcripts in enriched DR1/Env tetramer$^+$CD4$^+$ T cells *(gray bars)* and total PBMCs *(black bars)* were quantified by fluorescence with GeneScan software.

CD27 and CD28 staining, to separate antigen-specific CD4$^+$ T cells into 3 distinct functional subsets—CD27$^+$CD28$^+$, CD27$^-$CD28$^+$, and CD27$^-$CD28$^-$, which correlate with early, intermediate, and late phenotype, respectively [32]. A majority of HTLV-1–specific CD4$^+$ T cells were skewed to an early (mean ± SD, 56.43% ± 7.46%; median, 54.59%) to intermediate (mean ± SD, 28.27% ± 5.91%; median, 30.88%) memory phenotype in all 7 patients with HAM/TSP tested (figure 4*B*). Intracellular staining of IFN-γ in DR1/Env tetramer$^+$CD4$^+$ T cells after 6 h of in vitro stimulation with mitogen revealed that less than half of Env380–399–specific CD4$^+$ T cells express IFN-γ (mean ± SD, 32.23% ± 11.43%; median, 31.03%; $n = 6$) (figure 4C). We could not obtain data on HCs because the frequencies of DR1/Env tetramer$^+$CD4$^+$ T cells were very low; therefore, sufficient amounts of blood specimens were not available.

Expression of TCR-Vβ transcripts in enriched DR1/Env tetramer$^+$CD4$^+$ T cells and whole PBMCs from patients with HAM/TSP. TCR gene expression in enriched DR1/Env tetramer$^+$CD4$^+$ T cells and whole PBMCs is shown in figure 5. In contrast to the TCR-Vβ repertoire of whole PBMCs, which is composed of a diverse set of Vβ alleles, the Vβ repertoire of enriched DR1/Env tetramer$^+$CD4$^+$ T cells from 2 unrelated DRB1*0101-positive patients with HAM/TSP showed a similar and limited TCR-Vβ gene use. Namely, Vβ chains 2, 6, 7, 13S2, 15, 16, 18, and 20 were detected in enriched DR1/Env tetramer$^+$CD4$^+$ T cells derived from both HAM1 and HAM2, whereas Vβ13S1 was observed in only HAM1 and not in HAM2.

TCR junctional region sequences of enriched DR1/Env tetramer$^+$CD4$^+$ T cells. We have analyzed the nucleotide sequences of each different TCR-Vβ band. Conserved amino acid motifs were observed in the complementarity-determining region (CDR) 3 of enriched DR1/Env tetramer$^+$CD4$^+$ T cells derived from HAM1 and HAM2 (table 2). The T-X-G (where X indicates any amino acid) or S-X-T-G motifs were present in the CDR3 of Vβ2 PCR products of enriched DR1/Env tetramer$^+$CD4$^+$ cells. Similarly, the T-X-X-R, T-X-X-P, Q-E, P-G-X-G, and VG motifs were present in Vβ13S2, Vβ15, Vβ16, Vβ18, and Vβ20 CDR3 of the enriched DR1/Env tetramer$^+$CD4$^+$ cells derived from both HAM1 and HAM2, although we did not observe any amino acid motifs in Vβ7.

Table 2. T cell receptor junctional region sequences of enriched DRB1*0101/Env380–394 tetramer$^+$ T cells and Env380–394–specific T cell lines.

Subject	Vβ	N-D-N	Jβ	Cβ	No. of clones/total
HAM1	YICSA (Vβ2)	PTPGAS	EAFFGQGTRLTVV (Jβ1.1)	EDLNK	13/19
	YICSA (Vβ2)	SKTGV	NTEAFFGQGTRLTVV (Jβ1.1)	EDLNK	3/19
HAM2	YICSA (Vβ2)	SHTGGR	QPQHFGDGTRLSIL (Jβ1.5)	EDLNK	16/20
	YICSA (Vβ2)	GSGWP	NSPLHFGNGTRLTVT (Jβ1.6)	EDLNK	3/20
HAM1	YLCASS (Vβ6)	PRVPL	AKNIQYFGAGTRLSVL (Jβ2.4)	EDLKN	16/20
	YLCASS (Vβ6)	PFTSGRD	SYEQYFGPGTRLTVT (Jβ2.7)	EDLKN	2/20
HAM2	YLCASS (Vβ6)	SRTGGS	SNQPQHFGDGTRLSIL (Jβ1.5)	EDLNK	9/19
	YLCASS (Vβ6)	QTSGRPS	DTQYFGPGTRLTVL (Jβ2.3)	EDLKN	5/19
	YLCASS (Vβ6)	SDTLGS	YEQYFGPGTRLTVT (Jβ2.7)	EDLKN	3/19
HAM1	YLCASS (Vβ7)	LPWRT	YNSPLHFGNGTRLTVT (Jβ1.6)	EDLNK	16/19
	YLCASS (Vβ7)	QSSGVQES	QYFGPGTRLLVL (Jβ2.5)	EDLKN	2/19
HAM2	YLCASS (Vβ7)	QDPNY	TGELFFGEGSRLTVL (Jβ2.2)	EDLKN	20/20
HAM1	YFCASS (Vβ13S2)	TNKRTGDVA	QETQYFGPGTRLLVL (Jβ2.5)	EDLKN	20/20
HAM2	YFCASS (Vβ13S2)	TTRRGTGKF	NQPQHFGDGTRLSIL (Jβ1.5)	EDLNK	20/20
HAM1	YFCA (Vβ15)	TSAPETLK	QYFGPGTRLTVT (Jβ2.7)	EDLKN	17/17
HAM2	YFCA (Vβ15)	TVKPYGNE	QYFGPGTRLTVT (Jβ2.7)	EDLKN	20/20
HAM1	YFCASS (Vβ16)	QEAVSM	NYGYTFGSGTRLTVV (Jβ1.2)	EDLNK	20/20
HAM2	YFCASS (Vβ16)	QEKDM	NTEAFFGQGTRLTVV(Jβ1.1)	EDLNK	19/19
HAM1	YFCASS (Vβ18)	PGIGP	DTQYFGPGTRLTVL (Jβ2.3)	EDLKN	20/20
HAM2	YFCASS (Vβ18)	RLPGQGAT	GNTIYFGEGSWLTVV (Jβ1.3)	EDLNK	19/19
HAM1	YFCAW (Vβ20)	SVGGPGK	PQHFGDGTRLSIL (Jβ1.5)	EDLNK	11/19
	YFCAW (Vβ20)	SH	QETQYFGPGTRLLVL (Jβ2.5)	EDLKN	8/19
HAM2	YFCAW (Vβ20)	KVGA	NTGELFFGEGSRLTVL (Jβ2.2)	EDLKN	15/18
	YFCA (Vβ20)	GTYGI	YEQYFGPGTRLTVT (Jβ2.7)	EDLKN	3/18

NOTE. The common amino acid motifs found in clonotypes from HAM1 and HAM2 are indicated in boldface.

DISCUSSION

Until recently, studies of the HTLV-1–specific cellular immune response have focused on the CD8$^+$ CTL response, and the CD4$^+$ T cell response to HTLV-1 has been little studied. This is mainly because HTLV-1 predominantly infects CD4$^+$ T cells in vivo [29, 33] and because expression of HTLV-1 Tax in infected CD4$^+$ T cells leads to cell activation and to IFN-γ production and proliferation, which are the basis of the standard assays used to study the antigen-specific CD4$^+$ T cell response. To overcome this problem, we have used a synthetic tetramer of the disease susceptibility–associated allele DRB1*0101 and its immunodominant peptide to analyze HTLV-1–specific CD4$^+$ T cells ex vivo. The advantage of this technique is that we could directly detect HTLV-1 Env gp21–specific CD4$^+$ T cells among PBMCs from patients with HAM/TSP and HCs without in vitro cultivation, which may significantly alter the composition and functional properties of the T cells.

We found that there was no correlation between the frequency of DR1/Env tetramer$^+$CD4$^+$ T cells and HTLV-1 proviral load in either the patients with HAM/TSP alone, the HCs alone, or both groups combined, indicating that the higher frequency of HTLV-1–specific CD4$^+$ T cells observed in patients with HAM/TSP did not simply reflect the higher proviral load (i.e., more HTLV-1–infected T cells). This is consistent with the findings of previous studies by Goon et al. [34, 35]. Goon et al. also showed that the total frequency of HTLV-1–specific CD4$^+$ T cells was significantly higher in patients with HAM/TSP than in HCs with a similar proviral load, by use of an enzyme-linked immunospot assay to estimate the total frequency of HTLV-1–responsive CD4$^+$ cells that produce IFN-γ. That the 2 independent experimental techniques give the same qualitative result increases confidence that this conclusion is correct. We observed a significantly greater frequency of HTLV-1–specific CD4$^+$ T cells in patients with HAM/TSP than in HCs, although there was no significant difference between the groups with respect to mean proviral load. This observation suggests that more-efficient expansion of HTLV-1–specific CD4$^+$ T cell clones irrespective of proviral load does occur in patients with HAM/TSP, probably because of the greater chronic antigenic stimulation in these patients than in HCs with a similar proviral load. This suggestion is consistent with the previous observation by our group [36] and others [25] that HTLV-1 proviral expression in patients with HAM/TSP is greater than that in HCs at a given proviral load. A second factor might also contribute to the effi-

cient proliferation of HTLV-1–specific $CD4^+$ T cells: these cells are preferentially infected with HTLV-1, which, when expressed, will drive proliferation of the host cells.

To further characterize the DR1/Env $tetramer^+CD4^+$ T cells, we analyzed (1) TCR-Vβ use and CDR3 sequence, which is critical to antigen recognition [37, 38]; (2) cell surface phenotypes; and (3) Tax and IFN-γ expression after 6 h of cultivation in the DR1/Env $tetramer^+CD4^+$ T cells from patients with HAM/TSP for whom sufficient blood was available for assay. The higher frequency of HTLV-1–specific $CD4^+$ cells compared with the frequency of virus-specific $CD4^+$ T cells determined using a class II tetramer in other viral infections—such as influenza A virus [39], HIV [20, 21], Eptein-Barr virus [40], and hepatitis C virus [26]—made these experiments possible. For example, in influenza A virus infection, the frequency of hemagglutinin-specific $CD4^+$ T cells is typically only between 0.0012% and 0.0061% of circulating $CD4^+$ T cells [39], whereas the mean frequency of the DR1/Env $tetramer^+CD4^+$ T cells is >10-fold higher (0.20%) in the present study. As for TCR analysis, although the limited TCR-Vβ repertoire of virus-specific $CD4^+$ T cells has been reported in hepatitis C virus infection by use of a class II tetramer and Vβ monoclonal antibodies [26], the CDR3 sequences of directly isolated virus-specific $CD4^+$ T cells have not been reported elsewhere. In spite of the lower purity of enriched DR1/Env $tetramer^+CD4^+$ T cells (42.4% for HAM1 and 57.7% for HAM2), we found similar patterns of TCR-Vβ use and conserved amino acid motifs in different CDR3 regions. These unexpected findings suggest the possibility that, although the cells "negative" for tetramer in the enriched population were polyclonal, the cells "positive" for tetramer in the enriched population were oligoclonal. These results are also closely analogous to our previous findings for HTLV-1 Tax 11–19–specific $CD8^+$ T cells. Namely, an amino acid motif in the CDR3 of a particular TCR-Vβ chain was observed in freshly isolated HLA-A*0201/Tax11-19 $tetramer^+CD8^+$ T cells and muscle infiltrating cells from patients with HAM/TSP [30] and HTLV-1–infected patients with polymyositis [41]. It is therefore possible that the observed amino acid motifs are the result of in vivo selection by a complex of the particular MHC (DRB1*0101) and peptide (Env380–394) during the course of chronic infection. However, our data also suggest that DR1/Env $tetramer^+CD4^+$ T cells were preferentially infected by HTLV-1 in patients with HAM/TSP, again directly corroborating the findings of the previous study by Goon et al. [35], who showed that the frequency of $CD4^+$ T cells infected with HTLV-1 was greater among HTLV-1–specific cells than among cytomegalovirus-specific cells by both Tax expression and proviral load quantification (i.e., preferential infection of HTLV-1 in HTLV-1–specific $CD4^+$ T cells). Therefore, we cannot rule out the possibility that HTLV-1–specific $CD4^+$ T cells efficiently proliferate in response to infection. Nevertheless, in either case, it is evident that particular HTLV-1–specific $CD4^+$ T cell clones expand efficiently in vivo in patients with HAM/TSP.

Next, we ascertained surface phenotypes on the basis of CD27, CD28, CCR7, and CD45RA expression, which are considered to distinguish T cell differentiation phenotypes [42, 43] and to correlate with the cell's capacity to migrate to secondary lymphoid tissues (i.e., the central vs. the effector memory T cell distribution) [44]. Our data indicate that the vast majority of DR1/Env $tetramer^+CD4^+$ cells in patients with HAM/TSP were effector memory ($CCR7^-CD45RA^-$) T cells, which are able to leave the circulation and migrate into the parenchyma of peripheral tissues, including the CNS [45]. Interestingly, this effector memory T cell phenotype is the same as that of previously reported HIV-specific $tetramer^+CD4^+$ T cells [20]. Moreover, the maturational phenotype of memory $CD4^+$ T cells ascertained by CD27 and CD28 staining, which reflects the different phenotypic characteristics of $CD4^+$ T cells specific for different pathogens [43], indicated that the majority of DR1/Env $tetramer^+CD4^+$ cells were skewed to an early to intermediate memory phenotype, again the same as during HIV-1 infection [32]. As for HIV-1 infection, the relatively immature phenotype of HTLV-1–specific $CD4^+$ T cells may be due to a rapid turnover of HTLV-1–specific $CD4^+$ T cells during the course of chronic infection. These immature virus–specific $CD4^+$ T cells may produce a low frequency of IFN-γ production, leading to inefficient T cell surveillance and to the high proviral load seen in patients with HAM/TSP, given that we observed that more than half of DR1/Env $tetramer^+CD4^+$ T cells did not express IFN-γ after 6 h of in vitro stimulation with mitogen for all patients with HAM/TSP tested.

In conclusion, we have shown that HTLV-1–specific DR1/Env $tetramer^+CD4^+$ T cells that displayed a distinct early to intermediate effector memory phenotype expand more efficiently in vivo in patients with HAM/TSP than in HCs. These HTLV-1–specific $CD4^+$ T cells may be associated with HAM/TSP via an inappropriate regulation of cellular immunity, leading to activation, more-efficient proliferation, migration into the CNS, and subsequent bystander damage in patients with HAM/TSP [5, 19]. Further longitudinal study combined with single-cell analysis may provide useful information on how HTLV-1–specific $CD4^+$ T cells are involved in the initiation and pathogenesis of HAM/TSP.

Acknowledgments

We thank the staff and blood donors of Kagoshima University Hospital. We also thank Fumiko Inoue and Yoko Nishino of Kagoshima University and Sumie Saito of Kanazawa Medical University for their excellent technical assistance.

References

1. Poiesz BJ, Ruscetti FW, Gazdar AF, Bunn PA, Minna JD, Gallo RC. Detection and isolation of type C retrovirus particles from fresh and cultured lymphocytes of a patient with cutaneous T-cell lymphoma. Proc Natl Acad Sci USA **1980**; 77:7415–9.
2. Yoshida M, Miyoshi I, Hinuma Y. Isolation and characterization of retrovirus from cell lines of human adult T-cell leukemia and its implication in the disease. Proc Natl Acad Sci USA **1982**; 79:2031–5.

3. Gessain A, Barin F, Vernant JC, et al. Antibodies to human T-lymphotropic virus type-I in patients with tropical spastic paraparesis. Lancet **1985**; 2:407–10.
4. Osame M, Usuku K, Izumo S, et al. HTLV-I associated myelopathy, a new clinical entity. Lancet **1986**; 1:1031–2.
5. Bangham CR. The immune response to HTLV-I. Curr Opin Immunol **2000**; 12:397–402.
6. Jacobson S. Immunopathogenesis of human T cell lymphotropic virus type I-associated neurologic disease. J Infect Dis **2002**; 186(Suppl 2): S187–92.
7. Jacobson S, Shida H, McFarlin DE, Fauci AS, Koenig S. Circulating CD8+ cytotoxic T lymphocytes specific for HTLV-I pX in patients with HTLV-I associated neurological disease. Nature **1990**; 348:245–8.
8. Kannagi M, Harada S, Maruyama I, et al. Predominant recognition of human T cell leukemia virus type I (HTLV-I) pX gene products by human CD8+ cytotoxic T cells directed against HTLV-I-infected cells. Int Immunol **1991**; 3:761–7.
9. Parker CE, Daenke S, Nightingale S, Bangham CR. Activated, HTLV-1-specific cytotoxic T-lymphocytes are found in healthy seropositives as well as in patients with tropical spastic paraparesis. Virology **1992**; 188: 628–36.
10. Kubota R, Kawanishi T, Matsubara H, Manns A, Jacobson S. Demonstration of human T lymphotropic virus type I (HTLV-I) tax-specific CD8+ lymphocytes directly in peripheral blood of HTLV-I-associated myelopathy/tropical spastic paraparesis patients by intracellular cytokine detection. J Immunol **1998**; 161:482–8.
11. Jeffery KJ, Usuku K, Hall SE, et al. HLA alleles determine human T-lymphotropic virus-I (HTLV-I) proviral load and the risk of HTLV-I-associated myelopathy. Proc Natl Acad Sci USA **1999**; 96:3848–53.
12. Yamano Y, Kitze B, Yashiki S, et al. Preferential recognition of synthetic peptides from HTLV-I gp21 envelope protein by HLA-DRB1 alleles associated with HAM/TSP (HTLV-I-associated myelopathy/tropical spastic paraparesis). J Neuroimmunol **1997**; 76:50–60.
13. Kitze B, Usuku K, Yamano Y, et al. Human CD4+ T lymphocytes recognize a highly conserved epitope of human T lymphotropic virus type 1 (HTLV-1) env gp21 restricted by HLA DRB1*0101. Clin Exp Immunol **1998**; 111:278–85.
14. Jeffery KJ, Siddiqui AA, Bunce M, et al. The influence of HLA class I alleles and heterozygosity on the outcome of human T cell lymphotropic virus type I infection. J Immunol **2000**; 165:7278–84.
15. Sabouri AH, Saito M, Usuku K, et al. Differences in viral and host genetic risk factors for development of human T-cell lymphotropic virus type 1 (HTLV-1)-associated myelopathy/tropical spastic paraparesis between Iranian and Japanese HTLV-1-infected individuals. J Gen Virol **2005**; 86:773–81.
16. Moritoyo T, Reinhart TA, Moritoyo H, et al. Human T-lymphotropic virus type I-associated myelopathy and tax gene expression in CD4+ T lymphocytes. Ann Neurol **1996**; 40:84–90.
17. Umehara F, Izumo S, Nakagawa M, et al. Immunocytochemical analysis of the cellular infiltrate in the spinal cord lesions in HTLV-I-associated myelopathy. J Neuropathol Exp Neurol **1993**; 52:424–30.
18. Umehara F, Izumo S, Ronquillo AT, Matsumuro K, Sato E, Osame M. Cytokine expression in the spinal cord lesions in HTLV-I-associated myelopathy. J Neuropathol Exp Neurol **1994**; 53:72–7.
19. Ijichi S, Izumo S, Eiraku N, et al. An autoaggressive process against bystander tissues in HTLV-I-infected individuals: a possible pathomechanism of HAM/TSP. Med Hypotheses **1993**; 41:542–7.
20. Scriba TJ, Zhang HT, Brown HL, et al. HIV-1-specific CD4+ T lymphocyte turnover and activation increase upon viral rebound. J Clin Invest **2005**; 115:443–50.
21. Seth N, Kaufmann D, Lahey T, Rosenberg ES, Wucherpfennig KW. Expansion and contraction of HIV-specific CD4 T cells with short bursts of viremia, but physical loss of the majority of these cells with sustained viral replication. J Immunol **2005**; 175:6948–58.
22. Osame M. Review of WHO Kagoshima meeting and diagnostic guidelines for HAM/TSP. In: Blattner WA, ed. Human retrovirology: HTLV. New York: Raven Press, **1990**.
23. Olerup O, Zetterquist H. HLA-DR typing by PCR amplification with sequence-specific primers (PCR-SSP) in 2 hours: an alternative to serological DR typing in clinical practice including donor-recipient matching in cadaveric transplantation. Tissue Antigens **1992**; 39:225–35.
24. Nagai M, Usuku K, Matsumoto W, et al. Analysis of HTLV-I proviral load in 202 HAM/TSP patients and 243 asymptomatic HTLV-I carriers: high proviral load strongly predisposes to HAM/TSP. J Neurovirol **1998**; 4:586–93.
25. Yamano Y, Nagai M, Brennan M, et al. Correlation of human T-cell lymphotropic virus type 1 (HTLV-1) mRNA with proviral DNA load, virus-specific $CD8^+$ T cells, and disease severity in HTLV-1-associated myelopathy (HAM/TSP). Blood **2002**; 99:88–94.
26. Day CL, Seth NP, Lucas M, et al. Ex vivo analysis of human memory CD4 T cells specific for hepatitis C virus using MHC class II tetramers. J Clin Invest **2003**; 112:831–42.
27. Goon PK, Igakura T, Hanon E, et al. High circulating frequencies of tumor necrosis factor alpha- and interleukin-2-secreting human T-lymphotropic virus type 1 (HTLV-1)-specific CD4+ T cells in patients with HTLV-1-associated neurological disease. J Virol **2003**; 77: 9716–22.
28. Tanaka Y, Yoshida A, Takayama Y, et al. Heterogeneity of antigen molecules recognized by anti-tax1 monoclonal antibody Lt-4 in cell lines bearing human T cell leukemia virus type I and related retroviruses. Jpn J Cancer Res **1990**; 81:225–31.
29. Hanon E, Hall S, Taylor GP, et al. Abundant tax protein expression in CD4+ T cells infected with human T-cell lymphotropic virus type I (HTLV-I) is prevented by cytotoxic T lymphocytes. Blood **2000**; 95:1386–92.
30. Saito M, Taylor GP, Saito A, et al. In vivo selection of T-cell receptor junctional region sequences by HLA-A2 human T-cell lymphotropic virus type 1 Tax11-19 peptide complexes. J Virol **2001**; 75:1065–71.
31. Eiraku N, Hingorani R, Ijichi S, et al. Clonal expansion within CD4+ and CD8+ T cell subsets in human T lymphotropic virus type I-infected individuals. J Immunol **1998**; 161:6674–80.
32. Yue FY, Kovacs CM, Dimayuga RC, Parks P, Ostrowski MA. HIV-1-specific memory CD4+ T cells are phenotypically less mature than cytomegalovirus-specific memory CD4+ T cells. J Immunol **2004**; 172: 2476–86.
33. Richardson JH, Edwards AJ, Cruickshank JK, Rudge P, Dalgleish AG. In vivo cellular tropism of human T-cell leukemia virus type 1. J Virol **1990**; 64:5682–7.
34. Goon PK, Hanon E, Igakura T, et al. High frequencies of Th1-type $CD4^+$ T cells specific to HTLV-1 Env and Tax proteins in patients with HTLV-1-associated myelopathy/tropical spastic paraparesis. Blood **2002**; 99: 3335–41.
35. Goon PK, Igakura T, Hanon E, et al. Human T cell lymphotropic virus type I (HTLV-I)-specific CD4+ T cells: immunodominance hierarchy and preferential infection with HTLV-I. J Immunol **2004**; 172:1735–43.
36. Asquith B, Mosley AJ, Heaps A, et al. Quantification of the virus-host interaction in human T lymphotropic virus I infection. Retrovirology **2005**; 2:75.
37. Davis MM, Bjorkman PJ. T-cell antigen receptor genes and T-cell recognition. Nature **1988**; 334:395–402.
38. Garcia KC, Degano M, Stanfield RL, et al. An alphabeta T cell receptor structure at 2.5 A and its orientation in the TCR-MHC complex. Science **1996**; 274:209–19.
39. Lucas M, Day CL, Wyer JR, et al. Ex vivo phenotype and frequency of influenza virus-specific CD4 memory T cells. J Virol **2004**; 78:7284–7.
40. Ye M, Kasey S, Khurana S, et al. MHC class II tetramers containing influenza hemagglutinin and EBV EBNA1 epitopes detect reliably specific $CD4^+$ T cells in healthy volunteers. Hum Immunol **2004**; 65:507–13.
41. Saito M, Higuchi I, Saito A, et al. Molecular analysis of T cell clonotypes in muscle-infiltrating lymphocytes from patients with human T lymphotropic virus type 1 polymyositis. J Infect Dis **2002**; 186:1231–41.

42. Appay V, Dunbar PR, Callan M, et al. Memory CD8+ T cells vary in differentiation phenotype in different persistent virus infections. Nat Med **2002**; 8:379–85.
43. Amyes E, Hatton C, Montamat-Sicotte D, et al. Characterization of the CD4+ T cell response to Epstein-Barr virus during primary and persistent infection. J Exp Med **2003**; 198:903–11.
44. Sallusto F, Geginat J, Lanzavecchia A. Central memory and effector memory T cell subsets: function, generation, and maintenance. Annu Rev Immunol **2004**; 22:745–63.
45. Sallusto F, Lenig D, Forster R, Lipp M, Lanzavecchia A. Two subsets of memory T lymphocytes with distinct homing potentials and effector functions. Nature **1999**; 401:708–12.

ELSEVIER

Journal of the Neurological Sciences 266 (2008) 13 – 19

Journal of the Neurological Sciences

www.elsevier.com/locate/jns

Increased frequency of CD4+T cells expressing fractalkine receptor CX3CR1 in patients with HTLV-1 associated myelopathy/tropical spastic paraparesis (HAM/TSP), but its AIDS susceptible polymorphisms are not associated with the disease

Mineki Saito [a,*], Koichiro Usuku [b], Kimiyoshi Arimura [c], Shuji Izumo [d], Mitsuhiro Osame [c], Yoshiro Ohara [a]

[a] *Department of Microbiology, Kanazawa Medical University, 1-1 Daigaku, Uchinada-machi, Ishikawa 920-0293, Japan*
[b] *Department of Medical Information Technology and Administration Planning, Kumamoto University Hospital, 1-1-1 Honjo, Kumamoto 860-8556, Japan*
[c] *Department of Neurology and Geriatrics, Kagoshima University Graduate School of Medical and Dental Sciences, 8-35-1 Sakuragaoka, Kagoshima 890-8520, Japan*
[d] *Center for Chronic Viral Diseases, Kagoshima University Graduate School of Medical and Dental Sciences, 8-35-1 Sakuragaoka, Kagoshima 890-8520, Japan*

Received 28 May 2007; received in revised form 9 August 2007; accepted 14 August 2007
Available online 19 September 2007

Abstract

To investigate whether fractalkine receptor CX3CR1 polymorphisms that have been associated with rapid progression to AIDS among HIV-1 positive individuals also affects the risk of human T cell lymphotropic virus type 1 (HTLV-1) associated myelopathy/tropical spastic paraparesis (HAM/TSP), we compared the allele frequencies of V249I and T280M between 233 HAM/TSP patients and 213 HTLV-1 seropositive asymptomatic carriers (HCs). Although the frequency and absolute number of peripheral blood CX3CR1+CD4+T cells were significantly increased in HAM/TSP patients compared to HCs and uninfected controls independent of HTLV-1 trans-activator protein Tax, we could not observe any association between the two polymorphisms and the risk of HAM/TSP in our cohort.

Keywords: Fractalkine; CX3CR1; Gene polymorphism; HTLV-1; HAM/TSP

1. Introduction

Human T-cell lymphotropic virus type 1 (HTLV-1)-associated myelopathy/tropical spastic paraparesis (HAM/TSP) [1,2] is a chronic progressive myelopathy characterized by spastic paraparesis, sphincter dysfunction and mild sensory disturbance in the lower extremities [3] observed in only a minority of HTLV-1 infected individuals [4]. Because the main pathological features of HAM/TSP are chronic inflammation of the spinal cord characterized by perivascular lymphocytic cuffing and parenchymal lymphocytic infiltration [5], it is widely assumed that the immune response against HTLV-1 infection causes the bystander inflammatory spinal cord damage seen in HAM/TSP patients [6].

Fractalkine (also called CX3CL1) is a unique chemokine that functions not only as a chemoattractant but also as an adhesion molecule and is expressed in endothelial cells activated by proinflammatory cytokines such as interferon (IFN)-γ and tumor necrosis factor (TNF)-α [7,8]. The fractalkine receptor CX3CR1 is a chemotactic and adhesion receptor for the fractalkine, and is expressed in many tissues and IL-2 activated peripheral blood lymphocytes, monocytes, NK cells and cytotoxic T lymphocytes (CTL) containing high levels of intracellular perforin and granzyme B to mediate cell adhesion and migration through an inflamed

* Corresponding author. Tel.: +81 76 218 8097; fax: +81 76 286 3961.
E-mail address: mineki@kanazawa-med.ac.jp (M. Saito).

0022-510X/$ - see front matter © 2007 Elsevier B.V. All rights reserved.
doi:10.1016/j.jns.2007.08.022

Table 1
Frequencies of genotypes and alleles for the different polymorphisms in the CX3CR1 gene

SNP	Allele	HAM/TSP	HCs	*P* value[a]	Genotype	HAM/TSP	HCs	*P* value[b]
V249I	V	439 (94.2)[c]	409 (96.0)	0.330	VV	207 (88.8)	196 (92.0)	0.380
(Psp1406I)	I	27 (5.8)	17 (4.0)		VI	25 (10.7)	17 (8.0)	
					II	1 (0.4)	0 (0.0)	
	total	466	426		total	233	213	
T280M	T	439 (94.2)	409 (96.0)	0.330	TT	207 (88.8)	196 (92.0)	0.380
(BsmBI)	M	27 (5.8)	17 (4.0)		TM	25 (10.7)	17 (8.0)	
					MM	1 (0.4)	0 (0.0)	
	total	466	426		total	233	213	

HAM/TSP: HTLV-1-associated myelopathy/tropical spastic paraparesis.
HCs: asymptomatic HTLV-1 seropositive carriers.
[a] *P* values are calculated by χ^2-test with 2×2 contingency table.
[b] *P* values are calculated by χ^2-test with 2×3 contingency table.
[c] Numbers in parentheses are percentage.

endothelium [9–11]. It may therefore possible that CX3CR1 is involved in the HAM/TSP pathogenesis via migration of CTL and proinflammatory T cells to the site of inflammation. Furthermore, it has been reported that two non-synonymous polymorphisms in CX3CR1, which reduce its binding activity to fractalkine, are associated with more rapid disease progression to AIDS in HIV-1-infected individuals [12].

Since HAM/TSP is also caused by human retrovirus infection, and spinal cord inflammation seen in HAM/TSP is mediated by the T cell response including CTL, we analyzed whether these CX3CR1 polymorphisms are also associated with the risk of HAM/TSP. We also focused on the CX3CR1 expression on CD4+T cells, which are the main reservoir of HTLV-1 in vivo [13] and predominate in the mononuclear cell infiltrate that is found in early active inflammatory spinal cord lesions in HAM/TSP [14].

2. Patients and methods

2.1. Patients and cells

Two hundred thirty three cases of HAM/TSP and 213 HTLV-1 seropositive asymptomatic carriers (HCs) were analyzed for CX3CR1 genotyping. Peripheral blood mononuclear cells (PBMCs) were studied from 15 patients with HAM/TSP, 14 asymptomatic carriers and 12 normal uninfected controls by flow cytometry. All cases and controls were of Japanese and resided in Kagoshima Prefecture, where HTLV-1 is endemic in southern Japan. The diagnosis of HAM/TSP was made according to the World Health Organization diagnostic criteria [15]. The patients and controls gave their informed written consent for the study, which was approved by the institutional review boards of the authors' institutions.

2.2. Genotyping

Fresh PBMCs were obtained by Histopaque-1077 (Sigma) density gradient centrifugation and isolated samples were stored in liquid nitrogen until use. Genomic DNA was extracted from PBMCs using a QIAamp blood kit (Qiagen) according to the manufacturer's instructions. The CX3CR1 gene T280M and V249I polymorphisms were identified by PCR-RFLP analysis as described by Moatti et al [16]. Briefly, after amplification of a 588-base pair (bp) fragment by PCR using primers 5′-CCG AGG TCC TTC AGG AAA TCT-3′ and 5′-TCA GCA TCA GGT TCA GGA ACT C-3′, the 15 μl of PCR product was digested for 12 hr with an excess of restriction enzymes BsmBI and Psp1406I to check the T280M and V249I polymorphisms, respectively. Two restriction sites for BsmBI are present at positions 216 and 291 of the normal strand (T280), which was completely digested into 3 fragments of 75, 216, and 297 bp; the second site is disrupted in the mutated strand (M280), thus displaying only 2 fragments of 216 and 372 bp. In heterozygous subjects, 4 bands (75, 216, 297, and 372 bp) were present. The V249I polymorphism was detected using Psp1406I. One restriction site for Psp1406I is present at position 205 of the normal strand, which was split into 2 fragments of 205 and 383 bp. This site was disrupted in the mutated strand, which remained undigested (588 bp).

Table 2
Combined genotype frequencies of V249I and T280M polymorphisms of CX3CR1 gene in HAM/TSP patients and asymptomatic HTLV-1 seropositive carriers

Combined genotype	V249I	T280M	HAM/TSP	HCs
			(*n*=233)	(*n*=213)
1	VV	TT	207 (88.8)[a]	193 (90.6)
2	VV	TM	0 (0.0)	3 (1.4)
3	VV	MM	0 (0.0)	0 (0.0)
4	VI	TT	0 (0.0)	3 (1.4)
5	VI	TM	25 (10.7)	14 (6.6)
6	VI	MM	0 (0.0)	0 (0.0)
7	II	TT	0 (0.0)	0 (0.0)
8	II	TM	0 (0.0)	0 (0.0)
9	II	MM	1 (0.4)	0 (0.0)

HAM/TSP: HTLV-1-associated myelopathy/tropical spastic paraparesis.
HCs: asymptomatic HTLV-1 seropositive carriers.
[a] Numbers in parentheses are percentage.

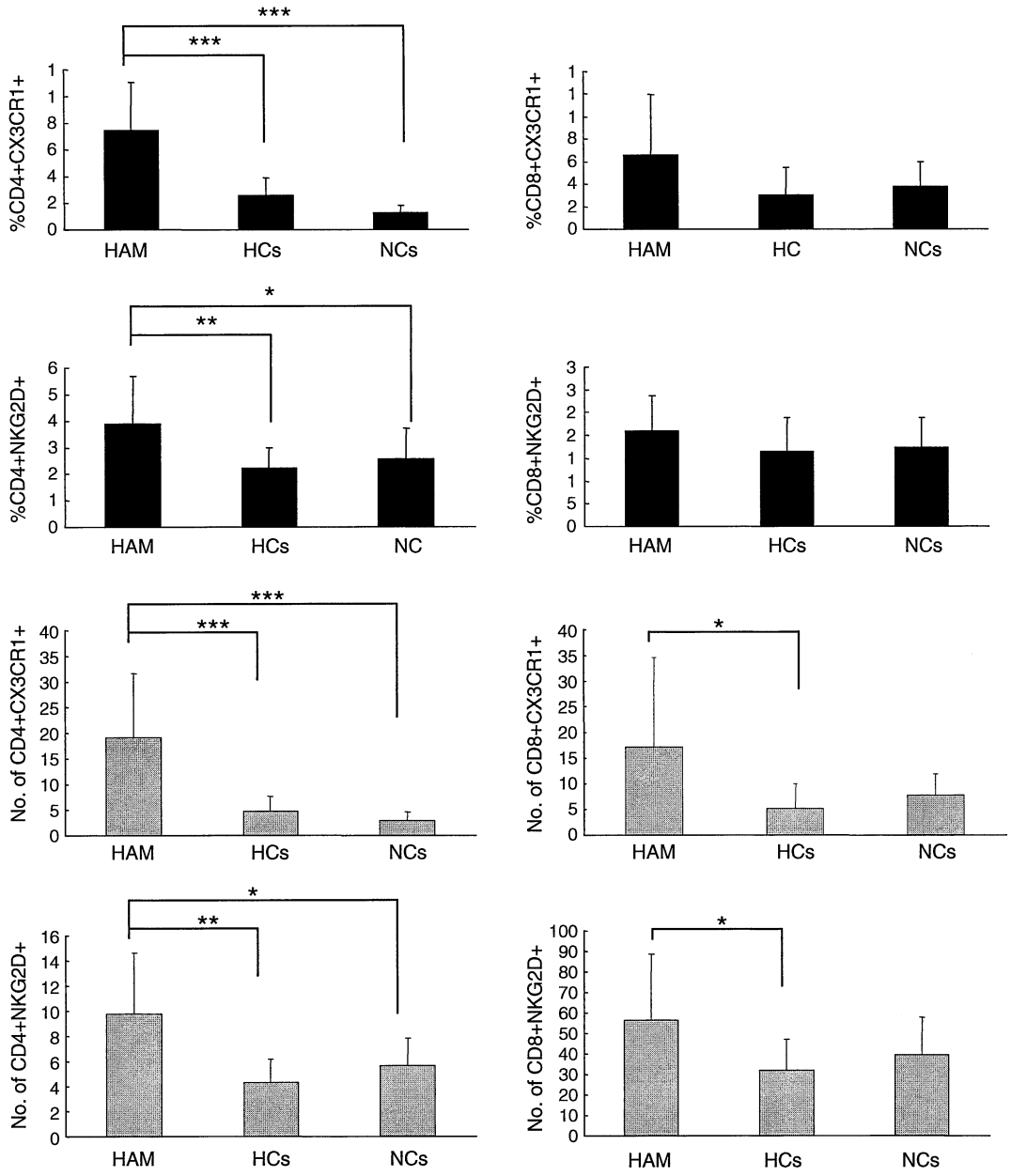

Fig. 1. The frequency and absolute number of CX3CR1 and NKG2D positive T cells in PBMCs from HAM/TSP patients, asymptomatic HTLV-1 carriers and normal controls. The percentage (black bar) and absolute number (gray bar) of CX3CR1 positive and NKG2D positive cells in peripheral blood CD4 positive and CD8 positive lymphocytes are shown. Values represent the mean±standard deviation (SD). One-factor ANOVA was done when variance of each group was equal by Bartlett test. If variance of each group was different, Kruskal–Wallis test was employed. For multiple comparisons, we used Sheffe's F to analyze statistical difference. ***$p<0.001$ **$p<0.01$ *$p<0.05$.

2.3. Quantification of HTLV-1 provirus load and anti-HTLV-1 antibody titers

To examine the HTLV-1 provirus load, we carried out quantitative PCR using an ABI Prism 7700™ (PE-Applied Biosystems) with 100 ng of genomic DNA (roughly equivalent to 10^4 cells) from PBMCs as reported previously [17]. Using β-actin as an internal control, the amount of HTLV-1 proviral DNA was calculated through the following formula: copy number of HTLV-1 (pX) per 1×10^4 PBMC= [(copy number of pX)/(copy number of β-actin/2)]$\times10^4$. All samples were performed in triplicate. Serum antibody titers to HTLV-1 were determined by the particle agglutination method (Serodia-HTLV-1®, Fujirebio). The antibody titers were achieved by performing a serial dilution of the patient serum and noting the highest dilution at which agglutination was still present.

2.4. HTLV-1 tax induction analysis

To investigate whether CX3CR1 is induced by HTLV-1 transactivator Tax protein, we employed a Jurkat derivative

cell line, JPX-9, in which the tax gene is under the control of an inducible metallothionein promoter [18]. JPX-9 was grown to a density of 5×10^5 cells/ml in 1640 RPMI medium supplemented with 10% fetal calf serum, glutamine and 1% penicillin/streptomycin (Sigma). Expression of Tax was induced by addition of $CdCl_2$ to 10 μM final concentration. The cells were harvested after the indicated times and analyzed by flow cytometry.

2.5. Flow cytometry

For cell surface staining, cells were washed and incubated on ice for 15 min with various combinations of fluorescence-conjugated monoclonal antibodies (mAbs) as follows: phycoerythrin (PE)-labeled anti-CX3CR1 (MBL), PE-labeled anti-NKG2D (Beckman Coulter), phycoerythrin-Cy5 (PC5)-labeled anti-CD4 (Beckman Coulter), energy-coupled dye (ECD)-labeled anti-CD8 (Beckman Coulter). Isotype matched mouse immunoglobulins were used as a control. For detection of Tax, JPX-9 cells were subjected to intracellular Tax staining with anti-Tax mAb [19] (Lt-4; IgG3) or isotype control mAb as described previously [20]. All samples were fixed in 2% formaldehyde and analyzed by an EPICS® XL flow cytometer and EXPO32® analysis software (Beckman Coulter) in the lymphocyte gate based on forward versus side scatter.

2.6. Statistical analysis

Comparisons of genotype frequency between HAM/TSP patients and HCs were calculated by the chi-squared test. To test for significant differences among the cell populations between three groups, one-factor ANOVA was done when the variance of each group was equal by Bartlett's test. If not, the Kruskal–Wallis test was employed. For multiple comparisons, we used Sheffe's F to analyze statistical difference. Correlations between variables were examined by Spearman rank correlation analysis. The results represent the mean±standard deviation (SD). Values of $p<0.05$ were considered statistically significant.

3. Results

3.1. CX3CR1 gene polymorphism in HAM/TSP patients and asymptomatic HTLV-1 carriers

In the present study, no significant differences were observed between HAM/TSP patients and HCs genotype or gene frequencies (Table 1). In both groups the genotype frequencies were distributed according to the Hardy–Weinberg equilibrium. The allele and genotype frequency of both SNPs in our present study was very similar to the recent report of 235 Japanese patients with ischemic cerebrovascular disease and 306 age- and sex-matched healthy controls [21]. The frequency of the combined genotype VV–TT in our population was highest, i.e. 88.8% in HAM/TSP and 90.6% in HCs, and other combinations appeared to be very low occurrences, which is again consistent with the previous result (Table 2) [21]. We concluded that CX3CR1 gene polymorphisms V249I and T280M are not associated with an increased risk for HAM/TSP in the southern Japanese population.

3.2. The percentage of CX3CR1+CD4+T cells was significantly increased in HAM/TSP patients

To determine whether the frequency and absolute number of CX3CR1+CD4+T cells differed between HAM/TSP patients

Table 3
Expression of CX3CR1 and NKG2D on peripheral blood T cells in HAM/TSP patients, asymptomatic HTLV-1 seropositive carriers and normal controls

	HAM/TSP (n=15)	HCs (n=14)	NCs (n=12)
CD4+ lymphocytes			
%CX3CR1+	7.5±3.6***†††	2.5±1.3	1.2±0.6
Absolute No. of CX3CR1+	190.3±125.5***†††	48.1±28.2	29.0±16.8
MFI of CX3CR1+	1028.4±375.2	1144.0±434.3	1006.5±258.5
% NKG2D+	3.9±1.8**†	2.2±0.8	2.6±1.1
Absolute No. of NKG2D+	97.6±48.4**†	42.7±18.9	56.0±22.1
MFI of NKG2D+	612.1±434.9	504.8±356.3	537.5±373.2
CD8+ lymphocytes			
%CX3CR1+	6.5±5.4	3.0±2.5	3.7±2.2
Absolute No. of CX3CR1+	171.9±174.3*	51.6±47.5	77.4±41.7
MFI of CX3CR1+	1392.6±782.9	1298.5±479.2	1140.8±316.2
% NKG2D+	21.1±7.7	16.5±7.3	17.3±6.6
Absolute No. of NKG2D+	564.3±322.8*	320.1±150.8	393.0±184.6
MFI of NKG2D+	1523.7±981.5	1241.6±558.2	1011.6±343.0

Absolute number: cells/mm^3.
HAM/TSP: HTLV-1-associated myelopathy/tropical spastic paraparesis.
HCs: asymptomatic HTLV-1 seropositive carriers NCs: normal uninfected controls.
MFI: mean fluorescence intensity.
***$p<0.001$ versus HCs **$p<0.01$ versus HCs *$p<0.05$ versus HCs.
†††$p<0.001$ versus NCs ††$p<0.01$ versus NCs †$p<0.05$ versus NCs.

and HCs as well as normal controls (NCs), we stained PBMCs with antibodies to CX3CR1, CD4 and CD8. Anti-NKG2D antibody was also used because previous reports indicated that NKG2D was highly expressed in CD8+T cells in HTLV-1 infected individuals with a low proviral load [22]; substantial proportions of CD4+T cells from HAM/TSP patients are positive for NKG2D [23], whereas NKG2D is normally absent on most CD4+T cells [24]. As shown in Fig. 1 and Table 3, both the percentages and absolute number of CX3CR1+CD4+T cells and NKG2D+CD4+T cells were significantly higher in HAM/TSP patients than in HCs and NCs; however, these differences were not observed between HCs and NCs, indicating selective increase in HAM/TSP patients. The percentages of CX3CR1+CD8+T cells and NKG2D+CD8+T cells also tended to be higher in HAM/TSP patients, but the difference did not reach a statistically significant level. In contrast, no difference was observed in the mean fluorescence intensity (MFI) of CX3CR1+CD4+, CX3CR1+CD8+, NKG2D+CD4+ and NKG2D+CD8+T cells among the groups (Table 3). Significant correlation between each cell phenotype and HTLV-1 proviral load or anti-HTLV-1 antibody titers was observed only between % CX3CR1+CD4+T cells and anti-HTLV-1 antibody titers (Spearman's rank correlation coefficient $r=0.411$, $P=0.031$).

3.3. CX3CR1 is not induced by HTLV-1 Tax

To investigate whether CX3CR1 is induced by Tax protein, we employed a Jurkat (human leukemic T cell line) subline carrying HTLV-1 Tax under the control of the metallothionein gene promoter. As shown in Fig. 2, induction of Tax by 10 μM $CdCl_2$ resulted in no activation of CX3CR1 and NKG2D, indicating that Tax may not responsible for the increased CX3CR1 and NKG2D expression in CD4+T cells.

4. Discussion

In this study, we examined the relation between HAM/TSP and two CX3CR1 SNPs, T280M and V249I, in HTLV-1 endemic southern Japanese population, and found no significant differences in polymorphisms between HAM/TSP patients and HCs. In both groups, the allele and genotype frequencies were very similar to those from healthy controls in a previously reported case control study in Japan [21]. We could confirm the previous observations that: 1) the frequency of the two SNPs V249I and T280M, (4.9 and 4.9%, present study) is significantly lower in the Japanese population than that in the Caucasian population (25.7 and 13.5%, respectively) [12]; 2) the V249-T280 haplotype has the highest proportion of

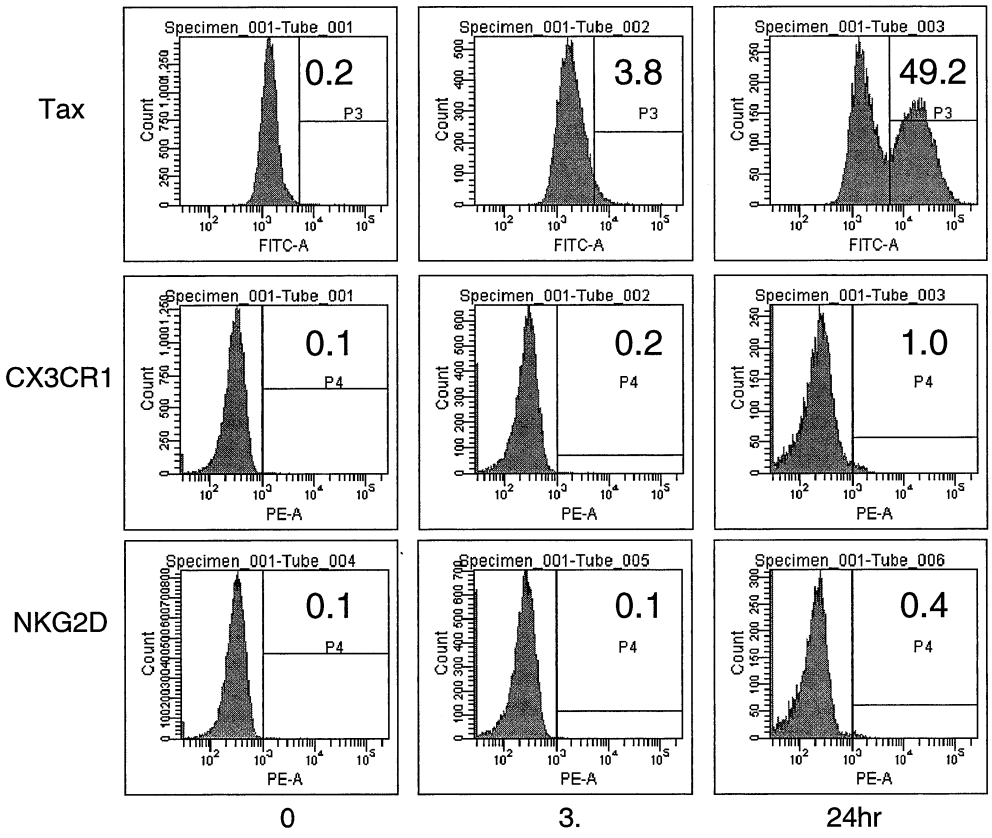

Fig. 2. Expression of CX3CR1 and NKG2D in JPX-9 cells after induction of Tax transactivator. JPX-9 cells were analyzed for Tax, CX3CR1 and NKG2D expression by flow cytometry at the indicated intervals after induction with 10 μM $CdCl_2$. The percentage represents the frequency of positive cells.

the nine possible combined genotypes in the Japanese population; and 3) we observed that 3 HCs with a VV+TM combined genotype, demonstrating that V249-M280, which has not been detected in Caucasians, is present in the Japanese population. Since there are indications that the relative importance of respective mechanisms of immune surveillance against HTLV-1 might differ quantitatively between populations [25,26] probably due to variation in the frequency of certain genetic polymorphisms, particularly HLA alleles, we cannot exclude the possibility that the difference in frequency of these SNPs between populations may have influenced our results. Further studies to test CX3CR1 SNPs in different HTLV-1 endemic populations will be of interest.

We next examined the CX3CR1 expression on CD4+T cells in HTLV-1 infected individuals and in uninfected controls, because CX3CR1 is a adhesion receptor for fractalkine that expressed on endothelial cells activated by proinflammatory cytokines such as interferon(IFN)-γ and tumor necrosis factor-α [7,8], and mediate cell adhesion and migration through an inflamed endothelium [9–11]. In HAM/TSP pathology, greater VCAM-1 and VLA-4 expression on the endothelium and infiltrating mononuclear cells, respectively, in the spinal cord lesions has been reported [27]. It may therefore possible that CX3CR1 also plays a role in the migration of infiltrating mononuclear cells into the spinal cord lesions of HAM/TSP. As a result, we found significantly increased frequency of CX3CR1+CD4+T cells in HAM/TSP patients by comparison with HCs or NCs. The percentages of CX3CR1+CD8+T cells were also tend to be higher in HAM/TSP patients, although the difference did not reach a statistically significant level. These results indicate that there was a selective increase of CX3CR1 expression on peripheral blood T cells in patients with HAM/TSP. Since both CX3CR1+CD4+T cells and CX3CR1+CD8+T cells predominantly express type 1 cytokines, i.e. representing Th1 and Tc1 cells [28], and the involvement of fractalkine and CX3CR1 has been reported in the immunopathogenesis of various Th1-dominated inflammatory diseases [8], it may also possible that CX3CR1 plays a role for HAM/TSP pathogenesis. Indeed, both Th1 and Tc1 cells were predominant in the peripheral blood of HAM/TSP patients [29–31], and HTLV-1-specific CD4+T cell response is dominated by IFNγ-producing pro-inflammatory Th1 cells in HAM/TSP patients [32].

To further investigate whether up-regulation of CX3CR1 is directly induced by HTLV-1-encoded transcriptional activator protein Tax, we employed a Jurkat derivative cell line, JPX-9, in which the tax gene is under the control of an inducible metallothionein promoter. Induction of Tax by 10 μM $CdCl_2$ resulted in no activation of CX3CR1 or of NKG2D in JPX-9 cells. In addition, we could not find any correlation between the percentage of CX3CR1+CD4+T cells and HTLV-1 proviral load in PBMCs of HAM/TSP patients, HCs or both. These data suggest that Tax does not play a major role for the higher CX3CR1 expression observed in HAM/TSP patients. However, there was a positive correlation between the percentage of CX3CR1+CD4+T cells and anti-HTLV-1 antibody titers if we included all the patients (HAM+HCs) enrolled in the study (Spearman's rank correlation coefficient $r=0.411$, $P=0.031$). This may be due to the fact that both the antibody titer and the percentage of CX3CR1+CD4+T cells are much higher in HAM/TSP patients than in HCs, although this is also the case for HTLV-1 proviral load. One possibility is that HTLV-1 infected individuals with high antibody reactivity, suggesting a more vigorous adaptive immune responses against HTLV-1, are more susceptible to systemic inflammatory conditions, and are thereby more closely associated with higher CX3CR1 expression.

In conclusion, we demonstrate that the percentages of CX3CR1+CD4+T cells were significantly higher in HAM/TSP patients than in HCs and NCs, but its AIDS susceptible polymorphisms are not associated with HAM/TSP in the Japanese population. Since higher CX3CR1 expression on CD4+T cells is not directly associated with the HTLV-1 Tax, increased frequency of CX3CR1+CD4+T cells in HAM/TSP patients may reflect by-stander manifestation of up-regulated Th1 cells. Further pathological studies are needed to clarify the contribution of CX3CR1 in the spinal cord inflammation observed in HAM/TSP.

Acknowledgments

We thank the staff and blood donors of Kagoshima University Hospital. The authors thank Ms. Fumiko Inoue and Yoko Nishino of Kagoshima University and Ms. Sumie Saito of Kanazawa Medical University for their excellent technical assistance. This work was supported by grant 17590886 from the Ministry of Education, Science, Sports and Culture, Japan, a Neuroimmunological Disease Research Committee grant from the Ministry of Health, Labour and Welfare of Japan and Grant for Promoted Research from Kanazawa Medical University (S2006-1).

References

[1] Gessain A, Barin F, Vernant JC, Gout O, Maurs L, Calender A, et al. Antibodies to human T-lymphotropic virus type-I in patients with tropical spastic paraparesis. Lancet 1985;2:407–10.
[2] Osame M, Usuku K, Izumo S, Ijichi N, Amitani H, Igata A, et al. HTLV-I associated myelopathy, a new clinical entity. Lancet 1986;1:1031–2.
[3] Nakagawa M, Nakahara K, Maruyama Y, Kawabata M, Higuchi I, Kubota H, et al. Therapeutic trials in 200 patients with HTLV-I-associated myelopathy/tropical spastic paraparesis. J Neurovirol 1996;2:345–55.
[4] Kaplan JE, Osame M, Kubota H, Igata A, Nishitani H, Maeda Y, et al. The risk of development of HTLV-I-associated myelopathy/tropical spastic paraparesis among persons infected with HTLV-I. J Acquir Immune Defic Syndr 1990;3:1096–101.
[5] Izumo S, Umehara F, Osame M. HTLV-I-associated myelopathy. Neuropathology 2000;20Suppl:S65–8.
[6] Osame M. Pathological mechanisms of human T-cell lymphotropic virus type I-associated myelopathy (HAM/TSP). J Neurovirol 2002;8:359–64.
[7] Fraticelli P, Sironi M, Bianchi G, D'Ambrosio D, Albanesi C, Stoppacciaro A, et al. Fractalkine (CX3CL1) as an amplification circuit of polarized Th1 responses. J Clin Invest 2001;107:1173–81.
[8] Umehara H, Bloom ET, Okazaki T, Nagano Y, Yoshie O, Imai T. Fractalkine in vascular biology: from basic research to clinical disease. Arterioscler Thromb Vasc Biol 2004;24:34–40.

[9] Imai T, Hieshima K, Haskell C, Baba M, Nagira M, Nishimura M, et al. Identification and molecular characterization of fractalkine receptor CX3CR1, which mediates both leukocyte migration and adhesion. Cell 1997;91:521–30.
[10] Fong AM, Robinson LA, Steeber DA, Tedder TF, Yoshie O, Imai T, et al. Fractalkine and CX3CR1 mediate a novel mechanism of leukocyte capture, firm adhesion, and activation under physiologic flow. J Exp Med 1998;188:1413–9.
[11] Nishimura M, Umehara H, Nakayama T, Yoneda O, Hieshima K, Kakizaki M, et al. Dual functions of fractalkine/CX3C ligand 1 in trafficking of perforin+/granzyme B+cytotoxic effector lymphocytes that are defined by CX3CR1 expression. J Immunol 2002;168:6173–80.
[12] Faure S, Meyer L, Costagliola D, Vaneensberghe C, Genin E, Autran B, et al. Rapid progression to AIDS in HIV+ individuals with a structural variant of the chemokine receptor CX3CR1. Science 2000;287:2274–7.
[13] Moritoyo T, Reinhart TA, Moritoyo H, Sato E, Izumo S, Osame M, et al. Human T-lymphotropic virus type I-associated myelopathy and tax gene expression in CD4+T lymphocytes. Ann Neurol 1996;40:84–90.
[14] Umehara F, Izumo S, Nakagawa M, Ronquillo AT, Takahashi K, Matsumuro K, et al. Immunocytochemical analysis of the cellular infiltrate in the spinal cord lesions in HTLV-I-associated myelopathy. J Neuropathol Exp Neurol 1993;52:424–30.
[15] Osame M. Review of WHO Kagoshima meeting and diagnostic guidelines for HAM/TSP. New York: Raven Press; 1990.
[16] Moatti D, Faure S, Fumeron F, Amara Mel W, Seknadji P, McDermott DH, et al. Polymorphism in the fractalkine receptor CX3CR1 as a genetic risk factor for coronary artery disease. Blood 2001;97:1925–8.
[17] Nagai M, Usuku K, Matsumoto W, Kodama D, Takenouchi N, Moritoyo T, et al. Analysis of HTLV-I proviral load in 202 HAM/TSP patients and 243 asymptomatic HTLV-I carriers: high proviral load strongly predisposes to HAM/TSP. J Neurovirol 1998;4:586–93.
[18] Nagata K, Ohtani K, Nakamura M, Sugamura K. Activation of endogenous c-fos proto-oncogene expression by human T-cell leukemia virus type I-encoded p40tax protein in the human T-cell line, Jurkat. J Virol 1989;63:3220–6.
[19] Tanaka Y, Yoshida A, Takayama Y, Tsujimoto H, Tsujimoto A, Hayami M, et al. Heterogeneity of antigen molecules recognized by anti-tax1 monoclonal antibody Lt-4 in cell lines bearing human T cell leukemia virus type I and related retroviruses. Jpn J Cancer Res 1990;81:225–31.
[20] Hanon E, Hall S, Taylor GP, Saito M, Davis R, Tanaka Y, et al. Abundant tax protein expression in CD4+T cells infected with human T-cell lymphotropic virus type I (HTLV-I) is prevented by cytotoxic T lymphocytes. Blood 2000;95:1386–92.
[21] Hattori H, Ito D, Tanahashi N, Murata M, Saito I, Watanabe K, et al. T280M and V249I polymorphisms of fractalkine receptor CX3CR1 and ischemic cerebrovascular disease. Neurosci Lett 2005;374:132–5.
[22] Vine AM, Heaps AG, Kaftantzi L, Mosley A, Asquith B, Witkover A, et al. The role of CTL in persistent viral infection: cytolytic gene expression in CD8+lymphocytes distinguishes between individuals with a high or low proviral load of human T cell lymphotropic virus type 1. J Immunol 2004;173:5121–9.
[23] Azimi N, Jacobson S, Tanaka Y, Corey L, Groh V, Spies T. Immunostimulation by induced expression of NKG2D and its MIC ligands in HTLV-1-associated neurologic disease. Immunogenetics 2006;58:252–8.
[24] Bauer S, Groh V, Wu J, Steinle A, Phillips JH, Lanier LL, et al. Activation of NK cells and T cells by NKG2D, a receptor for stress-inducible MICA. Science 1999;285:727–9.
[25] Hisada M, Stuver SO, Okayama A, Li HC, Sawada T, Hanchard B, et al. Persistent paradox of natural history of human T lymphotropic virus type I: parallel analyses of Japanese and Jamaican carriers. J Infect Dis 2004;190:1605–9.
[26] Sabouri AH, Saito M, Usuku K, Bajestan SN, Mahmoudi M, Forughipour M, et al. Differences in viral and host genetic risk factors for development of human T-cell lymphotropic virus type 1 (HTLV-1)-associated myelopathy/tropical spastic paraparesis between Iranian and Japanese HTLV-1-infected individuals. J Gen Virol 2005;86:773–81.
[27] Umehara F, Izumo S, Takeya M, Takahashi K, Sato E, Osame M. Expression of adhesion molecules and monocyte chemoattractant protein-1 (MCP-1) in the spinal cord lesions in HTLV-I-associated myelopathy. Acta Neuropathol (Berl) 1996;91:343–50.
[28] Nanki T, Imai T, Nagasaka K, Urasaki Y, Nonomura Y, Taniguchi K, et al. Migration of CX3CR1-positive T cells producing type 1 cytokines and cytotoxic molecules into the synovium of patients with rheumatoid arthritis. Arthritis Rheum 2002;46:2878–83.
[29] Horiuchi I, Kawano Y, Yamasaki K, Minohara M, Furue M, Taniwaki T, et al. Th1 dominance in HAM/TSP and the optico-spinal form of multiple sclerosis versus Th2 dominance in mite antigen-specific IgE myelitis. J Neurol Sci 2000;172:17–24.
[30] Wu XM, Osoegawa M, Yamasaki K, Kawano Y, Ochi H, Horiuchi I, et al. Flow cytometric differentiation of Asian and Western types of multiple sclerosis, HTLV-1-associated myelopathy/tropical spastic paraparesis (HAM/TSP) and hyperIgEaemic myelitis by analyses of memory CD4 positive T cell subsets and NK cell subsets. J Neurol Sci 2000;177:24–31.
[31] Ochi H, Wu XM, Osoegawa M, Horiuchi I, Minohara M, Murai H, et al. Tc1/Tc2 and Th1/Th2 balance in Asian and Western types of multiple sclerosis, HTLV-I-associated myelopathy/tropical spastic paraparesis and hyperIgEaemic myelitis. J Neuroimmunol 2001;119:297–305.
[32] Goon PK, Hanon E, Igakura T, Tanaka Y, Weber JN, Taylor GP, et al. High frequencies of Th1-type CD4(+) T cells specific to HTLV-1 Env and Tax proteins in patients with HTLV-1-associated myelopathy/tropical spastic paraparesis. Blood 2002;99:3335–41.

Impaired function of human T-lymphotropic virus type 1 (HTLV-1)–specific CD8$^+$ T cells in HTLV-1–associated neurologic disease

Amir H. Sabouri,[1] Koichiro Usuku,[2] Daisuke Hayashi,[1] Shuji Izumo,[3] Yoshiro Ohara,[4] Mitsuhiro Osame,[1] and Mineki Saito[4]

[1]Department of Neurology and Geriatrics, Kagoshima University Graduate School of Medical and Dental Sciences, Kagoshima; [2]Department of Medical Information Technology and Administration Planning, Kumamoto University Hospital, Kumamoto; [3]Center for Chronic Viral Diseases, Kagoshima University Graduate School of Medical and Dental Sciences, Kagoshima; and [4]Department of Microbiology, Kanazawa Medical University, Ishikawa, Japan

Despite abundant activated virus-specific cytotoxic T lymphocytes (CTLs), patients with human T-lymphotropic virus type 1 (HTLV-1)–associated myelopathy/tropical spastic paraparesis (HAM/TSP) showed a significantly higher frequency of infected T cells than did healthy virus carriers (HVCs). Here, we demonstrate that at a given proviral load, the frequency of CD8$^+$ T cells that are negative for specific co-stimulatory molecules was significantly higher in HAM/TSP than in age-matched HVCs and uninfected healthy controls (HCs), whereas the frequency of intracellular perforin-positive CD8$^+$ T cells was significantly lower in both HAM/TSP and HVCs than in HCs. An inverse correlation between HTLV-1 proviral load (PVL) and percent perforin-positive CD8$^+$ T cells were observed only in disease-protective allele HLA-A*02–positive HVCs, but not in HAM/TSP patients, whether HLA-A*02 positive or negative, nor in HLA-A*02–negative HVCs. Significantly lower perforin expression was observed in HTLV-1–specific than in cytomegalovirus-specific CD8$^+$ T cells. Majority of HTLV-1–specific CD8$^+$ T cells in HVCs showed a CD28$^-$CD27$^+$ phenotype, whereas HAM/TSP showed a CD28$^-$CD27$^-$ phenotype. HTLV-1–specific CD8$^+$ T cells from HAM/TSP patients showed significantly lower degranulation than HVCs by CD107a mobilization assay. These findings suggest that an impaired function of HTLV-1–specific CTLs is associated with failing antiviral control and disease HAM/TSP. (Blood. 2008;112:2411-2420)

Introduction

Human T-cell lymphotropic virus type 1 (HTLV-1) is a replication-competent human retrovirus[1,2] associated with adult T-cell leukemia (ATL)[3,4] and a slowly progressive neurologic disorder, HTLV-1–associated myelopathy/tropical spastic paraparesis (HAM/TSP).[5,6] The main pathologic features of HAM/TSP are chronic inflammation in the spinal cord, characterized by perivascular lymphocytic cuffing and parenchymal lymphocytic infiltration including HTLV-1–infected CD4$^+$ T cells.[7] Unlike human immunodeficiency virus (HIV), HTLV-1 causes no disease in a majority of infected subjects (healthy asymptomatic virus carriers, HVCs). However, approximately 2% to 3% develop ATL and another 2% to 3% develop a disabling chronic inflammatory disease involving the central nervous system (HAM/TSP), eyes, lungs, or skeletal muscles.[8] Our previous studies in HTLV-1 endemic to southern Japan indicated that the median proviral load (PVL) in peripheral blood mononuclear cells (PBMCs) of patients with HAM/TSP was more than 10 times higher than that in HVCs, and a high PVL was also associated with an increased risk of progression to disease.[9] In the same population, HLA-A*02 and HLA-Cw*08 genes were independently and significantly associated with a lower PVL and a lower risk of HAM/TSP.[10,11] Namely, possession of the HLA-A*02 allele, which efficiently presents several epitopes from HTLV-1 proteins to specific CTLs, was associated with protection against HAM/TSP as well as a lower PVL.[11] These data suggest that class I–restricted CD8$^+$ CTLs play an important part in controlling HTLV-1 PVL and reducing the risk of disease. Indeed, CD8$^+$ T cells in fresh PBMCs of HTLV-1–infected patients rapidly kill autologous CD4$^+$ cells naturally infected with HTLV-1 by a perforin-dependent mechanism.[12,13] However, because HTLV-1–specific CD8$^+$ T cells have the potential to produce proinflammatory cytokines,[14] there is a debate on the role of HTLV-1–specific CD8$^+$ T cells; that is, whether these cells contribute to the inflammatory and demyelinating processes of HAM/TSP, or whether the dominant effect of such cells in vivo is protective against disease, although these 2 mechanisms are not mutually exclusive.

Antigen-specific CTLs are crucial components of the immune response against viruses, and they have been shown to have an important role in limiting viral replication and controlling virus-associated diseases.[15] A decisive role of HTLV-1–specific CTLs has also been suggested by host genetics,[10,11] in vitro T-cell function,[12,13] and DNA expression microarray analysis.[16] However, in HTLV-1 infection, active and abundant HTLV-1–specific CTLs do not completely eliminate infected cells, especially in patients with HAM/TSP. We have therefore hypothesized that the differences in HTLV-1 PVL and associated differences in the risk of HAM/TSP should be associated with differences between patients in the efficiency of CTL-mediated lysis of infected cells. Because both positive and zero correlations have been found between the frequency of HTLV-1–specific CD8$^+$ T cells and PVL,[17-19] the frequency of HTLV-1–specific CTL itself is not an accurate indicator of CTL strength or effectiveness. Meanwhile, DNA expression microarray analysis suggested that a high level of expression of lymphocyte lysis-related genes, including granzymes, perforin, granulysin, and NKG2D, was associated with

Submitted February 18, 2008; accepted April 24, 2008. Prepublished online as *Blood* First Edition paper, May 27, 2008; DOI 10.1182/blood-2008-02-140335.

An Inside *Blood* analysis of this article appears at the front of this issue.

The online version of this article contains a data supplement.

The publication costs of this article were defrayed in part by page charge payment. Therefore, and solely to indicate this fact, this article is hereby marked "advertisement" in accordance with 18 USC section 1734.

Table 1. Characteristics of HTLV-1–infected patients and healthy uninfected controls

Patient characteristic	HAM/TSP n = 72	HVCs n = 96	HCs n = 20
Age, y, mean ± SE	55.9 ± 1.6	51.1 ± 1.2	55.2 ± 1.9
Sex			
Male	27	51	13
Female	45	45	7
Serum anti–HTLV-I antibody titer*			
Mean ± SE	36 932 ± 8414	2106 ± 990	N/A
Median	16 348	1024	N/A
HTLV-I provirus load in PBMCs†			
Mean ± SE	793.2 ± 677	245.0 ± 381	N/A
Median	537.0	109.0	N/A

HVCs indicates HTLV-1 carriers; HCs, uninfected healthy controls; N/A, not applicable.

*Anti–HTLV-1 antibodies were titrated by the particle agglutination method.

†HTLV-1 *tax* copy number per 10^4 PBMCs.

lower PVL both in patients with HAM/TSP and in HVCs.[16] Moreover, differentiation of $CD8^+$ T cells and their functional profile, such as secretion of cytotoxic molecules, cytokines, and degranulation markers, seems to play a key role in controlling several other chronic viral infections such as herpes simplex virus (HSV), Epstein-Barr virus (EBV), cytomegalovirus (CMV), and HIV.[20-22] In this study, based on these observations, we have evaluated the expression of costimulatory markers, cytotoxic granules (perforin and GzmB), and degranulation marker CD107a in $CD8^+$ T cells from HTLV-1–infected patients (HAM/TSP and HVCs) and age-matched healthy controls (HCs), and compared them with HTLV-1 PVL.

Methods

Patients and cells

Peripheral blood was studied from 72 patients with a clinical diagnosis of HAM/TSP, 96 HVCs, and 20 HCs in total. Characteristics of these patients are shown in Table 1. Fresh PBMCs were isolated on a Histopaque-1077 (Sigma-Aldrich, St Louis, MO) density gradient centrifugation, washed twice in RPMI 1640 with 10% heat-inactivated fetal calf serum (FCS), and stored in liquid nitrogen as stocked lymphocytes until use. All experiments were performed by using age-matched samples selected from stocked lymphocytes. The diagnosis of HAM/TSP was made according to the World Health Organization diagnostic criteria.[23] All patients and control subjects were Japanese and resided in Kagoshima Prefecture, an HTLV-1 endemic region in southern Japan. Samples from patients with HAM/TSP were studied only if the patients had never received any immunomodulators (oral steroid or interferon-α injection) or more than 10 years had passed since the last immune-modulating therapies. This research was approved by the institutional review boards of the authors' institutions and informed consent was obtained from all patients in accordance with the Declaration of Helsinki.

Lymphocyte phenotyping and perforin detection by flow cytometry

After thawing, cells were washed 3 times with phosphate-buffered saline (PBS) and fixed in PBS containing 2% paraformaldehyde (Sigma-Aldrich) for 20 minutes and resuspended in PBS at 4°C. Fixed cells were washed with PBS containing 7% of normal goat serum (Sigma-Aldrich) and then incubated for 15 minutes at room temperature with various combinations of fluorescence-conjugated monoclonal antibodies (mAbs) as follows: phycoerythrin-cyanin 5.1 (PC5)–labeled anti-CD27, PC5-labeled anti-CD28, PC5-labeled anti-CD8, energy-coupled dye (ECD)–labeled anti-CD8 (Beckman Coulter, Fullerton, CA), phycoerythrin (PE)–labeled anti-CD28, fluorescein isothiocyanate (FITC)–labeled antiperforin and GzmB (BD PharMingen, San Diego, CA). Isotype-matched mouse immunoglobulins were used as a control. The phenotype was determined by flow cytometry (EPICS XL: Beckman Coulter) in the lymphocyte gate based on forward versus side scatter. For intracellular staining of perforin and GzmB, PBMCs were first surface stained with the ECD-labeled anti-CD8 mAb for 15 minutes at room temperature. After cell-surface labeling, cells were washed and permeabilized with PBS/7% normal goat serum containing 0.2% saponin (PBS-SAPO; Sigma-Aldrich) for 10 minutes at room temperature. The cells were then washed twice and resuspended for 20 minutes at room temperature in PBS-SAPO containing FITC-labeled anticytotoxin mAbs (perforin, GzmB; BD PharMingen) or an isotype control mAb. Finally, the cells were washed twice and analyzed by an EPICS XL flow cytometer and EXPO32 analysis software (Beckman Coulter) in the lymphocyte gate based on forward versus side scatter.

Detection of HTLV-1 Tax– and CMV pp65–specific CTLs by HLA class I tetramer

To evaluate the expression of perforin in antigen-specific $CD8^+$ T cells, $CD8^+$ T cells were stained with fluorescent-labeled tetramers of HLA-A*02 + β2 microglobulin + Tax11-19 (LLFGYPVYV) or CMV pp65 (NLVPMVATV) peptides, which were purchased from Medical Biological Laboratories (Nagoya, Japan). PBMCs were incubated with each tetramer and ECD-labeled anti-CD8 mAb at 37°C for 25 minutes then washed 3 times in ice-cold PBS, fixed in 2% paraformaldehyde for 20 minutes at 4°C. Fixed PBMCs were then permeabilized with PBS/7% normal goat serum (NGS) containing 0.2% PBS-SAPO for 10 minutes at room temperature for intracellular staining of perforin and GzmB. The cells were washed again and resuspended for 20 minutes at room temperature in PBS-SAPO containing anticytotoxin mAbs (perforin, GzmB) or an isotype control mAb. Finally, the cells were washed and analyzed by flow cytometry. At least 5×10^4 events were collected in each assay.

Quantification of HTLV-1 proviral load and anti–HTLV-1 antibody titers

To examine the HTLV-1 PVL, we carried out a quantitative polymerase chain reaction (PCR) method using ABI Prism 7700 (Applied Biosystems, Foster City, CA) with 100 ng genomic DNA (roughly equivalent to 10^4 cells) from PBMC samples, as reported previously.[9] Based on the standard curve created by 4 known concentrations of template, the concentrations of unknown samples were determined. Using β-actin as an internal control, the amount of HTLV-1 proviral DNA was calculated by the following formula: copy number of HTLV-1 *tax* per 1×10^4 PBMC = [(copy number of *tax*) / (copy number of β-actin/2)] $\times 10^4$. All samples were performed in triplicate. Serum antibody titers to HTLV-1 were determined by a particle agglutination method.

CD107a mobilization assay

To evaluate cell-mediated cytotoxicity of HTLV-1–specific $CD8^+$ T cells in patients with HAM/TSP and HVCs, we performed a CD107a mobilization assay.[24,25] This assay enables rapid assessment of cell-mediated cytotoxicity via sensitive detection of CD107a exposed on the cell surface after antigen stimulation and subsequent secretion of the lytic granule contents such as perforin and granzymes. PBMCs (2×10^6) were cultured for 4 hours with or without 1 μg/mL HTLV-1 Tax peptide in combination with FITC-labeled anti-CD107a mAb and the secretion inhibitor monensin in RPMI 1640 complete medium with 50 IU/mL IL-2, according to the manufacturer's instruction (IMMUNOCYTO CD107a detection kit; MBL, Nagoya, Japan). After incubation, cell suspensions were washed with PBS and the cells were further stained with Tax-tetramer–PE and PC5-labeled anti-CD8 mAb (Beckman Coulter). A minimum of 3×10^4 $CD8^+$ T lymphocytes per sample were acquired by flow cytometry.

Statistical analysis

To test for significant differences among the cell populations between 3 different groups of subjects (HAM/TSP, HVCs, and HCs), one-factor

Table 2. Ex vivo frequency of CD8+ T cells lacking the costimulatory molecules in peripheral blood mononuclear cells from HTLV-1–infected patients and uninfected healthy controls

	n	Mean ± SE	*P* (ANOVA)	*P* (Sheffe F) HAM-HCs	*P* (Sheffe F) HVCs-HCs
All (PVL-unmatched)					
PVL					
HAM/TSP	16	805.1 ± 461.0	.001	N/A	N/A
HVCs	20	354.5 ± 106.2	(Mann-Whitney)		
%CD8+CD27− *					
HAM/TSP	16	31.6 ± 2.3			
HVCs	20	22.3 ± 1.7	.003	.004	.83
HCs	20	19.7 ± 1.3			
%CD8+CD28−					
HAM/TSP	16	31.4 ± 3.1			
HVCs	20	23.6 ± 1.5	.003	.003	.91
HCs	20	20.3 ± 1.5			
%CD8+CD80−					
HAM/TSP	16	36.4 ± 3.3			
HVCs	20	32.3 ± 1.6	.015	.012	.20
HCs	20	26.2 ± 1.7			
%CD8+CD86−					
HAM/TSP	16	35.3 ± 3.2			
HVCs	20	30.6 ± 1.5	.009	.007	.23
HCs	20	25.1 ± 1.5			
%CD8+CD152−					
HAM/TSP	16	35.6 ± 2.5			
HVCs	20	30.1 ± 1.9	.004	.003	.28
HCs	20	25.2 ± 1.7			
PVL-matched					
PVL					
HAM/TSP	8	529.8 ± 79.0	.79	N/A	N/A
HVCs	9	486.0 ± 104.5	(Mann-Whitney)		
%CD8+CD27−					
HAM/TSP	8	31.8 ± 5.9			
HVCs	9	19.8 ± 3.6	.012	.009	1.0
HCs	20	19.7 ± 1.3			
%CD8+CD28−					
HAM/TSP	8	30.6 ± 3.2			
HVCs	9	22.6 ± 2.4	.006	.007	.78
HCs	20	20.3 ± 1.5			
%CD8+CD80−					
HAM/TSP	8	39.5 ± 3.8			
HVCs	9	32.5 ± 2.1	.001	.001	.16
HCs	20	26.2 ± 1.7			
%CD8+CD86−					
HAM/TSP	8	35.3 ± 4.2			
HVCs	9	31.8 ± 1.8	.007	.013	.11
HCs	20	25.1 ± 1.5			
%CD8+CD152−					
HAM/TSP	8	31.0 ± 4.2			
HVCs	9	30.5 ± 2.8	.19	.32	.35
HCs	20	25.2 ± 1.7			

HVCs indicates HTLV-1 carriers; HCs, uninfected healthy controls; and PVL, proviral load.

One-factor ANOVA was done when variance of each group was equal by Levene test. If variance of each group was different, Kruskal-Wallis test was used. For multiple comparison, we used Sheffe F to analyze the statistical difference.

* % CD8+CD27− indicates the frequency of CD8+CD27− in PBMCs.

analysis of variance (ANOVA) was done when the variance of each group was equal by Levene test. If the variance of each group was different, the Kruskal-Wallis test was used. For multiple comparisons, we used Sheffe F to analyze statistical difference. The Mann-Whitney *U* test was used for comparing the differences in the frequencies of cell populations or PVL between patients with HAM/TSP and HVCs. The results represent the mean plus or minus the standard error (SE) where applicable. Correlations between variables were examined by Spearman rank correlation analysis. All statistical analyses were performed using SPSS version 13.5 software (SPSS, Chicago, IL). Values of *P* less than .05 were considered statistically significant.

Results

The expression of costimulatory molecules on T cells of HTLV-1–infected patients and uninfected controls

To determine whether the frequency of costimulatory molecules differed between patients with HAM/TSP and HVCs as well as HCs, we stained PBMCs with monoclonal antibodies to CD27,

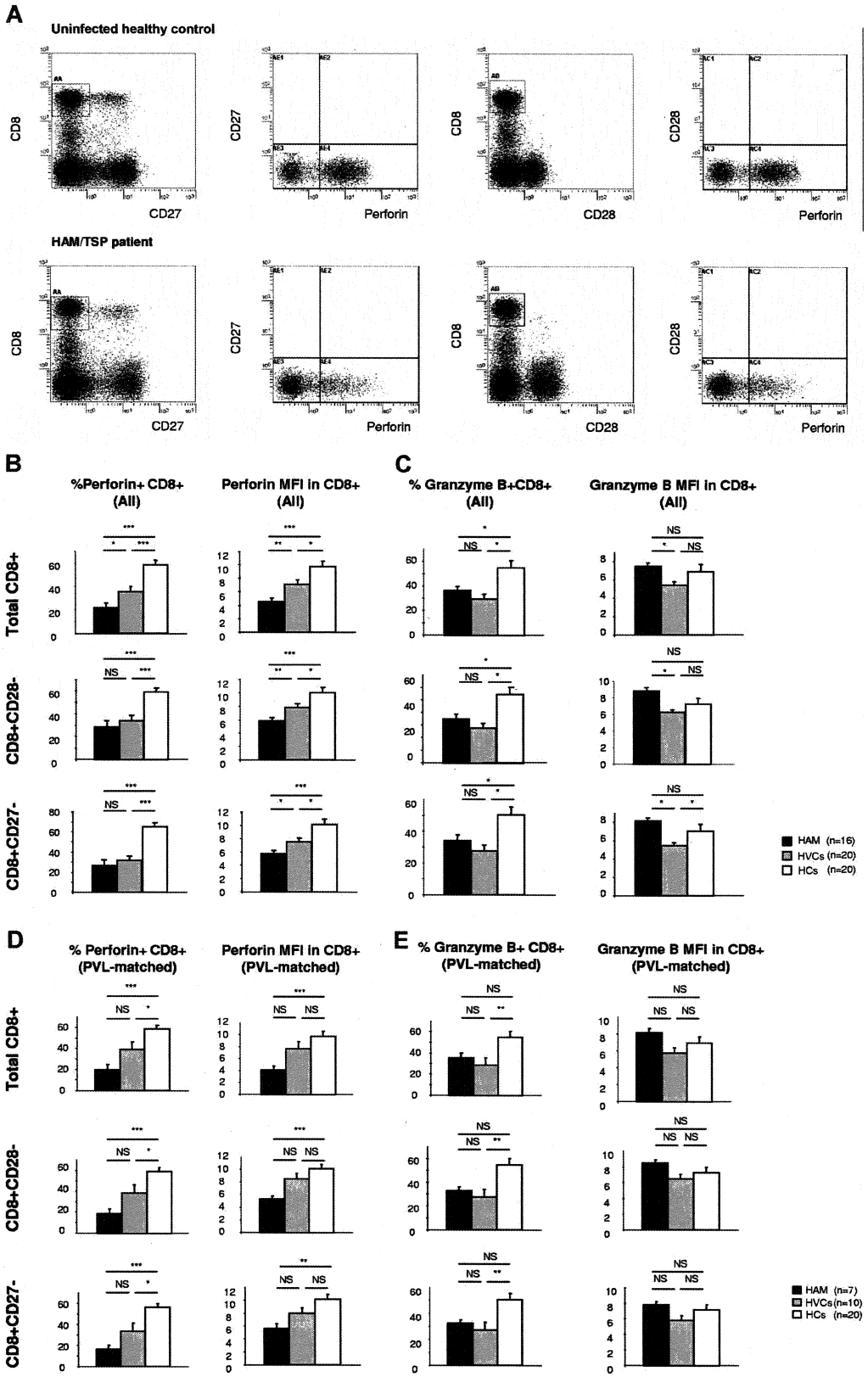

Figure 1. Frequencies and mean fluorescence intensities of perforin- and granzyme B–positive CD8⁺ T-cell populations in HTLV-1–infected patients. (A) Representative dot plots of PBMCs stained for cytotoxic function markers and costimulatory molecules. PBMCs from patients with HAM/TSP, asymptomatic healthy virus carriers (HVCs), and uninfected healthy controls (HCs) were costained for CD8, CD27, or CD28, and markers associated with cytotoxic function (ie, perforin or granzyme B [GzmB]). Cells in a $CD8^+$ lymphocyte gate were analyzed. Representative dot plots from 1 uninfected control and 1 HAM/TSP patient are shown. (B) The frequency and mean fluorescence intensity (MFI) of the perforin-positive $CD8^+$ T-cell population and its subpopulations ($CD8^+CD28^-$ and $CD8^+CD27^-$) in patients with HAM/TSP, HVCs, and HCs.

CD28, CD80, CD86, and CD152 (cytotoxic T-cell lymphocyte–associated antigen-4 [CTLA-4]) in 3 groups of age-matched patients with HAM/TSP, HVCs, and HCs (Table 2). The percentages of $CD8^+$ cells that were negative for costimulatory molecules were significantly higher in patients with HAM/TSP than in HCs; however, these differences were not observed between HVCs and HCs. Because the mean HTLV-1 PVL of the HAM/TSP group was significantly higher than that of the HVCs (HAM/TSP 805.1 ± 461.0 vs HVCs 354.5 ± 106.2, $P = .001$, Mann-Whitney), we further compared the frequencies of each costimulatory molecule between patients with HAM/TSP and the HVCs with a similar PVL (HAM/TSP 529.8 ± 79.0 vs HVCs 486.0 ± 104.5, $P = .79$, Mann-Whitney). The mean frequency of each costimulatory molecule was still significantly higher in patients with HAM/TSP than HCs except for $CD8^+$ $CD152^-$ (Table 2), and there was no correlation between the mean frequency of each costimulatory molecule and PVL (data not shown). These data indicate that the observed differences do not simply reflect differences in PVL (ie, in the frequency of HTLV-1–infected cells). Furthermore, although HTLV-1 mainly infects $CD4^+$ cells, the percentages of $CD4^+$ cells that were negative for costimulatory molecules were not significantly different between patients with HAM/TSP and HVCs or HCs (Table S1, available on the *Blood* website; see the Supplemental Materials link at the top of the online article), indicating that the mean frequency of each costimulatory molecule on $CD4^+$ cells was not influenced by the PVL.

Expression of perforin and granzyme B in $CD8^+CD28^-$ and $CD8^+CD27^-$ T-cell populations of patients with HAM/TSP and healthy virus carriers

We next focused on the $CD8^+CD28^-$ T cells and $CD8^+CD27^-$ T cells, because these subsets include CTLs and because abnormal expansion of these subsets was also described in chronic CMV,[26] EBV,[27] and HIV[20] infection. As shown in Table 2, both percent $CD8^+CD28^-$ and percent $CD8^+CD27^-$ T-cell populations in PBMCs were significantly higher in patients with HAM/TSP than in HVCs and HCs, whereas there were no significant differences of percent $CD8^+CD28^-$ and percent $CD8^+CD27^-$ T-cell populations between HVCs and HCs. Interestingly, as typical examples show in Figure 1A, the percentages of perforin$^+CD8^+$, perforin$^+CD8^+CD28^-$, and perforin$^+CD8^+CD27^-$ T cells were significantly lower in HTLV-1–infected patients (patients with HAM/TSP and HVCs) than in HCs, irrespective of PVL (Figure 1B,D). The differences between HVCs and patients with HAM/TSP were smaller than the differences between HCs and HVCs or patients with HAM/TSP alone, indicating that a selective decrease of perforin expression in $CD8^+$ T cells was associated with persistent HTLV-1 infection. The mean fluorescence intensity (MFI) of the perforin$^+CD8^+$, perforin$^+CD8^+CD28^-$, and perforin$^+CD8^+CD27^-$ T-cell populations were significantly lower in patients with HAM/TSP than in HCs, irrespective of PVL (Figure 1B,D). In contrast to the perforin expression, both the percentages and MFI of the GzmB$^+CD8^+$, GzmB $^+CD8^+CD28^-$, and GzmB $^+CD8^+CD27^-$ T-cell populations were not significantly different among the 3 subject groups (patients with HAM/TSP, HVCs, and HCs) when HTLV-1–infected patients were compared with a similar proviral load (Figure 1C,E).

There was a marginal negative correlation between percent perforin$^+CD8^+$ T cells and HTLV-1 PVL in all HTLV-1–infected patients (patients with HAM/TSP + HVCs; $P = .046$, $r = -0.29$ by Spearman rank correlation analysis) but not in patients with HAM/TSP or HVCs alone (Figure 2 left panels). Meanwhile, a significant negative correlation between percent perforin$^+CD8^+$ T cells and HTLV-1 PVL was observed in all HLA-A*02–positive HTLV-1–infected patients (patients with HAM/TSP + HVCs; $P = .003$, $r = -0.58$) and HVCs alone ($P = .024$, $r = -0.64$), but not in patients with HAM/TSP ($P = .15$, $r = -0.35$; Figure 2 right panels). No correlation was observed between expression of GrzB and HTLV-1 PVL in patients with HAM/TSP, HVCs, or both groups combined, irrespective of HLA status (data not shown).

Lower perforin expression in HTLV-1–specific $CD8^+$ T cells than in CMV-specific $CD8^+$ T cells within HTLV-1–infected patients

Perforin is essential for killing targets of CTLs by means of the granule exocytosis pathway, and its expression is more restricted than that of serine proteases. As we observed significant differences in perforin expression in $CD8^+$ T cells lacking the costimulatory molecules in PBMCs between HTLV-1–infected patients and healthy controls, and a significant negative correlation between percent perforin$^+CD8^+$ T cells and HTLV-1 PVL in HLA-A*02–positive HTLV-1–infected patients, we next focused on the perforin expression in HTLV-1–specific $CD8^+$ T cells and CMV-specific $CD8^+$ T cells in the same group of HTLV-1–infected patients (Figure 3A). Although there was no significant difference in percent perforin expression in virus-specific (both HTLV-1 Tax–specific and CMV-specific) $CD8^+$ T cells between patients with HAM/TSP and HVCs, the percentage perforin expression in HTLV-1 Tax–specific $CD8^+$ T cells was significantly lower than CMV-specific $CD8^+$ T cells in HTLV-1–infected patients (both patients with HAM/TSP and HVCs) (Figure 3B). The expression of perforin in CMV-specific $CD8^+$ T cells was always higher than the expression of perforin in Tax-specific $CD8^+$ T cells in the same patients in both patients with HAM/TSP and HVCs.

HTLV-1 Tax–specific $CD8^+$ T cells in patients with HAM/TSP and HVCs appear to be at different expression patterns of costimulatory molecule

Because it has been reported that the cell-surface phenotype of virus-specific cells was affected by the stage of infection (ie, acute or chronic) as well as by viral specificity,[20] we further investigated whether the cell-surface phenotype of HTLV-1–specific $CD8^+$ cells differed between patients with HAM/TSP and HVCs. According to a simple classification of 3 functional subsets based on CD28 and CD27 expression (ie, early [$CD28^+CD27^+$], intermediate

(C) Frequency and MFI of the GzmB-positive $CD8^+$ T-cell population and its subpopulations ($CD8^+CD28^-$ and $CD8^+CD27^-$) in patients with HAM/TSP, HVCs, and HCs. (D) Frequency and MFI of the perforin-positive $CD8^+$ T-cell population and its subpopulations ($CD8^+CD28^-$ and $CD8^+CD27^-$) in proviral load (PVL)–matched patients with HAM/TSP, HVCs, and HCs. (E) The frequency and MFI of the GzmB-positive $CD8^+$ T-cell population and its subpopulations ($CD8^+CD28^-$ and $CD8^+CD27^-$) in PVL-matched patients with HAM/TSP, HVCs, and HCs. The frequency of perforin- or GzmB-positive cells is shown as a percentage within each cell subset ($CD8^+$, $CD8^+CD28^-$, $CD8^-CD27^-$). Values represent the means plus or minus the standard error (SE). To test for significant differences among the cell populations between 3 different groups of subjects (HAM/TSP, HVCs, and HCs), one-factor ANOVA was done when the variance of each group was equal by Levene test. If the variance of each group was different, the Kruskal-Wallis test was used. For multiple comparisons, we used Sheffe F to analyze statistical difference. Values of $P < .05$ were considered statistically significant. $^{***}P < .001$; $^{**}P < .01$; $^{*}P < .05$.

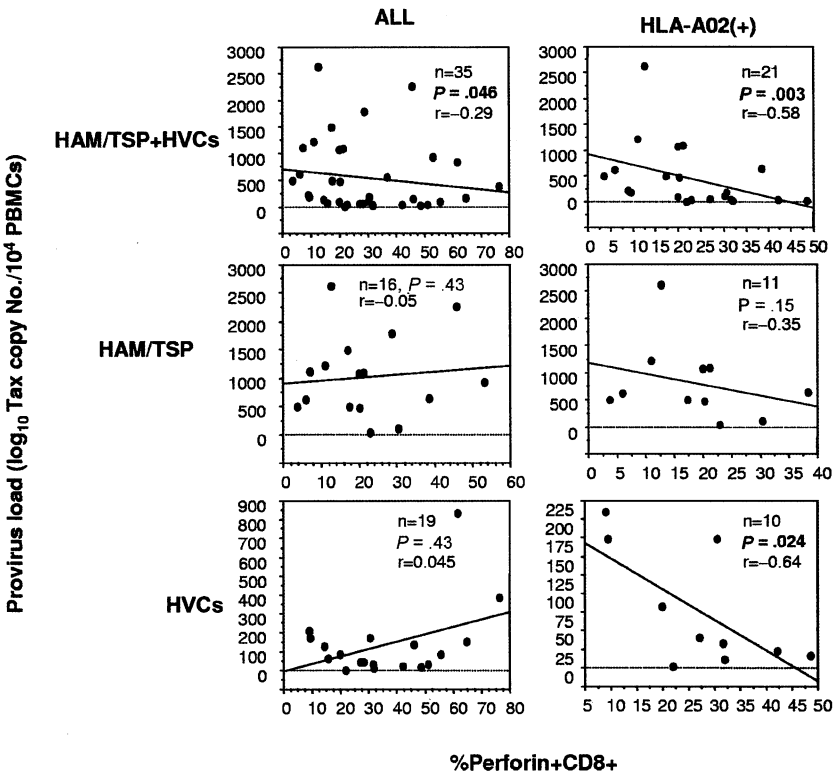

Figure 2. Perforin-positive CD8⁺ T cells and HTLV-1 proviral load in HTLV-1 infection. (Left panels) There was a marginal negative correlation between the percentages of perforin-positive CD8⁺ T cells and HTLV-1 proviral load (PVL) in whole HTLV-1–infected patients (HAM/TSP + HVCs; $P = .046$, $r = -0.29$ by Spearman rank correlation analysis), but not in patients with HAM/TSP or in HVCs alone. (Right panels) There was a significant negative correlation between the percentages of perforin-positive CD8⁻ T cells and HTLV-1 PVL in whole HLA-A*02–positive HTLV-1–infected patients (HAM/TSP + HVCs; $P = .003$, $r = -0.58$) and in HVCs alone ($P = .024$, $r = -0.64$), but not in patients with HAM/TSP ($P = .15$, $r = 0.35$). The x axis denotes percentage of perforin-positive CD8⁺ T cells, and the y axis denotes HTLV-1 PVL (copy number of HTLV-1 *tax* per 10^4 PBMCs = [(copy number of *tax*)/(copy number of β-actin/2)] × 10^4). Data were analyzed by Spearman rank correlation. The solid line represents a least-squares regression line.

[CD28⁻CD27⁺], and late [CD28⁻CD27⁻] differentiated T cells; Figure 4A),[20] more than 60% of HTLV-1 Tax–specific CD8⁺ T cells from patients with HAM/TSP showed late differentiated phenotype, whereas more than 60% of HTLV-1 Tax–specific CD8⁺ T cells from HVCs showed intermediate differentiated phenotype (Table 3 and Figure 4B,C). These phenotypes did not change even when we compared the frequencies between patients with HAM/TSP and the HVCs with a similar PVL ($P = .11$, Mann-Whitney U test, Table 3). As previously reported, more than 80% of CMV-tetramer–specific CD8⁺ T cells both from patients with HAM/TSP and HVCs showed a late differentiated phenotype (Table 3 and Figure 4B,C).[20] As shown in Figure 4D, there was a negative correlation between percent Tax-specific intermediate differentiated T cells and HTLV-1 PVL in the whole cohort ($n = 31$; $P = .008$, $r = -0.47$ by Spearman rank correlation analysis) whereas there was a positive correlation between percent Tax-specific late differentiated T cells and HTLV-1 PVL in the whole cohort ($n = 31$; $P = .005$, $r = 0.49$ by Spearman rank correlation analysis). There was no correlation between percent Tax-specific early differentiated T cells and HTLV-1 PVL in the whole cohort ($n = 31$; $P = .55$, $r = -0.1$ by Spearman rank correlation analysis).

CD107a mobilization assays

To determine the functional reactivity of HTLV-1 Tax-specific CD8⁺ T cells, we performed a CD107a mobilization assay (Figure 5). PBMCs derived from HLA-A*02–positive HTLV-1–infected patients (patients with HAM/TSP and HVCs) were stained with HLA-A*02/ Tax11-19 tetramer after incubation with Tax11-19 peptide and anti-CD107a monoclonal antibody for 4 hours. Significant anti-CD107a staining was observed on the Tax-tetramer–positive population after coculture with Tax11-19 peptide, whereas only background staining was seen without peptide (Figure 5A). We compared the frequency of expression of the degranulation marker CD107a in Tax-tetramer–positive cells, which allows measurement of cytolytic cell activation, between 10 patients with HAM/TSP and 14 HVCs. The percentage of CD107a⁺ HLA-A*02/Tax11-19 tetramer–positive cells within the HLA-A*02/Tax11-19 tetramer–positive gate (percent Tet⁺ CD107a⁺/ Tet⁺) was significantly lower in patients with HAM/TSP than in HVCs (Figure 5B). The same results were obtained in a comparison between 5 patients with HAM/TSP and 6 HVCs with similar PVL (patients with HAM/TSP 307.2 ± 125.3 vs HVCs 270.0 ± 92.2, $P = .57$, Mann-Whitney), indicating that the observed difference did not simply reflect the higher PVL (ie, the higher frequency of HTLV-1–infected T cells) in patients with HAM/TSP (Figure 5C).

Discussion

To characterize the HTLV-1–specific CD8⁺ T cells in infected patients, we first examined the expression of costimulatory molecules on CD4⁺ and CD8⁺ T cells, which have a significant impact on the cytokine profile and proliferation response. Interestingly, the percentages of CD8⁺ T cells that were negative for costimulatory molecules CD27, CD28, CD152 (CTLA-4), CD80 (B7-1), and CD86 (B7-2) were significantly higher in patients with HAM/TSP compared with HVCs or HCs, whereas this discrepancy was not found within the CD4⁺ T-cell population. Namely, there was a selective decrease of costimulatory molecule expression on CD8⁺ T cells in patients with HAM/TSP. It is noteworthy that the same differences were observed in a comparison between patients with HAM/TSP and HVCs with a similar PVL, whereas there were no significant differences between the patients with HAM/TSP and HVCs in either the frequency of CD4⁺ cells negative for costimulatory molecules or the PVL in PBMCs. These findings suggest that the expression of costimulatory molecules was influenced by the

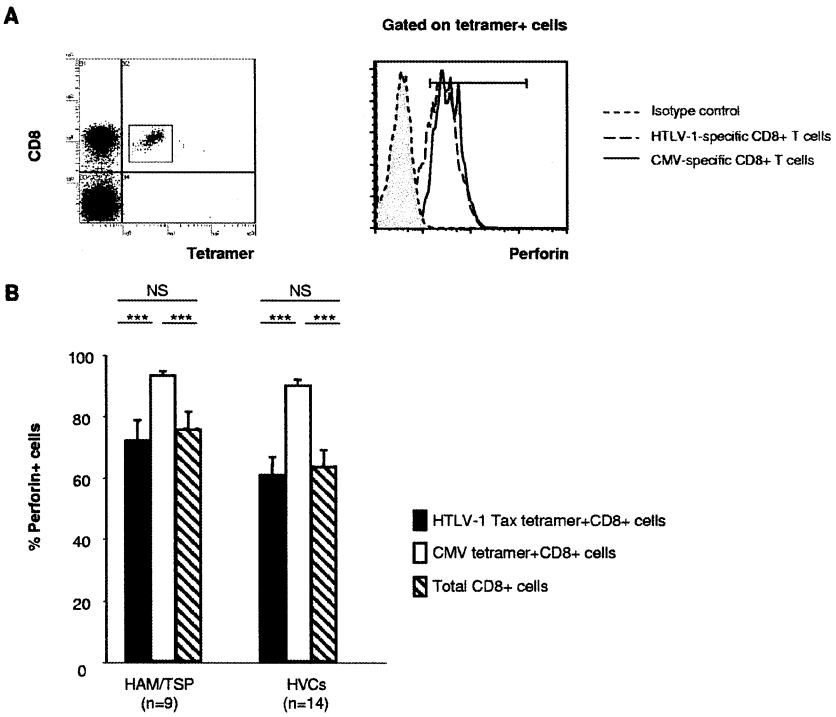

Figure 3. Perforin expression in HTLV-1 Tax– and CMV pp65–specific CD8+ T cells in HTLV-1 infection. (A) Left panel: Dot plots of HLA-A*02/Tax11-19 tetramer-PE (x axis) versus CD8-ECD fluorescence within the lymphocyte gate based on forward versus side scatter. Right panel: Histogram of perforin expression (x axis, arbitrary units, log scale) versus cell number (y axis) in gated virus-specific (tetramer-positive) cells. Representative dot plot from one patient with HAM/TSP is shown. (B) The perforin expression in HTLV-1 Tax– and CMV pp65–specific CD8+ T cells in HTLV-1–infected patients. Statistical analysis was done as described in the legend for Figure 1. ***$P < .001$

disease status rather than the PVL. The emergence of high frequencies of CD8+ T cells negative for costimulatory molecules might have been caused by a greater degree of continuous or repeated antigenic stimulation in patients with HAM/TSP than in HVCs at a similar PVL; such repeated antigenic stimulation might lead immune cells into a loss of antiviral CD8+ T-cell function, as suggested in HIV infection. In fact, it has been reported that the number of naive T cells was low in HTLV-1–infected patients compared with uninfected controls, whereas the number of memory T lymphocytes was greater in HTLV-1–infected patients.[28] This finding supports the rapid turnover of T cells by antigenic stimulation in HTLV-1–infected patients, which has recently been directly demonstrated by metabolic labeling of lymphocytes in vivo in human HTLV-1–infected subjects.[29] We next focused on the $CD8^+CD28^-$ T cells and $CD8^+CD27^-$ T cells, because these subsets include CTLs and abnormal expansion of these subsets was also described in chronic CMV,[26] EBV,[27] and HIV[20] infection. Especially, increased expression of $CD8^+CD28^-$ T cells was associated with disease activity and $CD8^+$ T-cell dysfunction in HIV infection.[30,31] As expected, the percentages of $CD8^+$ cells that were negative for CD28 or CD27 were significantly increased in patients with HAM/TSP by comparison with HVCs or HCs, irrespective of PVL.

Because impaired CTL-mediated lysis is a general feature of chronic HIV, CMV, and EBV infections,[32] especially when the antigen load is high,[33] it is important to examine the phenotypic and functional property of $CD8^+$ T cells in HTLV-1 infection. Our data showed that the frequency of perforin and $GzmB^+CD8^+$, $CD8^+CD28^-$, and $CD8^+CD27^-$ T cells in PBMCs was significantly lower in HTLV-1–infected patients (patients with HAM/TSP and HVCs) than in HCs. Interestingly, although both the percentage and MFI of $perforin^-CD8^+$, $perforin^+CD8^+CD28^-$, and $perforin^+CD8^+CD27^-$ T-cell populations were significantly lower in HTLV-1–infected patients (patients with HAM/TSP and HVCs) than in HCs, irrespective of PVL, the MFIs of $GzmB^+CD8^+$, $GzmB^+CD8^+CD28^-$, and $GzmB^+CD8^+CD27^-$ T-cell populations were not significantly different among patients with HAM/TSP, HVCs, and HCs compared with similar PVLs. Such discordant expression patterns between perforin and granzymes are a common feature of circulating virus-specific $CD8^+$ T cells in chronic HIV, CMV, and EBV infection.[32,34-37] Because perforin staining often lessens after T-cell activation, presumably because of the release of preformed perforin,[34] decreased perforin expression in HTLV-1 infection, especially patients with HAM/TSP, might arise from aberrant perforin secretion or from frequent discharge of perforin caused by constant antigenic stimulation.[38] In this case, the higher MFI of GzmB compared with perforin in $CD8^+$ T cells of patients with HAM/TSP might be a result of the lack of granzyme release caused by lower perforin levels. Interestingly, there was a significant negative correlation between percent $perforin^+CD8^+$ T cells and HTLV-1 PVL in HTLV-1–infected HLA-A*02–positive HVCs, but not in HLA-A*02–negative HVCs and patients with HAM/TSP who were either HLA-A*02 positive or negative. As the possession of HLA-A*02 was associated with a significant reduction in both HTLV-1 PVL and the risk of HAM/TSP,[11] these findings suggest that the HLA-A*02–restricted CTLs are particularly efficient at killing HTLV-1–infected cells.[39] The absence of correlation between perforin-expressing $CD8^+$ T cells and HTLV-1 PVL in patients with HAM/TSP also supports the hypothesis of $CD8^+$ T-cell inefficiency in the diseased situation.

A large number of phenotypic markers have been used to define different populations of antigen-specific $CD4^+$ and $CD8^+$ T cells, and these markers have been proposed to identify functionally distinct T-cell populations and different stages of T-cell function. A previous study indicated that HIV-specific $CD8^+$ T cells appear to have a different cell-surface phenotype from CMV-specific $CD8^+$ T cells,[20] and the lack of perforin in HIV-specific populations was correlated with decreased cytotoxic activity compared with CMV-specific populations.[34] In this study, we have also shown that the cell-surface phenotypes of virus-specific $CD8^+$ T cells are distinct among HVCs and patients with HAM/TSP, irrespective of

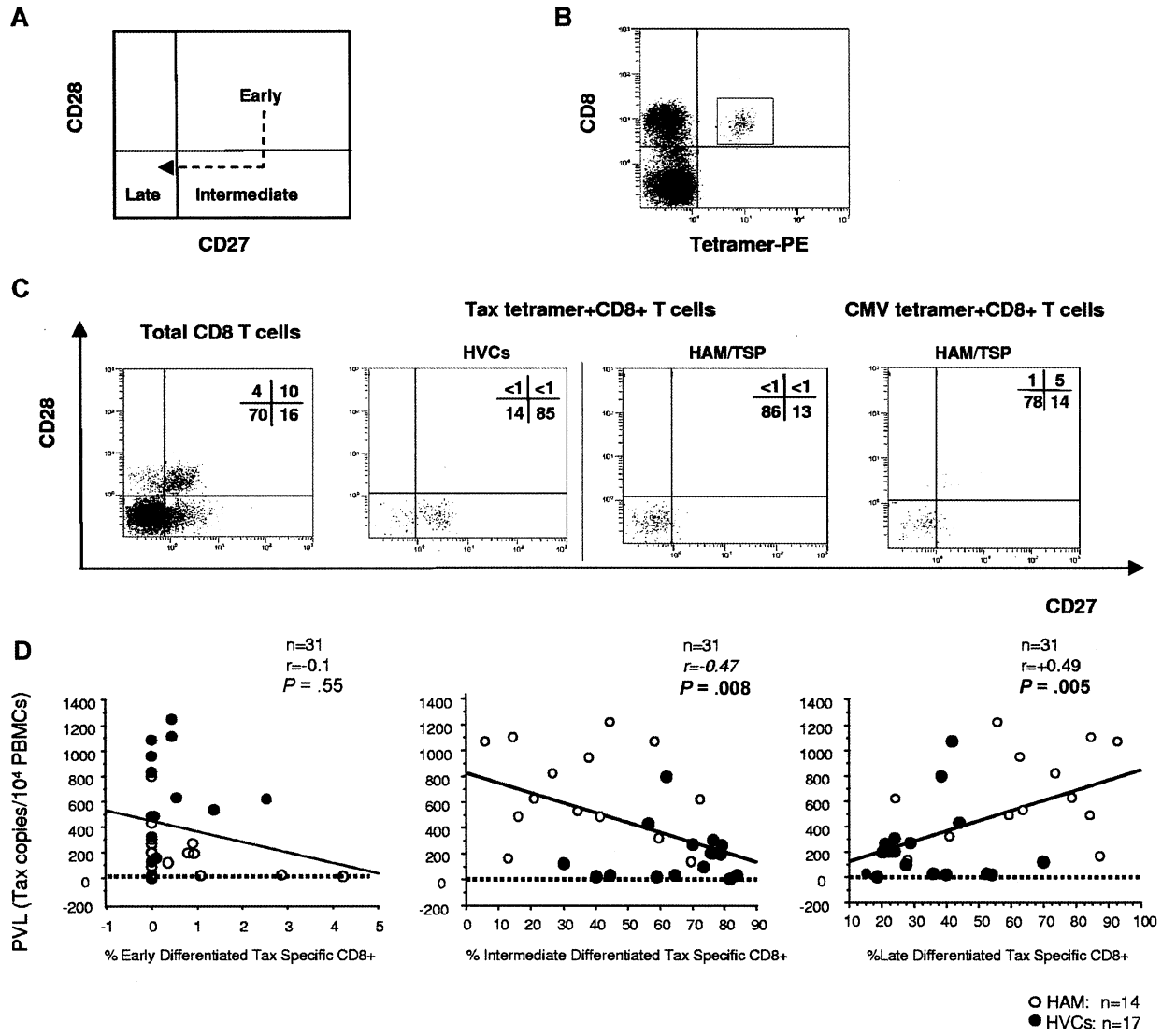

Figure 4. CD27 and CD28 coexpression on virus-specific CD8⁺ T cells in HTLV-1 infection. Flow cytometric analysis of CD27 and CD28 coexpression gated on HLA-A*02/Tax11-19 tetramer–positive cells. (A) The model of antigen-specific CD8⁺ T-cell differentiation based on the expression of CD27 and CD28. In the CD8⁺ T-cell population, early differentiated cells differentiate into late-differentiated cells, following a stage of intermediate cells that have down-regulated CD28, but not yet CD27. (B) Dot plots of HLA-A*02/Tax11-19 tetramer-PE (x axis) versus CD8-ECD fluorescence within the lymphocyte gate based on forward versus side scatter. (C) CD28/CD27 expression on total CD8⁺ T-cell– and HTLV-1– or CMV-specific T cells detected by tetramers were shown. The HTLV-1 Tax–specific CD8 T cells were enriched in intermediate-differentiated stage in HVCs and in late-differentiated stage in patients with HAM/TSP, whereas there was no difference in distribution of CMV pp65–specific CD8 T cells between patients with HAM/TSP and HVCs. Representative dot plots from 1 HVC and 1 patient with HAM/TSP for HTLV-1–specific cells, and 1 HAM/TSP patient for CMV-specific cells are shown. (D) Correlation between PVL (y axis; copy number of HTLV-1 *tax* per 10^4 PBMCs) and "early," "intermediate," or "late" phenotype of HTLV-1 Tax–specific cells (x axis; percentage of Tax-tetramer–positive cells in each subset) in PBMCs from HTLV-1–infected patients. Data were analyzed by Spearman rank correlation.

PVL, indicating distinct characteristics of the anti–HTLV-1 immune response in infected patients with different disease status. The observed increase in the frequencies of $CD8^+$, $CD8^+CD28^-$, and $CD8^+CD27^-$ T-cell population in PBMCs in HTLV-1 infection without correlation with perforin or granzyme expression in the corresponding cells suggests that the variation in perforin and GzmB staining among different subjects with HTLV-1 infection results from different levels of antigenic stimulation among these hosts. In addition, the costimulatory molecule expression, perforin content, and GzmB content might represent the state of activation of these cells when viral antigen expression reaches equilibrium with the CTL population. It is highly likely that this point of equilibrium will differ not only between different viral infections because of different kinetics of viral expression, but also between patients with a different "efficiency" of the HTLV-1–specific CTL response.

Finally, we performed a CD107a mobilization assay to compare the functional reactivity of HTLV-1–specific $CD8^+$ T cells between patients with HAM/TSP and HVCs, because the CD107a is much closer to the actual effector function than the equilibrium content of perforin and GzmB. After cultivation with Tax11-19 peptide, significantly higher anti-CD107a staining was observed in Tax-tetramer–positive $CD8^+$ T cells in HVCs than in patients with HAM/TSP. This was also the case when we compared patients with HAM/TSP and HVCs with a similar PVL, indicating that the observed differences were not attributable to the difference in PVL between patients with HAM/TSP and HVCs. Rather, the data suggest that the CTLs in PBMCs from patients with HAM/TSP

Table 3. Percentages of intermediate- and late-differentiated CD8+ T cells based on the expression of CD28 and CD27 in HTLV-1 Tax– and CMV pp65–specific CD8+ T cells of patients with HAM/TSP and HVCs

	Tax-specific		CMV-specific	
	Intermediate	Late	Intermediate	Late
HAM/TSP	38.1 ± 5.2 (n = 16)	61.0 ± 5.3 (n=16)	17.7 ± 5.8 (n = 12)	81.9 ± 5.8 (n = 12)
HVCs	66.3 ± 3.8 (n = 17)	32.7 ± 3.6 (n=17)	10.3 ± 4.0 (n = 8)	89.0 ± 2.4 (n = 8)
All	52.6 ± 4.0 (n = 33)	46.4 ± 4.0 (n=33)	14.8 ± 3.6 (n = 20)	84.7 ± 3.6 (n = 20)
*P**	< .001	< .001	.88	.88

	Tax-specific			
	Intermediate	Late	PVL	*P**
PVL-matched, HAM/TSP	39.2 ± 7.6 (n = 9)	56.6 ± 7.9 (n = 9)	470.3 ± 75.0	.11
PVL-matched, HVCs	68.2 ± 4.9 (n = 10)	31.4 ± 4.9 (n = 10)	303.5 ± 70.0	
PVL-matched, all	54.4 ± 5.5 (n = 19)	44.8 ± 4.9 (n = 19)	382.5 ± 50.4	
*P**	.004	.006		

Values represent the means plus minus SE.
*P values between HAM-HVCs were calculated by Mann-Whitney *U* test. PVL: HTLV-1 *tax* copy number per 10^4 PBMCs.

have discharged their granules much more recently because of the greater antigenic stimulus, and so have fewer lytic granules and less CD107a to discharge in the short-term in vitro assay. Because there is evidence that the concentration of antigen required to stimulate CD8+ T cells to produce cytokines is greater than the concentration required to induce CTL killing of target cells,[40] higher HTLV-1 PVL as well as higher antigen load in patients with HAM/TSP may deteriorate the function of CD8+ T cells. In this case, the abundance of antigen in patients with HAM/TSP might exceed the threshold required to stimulate the CD8+ T cells to produce inflammatory cytokines such as interferon-γ (IFN-γ) and tumor necrosis factor-α (TNF-α); therefore, the effect of CTLs is not protective but harmful for infected patients.

In conclusion, our present data indicate that CTL efficiency appears to be lower in patients with HAM/TSP than in HVCs. The different costimulatory molecule expression, perforin content, and GzmB content between patients with HAM/TSP and HVCs may reflect the different state of activation of the cells when viral antigen expression reaches equilibrium with the CTL population within infected patients. This point of equilibrium may differ not only between different viral infections (ie, different kinetics of viral expression), but also between HTLV-1–infected patients with a different "efficiency" of CTL response. Future studies investigating the nature of the defects in these T cells may provide opportunities to overcome such inefficient functions, and may hold the potential for reducing disease or eradicating persisting infection.

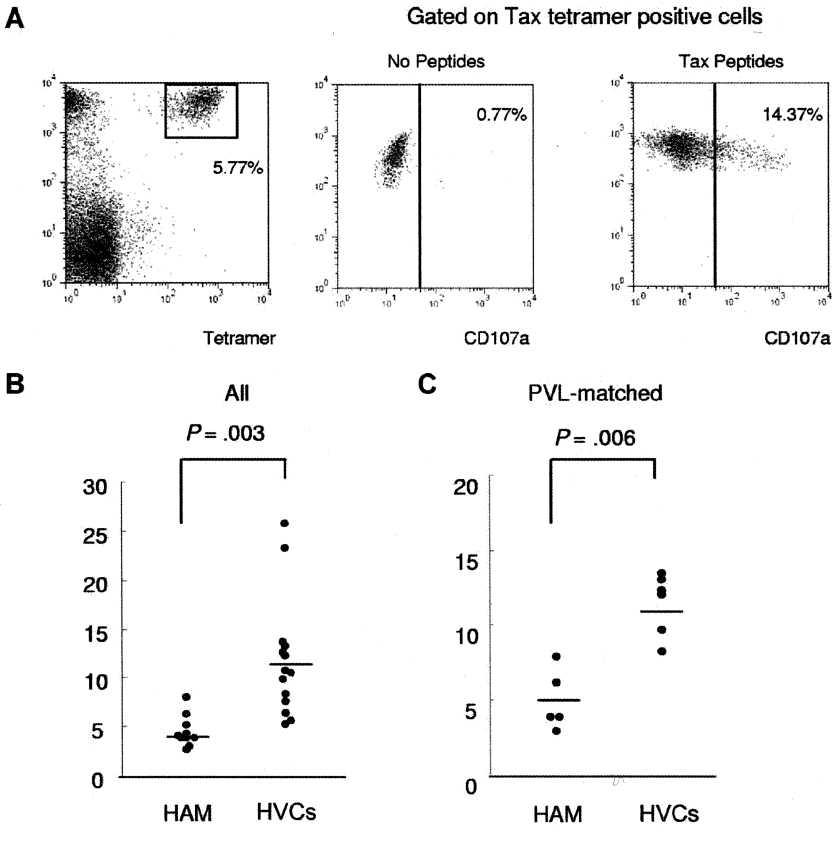

Figure 5. CD107a expression in patients with HAM/TSP and in HVCs after coculture with immunodominant Tax peptide. To determine the functional reactivity of HTLV-1 Tax–specific CD8+ T cells, we performed a CD107a mobilization assay. PBMCs derived from HLA-A*02–positive HTLV-1–infected patients (patients with HAM/TSP and HVCs) were stained with anti–CD8-PC5 and HLA-A*02/Tax11-19 tetramer after incubation with Tax11-19 peptide and anti-CD107a monoclonal antibody for 4 hours. (A) Left panel: Dot plots of HLA-A*02/Tax11-19 tetramer-PE (x axis) versus CD8-PC5 (y axis) fluorescence within the lymphocyte gate based on forward versus side scatter. Significant anti-CD107a staining was observed on the Tax-tetramer–positive population after coculture with Tax11-19 peptide (left panel), whereas only background staining was seen without peptide (center panel). (B) Comparison of degranulation marker CD107a expression in Tax-tetramer–positive cells between 10 patients with HAM/TSP and 14 HVCs. The percentage of CD107a+ Tax11-19 tetramer–positive cells/Tax11-19 tetramer–positive cells was significantly decreased in patients with HAM/TSP compared with HVCs ($P = .003$, Mann Whitney). (C) The CD107a staining was still significantly lower in patients with HAM/TSP than in HVCs compared between PVL-matched groups ($P = .006$, Mann-Whitney). Horizontal bars represent the median value of percent CD107a+ Tax11-19 tetramer–positive cells/Tax11-19 tetramer–positive cells.

Acknowledgments

We thank the staff and blood donors of Kagoshima University Hospital. The authors thank Ms Fumiko Inoue and Yoko Nishino of Kagoshima University and Ms Sumie Saito of Kanazawa Medical University for their excellent technical assistance.

This work was supported by the Ministry of Health, Labor and Welfare, Japan (Neuroimmunological Disease Research Committee Grant; S.I., M.O., and Y.O.); the Japan Society for the Promotion of Science (JSPS; grant 17590886; M.S.); the Japan Brain Foundation (M.S.); the Takeda Science Foundation (M.S.); Kanazawa Medical University (grants S2006-1, H2007-11, and C2007-5; M.S.). A.H.S. was supported by a Postdoctoral Fellowship for Foreign Researchers from JSPS.

Authorship

Contribution: A.H.S. designed and performed the experiments, analyzed the data, and wrote the paper; K.U. provided input into the data analyses and interpretation; M.O. and D.H. provided samples, clinical data, and advice; S.I., M.O., and Y.O. contributed to obtaining funding and gave advice; M.S. designed and supervised the research, performed experiments, and wrote the paper; and all authors checked the final version of the manuscript.

Conflict-of-interest disclosure: The authors declare no competing financial interests.

Correspondence: Mineki Saito, Department of Microbiology, Kanazawa Medical University, 1-1 Daigaku, Uchinada-machi, Ishikawa 920-0293, Japan; e-mail: mineki@kanazawa-med.ac.jp.

References

1. Poiesz BJ, Ruscetti FW, Gazdar AF, Bunn PA, Minna JD, Gallo RC. Detection and isolation of type C retrovirus particles from fresh and cultured lymphocytes of a patient with cutaneous T-cell lymphoma. Proc Natl Acad Sci U S A. 1980;77: 7415-7419.
2. Yoshida M, Miyoshi I, Hinuma Y. Isolation and characterization of retrovirus from cell lines of human adult T-cell leukemia and its implication in the disease. Proc Natl Acad Sci U S A. 1982;79: 2031-2035.
3. Hinuma Y, Nagata K, Hanaoka M, et al. Adult T-cell leukemia: antigen in an ATL cell line and detection of antibodies to the antigen in human sera. Proc Natl Acad Sci U S A. 1981;78:6476-6480.
4. Yoshida M, Seiki M, Yamaguchi K, Takatsuki K. Monoclonal integration of human T-cell leukemia provirus in all primary tumors of adult T-cell leukemia suggests causative role of human T-cell leukemia virus in the disease. Proc Natl Acad Sci U S A. 1984;81:2534-2537.
5. Gessain A, Barin F, Vernant JC, et al. Antibodies to human T-lymphotropic virus type-I in patients with tropical spastic paraparesis. Lancet. 1985;2: 407-410.
6. Osame M, Usuku K, Izumo S, et al. HTLV-I associated myelopathy, a new clinical entity. Lancet. 1986;1:1031-1032.
7. Izumo S, Umehara F, Osame M. HTLV-I-associated myelopathy. Neuropathology. 2000; 20(suppl):S65-68.
8. Uchiyama T. Human T cell leukemia virus type I (HTLV-I) and human diseases. Annu Rev Immunol. 1997;15:15-37.
9. Nagai M, Usuku K, Matsumoto W, et al. Analysis of HTLV-I proviral load in 202 HAM/TSP patients and 243 asymptomatic HTLV-I carriers: high proviral load strongly predisposes to HAM/TSP. J Neurovirol. 1998;4:586-593.
10. Jeffery KJ, Siddiqui AA, Bunce M, et al. The influence of HLA class I alleles and heterozygosity on the outcome of human T cell lymphotropic virus type I infection. J Immunol. 2000;165:7278-7284.
11. Jeffery KJ, Usuku K, Hall SE, et al. HLA alleles determine human T-lymphotropic virus-I (HTLV-I) proviral load and the risk of HTLV-I-associated myelopathy. Proc Natl Acad Sci U S A. 1999;96: 3848-3853.
12. Hanon E, Hall S, Taylor GP, et al. Abundant tax protein expression in CD4+ T cells infected with human T-cell lymphotropic virus type I (HTLV-I) is prevented by cytotoxic T lymphocytes. Blood. 2000;95:1386-1392.
13. Hanon E, Stinchcombe JC, Saito M, et al. Fratricide among CD8(+) T lymphocytes naturally infected with human T cell lymphotropic virus type I. Immunity. 2000;13:657-664.
14. Kubota R, Kawanishi T, Matsubara H, Manns A, Jacobson S. Demonstration of human T lymphotropic virus type I (HTLV-I) tax-specific CD8+ lymphocytes directly in peripheral blood of HTLV-I–associated myelopathy/tropical spastic paraparesis patients by intracellular cytokine detection. J Immunol. 1998;161:482-488.
15. Klenerman P, Hill A. T cells and viral persistence: lessons from diverse infections. Nat Immunol. 2005;6:873-879.
16. Vine AM, Heaps AG, Kaftantzi L, et al. The role of CTLs in persistent viral infection: cytolytic gene expression in CD8+ lymphocytes distinguishes between individuals with a high or low proviral load of human T cell lymphotropic virus type 1. J Immunol. 2004;173:5121-5129.
17. Kubota R, Kawanishi T, Matsubara H, Manns A, Jacobson S. HTLV-I specific IFN-gamma+ CD8+ lymphocytes correlate with the proviral load in peripheral blood of infected individuals. J Neuroimmunol. 2000;102:208-215.
18. Wodarz D, Hall SE, Usuku K, et al. Cytotoxic T-cell abundance and virus load in human immunodeficiency virus type 1 and human T-cell leukaemia virus type 1. Proc Biol Sci. 2001;268:1215-1221.
19. Goon PK, Biancardi A, Fast N, et al. Human T cell lymphotropic virus (HTLV) type-1–specific CD8+ T cells: frequency and immunodominance hierarchy. J Infect Dis. 2004;189:2294-2298.
20. Appay V, Dunbar PR, Callan M, et al. Memory CD8+ T cells vary in differentiation phenotype in different persistent virus infections. Nat Med. 2002;8:379-385.
21. Harari A, Vallelian F, Meylan PR, Pantaleo G. Functional heterogeneity of memory CD4 T cell responses in different conditions of antigen exposure and persistence. J Immunol. 2005;174: 1037-1045.
22. Betts MR, Nason MC, West SM, et al. HIV nonprogressors preferentially maintain highly functional HIV-specific CD8+ T cells. Blood. 2006; 107:4781-4789.
23. Osame M. Review of WHO Kagoshima meeting and diagnostic guidelines for HAM/TSP. New York, NY: Raven Press; 1990.
24. Rubio V, Stuge TB, Singh N, et al. Ex vivo identification, isolation and analysis of tumor-cytolytic T cells. Nat Med. 2003;9:1377-1382.
25. Burkett MW, Shafer-Weaver KA, Strobl S, Baseler M, Malyguine A. A novel flow cytometric assay for evaluating cell-mediated cytotoxicity. J Immunother (1997). 2005;28:396-402.
26. Gillespie GM, Wills MR, Appay V, et al. Functional heterogeneity and high frequencies of cytomegalovirus-specific CD8(+) T lymphocytes in healthy seropositive donors. J Virol. 2000;74:8140-8150.
27. Callan MF, Tan L, Annels N, et al. Direct visualization of antigen-specific CD8+ T cells during the primary immune response to Epstein-Barr virus in vivo. J Exp Med. 1998;187:1395-1402.
28. Yasunaga J, Sakai T, Nosaka K, et al. Impaired production of naive T lymphocytes in human T-cell leukemia virus type I–infected individuals: its implications in the immunodeficient state. Blood. 2001;97:3177-3183.
29. Asquith B, Zhang Y, Mosley AJ, et al. In vivo T lymphocyte dynamics in humans and the impact of human T-lymphotropic virus 1 infection. Proc Natl Acad Sci U S A. 2007;104:8035-8040.
30. Choremi-Papadopoulou H, Panagiotou N, Samouilidou E, et al. CD28 costimulation and CD28 expression in T lymphocyte subsets in HIV-1 infection with and without progression to AIDS. Clin Exp Immunol. 2000;119:499-506.
31. Vingerhoets JH, Vanham GL, Kestens LL, et al. Increased cytolytic T lymphocyte activity and decreased B7 responsiveness are associated with CD28 down-regulation on CD8+ T cells from HIV-infected subjects. Clin Exp Immunol. 1995;100: 425-433.
32. Zhang D, Shankar P, Xu Z, et al. Most antiviral CD8 T cells during chronic viral infection do not express high levels of perforin and are not directly cytotoxic. Blood. 2003;101:226-235.
33. Wherry EJ, Ahmed R. Memory CD8 T-cell differentiation during viral infection. J Virol. 2004;78: 5535-5545.
34. Appay V, Nixon DF, Donahoe SM, et al. HIV-specific CD8(+) T cells produce antiviral cytokines but are impaired in cytolytic function. J Exp Med. 2000;192:63-75.
35. Haridas V, McCloskey TW, Pahwa R, Pahwa S. Discordant expression of perforin and granzyme A in total and HIV-specific CD8 T lymphocytes of HIV infected children and adolescents. AIDS. 2003;17:2313-2322.
36. Chen G, Shankar P, Lange C, et al. CD8 T cells specific for human immunodeficiency virus, Epstein-Barr virus, and cytomegalovirus lack molecules for homing to lymphoid sites of infection. Blood. 2001;98:156-164.
37. Sandberg JK, Fast NM, Nixon DF. Functional heterogeneity of cytokines and cytolytic effector molecules in human CD8+ T lymphocytes. J Immunol. 2001;167:181-187.
38. Klingstrom J, Gudmundsdotter L, Zuber B, et al. Elevated levels of serum perforin in chronic HIV-1 and acute SIV/SHIV infection. AIDS. 2006;20: 125-127.
39. Bangham CR. The immune control and cell-to-cell spread of human T-lymphotropic virus type 1. J Gen Virol. 2003;84:3177-3189.
40. Valitutti S, Muller S, Dessing M, Lanzavecchia A. Different responses are elicited in cytotoxic T lymphocytes by different levels of T cell receptor occupancy. J Exp Med. 1996;183:1917-1921.

１．研究課題名：遺伝疾患原因遺伝子の探索（研究番号　S2006-2）

２．キーワード：１）ウェルナー症候群（Werner syndrome）
２）DNA マイクロアレイ（DNA microarray）
３）質量分析（Mass spectrometry）
４）老化（Ageing）
５）がん（Cancer）

３．研究者氏名：石垣　靖人・総合医学研究所・講師・共同利用部門

４．研 究 目 的

本研究の目的は、様々な疾患における遺伝子の変動や個体差を利用してバイオマーカーや原因遺伝子の同定に結びつけることである。各種がん、病態モデルについて本学に設置された先端機器を活用して解析手法を構築するとともに、各解析のリンクを行いオミックス型の遺伝子発現解析研究を実現することを目指している。

がんに加えて老化症候群における遺伝子発現を網羅的に解析することによって、ヒトの新たな老化経路を見いだすことを目指している。これによりアンチエイジングを目指した新しい標的分子の同定を試みたい。特に原因遺伝子既知のウェルナー症候群(WS)に加えて、未だに原因遺伝子が明らかにされていないが臨床症状は WS と近似した疑ウェルナー症候群(Q-WS)患者由来の細胞を解析するため、老化形質に直接かかわる遺伝子群を効率よく同定できる点が特色である。これらの疾患の解析に必要な手法を確立するとともに問題点について整理を目指した。

５．研 究 計 画

申請者は WS および Q-WS 患者由来細胞を収集しており、これを利用した研究について本学の遺伝子解析研究に関する倫理審査委員会の承認を得ている。これらの細胞について網羅的遺伝子発現解析を遺伝子およびタンパク質レベルで行い老化細胞での遺伝子発現プロファイルを明らかにする。プリファイリングには DNA、RNA およびタンパク質レベルでの網羅的な解析の組み合わせが有効であり、得られたデータ同士をネットワークのデータベースに落とし込んで俯瞰的に解析することが必要となる。これらの実験系の整備と手法を確立し、共同研究を実施するとともに、早老症の解析に応用する。

６．研 究 成 果

本学に導入された DNA マイクロアレイシステムは学内外の 10 以上の部門や研究グループで研究に活用されつつあるが、申請者は管理者として操作等に習熟し、学内の臨床系の研究支援を中心として広く共同研究を進めている。

発現プロファイルの解析についてはバイオインフォマテックスの手法を含めて一定の経験を積んできた（島崎ら、膵臓、2007)。また、病態モデルにおける遺伝子発現解析の基礎的な検討を行い、成果を発表してきた（Kiba *et al.*, Pancrea, 2007, Yamakawa *et al.*, Biol.Pharm.Bull. 印刷中)。さらに、SNPs 解析アレイについても

共同研究を行い、微細な染色体異常の検出にも有用であることを示してきた（尾崎と石垣、金沢医科大学雑誌、印刷中)。また質量分析装置によるタンパク質同定法についても、様々な検体について経験を積み論文を発表してきた（Takata *et al.*, Biol.Pharm.Bull. 印刷中)。また、１７年度の奨励研究の課題として上げた遺伝子ノックダウン法の改良については、従来の RNA 干渉誘導法に簡単な改良を加えるだけでノックダウンの効率を劇的に上げることに成功し、英文誌に成果を発表した（Nagao *et al.*, BBRC、2008)。さらに、外見上正常な方からの繊維芽細胞のデータセットを16例収集した。これにより、検出感度を飛躍的に上昇させるとともに、データのばらつきに基づいた新規の解析手法の解析を可能にできた。特に発現を欠失した原因遺伝子の特定が可能であることを原因遺伝子既知の色素性乾皮症細胞を用いて確認しており招待講演等で発表してきた（第６回北陸ポストゲノム研究フォーラム、2007)。これらの実験手法については更に実験技術の改良を行い、がん細胞の悪性化、mRNA 代謝機構および早老症の解析について論文を投稿、執筆中である。

特に早老症細胞のトランスクリプトーム解析結果から、炎症免疫遺伝子および細胞周期関連遺伝子の関与を示唆する結果を得ており、慢性的かつ軽度の炎症が早期老化の原因のひとつではないかと推定している。実際得られたデータセットから解析可能だった約２万個の遺伝子群から、患者においてのみ発現変動が認められる200個弱の遺伝子を抽出した。これらの発現量にもとづくクラスタリングは明瞭に患者群と正常コントロール群を判別することができ、疾患のマーカーとして有用であることが明らかとなった。この遺伝子群をパスウエイデータベース Ingenuity Pathways Analysis (IPA)において性格付けすると、WRN の細胞内機能から予想される細胞周期関連遺伝子に加えて、免疫応答と炎症に働く遺伝子群が患者でのみ変動していることが明らかとなった。さらに、早期老化症候群の典型的な症状を示す患者家系において血清タンパク質のプロテオミクス解析を行った。２次元電気泳動における解析は DNA マイクロアレイ解析と同様に患者特有のマーカーの存在を示唆していた。現在プロテオミクス手法を駆使して血清中のタンパク質マーカーを同定しつつあり、RNA レベルでの解析と IPA 上で統合することによって、*WRN*遺伝子の変異が引き起こす早期老化の分子パスウエイを提案していく予定である。また、疑ウェルナー症候群についても原因遺伝子の候補について絞り込みを行い、変異遺伝子の特定を急いでいる。

７．研究の考察・反省

疑ウェルナー症候群についても原因遺伝子の候補について絞り込みを行ったものの、決定的な変異を同定するにあたってなかなか進捗せず、この点に人手を育成してクローニングを成功させたいと考えている。今後は共同研究についてテーマを絞り込んで継続したい。

８．研 究 発 表

尾崎守、石垣靖人、SNPs ジェノタイピングアレイを用いた超微細染色体構造異常検出にむけた基礎的検討、金医大誌 2008; 33: 1-12.

Yamakawa JI, Ishigaki Y, Takano F, Takahashi T, Yoshida J, Moriya J, Takata T, Tatsuno T, Sasaki K, Ohta T, Takegami T, Yoshizaki F. The kampo medicines orengedokuto, bofutsushosan and boiogito have different activities to regulate gene expressions in differentiated rat white adipocytes: Comprehensive analysis of genetic profiles. Biol.Pharm.Bull. 2008; 31: 2083-2089.

金医大誌（J Kanazawa Med Univ）33：1－12, 2008

SNPsジェノタイピングアレイを用いた超微細染色体構造異常検出にむけた基礎的検討
－先天性多発奇形・精神発達遅滞の症例の場合－

尾崎　守[1)]，石垣靖人[2)]

要　約：目的：本研究では染色体検査の高度化を目指し，G-分染法とSNPsジェノタイピングアレイ（以下，SNPsアレイ）の組み合わせによる解析系の確立と臨床応用に向けた基礎的な検討を行った。

対象：健常者5名（男性3名，女性2名）。多発先天奇形・精神発達遅滞（Multiple congenital anomaly/Mental retardation MCA/MR）患者8名。

方法：ハプロイドセット400本レベルのG-分染法による染色体分析結果とAffymetrix社のSNPsアレイによるコピー数解析結果を比較検討するとともに，再現性確認試験を行った。

結果：健常者5例では，G-分染法，コピー数解析のいずれの方法においても異常は検出されなかった。MCA/MR患者では5例においてG-分染法で明らかな染色体構造異常が検出されたが，コピー数解析でははるかに高い分解能でコピー数異常部位が同定された。患者3例においては染色体異常が認められなかったが，そのうち1例では，コピー数解析により1q21.1バンド内に新たに約400kbの欠失が検出でされた。さらに，MCA/MR患者8例全てに7q11.23バンド内に約300kbの欠失が見られた。同一の検体で2回の解析を繰り返した試験では非常に良好な再現性が認められた。

考察：SNPsアレイのコピー数解析は，染色体構造異常の検出には高精度かつ正確な手法であることが明らかとなり，従来の染色体分析を補完する有用な検査法として利用価値は高いと結論した。

キーワード：　染色体異常，一塩基多型，コピー数多型，先天性多発奇形・精神発達遅滞，DNAマイクロアレイ

緒　　言

染色体異常は腫瘍や発達異常の主要マーカーのひとつで(1)，染色体分析はこれらの疾患の診断に広く利用されている。染色体異常は21トリソミーなどの「数的異常」と5p-症候群（猫泣き症候群）に代表される染色体の一部領域の欠失・重複の「構造異常」に大別される。構造異常の検出にはG-分染法が利用されている。G-分染法では染色体の長さによって縞模様の数が変わり，解像度も異なる。国際規約に基づくヒト細胞遺伝学的命名法（International System of human Cytogenetic Nomenclature 2005, ISCN2005）は長さに応じて分解精度を定義している。縞模様の総数により300から850本までの5段階の精度が定められている(2)。しかしながら，最高精度の850本レベルでも解像度は5Mb～10Mbレベルで，きわめて微細な構造解析には不十分である。

多発先天奇形・精神発達遅滞（以下Multiple congenital anomaly/Mental retardation MCA/MRと略す）は染色体の構造異常が原因と推定されるが，G-分染法で検出される割合はわずかに5%程度にすぎない(3)。蛍光標識したプローブで染色体末端部近傍のサブテロメア領域を検出するfluorescence in situ hybridization (FISH)法が開発され(4-6)，この領域の微細な相互転座（Cryptic Reciprocal Translocation）の検出が可能となったことから，MCA/MR患者の検出割合は，5～10%に向上した(7-9)。さらに，個々の染色体を染め分けるMultiplex-FISH法（M-FISH法）やSpectral Karyotyping法（SKY法）が開発され(9,10)，染色体異常部位の検出が可能となったが，M-FISH法とSKY法の解像度は，それぞれ3Mb，1.5Mb程度と低く，未だ不十分である(10-14)。

KallioniemiらはComparative Genomic Hybridization (CGH)法を開発し，ゲノムDNAの過剰，欠失，増幅などの染色体コピー数の変化を全染色体領域で検出することが可能となり(15)，腫

[1)]金沢医科大学総合医学研究所人類遺伝学研究部門臨床遺伝学
[2)]金沢医科大学総合医学研究所共同利用部門
石川県河北郡内灘町大学1-1
平成20年4月9日受理

瘍特異的な新規癌関連遺伝子の同定に利用された。しかしながら，解像度は増幅領域で2Mb，欠失領域で10Mb程度と未だ不十分であった (16)。

近年，標識した検体のゲノムDNAを，基板上の微小な区画上に植え込まれた1本鎖DNAに対して，ハイブリダイズさせて定量化するDNAマイクロアレイ法が開発され(17)，染色体のコピー数異常の検出に利用されるようになった(18)。これをCGH法に応用し，Pinkelらは腫瘍細胞における癌遺伝子や癌抑制遺伝子のコピー数変化の検出に成功した (19)。その後，プローブをcDNAからBacteria Artificial Chromosome (BAC)クローン(20)，Oligonucleotideに変更する改良 (21,22)，Single Nucleotide Polymorphisms(一塩基多型，SNPs) を検出するSNPsジェノタイピングアレイ (以下SNPsアレイと略す) などが開発されてきた (23,24)。SNPsアレイの開発後ただちに，染色体コピー数の検出ができる解析ソフトウエアが提供され，この結果，腫瘍組織やMCA/MRの染色体コピー数変動を検出できるようになった (1,25-28)。また，健常者にも認められるDNAの数kbから数Mbにおよぶ塩基配列領域の変動は，Copy Number Variants (CNV) と呼ばれるようになった (29,30)。32,447個のBACクローンを配置したCGHアレイでは230kbの重複が検出され (28)，Affymetrix社のSNPsアレイを用いた解析では178kb程度の小さな欠失が検出されるようになり，DNAアレイの解像度は飛躍的に改善された (1)。しかしながら，SNPsアレイによるコピー数解析ではコピー数の変動は判別できても，相互転座や逆位などのゲノムに過不足ない構造異常は検出できないという弱点がある。本研究では，MCA/MRの染色体構造異常の検出を目的に，G-分染法とコピー数変動の検出に高解像度解析が期待されるSNPsアレイ法を併用して，解析をおこなった。

対象および方法

対象

充分な説明の後に同意を得た健常者5名 (成人男性3名，女性2名)，また代諾者の同意を得たMCA/MR 患者8名の末梢血リンパ球を解析に用いた。なお，本研究は金沢医科大学遺伝子解析に関する生命倫理委員会の承認を得て行われた。

G-分染法

スライドガラス上に展開した染色体標本は，60℃で2時間孵置した後，60℃に加温した2×SSCに30分間浸漬し，洗浄乾燥後，0.5%トリプシン溶液に10秒間浸漬，洗浄乾燥した後，5%ギムザ氏液で10分間染色して各染色体にGバンドを描出した。

DNAの抽出

末梢静脈血をEDTA2Na入りの真空採血管 (テルモ) で5ml採血し，Quick Gene DNA whole blood kit (フジフィルム)を用いてゲノムDNAを調製した。DNA濃度の測定にはGeneQuant II (ファルマシア　バイオテック) 吸光度計を使用した。以上の方法で抽出したゲノムDNAは0.8%アガロースゲル中で電気泳動を行い，分解が起きていないことを確認した。

SNPsアレイによる解析

本研究で使用したSNPsアレイはAffymetrix 社製 GeneChip Human Mapping Array Kit Sty 250K である。250ngのゲノムDNAを出発材料とし，はじめに制限酵素*Sty I*でゲノムDNAを消化した。PCRプライマー配列を含むアダプターDNAを消化済みのDNA断片両端に付加し，1種類のプライマーでPCRを行えるようにした。PCRにはClonetech TITANIUM Taq DNA Polymerase (タカラバイオ(株)) を用い，200～1100bp程度のPCR産物を調製した。これを精製後，DNase Ⅰ処理によって約200bpまで断片化した。このDNA断片の末端をビオチンで標識しハイブリダイゼーション用のサンプルとした。49℃で16～18時間プローブへのハイブリダイゼーションを行った後，GeneChip Fluidics Station 450によりアレイの洗浄・染色を行ない，次いでGeneChip Scanner 7Gを用いてアレイのスキャニングを行った。

コピー数の解析

スキャン後はGeneChip Operating Software (GCOS，バージョン1.0，)によって画像の取得と定量化を行った。さらにジェノタイピング解析にはGeneChip Genotyping Analysis Software (GTYPE，バージョン4.1) を用いた。コピー数の解析にはChromosome Copy Number Analysis Tool (CNAT，バージョン4.0) を用いた。Integrated Genome Browser (IGB，バージョン5.0) は異常コピー数領域を拡大表示することが可能で，ヒトゲノム計画で得られた情報からその位置の塩基配列と近傍に座位する遺伝子を表示することができるので，コピー数解析に適用した。

国際HapMapプロジェクトで収集された日本人と中国人のデータの中から30名分のCNATを用いて得られたコピー数解析結果をリファレンスとして用い(31,32)，今回得られた各SNPsプローブにおける蛍光強度とリファレンスの蛍光強度の比を，2を底とする対数で求め，$\log_2$Ratioとして表示した。さらに変動部位をまとめて認識し易くするために，S/N比を低くする補正を加えて各プローブにおけるコピー数を決定し，CNStateとして表示した。コピー数が変化した領域は，IGBソフトによって，塩基配列とその領域に座位する遺伝子を表示した。実験の再現性を確認するために，健常者群から1例，MCA/MR群から2例を選択し，同じゲノムDNAサンプルを用いてコピー数解析を2回繰り返した。

結　　果

G-分染法による染色体分析

正常群5例において異常は検出されなかった。MCA/MR 患者8名のうち5例について，G-分染法による染色体分析の結果を表1にまとめた。患者群のうち残り3例は，臨床症状から染色体異常が示唆されたが，G-分染法では異常が見られなかった。なお，G-分染法による染色体検査は400本レベルで解析を行った。

健常者群におけるSNPsアレイ解析

健常者群5例におけるCNATによるコピー数解析結果を図1に示した。本アレイはY染色体を除く1番染色体からX染色体までを，約25万個のSNPs検出プローブで網羅しており，図1は健常者5名分の1番染色体からX染色体までのコピー数変動を$\log_2$Ratioで表示したものである。0.00のラインは2コピーを，0.50は3コピー，−0.50は1コピー分の配列の存在を示唆している。各染色体の動原体付近の繰返し配列領域では，SNPsの頻度が非常に低いためプローブ設定が困難であり，データ取得ができなかった。特に1番，9番，16番染色体の動原体付近では，広い領域で空白になっている。また，13番，14番，15番，21番，22番の各染色体は端部動原体染色体の短腕領域においても，繰返し配列領域のため，SNPsに対するプローブが設定できず，データが抜けたようになっている。またX染色体での$\log_2$Ratio値は，男性においておよそ1コピー，女性において2コピー程度であり，X染色体数の男女差を反映するとともに，コピー数解析の定量性を示している。このような解析条件下で様々なピークが散在しており，コピー数の変動が予想された。また個人特有のピークが観察される一方で，全ての健常人サンプルに共通するピークも認められた。

G-分染法で染色体構造異常が検出されたMCA/MR患者群5例での解析

図2に，症例番号3-001のG-分染法による4番染色体の部分核型と4番染色体のCNATによるコピー数解析結果を示した。コピー数解析結果の上段に$\log_2$Ratio表示，中段にコピー数のCNState表示，下段にG-分染法によるバンド位置が表示されている。CNState表示は2コピーからはずれたコピー数がバーで表示されており，3.00は3コピー，1.00は1コピー分のゲノム配列が検出されていることを示す。コピー数の異常が検出された部位を点線で四角く囲って示した。G-分染法で4番染色体短腕の重複が認められ，その重複領域は4p12→4pterとされたが，SNPsアレイによるコピー数解析でも4p12から4pterの領域が3コピーになっていることが明瞭に示された。

症例番号3-002のG-分染法による1番染色体部分核型と，CNATによる1番，18番染色体のコピー数解析結果を図3に示した。G-分染法により，1番染色体長腕1q44と18番染色体18q21を切断点とする相互転座から派生した不均衡型転座であって，1番染色体の片方が派生染色体であると判定した。コピー数解析では，1q44バンドが1コピーに，18q21.31バンドから18qter (18番染色体長腕末端)までが3コピーであることが判明した。SNPsアレイによる解析結果は，G-分染法による染色体分析の結果を再確認するだけでなく，18q21から18q21.31へと，より正確な推定を可能にした。

症例番号3-003のG-分染法による18番染色体の部分核型と，CNATによる18番染色体のコピー数解析結果を図4に示した。G-分染法では18番染色体長腕の同腕染色体と判定した。判定の詳細を図5に示したが，短腕部分が欠失し，長腕部分が重複して短腕の欠失部位と入れ替わった構造であると判断された。G-分染法による判定が正しければ，SNPsによるコピー数解析の結果は18番染色体短腕の全てが1コピーとなり長腕の全てが3コピーとなると予想されたが，実際には18番染色体短腕末端の18p11.32バンドが1コピー，18q12.3→18qterの領域が3コピーとなっていた。この結果は，最初のG-分染法の判定に何らかの誤りがあることを強く示唆している。両者の解析結果を共に満足させる判定は，図6に示したような複雑な逆位重複 (inverted duplication)であると考えられた。つまり，18番染色体短腕末端の18p11.2バンドが欠失し，18q12.3→18qterまでが重複し，欠失した18p11.2バンドのかわりに短腕側に付加したものと推定された。

表1．染色体構造異常の概要

症例番号	染色体核型	核型の説明
3-001	mos 46, XX, dup (4) (p12pter) [56]/46, XX[4]	60細胞中，4p12→4pter 領域が重複した細胞が56細胞，正常細胞が4細胞のモザイク
3-002	46, XX, der(1)t(1;18) (q44;q21)	1q44と18q21を切断点とする相互転座から派生した不均衡型転座
3-003	46, XY, i(q10)	18番染色体長腕同士による同腕染色体
3-004	46, XX, der(14)t(14;15) (p11.2;q24)	14p11.2と15q24を切断点とする相互転座から派生した不均衡型転座
5-001	46, XY, der(12)t(10:12) (q25;p13.3)	10q25と12p13.3を切断点とする相互転座から派生した不均衡型転座

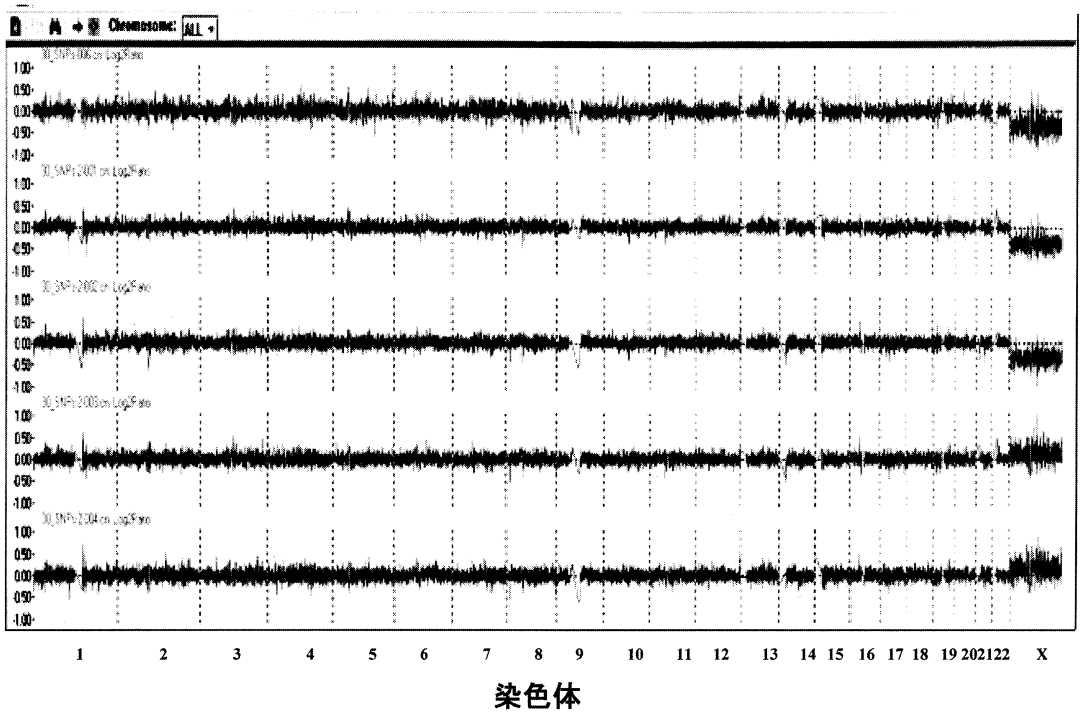

図1. 健常者群5例のコピー数解析結果

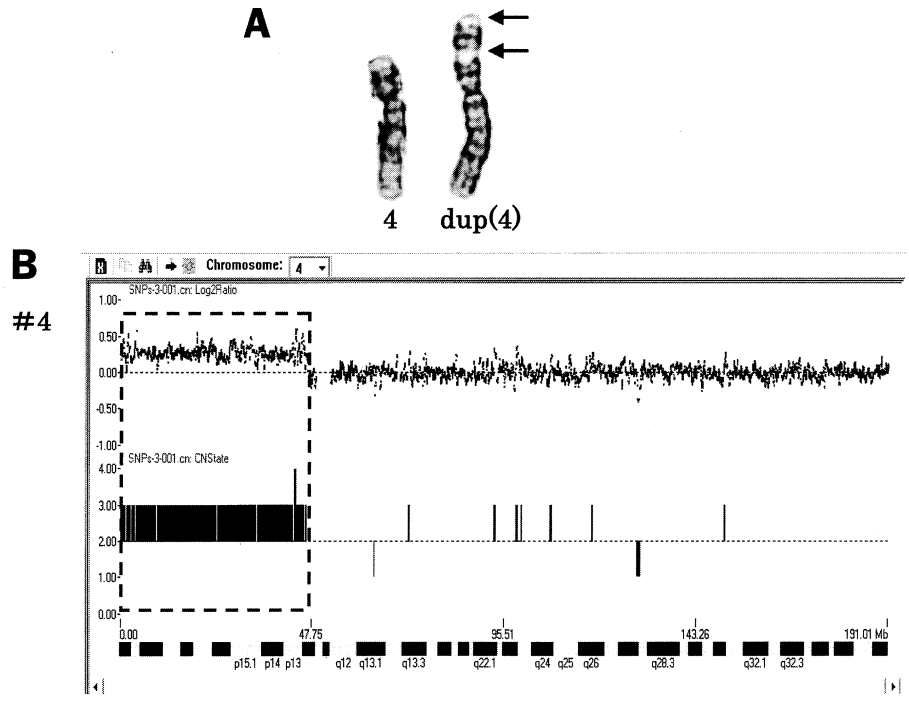

図2. 症例番号3－001の4番染色体の部分核型とコピー数解析結果
A：4番染色体部分核型　←の領域が重複領域
B：4番染色体のコピー数解析結果

4

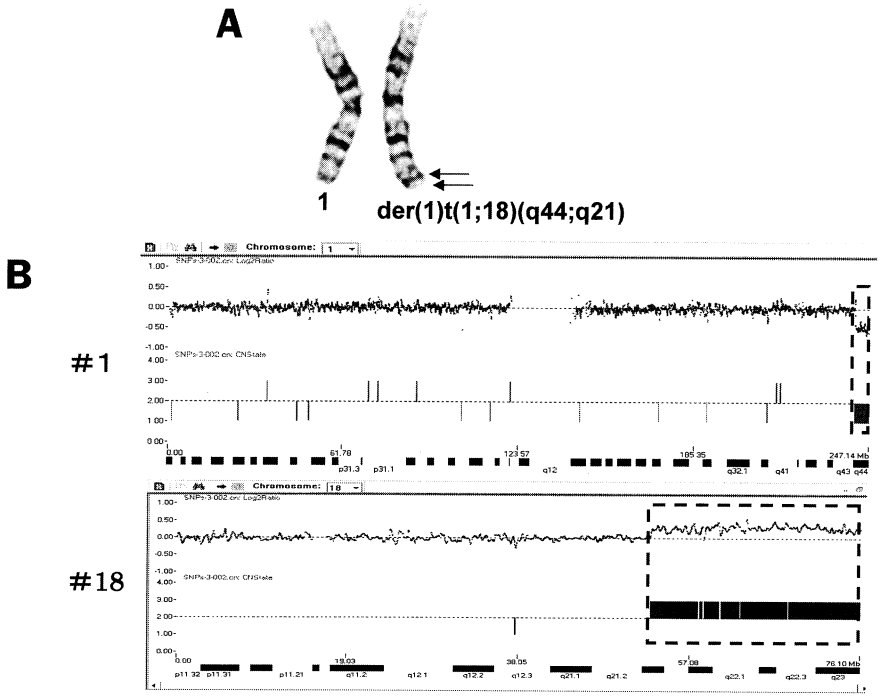

図3．症例番号3－002の1番染色体部分核型と1番染色体と18染色体コピー数解析結果
A：1番染色体の部分核型　←の領域が18q21.1→18qter
B：1番染色体と18番染色体のコピー数解析結果

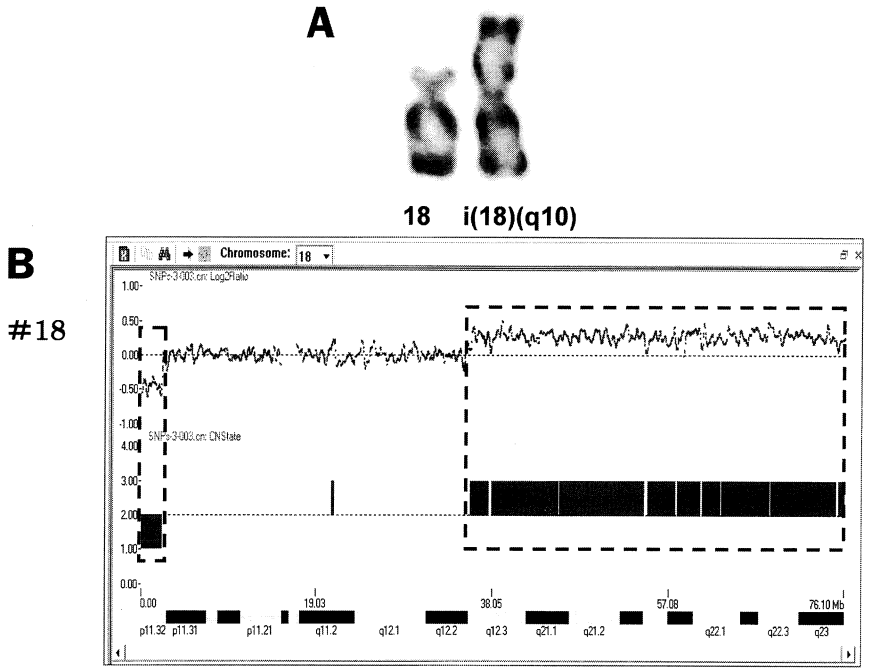

図4．症例番号3－003の18番染色体の部分核型とコピー数解析結果
A：18番染色体部分核型
B：18染色体のコピー数解析結果

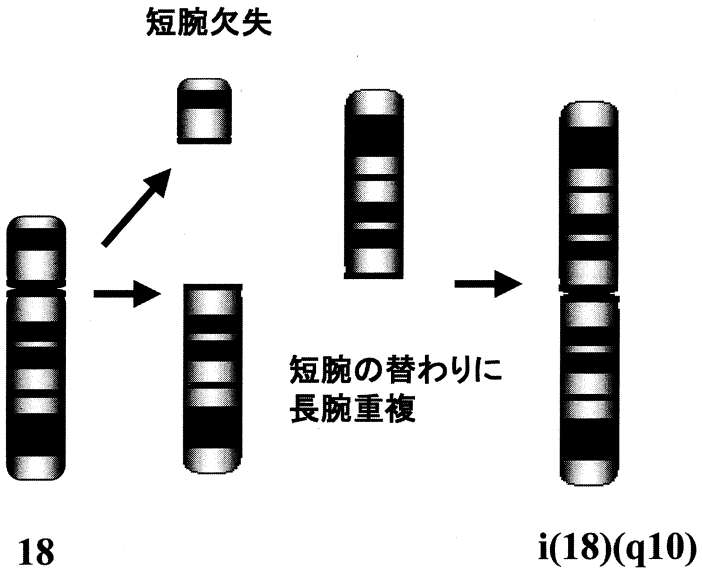

図5. 症例番号3－003の18番染色体長腕同腕染色体の形成

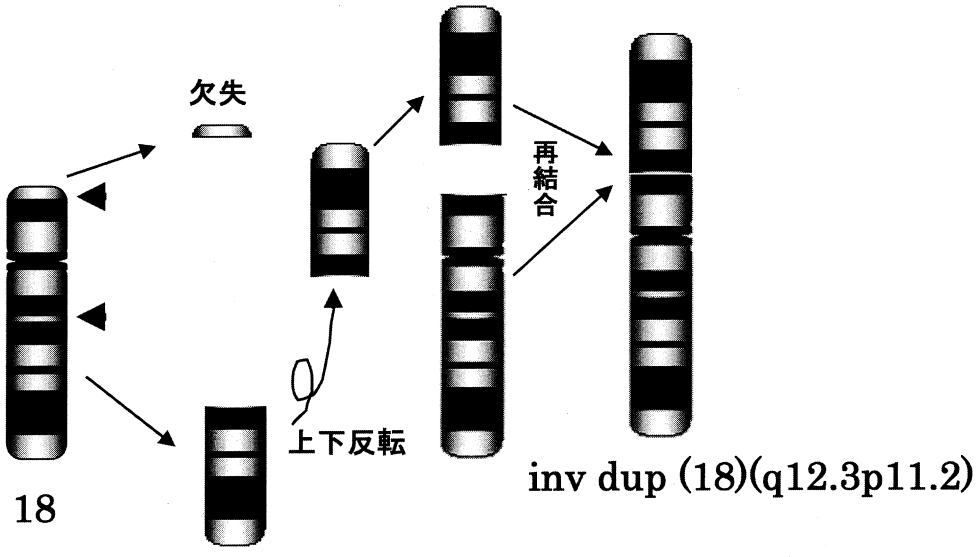

図6. 症例番号3－003の18番染色体逆位重複の形成

6

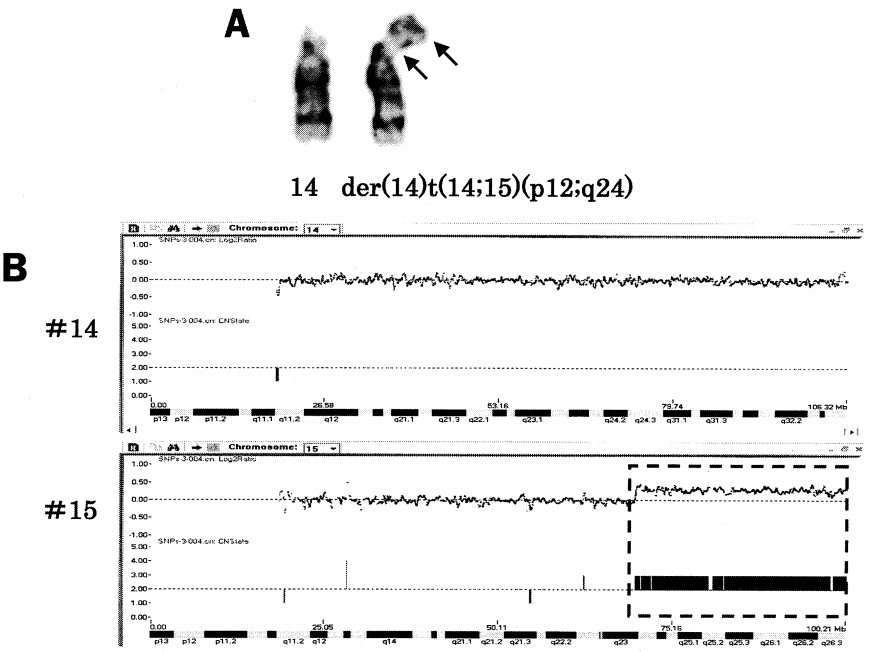

図7. 症例番号3－004の14番染色体部分核型と14番と15番染色体のコピー数解析結果
A：14番染色体の部分核型 ←の領域が15q24→15qter
B：14番染色体と15番染色体のコピー数解析結果

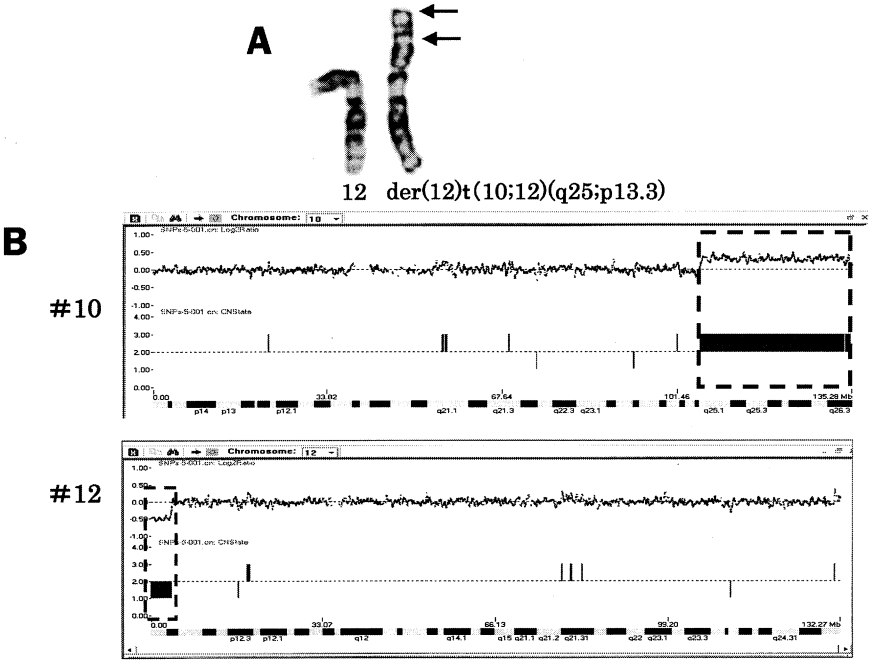

図8. 症例番号5-001の10番と12番染色体のコピー数解析結果
A：12番染色体の部分核型 ←の領域が10q25→10qter
B：10番染色体と12番染色体のコピー数解析結果

症例番号3-004のG-分染法による14番染色体の部分核型と，CNATによる14番，15番染色体のコピー数解析結果を図7に示した。G-分染法により，14p11.2と15q24を切断点とする相互転座から派生した不均衡型転座であって，14番染色体の片方が派生染色体であると判定した。前述のように，14番，15番染色体とも端部動原体染色体であるので，短腕領域は繰返し配列のためSNPsがなく，データの空白領域になっていた。15番染色体長腕15q24から15qterまでの領域がG-分染法の結果と一致して3コピーが存在した。

症例番号5-001のG-分染法による12番染色体と，CNATによる10番，12番染色体のコピー数解析結果を図8に示す。G-分染法による染色体分析では，10q25と12p13.3を切断点とする相互転座から派生した不均衡型転座であって，12番染色体の片方が派生染色体であると判定した。SNPsアレイによるコピー数解析は10q25.1から10qterまでの領域が3コピー分の存在比を示し，12p13.2バンドの中間部から12pterまでの領域が1コピーまで減少していた。この結果は，G-分染法とほぼ一致した結果であった。

G-分染法で染色体異常を検出されなかったMCA/MR群3例の解析

G-分染法によって染色体異常が検出されなかったMCA/MR患者の症例は3例あったが，SNPsアレイによるコピー数解析では，1例に病因となる可能性があるコピー数変化が見られた。症例番号5-003のCNATによるコピー数解析結果を図9に示したが，1番染色体長腕1q21.1バンド内に欠失を示唆する明瞭なピークが認められた。その欠失はIGBによって約400kbで，その領域におけるゲノム配列と遺伝子情報から*ZNF36*など複数の遺伝子の欠失が推定された。

MCA/MR群8例に共通に認められたコピー数変化

MCA/MR群8例と健常群5例の7番染色体のコピー数解析結果を図10に示した。MCA/MR群全例に，健常者群には全く認められなかった微細な欠失を示唆するピークが7番染色体長腕7q11.23バンド内に認められた。その欠失はIGBによって約300kbで，その領域におけるゲノム配列と遺伝子情報から*GTF2IRD2*など複数の遺伝子の欠失が推定された。

再現性確認試験

再現性を確認するために健常者群から1例，MCA/MR患者群から2例選択した計3例で独立したコピー数解析を2回行い，結果を比較したところ良好な再現性が認められた。代表例として症例番号5-003の18番染色体のコピー数解析結果を図11に示す。解析ごとに一定の範囲でばらつきは見られたが，切断点は再現性良く検出されており客観的かつ正確に1あるいは3コピー領域を同定できることが示された。

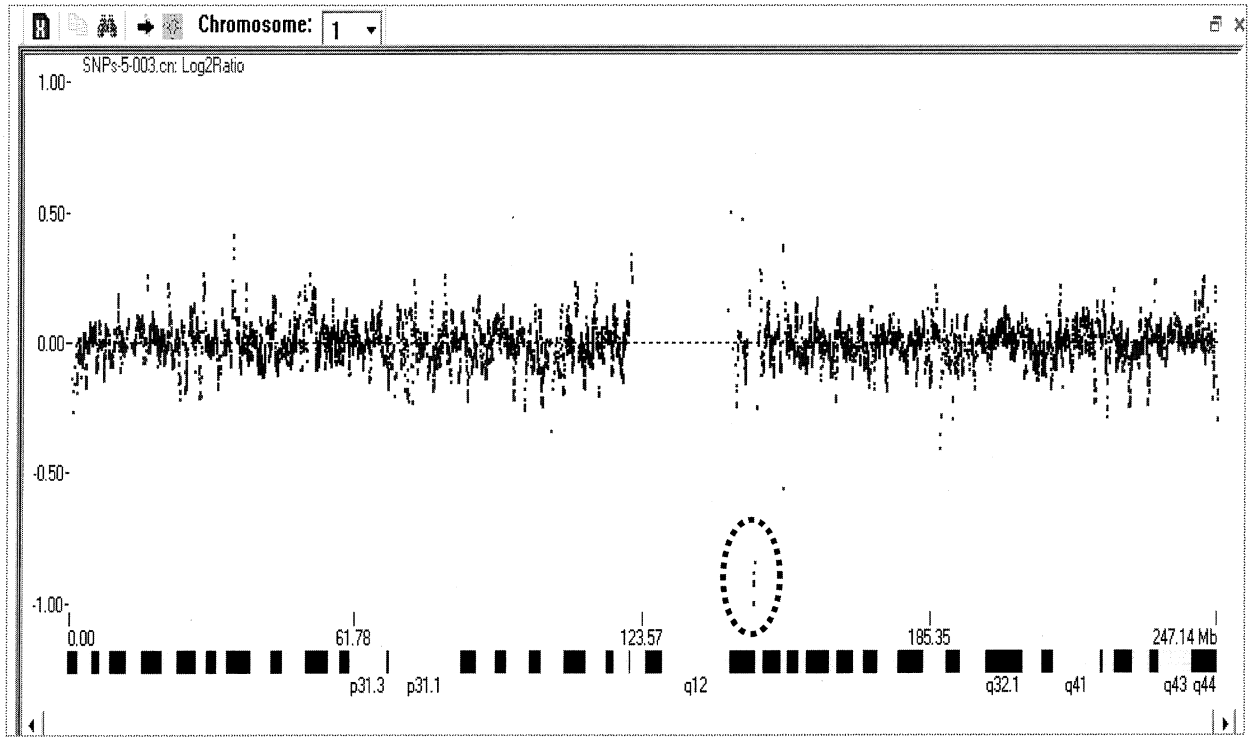

図9．症例番号5－003の1番染色体のコピー数解析結果

SNPsジェノタイピングアレイによる超微細染色体構造異常の検出

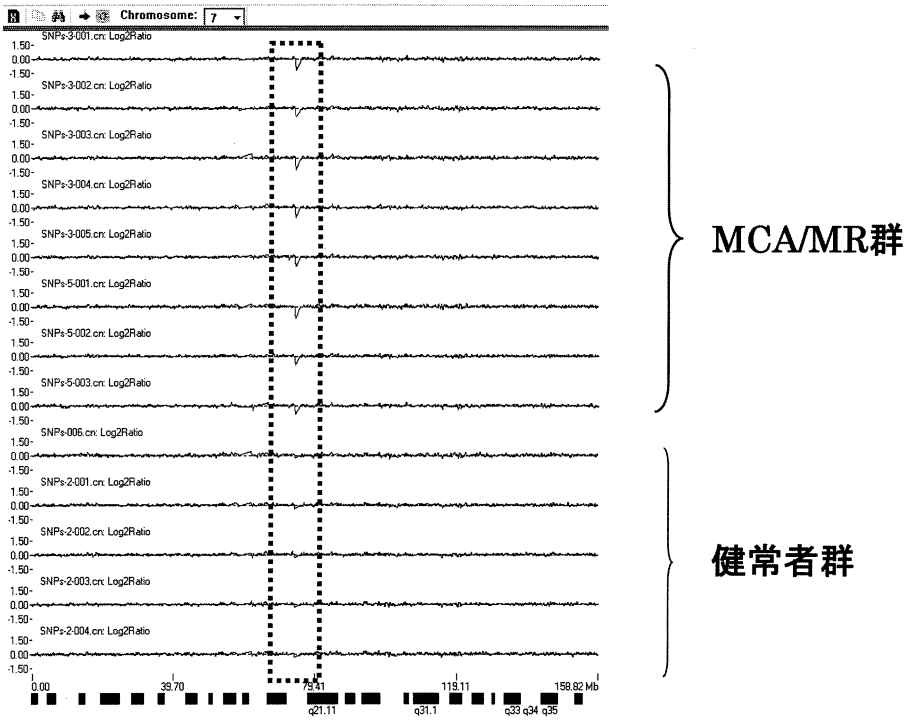

図10．MCA/MR群8例と健常者群5例の7番染色体のコピー数解析結果

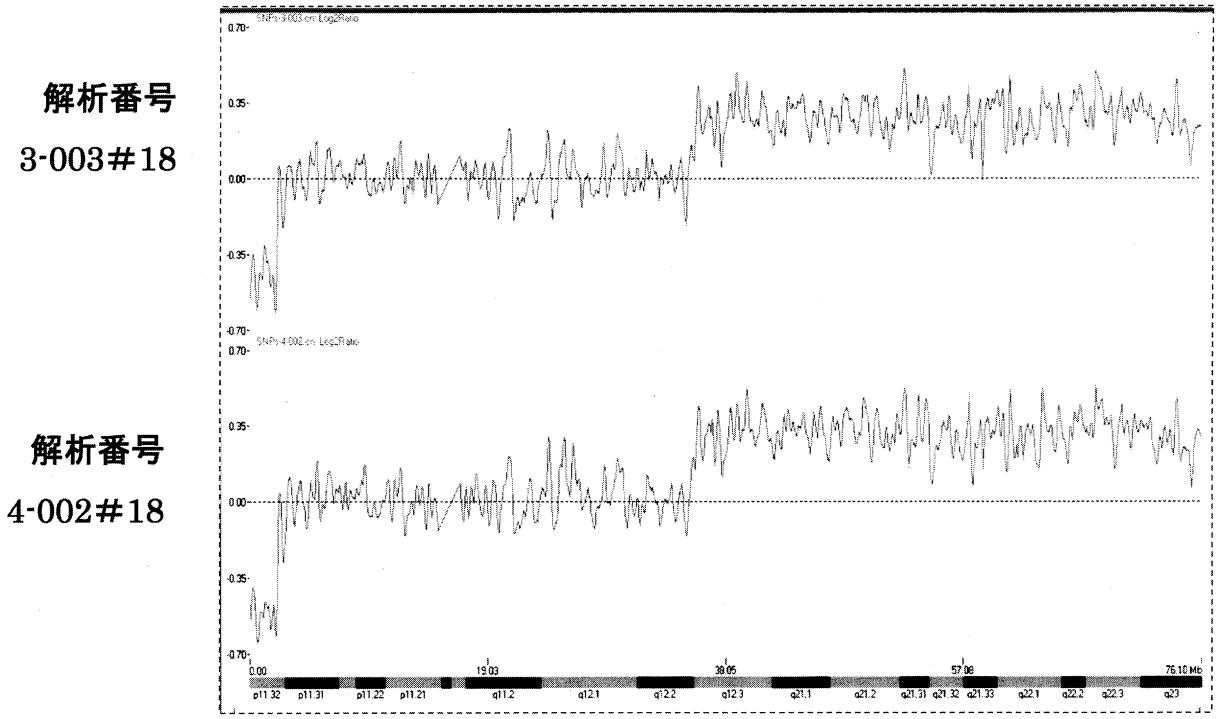

図11．再現性確認試験 症例5－003の18番染色体の独立した2回のコピー数解析結果

9

考　　察

本研究では，健常者，既知染色体構造異常患者，原因不明のMCA/MR患者を対象に，G-分染法とAffymetrix Mapping 250Kアレイを用いたSNPsアレイ解析を行った。後者のSNPsアレイ解析はG-分染法やFISH法などによる形態学的な観察では検出できないsubmicroscopicな微細な構造異常を全染色体領域で解析できる点が特徴である。マイクロアレイ解析法はAffymetrix社以外に，Illumina社，NimbleGen社，Agilent Technology社などから同様の解析法が提供されているが，DNAアレイは網羅的遺伝子発現解析用RNAアレイに比較すると低いコストで解析できる。今回の研究では，1検体あたり2～3万円のコストであった。

網羅的発現解析ではRNAを使用するため，従来から発現の変動や誤差が非常に大きいことが知られている.一方，SNPsアレイはサンプリングや解析条件に左右されないため再現性良い結果が本研究では得られた。マイクロアレイ解析では膨大なデータが得られるが，異常と正常のデータとの弁別はクリティカルである。本研究ではリファレンスデータとして中国人と日本人30例を使用し，健常者と既知染色体構造異常患者を明確に，再現性良く弁別できたことから，現在のところこのリファレンスデータを利用することは日本人の染色体構造異常解析に有用と考えられる。

SNPsアレイ解析は，G-分染法よりも，客観性と感度において優れていると考えられる。しかしながら，この解析法はコピー数異常が存在する位置情報は検出できない。したがって，位置情報を検出できるG-分染法を組み合わせる必要がある(33)。症例3-003でSNPsアレイによって発見された18q12.3→18qterまでが重複し，欠失した18p11.2バンドのかわりに短腕側に付加して発見された複雑な逆位重複は，G-分染法では18番染色体長腕の同腕染色体であると判定された。これは，SNPsアレイが高解像度であるという傍証となる。

原因不明のMCA/MRの症例で染色体分析を行う目的のひとつは，症例の臨床像である表現型と構造異常領域に座位する複数の遺伝子との関連性を調べ，その疾患の原因遺伝子を特定する点であった。SNPsアレイによるコピー数解析では，多くのCNVがゲノム全域に検出されてくる。このCNVの中から病気の原因となるpathogenicなCNVを選択するにはいくつかの工夫が必要となる。CNVは遺伝子のコピー数の変動といわれているが，実際は複数の遺伝子を含む数kbから数Mbの領域のコピー数が増減しているので，コピー数変動領域 (Copy Number Variation Regions: CNVRs) とも呼ばれ，これまでに1447個のCNVRsが報告されている (30)。MCA/MR患者群で検出された複数のCNVが健常者でも検出されたCNVであるならば，それらは病気とは直接的に関係のない良性なCNVと判断することができる。また，患者で検出されたCNV情報 (CNVのフィジカルマップの位置，染色体番号，G-分染法によるバンド名，欠失，重複など) をトロント大学が公開している公共データベース「Data of Genome Variants」(http // project tcag ca / variation) に登録されているCNVと照合することによっても，検出されたCNVの病原性を評価できる (34)。更に，両親のコピー数解析によって，両親のどちらかにみられるCNVは良性であり，両親には認められないCNVは病因となる可能性が高いと判断できる (35)。本研究では健常者を5名解析し，様々なCNVが検出された。個人特有のピークが観察される一方で，全ての健常人サンプルに一見共通するピークも認められた。このようなピークは解析の誤差によるものと，病的ではない良性のCNVである可能性が考えられる。全員に共通して検出されるピークは，リファレンスに使用した日本人および中国人30名分のデータの偏りによるものか良性のCNVかは，症例数を蓄積して解析する必要がある。

症例5-003の1q21.1バンド内に認められた約400kbの欠失は，FISH法や定量的PCR法で確認する必要がある(35)。この欠失が両親になければ，*de novo*な欠失で，病因となるCNVの可能性が高いと判断できる。IGBでは，1q21.1バンド内欠失領域に座位する数個の遺伝子の存在を確認している。この領域のCNVは先天性心疾患に関係するとの報告がある (36,37)。本症例との関連を検討する必要がある。健常人５例には検出されず，患者群8例にのみ共通に認められた7q11.23バンド内の約300kbの欠失についても，同様に確認する試験が必要となる。この場合，欠失領域の一部が奇形と精神発達を特徴とするWilliams-Beuren症候群の欠失領域と重なっているため，今後この欠失領域がいかなる機能を有しているかを解明する必要がある。

MCA/MRの症例では，従来，表現型が共通する症候群を確立し，その症例に共通する遺伝子型(遺伝子変異)を見つけることが主流であった。一方，SNPsアレイによるコピー数解析では，病因となるCNVを共に持つ症例に対して，逆に共通する表現型を見つけることによって，新たな症候群を発見することができる。17q21.31欠失症候群 (38,39) や12q14欠失症候群 (40) はこのような解析の成功例で，逆行異形学 (Reverse Dysmorphology) と呼ばれ，新しい疾患診断法として受け入れられつつある。

本研究では，SNPsアレイによる網羅的なコピー数解析法が，G-分染法を補完し，染色体構造異常の診断に有用であることを示した。この検査法によって，病因が明らかとなるMCA/MR症例の増加が予想される。しかしながら，このコピー数解析によっても病因が見つからない症例があることは事実である。特に症例数が少ない疾患では，SNPsアレイによるコピー数解析に加え，プロテオームやメタボローム解析法などを取り入れて，病因を総合的に判断していく必要がある。

本研究は，金沢医科大学奨励研究 (S2006-2) からの助成を受けました。

文　　献

1. Friedman TM, Agne Buross: Oligonucleotide microarray analysis of genomic imbalance in children with MR. AM J Hum Genet 2006; **79:** 500-13.
2. ISCN committee: Idiograms of G-banding for normal human chromosomes.

An international system for human cytogenetic nomenclature (2005) New York, Karger, 2005, 16-33.
3. de Varies BB, Dfundt R, Leisnk M et al: Diagnosis genome profiling mental retardation. Am J Hum Genet 2005; **77:** 606-16.
4. Kuwand A, Ledbteller SA, Dobyns WB et al: Detection of deletions and cryptic translocations in Miller-Dieker syndrome by in situ hybridization. Am J Hum Genet 1991; **49:** 707-14.
5. Alardo M, Bass HN, Coldwell S et al: Miller-Dieker syndrome. Detection of cryptic chromosome translocation using in situ hybridization in a family with multiple affected offsprings. Am J Dis Child 1993; **147:** 129-34.
6. Jauch A, Robsow L, Smith A: Investigations with fluorescence in situ hybridization (FISH) demonstrate loss of the telomeres on reciprocal chromosome in three unbalance translocations involving chromosome 15 in the Prader-Willli and Angelman syndromes. Hum Genet 1995; **96:** 345-9.
7. Ravan RB, Tepperberg JH, Papenhausen P et al: Subtelomere FISH analysis of 11688 cases: an evaluation of the frequency and pattern of subtelomere rearrangements in individuals with developmental disabilities. J Med Genet 2006; **43:** 478-89.
8. Walter S, Sandig K, Hinkel GK et al: Subtelomere FISH in 50 children with mental retardation and minor anomalies, identified by a checklist, detects 10 rearrangements including a de novo balanced translocation of chromosome 17p13.3 and 20q13.33. Am J Med Genet 2004; **128:** 364-73.
9. Bocian E, Heias-Rodzewicz Z, Suchenek K et al: Subtelomeric rearrangements: results from FISH studies in 84 families with idiopathic mental retardation. Med Sci Monit 2004; **20:** 143-51.
10. Speicer MR, Gwyn Bullard S, Ward DC: Karyotyping human chromosome by combinational multi-fluor FISH. Nat Genet 1996; **12:** 368-75.
11. Schrock F, du Manoir S, Veldman et al: Multicolor spectral karyotyping of human chromosomes. Science 1996; **26:** 494-7.
12. Uhrig S, Schuttenhauer S, Fauch C et al: Multiplex-FISH for pre and postnatal diagnosis applications. Am J Hum Genet 1999; **65:** 448-62.
13. Azoferia J, Fauth C, Kraus J et al: An optimized probe set for the detection of small interchromosomal aberration by use of 24 color FISH. Am J Hum Genetics 2000; **66:** 1684-88.
14. Haddad Br, Schorock E, Meck J et al: Identification of de novo chromosomal markers and derivatives by spectral karyotyping. Hum Genet 1998; **103:** 619-25.
15. Kallioniemi A, Kallioniemi O-P, Sudar D et al: Comparative genomic hybridization for molecular cytogenetic analysis of solid tumors. Science 1992; **258:** 818-21.
16. Houldsworth J, Chaganti RS Comparative genomic hybridization: An overview. Am J Pathol: 1994; **145:** 1253-60.
17. Schena M, Shalon D, Davis RW et al: Quantitative monitoring gene expression patterns with a complementary DNA microarray. Science 1995; **270:** 467-70, 371.
18. Solinas-Toldo S, Lampel S, Stilgenbauer S et al: Matrix-based comparative genomic hybridization: biochips to screen for genomic imbalances. Genes Chromosomes Cancer 1997; **20:** 207-11.
19. Pinkel D, Segraves R, Sudar D et al: High resolution analysis of DNA copy number variation using comparative genomic hybridization to microarrays. Nature Genet 1998; **20:** 207-11
20. Ishkanian S, Malloff CA, Watson SK et al: A tilling resolution DNA microarray with complete coverage of the human genome. Nat Genet 2004; **36:** 299-303.
21. Tyson C, Harrad C, Locker R et al: Submicroscopic deletions and duplications in individuals with intellectual disability deleted by array-CGH. Am J Med Genet 2005; **139:** 173-85.
22. Toruner GA, Streck DL, Schwalb MN et al: An oligonucleotide based array-CGH system for deletion of genome wide copy number changes including subtelomeric regions for genetic evaluation of mental retardation. Am J Med Genet 2007; **143:** 824-9
23. Fan JB, Chen X, Halushka MK et al: Parallel genotyping of human SNPs using high-density oligonucleotide tag assay. Genome Res 2000; **10:** 853-60.
24. Cutler DJ, Zwick ME, Carrasquillo MM et al: High-throughput variation detection and genotyping using microarrays. Genome Res 2001; **11:** 1913-25.
25. Howard RS, Dione KB, Hua R et al: High-resolution identification of chromosomal abnormalities using oligonucleotide arrays containing 116,204 SNPs. Am J Hum Genet 2005; **77:** 709-26.
26. Hoyer J, Dreweke A, Becker C et al: Molecular karyotyping in patients with mental retardation using 100K SNP array. J Med Genet 2007; **44:** 629-36.
27. Vissers L, de Vries B, Osoegawa K et al: Array-based comparative genomic hybridization for the genomewide detection of submicroscopic chromosome abnormalities. AM J Hum Genet 2003; **73:** 1261-70.
28. de Vries B, Pundt R, Leisink M et al: Diagnosis genome profiling mental retardation. Am J Hum Genet 2005; **77:** 606-15.
29. Iafrate AJ, Feuk L, Rivera MN et al: Detection large-scale variation in the human genome. Nat Genet 2004; **36:** 949-51.
30. Sebat J, Lakshmi B, Troge J et al: Large-scale copy number polymorphism in the human genome. Science 2004; **305:** 525-8.
31. Langer S, Geigl JB, Wagenstaller J, Lederer G et al: Delineation of a 2q deletion in a girl with dysmorphic features and epilepsy. Am J Med Genet 2006; **140:** 1354-5.
32. Rendon R, Ishikawa S, Fitch KR et al: Global variation in copy number in the human genome. Nature 2006; **444:** 444-54.
33. Wong K, deLeeuw R, Dosanjh N et al: A comprehensive analysis of copy-number variations in the human genome. Am J Hum Genet 2007; **80:** 91-104.
34. Zahir F, Friedman JM: The impact of array genomic hybridization on mental retardation research: a review of current technologies and clinical utility. Clin Genet 2007; **72:** 271-87.
35. Christiansen J, Dyck JD, Elyas BG et al: Chromosome 1q21.1 contiguous gene deletion is associated with congenital heart disease. Circ Res 2004; **94:** 1429-35.
36. Doggett NA, Xie G, Meincke LJ et al: A 360-kb interchromosomal duplication of the human HYDIN locus. Genomics 2006; **88:** 762-71
37. Sharp AJ, Hansen S, Seltzer RR et al: Discovery of previously unidentified genomic disorders from the duplication architecture of the human genomic. Nat Genet 2006; **38:** 1038-42.
38. Kollen DA, Vissers LE, Pfundt R et al: A new chromosome 17q21.31 microdeletion syndrome associated with a common inversion polymorphism. Nat Gent 2006; **38:** 999-1001.
39. Shaw-Smith C, Pittman AM, Willant L et al: Microdeletion encompassing MART at chromosome 17q21.3 is associated with development delay and learning disability. Nat Genet 2006; **38:** 1032-7.
40. Menten B, Buysse K, Zahir F et al: Osteopolikilosis, short stature and mental retardation as key features of a new microdeletion syndrome on 12q14. J Med Genet 2007; **44:** 264-68.

Comparative study of chromosomal analysis using SNPs genotyping arrays and G-banding in MCA/MR (multiple congenital abnormality / mental retardation) patients

Mamoru Ozaki[1], Yasuhito Ishigaki[2]

[1] *Clinical Genetics, Division of Human Genetics, Medical Research Institute, Kanazawa Medical University, Uchinada, Ishikawa 920-0293, Japan*

[2] *Division of Core Facility, Medical Research Institute, Kanazawa Medical University, Uchinada, Ishikawa 920-0293, Japan*

Chromosomal abnormalities are thought to be the main cause of the MCA/MR (multiple congenital anomaly/mental retardation) syndrome. G (Giemsa)-banding can detect chromosomal aberrations only in 5% of all patients with MCA/MR, and this low frequency appears to be due to the low resolution of chromosomal analysis using G-banding. Recently, CGH (comparative genome hybridization) arrays and SNPs genotyping arrays (single-nucleotide polymorphism genotyping arrays) have been developed and become available for the detection of minute chromosomal aberrations less than 1Mb. In this study, we analyzed 5 healthy subjects and 8 MCA/MR patients using a GeneChip Human Mapping Sty Array kit (Affymetrix) in combination with G-banding analysis. No abnormalities were detected by either G-banding analysis or the SNPs genome copy number analysis of the 5 healthy subjects. Chromosomal abnormalities were detected in the 5 MCA/MR patients by G-banding, and these results were clearly in accordance with those of the copy number analysis using SNPs arrays. SNPs array analysis detected an approximately 400 kb deletion at 1q21.1 in 1 of 3 MCA/MR patients in whom chromosomal abnormalities were not detected by G-banding; further, an approximately 300 kb deletion at 7q11.23 was detected by SNP array analysis in all patients. In addition to these results, copy number analysis using SNP arrays showed excellent signal reproducibility. We concluded that copy number analysis using SNPs arrays effectively complements the detection of chromosomal aberrations by G-banding.

Key Words: Chromosome abnormalities, SNPs (Single nucleotide polymorphisms), Copy number variants, Multiple congenital abnormality / Mental retardation, DNA microarray,

Highlighted paper selected by Editor-in-chief

The Kampo Medicines Orengedokuto, Bofutsushosan and Boiogito Have Different Activities to Regulate Gene Expressions in Differentiated Rat White Adipocytes: Comprehensive Analysis of Genetic Profiles

Jun-ichi YAMAKAWA,[a,e,#] Yasuhito ISHIGAKI,[b,#] Fumihide TAKANO,[*,c] Takashi TAKAHASHI,[a] Junko YOSHIDA,[d] Junji MORIYA,[a] Takanobu TAKATA,[c] Takanori TATSUNO,[c] Kenroh SASAKI,[e] Tomihisa OHTA,[b] Tsutomu TAKEGAMI,[f] and Fumihiko YOSHIZAKI[e]

[a] *Department of General Medicine, Kanazawa Medical University;* [b] *Division of Core Facility of Medical Research Institute, Kanazawa Medical University;* [d] *Department of Pharmacology, Kanazawa Medical University;* [f] *Division of Molecular Oncology and Virology, Medical Research Institute, Kanazawa Medical University; 1–1 Daigaku, Uchinada-machi, Kahoku-gun, Ishikawa 920–0293, Japan:* [c] *Department of Pharmacognosy and Chemistry of Natural Products, Graduate School of Natural Science and Technology, Kanazawa University; Kakuma-machi, Kanazawa 920–1192, Japan: and* [e] *Department of Pharmacognosy, Tohoku Pharmaceutical University; Komatsushima 4–4–1, Aoba-ku, Sendai 981–8558, Japan.* Received February 28, 2008; accepted August 20, 2008; published online August 21, 2008

Three Kampo medicines, Boiogito (BOT), Bofutsushosan (BTS) and Orengedokuto (OGT), used for obese patients were investigated for their effects on adipogenesis in cultured rat white adipocytes. Administration of the three extracts suppressed adipogenesis in concentration-dependent manners (1—100 μg/ml) without any cytotoxicity. Changes in mRNA expression levels were analyzed using a Rat 230 2.0 Affymetrix GeneChip® microarray system. DNA microarray analysis (total probe set: 31099) using cDNAs prepared from adipocytes revealed that BOT, BTS and OGT increased the expression of 133—150 genes and decreased the expression of 42—110 genes by ≥2-fold. We identified 329 downregulated genes and 189 upregulated genes among a total set of 514 probes (overlap: 4). Overall, genes related to cellular movement, cell death, cell growth/differentiation and immune responses were the most downregulated, while those related to lipid metabolism and cell signaling were the most upregulated. Semiquantitative reverse transcriptase-polymerase chain reaction (RT-PCR) assays were conducted to confirm the microarray results. Analysis of the clustering profiles of the microarray results revealed that BOT and BTS changed the expression levels of similar genes mainly involved in small molecule biochemistry and cell differentiation, while OGT altered 10 genes related to lipid metabolism, in contrast to the effects of BOT and BTS. We also measured mRNA expression levels of seven selected genes highly contributing to the lipid metabolism by using semiquantitative RT-PCR assay, that were acetyl-Coenzyme A carboxylase alpha (*ACACA*), AE binding protein 1 (*AEBP1*), patatin-like phospholipase domain containing 8 (*PNPLA8*), secretoglobin (*SCGB1A1*), adrenergic (*ADRB3*), adiponectin (*ADIPOQ*), monoglyceride lipase (*MGLL*). Beta-actin (*ACTB*) gene was used as an endogenous internal standard. The present findings indicate that these three herbal extracts have the potential to prevent adipogenesis in rat white adipocytes through different mechanisms *via* modulation of gene expression levels.

Key words Boiogito; Bofutsushosan; Orengedokuto; adipogenesis; rat white adipocyte; DNA microarray

Metabolic syndrome, wherein patients have both diabetes mellitus and dyslipidemia, is reaching epidemic proportions due to dietary factors and sedentary lifestyles.[1] A major cause of mortality in these patients is atherosclerotic macrovascular diseases, the majority of which result from dyslipidemia associated with insulin-resistant diabetes. Adipose tissues, which were once thought to function primarily as passive depots for storage of excess lipid, are now understood to play crucial roles in metabolic regulation, feeding behavior and secretion of a variety of metabolic hormones.[2,3] Excessive accumulation of adipose cells in obesity contributes to the development of metabolic and cardiovascular diseases, as well as certain cancers.[4,5]

Adipocytes accumulate energy in the form of triacylglycerols, which can be hydrolyzed and released as glycerol plus free fatty acids. When energy intake is dominant, excess lipid storage in white adipose tissues can be established through an increase in the size of mature adipocytes and/or recruitment of preadipocytes. This situation may lead not only to obesity but also to related pathophysiological conditions, such as type 2 diabetes mellitus, since adipose tissues are not only insulin-responsive tissues that convert glucose into fat stores, but also endocrine organs participating in energy balance regulation.[6,7] Adipogenesis has been extensively studied *in vitro* using murine preadipocyte lineages and rat white adipocytes. Adipose conversion from such fibroblastic precursors is divided into at least three steps, namely cell commitment, clonal amplification and phenotype expression.[8] The initial step involves the induction of expression of several adipose-specific genes, whereas later events result in the appearance of the functional characteristics of mature adipocytes, such as increased glucose transport capacity, through the expression of insulin-responsive glucose transporters, which represent a key step in lipogenesis, thereby leading to progressive lipid accumulation. As a key factor for controlling the adipose mass in adipocytes, examination of the inhibitory activities of substances on excess lipid storage in white adipocytes represents a rational strategy for preventing obesity.

Orengedokuto (OGT), Bofutsushosan (BTS) and Boiogito (BOT) are well-known Japanese, Korean and Chinese traditional herbal medicines used to clinically prevent or improve obesity. BTS has been reported to inhibit atherosclerosis,[9] obesity,[10] hypertension[11] and hyperglycemia.[12] However,

* To whom correspondence should be addressed. e-mail: takano@p.kanazawa-u.ac.jp
# These authors contributed equally to this work.

pharmacological evidence for the anti-obesity effects of OGT and BOT remains obscure. Using the well-established experimental model of excess lipid storage in cultured rat white adipocytes, we compared the pharmacological efficacies of OTG, BOT and BTS, and then investigated their effects on the expression levels of target genes responsible for obesity using DNA microarray analyses.

MATERIALS AND METHODS

Kampo Medicines and Test Sample Preparation Spray-dried powders of the herbal Kampo medicines OGT (TJ-15), BOT (TJ-20) and BTS (TJ-62) for clinical use were obtained from Tsumura & Co. (Tokyo, Japan). HPLC analyses of the ingredients of OGT, BOT and BTS were performed by photodiode array (PDA)-HPLC by Tsumura & Co. The PDA-HPLC profiles of the samples are shown in Fig. 1. Test samples were dissolved in phosphate-buffered saline (PBS) and sterilized with a membrane filter (pore size: 0.22 μm). Various concentrations of the test samples were added to cultured rat white adipocytes.

Cell Culture and Test Sample Treatment Rat white preadipocytes (RWPA) isolated from SD rats were purchased from TaKaRa Bio (Tokyo, Japan). RWPA were plated on type I collagen-coated dishes and cultured in serum-free Dulbecco's modified Eagle's medium supplemented with 10 μg/ml insulin at 37 °C in a humidified atmosphere containing 5% CO_2. Differentiation into adipocytes was achieved by incubating subconfluent undifferentiated white adipocytes with 10 μg/ml insulin, 2.5 μM dexamethasone and 0.5 mM 3-isobutyl-1-methylxanthine for 2 d. The medium was then replaced with medium containing 10 μg/ml insulin. All experiments with white adipocytes were performed within two passages. In the second experiment, cells on the seventh day of white adipocyte differentiation were incubated with various concentrations of the test samples or medium as a control.

Measurement of Adipogenesis in Cultured RWPA Intracellular lipid accumulation in RWPA was measured using a commercially available kit (AdipoRed™; Cambrex Bio, Walkersville, MD, U.S.A.) according to the manufacturer's instructions. This kit determined the effects of the test samples on the differentiation of adipocyte precursors based on the accumulation of intracellular triglycerides. Briefly, cell culture plates were washed twice with ice-cold PBS after completion of the experiment, and the cells were stained with AdipoRed reagent containing Nile Red. After 10 min, the fluorescence intensity of each well was measured using a U-3200 fluorophotometer (Hitachi, Tokyo, Japan) with excitation at 485 nm and emission at 538 nm. Intracellular lipid accumulation was calculated and indicated as the relative fluorescence units (RFU).

DNA Microarray Analysis[13] Total RNA was isolated from the cells using a commercially available kit (RNeasy Mini Kit; QIAGEN GmbH, Hilden, Germany). The isolated RNA was quantified by photometry at 260/280 nm, and the quality of the RNA was determined by the ratio of the 18S/28S ribosomal band intensities in an ethidium bromide-containing 1% agarose gel after electrophoresis. Preparation of cRNAs was carried out using a MessageAmp® II-Biotin Enhanced Kit (Ambion, Austin, TX, U.S.A.) and target hybridizations were performed using a Rat 230 2.0 GeneChip® microarray system (Affymetrix, High Wycombe, U.K.) according to the manufacturer's instructions. Double-stranded cDNAs were synthesized from 5 μg of total RNA and hybridized to the Affymetrix GeneChip® array for 16 h at 45 °C in a GeneChip® Hybridization Oven 640. After washing and staining in a GeneChip® Fluidics Station 450, the hybridized cRNAs were detected using a GeneChip® Scanner 3000. The digitalized image data were processed using the GeneChip® Operating Software (GCOS) version 1.4. The amounts of probe-specific transcripts were determined based on the average of the differences between the perfect-match and mismatch intensities. Since replicate assays were not performed, the signal intensities of selected genes that were upregulated or downregulated by at least 2-fold compared to a sham-control group were extracted by the GeneSpring GX software package version 7.3.1 (Agilent Technologies, Santa Clara, CA, U.S.A.). Ingenuity Pathway Analysis (IPA; Ingenuity Systems Inc., Redwood City, CA, U.S.A.) was used as an additional method for evaluating the functional significance of the drug-induced gene profiles. Fisher's exact test was used to calculate p values to determine the probabilities that the biological functions assigned to the different networks could be explained by chance alone.

Semiquantitative Reverse Transcriptase-Polymerase Chain Reaction (RT-PCR) for Gene Expression Semiquantitative RT-PCR analyses were performed by the methods described previously,[14] and PrimeScript one step RT-PCR kit version 2 (Takara Bio Inc., Otsu, Japan) was used. The sequences of the primers are shown in Table 1. First-strand cDNAs were synthesized by 1 cycle of reverse transcription at 50 °C for 30 min and 1 cycle of reverse transcriptase inactivation at 94 °C for 2 min. Second-strand cDNA synthesis and PCR amplification for acetyl-Coenzyme A carboxylase alpha (*ACACA*), AE binding protein 1 (*AEBP1*), patatin-like phospholipase domain containing 8 (*PNPLA8*), secretoglobin (*SCGB1A1*), adrenergic (*ADRB3*), adiponectin (*ADIPOQ*), monoglyceride lipase (*MGLL*) were carried out at 94 °C for 30 s, 53—57 °C for 30 s and 72 °C for 1 min. For each combination of primers, the kinetics of the PCR amplification was determined beforehand and semi-quantitative PCR was performed in the exponential range. The *beta-Actin* (*ACTB*) gene was used as an endogenous internal standard, and amplified with specific primers at the same time. The

Table 1. Primers Usued in Semiquantitative RT-PCR Analyses

Gene	Primer sequences
ACTB	Forward: 5′-CGTGCGTGACATTAAAGAGAAG-3′
	Reverse: 5′-TGGAAGGTGGACAGTGAGG-3′
ACACA	Forward: 5′-CCTCCAACCTCAACCACTAC-3′
	Reverse: 5′-AGCCTGTCATCCTCAATATCG-3′
AEBP1	Forward: 5′-CATCCGCATCTATCCACTAC-3′
	Reverse: 5′-ACCTCATCCTCGTCTTCTCC-3′
PNPLA8	Forward: 5′-AGGTGTGGTTGCTCTTCAG-3′
	Reverse: 5′-CTCGTGTATGTTGTGGTATTCC-3′
SCGB1A1	Forward: 5′-ATCGCCATCACAATCACTG-3′
	Reverse: 5′-AGGTCAAGGAGGGAGAGG-3′
ADRB3	Forward: 5′-GCCTTCCGTCGTCTTCTG-3′
	Reverse: 5′-CATTCTGTGGTCTAGTCATTGG-3′
ADIPOQ	Forward: 5′-CCGTGATGGCAGAGATGG-3′
	Reverse: 5′-TGGTCGTAGGTGAAGAGAAC-3′
MGLL	Forward: 5′-GCGGTGCCATCTCCATCC-3′
	Reverse: 5′-GCTCCTGCCACTGCTATCC-3′

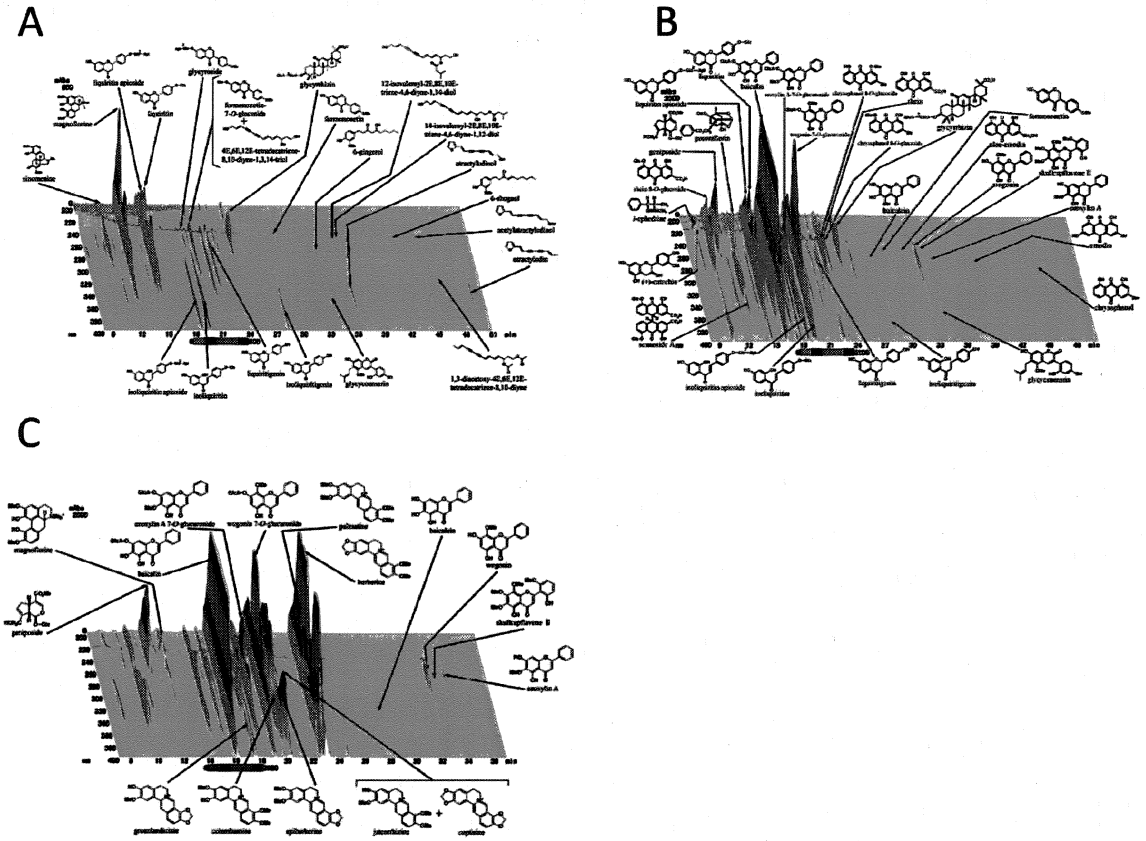

Fig. 1. PDA-HPLC Profiles of Three Kampo Extracts
Panel A: BOT (TJ-20); panel B: BTS (TJ-62); panel C: OGT (TJ-15).

PCR products were electrophoresed in a 1% agarose gel and visualized by ethidium bromide staining under UV-irradiation.

Data Analysis Data were analyzed using statistical analysis methods and graphing software (KaleidaGraph™; Synergy Software, Tokyo, Japan). All data are expressed as the mean±standard deviation (S.D.). The significance of differences among values was determined by Dunnett's multiple test after one-way analysis of variance (ANOVA) in comparison with control cultures, and values of $p<0.05$ were considered to indicate significance. Furthermore, Fisher's exact test was used to calculate a p value to determine the probability that the biological function assigned to each network could be explained by chance alone.

RESULTS

PDA-HPLC Profiles of Kampo Medicines As depicted in Fig. 1, PDA-HPLC analyses revealed broad peaks of chemical constituents for the three Kampo medicines that appeared at various retention times (Figs. 1A—C). UV and LC-MS/MS analyses of reference compounds indicated the presence of the following known active ingredients of BOT, BTS and OGT: isoquinoline alkaloids sinomenine (Fig. 1A) and magnoflorine (Figs. 1A, C) from rhizomes of *Sinomenium acutum* and *Coptis japonica*; triterpene glycosides glycyrrhizin (Figs. 1A, B) and flavone glycoside liquiritin from Glycyrrhiza (Figs. 1A, B); iridoid glucoside geniposide (Figs. 1B, C) from Gardenia Fructus; and flavone derivatives baicalin and wogonin (Figs. 1B, C) from *Scutellaria baicalensis*.

Effects of Kampo Medicines on Adipogenesis in Cultured RWPA We first investigated the *in vitro* effects of BOT, BTS and OGT on adipogenesis in RWPA. Cumulative lipogenesis was detected after 24 h of culture and increased until 48 h (Fig. 2C1). However, no further increase in lipogenesis was observed when the cells were further cultured until 72 h (data not shown). As shown in Fig. 2A, all extracts at a concentration of 100 μg/ml significantly inhibited intracellular lipid accumulation by 55—67% at 24 and 48 h after differentiation of RWPA. These effects were concentration-dependent in the range of 1—100 μg/ml (Fig. 2B). OGT seemed to be more effective than BTS and BOT (Fig. 2C4). Although no data are shown, BOT, BTS and OGT at 10—100 μg/ml, representing sufficient concentrations of Kampo extracts to inhibit adipogenesis, showed no cytotoxicity against RWPA.

Overview of DNA Microarray Analyses of RWPA after Administration of Kampo Medicines At the same biological endpoints after administration of Kampo extracts, various mRNA expression levels were analyzed using a DNA microarray. After treatments with all extracts at 100 μg/ml for 24 h, total RNA extracts were prepared. Whole histograms of the expression profiles resembled one another among the groups, implying that our data sets were comparable. The Affymetrix Rat 230 2.0 microarray consists of 31099 probe sets, but not all of the values were useful for

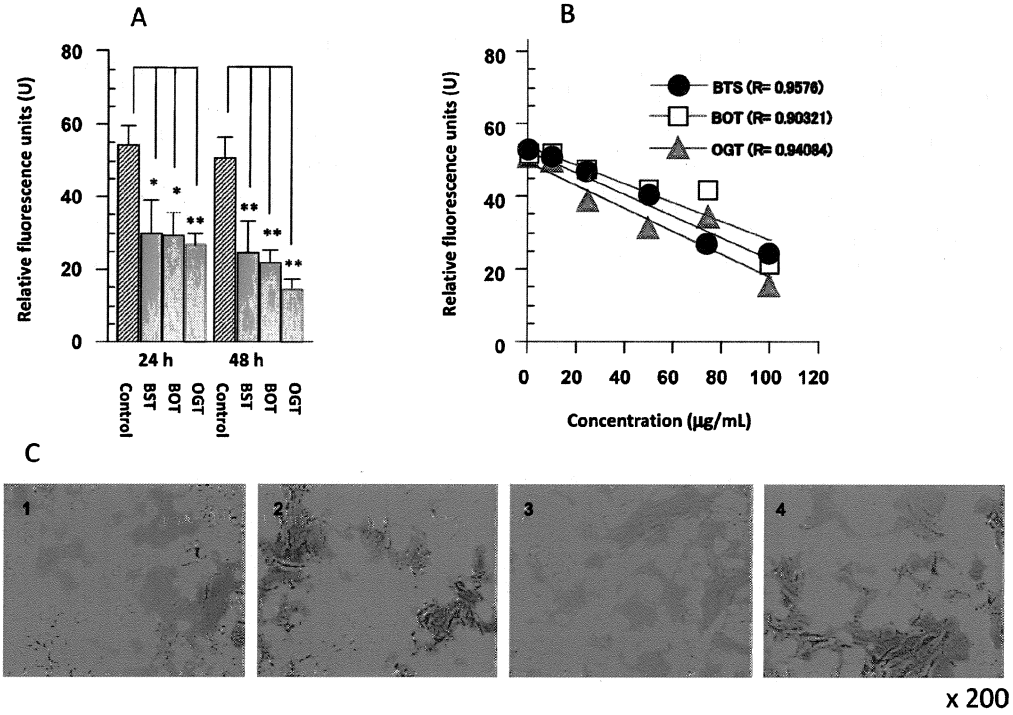

Fig. 2. Effects of BOT, BTS and OGT on Adipogenesis in Cultured RWPA

Panel A: At 100 μg/ml, all three extracts suppress intracellular lipid accumulation at 24 and 48 h after differentiation of RWPA. Panel B: The effects of the three extracts are concentration-dependent at concentrations ranging from 1—100 μg/ml on day 7 of RWPA differentiation. Panel C: Differences in cumulative lipogenesis in RWPA treated with medium alone (1), 100 μg/ml of BTS (2), BOT (3) and OGT (4) after 24 h of culture.

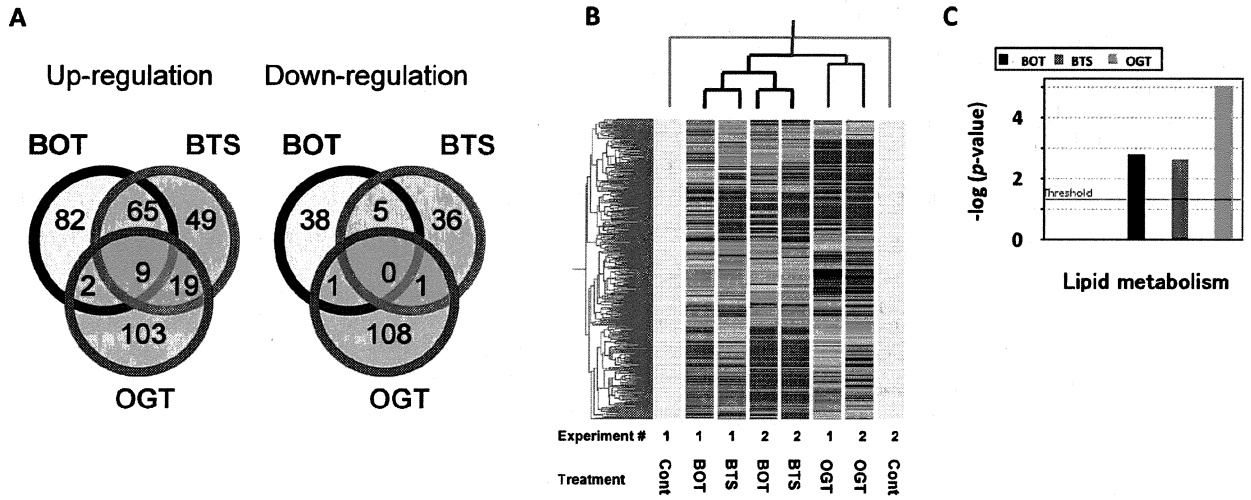

Fig. 3. Overview of DNA Microarray Analyses in Cultured RWPA after Administration of Three Kampo Medicines (BOT, BTS and OGT)

Panel A: Numbers of overlapping genes showing upregulation (left) or downregulation (right) among BOT, BTS and OGT. Panel B: Clustering of expression profiles among BOT, BTS, OGT and the control in two separate experiments. Panel C: Statistical scores for each functional regulatory network determined by IPA according to the network fit to the set of focus genes. The scores for expression of lipid metabolism-related genes are expressed as the negative log of p, and denote the likelihood of the focus genes in the network being found together due to chance.

measurements. Noise values were eliminated based on the flag determined by the GCOS software after normalization to the median. Finally, we picked up 18364 useful probe sets. Since we carried out two experiments for each medicine, genes that showed ≥2-fold changes in their expression levels in both experiments were defined as upregulated or downregulated genes. DNA microarray analyses (total probe set: 31099) of cDNAs prepared from adipocytes revealed that BOT, BTS and OGT increased the expression of 133—150 genes and decreased the expression of 42—110 genes by ≥2-fold. The number of overlapping genes between BOT and BTS was 65. However, there were only 2 (for BOT) or 19 (for BTS) genes whose expression was upregulated in common with OGT (Fig. 3A). On the other hand, very few commonly downregulated genes were detected. We clustered the data sets for upregulated or downregulated genes into a

condition tree using the Pearson correlation method and the resultant heat map is shown in Fig. 3B. The hierarchical clustering analysis produced similar results to the Venn diagram shown in Fig. 3A. BOT and OGT were closely clustered while OGT was clustered separately (Fig. 3B). Taken together, our results seem to imply that BOT and BTS have partial common effects on the gene expression profiles, whereas OGT does not. IPA uses a database depending on stored publications and enables us to identify functional regulatory networks from a gene list.[13] The gene list was used as a starting point for generating biological networks. To build these networks, the program uses its knowledge base to identify interactions between focus genes as well as other genes. IPA then determines a statistical score for each network according to the fit of the network to the set of focus genes. The score represents the negative log of p and denotes the likelihood of the focus genes in the network being found together due to chance (Fig. 3C). Biological functions, such as lipid metabolism, were assigned to each gene network by using findings extracted from the scientific literature and stored in the Ingenuity Pathways Knowledge Base. The biological functions assigned to each network are ranked according to the significance of that biological function to the network. IPA has its own gene ontology, and we analyzed the upregulated or downregulated genes categorized as "lipid metabolism"-related functions in IPA. As shown in Table 2, 10 genes affected by BOT, 20 genes affected by BTS and 22 genes affected by OGT were categorized into lipid metabolism-related functions. These genes seemed to coordinately affect lipid metabolism and result in the suppression of adipogenesis in RWPA. Several genes overlapped, as shown in Fig. 3A, but only OGT induced downregulation of multiple genes (Table 2). We measured mRNA expression levels of seven selected genes highly contributing to the lipid metabolism, that were *ACACA, AEBP1, PNPLA8, SCGB1A1, ADRB3, ADIPOQ, MGLL*. The modulated genes shown in bold in Table 2 were applied to the RT-PCR analyses.

Confirmation Using Semiquantitative RT-PCR To further validate the IPA analysis, the mRNA expression levels of *ACACA*, *AEBP1*, *PNPLA8*, *SCGB1A1*, *ADRB3*, *ADIPOQ*, and *MGLL*, which fluctuated by >2-fold relative to the control, were examined by semiquantitative RT-PCR. The results revealed significant increases or decreases in these genes in RWPA, as shown in Fig. 4.

Table 2. List of Upregulated and Downregulated Lipid Metabolism-Related Genes

Modulation	Extract		
	BOT	BTS	OGT
Upregulated	***ACACA***[a]	***ACACA***[a]	*ACOT2*
	AEBP1[a]	***AEBP1***[a]	*C3*[b]
	CXCL12[a]	*AKT2*	*CH25H*
	MSN	*ANGPTL4*	*HMOX1*
	MTMR1	*C3*[b]	*IFRD1*
	PAFAH1B1	*CXCL1*	*NQO1*
	PNPLA8[a]	*CXCL12*[a]	*PLA2G2A*[b]
	RAB5A	*EPAS1*	*PTGES*[b]
	SCD2	*HPX*	*SAT1*
		MMP3	***SCGB1A1***
		PCK1	*STAR*
		PI4K2A	*STC1*
		PLA2G2A[b]	
		PNPLA8[a]	
		PTGES	
		PTGS2[b]	
		RBP1	
		SCD2[a]	
		UCP1	
Downregulated	*PIK3R1*	***ADRB3***	*ABCD2*
			ACSL1
			ADIPOQ
			ANGPT2
			ELOVL2
			ELOVL6
			MGLL
			PRLR
			SEPP1
			UCP3

Lipid metabolism-related genes whose expression levels were changed by ≥2-fold compared with the control were picked up by the function analysis of IPA. The modulated genes indicated as bold-italic style in Table 2 were applied to the RT-PCR analyses. *a*) Common upregulated genes for BOT and BTS. *b*) Common upregulated genes for OGT and BTS.

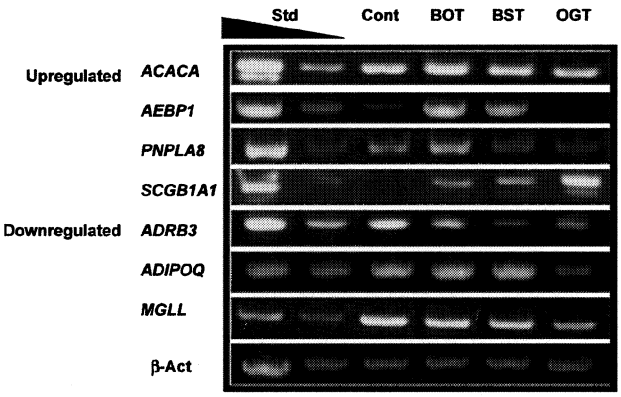

Fig. 4. Confirmation of the mRNA Expression Levels of *ACACA*, *AEBP1*, *PNPLA8*, *SCGB1A1*, *ADRB3*, *ADIPOQ*, and *MGLL* Using Semiquantitative RT-PCR

β-Actin gene expression is used as an endogenous internal standard.

DISCUSSION

In the present study, we have demonstrated that intracellular lipid accumulation in RWPA was significantly reduced over time by three different kinds of Kampo medicines in concentration-dependent manners. In a previous investigation,[15] we found that BOT inhibited obesity in ovariectomized rats. Nakayama *et al.*[16] recently reported that orally administered BTS lowered fatty acid droplet accumulation in the liver, and also reduced the levels of several plasma markers correlated to obesity as well as body growth in mice fed a high-fat diet. OGT contains four different herbs. Berberine, an isoquinoline alkaloid in Coptis rhizomes and Phellodendron cortex, is one of the major active constituents, and has been reported to have antihyperglycemic effects.[17—19] Therefore, adipocyte tissues represent one of the major target organs for the mechanisms by which BOT, BTS and OGT may prevent or improve obesity *in vivo*. To explore the mechanism of the anti-obesity effects of BOT, BTS and OGT, we exhaustively analyzed the mRNA expression levels in cultured RWPA after administration of these extracts using a DNA microarray at the same biological endpoints. In the cluster analysis, BOT and BTS downregulated and upregu-

lated the expression levels of various genes in RWPA, and their gene regulatory patterns were similar. However, OGT showed a different gene regulatory pattern compared to those of BOT and BTS. These findings indicate that BTS and BOT target and modulate the expression of similar genes in RWPA *in vitro*. Furthermore, lipid metabolism-related genes were modulated by administration of these extracts.

BOT and BTS individually upregulated 9 and 19 lipid-related genes, respectively, with *ACACA*, *AEBP1*, *CXCL12* and *PNPLA8* representing lipid metabolism-related genes upregulated by both extracts. Of these genes, *ACACA*,[20] *AEBP1*[21,22] and *PNPLA8*[23,24] were selected as determinants by the RT-PCR analyses, since the genes are reported to contribute to obesity through lipid metabolism. On the other hand, we measured mRNA expression levels of *ADRB3*[25] that was downregulated in the presence of BTS. This gene product, β-3 adrenalin receptor mainly observed in adipose tissue, is associated with liplid metabolism and thermal regulation. It is also known to related to activation of adenylate reductase induced by norepinephrine.

Interestingly, *C3*, *PLA2G2A* and *PTGES*, which are also related to lipid metabolism, were genes affected by both BTS and OGT in RWPA. It can therefore be assumed that the inhibitory effects of BTS on adipogenesis are partly induced through changes in gene expression levels that overlap between BOT or OGT. On the other hand, OGT was found to not only upregulate the expression of 19 genes but also downregulate the expression of 10 genes, which may explain why the effects of OGT on adipogenesis are greater than those of BOT and BTS. In fact, we measured mRNA expression levels of upregulated *SCGB1A1*[26,27] and downregulated *ADIPOQ*[23,24] and *MGLL*[28] in the presence of OGT with RT-PCR method, that is contributing to lipid metabolism. *ADIPOQ* expressed in adipose tissue is structurally highly homologous to collagen X/VIII and complementary factor C1q. It is thought to be collagen-like secretory protein. Triglyceride stored in fat and other cells is hydrolyzed into fatty acids and glycerol with *MGLL* and hormone-sensitive lipase. *MGLL* is also able to hydrolyze monoglyceride that is produced with metabolism of lipoprotein triglyceride. There are two limitations of poor reproducibility analyzed with this microarray and detailed mechanism of administerd drugs in our experiment, although we found the modulation of genes' expression related to differentiation of adipose cell and fat storage.

In summary, to the best of our knowledge, the present results provide the first evidence that three different herbal extracts, namely BOT, BTS and OGT, can suppress adipogenesis in cultured adipocytes, and that different regulatory genes corresponding to obesity are affected by the extracts. Hence, these herbal extracts may be useful for preventing or improving obesity in subjects who are clinically diagnosed with morbid obesity according to Kampo and genetic diagnoses. Kampo medicines could show potential pharmacological effects through transformation to active metabolites in the liver after their metabolism and absorption in the small intestine,[29—33] although confirmation of these effects using both *in vitro* and *in vivo* experiments is necessary.[34] We are currently planning to investigate the effects of *in vivo* administration of BOT, BTS and OGT on obesity in mice fed a high-fat diet, although it is also important to further clarify the usefulness of these three Kampo medicines in randomized control trials in clinical settings.

Acknowledgements This study was supported in part by a Grant-in-Aid for Scientific Research (C) from the Ministry of Education, Culture, Sports, Science and Technology of Japan (No. 17590605 to Dr. Yamakawa in 2005—2006), a research grant from the Japan Kampo Medicine Manufacturers Association (to Dr. Moriya in 2006), a research grant from the Institute of Kampo Medicine (Japan) (to Dr. Takahashi in 2006) and a grant for promoting research from Kanazawa Medical University (No. S2006-2 to Dr. Ishigaki in 2006). We would like to thank Tsumura & Co. for donating the PDA-HPLC profiles of Orengedokuto (TJ-15), Boiogito (TJ-20) and Bofutsushosan (TJ-62).

REFERENCES

1) Eckel R. H., Grundy S. M., Zimmet P. Z., *Lancet*, **365**, 1415—1428 (2005).
2) Camp H. S., Ren D., Leff T., *Trends Mol. Med.*, **8**, 442—447 (2002).
3) Korner J., Aronne L. J., *J. Clin. Invest.*, **111**, 565—570 (2003).
4) Must A., Spadano J., Coakley E. H., Field A. E., Colditz G., Dietz W. H., *JAMA*, **282**, 1523—1529 (1999).
5) Mokdad A. H., Bowman B. A., Ford E. S., Vinicor F., Marks J. S., Koplan J. P., *JAMA*, **286**, 1195—1200 (2001).
6) Kershaw E. E., Flier J. S., *J. Clin. Endocrinol. Metab.*, **89**, 2548—2556 (2004).
7) Guerre-Millo M., *Diabetes Metab.*, **30**, 13—19 (2004).
8) Fève B., Moldes M., El Hadri K., Lasnier F., Pairault J., *Médecine/Sci.*, **14**, 848—857 (1998).
9) Ohno K., Chung H.-W., Maruyama I., Tani T., *Biol. Pharm. Bull.*, **28**, 2162—2165 (2005).
10) Yoshida T., Sakane N., Wakabayashi Y., Umekawa T., Kondo M., *Int. J. Obes. Relat. Metab. Disord.*, **19**, 717—722 (1995).
11) Hioki C., Yoshimoto K., Yoshida T., *Clin. Exp. Pharmacol. Physiol.*, **31**, 614—619 (2004).
12) Morimoto Y., Sakata M., Ohno A., Maegawa T., Tajima S., *Yakugaku Zasshi*, **122**, 163—168 (2002).
13) Shimasaki T., Ishigaki Y., Minamoto T., Motoo Y., *Suizo*, **22**, 14—20 (2007).
14) Nagao A., Zhao X., Takegami T., Nakagawa H., Matsui S., Matsunaga T., Ishigaki Y., *Biochem. Biophys. Res. Commun.*, **370**, 301—305 (2008).
15) Yamakawa J., Moriya J., Takahashi T., Ishige A., Motoo Y., Yoshizaki F., Kanda T., *Evid. Based Complement. Alternat. Med.*, in press.
16) Nakayama T., Suzuki S., Kubo H., Sassa S., Nomura M., Sakamoto S., *J. Ethnopharmacol.*, **109**, 236—240 (2007).
17) Yin J., Hu R., Chen M., Tang J., Li F., Yang Y., Chen J., *Metabolism*, **51**, 1439—1443 (2002).
18) Leng S. H., Lu F. E., Xu L. J., *Acta Pharmacol. Sin.*, **25**, 469—502 (2004).
19) Bian X., He L., Yang G., *Bioorg. Med. Chem. Lett.*, **16**, 1380—1383 (2006).
20) Bodkin N. L., Pill J., Meyer K., Hansen B. C., *Horm. Metab. Res.*, **35**, 617—624 (2003).
21) Ro H. S., Zhang L., Majdalawieh A., Kim S. W., Wu X., Lyons P. J., Webber C., Ma H., Reidy S. P., Boudreau A., Miller J. R., Mitchell P., McLeod R. S., *Obesity*, **15**, 288—302 (2007).
22) Zhang L., Reidy S. P., Nicholson T. E., Lee H. J., Majdalawieh A., Webber C., Stewart B. R., Dolphin P., Ro H. S., *Mol. Med.*, **11**, 39—47 (2005).
23) Kubota N., Terauchi Y., Kubota T., Kumagai H., Itoh S., Satoh H., Yano W., Ogata H., Tokuyama K., Takamoto I., Mineyama T., Ishikawa M., Moroi M., Sugi K., Yamauchi T., Ueki K., Tobe K., Noda T., Nagai R., Kadowaki T., *J. Biol. Chem.*, **281**, 8748—8755 (2006).
24) Kralisch S., Klein J., Lossner U., Bluher M., Paschke R., Stumvoll M., Fasshauer M., *J. Endocrinol.*, **185**, R1—R8 (2005).
25) Serazin V., Dieudonné M. N., Morot M., de Mazancourt P., Giudicelli Y., *Am. J. Physiol. Endocrinol. Metab.*, **286**, E434—E438 (2004).

26) Pérez-Echarri N., Noel-Suberville C., Redonnet A., Higueret P., Martínez J. A., *J. Physiol. Biochem.*, **63**, 317—327 (2007).
27) Oort P. J., Knotts T. A., Grino M., Naour N., Bastard J. P., Clément K., Ninkina N., *J. Nutr. I.*, **38**, 841—348 (2008).
28) Bolduc C., Larose M., Yoshioka M., Ye P., Belleau P., Labrie C., Morissette J., Raymond V., Labrie F., St-Amand J., *J. Mol. Endocrinol.*, **33**, 429—444 (2004).
29) Tashiro S., "Tezukuri no Rinshoyakurigaku," Vol. I, Chap. 8, ed. by Tashiro S., Jiho, Tokyo, 1996, pp. 83—100.
30) Hattori M., Sakamoto T., Kobashi K., Namba T., *Planta Med.*, **48**, 38—42 (1983).
31) Hattori M., Shu Y.-Z., Shimizu M., Hayashi T., Morita N., Kobashi K., Xu G.-J., Namba T., *Chem. Pharm. Bull.*, **33**, 3838—3846 (1985).
32) Hattori M., Namba T., Akao T., Kobashi K., *Pharmacology*, **36** (Suppl. 1), 172—179 (1988).
33) Umeda M., Amagaya S., Ogihara Y., *J. Ethnopharmacol.*, **23**, 91—98 (1988).
34) Hayashi K., Imanishi N., Kashiwayama Y., Kawano A., Terasawa K., Shimada Y., Ochiai H., *Antiviral Res.*, **74**, 1—8 (2007).

１．研究課題名：腱鞘巨細胞腫における特異的融合遺伝子の検討（研究番号　S2006-3）

２．キーワード：１）腱鞘巨細胞腫（giant cell tumor of tendon sheath）
２）COL6A3-CSF1 融合遺伝子（COL6A3-CSF1 fusion gene）
３）Fluorescence *in situ* hybridization （FISH）
４）Reverse transcribed-polymerase chain reaction （RT-PCR）
５）パラフィン切片　（paraffin sections）

３．研究代表者：佐藤　勝明・医学部・講師・病理病態学（病理学Ⅱ）

４．研 究 目 的

近年、リンパ腫などの血液系腫瘍同様に、軟部固形腫瘍においても腫瘍発生に染色体特異的相互転座が深く関係している例が数多く報告されてきている。指などに好発する腱鞘巨細胞腫においては、1 番と 2 番の染色体の相互転座により、1 番染色体短腕(1p13)にある CSF1 遺伝子と 2 番染色体長腕(2q37)にある COL6A3 遺伝子が融合していることが報告された(PNAS 103:690-5, 2006)。そこで、我々は、腱鞘巨細胞腫多数例を用いて、この特異的染色体転座の有無をパラフィン切片上でのダブルカラーの fluorescent *in situ* hybridization (FISH)で検討し、特異的相互転座がどの割合で検出されるかを明らかにし、相互転座例を用いて RT-PCR 法による融合遺伝子検出法を確立することを目的とした研究を計画した。

５．研 究 計 画

１） CSF1 遺伝子および COL6A3 遺伝子をカバーするような BAC クローン、CSF1 遺伝子および COL6A3 遺伝子それぞれのセントロメア側とテロメア側に相当する BAC クローンを選定し、FISH のためのプローブを作成する。

２）腱鞘巨細胞腫 20 例以上のホルマリン固定パラフィン包埋切片について、ダブルカラーの FISH を行い、相互転座の有無を検討する。検出については、CSF1 遺伝子および COL6A3 遺伝子それぞれで dual color, break apart 法で検討するとともに、dual color、dual fusion 法で CSF1 遺伝子と COL6A3 遺伝子の特異的融合が認められるかも検討する。いずれの方法でも 100 個の細胞核の観察で、1 個でも所見を認めたものを陽性と判定した。

３）相互転座陽性例については、より短い BAC クローンから作成したプローブを用いて、遺伝子内での融合部位をより詳細に明らかにする。また、相互転座例を陽性コントロールとし、融合遺伝子を検出できるような RT-PCR 法のためのプライマー設定を検討する。

６．研 究 成 果

腱鞘巨細胞腫 28 例について検討した。症例の内訳は、年齢 11-73 歳（平均年齢 42 歳)、男：女＝11:17：、発生部位は手指 22 例で足趾 2 例、腫瘍最大径は 3-40㎜（平均径 16 ㎜）であった。

１）Dual color, dual fusion 法で検討したところ、3 例に COL6A3 遺伝子と CSF1 遺伝子の融合所見を認めた。2 例においてはシグナルが検出されず、評価不能であった。

2）Dual color, apart 法での、CSF1 遺伝子と COL6A3 遺伝子の split の有無を検討中である。

7．研究の考察・反省

腱鞘巨細胞腫において、FISH 法による COL6A3-CSF1 融合遺伝子の検出は予想以上に感度が低い結果であった。これまでの報告によると、腫瘍内に占める COL6A3-CSF1 融合ほかの遺伝子異常をもった腫瘍細胞の割合は低く、腫瘍細胞から過剰に発現される CSF1 により反応性に誘引された CSF1 receptor を発現する組織球が多くを占めることがわかってきた。今回の FISH では 100 個中 1 個の異常シグナルの検出で陽性と判定したが、それでも陽性例は少なくパラフィン切片における interphase FISH による融合遺伝子の検出の限界が示唆された。

最近、COL6A3-CSF1 融合遺伝子を RT-PCR で検討した報告がされ（Möller E, et al. Genes Chromosomes Cancer. 2008 47:21-5.）、6 例中の 3 例に融合遺伝子の転写産物が検出された。今後、Möller らの報告に従って RT-PCR でも COL6A3-CSF1 融合遺伝子の検出を試み、FISH の結果との比較検討を計画している。

8．研 究 発 表

当研究課題に関しての論文発表はない。

当研究過程で確立された BAC クローン由来のプローブ作成技術とパラフィン切片上での間期核 FISH の技術を用いて症例を検討し、以下の論文発表を行った。

Sato K, Ueda Y, Sugaya J, Ozaki M, Hisaoka M, Katsuda S. Extrauterine endometrial stromal sarcoma with JAZF1/JJAZ1 fusion confirmed by RT-PCR and interphase FISH presenting as an inguinal tumor. Virchows Arch 2007; 450: 349-353. (MLDB)

Sato K, Ueda Y, Miwa S, Yokogawa A, Ozaki M, Katsuda S. Low-grade malignant soft tissue perineurioma: lnterphase fluorescence in situ hybridization. Pathol Int. 2008; 58: 718-722. (MLDB)

Virchows Arch (2007) 450:349–353
DOI 10.1007/s00428-006-0345-8

CASE REPORT

Extrauterine endometrial stromal sarcoma with *JAZF1/JJAZ1* fusion confirmed by RT-PCR and interphase FISH presenting as an inguinal tumor

Katsuaki Sato · Yoshimichi Ueda · Junichi Sugaya · Mamoru Ozaki · Masanori Hisaoka · Shogo Katsuda

Received: 31 March 2006 / Accepted: 30 October 2006 / Published online: 18 January 2007

Abstract Endometrial stromal sarcomas are rare malignant mesenchymal tumors that usually develop in the uterine corpus and occasionally arise at various extrauterine sites. This report describes the first case of primary extrauterine endometrial stromal sarcoma arising in the extraperitoneal portion of the round ligament presenting as a solitary inguinal mass in a 46-year-old woman. The patient presented gradually growing tumor in the right inguinal region. Local tumor resection was performed and no recurrence or metastasis was found at 15 months after the operation. Histological examination revealed that the tumor comprised uniform, spindle-shaped cells with blunt nuclear figure and scattered small arteries, and infiltrated into adjacent tissue. No endometriosis was morphologically identified in the lesion. Immunohistochemically, the tumor cells were positive for CD10, estrogen receptor, progesterone receptor, α-smooth muscle actin, and calponin. We confirmed *JAZF1/JJAZ1* fusion by reverse transcription–polymerase chain reaction and the corresponding chromosomal translocation by interphase fluorescence in situ hybridization on paraffin sections. It is essential that the inguinal region should be recognized as a possible primary site of endometrial stromal sarcoma, and the detection of a *JAZF1/JJAZ1* fusion can be useful when the diagnosis is not confirmed by microscopic observation or immunohistochemistry for the tumor arising in extrauterine sites.

Keywords Endometrial stromal sarcoma · Inguinal hernia · Round ligament · *JAZF1/JJAZ1* · Interphase FISH

K. Sato (✉) · Y. Ueda · S. Katsuda
Department of Pathophysiological and Experimental Pathology,
Kanazawa Medical University,
1-1 Daigaku, Uchinada, Kahoku,
Ishikawa 920-0293, Japan
e-mail: sato-k@kanazawa-med.ac.jp

J. Sugaya
Department of Surgical Oncology, Kanazawa Medical University,
Ishikawa, Japan

M. Ozaki
Division of Human Genetics, Medical Research Institute,
Kanazawa Medical University,
Ishikawa, Japan

M. Hisaoka
Department of Pathology and Oncology, School of Medicine,
University of Occupational and Environmental Health,
Kitakyushu, Japan

Introduction

Endometrial stromal sarcoma (ESS) is a rare type of uterine tumor that accounts for less than 10% of uterine sarcomas [10]. The World Health Organization's classification of tumors of the breast and female genital organs subclassified endometrial stromal tumors into three categories: endometrial stromal nodule, low-grade ESS, and undifferentiated endometrial sarcoma (UES) [3]. The tumors traditionally called high-grade ESS were recently reclassified as UES due to their lack of specific differentiation and histological resemblance to endometrial stroma [3]. Accordingly, ESS only means low-grade ESS. ESS was distinguished from the endometrial stromal nodule based on the presence of an infiltrative growing character or vascular invasion in ESS [4, 5, 7, 8].

Recently, a fusion of two zinc finger genes, *JAZF1* and *JJAZ1*, caused by a reciprocal translocation t(7;17)(p15;q21) was detected in more than 80% of ESS cases [4, 5, 7, 8]. Furthermore, *JAZF1/PHF1* or *EPC1/PHF1* fusion also presented in a small number of ESS cases [9]. Diagnosis of

ESS has been dependent on histological findings supported by immunohistochemical examination. However, it could be difficult to get to a definite diagnosis for monophasic spindle cell tumors, especially when an unusual location was involved. Molecular detection of specific fusion transcripts could overcome these problems and should become a potent diagnostic tool for ESS.

ESS's usually develop as primary uterine tumor, but ESS's of extrauterine origin, such as the ovary, fallopian tube, pelvic cavity, abdominal cavity, omentum, retroperitoneum, vagina, vulva, and sigmoid colon, have been reported [2, 6]. The round ligament passes through the inguinal canal and comprises mainly smooth muscle, fibrous tissue, blood vessels, and nerves [12]. Most round ligament tumors are leiomyomas or fibromas, and there is no previous report of ESS arising in the inguinal portion of the round ligament.

We described the first case of primary extrauterine ESS arising from the round ligament in the inguinal canal, unassociated with endometriosis, with a confirmed *JAZF1/JJAZ1* fusion by reverse transcription–polymerase chain reaction (RT-PCR) and interphase fluorescence in situ hybridization (FISH) analysis.

Clinical history

A 46-year-old woman, para 3 and gravida 3, presented with an indolent mass in the right inguinal region. Her menstrual cycle was regular, and her gynecologic history was unremarkable. Physical examination suggested an inguinal hernia. The MRI showed a demarcated 3.0-cm solid mass in the right inguinal canal (Fig. 1a), and no significant lesion in the uterus. Tumor resection was performed. At the operation, the tumor was not covered with a hernia sac nor adhered to the peritoneum but attached to the extraperitoneal portion of the round ligament. There was no evidence of recurrence or metastasis 15 months after surgery.

Materials and methods

Surgically resected specimen was fixed in 10% neutral-buffered formalin, cut into 6 tissue blocks of 5 mm in thickness, and embedded in paraffin. Sections, 4-μm thick, were used for hematoxylin and eosin staining, immunohistochemical studies, molecular analysis, and interphase FISH.

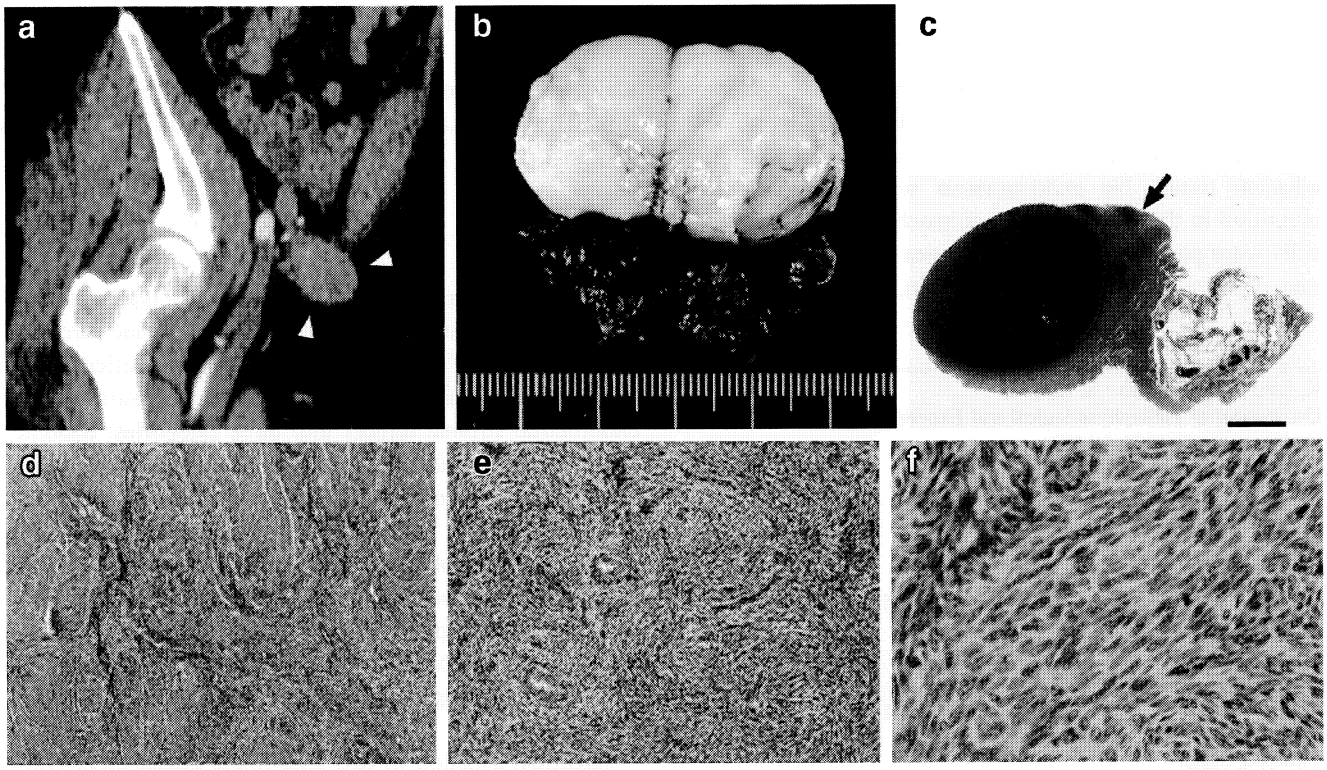

Fig. 1 **a** MRI showing a mass (*arrow head*) in the right inguinal canal. **b** Macroscopic appearance of the cut surface of the tumor showing a yellow-white tumor. **c** Panoramic view of the tumor demonstrating invasion to adjacent tissue (*arrow*). H & E staining; scale bar, 5 mm. **d** The tumor cells infiltratively growth into the adjacent smooth muscle tissue of the round ligament. H & E staining (original magnification ×40). **e** The tumor is densely cellular, and whorls around small arteries are observed. H & E staining (original magnification ×100). **f** The tumor cells are uniform, short, and spindle shaped. H & E staining (original magnification ×400)

Immunohistochemistry

Immunohistochemical examinations were performed on deparaffinized thin sections using the standard avidin–biotin–peroxidase complex method with an automated immunostainer (Ventana Medical System, Tucson, AZ, USA). Primary antibodies against following antigens were used: low molecular weight cytokeratin (CAM5.2, prediluted, Becton–Dickinson, San Jose, CA, USA), high molecular weight cytokeratin (34βE12, 1:75, Dako, Glostrup, Denmark), vimentin (V9, 1:100, Dako), α-smooth muscle actin (1A4, 1:200, Dako), desmin (D33, 1:100, Dako), calponin (CALP, 1:75, Dako), high-molecular-weight caldesmon (h-caldesmon; h-CD, 1:100, Dako), bcl-2 (124, 1:50, Dako), E-cadherin (NCH-38, 1:100, Dako), epithelial membrane antigen (EMA; E29, 1:100, Dako), CD10 (56C6, 1:20, Novocastra, Newcastle upon Tyne, UK), CD34 (NU-4A1, 1:100, Nichirei, Tokyo, Japan), CD117 (c-kit; polyclonal, 1:80, Dako), estrogen receptor (1D5, 1:50, Dako), progesterone receptor (PgR636, 1:800, Dako), calretinin (polyclonal, prediluted, Invitrogen, Carlsbad, CA, USA), inhibin-α (R1, 1:50, Dako), S-100 protein (2A10, Immuno-Biological Laboratories, Gunma, Japan), and Ki-67 (MIB-1, 1:50, Dako). Antigen retrieval was carried out with appropriate methods for each antibody.

Molecular analysis

Three sections cut from paraffin-embedded tissue were prepared for RT-PCR. The RNA extraction and RT-PCR to identify the *JAZF1/JJAZ1* fusion was carried out as previously described using the following primers: JAZF1-369-FW (5′-CCACCCATCACCCCCTCCT-3′) and JJAZ1-400-RV (5′-TGCTATGAGATTCCGAGTTC-3′) [5]. To confirm the *JAZF1/JJAZ1* fusion, PCR products extracted from a corresponding band in agarose gel were analyzed by direct sequencing. The RT-PCR for detection of *SYT/SSX* fusion transcripts, frequently observed in synovial sarcoma, were performed as reported elsewhere [11, 13].

Interphase fluorescence in situ hybridization

The interphase FISH was performed on the paraffin-embedded tissue sections. The probes used were derived from bacterial artificial chromosomes (BAC). BAC clones were commercially purchased from Invitrogen. To detect chromosomal translocations, *JAZF1/JJAZ1* fusion, the probes were selected as follows: RP11-350G16 encompassing the entire *JAZF1* gene mapping to 7p15 and CTD-3205H10 fully covering the *JJAZ1* gene mapping to 17q21 according to the mapping data at the NCBI map viewer website (http://www.ncbi.nlm.nih.gov/mapview/static/MVstart.html). RP11-350G16 and CTD-3205H10 were labeled with digoxigenin and biotin, respectively, with Nick translation mix (Roche Diagnostics, Basel, Switzerland). The slides were deparaffinized in xylene and rehydrated in ethanol. The slides were pretreated by microwaving in 10-mmol citrate buffer (pH 6.0) at 90°C for 15 min. The extracellular matrix in the tissue section was digested using 0.2% pepsin (in 0.01 NHCl) for 10 min at 37°C. The DNA in the tissue sections and the probes were codenatured for 10 min at 90°C, and incubated in a humidified box at 37°C for 48 h. Digoxigenin-labeled probes were detected with rhodamine-conjugated antidigoxigenin antibody, and biotinylated probes were detected with conjugated avidin (Alexa Fluor 488, Molecular Probes, Eugene, OR, USA). The nuclei were counterstained with mounting medium containing 4′,6-diamidino-2-phenylindole (Vector, Burlingame, CA, USA). The probe signals were detected using a fluorescence microscope with a digital camera, with rhodamine as red and Alexa Fluor 488 as green label. For each slide, more than 100 nuclei of tumor cells were analyzed. The composed images were reconstructed with Adobe Photoshop 6.0 software (Adobe, San Jose, CA, USA).

Results

Macroscopically, the tumor was demarcated, adhered to fibromuscular tissue of the round ligament, and had a maximum diameter of 3 cm. The cutting surface of the tumor displayed a yellow-white color and had an elastic hard consistency (Fig. 1b). No necrosis or hemorrhage was apparent.

Microscopically, the tumor cells infiltrated the adjacent smooth muscle tissue of the round ligament at the periphery, 10 mm away from the main mass (Fig. 1c and d). The tumor was highly cellular, and whorls of the tumor cells around small arteries were observed (Fig. 1e). The tumor cells were uniform and spindle-shaped, and had bland nuclei and indistinct cytoplasmic margins (Fig. 1f). Mitotic figures were rare. There was no evidence of vascular invasion or endometriosis throughout the entire specimen.

Immunohistochemically, the tumor cells were positive for CD10, estrogen receptor, progesterone receptor, bcl-2, vimentin, α-smooth muscle actin, and calponin but negative for low and high molecular weight cytokeratin, desmin, h-caldesmon, E-cadherin, EMA, CD34, CD117, calretinin, inhibin-α, and S-100 protein. Less than 1% of tumor cells were positive for Ki-67.

The RT-PCR for the detection of the *JAZF1/JJAZ1* fusion transcript showed a fusion product at the expected level of 93 bp as previously reported (Fig. 2a). The fusion of *JAZF1* and *JJAZ1* genes was confirmed by direct sequencing (Fig. 2b). No *SYT–SSX1* or *SYT–SSX2* fusions were detected.

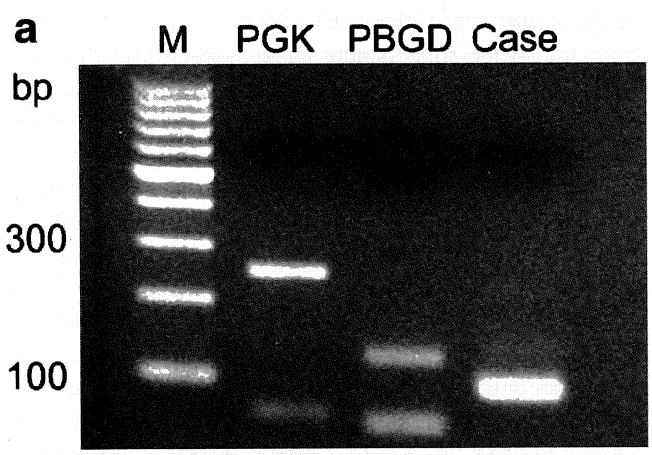

Fig. 2 Detection of the *JAZF1/JJAZ1* fusion transcript. **a** Fusion transcript is amplified and identified in the expected range of 93 bp. **b** Partial chromatogram showing the junction of the *JAZF1/JJAZ1* fusion gene (*arrows*). *M* 100-bp DNA ladder, *PGK* phosphoglycerate kinase (247 bp, internal control), *PBGD* porphobilinogen deaminase (127 bp, internal control), *Case* RNA extracted from the present tumor

The interphase FISH revealed a *JAZF1/JJAZ1* fusion as a result of a reciprocal translocation between 7p15 and 17q21 (Fig. 3).

Discussion

ESS's usually arise in the uterine corpus and are composed of uniform ovoid to slightly spindle-shaped cells. However, these tumors occasionally present elongated spindle-shaped cells that are hard to distinguish from various spindle cell tumors and may be confused with other tumors. In this case, histological diagnosis was difficult because the tumor developed in the extrauterine site, the inguinal region, and comprised uniform, elongated spindle-shaped cells.

Fig. 3 Interphase FISH analysis on a paraffin section. Two fusion spots (merge signal, *arrows*), one red spot and one green spot, indicate *JAZF1/JJAZ1* fusion originating from a reciprocal translocation between 7p15 and 17q21

Immunohistochemical findings supported the differential diagnosis for spindle cell tumor. The present tumor was positive for CD10, estrogen receptor, progesterone receptor, α-smooth muscle actin, calponin but negative for desmin and h-caldesmon. These findings supported the diagnosis of ESS. Monophasic fibrous synovial sarcoma (MFSS) is a representative spindle-shaped soft tissue tumor that resembles ESS histologically, demonstrating *SYT/SSX1* or *SYT/SSX2* chimera gene in more than 90% of the cases [13]. In this case, although these chimera genes were not revealed by RT-PCR using RNA extracted from paraffin-embedded tissues, the diagnosis of MFSS could not completely be excluded from these negative results only.

Previous studies examining the genetic aspects of ESS's revealed frequent chromosomal abnormalities of 6p, 7p, and 17q [8]. In recent years, a specific chromosomal rearrangement t(7;17)(p15;q21) resulting in a *JAZF1/JJAZ1* fusion transcript was reported in ESS [4, 5, 7, 8]. The *JAZF1/JJAZ1* fusion in ESS was described in 5 of 5 cases by Koontz et al. [7], 1 of 3 cases by Micci et al. [8], 3 of 13 cases including variant types by Huang et al. [4], and 16 of 20 cases by Hrzenjak et al. [5]. Micci et al. [9] identified ESS cases with two other genetic alterations, t(6;7)(p21;p15) leading to a *JAZF1/PHF1* fusion gene and t(6;10;10)(p21;q22;p11) causing a *EPC1/PHF1* fusion gene. The *JAZF1*, *JJAZ1*, and *PHF1* genes all encode zinc finger domains often found in DNA-binding proteins, and fusion genes previously reported in ESS, *JAZF1/JJAZ1*, *JAZF1/PHF1*, and *EPC1/PHF1* could express unusual proteins with zinc finger motifs. Wild-type *JAZF1* is expressed in normal endometrium, and loss of expression for normal *JAZF1* was demonstrated in some ESS cases [7]. The function of the *JAZF1* gene has not been elucidated, but it has been suggested that *JAZF1* might have a role in tumor suppression, and abnormal fusion proteins with DNA-

binding activities could deregulate the transcriptional process of other genes [7, 9]. The recognition of the *JAZF1/JJAZ1* fusion gene was crucial and unique in diagnosing ESS. The detection of these chimera genes should become a specific diagnostic tool, especially when the ESS arises at an extrauterine site. In this case, *JAZF1/JJAZ1* fusion was confirmed by RT-PCR and interphase FISH.

Primary ESS's have been reported in various extrauterine locations [2, 6]. Irvin et al. [6] reported a case of ESS that occurred in the endometriosis of the vulva in association with the extrapelvic portion of the round ligament; however, an ESS arising from the round ligament in the inguinal canal has not been described. Some cases of extrauterine ESS included endometriosis, but many of the extrauterine ESS's described in the literature have been unassociated with endometriosis [2]. There are many reports of inguinal endometriosis often presenting as an inguinal hernia, and approximately 90% of these cases have right-side lesion [1]. The present case showed a right groin mass, but there was no endometriosis within the lesion as determined by histological examination.

In conclusion, it is important to recognize that ESS can develop in extrauterine sites such as the inguinal region, and the detection of *JAZF1/JJAZ1* fusion can be useful when the diagnosis is not definitive by other studies including light microscopy and immunohistochemistry.

Acknowledgment The authors thank Hideaki Ninomiya and Yoshitame Yanaida (Department of Pathology, Kanazawa Medical University Hospital, Ishikawa, Japan) for the immunohistochemistry. This work was supported by a grant for promoted research from Kanazawa Medical University (S2006-3).

References

1. Candiani GB, Vercellini P, Fedele L, Vendola N, Carinelli S, Scaglione V (1991) Inguinal endometriosis: pathogenetic and clinical implications. Obstet Gynecol 78:191–194
2. Chang KL, Crabtree GS, Lim-Tan SK, Kempson RL, Hendrickson MR (1993) Primary extrauterine endometrial stromal neoplasms: a clinicopathologic study of 20 cases and a review of the literature. Int J Gynecol Pathol 12:282–296
3. Hendrickson MR, Tavassoli FA, Kempson RL, McCluggage WG, Haller U, Kubik-Huch RA (2003) Mesenchymal tumours and related lesions. In: Tavassoli FA, Devilee P (eds) World Health Organization classification of tumours. Pathology and genetics of tumours of the breast and female genital organs. IARC, Lyon, pp 233–244
4. Huang HY, Ladanyi M, Soslow RA (2004) Molecular detection of *JAZF1–JJAZ1* gene fusion in endometrial stromal neoplasms with classic and variant histology: evidence for genetic heterogeneity. Am J Surg Pathol 28:224–232
5. Hrzenjak A, Moinfar F, Tavassoli FA, Strohmeier B, Kremser ML, Zatloukal K, Denk H (2005) *JAZF1/JJAZ1* gene fusion in endometrial stromal sarcomas: molecular analysis by reverse transcriptase–polymerase chain reaction optimized for paraffin-embedded tissue. J Mol Diagn 7:388–395
6. Irvin W, Pelkey T, Rice L, Andersen W (1998) Endometrial stromal sarcoma of the vulva arising in extraovarian endometriosis: a case report and literature review. Gynecol Oncol 71:313–316
7. Koontz JI, Soreng AL, Nucci M, Kuo FC, Pauwels P, van Den Berghe H, Cin PD, Fletcher JA, Sklar J (2001) Frequent fusion of the *JAZF1* and *JJAZ1* genes in endometrial stromal tumors. Proc Natl Acad Sci USA 98:6348–6353
8. Micci F, Walter CU, Teixeira MR, Panagopoulos I, Bjerkehagen B, Saeter G, Heim S (2003) Cytogenetic and molecular genetic analyses of endometrial stromal sarcoma: nonrandom involvement of chromosome arms 6p and 7p and confirmation of *JAZF1/JJAZ1* gene fusion in t(7;17). Cancer Genet Cytogenet 144:119–124
9. Micci F, Panagopoulos I, Bjerkehagen B, Heim S (2006) Consistent rearrangement of chromosomal band 6p21 with generation of fusion genes *JAZF1/PHF1* and *EPC1/PHF1* in endometrial stromal sarcoma. Cancer Res 66:107–112
10. Moinfar F, Gogg-Kamerer M, Sommersacher A, Regitnig P, Man YG, Zatloukal K, Denk H, Tavassoli FA (2005) Endometrial stromal sarcomas frequently express epidermal growth factor receptor (EGFR, HER-1): potential basis for a new therapeutic approach. Am J Surg Pathol 29:485–489
11. Okamoto S, Hisaoka M, Daa T, Hatakeyama K, Iwamasa T, Hashimoto H (2004) Primary pulmonary synovial sarcoma: a clinicopathologic, immunohistochemical, and molecular study of 11 cases. Hum Pathol 35:850–856
12. Smith P, Heimer G, Norgren A, Ulmsten U (1993) The round ligament: a target organ for steroid hormones. Gynecol Endocrinol 7:97–100
13. Tsuji S, Hisaoka M, Morimitsu Y, Hashimoto H, Shimajiri S, Komiya S, Ushijima M, Nakamura T (1998) Detection of SYT-SSX fusion transcripts in synovial sarcoma by reverse transcription–polymerase chain reaction using archival paraffin-embedded tissues. Am J Pathol 153:1807–1812

Pathology International 2008; **58**: 718–722 doi:10.1111/j.1440-1827.2008.02299.x

Case Report

Low-grade malignant soft-tissue perineurioma: Interphase fluorescence *in situ* hybridization

Katsuaki Sato,[1] Yoshimichi Ueda,[1] Shinji Miwa,[2] Akio Yokogawa,[2] Mamoru Ozaki[3] and Shogo Katsuda[1]

[1]Department of Pathophysiological and Experimental Pathology, [3]Division of Human Genetics, Medical Research Institute, Kanazawa Medical University and [2]Department of Orthopedics, Saiseikai Kanazawa Hospital, Ishikawa, Japan

Perineuriomas are usually benign soft-tissue tumors that arise from perineurial cells of the peripheral nerve sheath. Low-grade malignant perineurioma is a rare type of perineurioma, presenting with infiltrative growth, low mitotic activity, and a lack of necrosis. This report describes a case of low-grade malignant perineurioma in a 60-year-old man who presented with a growing tumor on the dorsal side of his left wrist. The tumor was surgically excised and showed no adhesion to the surrounding muscle and no continuity with nerves. There was no evidence of recurrence or metastases 12 months after surgery. Histology indicated that the tumor contained hypercellular and hypocellular areas with spindle-shaped cells proliferating in storiform patterns or perivascular whorling. There was moderate infiltrative growth into the surrounding tissue. There was an evident central infarction but no coagulative necrosis. Mitotic figures were observed at 5/10 high-power fields. On immunohistochemistry tumor cells were found to be positive for epithelial membrane antigen, glucose transporter protein 1, and claudin-1. Approximately 18.4% of tumor nuclei were labelled for Ki-67. Interphase fluorescence *in situ* hybridization on paraffin sections indicated a loss of chromosome 13. This suggests that chromosome 13 abnormalities could also be involved in perineurioma with low-grade malignant potential.

Key words: chromosome 13, claudin-1, Glut1, interphase fluorescence *in situ* hybridization, low-grade malignant, perineurioma, soft-tissue

Perineurioma is a rare tumor type that arises from perineurial cells of the peripheral nerve sheath and was first described by Lazarus and Trombetta.[1] Four clinicopathological variants are recognized: soft-tissue perineurioma, sclerosing perineurioma, reticular perineurioma, and intraneural perineurioma.[2] These conventional perineuriomas almost always follow a benign course but a rare malignant subtype of perineurioma, malignant peripheral nerve sheath tumor (MPNST) showing perineurial cell differentiation, was reported by Hirose *et al.*[3,4] Furthermore, Hirose *et al.* presented three cases of low-grade malignant perineurioma (LGMPN) with lower mitotic activity than malignant perineurioma and no necrosis.[5] According to the World Health Organization (WHO) classification, malignant perineuriomas characterized by hypercellularity, hyperchromasia, variable mitotic activity, and no necrosis are defined as WHO grade II, corresponding to low-grade malignancy, whereas necrosis is a feature of WHO grade III tumors.[6] There have been only seven reported cases of LGMPN[5,7–10] and the clinical course of these tumors is unknown.

Cytogenetic examination indicated chromosome 22 abnormalities in perineuriomas,[11–14] rearrangements and/or deletions of chromosome 10q in sclerosing perineurioma,[15] and loss of chromosome 13 in soft-tissue perineurioma.[16] These were all cases of conventional perineuriomas. Cytogenetic abnormalities in perineuriomas with a malignant potential have not been reported so far.

In the current report we present a literature review on soft-tissue LGMPN, as well as a soft-tissue LGMPN with cytogenetic abnormalities confirmed on interphase fluorescence *in situ* hybridization (FISH).

CASE REPORT

Clinical summary

A 60-year-old man noticed a growing mass on the dorsal side of his left wrist. The family and medical history were unremarkable. Upon excision it was found that the tumor was

Correspondence: Katsuaki Sato, MD, Department of Pathophysiological and Experimental Pathology, Kanazawa Medical University, 1-1 Daigaku, Uchinada, Kahoku, Ishikawa 920-0293, Japan. Email: sato-k@kanazawa-med.ac.jp

Received 25 March 2008. Accepted for publication 26 June 2008.

located in the subcutaneous tissue and showed no adhesion to the surrounding muscle and no continuity with nerves. There was no evidence of recurrence or metastases 12 months after surgery.

Procedure

Surgically resected specimens were fixed in 10% neutral-buffered formalin, embedded in paraffin and cut into 4 μm-thick sections. Sections were used for HE staining, immunohistochemistry, and interphase FISH. For ultrastructural examination, paraffin-embedded tissue was fixed in 2.5% glutaraldehyde solution, post-fixed in 2% osmium tetroxide, dehydrated, and embedded in epoxy resin. Ultrathin sections were examined under electron microscope (JEM1200EXII, JEOL, Tokyo, Japan).

Immunohistochemistry

Immunohistochemical examination was performed on deparaffinized sections using the standard avidin–biotin–peroxidase complex method with an automated immunostainer (Ventana Medical System, Tucson, AZ, USA). The following primary antibodies were used: pancytokeratin (AE1/AE3, 1:100; Dako, Glostrup, Denmark), vimentin (V9, 1:100; Dako), S-100 protein (2A10, 1:50; IBL, Takasaki, Japan), α-smooth muscle actin (α-SMA; 1A4, 1:200; Dako), desmin (D33, 1:100; Dako), epithelial membrane antigen (EMA; E29, non-diluted; Dako), glucose transporter protein 1 (Glut1; polyclonal, 1:100; Dako), claudin-1 (polyclonal, 1:200; Lab Vision, Fremont, CA, USA), CD21 (1F8, 1:50; Dako), CD34 (NU-4A1, 1:100; Nichirei, Tokyo, Japan), CD117 (c-kit; polyclonal, 1:80; Dako), CD56 (1B6, 1:100; Novocastra, Newcastle upon Tyne, UK), CD68 (KP1, 1:100; Dako), collagen IV (CIV, 1:100; Dako), laminin (polyclonal, 1:800; Dako), and Ki-67 (MIB-1, 1:50; Dako). Appropriate antigen retrieval was carried out for each antibody according to the manufacturers' instructions.

Interphase fluorescence *in situ* hybridization

Interphase FISH was performed on paraffin-embedded tissue sections as previously described.[17] The Human Centromeric Probe was used for chromosomes 13/21 (Cambio, Cambridge, UK). Subtelomeric probes for 13q, 21q, and 22q originated from BAC clones, RP11-960N29, RP11-430O7, and CTD-255204, respectively.

Pathological findings

The excised tumor had a maximum diameter of 2.8 cm. The cut surface of the tumor had a white-tan color (Fig. 1a). Microscopy indicated that the tumor had no capsule and a central infarction with hemorrhage. No coagulative necrosis was found. There was a hypercellular area consisting of mild atypical tumor cells with oval nuclei and eosinophilic cytoplasm and a hypocellular area consisting of spindle cells with elongated nuclei and thin cytoplasmic processes and edematous stroma. Pleomorphism of tumor cells was not evident. There were characteristic features indicative of a storiform pattern (Fig. 1b) and perivascular whorling (Fig. 1c). Moderate infiltration into the surrounding tissue was seen but no invasion of muscle tissue. Mitotic figures were evident at 5/10 high-power fields (HPF) on average but without atypical forms (Fig. 1d). On immunohistochemistry the tumor cells were positive for vimentin, Glut1 (Fig. 2a), and claudin-1 (Fig. 2b) but negative for pancytokeratin, S-100 protein, α-SMA, desmin, CD21, CD34, c-kit (CD117), CD56, CD68, type IV collagen, and laminin. Immunoreactivity for EMA was diffusely observed when non-diluted primary antibody was used (Fig. 2c), but was not seen when 1:20 diluted primary antibody was applied. Approximately 18.4% of tumor nuclei were immunoreactive for Ki-67 (Fig. 2d). Ultrastructural examination indicated parallel thin cytoplasmic processes separated by collagen fibers containing a few pinocytotic vesicles (Fig. 3). No external lamina was detected. Interphase FISH demonstrated that >70% of observed nuclei had a decreased signal for the centromeric probe for chromosomes 13/21 (Fig. 4a). More than 85% of nuclei had one signal for the 13q subtelomeric probe (Fig. 4b). No abnormality was found with the 21q (Fig. 4c) or 22q (Fig. 4d) subtelomeric probe.

DISCUSSION

Perineurioma is usually a benign soft-tissue tumor derived from perineurial cells. The malignant subtype of perineurioma has been occasionally described as MPNST with perineurial cell differentiation.[3,4,18] Tumors with an intermediate malignancy have also been reported by Hirose *et al.*[5] These tumors presented with a relatively small number of mitoses, infiltrative growth and no necrosis. Only seven of these tumors with low-grade malignant potential have been reported and the clinicopathological features are summarized in Table 1. Age at diagnosis ranged between 11 and 76 years. There is a slight male predominance and no predilection for tumor location. No necrosis was detected and only the current patient presented with hemorrhage. Mitotic figures were seen occasionally and there was a moderate increase in Ki-67 index (<20%). In three out of the seven described cases the tumor recurred locally. Only one patient with overt malignant transformation 10 years after the initial presentation developed multiple distant metastases and died of the disease.[7]

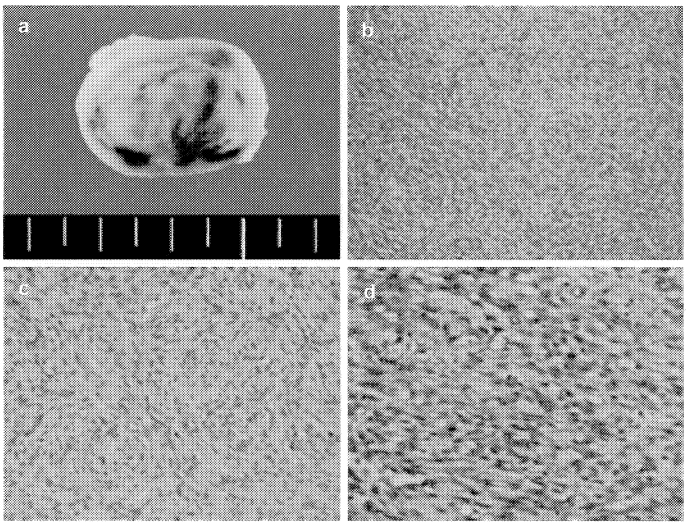

Figure 1 Pathological tumor features. (**a**) Cut surface showing a demarcated tumor presenting with a central infarction and focal hemorrhage. (**b**) Microscopic appearance of the tumor showing spindle cells proliferating in a storiform architecture (HE). (**c**) Tumor cells presenting with perivascular whorls (HE). (**d**) Mitotic figures are observed at 5/10 high-power fields on average (HE).

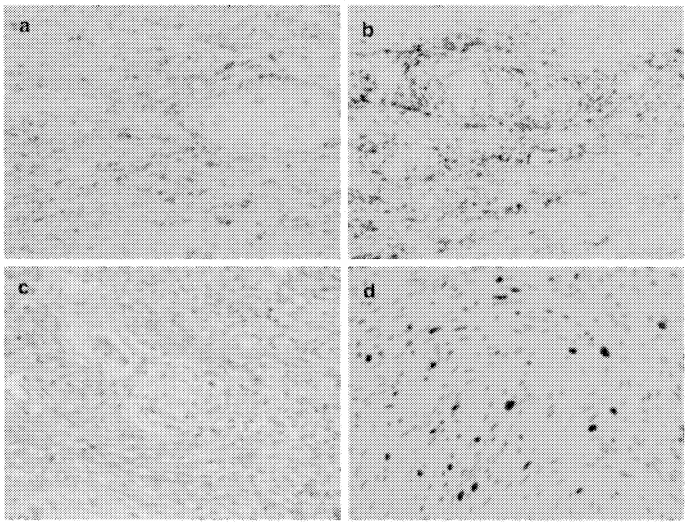

Figure 2 Immunohistochemical tumor features. (**a**) Cell membrane is stained diffusely for glucose transporter protein 1. (**b**) Claudin-1 had a granular expression pattern in the cytoplasm. (**c**) Epithelial membrane antigen is diffusely positive when non-diluted primary antibody is applied. (**d**) Ki-67 index is approximately 18.4%.

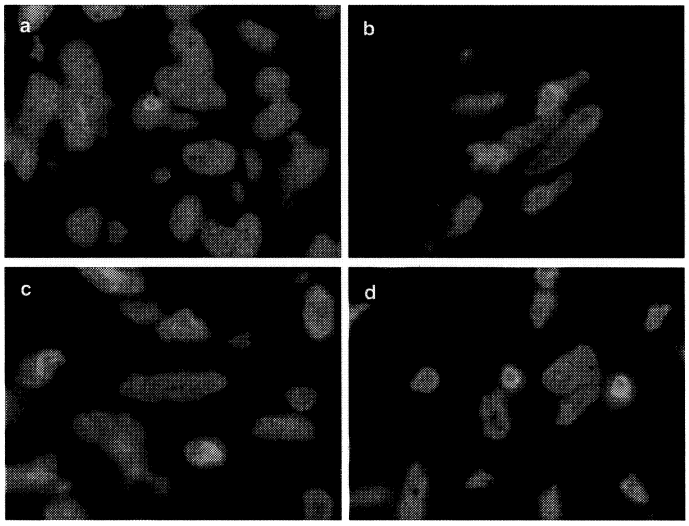

Figure 4 Interphase fluorescence *in situ* hybridization (FISH) on paraffin section. (**a**) Less than three signals are apparent in >70% of the observed nuclei using the centromeric probe for chromosome 13/21. (**b**) More than 85% of nuclei demonstrate one signal using the 13q subtelomeric probe. (**c**) More than 70% of nuclei present with two signals using the 21q subtelomeric probe. (**d**) More than 80% of nuclei show two signals using the 22q subtelomeric probe.

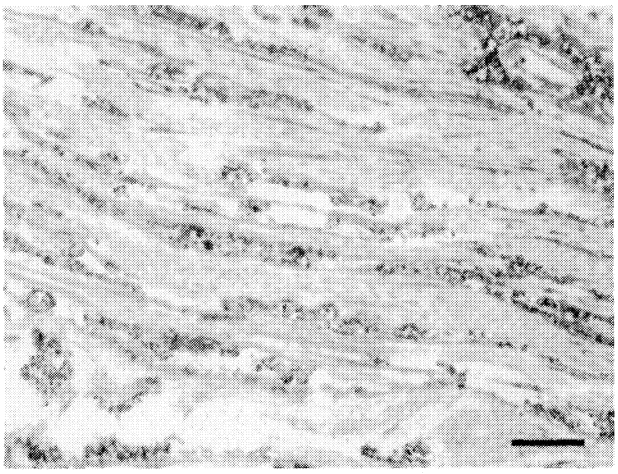

Figure 3 Ultrastructural image of the tumor showing thin cytoplasmic processes organized in parallel and separated by collagen fibers. A few pinocytotic vesicles are visible but no external lamina. Scale bar, 2 μm.

Hornick and Fletcher reported 14 cases of perineurioma with the following atypical features: scattered pleomorphic cells, an abrupt transition from typical morphology to a markedly hypercellular area with cytological atypia, diffuse infiltration of skeletal muscle, and what they called 'atypical perineurioma'.[19] These atypical histological features are recognized as degenerative changes seen in ancient schwannomas and atypical neurofibromas.[19] Atypical perineurioma cases contained very low mitotic figures (0–7/30 HPF), nearly equal to those of conventional perineurioma cases (0–13/30 HPF), and no necrosis.[19] The present tumor demonstrated a transition from a conventional appearance to a hypercellular area, but no marked cytological atypia. No pleomorphic cells or skeletal muscle invasion was observed. Mitotic figures were easily observed (5/10 HPF). According to the morphological criteria described by Hornick and Fletcher,[19] the present case cannot be classified as 'atypical perineurioma' because of this brisk mitotic activity and lack of cytological atypia suggestive of degeneration.

Perineuriomas are benign tumors and usually lack mitotic figures and necrosis.[2] In contrast, MPNST with perineurial cell differentiation (malignant perineurioma) usually have obvious mitoses and necrosis.[5] The present tumor had a relatively low mitosis count and no coagulative necrosis. Larger perineurioma tumors might cause central infarction.[19] Accordingly, the present case was considered to be an intermediate grade of perineurial tumor in between conventional perineurioma and malignant perineurioma (WHO grade III), and should be included in the group of LGMPN proposed by Hirose *et al.*[4] corresponding to WHO grade II tumors.

The diagnosis of malignant perineurioma can be difficult without ultrastructural examination. Immunoreactivity for EMA is often faint or focal, and positive EMA staining is not specific for perineurioma. Recent reports showed that Glut1 and claudin-1 can be useful markers for the diagnosis of perineurioma,[20,21] but these markers have not been studied in malignant perineurioma. Immunoreactivity for EMA in the present tumor was observed when non-diluted primary antibody was used but was not seen when primary antibody was applied at the concentration recommended by the manufacturer. This tumor did not show any immunohistochemical staining for type IV collagen but was positive for Glut1 and claudin-1, suggesting that Glut1 and claudin-1 are also useful markers for the diagnosis of LGMPN.

Cytogenetic studies of perineurioma have shown abnormalities of chromosome 22 or the *NF2* gene (22q12) in many cases.[11–14] Loss of chromosome 13 has been reported in only one case of soft-tissue perineurioma without malignant features.[16] Cytogenetic abnormalities in malignant perineurioma have not been examined and described so far. In the current case interphase FISH indicated a loss of signal for the 13/21 centromeric probe and the 13q subtelomeric probe but no abnormality for the 21q subtelomeric probe, thereby confirming loss of chromosome 13. Furthermore, interphase FISH using the 22q subtelomeric probe demonstrated no loss of signal. These results suggest that a chromosome 13 abnormality without a chromosome 22 disorder might also be involved in LGMPN.

Table 1 Clinicopathological features of low-grade malignant soft-tissue perineurioma

Authors	Age/Sex	Tumor location	Tumor size (cm)	Necrosis/ Hemorrhage	Mitoses (HPF)	Ki-67 index (%)	Recurrence/ Metastasis	Treatment	Follow up
Hirose *et al.*[5]	11/M	R, face	1.5	–/ND	ND	10.7	–/–	Ex + Ch + Ra	AWOD 56 months
	26/M	L, back	11	–/ND	ND	9.8	+/–	Ex + Ra	AWOD 75 months
	55/F	R, thigh	7	–/ND	ND	6.9	+/–	Ex	AWOD 55 months
Karaki *et al.*[7]	39/M	R, paravertebra	6	ND/ND	–	ND	+/+	Ex	DOD 10 years
Zamecnik *et al.*[8]	25/F	L, groin	2	ND/ND	1/20	2	–/–	Ex	AWOD 32 months
Rosenberg *et al.*[9]	70/M	L, arm	3	–/–	1/10	ND	–/–	Ex	AWOD 8 months
Suster *et al.*[10]	76/F	R, thigh	6.5	–/–	1–2/10	ND	ND	Ex	ND
Present case	60/M	L, wrist	2.8	–/+	5/10	18.4	–/–	Ex	AWOD 12 months

AWOD, alive without disease; Ch, chemotherapy; DOD, died of disease; Ex, surgical excision; HPF, high-power fields; L, left; ND, not determined; R, right; Ra, radiation therapy.

Local recurrence and distant metastases are rare in malignant perineuriomas, which is why the prognosis for malignant perineurioma is more favorable than for conventional MPNST.[5] LGMPN also sporadically displays recurrences and rare metastases (Table 1). A patient with LGMPN showing malignant transformation developed metastases after 10 years and died of the disease.[7] Although only eight LGMPN have been described in the past, there are only minor differences between the prognoses for malignant and low-grade malignant perineurioma, and these tumors are identified mainly by morphological features and proliferative activity. Further analysis of additional cases and longer follow-up periods are needed to distinguish between LGMPN (WHO grade II) and malignant perineurioma (WHO grade III).

ACKNOWLEDGMENTS

The authors thank Dr Takanori Hirose (Department of Pathology, Saitama Medical School, Saitama, Japan) and Dr Masanori Hisaoka (Department of Pathology and Oncology, School of Medicine, University of Occupational and Environmental Health, Kitakyushu, Japan) for their useful comments. This work was supported by a Grant for Promoted Research from Kanazawa Medical University (S2006-3).

REFERENCES

1 Lazarus SS, Trombetta LD. Ultrastructural identification of a benign perineurial cell tumor. *Cancer* 1978; **41**: 1823–9.
2 Macarenco RS, Ellinger F, Oliveira AM. Perineurioma: A distinctive and underrecognized peripheral nerve sheath neoplasm. *Arch Pathol Lab Med* 2007; **131**: 625–36.
3 Hirose T, Sano T, Hizawa K. Heterogeneity of malignant schwannomas. *Ultrastruct Pathol* 1988; **12**: 107–16.
4 Hirose T, Sumitomo M, Kudo E *et al.* Malignant peripheral nerve sheath tumor (MPNST) showing perineurial cell differentiation. *Am J Surg Pathol* 1989; **13**: 613–20.
5 Hirose T, Scheithauer BW, Sano T. Perineurial malignant peripheral nerve sheath tumor (MPNST): A clinicopathologic, immunohistochemical, and ultrastructural study of seven cases. *Am J Surg Pathol* 1998; **22**: 1368–78.
6 Scheithauer BW, Woodruff JM, Antonescu CR. Perineurioma. In: Louis DN, Ohgaki H, Wiestler OD, eds. *WHO Classification of Tumours of the Central Nervous System.* Lyon: IARC Press, 2007; 158–9.
7 Karaki S, Mochida J, Lee YH, Nishimura K, Tsutsumi Y. Low-grade malignant perineurioma of the paravertebral column, transforming into a high-grade malignancy. *Pathol Int* 1999; **49**: 820–25.
8 Zamecnik M, Koys F, Gomolcak P. Atypical cellular perineurioma. *Histopathology* 2002; **40**: 296–9.
9 Rosenberg AS, Langee CL, Stevens GL, Morgan MB. Malignant peripheral nerve sheath tumor with perineurial differentiation: "Malignant perineurioma". *J Cutan Pathol* 2002; **29**: 362–7.
10 Suster D, Plaza JA, Shen R. Low-grade malignant perineurioma (perineurial sarcoma) of soft tissue: A potential diagnostic pitfall on fine needle aspiration. *Ann Diagn Pathol* 2005; **9**: 197–201.
11 Emory TS, Scheithauer BW, Hirose T, Wood M, Onofrio BM, Jenkins RB. Intraneural perineurioma. A clonal neoplasm associated with abnormalities of chromosome 22. *Am J Clin Pathol* 1995; **103**: 696–704.
12 Giannini C, Scheithauer BW, Jenkins RB *et al.* Soft-tissue perineurioma. Evidence for an abnormality of chromosome 22, criteria for diagnosis, and review of the literature. *Am J Surg Pathol* 1997; **21**: 164–73.
13 Sciot R, Cin PD, Hagemeijer A, De Smet L, Van Damme B, Van den Berghe H. Cutaneous sclerosing perineurioma with cryptic NF2 gene deletion. *Am J Surg Pathol* 1999; **23**: 849–53.
14 Lasota J, Fetsch JF, Wozniak A, Wasag B, Sciot R, Miettinen M. The neurofibromatosis type 2 gene is mutated in perineurial cell tumors: A molecular genetic study of eight cases. *Am J Pathol* 2001; **158**: 1223–9.
15 Brock JE, Perez-Atayde AR, Kozakewich HP, Richkind KE, Fletcher JA, Vargas SO. Cytogenetic aberrations in perineurioma: Variation with subtype. *Am J Surg Pathol* 2005; **29**: 1164–9.
16 Mott RT, Goodman BK, Burchette JL, Cummings TJ. Loss of chromosome 13 in a case of soft tissue perineurioma. *Clin Neuropathol* 2005; **24**: 69–76.
17 Sato K, Ueda Y, Sugaya J, Ozaki M, Hisaoka M, Katsuda S. Extrauterine endometrial stromal sarcoma with JAZF1/JJAZ1 fusion confirmed by RT-PCR and interphase FISH presenting as an inguinal tumor. *Virchows Arch* 2007; **450**: 349–53.
18 Fisher C, Carter RL, Ramachandra S, Thomas DM. Peripheral nerve sheath differentiation in malignant soft tissue tumours: An ultrastructural and immunohistochemical study. *Histopathology* 1992; **20**: 115–25.
19 Hornick JL, Fletcher CD. Soft tissue perineurioma: Clinicopathologic analysis of 81 cases including those with atypical histologic features. *Am J Surg Pathol* 2005; **29**: 845–58.
20 Hirose T, Tani T, Shimada T, Ishizawa K, Shimada S, Sano T. Immunohistochemical demonstration of EMA/Glut1-positive perineurial cells and CD34-positive fibroblastic cells in peripheral nerve sheath tumors. *Mod Pathol* 2003; **16**: 293–8.
21 Folpe AL, Billings SD, McKenney JK, Walsh SV, Nusrat A, Weiss SW. Expression of claudin-1, a recently described tight junction-associated protein, distinguishes soft tissue perineurioma from potential mimics. *Am J Surg Pathol* 2002; **26**: 1620–26.

１．研究課題名：デオキシリボ核酸分解酵素Ⅰ（DNase Ⅰ）による急性冠症候群の迅速診断
（研究番号　S2006-4）

２．キーワード：１）デオキシリボ核酸分解酵素Ⅰ（Deoxyribonuclease Ⅰ）
２）急性冠症候群（Acute Coronary Syndrome）
３）診断マーカー（Diagnostic Marker）
４）不安定狭心症（Unstable Angina Pectoris）

３．研究代表者：河合　康幸・医学部・助教・循環制御学（循環器内科学）

４．研 究 目 的

これまで我々は血清デオキシリボ核酸分解酵素Ⅰ（DNase Ⅰ）活性が急性心筋梗塞（AMI）診断の有用な診断マーカーになり得ること、さらに一過性心筋虚血の診断マーカーとしても有用であることを報告してきた。現在ではAMIと不安定狭心症(UAP)はいずれも不安定プラークの崩壊とそれに引き続く血栓形成が原因で発症することが知られ、急性冠症候群として包括されている。しかしUAPは患者受診時の自覚症状および心電図変化に乏しいこと、既存の心筋逸脱マーカーが陰性であることが多いことなどがその確定診断を困難にしてきた。さらにUAPを疑い緊急冠動脈造影検査を施行しても冠動脈病変を認めない、いわゆる胸痛症候群（CPS）患者であることも多く、患者負担や医療経済上もUAPを簡便かつ的確に診断できるマーカーが望まれる。上述の結果よりDNase ⅠはAMIのみならずUAPにおいても上昇を示す可能性がある。したがって本研究の目的は通常の非侵襲的検査では診断し得ないUAP診断に血清DNase Ⅰ活性が有用であるかを明らかにすること、またそのための迅速診断キットを開発することである。

５．研 究 計 画

(1) UAPの診断マーカーとしての血清DNase Ⅰ活性測定の有用性の検証

対象は胸痛後6時間以内に来院したUAPが疑われる患者である。ただしST上昇型急性心筋梗塞、UAP以外の器質的疾患（大動脈解離、急性肺血栓塞栓症、消化器疾患など）を除外する。問診、心電図、血液生化学的検査を行った後、全例緊急冠動脈造影を施行し、冠動脈病変の有無を確認する。すべての患者に同意を得て、来院時、3、6、12、24時間後に経静脈的に採血を行う。採血したサンプルは活性測定まで-80℃の冷凍庫に保存する。血清DNase Ⅰ活性はsingle radial diffusion method（SRED法）にて行う。血清DNase Ⅰ活性の最大値とその3時間前後の活性値から変化率（%）を算出する。冠動脈造影で冠動脈に器質的有意狭窄を認めず、他の器質的疾患が除外され、冠攣縮誘発試験が陰性で、冠スパズムが否定された症例を胸痛症候群（CPS）と定義し、UAPに対するコントロールとした。

(2) 血清DNase Ⅰ活性の迅速測定法の開発

SRED法での血清DNase Ⅰ活性測定は約20時間を要し、迅速な対応が要求されるUAPの診断に利用することができない。そこで抗DNase Ⅰ抗体を用いて、抗原・抗体法による血清DNase Ⅰ濃度測定法を研究する。さらにこの抗原・抗体法にて迅速定量キットを開発する。

(3) 多施設共同研究によるUAP診断マーカーとしての有用性の検証と血清DNase Ⅰ検査法の標準化

迅速定量キットを用いて、他の施設に協力を依頼し、多施設共同研究によるUAP診断マーカーとしての有用性の検証と血清DNase Ⅰ検査法の標準化を行う。この研究からDNase ⅠのUAP診断マーカーとしての診断感度・特異度を検討する。

６．研 究 成 果

(1) UAPの診断マーカーとしての血清DNase Ⅰ活性測定の有用性の検証

UAP群（N=13）の患者背景は、平均年齢62±11歳、男性10人（77%）であった。UAP群では来

院時、全例胸痛はなく、心電図異常を認めない患者が８人（62%）、トロポニンＴあるいはFABPが陰性の患者が６人(46%)であった。一方、CPS群（N=8）は平均年齢67±15歳、男性６人（75%）であった。最大血清DNase Ⅰ活性はUAP群20.0±13.9×10^{-6} U/μlでCPS群9.7±2.5×10^{-6} U/μlと比較して有意に高値であった（P=0.03）。また血清DNase Ⅰ活性の変化率もUAP群30.6±28.1%、CPS群11.1±9.9%とUAP群で有意ではないものの高値であった（P=0.053）。

心電図異常および経過中にトロポニンＴの上昇を認めない症例は４例(31%)であり、最大DNase Ⅰ活性、血清DNase Ⅰ活性変化率はそれぞれ23.2±14×10^{-6} U/μl、52.2±44%でいずれもコントロールに比べて有意に高値であった（P=0.02、P=0.02）。

(2) 血清DNase Ⅰ活性の迅速測定法の開発

抗DNase Ⅰ抗体を用いて抗原・抗体法による血清DNase Ⅰ濃度測定法を開発した。図１に示すように、r=0.846と血清DNase Ⅰ活性との良好な相関を認めた。

(3) 多施設共同研究によるUAP診断マーカーとしての有用性の検証と血清DNase Ⅰ検査法の標準化

現在、他施設との共同研究を検討中で、期間内に行うことができなかった。

７．研究の考察・反省

これまで来院時胸痛の自覚がなく、心電図異常やこれまでに知られている心筋逸脱酵素の有意な上昇がない、UAP患者を診断し得る血液生化学マーカーはほとんど報告がない。(1)の結果から血清DNase ⅠはUAPの有用な診断マーカーになる可能性が示唆された。

また血清DNase Ⅰ濃度が血清DNase Ⅰ活性と良好な相関を示すことより、検査室や救急室での血清DNase Ⅰレベルの測定できる可能性がある。

図１

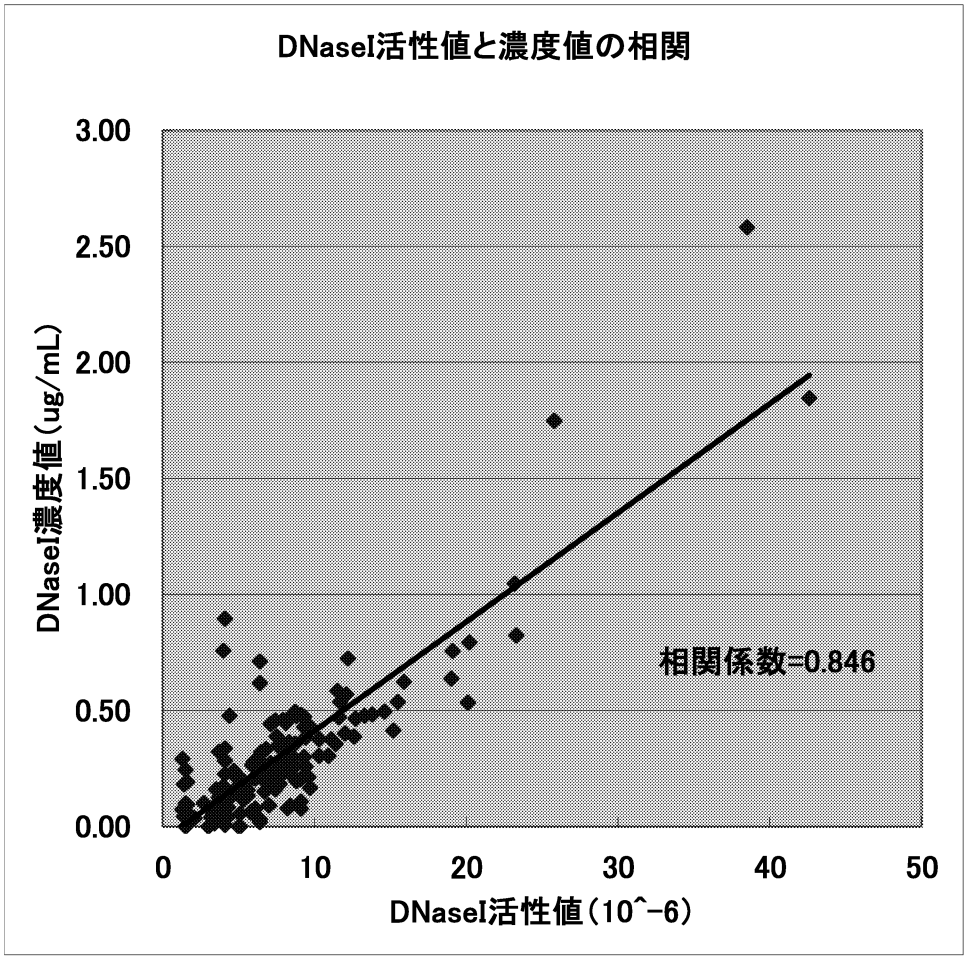

本研究の反省点

(1) 採血のシステム作りに時間がかかり十分な症例を集めることができなかったことから、研究発表や論文作成に至らなかった。平成21年度中に学会発表と論文投稿を予定している。

(2) 使用した抗体は抗ヒトDNase Ⅰポリクロナール抗体であり、臨床応用のためには血清DNase Ⅰ活性と良好な相関を示すモノクロナール抗体を作成する必要がある。平成20年度から21年にかけてモノクロナール抗体を作成する。

(3) 多施設での共同研究に至っていない。迅速キットが開発できれば多施設共同研究を行う。

以上が本研究の反省点である。

８．研 究 発 表

統計処理に十分な症例数が得られた時点で、研究発表を行う。

１．研究課題名：能登地方における遺伝性神経疾患の特徴について（研究番号 S2006-5）

２．キーワード：１）遺伝性神経疾患　(hereditary neurological disease)
２）遺伝子変異　(gene mutation)
３）遺伝性痙性対麻痺（hereditary spastic paraplegia）
４）VWM 型白質脳症（leukoencephalopathy with vanishing white matter）
５）遺伝性脊髄小脳変性症（hereditary spinocerebellar degeneration）

３．研究代表者：松井　大・医学部・講師・脳脊髄神経治療学（神経内科学）

４．研 究 目 的

近年の分子生物学の進歩により、遺伝性の神経疾患において次々と原因遺伝子が同定されてきた。一方、これらの基礎研究成果が臨床の現場に必ずしも反映されているとは限らず、能登地方は、神経難病が多いと推定されているものの、遺伝子診断による確定診断が遅れており、どのような割合で遺伝性神経疾患が存在するのか実態は明らかになっていない。金沢は、加賀藩のもとで築かれた文化の中で、歴史的には他の領域との交流が少なかったことも予測され、能登地方の遺伝性神経疾患の特徴について調査することは極めて重要であると思われる。能登地方における遺伝性神経疾患の実態を明らかにし、個々の症例の臨床知見と遺伝子検査結果との関連を調べることを本研究の目的とする。

５．研 究 計 画

金沢医科大学神経内科および関連病院に入院中あるいは外来に通院中の神経疾患患者の末梢血から genomic DNA を抽出する。Hereditary spastic paraplegia（以下 HSP と略）に関しては、SPG3A(atlastin)の exon12 の変異 Tyr459Cys の RFLP 解析を試行する。具体的には、PCR プライマー(SPG3A exon 12F:CCAGTCCCATTTATAGTCATGCCTCG, SPG3A exon 12R: GTGTGCTGAATT TAGTT G) を作成し, genomic DNA に対して、PCR を試行する。PCR 産物を 1.2% アガロースゲルに泳動して確認後、PCR 産物から DNA を抽出し、Afl III を反応させ、1.2 %アガロースゲルで泳動する。

Leukoencepalopathy with vanishing white matter に関しては、 EIF2B5(E1)-F: TACTGCGTGCGGTGGCAGCTT,EIF2B5(E1)-R:GCCGAAATGAGAACTTGCTCC,EIF2B5(E2)-F:CACTGT TTGGAAATACGAATAGAGG,EIF2B5(E2)-R:CCCCTTAGTTACATTCATCCTG,EIF2B5(E3/4/5)-F:CGA GAA GGACTGTGAGTGCTGA,EIF2B5(E3/4/5)-R:GGCCTTCTAAGGGGACAATAAC の６種類のプライマーを作成し、PCR を試行する。次に PCR 産物から直接塩基配列を解析する。解析は、GENETYX-MAC を用いる。遺伝性脊髄小脳変性症に関しては、国内で頻度の高い SCA-1,2,3,6, DRPLA から解析を始める。

６．研 究 成 果

100 症例に対して、HSP SPG3A の exon 12 の変異 Tyr459Cys の RFLP 解析を行った所、626bp のバンドを認めるのみで、AflIII で切断される PCR 産物は認めなかった。もし変異があれば 410bp と 216bp の２本のバンドを認めるため、検索した 100 症例におい

ては、SPG3A の Tyr459Cys の変異は認めないことがわかった。

遺伝歴があり軽度知能低下、先天性白内障を合併した HSP の症例に関しては、イタリアの IRCCS(Istituto di Ricovero e Cura a Carattere Scientifico)と共同で、現在遺伝子変異を解析中である。 Leukoencephalopathy with vanishing white matter に関しては、上記 PCR プライマーにて、PCR 産物を認め、一部は塩基配列の決定が可能であることを確認している。

原因不明の白質脳症を呈する当科入院患者において京都府立医科大学神経内科と共同で CADASIL(Cerebral autosomal dominant arteriopathy with subcortical infarcts and leukoencephalopathy) の原因遺伝子である Notch 3 Arg182Cys の遺伝子変異を見出した。 この変異は、CADASIL の中でも頻度が高い変異として報告されているものである。また、国立病院機構　新潟病院と共同で当科入院患者において遺伝性脊髄小脳変性症の中の SCA6 の遺伝子異常である Ca チャネルのトリプレットリピートの延長を見出した。

７．研究の考察・反省

当初の予想通り、まだ確定診断のついていない遺伝性神経疾患が多数存在する可能性があることが考えられた。能登地方の遺伝性神経疾患の特徴を見出すには、長期間にわたる地道な遺伝子解析のデータの蓄積が必要であると思われた。そして、大学病院だけでなく､能登地方の様々な病院からの症例の紹介が必要であるように思われた。

残念ながら、研究代表者は、県外の他施設に異動となったため、能登地方の遺伝性神経疾患の解析を継続することは困難な状況となった。

８．研 究 発 表

特になし。

１．研究課題名：心室筋における異常自動能の発生機序とバイオペースメーカーシステム設計に関する非線形力学的解析（研究番号　S2006-6）

２．キーワード：１）ヒト心室筋細胞（human ventricular myocyte）
２）異常自動能（abnormal automaticity）
３）バイオロジカル・ペースメーカー（biological pacemaker）
４）分岐理論（bifurcation theory）
５）コンピュータ・シミュレーション（computer simulation）

３．研究代表者：倉田　康孝・医学部・准教授・生理機能制御学（生理学Ⅱ）

４．研 究 目 的

心室筋異常自動能の発生機序を解明することは、心臓生理学並びに不整脈学の最も重要な課題である。特に心室筋の早期後脱分極（ＥＡＤ）はＱＴ延長症候群（ＬＱＴＳ）における致死的不整脈の成因と考えられており、ＥＡＤの発生機序と最適制御方法を検討することがＬＱＴＳにおける致死的不整脈の予防・治療法の確立に必要不可欠である。また近年、徐脈性不整脈の新たな治療法としてバイオペースメーカー（ＢＰ）の開発が期待されているが、最適ＢＰシステムの設計を行うためには、心筋自動能の発生機序を深く理解する必要がある。心筋における自動能の発現は、非線形システムに生じる分岐現象（安定性・ダイナミクスの質的変化）の一つと考えられ、従ってその発生機序の解明には、非線形力学系の分岐理論に基づく新たな理論的・実験的アプローチが必要不可欠であると考えられる。

本研究の目的は、非線形力学的解析手法により、1）心室筋細胞の自動能発現過程における分岐構造（安定性とダイナミクスの変化）を解析して異常自動能（ＥＡＤ）発現の非線形力学的機序を解明すること、さらに 2）心室筋由来ＢＰ作成・機能強化のためのシステム設計を行うことである。分岐理論を基礎とした新しいアプローチにより、心筋自動能発生機序の統一的理解と体系的記述、人工ペースメーカーに代わるＢＰ開発のための理論的基盤を確立することを最終目標とする。

５．研 究 計 画

本研究では、まずヒト心室筋細胞の非線形力学系モデル（実験的に観測される異常自動能の再現が可能であり、かつ分岐構造解析に適したもの）を用い、本モデルシステムの平衡点と活動電位ダイナミクス及びその安定性のパラメータ依存性変化を解析するためのプログラム群を構築する。モデルシステムのパラメータ依存性ダイナミクスを表わす分岐図を作成することにより、心室筋における異常自動能（ＥＡＤ・脱分極誘発自動能）発現の条件と力学的機序（各イオンチャネル電流系の役割）を明らかにする。

さらに、ヒト心室筋由来ＢＰ細胞と非ペースメーカー細胞（ＮＰ細胞）をギャップコンダクタンス（ＧＣ）で連結した２細胞カップルモデルを構築し、ＢＰ細胞の電気緊張性負荷に対するロバスト性と心室筋ドライブ機能を評価するためのプログラム群を作成する。ＢＰ細胞の構造安定性（過分極負荷に対するロバスト性）と心室筋ドライ

ブ機能強化における各種自動能調節チャネル電流系（ペースメーカー電流）導入の効果を比較解析することにより、ヒト心室筋細胞を用いた最適ＢＰ作成のためのシステム設計を試みる。

６．研 究 成 果

（１）心室筋におけるＥＡＤの発生機序：ヒト心室筋細胞モデルを用いた解析

まず、本研究で開発した分岐構造解析システムを用いて、ヒト心室筋細胞モデルにおけるＥＡＤの発現条件・機序並びにその最適制御方法を非線形力学的観点から検証した。本研究では、イオンチャネル遺伝子の異常に起因する先天性ＬＱＴＳとして、①遅延整流K^+チャネル電流の遅い活性化成分(IKs)の機能異常（ＬＱＴ１）、②遅延整流K^+チャネル電流の速い活性化成分(IKr)の機能異常（ＬＱＴ２）、③INaの非不活性化成分の出現（ＬＱＴ３）に注目し、パラメータ（チャネルコンダクタンス）を調節することによりＬＱＴＳにおける活動電位持続時間の延長とＥＡＤをシミュレート(再現)することができた。モデルシステムの平衡点（零電流電位）とその安定性及び活動電位ダイナミクスのパラメータ依存性変化を分岐図で解析することにより、以下の結論を得た。

① ＬＱＴ２及び３におけるＥＡＤは、IKsの遅い活性化(再分極遅延)に伴う脱分極側平衡点の不安定化(ホップ分岐)によって生じる一過性のリミットサイクルとみなすことができる。

② ＬＱＴ２及び３では、IKs活性化を促進(加速)することがＥＡＤの抑制に最も有効である。

これらの成果は、ＥＡＤ制御―ＬＱＴＳにおける致死的不整脈の予防と治療―の問題を分岐制御の問題に帰着できる可能性を示すものである。

（２）ヒト心室筋由来ＢＰの機能強化におけるペースメーカー電流導入の意義

先の研究でモデル細胞自動能の過分極負荷に対する構造安定性を検討した結果、心室筋由来ＢＰの過分極負荷に対するロバスト性は洞結節に比べて低いことが明らかとなった。既存のイオン電流系の修飾では過分極負荷に対する構造安定性の強化は不可能であり、洞結節に存在する（正常心室筋にはない）自動能調節チャネル（ペースメーカー電流）の導入・発現が不可欠であると考えられた。そこで、ＢＰ細胞とＮＰ細胞を連結した２細胞カップルモデルを用い、ヒト心室筋由来ＢＰ細胞モデルの電気緊張性負荷に対するロバスト性と心室筋ドライブ機能に対する各ペースメーカー電流（①過分極活性化陽イオンチャネル電流Ih、②Ｔ型Ca^{2+}チャネル電流ICa,T、③持続性内向き電流Ist、④低電位活性化Ｌ型Ca^{2+}チャネル電流ICa,LD）導入の影響を解析した。各電流の導入における分岐構造(平衡点・ダイナミクス及び分岐点)の変化を解析した結果、以下の結論を得た。

① ＢＰ細胞の電気緊張性負荷に対する構造安定性及び心室ドライブ機能の強化には、比較的不活性化の遅いペースメーカー電流Istの導入が最も有効である。

② Ihは心室筋からの電気緊張性負荷に対するＢＰ細胞の構造安定性及び心室筋ドライブ機能を強化できないが、Istとの共発現によりＢＰ細胞の過分極負荷に対する構造安定性は劇的に増大する。

③ ICa,T及びICa,LDもＢＰ細胞の電気緊張性負荷に対する構造安定性及び隣接心筋

ドライブ機能を強化できるが、その作用は比較的弱い（高密度が必要である）。これらの成果は、心筋細胞モデルの分岐構造解析が、チャネル遺伝子発現調節によるＢＰ機能強化方法の開発・確立（ＢＰシステム設計）をも可能にすることを示唆している。

７．研究の考察・反省

本研究では、モデル心筋細胞の分岐構造解析により、１）ヒト心室筋におけるＥＡＤの発生機序と制御方法、２）ヒト心室筋由来ＢＰ細胞の構造安定性・心室ドライブ機能の強化方法を明らかにした。さらに、本研究で確立した分岐構造解析手法を「洞結節自動能の発生機序及び構造安定性における結節内部位差とそのイオン機序（Na^+チャネル電流の役割）」の解析にも適用し、洞結節の辺縁部細胞は中心部細胞に比べて過分極負荷に対する構造安定性が高いこと、ペースメーカーの安定な歩調取りとドライブ機能の維持にはNa^+チャネル電流が不可欠であることを明らかにした（研究論文２）。これらの成果は、自動能発生機序及びその制御方法の解明やＢＰシステム設計において、非線形力学系理論に基づく心筋細胞分岐構造の解析が極めて有用であることを示している。

このように非線形システム論的アプローチは有用かつ不可欠な方法論であると考えられるが、現時点では問題点も多い。その第一は、モデル自体の完成度が低いことである。現在までに多くの心筋細胞モデルが開発されているが、いずれも実在の心筋システムの特性を十分に再現できるものではなく、さらなる実験的検証とモデルの継続的改良が必要であろう。また、現実の心臓システムは多細胞システムであり、組織として機能する。従って将来的には、多細胞モデルを用いた組織レベルでの心臓システムの分岐構造を解析する必要があると考えられる。このようなアプローチが、臓器レベルでの不整脈発生機序の統一的理解と体系的記述を可能にすると共に、徐脈性不整脈の新しい治療法としてのＢＰシステムの設計や頻脈性不整脈の合理的制御方法の確立を可能にする（理論的基盤を与える）と信じている。

８．研 究 発 表

(1) Kurata Y, Matsuda H, Hisatome I, Shibamoto T. Effects of pacemaker currents on creation and modulation of human ventricular pacemaker: theoretical study with application to biological pacemaker engineering. Am J Physiol Heart Circ Physiol 2007; 292: H701-H718.（MLDB）

(2) Kurata Y, Matsuda H, Hisatome I, Shibamoto T. Regional difference in dynamical property of sinoatrial node pacemaking: Role of Na^+ channel current. Biophys J 2008; 95: 951-977.（MLDB）

Am J Physiol Heart Circ Physiol 292: H701–H718, 2007.
First published September 22, 2006; doi:10.1152/ajpheart.00426.2006.

Effects of pacemaker currents on creation and modulation of human ventricular pacemaker: theoretical study with application to biological pacemaker engineering

Yasutaka Kurata,[1] Hiroyuki Matsuda,[1] Ichiro Hisatome,[2] and Toshishige Shibamoto[1]

[1]*Department of Physiology, Kanazawa Medical University, Ishikawa, and* [2]*Division of Regenerative Medicine and Therapeutics, Tottori University Graduate School of Medical Science, Yonago, Japan*

Submitted 28 April 2006; accepted in final form 16 September 2006

Kurata Y, Matsuda H, Hisatome I, Shibamoto T. Effects of pacemaker currents on creation and modulation of human ventricular pacemaker: theoretical study with application to biological pacemaker engineering. *Am J Physiol Heart Circ Physiol* 292: H701–H718, 2007. First published September 22, 2006; doi:10.1152/ajpheart.00426.2006.—A cardiac biological pacemaker (BP) has been created by suppression of the inward rectifier K^+ current (I_{K1}) or overexpression of the hyperpolarization-activated current (I_h). We theoretically investigated the effects of incorporating I_h, T-type Ca^{2+} current ($I_{Ca,T}$), sustained inward current (I_{st}), and/or low-voltage-activated L-type Ca^{2+} channel current ($I_{Ca,LD}$) on *1*) creation of BP cells, *2*) robustness of BP activity to electrotonic loads of nonpacemaking (NP) cells, and *3*) BP cell ability to drive NP cells. We used a single-cell model for human ventricular myocytes (HVMs) and also coupled-cell models composed of BP and NP cells. Bifurcation structures of the model cells were explored during changes in conductance of the currents and gap junction. Incorporating the pacemaker currents did not yield BP activity in HVM with normal I_{K1} but increased the critical I_{K1} conductance for BP activity to emerge. Expressing I_h appeared to be most helpful in facilitating creation of BP cells via I_{K1} suppression. In the coupled-cell model, I_{st} significantly enlarged the gap conductance (G_C) region where stable BP cell pacemaking and NP cell driving occur, reducing the number of BP cells required for robust pacemaking and driving. In contrast, I_h enlarged the G_C region of pacemaking and driving only when I_{K1} of the NP cell was relatively low. $I_{Ca,T}$ or $I_{Ca,LD}$ exerted effects similar to those of I_{st} but caused shrinkage or irregularity of BP oscillations. These findings suggest that expressing I_{st} most effectively improves the structural stability of BPs to electrotonic loads and the BP ability to drive the ventricle.

mathematical model; bifurcation analysis; computer simulation

A CARDIAC BIOLOGICAL PACEMAKER (BP) has recently been created by genetic suppression of the inward rectifier K^+ current (I_{K1}) in guinea pig ventricular myocytes (28) or overexpression of the hyperpolarization-activated current (I_h) in canine atrial or Purkinje myocytes (32, 36), suggesting possible development of the functional BP as a therapeutic alternative to the electronic pacemaker (8, 37).

A first step for creation of the functional BP would be engineering of single BP cells, which requires deep understanding of the BP mechanisms. By bifurcation analyses of a mathematical model for human ventricular myocytes (HVMs), we have elucidated (22) the dynamical mechanisms of BP generation in I_{K1}-downregulated HVMs and the roles of individual sarcolemmal currents in HVM pacemaking. We have suggested that *1*) BP activity can be developed by reducing I_{K1} alone in HVMs as in guinea pig ventricular myocytes (41), *2*) the instability of an equilibrium point (EP) with depolarized potentials is essentially important for BP generation, and *3*) the dynamical mechanism of ventricular pacemaking is essentially the same as that of natural sinoatrial (SA) node pacemaking as reported by Kurata et al. (21). In the previous study, however, whether BP cells can be developed from HVMs by incorporating "pacemaker currents," which contribute to phase 4 depolarization in SA node pacemaking, was not clearly shown, with the most efficient way to create BP cells remaining unknown; the pacemaker currents include I_h, T-type Ca^{2+} channel current ($I_{Ca,T}$), sustained inward current (I_{st}), and low-voltage-activated L-type Ca^{2+} channel current ($I_{Ca,LD}$). Therefore, we first investigated whether incorporating these pacemaker currents can yield BP activity and how this affects BP generation during I_{K1} suppression in the model HVM. Our findings suggested that I_h facilitates BP generation during I_{K1} suppression in combination with the other pacemaker currents, although I_{K1} downregulation is necessary for constructing BP cells from HVMs.

Our preliminary study also revealed some drawbacks of the I_{K1}-downregulated HVM pacemaker, compared with the SA node pacemaker, to prevent the creation of functional BPs. They include *1*) relatively low robustness to hyperpolarizing (electrotonic) loads and *2*) low ability to drive adjacent nonpacemaker cells, which may be due to the lack of pacemaker currents. Using a coupled-cell model composed of I_{K1}-deleted BP cells and a nonpacemaking HVM [referred to as "nonpacemaking (NP) cell"], therefore, we further explored the effects of incorporating pacemaker currents on the structural stability of BP cells (robustness of BP activity) to electrotonic modulations and BP cell ability to drive the adjacent NP cell. Our results suggested that $I_{Ca,T}$, I_{st}, and $I_{Ca,LD}$ can, but I_h cannot, significantly improve the structural stability of BPs to electrotonic loads of HVMs and the BP ability to drive the ventricle.

This study indicates that the theoretical approach based on nonlinear dynamics and bifurcation theory may allow us to predict the effects of current modulations on pacemaker cell dynamics accurately and find out how to control the dynamical properties of real myocytes properly. Exploring bifurcation structures of the mathematical model would provide a theoret-

Address for reprint requests and other correspondence: Y. Kurata, Dept. of Physiology, Kanazawa Medical Univ., 1-1 Daigaku, Uchinada-machi, Kahoku-gun, Ishikawa 920-0293, Japan (e-mail: yasu@kanazawa-med.ac.jp).

The costs of publication of this article were defrayed in part by the payment of page charges. The article must therefore be hereby marked "*advertisement*" in accordance with 18 U.S.C. Section 1734 solely to indicate this fact.

ical background for engineering of BP cells and functional BPs from native cardiomyocytes or embryonic stem (ES) cells, i.e., for gene or cell therapy of bradyarrhythmias (8, 37). This study also provides novel insights into the roles of the pacemaker currents in natural SA node pacemaking. Definitions of terms specific to nonlinear dynamics and bifurcation theory are given at the end of THEORY AND METHODS (see also Refs. 21–23, 30).

THEORY AND METHODS

Base Mathematical Model for Human Ventricular Myocytes

We used our HVM model (22) as a modified version of the Priebe-Beuckelmann model (33). More elaborate HVM models were recently developed by Iyer et al. (12) and ten Tusscher et al. (42), which are probably superior to the original or modified Priebe-Beuckelmann model in reproducing experimental data. Nevertheless, these models are much more complex or include vector field functions that are not continuous or smooth, being less suitable for bifurcation analyses (for more details, see Ref. 22). We have therefore chosen to use our model, which is more suitable for bifurcation analyses.

The standard model for the normal activity of single HVMs is described as a nonlinear dynamical system of 15 first-order ordinary differential equations. The membrane current system includes the L-type Ca^{2+} channel current ($I_{Ca,L}$), rapid and slow components of delayed rectifier K^+ currents (denoted I_{Kr} and I_{Ks}, respectively), 4-aminopyridine-sensitive transient outward current (I_{to}), Na^+ channel current (I_{Na}), I_{K1}, background Na^+ ($I_{Na,b}$) and Ca^{2+} ($I_{Ca,b}$) currents, Na^+-K^+ pump current (I_{NaK}), Na^+/Ca^{2+} exchanger current (I_{NaCa}), and Ca^{2+} pump current (I_{pCa}). Time-dependent changes in the membrane potential (V) are described by the equation

$$dV/dt = I_{stim} - (I_{Ca,L} + I_{Kr} + I_{Ks} + I_{to} + I_{Na} + I_{K1} + I_{Na,b} + I_{Ca,b} + I_{NaK} + I_{NaCa} + I_{pCa}) \quad (1)$$

where I_{stim} represents the stimulus current (in pA/pF), being set equal to zero for simulations of BP activity. Details on modifications and expressions of the HVM model are described in our previous article (22).

Our full system includes material balance expressions to define the temporal variation in intracellular Ca^{2+}, Na^+, and K^+ concentrations ($[Ca^{2+}]_i$, $[Na^+]_i$, and $[K^+]_i$), whereas extracellular Ca^{2+}, Na^+, and K^+ concentrations ($[Ca^{2+}]_o$, $[Na^+]_o$, and $[K^+]_o$) were fixed at 2, 140 and 5.4 mM, respectively. As pointed out by Hund et al. (11) and Krogh-Madsen et al. (18), the second-generation model incorporating ion concentration changes exhibits degeneracy (i.e., nonuniqueness of steady-state solutions), not suitable for bifurcation analysis to be applicable to isolated equilibria. One of the ways to remove degeneracy and thus allow bifurcation analyses of isolated equilibria is to make some ionic concentrations fixed (18). Variations in $[K^+]_i$ during changes in bifurcation parameters were relatively small, not significantly altering the model cell behaviors. For stability and bifurcation analyses, therefore, $[K^+]_i$ was fixed at 140 mM.

Incorporation of Pacemaker Currents

To investigate how pacemaker currents contributing to phase 4 depolarization in SA node pacemaking affect bifurcation structures of HVM model cells, we incorporated the formulas of I_h, $I_{Ca,T}$, and I_{st}, which were used for our SA node model (20) or experimentally determined for human cardiomyocytes. The low voltage-activated L-type Ca^{2+} channel (D-LTCC) was recently reported to activate at pacemaker potential regions, i.e., at potentials 10–20 mV more negative than the high-voltage-activated Ca^{2+} channel, contributing to mouse SA node pacemaking (16, 27, 31, 51). Therefore, we also tested the effect of the current mediated by D-LTCC (denoted as $I_{Ca,LD}$). The formulas for individual pacemaker currents are given in APPENDIX B. The origins of the expressions and conductance values tested for each current, as well as those chosen for the original SA node models as mean experimental values, are summarized in Table 1 (for details, see below).

For comparison of the voltage-dependent gating behaviors of the currents tested, steady-state probabilities and time constants of gating variables, as well as the steady-state (window) currents calculated by the steady-state equations for the gating variables, are shown in Fig. 1. To determine the conductance range to be tested for individual currents, we first examined their effects on stability and dynamics of a single BP cell (Fig. 2). Higher conductance of I_h caused a saddle-node bifurcation and cessation of BP activity with drastic increases in $[Na^+]_i$ and $[Ca^{2+}]_i$; higher conductance of $I_{Ca,T}$, I_{st}, or $I_{Ca,LD}$ caused shrinkage of BP oscillations with decrease in upstroke velocity and then cessation of BP activity via Hopf bifurcations. The maximum conductance value to be tested was limited for each current so as not to significantly shrink BP oscillations or not to cause Na^+- or Ca^{2+}-overload conditions (for more details, see below).

I_h. The expressions for I_h were adopted from the rabbit SA node model (20, 49), as well as from experimental studies for human I_h (3, 29). Although all the I_h formulas exerted qualitatively the same effects, the effect of the rabbit SA node I_h was most dramatic, which is probably due to the most positive activation threshold. Thus we show data only for the rabbit SA node I_h. The maximum conductance (g) value for I_h (g_h), 0.375 nS/pF in the original SA node model (20, 49), was limited to 0.12 nS/pF (for the effects on BP generation) or 0.5 nS/pF (for the effects on pacemaking and driving ability of BP cells); higher g_h caused inaccurate calculations of steady states with drastic increases of $[Na^+]_i$ and $[Ca^{2+}]_i$ to unreasonable values.

$I_{Ca,T}$. The expressions for $I_{Ca,T}$ were adopted from the rabbit SA node (5, 20) and ventricular (34) models. The effects of these $I_{Ca,T}$ currents were qualitatively the same, with the effect of the SA node $I_{Ca,T}$ being more remarkable; thus the data for the rabbit SA node $I_{Ca,T}$ are shown. Relatively high $g_{Ca,T}$ was required to affect dynamical properties of the model cell, probably because the window region (i.e., overlap of activation and inactivation curves) of the model $I_{Ca,T}$ is relatively small (see Fig. 1). Therefore, the $g_{Ca,T}$ value was increased up to 3 nS/pF, although it was 0.458 nS/pF in the original SA node model (5, 20). Further

Table 1. *Equations and conductance values tested for individual pacemaker currents*

Species and Expression Systems	References	Conductance, nS/pF	
		BP	SAN
I_h			
Rabbit SA node	Kurata et al. (20), Wilders et al. (49)	0–0.5	0.375
Human ventricle	Cerbai et al. (3)	0–1	
HCN2 (expressed in HEK cells)	Moroni et al. (29)	0–1	
$I_{Ca,T}$			
Rabbit SA node	Kurata et al. (20), Demir et al. (5)	0–3	0.458
Rabbit ventricle	Puglisi and Bers (34)	0–3	
I_{st}			
Rabbit SA node	Kurata et al. (20)	0–0.02	0.015
Rat SA node	Shinagawa et al. (40)	0–0.1	0.0669
$I_{Ca,LD}$			
Mouse SA node	Mangoni et al. (27), Platzer et al. (31)	0–1	0.58

I_h, hyperpolarization-activated current; $I_{Ca,T}$, T-type Ca^{2+} current; I_{st}, sustained inward current; $I_{Ca,LD}$, low-voltage-activated L-type Ca^{2+} channel current; SA, sinoatrial; SAN, SA node; BP, biological pacemaker. BP values are ranges of the maximum conductance tested for each current in this study. SAN values are the maximum conductance of each current used for the original SA node models (5, 20, 40, 49); the value used for the SA node high-voltage-activated Ca^{2+} channel current ($I_{Ca,LC}$) (20) is shown for $I_{Ca,LD}$.

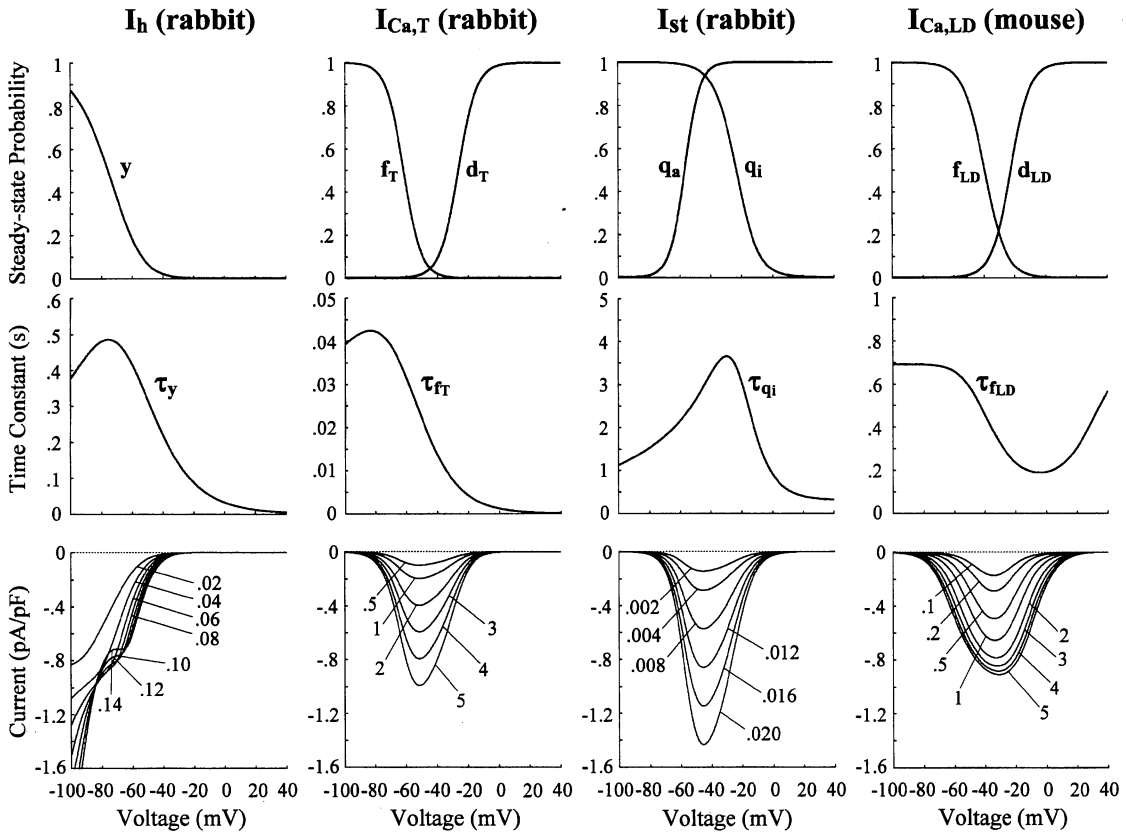

Fig. 1. Voltage-dependent kinetics of the rabbit sinoatrial (SA) node hyperpolarization-activated current (I_h), T-type Ca^{2+} current ($I_{Ca,T}$), and sustained inward current (I_{st}) as well as mouse SA node low-voltage-activated L-type Ca^{2+} channel current ($I_{Ca,LD}$). *Top* and *middle*: voltage dependence of the steady-state probabilities (*top*) and time constants (τ, *middle*) for activation and inactivation gating variables of individual pacemaker currents. *Bottom*: steady-state (window) currents calculated by the steady-state equations for the gating variables. Numbers in each panel represent the maximum current conductance in nS/pF. See APPENDIX A for symbol definitions.

increases in $g_{Ca,T}$ caused shrinkage of BP oscillations and stabilization of an EP via a Hopf bifurcation (see Fig. 2).

I_{st}. The formulas for I_{st} were adopted from the rabbit SA node model (20) and the experimental report for the rat SA node (40). The effects of the two I_{st} currents were essentially the same; thus only data for the rabbit SA node I_{st} are shown. The g_{st} value, 0.015 nS/pF in the original SA node model (20), was limited to 0.02 nS/pF; further increases in g_{st} yielded extremely large window currents leading to Na^+-overload conditions, because the window region of the model I_{st} is relatively large (see Fig. 1).

$I_{Ca,LD}$. The kinetics of $I_{Ca,LD}$ was formulated on the basis of experimental data from mouse SA node cells (27, 31, 51) and human embryonic kidney cells expressing D-LTCC (16). These previous studies suggested that *1*) the voltage dependence of the activation and inactivation of $I_{Ca,LD}$ is 10–20 mV more negative than that of the high-voltage-activated Ca^{2+} channel current ($I_{Ca,LC}$), *2*) the activation of $I_{Ca,LD}$ is faster than that of $I_{Ca,LC}$, and 3) the inactivation of $I_{Ca,LD}$ is 1.5–2 times slower than that of $I_{Ca,LC}$. According to these data, therefore, we formulated the kinetics of $I_{Ca,LD}$ as provided in APPENDIX B (*Eqs. A38–A42*). Because the effects on model cell dynamics of the model $I_{Ca,LD}$ were relatively small, the $g_{Ca,LD}$ value was increased up to 1 nS/pF. Further increases in $g_{Ca,LD}$ caused Ca^{2+}-overload conditions as well as shrinkage of BP oscillations (see Fig. 2).

Formulation of Coupled-Cell Model

To investigate the electrotonic influences of adjacent HVMs on stability and dynamics of BP cells as well as BP cell ability to drive adjacent HVMs, we used a coupled-cell model (Fig. 3), in which I_{K1}-deleted BP cells were connected to a NP cell with normal or reduced I_{K1} via the gap junction conductance (G_C) of 0–20 nS. One NP cell was connected with one to seven BP cells; more than one BP cells were assumed to be well-coupled enough to synchronize completely and act as a cluster of isopotential cells (or assumed to connect with the NP cell via an identical G_C). Pacemaker currents were incorporated into the BP cells only (not into the NP cell).

Time-dependent changes in the membrane potentials of the BP (V_{BP}) and NP (V_{NP}) cells were calculated by the equations

$$dV_{BP}/dt = I_{stim} - I_{total(BP)} - I_{GJ}/C_{BP} \quad (2)$$

$$dV_{NP}/dt = -I_{total(NP)} + I_{GJ}/C_{NP} \quad (3)$$

where C_{BP} and C_{NP} represent the membrane capacitance of the BP and NP cells, respectively. $I_{total(BP)}$ and $I_{total(NP)}$ are the sum of sarcolemmal ionic currents in the BP and NP cells, with I_{GJ} denoting the gap junction current. I_{stim} is the stimulus current applied to the BP cells, usually set equal to zero. The units for V, C, I_{total} (I_{stim}), and I_{GJ} are millivolts, picofarads, picoamperes per picofarad, and picoamperes, respectively. Time-dependent changes in all the other state variables of the BP and NP cells were computed independently, as described for the single HVM in our previous article (22).

Numerical Methods for Dynamic Simulations and Bifurcation Analyses

Dynamic behaviors of the model cells were determined by solving a system of nonlinear ordinary differential equations numerically. Numerical integration as well as bifurcation analyses were performed

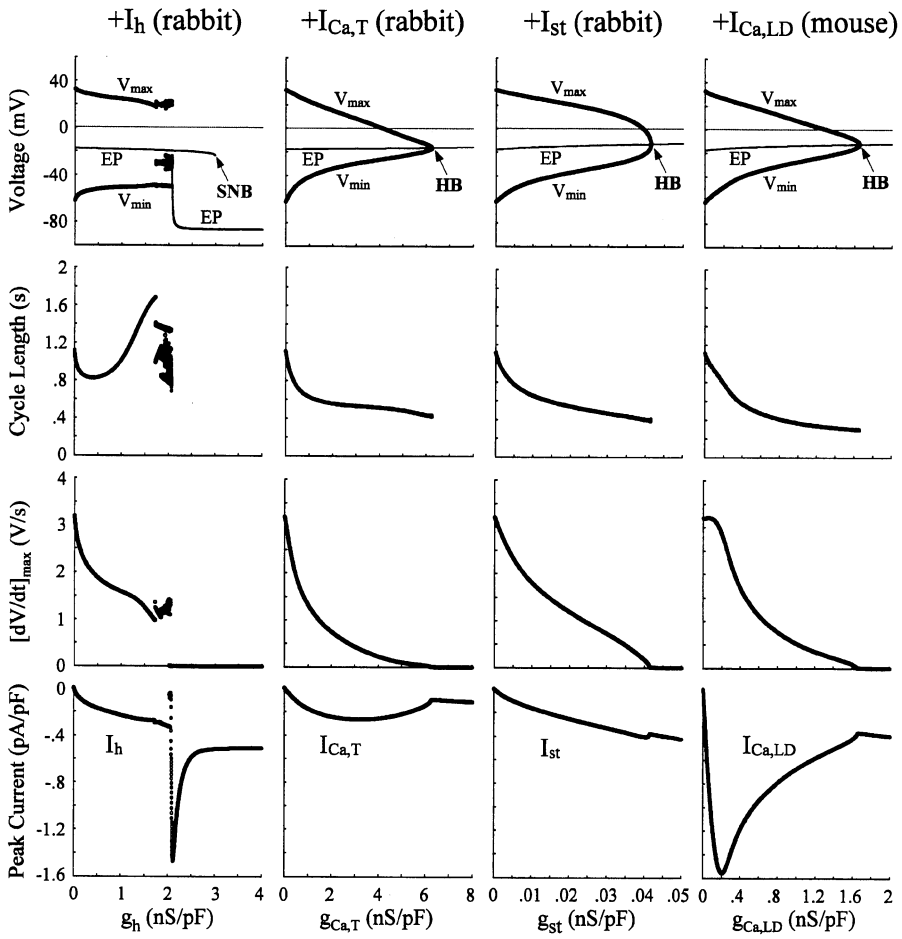

Fig. 2. Changes in stability and dynamics of a single biological pacemaker (BP) cell with increase of each pacemaker current. To induce BP activity, the inward rectifier K^+ current (I_{K1}) conductance (g_{K1}) was reduced to 15% of the control. The steady-state (equilibrium point, EP) and stable periodic [maximum diastolic potential (V_{min}) and peak overshoot potential (V_{max})] branches (*top*), as well as the cycle length (CL) (*second*) and maximum upstroke velocity ($[dV/dt]_{max}$) (*third*) of potential oscillations, are shown as functions of the maximum conductance (g). Peak amplitudes of the pacemaker currents during BP oscillations are also plotted (*bottom*). Steady-state BP dynamics were computed by numerically solving differential equations for 1 min at each conductance value (for details, see Ref. 22), with the initial Na^+ concentration ($[Na^+]_i$) set equal to 6.55 mM in the absence of pacemaker currents; the conductance value was increased at an interval of 1 pS/pF (for g_h, $g_{Ca,T}$, and $g_{Ca,LD}$) or 0.01 pS/pF (for g_{st}) until a bifurcation occurred. Hopf bifurcation points at which stability of an EP reverses (labeled HB at $g_{Ca,T}$ = 6.253, g_{st} = 0.04141, and $g_{Ca,LD}$ = 1.654 nS/pF) and a saddle-node bifurcation point at which an EP disappears (labeled SNB at g_h = 2.982 nS/pF) are shown.

on Workstation CELSIUS X630 (Fujitsu, Tokyo, Japan) with MATLAB 7 (MathWorks, Natick, MA). We used the numerical algorithms available as MATLAB ODE solvers: *1*) a fourth-order adaptive-step Runge-Kutta algorithm that includes an automatic step-size adjustment based on an error estimate (*ode45*) (6) and *2*) a variable time-step numerical differentiation approach selected for its suitability to stiff systems (*ode15s*) (39). Both solvers usually yielded nearly identical results. The latter, much more efficient than the former, was usually used; the former as the best function for most problems was only sometimes used to confirm the accuracy of calculations. The maximum relative error tolerance for the integration methods was set to 1×10^{-6}.

Stability and Bifurcation Analyses

We examined how the stability and dynamics of the model cells alter with changes in bifurcation parameters and constructed bifurcation diagrams for one or two parameters. Bifurcation parameters chosen in this study were the maximum conductance of I_{K1} (g_{K1}) and pacemaker currents (g_h, $g_{Ca,T}$, g_{st}, $g_{Ca,LD}$) as well as G_C; g_{K1} is expressed as a normalized value, i.e., in ratio to the control value of 3.9 nS/pF, unless otherwise stated. The methods for bifurcation analyses of the single BP or NP cell are described in our previous article (22).

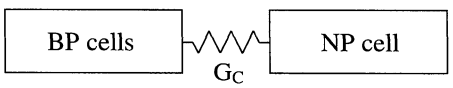

Fig. 3. Coupled-cell model. NP, nonpacemaking; G_C, gap conductance.

Although the methods of bifurcation analyses for the coupled-cell system are essentially the same as for the single cell, the number of state variables increases twice: in the coupled-cell system with fixed $[K^+]_i$, 28 state variables define a 28-dimensional state point in the 28-dimensional state space of the system. We calculated EPs, i.e., steady-state values of the variables, and periodic orbits in the state space of the coupled-cell system. Steady-state values of the variables were calculated by *Eqs. A53–A58* in APPENDIX C. Asymptotic stability of the EP was also determined by computing 28 eigenvalues of a 28 × 28 Jacobian matrix derived from the linearization of the nonlinear system around the EP (for details, see Ref. 45). Periodic orbits were located with the MATLAB ODE solvers. When spontaneous oscillation (BP activity) appeared, the action potential amplitude (APA) as a voltage difference between the maximum diastolic potential (V_{min}) and peak overshoot potential (V_{max}) as well as the cycle length (CL) were determined for each calculation of a cycle. Numerical integration was continued until the differences in both APA and CL between the newly calculated cycle and the preceding one became $<1 \times 10^{-3}$ of the preceding APA and CL values. Potential extrema (V_{min}, V_{max}) and CL of the steady-state oscillation were plotted against bifurcation parameters. When periodic behavior was irregular or unstable, model dynamics were computed for 60 s; all potential extrema and CL values were then plotted.

We constructed one-parameter bifurcation diagrams for G_C and two-parameter bifurcation diagrams for G_C and pacemaker current conductance. For construction of one-parameter bifurcation diagrams, the membrane potential at EPs (steady-state branches) and local potential extrema (V_{min}, V_{max}) of periodic orbits (periodic branches) were determined and plotted as a function of G_C, which was system-

atically changed while keeping all other parameters at their standard values. The saddle-node bifurcation point at which two EPs coalesce and disappear with emergence of robust BP activity was determined; the Hopf bifurcation point at which an unstable EP is stabilized with cessation of BP activity was also located. For construction of two-parameter bifurcation diagrams, the critical G_C values at bifurcation points were determined as functions of the secondary parameters such as the pacemaker current conductance, the number of BP cells, and NP cell g_{K1}; the primary parameter (G_C) was systematically changed, with the secondary parameter fixed at various different values. The path of Hopf and saddle-node bifurcation points was traced in the parameter plane, i.e., bifurcation values for the primary parameter were plotted as a function of the secondary parameter.

We also evaluated the "structural stability" of BP cells, which is defined as the robustness of BP activity to various interventions or modifications that may cause a bifurcation to quiescence or irregular dynamics (21, 22). In this study, we tested the structural stability of BP cells to electrotonic (hyperpolarizing) loads of an adjacent NP cell, using the coupled-cell system, which is also useful in exploring BP cell ability to drive the adjacent NP cell. The method of evaluating the structural stability to electrotonic loads is essentially the same as that for constant bias currents as described in our previous articles (21, 22). In the unstable G_C region where the system has no stable EP, the system usually exhibited robust pacemaking and driving without annihilation (9, 24). When the system removes to the stable G_C region with a stable EP, it will come to a rest at the stable EP via gradual decline of limit cycles, annihilation, or irregular dynamics, as reported by Guevara and Jongsma (9). In the coupled-cell system, the larger the G_C region over which all EPs are unstable (there is no stable EP) and thus BP activity appears is, the more structurally stable the BP system is (for more detail, see Ref. 22).

Definitions of Terms Specific to Nonlinear Dynamics and Bifurcation Theory

Equilibrium point. The equilibrium point (EP) is a time-independent steady-state point at which the vector field vanishes in the state space of a dynamical system, constructing the steady-state branch in one-parameter bifurcation diagrams. This state point corresponds to the zero-current crossing in the steady-state current-voltage (*I-V*) curve, i.e., a quiescent (resting) state of a cell if it is stable.

Periodic orbit. A periodic orbit is a closed trajectory in the state space of a system, constructing the periodic branch in one-parameter bifurcation diagrams.

Limit cycle. The limit cycle is a periodic limit set onto which a trajectory is asymptotically attracted. A stable limit cycle corresponds to an oscillatory state, i.e., pacemaker activity, of a cell.

Bifurcation. Bifurcation is a qualitative change in a solution of differential equations caused by altering parameters, e.g., a change in the number of EPs or periodic orbits, a change in the stability of an EP or periodic orbit, and a transition from a periodic to a quiescent state. Bifurcation phenomena we can see in cardiac myocytes include generation or cessation of pacemaker activity and occurrence of irregular dynamics such as skipped-beat runs and early afterdepolarizations.

Saddle-node bifurcation. Saddle-node bifurcation is a bifurcation at which two EPs (steady-state branches) or two periodic solutions (periodic branches) emerge or disappear. The saddle-node bifurcation of EPs occurs when one of the eigenvalues of a Jacobian matrix for the EP is zero.

Hopf bifurcation. The Hopf bifurcation is a bifurcation at which the stability of an EP reverses with emergence or disappearance of a limit cycle, occurring when eigenvalues of a Jacobian matrix have a single complex conjugate pair and its real part reverses the sign through zero.

RESULTS

Effects of Pacemaker Currents on BP Generation in Single HVM Model

Our preceding study (22) suggests that I_{K1} downregulation, ensuring both the occurrence of a saddle-node bifurcation and instability of the EP with depolarized potentials, yields spontaneous oscillations (BP activity) in HVMs without incorporating any pacemaker current. However, a saddle-node bifurcation to induce BP activity may also be yielded by incorporating pacemaker currents such as I_h, $I_{Ca,T}$, I_{st}, and $I_{Ca,LD}$, which are abundant in SA node primary pacemaker cells but absent or very small in native HVMs. In the preliminary study, we found that these pacemaker currents could not yield BP generation in the model HVM with normal I_{K1} (g_{K1} = 1): BP activity did not appear when g_h, $g_{Ca,T}$, g_{st}, and $g_{Ca,LD}$ were increased up to the limited values of 0.12, 3, 0.02 and 1 nS/pF, respectively (see THEORY AND METHODS) or even when $g_{Ca,T}$, g_{st}, or $g_{Ca,LD}$ was further increased to the critical value above which an EP at depolarized potentials would be stable and thus BP oscillations could not occur (see Fig. 2). Nevertheless, incorporating the pacemaker currents is expected to accelerate BP generation during I_{K1} suppression by increasing the critical g_{K1} value at which a saddle-node bifurcation occurs and thus BP oscillations emerge. We therefore investigated how these currents affect the saddle-node bifurcation and BP generation during I_{K1} suppression.

Effects of incorporating each pacemaker current on BP generation during I_{K1} suppression. As clearly shown in Fig. 4, the saddle-node bifurcation point below which BP oscillations occur shifted toward higher g_{K1} values with increasing g_h, suggesting that expression of I_h accelerates BP generation during I_{K1} suppression by increasing the critical g_{K1} value to induce BP activity. To further examine the effects of incorporating the pacemaker currents on BP generation in the I_{K1}-reduced HVM, we determined the critical g_{K1} value for BP generation (i.e., g_{K1} value at a saddle-node bifurcation) as functions of g_h, $g_{Ca,T}$, g_{st}, or $g_{Ca,LD}$, as well as exploring the influences of the pacemaker currents on the steady-state *I-V* relation at g_{K1} = 1 (Fig. 5). The inward pacemaker currents counteracted the outward component of I_{K1}, inwardly shifting the steady-state *I-V* curve. The critical g_{K1} value increased with increasing g_h; however, it did not reach the control g_{K1} value but reached the maximum of 0.287 (28.7%) at g_h = 0.1039 nS/pF. $I_{Ca,T}$ at higher densities ($g_{Ca,T} \leq 3$ nS/pF) also increased the critical g_{K1}, with its increase limited to <0.266 (26.6%). The effects of I_{st} and $I_{Ca,LD}$ were relatively small within the limited conductance ranges of ≤0.02 and ≤1 nS/pF, respectively.

Effects of coexpression of I_h and other pacemaker currents on BP generation. The critical g_{K1} value did not reach the control g_{K1} value when the conductance of individual currents was increased up to the limited values, or even when $g_{Ca,T}$, g_{st}, or $g_{Ca,LD}$ was increased to more than the Hopf bifurcation point at which BP oscillation would disappear (see Fig. 2). However, the critical g_{K1} may further be increased by coexpression of I_h and the other pacemaker currents that have a different voltage range of activation. As shown in Fig. 6, therefore, we also examined the effects of coexpressing I_h and $I_{Ca,T}$, I_{st}, or $I_{Ca,LD}$ on BP generation

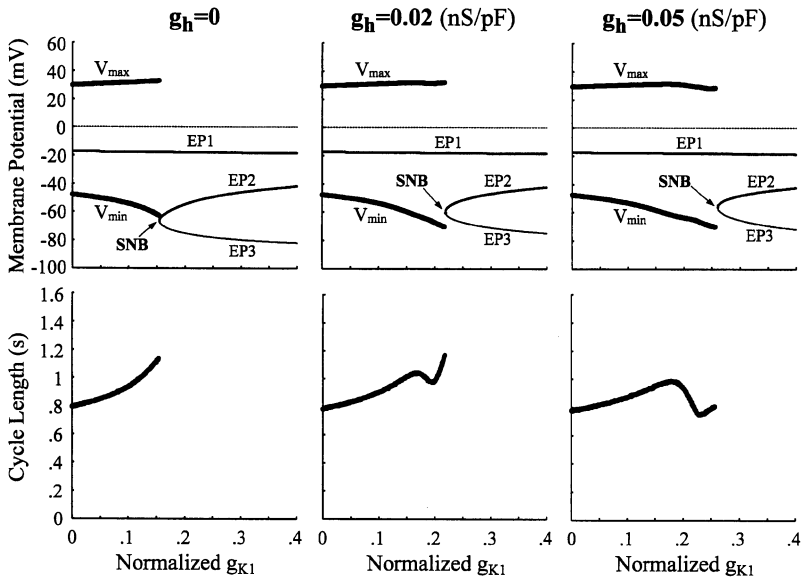

Fig. 4. Bifurcation structures during g_{K1} decreases of the model human ventricular myocyte (HVM) in the absence or presence of the rabbit SA node type I_h. One-parameter bifurcation diagrams for g_{K1} with the steady-state (EP1–3) and stable periodic (V_{min}, V_{max}) branches (*top*), as well as CL of potential oscillations as a function of g_{K1} (*bottom*), are shown for g_h of 0 (*left*), 0.02 (*center*), and 0.05 (*right*) nS/pF. Steady-state BP dynamics were computed by numerically solving differential equations for 60 min at each g_{K1} value (for details see APPENDIX B). The g_{K1} value was reduced at an interval of 0.001, with the initial $[Na^+]_i$ set equal to 5.75 mM at g_{K1} = 0.4. The saddle-node bifurcation point at which EP2 and EP3 merge together and disappear is shown (labeled SNB at g_{K1} = 0.154, 0.219, and 0.260).

during I_{K1} suppression. $I_{Ca,T}$, I_{st}, or $I_{Ca,LD}$ coexpressed with I_h further increased the critical g_{K1} value, i.e., enhanced the accelerating effect of I_h. Nevertheless, the increase in the critical g_{K1} was limited even when I_h and the other pacemaker currents were coexpressed. Drastic increases of $[Na^+]_i$ and $[Ca^{2+}]_i$ at the bifurcation points were caused by coexpression of I_h and the other currents at higher conductance.

Structural Stability and Driving Ability of HVM Pacemaker

One of the drawbacks of the I_{K1}-downregulated HVM pacemaker may be the relatively low structural stability to hyperpolarizing loads such as electrotonic modulations of surrounding nonpacemaker cells, because it lacks the pacemaker currents that are abundant in SA node primary pacemaker cells and contribute to pacemaker depolarization. We therefore ex-

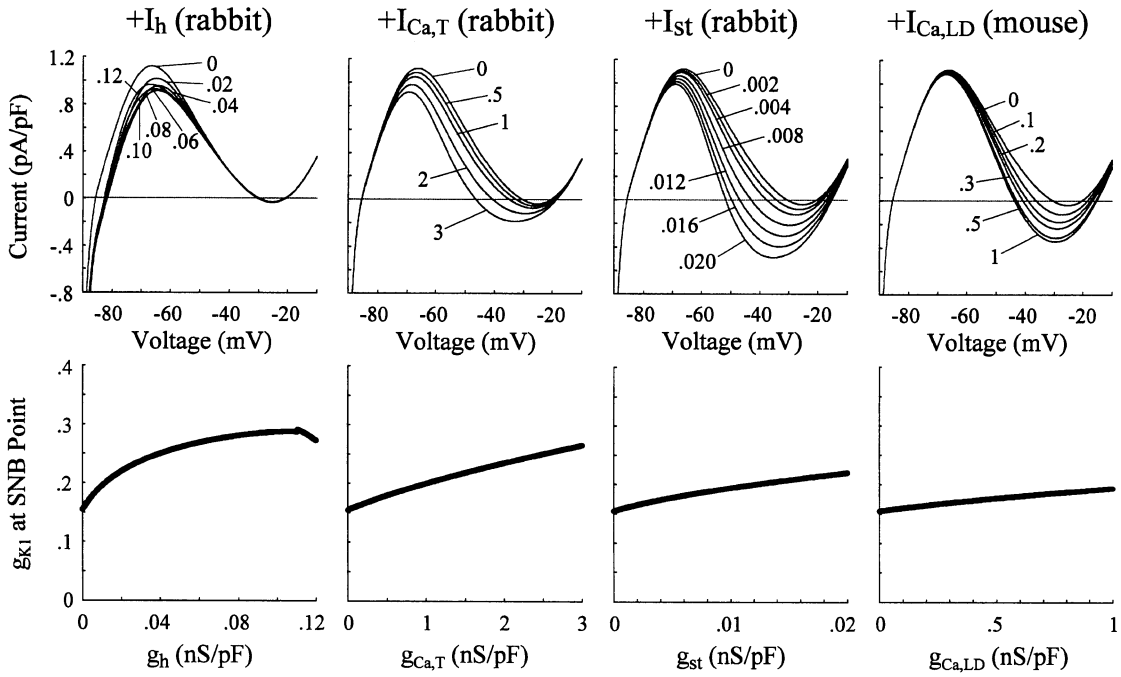

Fig. 5. Effects of incorporating the rabbit SA node I_h, $I_{Ca,T}$, or I_{st} or the mouse SA node $I_{Ca,LD}$ on the steady-state current-voltage (*I-V*) relation and BP generation during I_{K1} inhibition. *Top*: effects on the steady-state *I-V* curve for a HVM with normal I_{K1}. $[K^+]_i$ was fixed at 140 mM. The values of g_h, $g_{Ca,T}$, g_{st}, and $g_{Ca,LD}$ were increased up to 0.12, 3, 0.02, and 1 nS/pF, respectively. *Bottom*: 2-parameter bifurcation diagrams for g_{K1} (*y*-axis) and g_h, $g_{Ca,T}$, g_{st}, or $g_{Ca,LD}$ (*x*-axis), depicting changes in the critical g_{K1} value, i.e., displacements of saddle-node bifurcation points at which BP activity emerges, with increasing g_h, $g_{Ca,T}$, g_{st}, or $g_{Ca,LD}$ at an interval of 0.1 (for g_h and g_{st}) or 1 (for $g_{Ca,T}$ and $g_{Ca,LD}$) pS/pF. The g_{K1} value was reduced at an interval of 0.001–0.0001 for searching for bifurcation points.

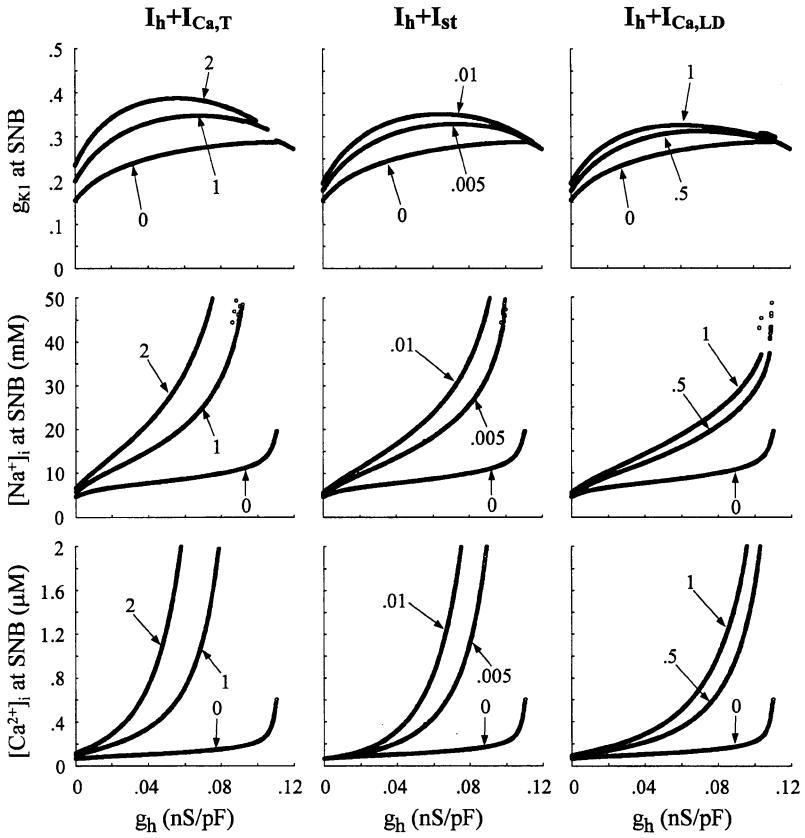

Fig. 6. Effects of coexpression of I_h and $I_{Ca,T}$ (*left*), I_{st} (*center*), or $I_{Ca,LD}$ (*right*) on BP generation during I_{K1} inhibition. *Top*: 2-parameter bifurcation diagrams for g_{K1} (*y*-axis) and g_h (*x*-axis) depicting displacements of saddle-node bifurcation points with increasing g_h at an interval of 0.1 pS/pF. $I_{Ca,T}$, I_{st}, or $I_{Ca,LD}$ was incorporated with maximum conductance set equal to 1–2, 0.005–0.01, and 0.5–1 nS/pF, respectively. The g_{K1} value was reduced at an interval of 0.0001 for searching for bifurcation points. Calculations were stopped when $[Na^+]_i$ exceeded extracellular Na^+ concentration ($[Na^+]_o$) or when $[Ca^{2+}]_i$ exceeded $[Ca^{2+}]_o$. *Middle* and *bottom*: steady-state $[Na^+]_i$ (*middle*) and $[Ca^{2+}]_i$ (*bottom*) at the bifurcation points are shown as functions of g_h.

amined the structural stability of BP cells to electrotonic loads of the adjacent NP cell, using a coupled-cell model in which BP cells (g_{K1} = 0) were connected to a NP cell (g_{K1} = 0.2–1) via the G_C ranging from 0 to 20 nS. The coupled-cell system is also useful in exploring BP cell ability to drive adjacent NP cells.

G_C-dependent behaviors of the coupled-cell system. In the system with one BP cell and one normal HVM (g_{K1} = 1), an EP was stabilized via a Hopf bifurcation at G_C = 0.689 nS, with the BP cell not exhibiting pacemaker activity at G_C values higher than the bifurcation value. Thus the coupling of one BP cell to one normal HVM produced either *1*) BP cell pacemaking at slower rates without driving the NP cell for lower G_C values or *2*) inhibition of BP cell pacemaking for higher G_C values. We could not find a G_C value for which one BP cell could exhibit pacemaking itself and drive the normal HVM but found that three or more BP cells, assumed to be well coupled to form a cluster, were required for driving the normal HVM.

Figure 7 shows the simulated membrane potentials and I_{GJ} at various G_C values for the coupled-cell system composed of five BP cells and one normal HVM. With increasing G_C, the BP rate decreased, with the oscillation amplitude getting larger. The BP cells could induce only subthreshold responses of the HVM at G_C = 2.0 nS, whereas they induced driven action potentials at G_C = 2.5–3.5 nS. Further increase in G_C to 5.0 nS abolished BP activity, which was probably due to hyperpolarizing loads of the NP cell as indicated by positive I_{GJ}.

Influences of size factor and NP cell g_{K1} on G_C-dependent bifurcation structures. The structural stability and driving ability of pacemaker systems are known to depend on the size factor (i.e., the number of BP cells relative to that of NP cells) and g_{K1} of adjacent NP cells (13, 14, 19, 47), which are practically important for engineering of functional BPs in vivo. Therefore, we more minutely explored the effects of the size factor and NP cell g_{K1} on G_C-dependent bifurcation structures of coupled-cell systems.

Stability and dynamics during G_C increases of the coupled-cell system composed of one to seven BP cells and one normal HVM are shown in Fig. 8*A*. EPs and potential extrema were determined for both the BP and NP cells, plotted as functions of G_C values. Hopf and saddle-node bifurcation points were also determined and located in the bifurcation diagrams. In the systems with one to five BP cells, hyperpolarizing loads of the NP cell caused *1*) prolongation of CL with an increase in oscillation amplitude, *2*) irregular dynamics, and then *3*) a bifurcation to quiescence (Hopf bifurcation), with increasing G_C. These behaviors are essentially the same as those reported for interactions of the SA node cell and the atrial or ventricular myocyte (13, 44, 47, 48). The critical G_C value at the Hopf bifurcation to cause stabilization of EPs and cessation of BP activity increased with increasing number of BP cells. One or two BP cells could not drive the normal HVM. With three to five BP cells, the increase in G_C yielded a BP cell ability to drive the normal HVM; however, further increases in G_C led to the cessation of pacemaking and driving via the Hopf bifurcation. The G_C region of driving the normal HVM was very limited with three to five BP cells, whereas it dramatically enlarged when the number of BP cells increased to more than five. With six or more BP cells, a saddle-node bifurcation at which two EPs (EP2, EP3) disappear occurred to ensure the

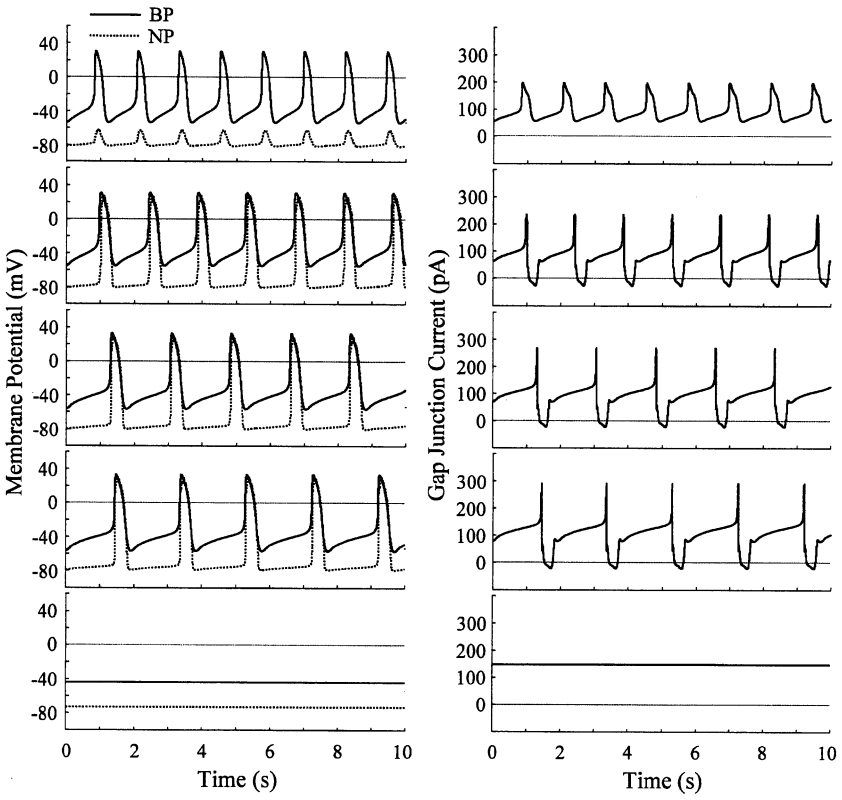

Fig. 7. Simulated dynamic behaviors of a coupled-cell system at various G_C values of 2.0, 2.5, 3.0, 3.5, and 5 nS (from *top* to *bottom*). One normal HVM (g_{K1} = 1) was connected to 5 BP cells (g_{K1} = 0), which were assumed to be well coupled enough to act as a cluster. Membrane potentials of the BP cells and normal HVM (NP), as well as gap junction currents, were computed by numerically solving differential equations for 60 min at each G_C value (for details, see APPENDIX B); the potential and current behaviors during the last 10 s are shown.

robust pacemaking and driving without annihilation (see Fig. 8*A*, *far right*, for 7 BP cells).

The relatively low ability to drive the normal HVM and low structural stability to electrotonic loads of the BP cell appeared to be due to the relatively high I_{K1} density in the normal HVM (14). Therefore, we also explored stability and dynamics during G_C increases of a coupled-cell system consisting of one BP cell and one NP cell with reduced I_{K1}, as shown in Fig. 8*B* for the normalized NP cell g_{K1} of 0.35, 0.30, and 0.25. With the reduced g_{K1} of 0.30 (1.17 nS/pF) or less, increasing G_C did not cause a Hopf bifurcation to quiescence but yielded a saddle-node bifurcation to ensure robust pacemaking and driving.

Effects of Pacemaker Currents on Structural Stability and Driving Ability of HVM Pacemaker

Using the coupled-cell model, we examined how incorporating the pacemaker currents affects the structural stability of BP cells to electrotonic loads of the adjacent NP cell, as well as BP cell ability to drive the NP cell. Figure 8 suggests that a Hopf bifurcation point is just at or close to the point at which BP activity is abolished by hyperpolarizing loads of the NP cell, whereas a saddle-node bifurcation point is the point above which robust pacemaking and driving occur. To assess the effects of the pacemaker currents on the structural stability and driving ability of BP cells, therefore, we focused on the shift in the Hopf bifurcation point, as well as emergence of a saddle-node bifurcation.

Effects of incorporating pacemaker currents on G_C-dependent bifurcation structures. Bifurcation structures during G_C increases were first determined at various conductances of each pacemaker current. We constructed two-parameter bifurcation diagrams in which the critical G_C value at Hopf or saddle-node bifurcation points was plotted as functions of the maximum current conductance. Figure 9 shows the effects of incorporating I_h, $I_{Ca,T}$, I_{st}, or $I_{Ca,LD}$ on the bifurcation structure during G_C increases of the coupled-cell system in which three BP cells were connected to one normal HVM or one BP cell was connected to one NP cell with reduced I_{K1} (g_{K1} = 0.35). Stability and dynamics during G_C increases of the coupled-cell systems incorporating each pacemaker current are illustrated in Fig. 10. The results suggest that individual pacemaker currents affect the G_C-dependent bifurcation structure of the system in different ways.

I_H EFFECT. In the coupled-cell system with three BP cells and one normal HVM, incorporation of I_h (~0.5 nS/pF) did not significantly change the critical G_C value at Hopf bifurcations where an EP is stabilized and BP activity is abolished, not enlarging the region of pacemaking labeled "$P^+D^{\pm}$" (Fig. 9, *top*). As shown in Fig. 10*A*, I_h (0.2 nS/pF) did not enlarge the G_C region where all EPs are unstable and BP activity appears. When I_{K1} of the NP cell was relatively small (g_{K1} = 0.35), however, I_h enlarged the pacemaking and driving region labeled P^+D^+ by producing a saddle-node bifurcation (Fig. 9, *bottom*; Fig. 10*B*). Overexpression of I_h (g_h > 0.2043 nS/pF) caused cessation of BP activity at higher G_C values, with a stable resting potential dramatically hyperpolarized probably via drastic increases in $[Na^+]_i$ and $[Ca^{2+}]_i$.

$I_{CA,T}$ EFFECT. Similar to I_h, $I_{Ca,T}$ (~3 nS/pF) did not significantly change the critical G_C value at Hopf bifurcations, not enlarging the $P^+D^{\pm}$ region, in the coupled-cell system with three BP cells and one normal HVM (Fig. 9, *top*). However, higher densities of $I_{Ca,T}$ yielded a saddle-node bifurcation and

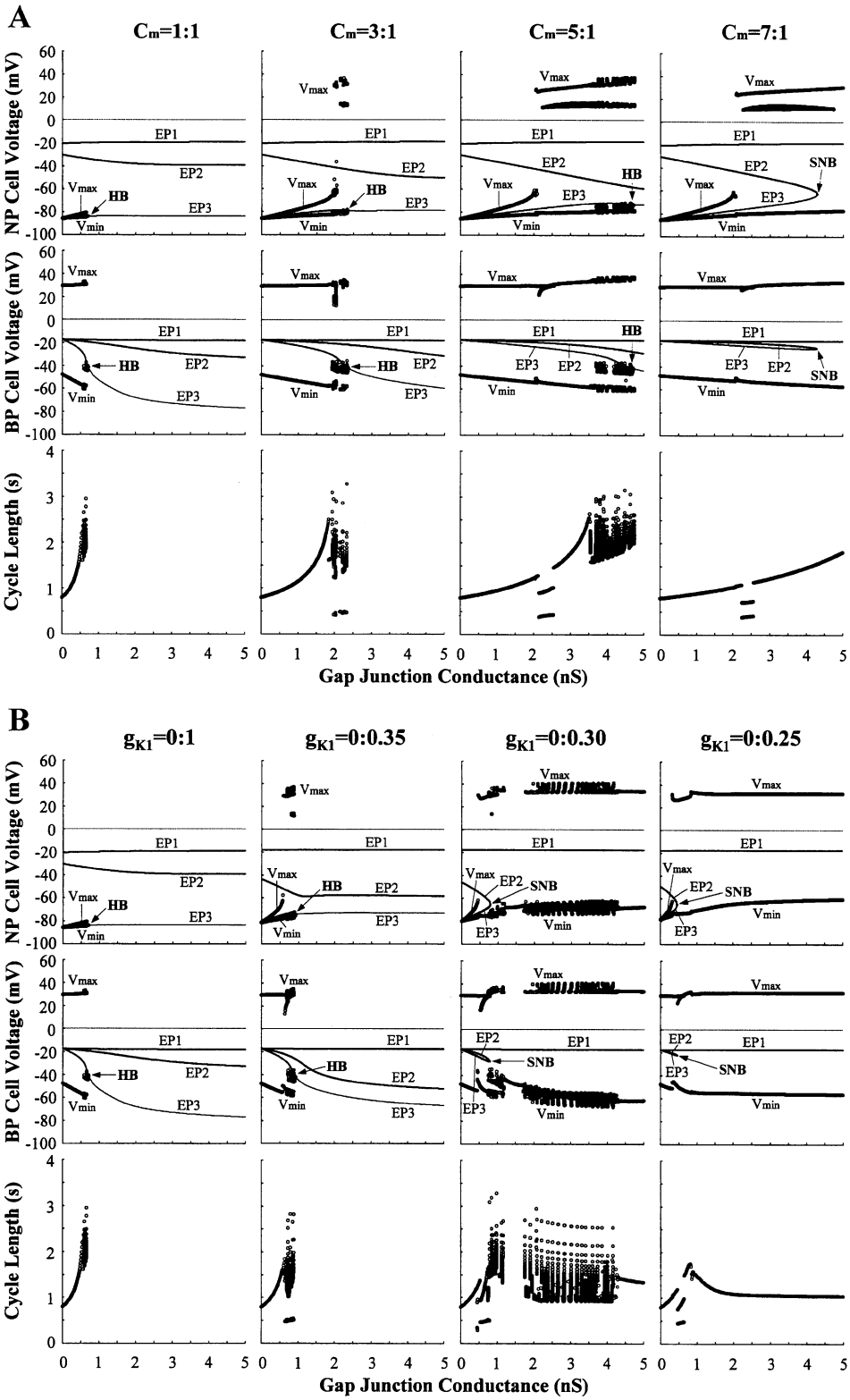

Fig. 8. Stability and dynamics during G_C increases of the coupled-cell systems with various size factors (*A*) or NP cell g_{K1} (*B*). One normal HVM was connected to 1, 3, 5, or 7 I_{K1}-deleted BP cells with all the BP cells assumed to be well coupled (*A*), or 1 I_{K1}-reduced NP cell (g_{K1} = 0.35, 0.30, 0.25) was connected to 1 BP cell (*B*). One-parameter bifurcation diagrams for G_C depicting EPs, Hopf bifurcation, and saddle-node bifurcation points, as well as extrema of potential oscillations (V_{min}, V_{max}), of NP (*top*) and BP (*middle*) cells are shown; CL of BP oscillations is also shown as functions of G_C (*bottom*). Steady-state model cell dynamics were computed by numerically solving the differential equations for 60–120 min at each G_C value. The G_C value was increased up to 5 nS at an interval of 0.01 nS. C_m, cell membrane capacitance.

thus enlarged the P^+D^+ region; $I_{Ca,T}$ at 2 nS/pF enlarged the G_C region where all EPs are unstable and BP activity appears (Fig. 10*A*). When the NP cell I_{K1} was relatively small, $I_{Ca,T}$ dramatically enlarged the P^+D^+ region by producing a saddle-node bifurcation (Fig. 9, *bottom*; Fig. 10*B*). With relatively high conductance of $I_{Ca,T}$, the amplitudes of BP oscillations and driven action potentials of the NP cell were relatively small.

I_{ST} EFFECT. In contrast to I_h or $I_{Ca,T}$, incorporation of I_{st} (~0.02 nS/pF) dramatically shifted Hopf bifurcation points

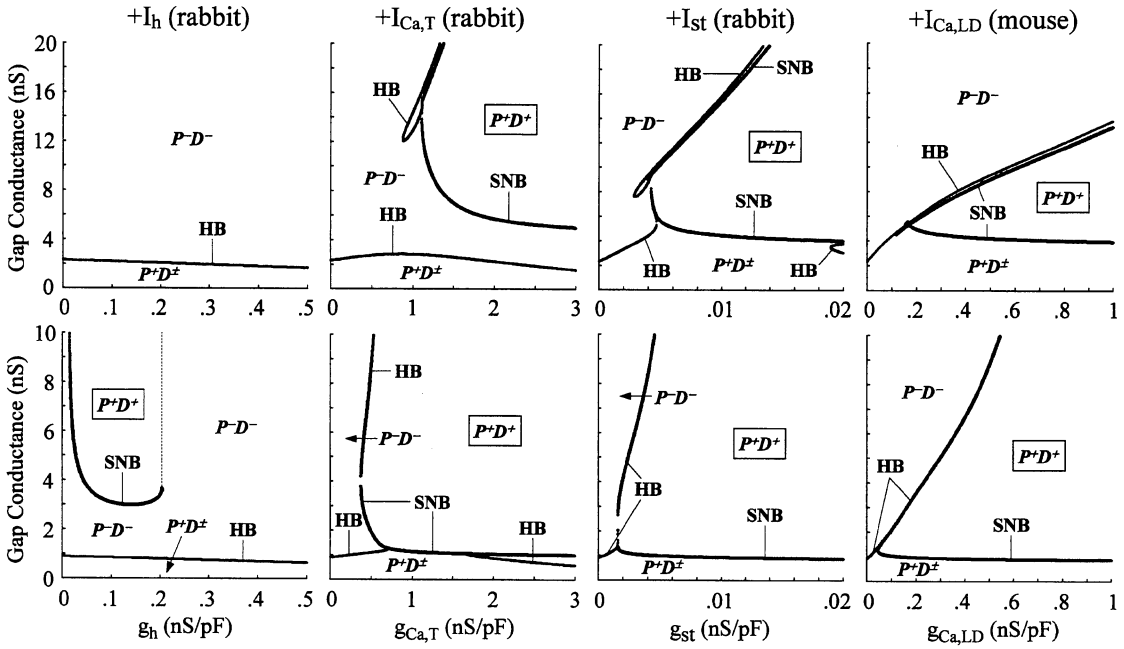

Fig. 9. Effects of incorporating pacemaker currents on bifurcation structures during G_C increases of the coupled-cell model. Three BP cells were connected to 1 normal HVM (*top*), or 1 BP cell was connected to 1 NP cell with a reduced g_{K1} of 0.35 (*bottom*). The rabbit SA node I_h (g_h = 0–0.5 nS/pF), $I_{Ca,T}$ ($g_{Ca,T}$ = 0–3 nS/pF), or I_{st} (g_{st} = 0–0.02 nS/pF) or mouse SA node $I_{Ca,LD}$ ($g_{Ca,LD}$ = 0–1 nS/pF) was incorporated into the BP cells. Two-parameter bifurcation diagrams for G_C and the pacemaker current conductance are shown; the critical G_C values at Hopf bifurcation and saddle-node bifurcation points were plotted as functions of the maximum current conductance. The G_C value was increased up to 10–20 nS at an interval of 0.01 nS for searching for bifurcations. The parameter plane should be divided into 3 areas with different steady states: *1*) nonpacemaking and nondriving (P^-D^-), where BP activity is abolished; 2) pacemaking and driving (P^+D^+), where BP cells exhibit pacemaker activity and drive the NP cell; and *3*) pacemaking and nondriving (P^+D^-), where BP cells exhibit pacemaker activity but do not drive the NP cell. The loci of Hopf and saddle-node bifurcation points actually divided the parameter plane into 3 areas, P^-D^-, P^+D^+, and $P^+D^\pm$ (not P^+D^-). The symbol $P^+D^\pm$ was used for the G_C region lower than the 1st bifurcation point, because NP cell driving might appear in the vicinity of the 1st bifurcation point (see Fig. 8), but it was not possible to determine the critical G_C value at which NP cell driving occurs by this analysis.

toward higher G_C values and further produced a saddle-node bifurcation to ensure robust pacemaking and driving, i.e., enlarged the P^+D^+ region (Fig. 9). I_{st} at 0.01 nS/pF dramatically enlarged the G_C region where BP oscillations occur, with CL of BP oscillations being relatively stable during increases in G_C (Fig. 10).

$I_{CA,LD}$ EFFECT. The effects of $I_{Ca,LD}$ were similar to those of I_{st}, although much larger conductance was required for $I_{Ca,LD}$ to exert the effects as dramatically as I_{st}. Incorporation of $I_{Ca,LD}$ (~1 nS/pF) increased the Hopf bifurcation value and produced a saddle-node bifurcation to enlarge the P^+D^+ region (Fig. 9). As shown in Fig. 10, $I_{Ca,LD}$ (0.5 nS/pF) enlarged the G_C region where BP oscillations occur. However, $I_{Ca,LD}$ at high densities of 0.5–1 nS/pF caused unstable CL and irregular dynamics during increases in G_C.

Influences of altering pacemaker current kinetics on their modulation of bifurcation structures. Individual pacemaker currents affected the G_C-dependent bifurcation structure in different ways, as well as with different potencies. The effects of I_h were completely different from those of the other pacemaker currents, which probably resulted from the difference in the voltage range of activation. Furthermore, the effects of $I_{Ca,T}$, I_{st}, and $I_{Ca,LD}$ were apparently different in the system with three BP cells and one normal HVM: the locus of Hopf bifurcation points at lower G_C was separated from that of saddle-node bifurcation points with $I_{Ca,T}$, but not with I_{st} or $I_{Ca,LD}$. The differences in their effects may result from the large differences in their inactivation kinetics, whereas the different potencies are probably due to the different degrees of the overlap of activation and inactivation curves (see Fig. 1). Thus we examined the effects of incorporating the modified $I_{Ca,T}$ or I_{st} with slowed or accelerated inactivation on G_C-dependent bifurcation structures of the system with three BP cells and one normal HVM (Fig. 11). Changing the inactivation kinetics altered the loci of Hopf bifurcations: the modified $I_{Ca,T}$ with the inactivation time constant (τ_{fT}) 10 times higher than the control yielded a bifurcation diagram similar to that for the original I_{st}; in contrast, the modified I_{st} with the inactivation time constant (τ_{qi}) decreased to 0.01 of the control yielded a locus of Hopf bifurcations separated from that of saddle-node bifurcations, like the original $I_{Ca,T}$. Thus the different effects of the pacemaker currents are at least in part ascribable to the difference in their inactivation kinetics, which appeared to affect the Hopf bifurcation, i.e., stability of EPs, but not the saddle-node bifurcation.

Effects of pacemaker currents on size factor or NP cell g_{K1}-dependent bifurcation structures. To further examine how the pacemaker currents affect the pacemaking and driving of BP cells, bifurcation structures during G_C increase were determined with change in the size factor (the number of BP cells) or NP cell g_{K1} for the modified systems with BP cells incorporating I_h, $I_{Ca,T}$, I_{st}, or $I_{Ca,LD}$, as well as for the standard system not including a pacemaker current (control). We constructed two-parameter bifurcation diagrams in which the critical G_C value at saddle-node or Hopf bifurcation points was plotted as functions of the size factor or normalized NP cell

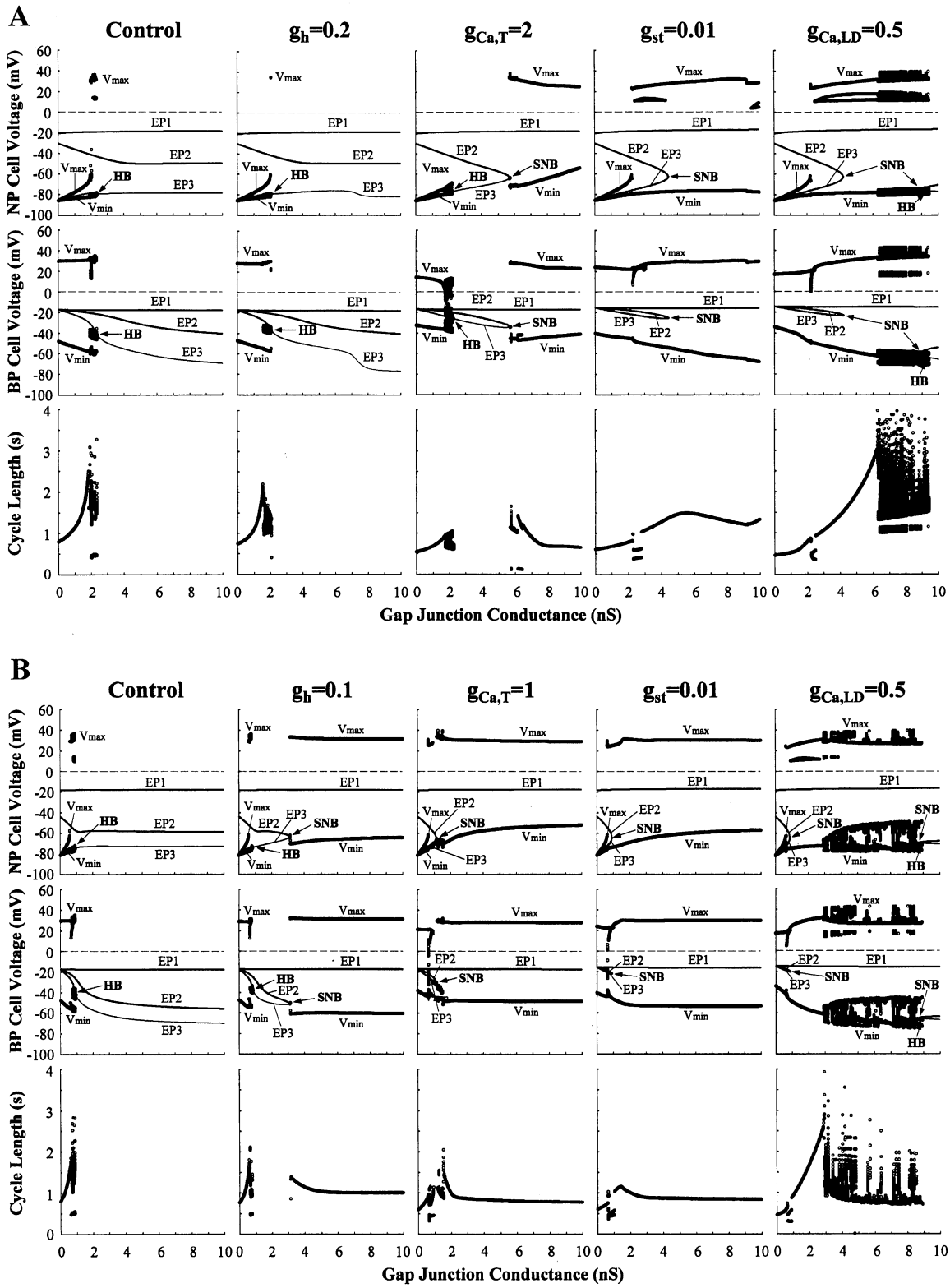

Fig. 10. Stability and dynamics during G_C increases of the coupled-cell systems composed of 3 BP cells and 1 normal HVM (*A*) or 1 BP cell and 1 NP cell with reduced g_{K1} of 0.35 (*B*). I_h (g_h = 0.1–0.2 nS/pF), $I_{Ca,T}$ ($g_{Ca,T}$ = 1–2 nS/pF), I_{st} (g_{st} = 0.01 nS/pF), or $I_{Ca,LD}$ ($g_{Ca,LD}$ = 0.5 nS/pF) was incorporated into the BP cells. Bifurcation diagrams depicting EPs, Hopf bifurcation, and/or saddle-node bifurcation points, as well as dynamics (V_{min}, V_{max}, CL) of the NP and BP cells, are shown as functions of G_C. Steady-state dynamics were computed by numerically solving the differential equations for 30–60 min at each G_C value, which was increased up to 10 nS at an interval of 0.01 nS.

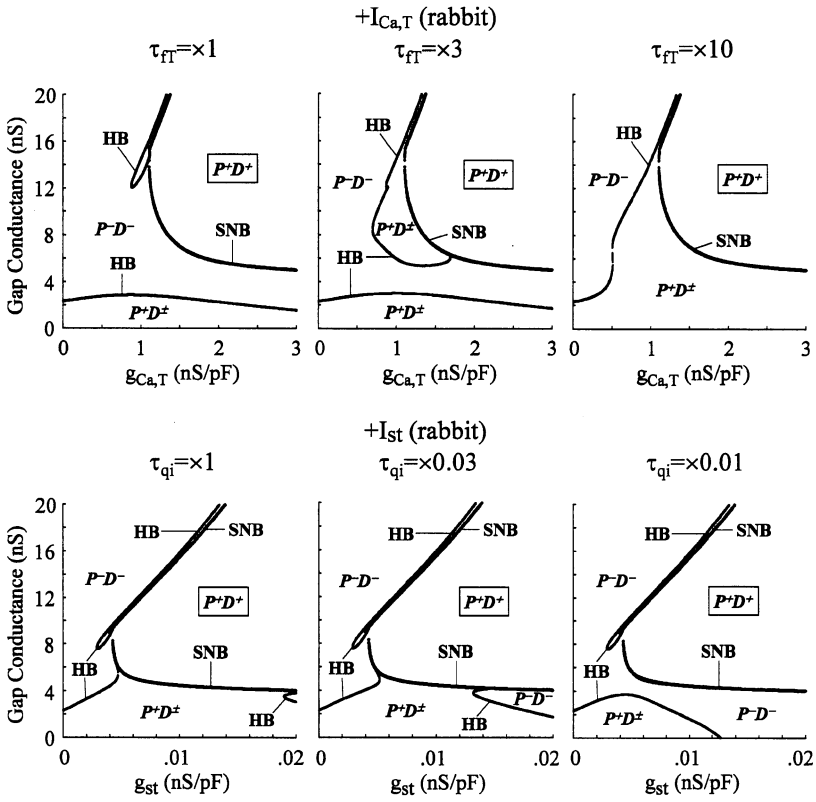

Fig. 11. Effects of the pacemaker currents with different inactivation kinetics on G_C-dependent bifurcation structures of the coupled-cell system composed of 3 BP cells and 1 normal HVM. $I_{Ca,T}$ ($g_{Ca,T}$ = 0–3 nS/pF) or I_{st} (g_{st} = 0–0.02 nS/pF) was incorporated into the BP cells, with their inactivation time constants (τ_{fT}, τ_{qi}) increased or decreased to the values shown as ratios to the control values. Two-parameter bifurcation diagrams for G_C and the pacemaker current conductance were constructed as for Fig. 9.

g_{K1}; one to six BP cells were connected to one normal HVM (Fig. 12) or one BP cell was connected to one NP cell with reduced g_{K1} of 0.2–0.7 (Fig. 13).

Incorporating I_h (0.1–0.2 nS/pF) exerted relatively small effects on the size factor-dependent bifurcation structure of the coupled-cell system with a normal HVM, enlarging the P^+D^+ area only in the region of relatively large size factors and high G_C values (Fig. 12). Decreasing g_{K1} of the NP cell, I_h enlarged the P^+D^+ area by producing a saddle-node bifurcation at relatively low g_{K1} values (Fig. 13). In contrast to I_h, I_{st} (0.01–0.02 nS/pF) dramatically enlarged the P^+D^+ area by facilitating the emergence of saddle-node bifurcations at

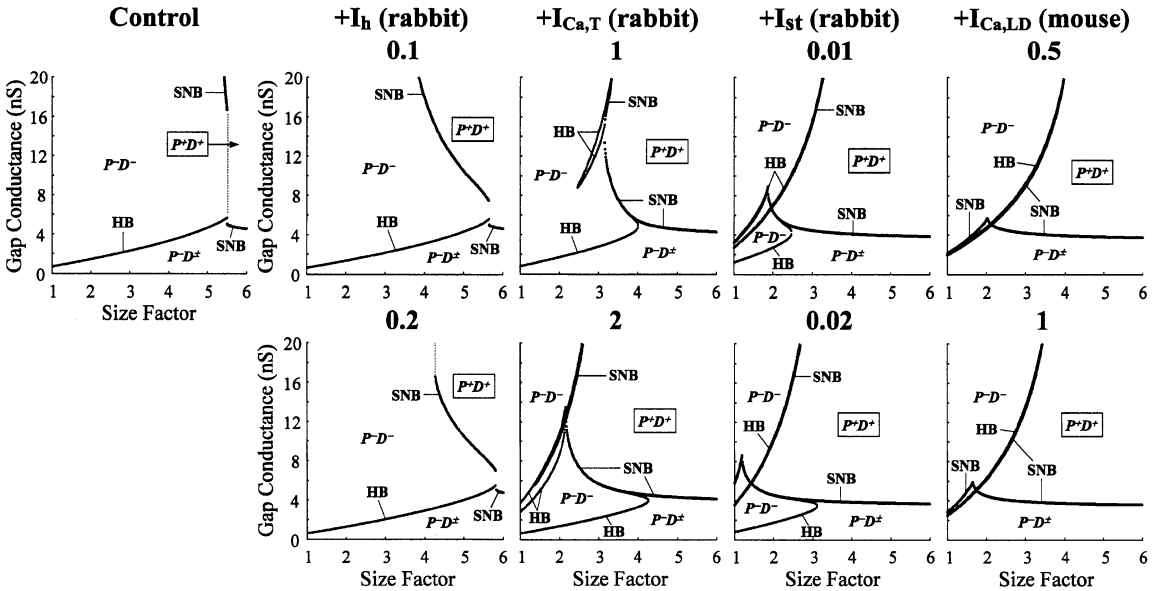

Fig. 12. Effects of incorporating the pacemaker currents on size factor-dependent bifurcation structures of the coupled-cell systems. One to six BP cells were connected to 1 normal HVM. Rabbit SA node I_h (g_h = 0.1–0.2 nS/pF), $I_{Ca,T}$ ($g_{Ca,T}$ = 1–2 nS/pF), or I_{st} (g_{st}=0.01–0.02 nS/pF) or mouse SA node $I_{Ca,LD}$ ($g_{Ca,LD}$ = 0.5–1 nS/pF) was incorporated into the BP cells. Two-parameter bifurcation diagrams depicting the displacement of saddle-node bifurcation and Hopf bifurcation points are shown; the critical G_C value at the bifurcation points was plotted as functions of the size factor (i.e., the number of BP cells) increased at an interval of 0.01. The G_C value was increased up to 20 nS at an interval of 0.01 nS for searching for bifurcations.

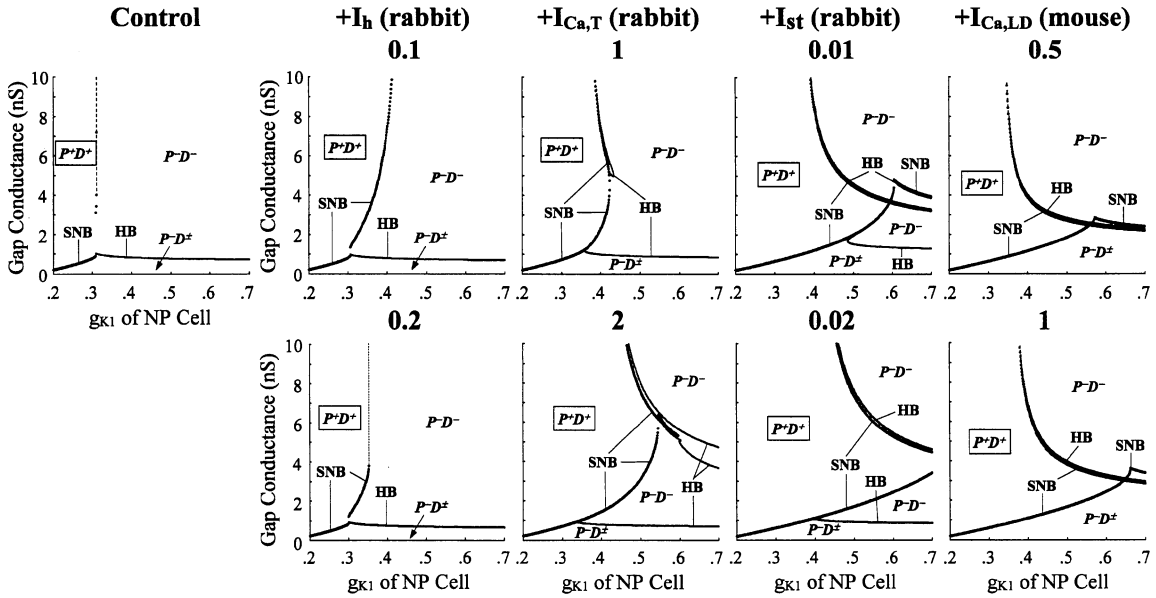

Fig. 13. Effects of incorporating the pacemaker currents on NP cell g_{K1}-dependent bifurcation structures of the coupled-cell systems. One BP cell was connected to 1 NP cell with g_{K1} = 0.2–0.7. I_h (g_h = 0.1–0.2 nS/pF), $I_{Ca,T}$ ($g_{Ca,T}$ = 1–2 nS/pF), I_{st} (g_{st} = 0.01–0.02 nS/pF), or $I_{Ca,LD}$ ($g_{Ca,LD}$ = 0.5–1 nS/pF) was incorporated into the BP cell. The critical G_C value at the bifurcation points was plotted as functions of the normalized g_{K1} of the NP cell decreased at an interval of 0.001. The G_C value was increased up to 10 nS at an interval of 0.01 nS for searching for bifurcations.

smaller size factors and higher g_{K1} values. The effects of $I_{Ca,T}$ (1–2 nS/pF) or $I_{Ca,LD}$ (0.5–1 nS/pF) were similar to those of I_{st}, although much larger conductance was required for $I_{Ca,T}$ or $I_{Ca,LD}$ to exert effects as dramatically as I_{st}.

DISCUSSION

Possible Roles of Pacemaker Currents in Creation of BP Cells

We first investigated whether incorporating pacemaker currents exerts beneficial effects on creation of BP cells by constructing two-parameter bifurcation diagrams in which the critical g_{K1} value (saddle-node bifurcation point) to produce BP activity was plotted as functions of the maximum current conductance.

Pacemaker currents facilitate BP generation during I_{K1} suppression. Our results suggest that the pacemaker currents, especially I_h, can facilitate BP generation during I_{K1} suppression, although their effects were limited (Fig. 5). The mechanism underlying the facilitation of BP generation appears to be relatively simple: the inward pacemaker currents counteract the outward component of I_{K1}, inwardly shift the steady-state *I-V* curve, and thus lead to a saddle-node bifurcation at a higher g_{K1} value (see Fig. 5, *top*). Nevertheless, the critical g_{K1} value never reached the control value of 1, suggesting that any pacemaker currents cannot yield BP activity in the HVM with normal I_{K1}.

I_{K1} downregulation is a requisite for BP generation in HVM. The limited effects of the pacemaker currents appear to be due to the induction of intracellular Na^+ and Ca^{2+} overloads: as shown in Fig. 6, overexpressions of the pacemaker currents cause increases in $[Na^+]_i$ and $[Ca^{2+}]_i$, which enhance the outward Na^+-K^+ pump current, attenuate the inward background Na^+ and Ca^{2+} currents (by decreasing the driving force for Na^+ and Ca^{2+}), and thus counteract the inward shift of *I-V* curves that leads to a saddle-node bifurcation. When $[Na^+]_i$, which is a state variable in the standard system, was fixed at the control value of 6.14 mM (for g_{K1} = 1) to prevent the pacemaker currents causing Na^+ and Ca^{2+} overloads, increasing the pacemaker currents led to BP generation via a saddle-node bifurcation without inhibition of I_{K1}, albeit with the requirement of very high conductance (e.g., $g_h > 0.996$ nS/pF) (data not shown). Thus Na^+ and Ca^{2+} overloads would prevent a bifurcation to BP generation during enhancements of the pacemaker currents. In conclusion, incorporating I_h and/or the other pacemaker currents would not yield BP generation in HVMs with normal I_{K1}, and thus I_{K1} downregulation would be necessary for constructing a BP cell system from HVMs. Inconsistent with our result, Viswanathan et al. (46) reported that the rabbit SA node I_h could induce BP activity in the Luo-Rudy guinea pig ventricular model without reducing I_{K1}. We are not sure about the reason for this inconsistency. Further studies are required to clarify whether the effects of I_h and other pacemaker currents depend on species (human vs. guinea pig) or on the property of a model itself as well as whether expressing I_h can actually induce BP activity in real NP myocytes of the ventricle.

Overexpression of I_h has been reported to induce BP activity (or increase BP rates) in canine atrial or Purkinje myocytes (32, 36). Figure 5 indicates that increasing I_h alone can induce BP activity via a saddle-node bifurcation if g_{K1} is smaller than the control value of 3.9 nS/pF, e.g., when a g_{K1} value is 25% of the control value (0.975 nS/pF), increasing g_h to 0.0403 nS/pF or more yields BP generation. Koumi et al. (17) reported that a slope conductance at a reversal (K^+ equilibrium) potential of the human atrial I_{K1} (0.134 nS/pF) is only 18.3% of that of the human ventricular I_{K1} (0.732 nS/pF). As suggested by previous reports (14, 32, 36), expression of I_h alone would induce pacemaker activity in myocytes with relatively low density of I_{K1}, such as atrial and Purkinje myocytes.

Possible Roles of Pacemaker Currents in Robust Pacemaking and Driving of Functional BP

Using the coupled-cell model, we examined whether incorporation of pacemaker currents exerts beneficial effects on BP functions, i.e., whether it improves the structural stability of BPs to electrotonic loads of adjacent NP cells and the BP ability to drive the ventricle. The results suggest that individual pacemaker currents affect the BP functions in different ways.

I_h effect is relatively small and NP cell g_{K1} dependent. The effects of I_h on G_C-dependent bifurcation structures were quite different from those of the other pacemaker currents, which is probably due to the difference in the voltage range of activation. I_h did not significantly improve the structural stability of BP cells to electrotonic loads of the normal HVM or the BP cell ability to drive the normal HVM (Figs. 9 and 10*A*). When NP cell I_{K1} was relatively small, however, I_h improved the structural stability and driving ability of BP cells by producing a saddle-node bifurcation (Figs. 9 and 10*B*). Moreover, the effects of I_h were shown to depend on I_{K1} density of the NP cell, as well as the size factor (Figs. 12 and 13). These results suggest that I_h can support the robust pacemaking and driving of BPs only when I_{K1} density in adjacent NP cells is relatively small. I_{K1} density is much larger in the human ventricle than in the human atrium (17); thus I_h may support the robust pacemaking and driving of BPs (as well as the SA node) in the atrium with relatively small I_{K1}, but not in the ventricle with relatively large I_{K1}. Possible roles of I_h in the working of ventricular BPs could be to modulate pacemaker frequency in response to autonomic regulations, as well as to prevent excess hyperpolarization, rather than to improve the structural stability and driving ability by destabilizing EPs or yielding saddle-node bifurcations.

$I_{Ca,T}$ effect is NP cell g_{K1} dependent and characterized by shrinkage of voltage oscillations. Similar to I_h, $I_{Ca,T}$ did not improve the structural stability of BP cells to electrotonic loads of the normal HVM by shifting the Hopf bifurcation point at lower G_C values (Fig. 9, *top*); the low efficacy of $I_{Ca,T}$ appeared to be due to the rapid inactivation kinetics, because the modified $I_{Ca,T}$ with slowed inactivation significantly increased the Hopf bifurcation value (Fig. 11). Nevertheless, higher densities of $I_{Ca,T}$ improved the structural stability and driving ability of BP cells by producing a saddle-node bifurcation. The effects of $I_{Ca,T}$ also depend on the NP cell I_{K1}, as well as the size factor (Figs. 9, 12, and 13); $I_{Ca,T}$ may effectively improve the functions of BPs in the atrium, whereas much larger $I_{Ca,T}$ is required for the ventricle. However, higher densities of $I_{Ca,T}$ caused shrinkage in BP oscillations and driven action potentials of the NP cell (Fig. 10), which is probably due to the rapid kinetics of $I_{Ca,T}$ inactivation and is not desirable for functional BPs.

I_{st} most dramatically improves structural stability and driving ability of BP cells. In contrast to I_h or $I_{Ca,T}$, I_{st} at relatively low conductance dramatically improved the structural stability and driving ability of BP cells by shifting Hopf bifurcation points toward higher G_C values and yielding a saddle-node bifurcation (Fig. 9), producing BP oscillations with stable frequency over the broad G_C range (Fig. 10). Furthermore, I_{st}, as well as $I_{Ca,T}$ and $I_{Ca,LD}$, may contribute to reducing the critical size of a BP system (i.e., the number of BP cells) to be required for driving the ventricle: with I_{st} at 0.01 nS/pF, four BP cells are enough to yield robust pacemaking and driving of a normal HVM via creation of a saddle-node bifurcation, whereas more than five BP cells are required without a pacemaker current (see Fig. 12). Our results suggest that I_{st}, exhibiting relatively slow inactivation kinetics, most dramatically improves the structural stability and driving ability of the HVM pacemaker. I_{st} may be indispensable for robust pacemaking and driving of ventricular BPs.

$I_{Ca,LD}$ effect is similar to I_{st} effect but characterized by generation of irregular dynamics. The effects of $I_{Ca,LD}$ were qualitatively similar to those of I_{st}, although its potency was much smaller (Figs. 9, 12, and 13). However, $I_{Ca,LD}$ at high densities caused unstable CL and irregular dynamics during increases in G_C, which is possibly a consequence of producing Ca^{2+} overload conditions, not desirable for functional BPs. We suppose that the role of $I_{Ca,LD}$ in the working of pacemaker systems is essentially the same as that of $I_{Ca,LC}$: $I_{Ca,LD}$ may play a major role in producing the action potential upstroke as well as excitation-contraction coupling, rather than in supporting robust pacemaking and driving.

Implications and Significance of Study

In the present study, we used stability and bifurcation analyses to investigate the effects of pacemaker currents on creation and modulations of the HVM pacemaker. Previous reports indicate that exploring bifurcation structures of SA node or ventricular models is useful for general understanding and systematic descriptions of the dynamical mechanisms of normal and abnormal pacemaker activities, e.g., the roles of individual currents in pacemaking (4, 9, 21, 22, 24, 45). Pacemaker currents are not indispensable for basal pacemaking of SA node cells (20, 21) or BP cells (22, 46). As shown in this study for BP cells, however, the pacemaker currents may be necessary for constructing a pacemaker system with high structural stability and high driving ability, as well as for finer regulations of pacemaking rates.

Bifurcation analyses of model cell systems may also allow us to accurately predict and properly control the dynamics and bifurcation structures of real cells, possibly applicable to cell system engineering to develop functional BPs from native cardiomyocytes or ES cells for gene or cell therapy of bradyarrhythmias (8, 10, 15, 25, 28, 32, 36, 50). Pacemaker currents are not necessarily required for creating BP cells (22, 46). Nevertheless, stable transfection of pacemaker channel genes or transplantation of BP cells expressing pacemaker channels (e.g., ES cell-derived SA node cells) to host tissues may be helpful or even necessary for creating functional BPs with robust pacemaking and driving, as well as responsiveness to autonomic regulations. This study suggests that *1*) expression of I_h (or the other pacemaker currents) is not indispensable but is helpful for creating BP cells from HVMs, *2*) expression of I_h improves structural stability and driving ability of BPs when I_{K1} density in adjacent NP cells is relatively small, as in the atrium, and *3*) expression of I_{st}, i.e., a pacemaker current with relatively slow inactivation kinetics, may especially be effective in yielding robust BP activity with stable frequency.

Limitations and Perspectives of Study

As mentioned in our previous article (22), the limitations of our study include incompleteness of the HVM model due to the

lack of experimental data from HVMs as well as the lack of experimental evidence for bifurcation structures of real myocytes. More elaborate HVM models, such as recently published ones (12, 42), with refinements of formulas to be suitable for bifurcation analyses would have to be developed for more detailed investigations using the theoretical approach. In addition, the pacemaker current formulas based on experiments for human cardiomyocytes should be used in future studies.

As suggested by Silva and Rudy (41), a potential advantage of the BP over the electronic pacemaker is responsiveness to β-adrenergic stimulation (β-AS). BP responsiveness to β-AS was very limited in the guinea pig ventricular model (41). We also found in the simulations according to their method that the HVM pacemaker did not exhibit a significant rate increase in response to β-AS, suggesting that the ventricular pacemaker is less sensitive to β-AS than the SA node pacemaker. Such low sensitivity to β-AS of the ventricular pacemaker would be due at least in part to the lack of the pacemaker currents that are abundant in SA node primary pacemaker cells (20, 21, 27, 31, 51) and are known to be enhanced by β-AS (26, 35, 43). Nevertheless, we did not show the data on this issue, because it is very important but beyond the aim of this study and because our model lacks the intracellular modulating factors such as cAMP and protein kinases. Further sophisticated models incorporating the modulating factors, as developed by Saucerman et al. (38), would be required.

We used the simple coupled-cell system to investigate the structural stability and driving ability of BP cells, believing that this study is valuable as a first step toward development of a theoretical background for engineering of functional BPs. Nevertheless, a real pacemaker system such as the intact SA node has much more complex architectures to facilitate optimization of the electrical loading by surrounding atrial or ventricular tissues (1, 2, 14, 44). Thus more elaborate multicellular models are required for investigation of the structural stability to electrotonic loads and ability to drive the heart of a BP system in vivo and of how to create BP systems with robust pacemaking and driving. In the coupled-cell model, the critical size factor (the critical number of BP cells) for stable driving of a normal HVM was quite large, e.g., at least six BP cells were required in the absence of a pacemaker current (see Figs. 8*A* and 12). A similar size effect, a size factor of 5, was previously reported for other coupled-cell systems composed of SA node cells and ventricular myocytes (19, 47). However, the coupled-cell model cannot predict the critical size of a BP to be required for stable driving of the ventricle. Using a two-dimensional system in which real atrioventricular node or model SA node cells were coupled to ventricular or atrial model cells, Joyner et al. (14) determined the critical size of the pacemaker cells for driving the surrounding quiescent cells and suggested that the critical size depends on the scale of the systems, I_{K1} density in surrounding NP cells, G_C values, and many other factors. Moreover, the roles of pacemaker currents in pacemaking and driving of BPs may also change depending on the dimension of the systems, as well as the number of BP cells, I_{K1} of adjacent NP cells, and G_C values (see Figs. 12 and 13). Further studies using multicellular (2 or 3 dimensional) models are required to determine the critical BP size for driving the ventricle and to determine how incorporating pacemaker currents affects critical BP size and BP functions.

APPENDIX A: GLOSSARY

General

F	Faraday constant
V	Membrane potential (mV)

Cell Geometry

C_m	Cell membrane capacitance
C_{BP}	C_m of BP cells
C_{NP}	C_m of NP cells
V_i	Myoplasmic volume available for Ca^{2+} diffusion
V_{rel}	Volume of junctional SR (Ca^{2+} release store)
V_{up}	Volume of network SR (Ca^{2+} uptake store)

Ionic Concentrations

$[Na^+]_o$	Extracellular Na^+ concentration
$[K^+]_o$	Extracellular K^+ concentration
$[Ca^{2+}]_o$	Extracellular Ca^{2+} concentration
$[Na^+]_i$	Intracellular Na^+ concentration
$[K^+]_i$	Intracellular K^+ concentration
$[Ca^{2+}]_i$	Myoplasmic Ca^{2+} concentration
$[Ca^{2+}]_{rel}$	Ca^{2+} concentration in junctional SR
$[Ca^{2+}]_{up}$	Ca^{2+} concentration in network SR

Equilibrium Potentials

E_{Na}	Equilibrium (Nernst) potential for Na^+
E_K	Equilibrium (Nernst) potential for K^+

Sarcolemmal Ionic Currents

g_h	Maximum I_h conductance
$g_{Ca,T}$	Maximum $I_{Ca,T}$ conductance
g_{st}	Maximum I_{st} conductance
$g_{Ca,LD}$	Maximum $I_{Ca,LD}$ conductance
d_L	Activation gating variable for $I_{Ca,L}$
f_L	Voltage-dependent inactivation gating variable for $I_{Ca,L}$
d_T	Activation gating variable for $I_{Ca,T}$
f_T	Inactivation gating variable for $I_{Ca,T}$
p_a	Activation gating variable for I_{Kr}
n	Activation gating variable for I_{Ks}
q	Inactivation gating variable for I_{to}
y	Activation gating variable for I_h
q_a	Activation gating variable for I_{st}
q_i	Inactivation gating variable for I_{st}
α_{qa}	Opening rate constant for q_a
β_{qa}	Closing rate constant for q_a
α_{qi}	Opening rate constant for q_i
β_{qi}	Closing rate constant for q_i
d_{LD}	Activation gating variable for $I_{Ca,LD}$
f_{LD}	Voltage-dependent inactivation gating variable for $I_{Ca,LD}$
$f_{Ca,\infty}$	Ca^{2+}-dependent inactivation gating variable for $I_{Ca,LD}$
h	Inactivation gating variable for I_{Na}
x_∞	Steady-state value of a gating variable x
τ_x	Time constant for a gating variable x
$J_{Ca,net}$	Net Ca^{2+} flux through the sarcolemmal membrane
$J_{Na,net}$	Net Na^+ flux through the sarcolemmal membrane

Intracellular Ca^{2+} Dynamics (SR Function and Ca^{2+} Buffering)

J_{rel}	Ca^{2+} release flux from junctional SR to subspace
J_{up}	Ca^{2+} uptake flux from myoplasm to network SR

J_{tr}	Ca^{2+} transfer flux from network SR to junctional SR
J_{leak}	Ca^{2+} leak flux from network SR to myoplasm
$[CM]_{tot}$	Total calmodulin concentration
$[CQ]_{tot}$	Total calsequestrin concentration
$[TC]_{tot}$	Total concentration of troponin-Ca complex
f_{TC}	Fractional occupancy of troponin-Ca complex by Ca^{2+}
f_{CM}	Fractional occupancy of calmodulin by Ca^{2+} in myoplasm
f_{CQ}	Fractional occupancy of calsequestrin by Ca^{2+}
K_{dCM}	Ca^{2+}-binding constant for calmodulin
K_{dCQ}	Ca^{2+}-binding constant for calsequestrin
B_{CM}	Scaling factor for fast Ca^{2+} buffering by calmodulin
B_{CQ}	Scaling factor for fast Ca^{2+} buffering by calsequestrin

APPENDIX B: MODEL EQUATIONS

The mathematical expressions used for the pacemaker currents (I_h, $I_{Ca,T}$, I_{st}, $I_{Ca,LD}$), as well as differential equations for state variables of the coupled-cell system, are given below. Units are millivolts, picoamperes, nanosiemens, picofarads, milliseconds, millimolar, and liters. The temperature assumed for the model is 37°C. The symbols used and their definitions are the same as those in our rabbit SA node model (20). Expressions for other currents and dynamics of SR Ca^{2+} handling, as well as standard parameter values and initial conditions for computations, are given in our previous article (22). See APPENDIX A for symbol definitions.

Hyperpolarization-Activated Current (I_h)

Rabbit SA node I_h from Kurata et al. (20) model [adopted from Wilders et al. (49) model].

$$I_{hK} = 0.6167 \cdot g_h \cdot (V - E_K) \cdot y^2 \quad (A1)$$

$$I_{hNa} = 0.3833 \cdot g_h \cdot (V - E_{Na}) \cdot y^2 \quad (A2)$$

$$I_h = I_{hK} + I_{hNa} \quad (A3)$$

$$y_\infty = 1/\{1 + \exp[(V + 64)/13.5]\} \quad (A4)$$

$$\tau_y = 0.71665/\{\exp[-(V + 386.9)/45.302] + \exp[(V - 73.08)/19.231]\} \quad (A5)$$

Human ventricle I_h from Cerbai et al. (3).

$$I_{hK} = 0.6167 \cdot g_h \cdot (V - E_K) \cdot y \quad (A6)$$

$$I_{hNa} = 0.3833 \cdot g_h \cdot (V - E_{Na}) \cdot y \quad (A7)$$

$$I_h = I_{hK} + I_{hNa} \quad (A8)$$

$$y_\infty = 1/\{1 + \exp[(V + 80.6)/6.8]\} \quad (A9)$$

$$\tau_y = 1{,}000/[\exp(-2.9\text{–}0.04 \cdot V) + \exp(3.6 + 0.11 \cdot V)] \quad (A10)$$

Human HCN2 current from Moroni et al. (29).

$$I_{hK} = 0.6167 \cdot g_h \cdot (V - E_K) \cdot y^2 \quad (A11)$$

$$I_{hNa} = 0.3833 \cdot g_h \cdot (V - E_{Na}) \cdot y^2 \quad (A12)$$

$$I_h = I_{hK} + I_{hNa} \quad (A13)$$

$$y_\infty = 1/\{1 + \exp[(V + 83.1)/7.89]\} \quad (A14)$$

$$\tau_y = 438.6/[0.00053 \cdot \exp(-V/13.16) + 141.17 \cdot \exp(V/13.16))] \quad (A15)$$

T-type Ca^{2+} Channel Current ($I_{Ca,T}$)

Rabbit SA node $I_{Ca,T}$ from Kurata et al. (20) model [adopted from Demir et al. (5) model].

$$I_{Ca,T} = g_{Ca,T} \cdot (V - 45) \cdot d_{T,\infty} \cdot f_T \quad (A16)$$

$$d_{T,\infty} = 1/\{1 + \exp[-(V + 26.3)/6]\} \quad (A17)$$

$$f_{T,\infty} = 1/\{1 + \exp[(V + 61.7)/5.6]\} \quad (A18)$$

$$\tau_{fT} = 1/(0.0153 \cdot \exp[-(V + 61.7)/83.3] + 0.015 \cdot \exp[(V + 61.7)/15.38)] \quad (A19)$$

Rabbit ventricle $I_{Ca,T}$ from Pugligi-Bers (34) model.

$$I_{Ca,T} = g_{Ca,T} \cdot (V - E_{Ca}) \cdot d_{T,\infty} \cdot f_T \quad (A20)$$

$$d_{T,\infty} = 1/\{1 + \exp[-(V + 48)/6.1]\} \quad (A21)$$

$$f_{T,\infty} = 1/\{1 + \exp[(V + 66)/6.6]\} \quad (A22)$$

$$\tau_{fT} = 32/\{1 + \exp[(V + 65)/5]\} + 8 \quad (A23)$$

Sustained Inward Current (I_{st})

Rabbit SA node I_{st} from Kurata et al. (20) model.

$$I_{st} = g_{st} \cdot (V - 37.4) \cdot q_{a,\infty} \cdot q_i \quad (A24)$$

$$q_{a,\infty} = 1/\{1 + \exp[-(V + 57)/5]\} \quad (A25)$$

$$\alpha_{qi} = 1[3{,}100 \cdot \exp(V/13) + 700 \cdot \exp(V/70)] \quad (A26)$$

$$\beta_{qi} = 1/[95 \cdot \exp(-V/10) + 50 \cdot \exp(-V/700)] + 0.000229/[1 + \exp(-V/5)] \quad (A27)$$

$$q_{i,\infty} = \alpha_{qi}/(\alpha_{qi} + \beta_{qi}) \quad (A28)$$

$$\tau_{qi} = 6.65/(\alpha_{qi} + \beta_{qi}) \quad (A29)$$

Rat SA node I_{st} from Shinagawa et al. (40).

$$I_{st} = g_{st} \cdot (V - 18) \cdot q_{a,\infty} \cdot q_i \quad (A30)$$

$$\alpha_{qa} = 1/[0.15 \cdot \exp(-V/11) + 0.2 \cdot \exp(-V/700)] \quad (A31)$$

$$\beta_{qa} = 1/[16 \cdot \exp(V/8) + 15 \cdot \exp(V/50)] \quad (A32)$$

$$q_{a,\infty} = \alpha_{qa}/(\alpha_{qa} + \beta_{qa}) \quad (A33)$$

$$\alpha_{qi} = 1/[3{,}100 \cdot \exp(V/13) + 700 \cdot \exp(V/70)] \quad (A34)$$

$$\beta_{qi} = 1/[95 \cdot \exp(-V/10) + 50 \cdot \exp(-V/700)] + 0.000229/[1 + \exp(-V/5)] \quad (A35)$$

$$q_{i,\infty} = \alpha_{qi}/(\alpha_{qi} + \beta_{qi}) \quad (A36)$$

$$\tau_{qi} = 1/(\alpha_{qi} + \beta_{qi}) \quad (A37)$$

Low-Voltage-Activated L-Type Ca^{2+} Channel Current ($I_{Ca,LD}$)

$$I_{Ca,LD} = g_{Ca,LD} \cdot (V - 52.8) \cdot d_{LD,\infty} \cdot f_{LD} \cdot f_{Ca,\infty} \quad (A38)$$

$$d_{LD,\infty} = 1/\{1 + \exp[-(V + 7.64)/6.32]\} \quad (A39)$$

$$f_{LD,\infty} = 1/\{1 + \exp[(V + 24.6)/6.9]\} \quad (A40)$$

$$\tau_{fLD} = 17.925/(0.1389 \cdot \exp\{-[0.0358 \cdot (V - 10.9)]^2\} + 0.0519) \quad (A41)$$

$$f_{Ca,\infty} = 1/[1 + ([Ca^{2+}]_i/0.00035)] \quad (A42)$$

Differential Equations for State Variables

Membrane potential (V).

$$dV_{BP}/dt = I_{stim} - I_{total(BP)} - I_{GC}/C_{BP} \quad (A43)$$

$$dV_{NP}/dt = -I_{total(NP)} + I_{GC}/C_{NP} \quad (A44)$$

$$I_{total} = I_{Ca,L} + I_{Kr} + I_{Ks} + I_{to} + I_{Na} + I_{K1} + I_{Na,b} + I_{Ca,b} + I_{NaK} + I_{NaCa} + I_{pCa} + I_h + I_{Ca,T} + I_{st} + I_{Ca,LD} \quad (A45)$$

Gating variables.

$$dx/dt = (x_\infty - x)/\tau_x \quad [x = d_L f_L, p_a, n, q, h, d_R, f_R, y, d_T, f_T, q_a, q_i, d_{LD}, f_{LD}] \tag{A46}$$

Intracellular ion concentrations.

$$d[Ca^{2+}]_i/dt = B_{CM} \cdot [(-J_{Ca,net} + J_{rel} \cdot V_{rel} - J_{up} \cdot V_{up} + J_{leak} \cdot V_{up})/V_i - [TC]_{tot} \cdot df_{TC}/dt] \tag{A47}$$

$$B_{CM} = 1/\{1 + [CM]_{tot} \cdot K_{dCM}/(K_{dCM} + [Ca^{2+}]_i)^2\} \tag{A48}$$

$$d[Ca^{2+}]_{rel}/dt = B_{CQ} \cdot (J_{tr} - J_{rel}) \tag{A49}$$

$$B_{CQ} = 1/\{1 + [CQ]_{tot} \cdot K_{dCQ}/(K_{dCQ} + [Ca^{2+}]_{rel})^2\} \tag{A50}$$

$$d[Ca^{2+}]_{up}/dt = J_{up} - J_{tr} \cdot V_{rel}/V_{up} - J_{leak} \tag{A51}$$

$$d[Na^{2+}]_i/dt = -J_{Na,net}/V_i \tag{A52}$$

$$J_{Ca,net} = (I_{Ca,L} + I_{Ca,b} - 2 \cdot I_{NaCa} + I_{pCa} + I_{Ca,T} + I_{Ca,LD}) \cdot C_m/(2 \cdot F) \tag{A53}$$

$$J_{Na,net} = (I_{Na} + I_{Na,b} + 3 \cdot I_{NaK} + 3 \cdot I_{NaCa} + I_{hNa} + I_{st}) \cdot C_m/F \tag{A54}$$

APPENDIX C: DETERMINATION OF EPS AS INITIAL CONDITIONS

The methods for determination of EPs as initial conditions for the single cell were described previously (22). To determine an EP of the coupled-cell system, steady-state values of the state variables V, $[Ca^{2+}]_i$, $[Na^+]_i$, $[Ca^{2+}]_{rel}$, and $[Ca^{2+}]_{up}$ for BP and NP cells were calculated numerically by the algebraic method with a nonlinear equation solver available in MATLAB 7. For bifurcation analyses and simulations using the $[K^+]_i$-fixed system, steady-state values of the state variables for BP and NP cells were computed by the following algebraic equations derived from the differential equations.

$$I_{total(BP)} + I_{GJ}/C_{BP} = 0 \; (dV_{BP}/dt = 0) \tag{A55}$$

$$I_{total(NP)} - I_{GJ}/C_{NP} = 0 \; (dV_{NP}/dt = 0) \tag{A56}$$

$$J_{Ca,net} = 0 \; (d[Ca^{2+}]_i/dt = 0) \tag{A57}$$

$$J_{rel} - J_{tr} = 0 \; (d[Ca^{2+}]_{rel}/dt = 0) \tag{A58}$$

$$J_{up} - J_{tr} \cdot V_{rel}/V_{up} - J_{leak} = 0 \; (d[Ca^{2+}]_{up}/dt = 0) \tag{A59}$$

$$J_{Na,net} = 0 \; (d[Na^+]_i/dt = 0) \tag{A60}$$

Equations A57–A60 are for either the BP or the NP cell; in total, 10 equations are required for calculating the steady state of the coupled-cell system.

ACKNOWLEDGMENTS

Present address of H. Matsuda: Group in Leading Project for Biostimulation, Kyoto Univ., Kyoto, Japan.

GRANTS

This work was supported in part by Ministry for Education, Science, Sports and Culture of Japan Grant-in-Aid for Scientific Research (C) 17590192 (to Y. Kurata and T. Shibamoto), Kanazawa Medical University Grant for Collaborative Research C2005-1 (to Y. Kurata and T. Shibamoto), and Kanazawa Medical University Grant for Promoted Research S2006-6 (to Y. Kurata).

REFERENCES

1. **Boyett MR, Dobrzynski H, Lancaster MK, Jones SA, Honjo H, Kodama I.** Sophisticated architecture is required for the sinoatrial node to perform its normal pacemaker function. *J Cardiovasc Electrophysiol* 14: 104–106, 2003.
2. **Boyett MR, Honjo H, Kodama I.** The sinoatrial node, a heterogeneous pacemaker structure. *Cardiovasc Res* 47: 658–687, 2000.
3. **Cerbai E, Pino R, Portiatti F, Sani G, Toscano M, Maccherini M, Giunti G, Mugelli A.** Characterization of the hyperpolarization-activated current, I_f, in ventricular myocytes from human failing heart. *Circulation* 95: 568–571, 1997.
4. **Chay TR, Lee YS.** Phase resetting and bifurcation in the ventricular myocardium. *Biophys J* 47: 641–651, 1985.
5. **Demir SS, Clark JW, Murphey CR, Giles WR.** A mathematical model of a rabbit sinoatrial node cell. *Am J Physiol Cell Physiol* 266: C832–C852, 1994.
6. **Dormand JR, Prince PJ.** A family of embedded Runge-Kutta formulae. *J Comput Appl Math* 6: 19–26, 1980.
7. **Garny A, Kohl P, Hunter PJ, Boyett MR, Noble D.** One-dimensional rabbit sinoatrial node models: benefits and limitations. *J Cardiovasc Electrophysiol* 14: S121–S132, 2003.
8. **Gepstein L, Feld Y, Yankelson L.** Somatic gene and cell therapy strategies for the treatment of cardiac arrhythmias. *Am J Physiol Heart Circ Physiol* 286: H815–H822, 2004.
9. **Guevara MR, Jongsma HJ.** Three ways of abolishing automaticity in sinoatrial node: ionic modeling and nonlinear dynamics. *Am J Physiol Heart Circ Physiol* 262: H1268–H1286, 1992.
10. **He JQ, Ma Y, Lee Y, Thomson JA, Kamp TJ.** Human embryonic stem cells develop into multiple types of cardiac myocytes: action potential characterization. *Circ Res* 93: 32–39, 2003.
11. **Hund TJ, Kucera JP, Otani NF, Rudy Y.** Ionic charge conservation and long-term steady state in the Luo-Rudy dynamic cell model. *Biophys J* 81: 3324–3331, 2001.
12. **Iyer V, Mazhari R, Winslow RL.** A computational model of the human left-ventricular epicardial myocyte. *Biophys J* 87: 1507–1525, 2004.
13. **Joyner RW, Kumar R, Golod DA, Wilders R, Jongsma HJ, Verheijck EE, Bouman L, Goolsby WN, van Ginneken AC.** Electrical interactions between a rabbit atrial cell and a nodal cell model. *Am J Physiol Heart Circ Physiol* 274: H2152–H2162, 1998.
14. **Joyner RW, Wang YG, Wilders R, Golod DA, Wagner MB, Kumar R, Goolsby WN.** A spontaneously active focus drives a model atrial sheet more easily than a model ventricular sheet. *Am J Physiol Heart Circ Physiol* 279: H752–H763, 2000.
15. **Kehat I, Khimovich L, Caspi O, Gepstein A, Shofti R, Arbel G, Huber I, Satin J, Itskovitz-Eldor J, Gepstein L.** Electromechanical integration of cardiomyocytes derived from human embryonic stem cells. *Nat Biotechnol* 22: 1282–1289, 2004.
16. **Koschak A, Reimer D, Huber I, Grabner M, Glossmann H, Engel J, Striessnig J.** α_{1C} ($Ca_V1.3$) subunits can form L-type Ca^{2+} channels activating at negative voltages. *J Biol Chem* 276: 22100–22106, 2001.
17. **Koumi S, Backer CL, Arentzen CE.** Characterization of inwardly rectifying K^+ channel in human cardiac myocytes: alterations in channel behavior in myocytes isolated from patients with idiopathic dilated cardiomyopathy. *Circulation* 92: 164–174, 1995.
18. **Krogh-Madsen T, Schaffer P, Skriver AD, Taylor LK, Pelzmann B, Koidl B, Guevara MR.** An ionic model for rhythmic activity in small clusters of embryonic chick ventricular cells. *Am J Physiol Heart Circ Physiol* 289: H398–H413, 2005.
19. **Kumar R, Wilders R, Joyner RW, Jongsma HJ, Verheijck EE, Golod DA, van Ginneken ACG, Goolsby WN.** Experimental model for an ectopic focus coupled to ventricular cells. *Circulation* 94: 833–841, 1996.
20. **Kurata Y, Hisatome I, Imanishi S, Shibamoto T.** Dynamical description of sinoatrial node pacemaking: improved mathematical model for primary pacemaker cell. *Am J Physiol Heart Circ Physiol* 283: H2074–H2101, 2002.
21. **Kurata Y, Hisatome I, Imanishi S, Shibamoto T.** Roles of L-type Ca^{2+} and delayed-rectifier K^+ currents in sinoatrial node pacemaking: insights from stability and bifurcation analyses of a mathematical model. *Am J Physiol Heart Circ Physiol* 285: H2804–H2819, 2003.
22. **Kurata Y, Hisatome I, Matsuda H, Shibamoto T.** Dynamical mechanisms of pacemaker generation in I_{K1}-downregulated human ventricular myocytes: insights from bifurcation analyses of a mathematical model. *Biophys J* 89: 1–23, 2005.
23. **Kuznetsov YA.** *Elements of Applied Bifurcation Theory* (3rd ed.). New York: Springer, 2003.
24. **Landau M, Lorente P, Michaels D, Jalife J.** Bistabilities and annihilation phenomena in electrophysiological cardiac models. *Circ Res* 66: 1658–1672, 1990.
25. **Lin G, Cai J, Jiang H, Shen H, Jiang X, Yu Q, Song J.** Biological pacemaker created by fetal cardiomyocyte transplantation. *J Biomed Sci* 12: 513–519, 2005.

26. **Lonardo G, Cerbai E, Casini S, Giunti G, Bonacchi M, Battaglia F, Fiorani B, Stefano PL, Sani G, Mugelli A.** Pharmacological modulation of the hyperpolarization-activated current (I_f) in human atrial myocytes: focus on G protein-coupled receptors. *J Mol Cell Cardiol* 38: 453–460, 2005.
27. **Mangoni ME, Couette B, Bourinet E, Platzer J, Reimer D, Striessnig J, Nargeot J.** Functional role of L-type $Ca_v1.3$ Ca^{2+} channels in cardiac pacemaker activity. *Proc Natl Acad Sci USA* 100: 5543–5548, 2003.
28. **Miake J, Marbán E, Nuss HB.** Gene therapy: biological pacemaker created by gene transfer. *Nature* 419: 132–133, 2002.
29. **Moroni A, Barbuti A, Altomare C, Viscomi C, Morgan J, Baruscotti M, DiFrancesco D.** Kinetic and ionic properties of the human HCN2 pacemaker channel. *Pflügers Arch* 439: 618–626, 2000.
30. **Parker TS, Chua LO.** *Practical Numerical Algorithms for Chaotic Systems*. New York: Springer, 1989.
31. **Platzer J, Engel J, Schrott-Fischer A, Stephan K, Bova S, Chen H, Zheng H, Striessnig J.** Congenital deafness and sinoatrial node dysfunction in mice lacking class D L-type Ca^{2+} channels. *Cell* 102: 89–97, 2000.
32. **Plotnikov AN, Sosunov EA, Qu J, Shlapakova IN, Anyukhovsky EP, Liu L, Janse MJ, Brink PR, Cohen IS, Robinson RB, Danilo P Jr, Rosen MR.** Biological pacemaker implanted in canine left bundle branch provides ventricular escape rhythms that have physiologically acceptable rates. *Circulation* 109: 506–512, 2004.
33. **Priebe L, Beuckelmann DJ.** Simulation study of cellular electric properties in heart failure. *Circ Res* 82: 1206–1223, 1998.
34. **Puglisi JL, Bers DM.** LabHEART: an interactive computer model of rabbit ventricular myocyte ion channels and Ca transport. *Am J Physiol Cell Physiol* 281: C2049–C2060, 2001.
35. **Qu Y, Baroudi G, Yue Y, El-Sherif N, Boutjdir M.** Localization and modulation of α_{1D} (Cav1.3) L-type Ca channel by protein kinase A. *Am J Physiol Heart Circ Physiol* 288: H2123–H2130, 2005.
36. **Qu J, Plotnikov AN, Danilo P Jr, Shlapakova I, Cohen IS, Robinson RB, Rosen MR.** Expression and function of a biological pacemaker in canine heart. *Circulation* 107: 1106–1109, 2003.
37. **Robinson RB, Brink PR, Cohen IS, Rosen MR.** I_f and the biological pacemaker. *Pharmacol Res* 53: 407–415, 2006.
38. **Saucerman JJ, Brunton LL, Michailova AP, McCulloch AD.** Modeling β-adrenergic control of cardiac myocytes contractility in silico. *J Biol Chem* 278: 47997–48003, 2003.
39. **Shampine LF, Reichelt MW.** The MATLAB ODE Suite. *SIAM J Sci Comput* 18: 1–22, 1997.
40. **Shinagawa Y, Satoh H, Noma A.** The sustained inward current and inward rectifier K^+ current in pacemaker cells dissociated from rat sinoatrial node. *J Physiol* 523: 593–605, 2000.
41. **Silva J, Rudy Y.** Mechanism of pacemaking in I_{K1}-downregulated myocytes. *Circ Res* 92: 261–263, 2003.
42. **ten Tusscher KHWJ, Noble D, Noble PJ, Panfilov AV.** A model for human ventricular tissue. *Am J Physiol Heart Circ Physiol* 286: H1573–H1589, 2004.
43. **Toyoda F, Ding WG, Matsuura H.** Responses of the sustained inward current to autonomic agonists in guinea-pig sino-atrial node pacemaker cells. *Br J Pharmacol* 144: 660–668, 2005.
44. **Verheijck EE, Wilders R, Bouman LN.** Atrio-sinus interaction demonstrated by blockade of the rapid delayed rectifier current. *Circulation* 105: 880–885, 2002.
45. **Vinet A, Roberge FA.** A model study of stability and oscillations in the myocardial cell membrane. *J Theor Biol* 147: 377–412, 1990.
46. **Viswanathan PC, Coles JA Jr, Sharma V, Sigg DC.** Recreating an artificial biological pacemaker: insights from a theoretical model. *Heart Rhythm* 3: 824–831, 2006.
47. **Wagner MB, Golod D, Wilders R, Verheijck EE, Joyner RW, Kumar R, Jongsma HJ, van Ginneken ACG, Goolsby WN.** Modulation of propagation from an ectopic focus by electrical load and by extracellular potassium. *Am J Physiol Heart Circ Physiol* 272: H1759–H1796, 1997.
48. **Watanabe EI, Honjo H, Anno T, Boyett MR, Kodama I, Toyama J.** Modulation of pacemaker activity of sinoatrial node cells by electrical load imposed by an atrial cell model. *Am J Physiol Heart Circ Physiol* 269: H1735–H1742, 1995.
49. **Wilders R, Jongsma HJ, van Ginneken ACG.** Pacemaker activity of the rabbit sinoatrial node: a comparison of mathematical models. *Biophys J* 60: 1202–1216, 1991.
50. **Xue T, Cho HC, Akar FG, Tsang SY, Jones SP, Marbán E, Tomaselli GF, Li RA.** Functional integration of electrically active cardiac derivatives from genetically engineered human embryonic stem cells with quiescent recipient ventricular cardiomyocytes: insights into the development of cell-based pacemakers. *Circulation* 111: 11–20, 2005.
51. **Zhang Z, Xu Y, Song H, Rodriguez J, Tuteja D, Namkung Y, Shin HS, Chiamvimonvat N.** Functional roles of $Ca_v1.3$ (α_{1D}) calcium channel in sinoatrial nodes: insight gained using gene-targeted null mutant mice. *Circ Res* 90: 981–987, 2002.

Biophysical Journal Volume 95 July 2008 951–977

Regional Difference in Dynamical Property of Sinoatrial Node Pacemaking: Role of Na^+ Channel Current

Yasutaka Kurata,* Hiroyuki Matsuda,* Ichiro Hisatome,† and Toshishige Shibamoto*
*Department of Physiology, Kanazawa Medical University, Ishikawa 920-0293, Japan, and †Division of Regenerative Medicine and Therapeutics, Tottori University Graduate School of Medical Science, Yonago 683-0826, Japan

ABSTRACT To elucidate the regional differences in sinoatrial node pacemaking mechanisms, we investigated 1), bifurcation structures during current blocks or hyperpolarization of the central and peripheral cells, 2), ionic bases of regional differences in bifurcation structures, and 3), the role of Na^+ channel current (I_{Na}) in peripheral cell pacemaking. Bifurcation analyses were performed for mathematical models of the rabbit sinoatrial node central and peripheral cells; equilibrium points, periodic orbits, and their stability were determined as functions of parameters. Structural stability against applications of acetylcholine or electrotonic modulations of the atrium was also evaluated. Blocking L-type Ca^{2+} channel current ($I_{Ca,L}$) stabilized equilibrium points and abolished pacemaking in both the center and periphery. Critical acetylcholine concentration and gap junction conductance for pacemaker cessation were higher in the periphery than in the center, being dramatically reduced by blocking I_{Na}. Under hyperpolarized conditions, blocking I_{Na}, but not eliminating $I_{Ca,L}$, abolished peripheral cell pacemaking. These results suggest that 1), $I_{Ca,L}$ is responsible for basal pacemaking in both the central and peripheral cells, 2), the peripheral cell is more robust in withstanding hyperpolarizing loads than the central cell, 3), I_{Na} improves the structural stability to hyperpolarizing loads, and 4), I_{Na}-dependent pacemaking is possible in hyperpolarized peripheral cells.

INTRODUCTION

Elucidation of the mechanisms of the sinoatrial (SA) node pacemaking is one of the most important subjects in cardiac electrophysiology. A large body of information on the ionic mechanisms of SA node pacemaking has been obtained from numerous experimental and theoretical studies (1). From the bifurcation analysis of a mathematical model for SA node primary pacemaker cells, we have elucidated the dynamical mechanisms of the natural SA node pacemaking and the roles of L-type Ca^{2+} channel current ($I_{Ca,L}$) and rapidly activating delayed-rectifier K^+ current (I_{Kr}) in basal pacemaking (2). We have suggested that 1), the instability of an equilibrium point (EP) is essentially important for pacemaker generation; 2), $I_{Ca,L}$ is responsible for EP instability and pacemaker generation, whereas I_{Kr} is not necessarily required for constructing a pacemaker cell system; and 3), I_{Kr} acts as an oscillation amplifier and frequency stabilizer as well as plays an important role in preventing bifurcation to quiescence of the system. Nevertheless, the pacemaking mechanism addressed in our previous article is for primary pacemaker cells in the central SA node. We expect that the same mechanisms underlie the pacemaking of transitional or peripheral SA node cells. However, previous reports suggest regional differences in pacemaker mechanisms, e.g., blocking $I_{Ca,L}$ abolished spontaneous activity in central SA node tissues, but not in peripheral tissues (3). In the peripheral SA node, the Na^+ channel current (I_{Na}), not present in the central SA node, might contribute to EP instability and pacemaker generation. Hyperpolarization-activated cation current (I_h) has also been suggested to play a predominant role in the subsidiary pacemaker mechanisms (4–6). Thus, regional differences in pacemaker mechanisms and roles of sarcolemmal currents, such as I_{Na} or I_h, remain to be clarified.

The aim of this study was to elucidate the regional differences in the mechanisms for basal pacemaking of SA node cells in terms of the nonlinear dynamical system theory. We particularly focused on the roles of I_{Na} in peripheral cell pacemaking, as well as the regional differences in the robustness of pacemaker activity to current blocks or hyperpolarizing loads. In previous studies, bifurcation structures (i.e., ways of changes in the number or stability of equilibrium and periodic states) of ventricular or SA node model systems were investigated for elucidating the mechanisms of normal and abnormal pacemaker activities (2,7–13). These theoretical works indicate that the initiation or cessation of pacemaker activity is considered as a bifurcation phenomenon, and that the mathematical approach—bifurcation analysis—provides a convenient way of understanding how individual currents contribute to pacemaker activities. In this study, therefore, we compared the bifurcation structures during current blocks or hyperpolarization of the central and peripheral SA node cells and also explored the ionic bases of the regional differences in bifurcation structures. Furthermore, we explored the manner in which I_{Na} contributes to the robustness of peripheral cell pacemaking and whether I_{Na}-dependent pacemaking is possible in the peripheral cell.

Local stability and bifurcation analyses were performed for the modified versions of our SA node model (14), as well as Zhang et al. models (15,16), for central and peripheral cells.

Submitted May 15, 2007, and accepted for publication March 25, 2008.

Address reprint requests to Yasutaka Kurata, Dept. of Physiology, Kanazawa Medical University, 1-1 Daigaku, Uchinada-machi, Kahoku-gun, Ishikawa 920-0293, Japan. E-mail: yasu@kanazawa-med.ac.jp

Editor: Edward H. Egelman.

0006-3495/08/07/951/27 $2.00

doi: 10.1529/biophysj.107.112854

We constructed bifurcation diagrams by calculating EPs, periodic orbits (POs), stability of EPs and POs, and bifurcation points as functions of bifurcation parameters such as the maximum current conductance. The structural stability of the model cells (robustness of pacemaker activity) was also evaluated by computing the stability and dynamics of the systems during applications of constant bias currents (I_{bias}) or acetylcholine (ACh), or during electrotonic modulations by the atrium.

A salient point of this study is that the theory of bifurcations of nonlinear dynamical systems was used to obtain significant insights into the region-dependent mechanisms of SA node pacemaking. Elucidating the regional differences in bifurcation structures of SA node cells would lead to a deeper understanding of the pacemaker mechanisms and may also provide a theoretical background for engineering a biological pacemaker (13,17,18). Definitions of the specific terms for the nonlinear dynamics and bifurcation theory are given at the end of the Theory and Methods section (see also (19–21)).

THEORY AND METHODS

Mathematical formulation

Base models for central and peripheral SA node cells

Zhang et al. (15) were the first to develop single-cell models for central and peripheral SA node cells of the rabbit that were based on the experimentally observed regional differences in action potential (AP) parameters, ionic current densities, and pharmacological responses. Their models are simplified versions that do not include intracellular Ca^{2+} dynamics or other intracellular factors. Nevertheless, we first chose to use their models, which have been corrected by Garny et al. (16), for the following reasons:

1. There was no other peripheral SA node model suitable for bifurcation analysis.
2. Their models could accurately reproduce the experimental data for the regional differences in AP dynamics and effects of various channel blockers, as summarized in Zhang et al. (15).
3. In our preliminary study, the bifurcation structures of their central cell model were essentially the same as those of our primary pacemaker model incorporating the dynamics of intracellular ion concentrations (2,14).
4. Their simple models are more suitable for bifurcation analyses than other more complex models.
5. Their cell models have been used for constructing SA node tissue models (16,22).

We found that EPs of their original models are stable, and thus they exhibit "bistability" (i.e., coexistence of stable steady and periodic states) under normal conditions. This implies that "annihilation" can easily occur in SA node cells; however, annihilation is seldom observed in SA node preparations (9). In the aspects of the nonlinear dynamics and bifurcation theory, pacemaker activity could be defined as a stable limit cycle (LC) around an unstable EP; thus, the most important dynamical property of the SA node cell system for robust pacemaking appears to be the instability of an EP (2). Other previous SA node models appear not to have a stable EP (2,23–26). Thus, we believe that EPs of SA node cell models must be unstable under normal conditions. To make the EPs unstable, therefore, the steady-state activation ($d_{L\infty}$) and inactivation ($f_{L\infty}$) curves for $I_{Ca,L}$ were positively shifted by 5 and 10 mV, respectively, with the maximum conductance ($g_{Ca,L}$) being reduced by 5%; the shifts of $d_{L\infty}$ and $f_{L\infty}$ curves were determined so as to lie within the experimental ranges as shown in Fig. 2 of Zhang et al. (15). This modification only slightly altered the AP waveforms. A complete list of the equations and standard parameter values for their models has been provided in previous articles (15,16). The formulas for the modified $I_{Ca,L}$ are given in Appendix A.

Intracellular Ca^{2+} dynamics is known to exert substantial effects on the dynamics of pacemaker cells and may also significantly affect the bifurcation structures of SA node cells. Therefore, we also used models that incorporated intracellular Ca^{2+} dynamics. On the basis of the Zhang et al. models (15) and related experimental data, we developed the central and peripheral versions of our SA node model (14). Although the expressions for individual components of our modified models (referred to as the Kurata et al. models) are essentially the same as in the previous article (14), the original formulas for I_{Na} and I_h were replaced by those of the Zhang et al. models for the following reasons: 1), the I_{Na} formulas of the Zhang et al. model yielded better fits to the experimental data for SA node I_{Na} kinetics (27,28), and 2), voltage dependence of the original formula for I_h activation (y^2) was so steep that I_h became too large for the peripheral cell model and yielded irregular dynamics. Standard parameter values for the Kurata et al. models are provided in Table 1. Dynamics of the Kurata et al. models, as well as the Zhang et al. models, with the standard parameter values are shown in Appendix A (see Fig. 17).

In our original or other SA node models, the contribution of sarcoplasmic reticulum (SR) Ca^{2+} cycling to pacemaker activity was small; the suppression of SR Ca^{2+} release did not slow pacemaking as dramatically as did the application of ryanodine or BAPTA in experiments (see Table 4 of Kurata et al. (14)). To examine how SR Ca^{2+} release affects the stability, dynamics, and bifurcation of SA node cells, we developed the modified versions of our SA node model for which SR Ca^{2+} cycling was enhanced by increasing the rate constants of Ca^{2+} uptake (P_{up}) and release (P_{rel}). The central cell model with increased P_{up} and P_{rel} could exhibit a 68.1–112.2% increase in CL on minimizing SR Ca^{2+} release, whereas a peripheral version of such a large response could not be developed, probably because of the presence of large I_{Na} (data not shown). Bifurcation structures of our original model and the modified models with enhanced SR Ca^{2+} cycling were essentially the same (data not shown). Thus, only the data from the models of the medium response (yielding 11.8–23.7% increases in CL) are shown in this article.

The standard models for the normal pacemaker activity include 13–14 membrane current components. The time-dependent change in the membrane potential (V_S) is described by

$$dV_S/dt = -(I_{Ca,L} + I_{Ca,T} + I_{Na} + I_h + I_{st} + I_{Kr} + I_{Ks} + I_{to} + I_{sus} + I_{b,Na} + I_{b,Ca} + I_{b,K} + I_{NaK} + I_{NaCa})/C_S, \quad (1)$$

where $I_{Ca,L}$ and $I_{Ca,T}$ represent the L-type and T-type Ca^{2+} channel currents, respectively. The rapid and slow components of the delayed-rectifier K^+ currents are denoted as I_{Kr} and I_{Ks}, respectively. The membrane current system also includes I_{Na}, I_h, the sustained inward current (I_{st}), four AP-sensitive currents consisting of transient (I_{to}) and sustained (I_{sus}) components, background currents carried by Na^+ ($I_{b,Na}$), Ca^{2+} ($I_{b,Ca}$) and K^+ ($I_{b,K}$), Na^+-K^+ pump current (I_{NaK}), and Na^+/Ca^{2+} exchanger current (I_{NaCa}). All the currents charge the membrane capacitance (C_S).

Incorporation of ACh effects on ionic currents

To investigate the bifurcation structure of the model cells during applications of ACh, we incorporated the formulas of Dokos et al. (29) or Zhang et al. (30) for the muscarinic K^+ channel current ($I_{K,ACh}$), as well as for the modifications of $I_{Ca,L}$ and I_h by ACh, into the base models. Both the formula sets yielded qualitatively the same results; thus, only the results obtained with the formulas of Dokos et al. (29) are shown. It is unknown whether the density of the muscarinic K^+ channel varies between the center and periphery of the SA node, whereas the density of the muscarinic M_2 receptor as well as vagal innervation may be greater in the center than in the periphery (31,32). In this study, therefore, it was assumed that the $I_{K,ACh}$ density is the same in central and peripheral cells, as in Zhang et al. (30). Sensitivities to ACh of $I_{K,ACh}$, $I_{Ca,L}$, and I_h were also assumed to be independent of the regions. The ex-

TABLE 1 Standard parameter values for the original and modified Kurata et al. models

Parameters	Units	Original central*	Modified central	Modified peripheral
C_m	pF	32	20	65
V_{cell}	pL	3.5186	2.19911	7.147123
V_{sub}	pL	0.0351	0.021936	0.0712925
V_i	pL	1.5835	0.98965	3.216384
V_{rel}	pL	0.0042	0.0026389	0.00857654
V_{up}	pL	0.0408	0.0255097	0.0829066
$[K^+]_o$	mM	5.4	5.4	5.4
$[K^+]_i$	mM	Variable	140	140
$g_{Ca,L}$	nS/pF	0.58	0.58	1.6008
g_{Kr}	nS/pF	$0.025 \times [K^+]_o^{0.59}$	$0.025 \times [K^+]_o^{0.59}$	$0.09255 \times [K^+]_o^{0.59}$
g_{Ks}	nS/pF	0.0259	0.0259	0.0958818
g_{to}	nS/pF	0.18	0.18	0.4194
g_{sus}	nS/pF	0.02	0.02	0.0466
g_{Na}†		0	*0*	*1.204×10^{-15}*
$g_{Ca,T}$	nS/pF	0.458	0.458	0.458
g_h†	nS/pF	0.375	*0.05465*	*0.1565*
g_{st}	nS/pF	0.015	0.0075	0
$g_{Na,b}$	nS/pF	0.0054	0.0054	0.0093312
$g_{K,ACh}$	$pA \times mM^{-1} \times pF^{-1}$	$0.0011 \times [K^+]_o^{0.41}$	$0.0011 \times [K^+]_o^{0.41}$	$0.0011 \times [K^+]_o^{0.41}$
I_{NaKmax}	pA/pF	3.6	3.6	9.72‡
k_{NaCa}	pF^{-1}	125	125	187.5‡
$T_{dif,Ca}$	ms	0.04	0.01	0.01
P_{rel}	ms^{-1}	0.5	1.25	2.50
P_{up}	$mM \times ms^{-1}$	0.005	0.01	0.02
$k\tau_q$§		1	0.670	0.670
$k\tau_r$§		1	0.303	0.303

*Parameter values used for the original Kurata et al. model (14) are given for comparison.
†Values are shown in *italic*, because the formulas used in this study are different from those of the original model and thus direct comparison is impossible.
‡Higher activities of Na^+-K^+ pump and Na^+/Ca^{2+} exchanger were required to counteract the increased Ca^{2+} and Na^+ influx via Na^+ and Ca^{2+} channels.
§Scaling factors for the activation and inactivation time constants of I_{to} and I_{sus}, which were determined for the peripheral model to reproduce the AP waveform experimentally observed in the periphery of SA node tissues (15).

pressions for these currents with the ACh modifications of Dokos et al. (29) are given in Appendix A.

Formulation of a coupled-cell model

To investigate the electrotonic influences of atrial myocytes on stability and dynamics of SA node cells, we used a coupled-cell model as introduced by Watanabe et al. (33). According to their method, a SA node cell was connected to a passive membrane model (resistance-capacitance (R-C) circuit) for an atrial myocyte via the gap junction conductance (G_C) of 0–20 nS. We used an atrial membrane capacitance (C_A) of 51 pF and an atrial membrane resistance (R_A) of 0.22 GOhm, as in Watanabe et al. (33), for the central cell ($C_S = 20$ pF). For the peripheral cell with a larger capacitance ($C_S = 65$ pF), the C_A and R_A values were scaled by multiplying 3.25 and 3.25^{-1}, respectively, to yield the same capacitance ratio (C_S/C_A) for the peripheral cell as for the central cell. An offset voltage, corresponding to a resting potential of the atrial myocyte, was set equal to −80 mV.

Time-dependent changes in the membrane potentials of the SA node cell (V_S) and atrial myocyte (V_A) were calculated by the equations

$$dV_S/dt = -(I_{total} + I_C/C_S) \quad (2)$$

$$dV_A/dt = (I_C - I_A)/C_A \quad (3)$$

$$I_C = G_C(V_S - V_A) \quad (4)$$

$$I_A = (V_A + 80)/R_A, \quad (5)$$

where I_{total} and I_A represent the sum of sarcolemmal ionic currents in the SA node cell (pA/pF) and the atrial membrane current (pA), respectively. I_C denotes the gap junction current (pA).

Bifurcation analysis

The model cells are 15- or 26-order autonomous continuous-time dynamical systems, each of which is described as a set of 15 or 26 first-order, nonlinear ordinary differential equations. Dynamical properties and bifurcation structures of a model cell system were determined by analytically and numerically handling the differential equations. Numerical computations were performed with MATLAB 7 for Windows XP (The MathWorks, Natick, MA) on Workstation HP xw9300 (Hewlett-Packard, Tokyo, Japan) and CELSIUS X630 (Fujitsu, Tokyo, Japan).

Locating EPs and LCs

In the model cell systems, 15 or 26 state variables define a 15- or 26-dimensional state point in the 15- or 26-dimensional state space. We calculated EPs and LCs (isolated POs) in the state space. An EP was determined as a point at which the vector field vanishes. A steady-state value of the state variable V_S (for $dV_S/dt = 0$) was calculated by the Newton-Raphson algorithm, practically with a nonlinear equation solver (fsolve) available in MATLAB 7 (optimization toolbox); then, steady-state values of the gating variables for individual currents were computed. A stable LC was located by the brute-force approach or autonomous shooting method (20) using the numerical algorithms available as MATLAB ODE solvers, i.e., 1), a variable time-step numerical differentiation approach selected for its suitability to stiff systems (ode15s) and 2), a fourth-order adaptive-step Runge-Kutta algorithm (ode45). When a stable LC appeared, the AP amplitude (APA) as a voltage difference between the local potential minimum (V_{min}) and maximum (V_{max}), as well as the cycle length (CL), was determined for each calculation of a cycle. Numerical integration was continued until the differences in both APA and CL between the newly calculated cycle and the preceding one became

$<1 \times 10^{-3}$ of the preceding APA and CL values. To locate an unstable LC, we used CL_MATCONT, a continuation toolbox for MATLAB (34).

Constructing one-parameter bifurcation diagrams

To examine how the stability and dynamics of the model cells alter with changes in bifurcation parameters, we constructed one-parameter bifurcation diagrams in which values of a state variable at EPs and extrema of LCs are plotted as functions of the bifurcation parameters. Bifurcation parameters chosen in this study include 1), the maximum conductance of $I_{Ca,L}$ ($g_{Ca,L}$), I_{Kr} (g_{Kr}), I_{Na} (g_{Na}), I_h (g_h), and $I_{Ca,T}$ ($g_{Ca,T}$); 2), amplitude of I_{bias}; 3), ACh concentration ([ACh]); and 4), G_C. The maximum conductance is expressed as normalized values, i.e., ratios to the control value.

A single bifurcation parameter was systematically changed while keeping all other parameters at their standard values. The steady-state membrane potential (V_E) at EPs (steady-state branches) and local potential extrema (V_{min}, V_{max}) of LCs (periodic branches), as well as the CL of LCs, were determined and plotted for each value of the bifurcation parameter. When periodic behavior was irregular, model cell dynamics were computed for 60 s; all potential extrema and CL values sampled during the last 10 s were then plotted in the diagrams.

Detecting codimension-one bifurcations (determination of EP and LC stabilities)

The critical parameter value (bifurcation point) at which a codimension-one bifurcation occurs was determined by evaluating the existence and stability of EPs and LCs at each value of a relevant parameter (one-parameter bifurcation analysis). The asymptotic stability of an EP was determined by computing eigenvalues of a Jacobian matrix derived from the linearization of the nonlinear systems around the EP (for details, see Appendix B). The stability of an LC was determined by its characteristic multipliers, which were calculated as eigenvalues of the solution of the variational equation (for more details, see (9,12,20)).

The Hopf bifurcation point at which the stability of an EP reverses was determined by the stability analysis. The saddle-node (SN) bifurcation point at which two EPs coalesce and disappear was also detected as a point at which the steady-state current-voltage (I/V) curve and zero-current axis come in contact with each other. Moreover, the saddle-node, period-doubling, and Neimark-Sacker bifurcations were detected for LCs (for details, see "Definitions of Terms" at the end of this section and also (9,21)).

Constructing two-parameter bifurcation diagrams

We further constructed two-parameter bifurcation diagrams in which the path of codimension-one bifurcation determined by the one-parameter bifurcation analysis is traced in a parameter plane. The primary parameter was systematically changed with the secondary parameter fixed at a constant value. The critical value of the primary parameter at which Hopf or saddle-node bifurcations occur on the steady-state branch was determined for various different values of the secondary parameter. Bifurcation values for the primary parameter were plotted as a function of the secondary parameter. Codimension-two saddle-node bifurcation at which two loci of codimension-one (Hopf) bifurcation points coalesce and disappear was detected.

Definition and evaluation of structural stability

We also evaluated the structural stability of SA node cells, which is defined as the robustness of pacemaker activity to various interventions or modifications that may cause a bifurcation to quiescence or irregular dynamics (for details, see Kurata et al. (2)). In this study, we tested the structural stability against applications of hyperpolarizing (or depolarizing) I_{bias} or ACh and against electrotonic loads of an adjacent atrial myocyte.

The manner of evaluating the structural stability to I_{bias} is essentially the same as described in our previous articles (2,13). Changes in V_E and its stability during I_{bias} applications were depicted as the I_{bias}-V_E curve (for more details, see Fig. 4 in the Results section; see also Fig. 1 of Kurata et al. (2)). Hopf and saddle-node bifurcation points in the I_{bias}-V_E curve were determined as functions of bifurcation parameters and plotted on both the potential and current coordinates. Changes in EPs, LC dynamics, and their stability were also determined with increasing [ACh] or G_C; the Hopf bifurcation for EP stabilization, as well as the saddle-node, period-doubling, or Neimark-Sacker bifurcation causing cessation or destabilization of LCs, were detected.

In the unstable I_{bias}, [ACh] or G_C region, a system has an unstable EP only (no stable EP), generally exhibiting robust pacemaking (stable LCs) without annihilation. When the system removes to the stable I_{bias}, [ACh] or G_C region with a stable EP, it would, however, come to a rest at the stable EP via gradual decline of LCs, annihilation, or irregular dynamics (9). Thus, the larger the unstable I_{bias}, [ACh], or G_C range is, the more structurally stable the pacemaker system is.

Definitions of terms specific to nonlinear dynamics and bifurcation theory

Autonomous system

An nth-order autonomous continuous-time dynamical system is defined by the state equation, $d\mathbf{x}/dt = \mathbf{f}(\mathbf{x})$, where the vector field $\mathbf{f}$ does not depend on time but depends only on the state variable $\mathbf{x}$ (20). A dynamical system is nonautonomous when the vector field $\mathbf{f}$ explicitly contains time $\mathbf{t}$.

Limit set

The set of points in state space that a trajectory repeatedly visits in autonomous systems.

Equilibrium point

A time-independent steady-state point at which the vector field vanishes (i.e., $d\mathbf{x}/dt = 0$) in the state space of an autonomous system, constructing the steady-state branch in one-parameter bifurcation diagrams. This state point corresponds to the zero-current crossing in the steady-state I/V curve, i.e., a quiescent state of a cell if it is stable.

Periodic orbit

A closed trajectory in the state space of a system, constructing the periodic branch in one-parameter bifurcation diagrams.

Limit cycle

An isolated periodic limit set onto which a trajectory is asymptotically attracted in an autonomous system. A stable LC corresponds to an oscillatory state—i.e., pacemaker activity—of a cell.

Bifurcation

A qualitative change in a limit set (i.e., in a solution of ordinary differential equations) caused by altering parameters, *e.g.*, a change in the number of EPs or LCs, a change in the stability of an EP or LC, and a transition from a periodic to quiescent state. Bifurcation phenomena that can be observed in cardiac cells include a cessation or generation of pacemaker activity and occurrence of irregular dynamics such as skipped-beat runs (9).

Hopf bifurcation

This is a bifurcation at which the stability of an EP reverses with emergence or disappearance of a LC, occurring when the eigenvalues of a Jacobian matrix for the EP have a single complex conjugate pair and its real part reverses the sign through zero. It is supercritical when a stable EP becomes unstable with the emergence of a stable LC; it is subcritical when an unstable EP becomes stable with emergence of an unstable LC (21).

Saddle-node bifurcation

This is a bifurcation at which two EPs (steady-state branches) or two periodic solutions (periodic branches) coalesce and disappear, also called a fold or limit point bifurcation. The saddle-node bifurcation of EPs occurs when one of eigenvalues of a Jacobian matrix is zero; that of LCs occurs when one of characteristic multipliers becomes >1.

Period-doubling bifurcation

This is a bifurcation at which a stable period-K solution becomes unstable and spawns a stable period-2K solution (20), also referred to as a flip bifurcation. This occurs when one of characteristic multipliers becomes <-1.

Neimark-Sacker bifurcation

This is a bifurcation at which a stable LC becomes unstable with emergence of torus trajectories; it is thus also called a torus bifurcation. This bifurcation occurs when a complex conjugate pair of characteristic multipliers comes outside of a unit circle in the complex plane.

Codimension

The codimension of a bifurcation is the minimum dimension of the parameter space in which the bifurcation may occur in a persistent way (19,35). In other words, the codimension is the number of independent conditions determining the bifurcation (21). A bifurcation with codimension 1 is a point in one-parameter bifurcation diagrams or a line in two-parameter bifurcation diagrams, whereas a bifurcation with codimension 2 is a point in the two-parameter space.

Bistability

This means the coexistence of two stable structures in the phase space of a system. In the region of bistability, two stable EPs or stable LCs coexist, or a stable LC coexists with a stable EP (7,9,10,12). Thus, the system has two stable solutions at the same time in the bistable zone. Bistability links to the transition between two stable states; e.g., annihilation (transition from LC to EP) and single-pulse triggering (transition from EP to LC) could be achieved.

Annihilation

Permanent stable extinction of spontaneous activity, which depends upon the polarity, timing, and magnitude of the applied stimuli (9,10,12).

RESULTS

Regional differences in bifurcation structures of SA node cells

To elucidate the regional differences in pacemaker mechanisms and robustness of pacemaker activity, we compared the stability, dynamics, and bifurcation structures of the central and peripheral cells during sarcolemmal ionic current blocks or hyperpolarization.

Effects of blocking ionic currents or SR Ca^{2+} release on pacemaker activities

We first simulated the effects of blocking sarcolemmal ionic currents or SR Ca^{2+} release current (I_{rel}) on pacemaker activity by decreasing the current conductance. Dynamic behaviors of the central and peripheral cell models with normal and decreased conductance are shown in Fig. 1. When $I_{Ca,L}$ or I_{Kr} was completely blocked, spontaneous activity ceased in both the central and peripheral cells. In contrast, the elimination of I_{Na}, I_h, or $I_{Ca,T}$, although slowing pacemaking, did not abolish pacemaker activity of either the central or peripheral cell. These simulated results are consistent with those shown in the original article of Zhang et al. (15), except that peripheral cell pacemaking ceased during the $I_{Ca,L}$ block. Decreasing I_{NaCa} also abolished spontaneous oscillations in the Kurata et al. models, although it did not do so in the Zhang et al. models. This is a consequence of the Ca^{2+}-dependent inactivation of $I_{Ca,L}$ under Ca^{2+} overload conditions because pacemaker activities of the Kurata et al. models did not cease during the inhibition of I_{NaCa} when Ca^{2+}-dependent inactivation of $I_{Ca,L}$ was removed or when intracellular Ca^{2+} concentrations were fixed (data not shown). In the Kurata et al. models, spontaneous oscillations were slowed but not abolished by decreasing I_{rel}.

Comparison of bifurcation structures during inhibition of $I_{Ca,L}$ or I_{Kr}

Blocking $I_{Ca,L}$ or I_{Kr}, but not blocking other currents, abolished pacemaker activity in both the central and peripheral cells. Thus, we explored the stability, dynamics, and bifurcation structures of the model cells during the inhibition of $I_{Ca,L}$ or I_{Kr}. Figs. 2 and 3 show the bifurcation diagrams constructed for $g_{Ca,L}$ and g_{Kr}, respectively, depicting the V_E at EPs (steady-state branch), local potential extrema of LCs (periodic branches), and the CL of LCs as functions of $g_{Ca,L}$ or g_{Kr}.

During the block of $I_{Ca,L}$ (decrease in $g_{Ca,L}$), the EP was stabilized via a Hopf bifurcation with emergence of an unstable LC or disappearance of a stable LC. In the Zhang et al. models and Kurata et al. peripheral model, stable and unstable LCs (periodic branches) abruptly disappeared via a saddle-node bifurcation, with the cells coming to quiescence. In the Kurata et al. central model, irregular dynamics emerged via a Neimark-Sacker bifurcation before cessation of spontaneous activity. It should be noted that the critical $g_{Ca,L}$ values at the bifurcation points were smaller in the peripheral cell than in the central cell and that the Zhang et al. models and Kurata et al. peripheral model exhibited bistability, i.e., the coexistence of a stable EP and a stable LC.

The block of I_{Kr} (decrease in g_{Kr}) also caused EP stabilization via a Hopf bifurcation. Stable and unstable LCs of the Zhang et al. central model abruptly vanished via a saddle-node bifurcation, whereas the stable LC of the other model cells gradually contracted in size and collapsed at the Hopf bifurcation point. The critical g_{Kr} value at which the saddle-node or Hopf bifurcation to quiescence occurs was lower in the peripheral cell than in the central cell.

Influences of blocking $I_{Ca,L}$ or I_{Kr} on stability and bifurcations during I_{bias} applications

We also examined the influences of blocking $I_{Ca,L}$ or I_{Kr} on bifurcation structures (stability, dynamics, and bifurcations) during I_{bias} applications of the model cells. In Fig. 4, changes

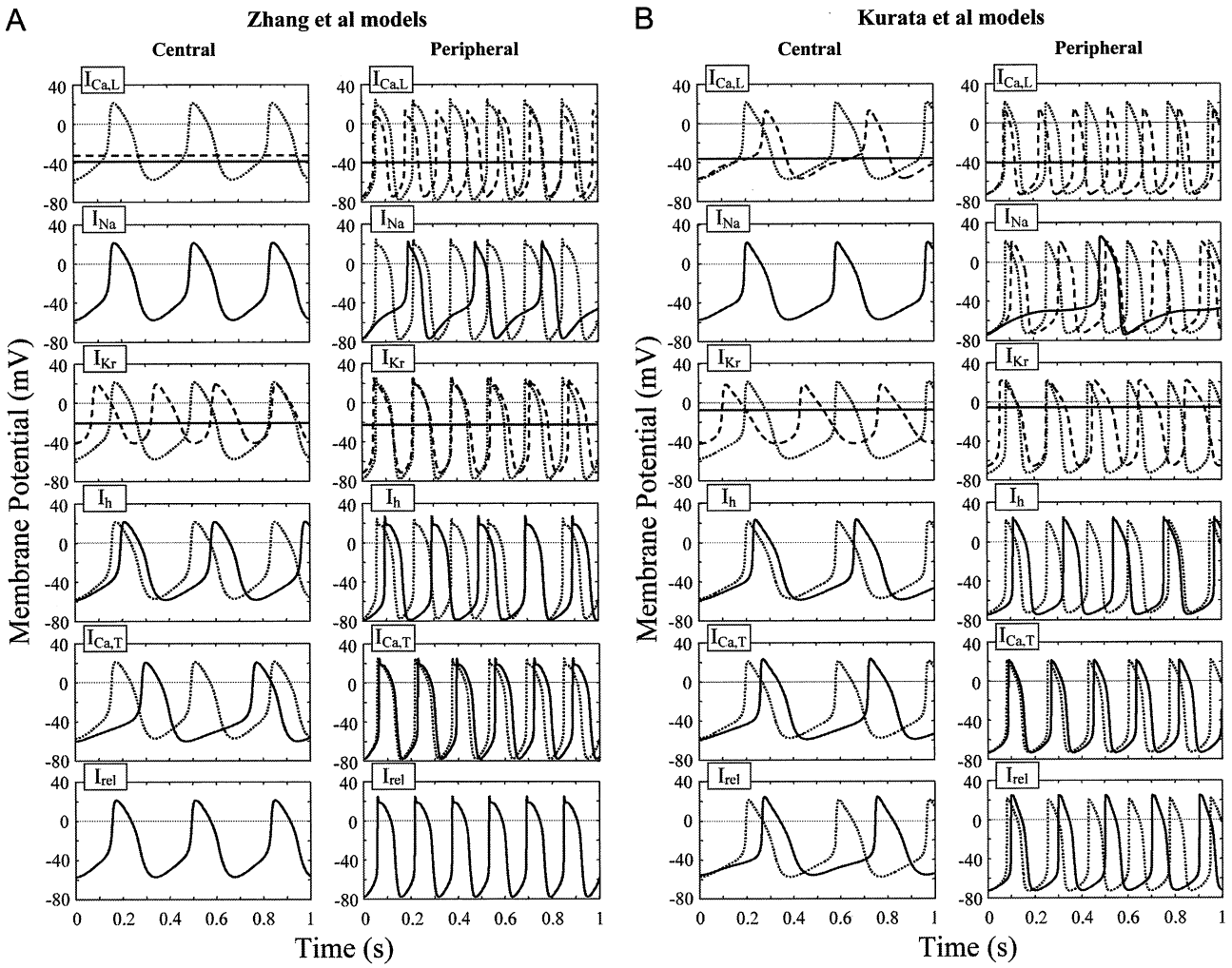

FIGURE 1 Simulated effects of blocking individual sarcolemmal currents or SR Ca^{2+} release on pacemaker activity of the Zhang et al. (*A*) and Kurata et al. (*B*) models for the central and peripheral cells. Membrane potential behaviors on decreasing one of $I_{Ca,L}$, I_{Na}, I_{Kr}, I_h, $I_{Ca,T}$, and the SR Ca^{2+} release current I_{rel} (from *top* to *bottom*) are shown. Effects of the complete block of each current (*solid lines*) and 50% block of $I_{Ca,L}$, I_{Na}, or I_{Kr} (*dashed lines*) were tested. The SR Ca^{2+} release rate (P_{rel}) was reduced to 1% of the control value. Control APs are superimposed in each panel (*dotted lines*). Differential equations of the model systems were numerically solved for 11 s (*A*) or 301 s (*B*), with an initial condition appropriate to an EP and a 1-ms stimulus of 1 pA/pF; the membrane potential behaviors during the last 1 s (starting from a maximum diastolic potential) were depicted.

in V_E and its stability during I_{bias} applications are depicted as the I_{bias}-V_E curves for the normal, $I_{Ca,L}$-removed and I_{Kr}-removed versions of the Kurata et al. models. The control EP (V_E) at $I_{bias} = 0$ is unstable in the normal systems because two eigenvalues of a Jacobian matrix for the EP are positive real numbers; in contrast, those in the $I_{Ca,L}$- and I_{Kr}-removed systems are stable because all the real parts of eigenvalues (Re[λ]) are negative. There are 2–4 Hopf bifurcation points (labeled as H1–H4), where real parts of a pair of the complex conjugate eigenvalues go through zero and reverse their sign. In the whole interval between H1 and H2, the systems have no stable EP but have only one unstable EP, generating LC oscillations (Fig. 5). Saddle-node bifurcations at which multiple EPs emerge occurred in the I_{Kr}-removed systems.

Figs. 6 and 7 show the displacement of Hopf and saddle-node bifurcation points in the I_{bias}-V_E curve, as well as the shift in the control V_E at $I_{bias} = 0$ (V_0), with decreases in $g_{Ca,L}$ and g_{Kr}, respectively. Bifurcation points were plotted as functions of $g_{Ca,L}$ or g_{Kr} on both the potential (V_E) and current (I_{bias}) coordinates. In the central cells, the unstable V_E and I_{bias} regions between H1 and H2 shrunk with decreasing $g_{Ca,L}$, and finally disappeared via a codimension-two saddle-node bifurcation. In contrast, the unstable regions of the peripheral cells did not vanish even when $I_{Ca,L}$ was completely blocked. Reducing g_{Kr} did not significantly shrink the unstable V_E range in either the central or peripheral cells. The unstable I_{bias} regions did not disappear even when I_{Kr} was removed. The $I_{Ca,L}$-removed peripheral cells as well as the I_{Kr}-removed cells—quiescent at $I_{bias} = 0$—resumed spontaneous oscillations when an EP was destabilized by applications of hyperpolarizing I_{bias} (see Fig. 5).

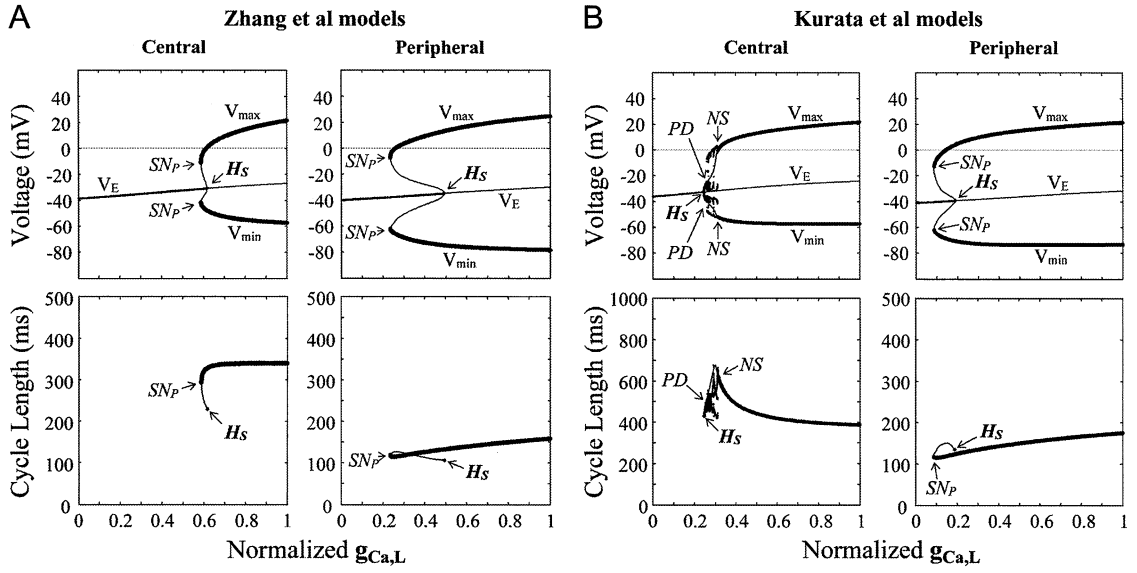

FIGURE 2 Effects of reducing $g_{Ca,L}$ on the EP stability and oscillation dynamics of the Zhang et al. (*A*) and Kurata et al. (*B*) models for central and peripheral cells. One-parameter bifurcation diagrams for $g_{Ca,L}$ with the steady-state branch as a locus of V_E and the periodic branches as the potential extrema of LCs (V_{min}, V_{max}) are shown (*top*); the CL of LCs is also plotted as a function of $g_{Ca,L}$ (*bottom*). The steady-state and periodic branches consist of the stable (*thick lines*) and unstable (*thin lines*) segments. The normalized $g_{Ca,L}$ value was reduced at an interval of 0.001 for calculations of EPs and stable LCs. The points of Hopf bifurcation of EPs, saddle-node bifurcation of LCs, period-doubling bifurcation of LCs, and Neimark-Sacker bifurcation of LCs are located, as labeled H_S, SN_P, *PD*, and *NS*, respectively: (*A*) H_S at $g_{Ca,L} = 0.6178$ (*central*) and 0.4912 (*peripheral*); SN_P at $g_{Ca,L} = 0.5890$ (*central*) and 0.2337 (*peripheral*). (*B*) H_S at $g_{Ca,L} = 0.2457$ (*central*) and 0.1891 (*peripheral*); SN_P at $g_{Ca,L} = 0.085$ (*peripheral*); *PD* at $g_{Ca,L} = 0.257$ (*central*); and *NS* at $g_{Ca,L} = 0.312$ (*central*).

Bifurcation structures during ACh applications or electrotonic modulations

We further examined the regional differences in the structural stability against hyperpolarizing loads by comparing the bifurcation structures of the central and peripheral cells during ACh applications or electrotonic modulations. Figs. 8 and 9 show the stability, dynamics, and bifurcations of the model cells as functions of [ACh] and G_C, respectively.

During increases in [ACh], EPs of the central and peripheral cells were destabilized via Hopf bifurcations. In the Zhang et al. central model, a stable LC abruptly vanished via a saddle-node bifurcation, with the cell coming to a rest;

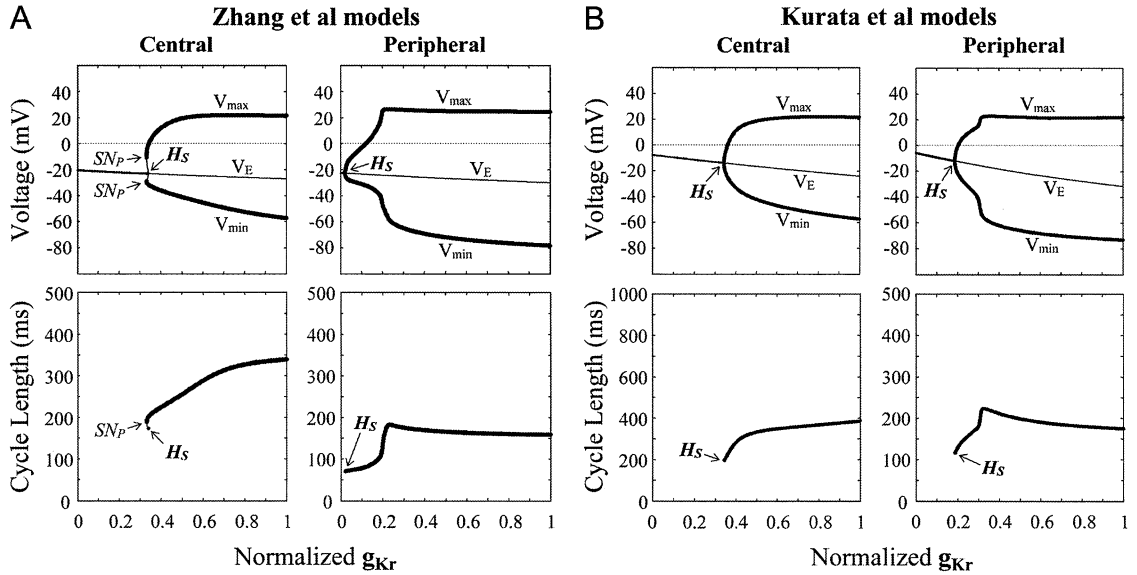

FIGURE 3 Effects of reducing g_{Kr} on the EP stability and oscillation dynamics of the Zhang et al. (*A*) and Kurata et al. (*B*) models. One-parameter bifurcation diagrams for g_{Kr} with the steady-state branch (V_E) and the periodic branches (V_{min}, V_{max}) are shown (*top*); the CL of LCs is also plotted as a function of g_{Kr} (*bottom*). The normalized g_{Kr} value was reduced at an interval of 0.001 for calculations of EPs and stable LCs. The points of Hopf bifurcation of EPs (H_S) and saddle-node bifurcation of LCs (SN_P) are located: (*A*) H_S at $g_{Kr} = 0.3384$ (*central*) and 0.0228 (*peripheral*); SN_P at $g_{Kr} = 0.3298$ (*central*). (*B*) H_S at $g_{Kr} = 0.3440$ (*central*) and 0.1867 (*peripheral*).

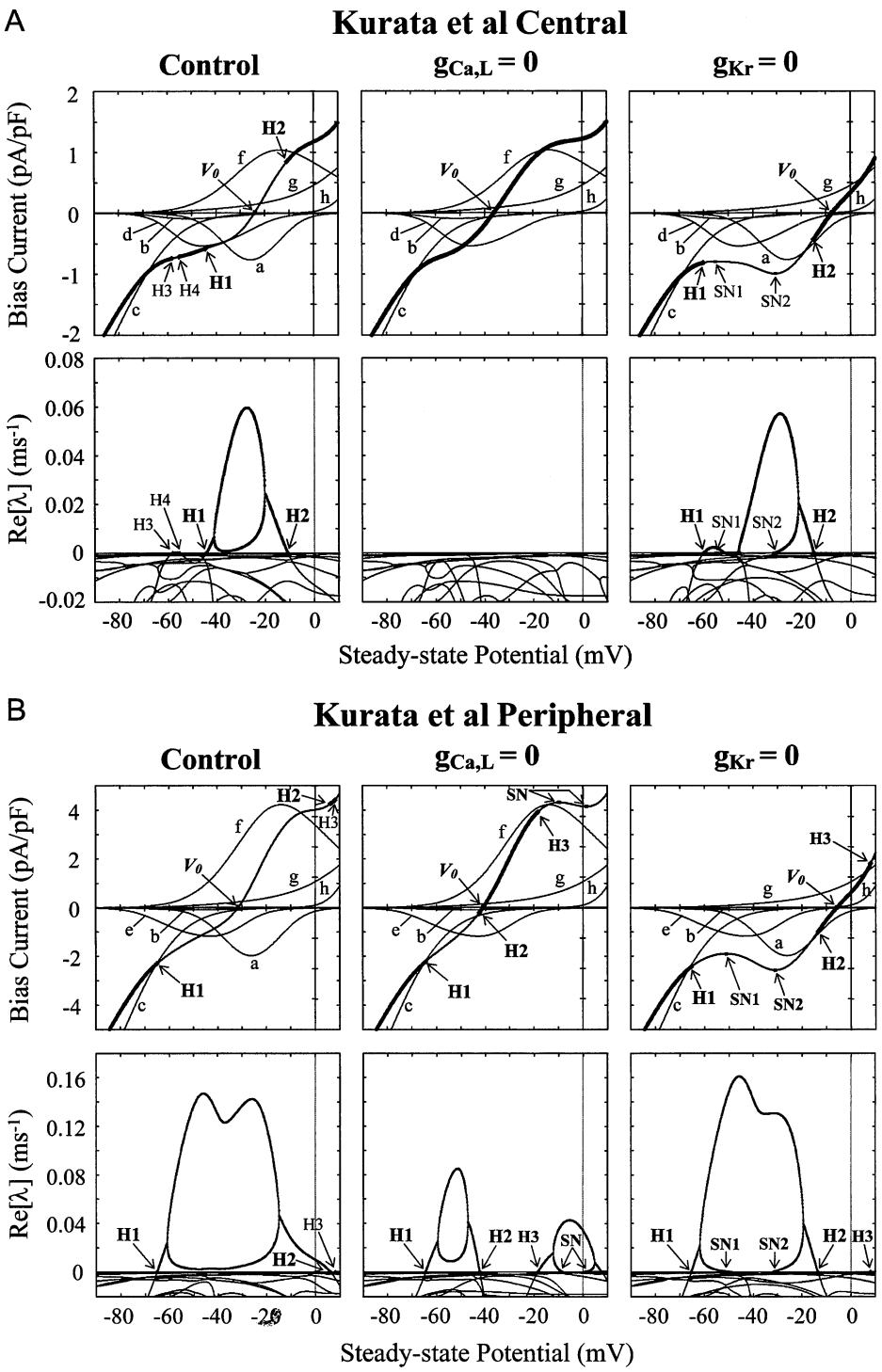

FIGURE 4 Changes in EPs and their stability during I_{bias} applications of the normal (*control*), $I_{Ca,L}$-removed ($g_{Ca,L} = 0$), and I_{Kr}-removed ($g_{Kr} = 0$) versions of the Kurata et al. central (*A*) and peripheral (B) models. Shown are the I_{bias}-V_E curves illustrating how V_E and its stability changed when I_{bias} was applied (*top*). V_E was systematically changed by applying hyperpolarizing (negative) or depolarizing (positive) I_{bias} of various amplitudes; the resulting relationship between V_E (abscissa) and I_{bias} amplitude (ordinate) is depicted. Stability of EPs was evaluated by the stability analysis based on the linear stability theory (see Appendix B); real parts of eigenvalues (Re[λ]) of a Jacobian matrix for each EP (V_E) representing the rate constants (ms^{-1}) of a system to be attracted to or go away from an EP are shown (*bottom*). In the I_{bias}-V_E curve, the segments of thin lines designate the loci of unstable EPs with two positive Re[λ] values; those of thick lines are the stable EPs for which Re[λ] values are all negative. There are 2–4 Hopf bifurcation points (*H1–H4*), corresponding to the zero crossings of Re[λ]. Saddle-node bifurcation points are also located (labeled *SN*). Individual time-dependent current components in steady state are superimposed to show the contribution of each current to the stability of EPs: *a*, $I_{Ca,L}$; *b*, $I_{Ca,T}$; *c*, I_h; *d*, I_{st}; *e*, I_{Na}; *f*, I_{Kr}; *g*, $I_{to} + I_{sus}$; and *h*, I_{Ks}.

in their peripheral model and Kurata et al. models, an LC became unstable via a period-doubling bifurcation with emergence of irregular dynamics between the period-doubling and Hopf bifurcation points. Destabilization of EPs via Hopf bifurcations was also observed during increases of G_C in the coupled-cell models. A stable LC of the Zhang et al. central cell abruptly vanished via a saddle-node bifurcation leading to quiescence; in their peripheral model and Kurata et al. models, an LC became unstable via a saddle-node, period-doubling, or Neimark-Sacker bifurcation with emergence of irregular dynamics. The critical [ACh] and G_C values at the bifurcations to quiescence were much greater for the peripheral cell than for the central cell.

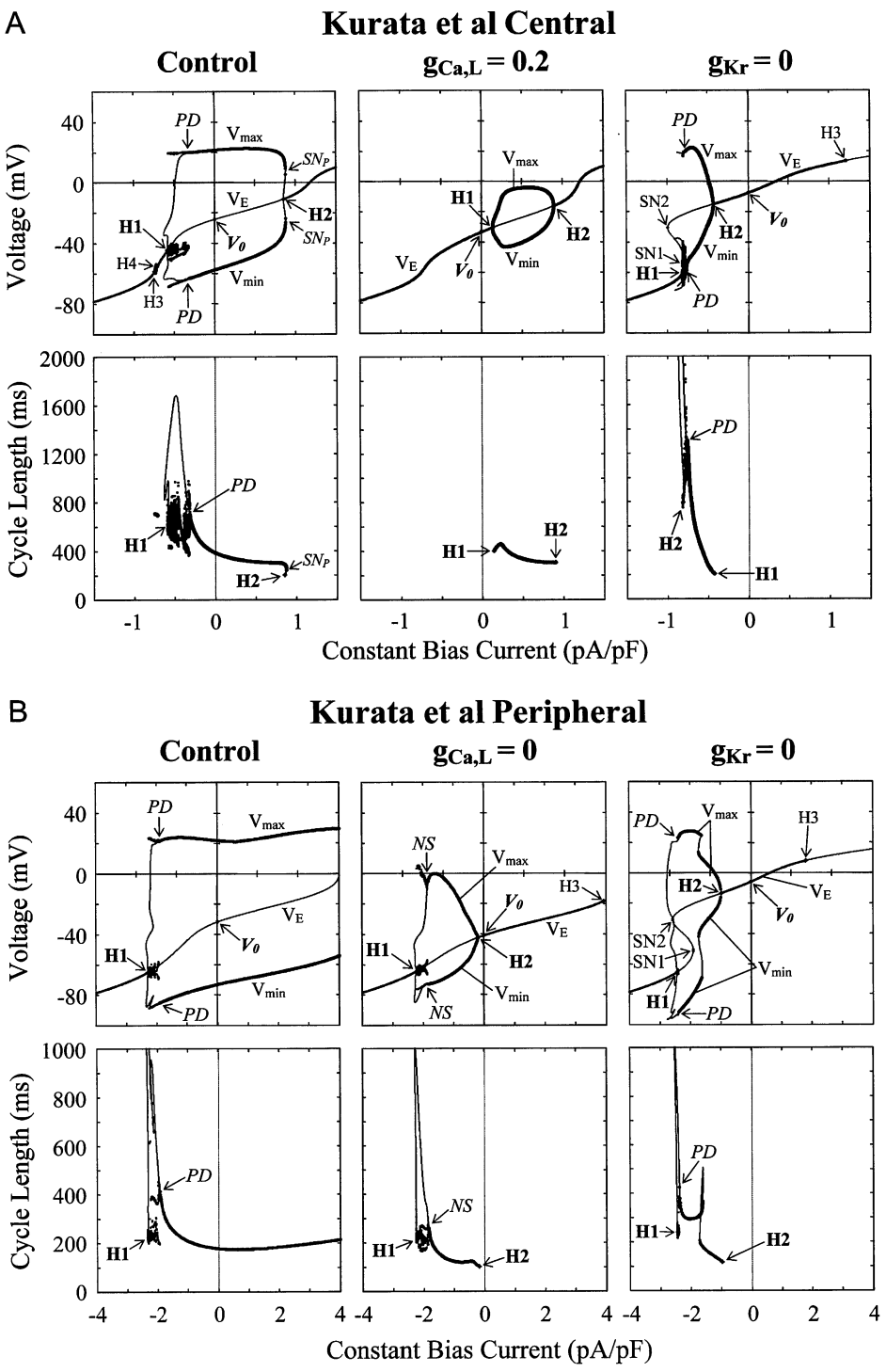

FIGURE 5 Oscillation dynamics during I_{bias} applications of the normal (*control*), $I_{Ca,L}$-reduced ($g_{Ca,L}$ = 0.2 or 0), and I_{Kr}-removed (g_{Kr} = 0) versions of the Kurata et al. central (*A*) and peripheral (*B*) models. A bifurcation diagram for I_{bias} with the steady-state (V_E) and stable periodic (V_{min}, V_{max}) branches is shown; CL is also plotted against I_{bias}. Various amplitudes of hyperpolarizing (negative) or depolarizing (positive) I_{bias} were applied at an interval of 0.001 pA/pF. Hopf (*H1–H3*) or saddle-node (*SN1*, *SN2*) bifurcation of EPs, and saddle-node (SN_P), period-doubling (*PD*), or Neimark-Sacker (*NS*) bifurcation of LCs are located.

Ionic bases of regional differences in bifurcation structures

Our results above suggest certain regional differences in bifurcation structures that can be summarized as follows: 1), the unstable V_E (EP) region determined by applications of hyperpolarizing I_{bias} was abolished by blocking $I_{Ca,L}$ in the central cells but not in the peripheral cells (Fig. 6), and 2), the critical [ACh] and G_C values for the stabilization of EPs and abolition of stable LCs were much greater in the periphery than in the center (Figs. 8 and 9). To elucidate the ionic bases of these regional differences, we further explored how blocking individual sarcolemmal currents affects EP stability, oscillation dynamics, and bifurcation structures of the model systems. We particularly focused on the contributions of I_{Na} and I_h, the densities of which are much greater in the periphery than in the center.

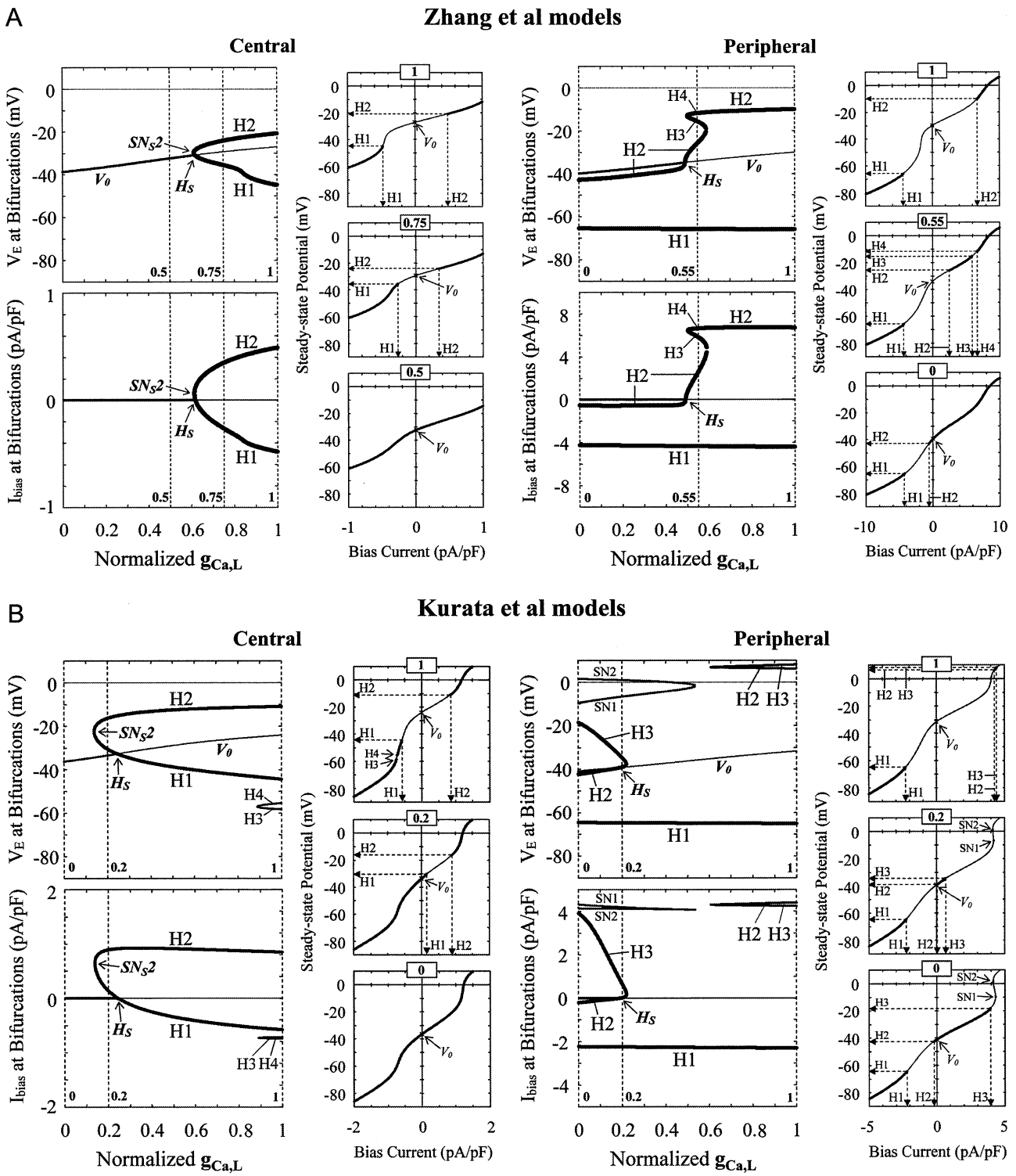

FIGURE 6 Effects of reducing $g_{Ca,L}$ on bifurcation structures (stability and bifurcation of EPs) during I_{bias} applications of the Zhang et al. (*A*) and Kurata et al. (*B*) models for central and peripheral cells. Displacements of Hopf (*H1–H4*) and saddle-node (*SN1*, *SN2*) bifurcation points in the I_{bias}-V_E curve with decreasing $g_{Ca,L}$ at an interval of 0.001 are shown on the potential (V_E) coordinates (*top*) and current (I_{bias}) coordinates (*bottom*). The path of the control V_E at $I_{bias} = 0$ is also shown on the potential coordinates (V_0), intersecting the locus of H1 or H2 at the Hopf bifurcation points (H_S) as shown in Fig. 2. In the insets, V_E and its stability, as well as bifurcation points, are shown as functions of I_{bias} for $g_{Ca,L} = 1$, 0.75, and 0.5 (*A*, *central*); $g_{Ca,L} = 1$, 0.55, and 0 (*A*, *peripheral*); or $g_{Ca,L} = 1$, 0.2, and 0 (*B*), as indicated by the dashed lines. The unstable regions where spontaneous oscillations occur are as follows: *A*, between H1 and H2 (or H3 and H4 in the periphery); *B* (*central*), between H1 and H2 (or H3 and H4); *B* (*peripheral*), between H1 and H2, or above H3 (or above H1 at $g_{Ca,L} = 0.221$–0.605). A codimension-two saddle-node bifurcation point at which the loci of H1 and H2 merge together, i.e., the unstable region disappears, is labeled SN_S2 (codimension-two saddle-node bifurcation of EPs) at $g_{Ca,L} = 0.6131$ (*A*, *central*) and 0.1382 (*B*, *central*).

Effects of blocking ionic currents on bifurcations during I_{bias} applications

To clarify the contributions of sarcolemmal currents to EP instability during applications of I_{bias}, we examined the effects of blocking I_{Na}, I_h or other time-dependent currents on the unstable V_E and I_{bias} regions in the I_{bias}-V_E curve. Hopf and saddle-node bifurcation points in the I_{bias}-V_E curve were determined with decreasing the maximum current conductance and plotted on the potential and current coordinates. The results after the I_{Na} and I_h blocks in the $I_{Ca,L}$-removed systems are shown in Fig. 10. The manner in which blocking each current shrinks the unstable V_E range where spontaneous oscillations occur should be noted; the more prominent the shrinkage in the unstable V_E region, the greater is the contribution of the current to EP instability.

The unstable V_E regions at negative potentials (between H1 and H2) shrunk with decreasing g_{Na} but not with decreasing g_h. In the $I_{Ca,L}$-removed systems, the unstable regions disappeared via a codimension-two saddle-node bifurcation; in contrast, reducing g_h did not shrink the unstable V_E range, not causing a saddle-node bifurcation. Decreases in either g_{Na} or g_h shrunk the unstable current region for hyperpolarizing I_{bias}. The effects of blocking other time-dependent currents were relatively small (data not shown).

Effects of blocking ionic currents on bifurcations during hyperpolarization

For further clarifying how sarcolemmal currents contribute to the relatively high structural stability of the peripheral cells to hyperpolarizing loads, we also examined the effects of blocking individual currents on bifurcation structures of the peripheral cells during ACh applications or electrotonic modulations. Figs. 8 and 9 indicate that a Hopf bifurcation point in the steady-state branch is just or close to the point at which spontaneous activity is abolished by hyperpolarizing loads. To assess the contribution of each current to the structural stability of the peripheral cells, we therefore focused on the changes in Hopf bifurcation points (unstable EP regions). In Figs. 11 and 12, the critical [ACh] or G_C values at which Hopf bifurcations occur are shown as functions of the maximum current conductance.

The critical [ACh] and G_C values most dramatically reduced with decreasing g_{Na}; decreases in g_h or $g_{Ca,L}$ also reduced the critical [ACh] and G_C, but their effects were relatively small. Thus, the robustness against hyperpolarizing loads was most dramatically attenuated by inhibiting I_{Na}. At lower $g_{Ca,L}$ values, two Hopf bifurcation points (H1 and H2) appeared, with the unstable regions where LCs emerge lying between H1 and H2. It should be noted that the unstable regions did not disappear even when $I_{Ca,L}$ was completely blocked. With decreases in g_{Na}, the unstable regions of the $I_{Ca,L}$-removed systems shrunk and finally vanished via codimension-two saddle-node bifurcations; in contrast, they were not significantly or only slightly shrunk by reductions of g_h or $g_{Ca,T}$ (data not shown).

Bifurcation structures of I_{Na}- or I_h-removed peripheral cells

We compared the bifurcation structures during the $I_{Ca,L}$ block of the normal, I_{Na}-removed, and I_h-removed peripheral cells (data not shown). In all the model cells, blocking $I_{Ca,L}$ caused EP stabilization via a Hopf bifurcation. LCs of the I_{Na}-removed systems became unstable via a period-doubling bifurcation with emergence of irregular dynamics, which vanished at the Hopf bifurcation point. The critical $g_{Ca,L}$ values for the bifurcations were higher in the I_{Na}-removed systems than in the control systems. The I_h-removed cells exhibited nearly the same stability, dynamics, and bifurcations during $g_{Ca,L}$ decreases as the normal cells.

Figs. 13 and 14 show the bifurcation structures of the I_{Na}-removed cells as well as of the normal cells during increases of [ACh] and G_C, respectively. In the I_{Na}-removed systems, EPs were stabilized via Hopf bifurcations at smaller [ACh] and G_C values than in the control systems. Stable LCs of the I_{Na}-removed cells became unstable via period-doubling bifurcations, with irregular dynamics emerging between the period-doubling and Hopf bifurcations. The bifurcation values for irregular dynamics and quiescence were far smaller in the I_{Na}-removed systems than in the control systems. The critical [ACh] or G_C value for bifurcations of the I_h-removed cells was also smaller than that of the normal cells but much larger than that of the I_{Na}-removed cells (data not shown; see Figs. 11 and 12).

Searching for I_{Na}-dependent pacemaking in peripheral cells

The $I_{Ca,L}$-removed peripheral cell has an unstable EP region during hyperpolarization (Figs. 4 and 5), which disappears by blocking I_{Na} (Fig. 10). As shown in Fig. 5 *B*, the application of hyperpolarizing I_{bias} to the $I_{Ca,L}$-eliminated peripheral cells yielded destabilization of an EP via a Hopf bifurcation, at which the cells resumed spontaneous activity. Increasing [ACh] or G_C also induced EP destabilization and emergence of a stable LC in the $I_{Ca,L}$-removed peripheral systems (data not shown). Under hyperpolarized conditions, therefore, I_{Na} may be responsible for EP instability and may possibly yield spontaneous oscillations independent of $I_{Ca,L}$. These findings further suggest that the "I_{Na}-dependent pacemaking" occurs in hyperpolarized peripheral cells. We assumed that pacemaker activity is I_{Na}-dependent when I_{Na} (not $I_{Ca,L}$) is responsible for the instability of an EP and, thus, an I_{Na} block (but not an $I_{Ca,L}$ block) causes EP stabilization and cessation of spontaneous activity. To determine whether and how the I_{Na}-dependent pacemaking is possible, we further explored bifurcation structures of the hyperpolarized peripheral cells during the I_{Na} and/or $I_{Ca,L}$ blocks.

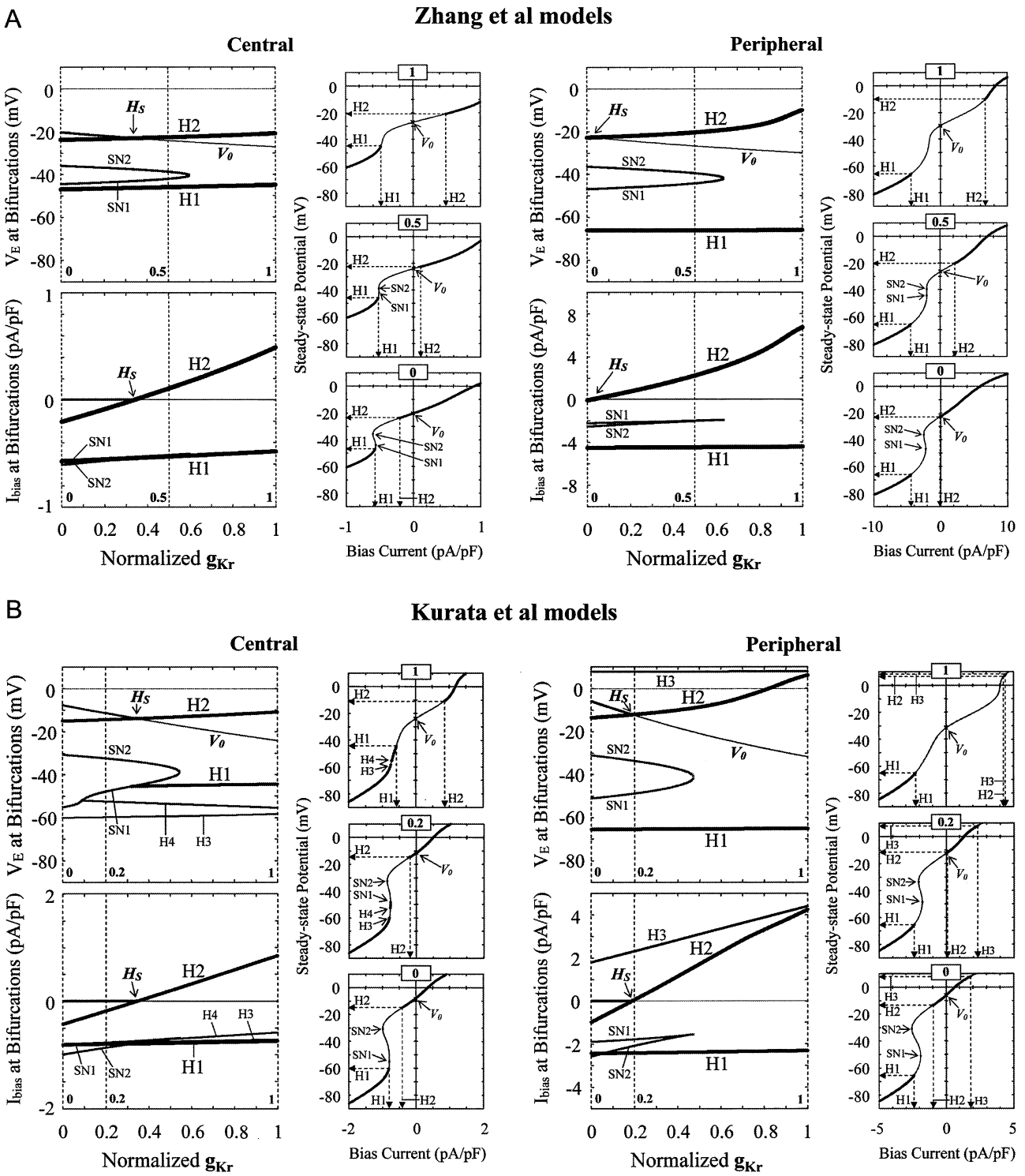

FIGURE 7 Effects of reducing g_{Kr} on bifurcation structures during I_{bias} applications of the Zhang et al. (*A*) and Kurata et al. (*B*) models. Displacements of Hopf (*H1–H4*) and saddle-node (*SN1*, *SN2*) bifurcation points in the I_{bias}-V_E curve with decreasing g_{Kr} at an interval of 0.001 are shown on the potential (*top*) and current (*bottom*) coordinates. The path of V_0 is also shown on the potential coordinates, intersecting the locus of H1 or H2 at the Hopf bifurcation points (H_S) as shown in Fig. 3. In the insets, V_E and its stability, as well as bifurcation points, are shown as functions of I_{bias} for $g_{Kr} = 1$, 0.5, and 0 (*A*) or $g_{Kr} = 1$, 0.2, and 0 (*B*), as indicated by the dashed lines. The unstable regions are as follows: *A*, between H1 and H2; *B* (*central*), between H1 and H2 (or SN1 and H2 at $g_{Kr} < 0.318$), and H3 and H4 (or H3 and SN1 at $g_{Kr} < 0.090$); *B* (*peripheral*), between H1 and H2, and above H3.

Influences of hyperpolarization on bifurcations during inhibition of $I_{Ca,L}$ and/or I_{Na}

We constructed two-parameter bifurcation diagrams in which the loci of Hopf bifurcation of EPs are plotted as functions of $g_{Ca,L}$ and g_{Na} (Fig. 15). ACh was applied to the peripheral cells at various concentrations. The critical $g_{Ca,L}$ value at which a Hopf bifurcation occurs was determined by the stability analysis with g_{Na} fixed at various different values, and was plotted as a function of g_{Na} (for more details, see Appendix C). Note that the right-top corner of the diagrams corresponds to the control condition. In the absence of ACh, an EP was stabilized by reducing $g_{Ca,L}$ but not by reducing g_{Na} (with normal $g_{Ca,L}$). However, increasing [ACh] shifted the loci of Hopf bifurcation points, i.e., changed the stable and unstable regions, in the g_{Na}-$g_{Ca,L}$ plane. With ACh at higher concentrations (Fig. 15, *f–h*), an EP was stabilized by decreasing g_{Na} but not by decreasing $g_{Ca,L}$ (with normal g_{Na}).

Bifurcation structures of hyperpolarized peripheral cells during inhibition of $I_{Ca,L}$ or I_{Na}

Fig. 16 shows the stability, dynamics, and bifurcations of the peripheral cells during $I_{Ca,L}$ or I_{Na} block in the absence and presence of ACh at $1 \times 10^{-6.8}$ M (158.5 nM) for the Zhang et al. model and $1 \times 10^{-7.0}$ M (100 nM) for the Kurata et al. model. Under normal conditions at [ACh] = 0, reducing $I_{Ca,L}$ stabilized an EP and abolished LCs, whereas reducing I_{Na} did not. Under the hyperpolarized conditions, however, blocking I_{Na} caused 1), LC destabilization to induce irregular dynamics via a period-doubling or Neimark-Sacker bifurcation, and 2), EP stabilization via a Hopf bifurcation below which quiescence occurred. In contrast, the abolition (or destabilization) of the stable LC or EP stabilization did not occur during the inhibition of $I_{Ca,L}$ in the hyperpolarized cells.

DISCUSSION

Regional differences in pacemaker mechanism and structural stability

Mechanisms of normal pacemaking are essentially the same for center and periphery

It has been reported that $I_{Ca,L}$ is responsible for EP instability and spontaneous oscillations of the primary pacemaker cell in the rabbit SA node, i.e., natural pacemaking is $I_{Ca,L}$-dependent (2). In the center of the SA node, $I_{Ca,L}$ would contribute to EP destabilization as a prerequisite for robust pacemaking, whereas other time-dependent currents are not necessary for basal pacemaking, rather playing pivotal roles in regulations of pacemaker activity. In this study, pacemaker activities of the peripheral cell models were abolished by blocking $I_{Ca,L}$ but not by blocking I_{Na} or I_h, as in the central cell models (Fig. 1). Bifurcation structures during the $I_{Ca,L}$ block of the

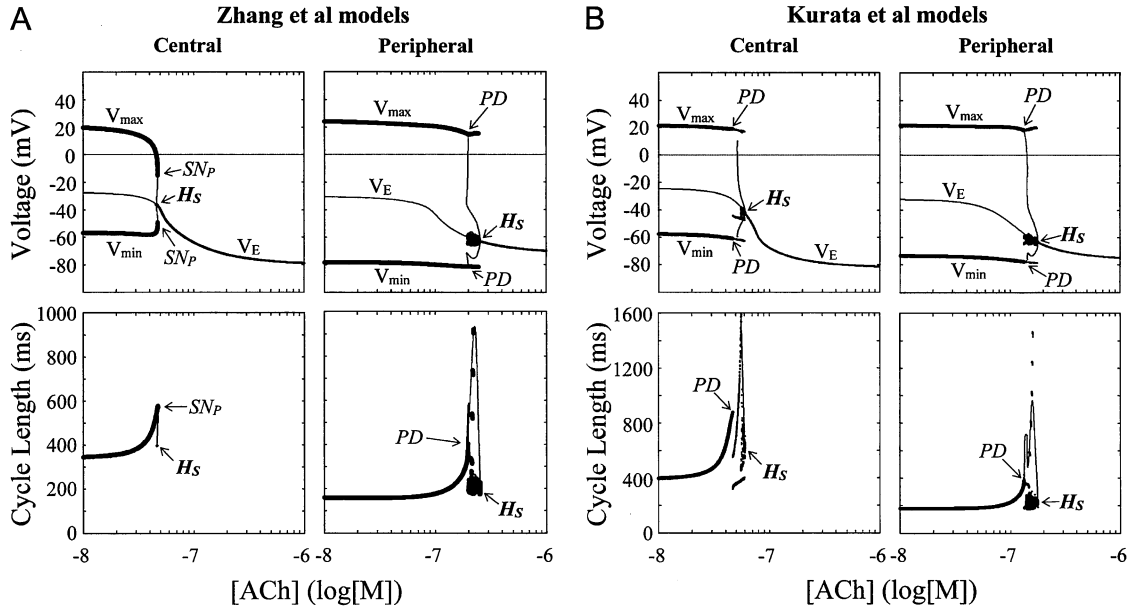

FIGURE 8 Effects of ACh applications (increases in [ACh]) on the stability and dynamics of the Zhang et al. (*A*) and Kurata et al. (*B*) models. One-parameter bifurcation diagrams for [ACh] (log[M]) depicting a locus of V_E and the potential extrema of LCs (V_{min}, V_{max}) are shown (*top*); the CL of LCs is also shown as functions of log[ACh] (*bottom*). For calculations of EPs and stable LCs, the log[ACh] values were increased at the interval of 0.001. Hopf bifurcation points on the steady-state branches are labeled H_S: *A*, at log[ACh] = −7.3332 (*central*) and −6.6059 (*peripheral*); *B*, at log[ACh] = −7.2218 (*central*) and −6.7545 (*peripheral*). The points at which a saddle-node (SN_P) or period-doubling (*PD*) bifurcation of LCs occurs with disappearance of stable LCs are located on the periodic branches: *A*, SN_P at log[ACh] = −7.3239 (*central*); *PD* at log[ACh] = −6.7148 (*peripheral*); *B*, *PD* at log[ACh] = −7.329 (*central*) and −6.874 (*peripheral*). Potential extrema and CLs of the irregular dynamics emerging between *PD* and H_S are also superimposed.

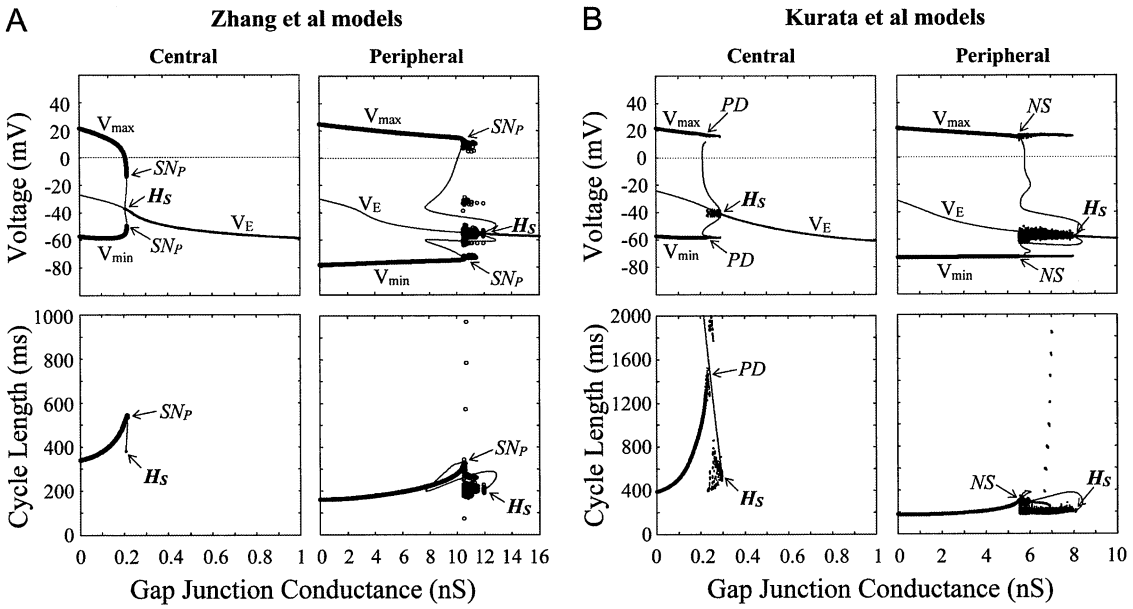

FIGURE 9 Effects of electrotonic loads of the atrium (increases in G_C) on the stability and dynamics of the Zhang et al. (*A*) and Kurata et al. (*B*) models. One-parameter bifurcation diagrams for G_C (nS) depicting a locus of V_E and the potential extrema of LCs (V_{min}, V_{max}) are shown (*top*); the CL of LCs is also shown as functions of G_C (*bottom*). G_C values for the central and peripheral cells were increased at the interval of 0.001 and 0.01 (nS), respectively. Hopf bifurcation points are labeled H_S: *A*, at $G_C = 0.2067$ (*central*) and 11.953 (peripheral); *B*, at $G_C = 0.2925$ (*central*) and 8.0688 (*peripheral*). The points at which a saddle-node (SN_P), period-doubling (*PD*), or Neimark-Sacker (*NS*) bifurcation of LCs occurs are located: *A*, SN_P at $G_C = 0.2152$ (*central*) and 10.484 (*peripheral*); *B*, *PD* at $G_C = 0.230$ (*central*); *NS* at $G_C = 5.51$ (*peripheral*). Potential extrema and CLs of the irregular dynamics emerging between the bifurcation of LCs and H_S are also superimposed.

central and peripheral cells were the same in that an EP was stabilized via a Hopf bifurcation, although the ways of abolishing automaticity were model-dependent (Fig. 2). These findings suggest that the dynamical mechanism of peripheral cell pacemaking is essentially the same as that of central cell pacemaking (2) and that basal pacemaking of the peripheral cell, as well as the central cell, is $I_{Ca,L}$-dependent.

Inconsistent with our simulated results, however, Kodama et al. (3) reported that applications of 2 μM nifedipine causing ~99% block of $I_{Ca,L}$ abolished spontaneous activity in the central region but not in the peripheral region, suggesting an $I_{Ca,L}$-independent pacemaker mechanism for the peripheral SA node. This inconsistency may reflect the relatively small $g_{Ca,L}$ value for bifurcation to quiescence in the peripheral cell (Fig. 2), as well as the incomplete block of $I_{Ca,L}$ or modulations of other currents by the agent in their preparations. Under hyperpolarized conditions, peripheral cell pacemaking was abolished not by blocking $I_{Ca,L}$ but by blocking I_{Na}, i.e., I_{Na}-dependent (Fig. 16). Furthermore, eliminating $I_{Ca,L}$ did not cause either stabilization of an EP (Hopf bifurcation) or cessation of pacemaker activity when relatively high $[Na^+]_i$ was assumed (data not shown). Thus, it is also possible that peripheral cell pacemaking was not $I_{Ca,L}$-dependent in their preparations due to hyperpolarization (outward shift in the net background current) or other unknown reasons. Previous reports also suggest that I_h plays a predominant role in the subsidiary pacemaker mechanisms (4–6). I_{Na} or I_h might contribute to EP destabilization and pacemaker generation in hyperpolarized peripheral SA node cells.

Structural stability to hyperpolarization of peripheral cell is greater than that of central cell

Our results suggest that the peripheral cell is considerably more robust than the central cell against hyperpolarizing loads such as applications of ACh (or hyperpolarizing I_{bias}) and electrotonic modulations by atrial myocytes (Figs. 6–9). Zhang et al. (30) also reported the lower sensitivity of the peripheral cell model to ACh. It should be noted that the structural stability of the peripheral cell against electrotonic loads was much greater than that of the central cell (Fig. 9). The higher structural stability of the peripheral cell is reasonable because in vivo peripheral cells are directly exposed to electrotonic loads of adjacent atrial myocytes, and thus must be more robust against hyperpolarizing loads than central cells.

The higher structural stability to hyperpolarization of the peripheral cell may be related to the pacemaker shift from the center to the periphery in SA node tissues under hyperpolarized conditions (36,37). Although it is not known whether there is a regional difference in the density of muscarinic K^+ channels, that of muscarinic M_2 receptors as well as vagal innervation was reported to be greater in the center than in the periphery (31,32). As Shibata et al. (37) suggested, the pacemaker shift may be the result of the regional differences in the robustness against hyperpolarizing loads,

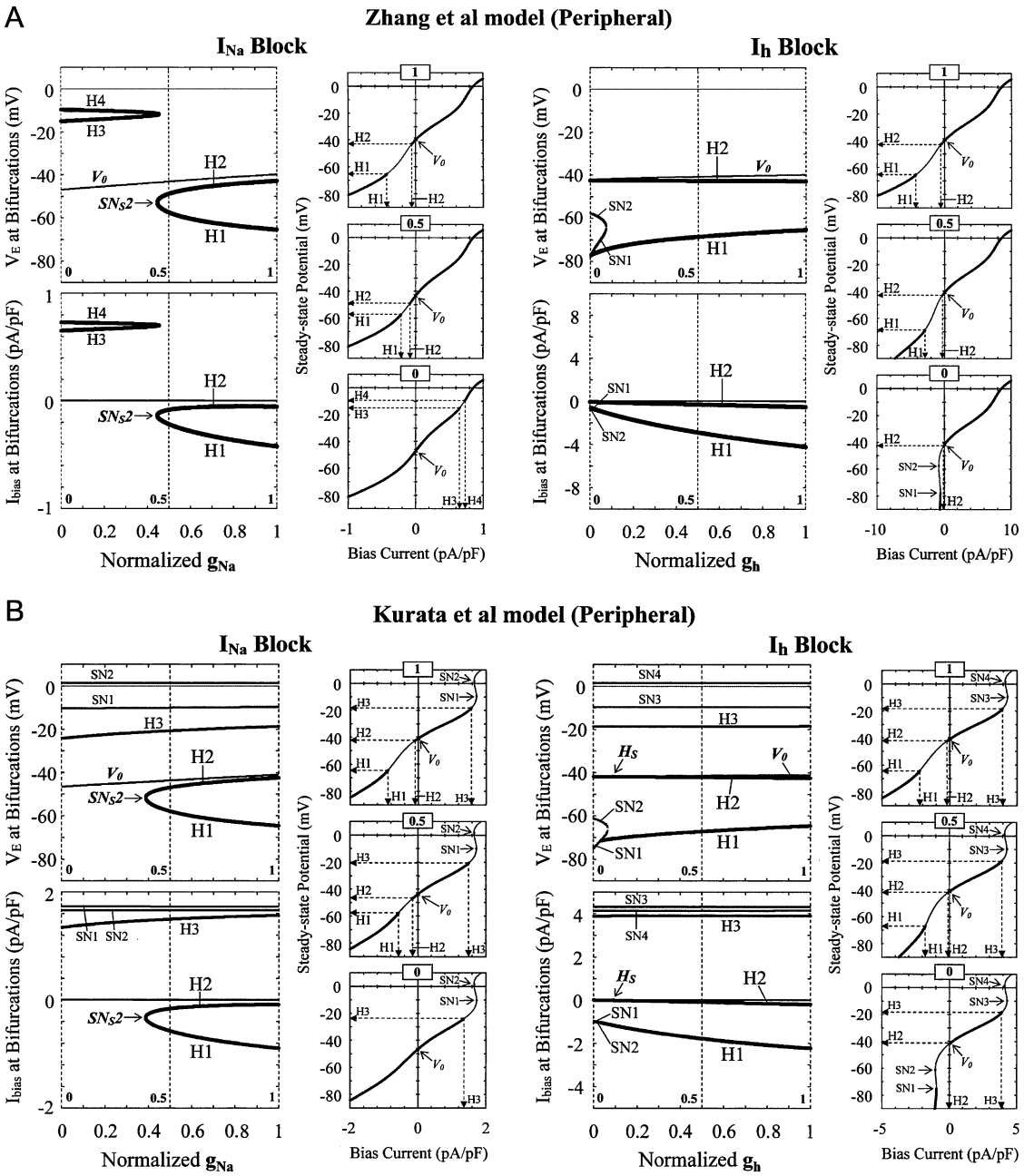

FIGURE 10 Effects of blocking I_{Na} or I_h on bifurcation structures during I_{bias} applications of the $I_{Ca,L}$-removed Zhang et al. (*A*) and Kurata et al. (*B*) peripheral models. Displacements of Hopf (*H1–H4*) and saddle-node (*SN1–SN4*) bifurcation points in the I_{bias}-V_E curve with decreasing g_{Na} or g_h at an interval of 0.001 are shown on the potential (*top*) and current (*bottom*) coordinates. The path of V_0 is also shown on the potential coordinates. In the insets, V_E and its stability, as well as bifurcation points, are shown as functions of I_{bias} for $g_{Ca,L} = 1$, 0.5, and 0, as indicated by the dashed lines. The unstable regions where spontaneous oscillations occur are as follows: *A*, between H1 and H2 (or H3 and H4); *B*, between H1 (or SN1) and H2, or above H3. A codimension-two saddle-node bifurcation point at which the loci of H1 and H2 merge together is labeled SN_S2 at $g_{Na} = 0.4470$ (*A*) and 0.388 (*B*).

M_2 receptor density, vagal innervation, and possibly $I_{K,ACh}$ density as well.

Contribution of intracellular Ca^{2+} dynamics to regional differences

Lancaster et al. (38) reported that the effect of 2–30 μM ryanodine on CL was greater in peripheral cells (24 ± 6% increase) than in central cells (3.5 ± 2% increase). This may be related to heterogeneous expression of Ca^{2+} handling proteins (39), which might contribute to the regional differences in dynamical properties of pacemaker activities. Inconsistent with their experimental findings, our peripheral model could exhibit only a small increase in CL (10.7–14.0%) on minimizing the SR Ca^{2+} release, whereas a central version with a larger response (~112.2% increase in CL) could be devel-

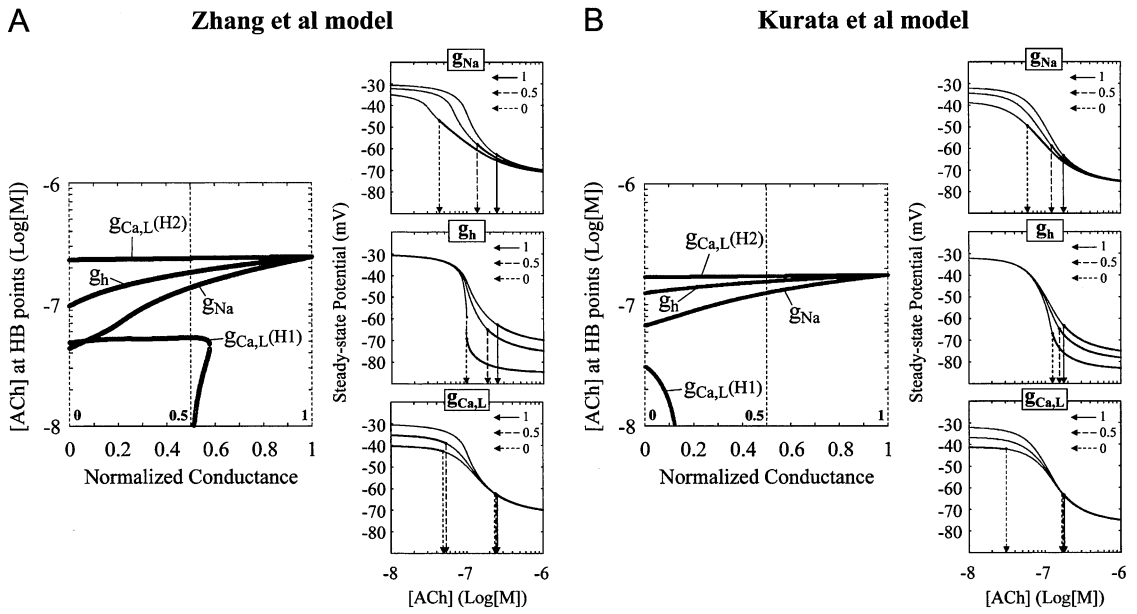

FIGURE 11 Effects of blocking individual currents on bifurcations during ACh applications of the Zhang et al. (*A*) and Kurata et al. (*B*) peripheral models. Two-parameter bifurcation diagrams for the normalized maximum current conductance (abscissa) and log[ACh] (ordinate) are shown; the critical [ACh] values at Hopf bifurcation points were plotted as functions of the conductance, which was decreased at an interval of 0.001. The values of [ACh] (log[M]) were increased at an interval of 0.001 for searching for bifurcation points. In the insets, one-parameter bifurcation diagrams for log[ACh] used for construction of the two-parameter diagrams are shown for g_{Na}, g_h, and $g_{Ca,L}$ at 1, 0.5, and 0, as indicated by the dashed lines in the two-parameter diagrams.

oped. The relatively small response of the peripheral model appeared to be due to the presence of large I_{Na} because the model cell with reduced I_{Na} exhibited much greater response, e.g., 34.3–39.6% increases in CL with $g_{Na} = 0.3$ (data not shown). In addition, ryanodine or BAPTA are known to affect sarcolemmal ion channel currents probably via decreasing intracellular Ca^{2+} concentrations (40); their secondary (or direct) effects on ionic channels may result in more dramatic responses of peripheral cells with higher densities of the channels.

To clarify whether SR Ca^{2+} cycling and intracellular Ca^{2+} dynamics substantially alter the dynamical properties of SA node cells and contribute to the regional differences in bifurcation structures, we explored their influences on stability and bifurcation of the Kurata et al. models (see Theory and Methods). Changes in SR Ca^{2+} uptake and release rates only slightly affected the stability and bifurcation of the model cells; bifurcation structures of the modified models with larger responses to the suppression of SR Ca^{2+} release were essentially the same as those of the original systems with smaller responses (data not shown). We therefore believe that neither SR Ca^{2+} cycling nor intracellular Ca^{2+} dynamics exerts substantial effects on the dynamical properties of SA node cells, not significantly contributing to the regional differences in bifurcation structures. This idea is also supported by the fact that the bifurcation structures of the Kurata et al. models incorporating the intracellular Ca^{2+} dynamics were essentially the same as those of the Zhang et al. models with fixed $[Ca^{2+}]_i$.

Roles of I_{Na} in peripheral cell pacemaking

I_{Na} contributes to high structural stability of peripheral cell

The I_{Na} block most dramatically shrunk the [ACh] and G_C regions, as well as the I_{bias} region, of unstable EP where LCs emerge (Figs. 10–12), suggesting that I_{Na} mainly contributes to the relatively high structural stability of peripheral cells. This idea was further supported by the finding that the I_{Na}-incorporated system exhibited robust pacemaking over the broader ranges of [ACh] and G_C than the I_{Na}-removed system; spontaneous oscillations of the I_{Na}-removed system were unstable in frequency and ceased at relatively low [ACh] or G_C values (Figs. 13 and 14). Consistent with our result, Watanabe et al. (33) reported that an SA node cell with a relatively small maximum upstroke velocity (i.e., including only small I_{Na}) had a relatively low threshold G_C (0.58 nS) in causing bifurcation to quiescence or irregular dynamics. Thus, I_{Na} may dramatically improve the structural stability of peripheral cells, playing a pivotal role in preventing a bifurcation to quiescence or irregular dynamics, as well as an excess increase in CL, during hyperpolarization.

I_{Na} in peripheral cells is also suggested to help the SA node in driving the atrium, i.e., it plays an important role in the conduction of pacemaker activity to atrial myocytes. Reduction of I_{Na} in the peripheral SA node slows down the pacemaking rate (not only in the periphery but also in the center), decreases the conduction velocity, and causes exit block or sinus arrest (41,42). Thus, SA node dysfunctions in

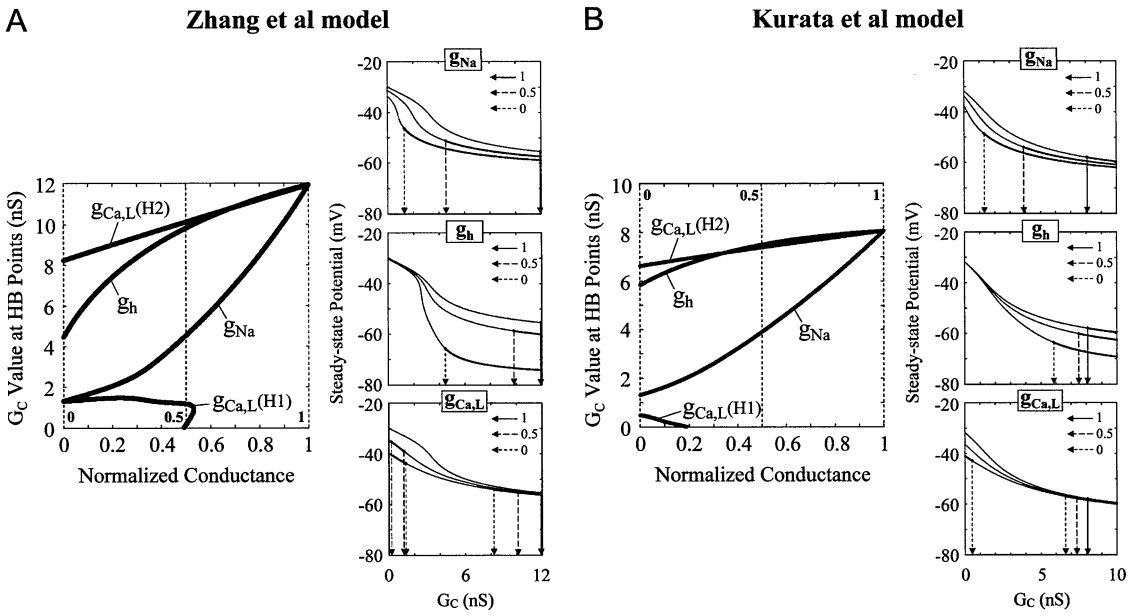

FIGURE 12 Effects of blocking individual currents on bifurcations during electrotonic modulations of the Zhang et al. (*A*) and Kurata et al. (*B*) peripheral models. Two-parameter bifurcation diagrams for the normalized maximum current conductance (abscissa) and G_C (ordinate) are shown; the critical G_C values at Hopf bifurcation points were plotted as functions of the conductance, which was decreased at an interval of 0.001. The values of G_C (nS) were increased at an interval of 0.01 for searching for bifurcation points. In the insets, one-parameter bifurcation diagrams for G_C used for construction of the two-parameter diagrams are shown for g_{Na}, g_h, and $g_{Ca,L}$ at 1, 0.5, and 0, as indicated by the dashed lines in the two-parameter diagrams.

congenital sick sinus syndromes and aged hearts may be at least in part due to the I_{Na} decrease in peripheral cells (43,44). Our results and these reports suggest that I_{Na} is indispensable for the robust maintenance of SA node pacemaking and driving against electrotonic loads of the atrium.

Possible I_{Na}-dependent pacemaking in hyperpolarized peripheral cell

The $I_{Ca,L}$-removed peripheral cell resumed spontaneous activity when an EP was destabilized via a Hopf bifurcation by hyperpolarizing loads (Fig. 5). In the $I_{Ca,L}$-removed periph-

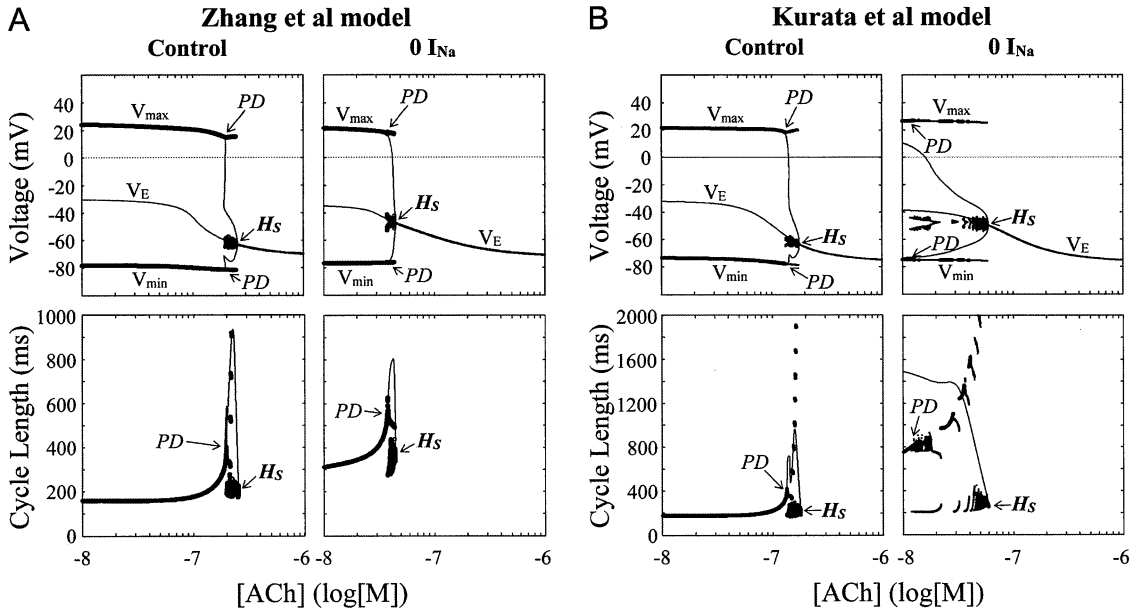

FIGURE 13 Bifurcation structures during ACh applications of the normal (*control*) and I_{Na}-removed (0 I_{Na}) versions of the Zhang et al. (*A*) and Kurata et al. (*B*) peripheral models. One-parameter bifurcation diagrams for log[ACh] depicting the steady-state (V_E) and periodic (V_{min}, V_{max}) branches are shown (*top*); the CL of LCs is also shown as functions of log[ACh] (*bottom*). Procedures of the calculations are the same as for Fig. 8. Hopf (H_S) and period-doubling (*PD*) bifurcation points are located: *A*, H_S at log[ACh] = −6.6059 (*control*) and −7.3586 (0 I_{Na}); *PD* at log[ACh] = −6.7148 (*control*) and −7.4250 (0 I_{Na}); *B*, H_S at log[ACh] = −6.7545 (*control*) and −7.2241 (0 I_{Na}); *PD* at log[ACh] = −6.874 (*control*) and −7.930 (0 I_{Na}).

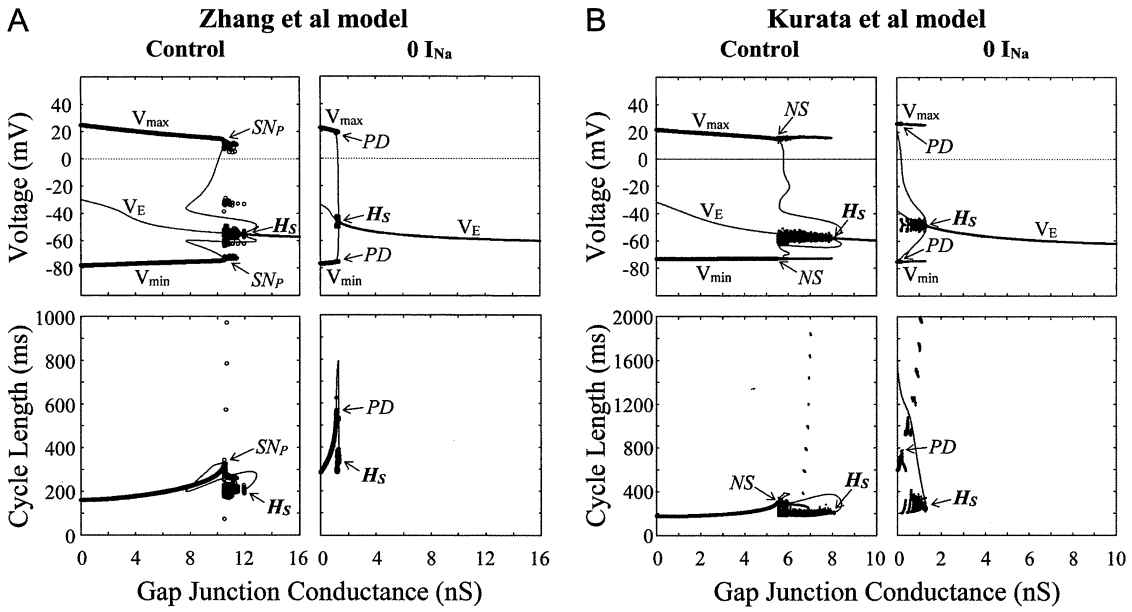

FIGURE 14 Bifurcation structures during electrotonic modulations of the normal (*control*) and I_{Na}-removed (0 I_{Na}) versions of the Zhang et al. (*A*) and Kurata et al. (*B*) peripheral models. One-parameter bifurcation diagrams for G_C depicting the steady-state (V_E) and periodic (V_{min}, V_{max}) branches are shown (*top*); the CL of LCs is also shown as functions of G_C (*bottom*). Procedures of the calculations are the same as for Fig. 9. Hopf (H_S), saddle-node (SN_P), period-doubling (*PD*), and Neimark-Sacker (*NS*) bifurcation points are located: *A*, H_S at $G_C = 11.953$ (*control*) and 1.3152 (0 I_{Na}); SN_P at $G_C = 10.484$ (*control*); *PD* at $G_C = 1.1380$ (0 I_{Na}); *B*, H_S at $G_C = 8.0688$ (*control*) and 1.3170 (0 I_{Na}); *PD* at $G_C = 0.15$ (0 I_{Na}); *NS* at $G_C = 5.51$ (*control*).

eral cell, the unstable I_{bias}, [ACh], or G_C region where stable or unstable LCs appear vanished via a codimension-two saddle-node bifurcation during I_{Na} inhibition, but not during I_h or $I_{Ca,T}$ inhibition (Fig. 10). These results suggest that the spontaneous oscillation of the $I_{Ca,L}$-removed system is I_{Na}-dependent and that I_{Na} destabilizes an EP and induces spontaneous oscillations independent of $I_{Ca,L}$ in hyperpolarized peripheral cells.

Our results further suggest that I_{Na}-dependent pacemaking is possible under hyperpolarized conditions (Figs. 15 and 16). An I_{Na} block by tetrodotoxin abolished pacemaker activity of the peripheral region of the intact SA node that suffers electrotonic loads of the atrium (41,42). Previous studies also suggest the requirement of I_{Na} for murine SA node pacemaking (41,42) and for pacemaking in human embryonic stem cell-derived cardiomyocytes that did not require $I_{Ca,L}$ or I_h (45). Thus, I_{Na}-dependent pacemaking may actually occur in hyperpolarized peripheral SA node cells, as well as in other pacemaker cells.

Significance of applying bifurcation theory to pacemaker system analyses

In this study, we employed stability and bifurcation analyses to investigate the regional difference in the mechanisms and robustness of pacemaker activity, and also the roles of I_{Na} in peripheral cell pacemaking. Our work clearly shows that the nonlinear dynamical approach allows us to identify key variables or parameters responsible for pacemaker generation and to define the contribution of each current to pacemaking. As previous studies have indicated, bifurcation analyses of SA node or ventricular models are necessary for general understanding and systematic descriptions of the dynamical mechanisms of natural pacemaking (2), abnormal automaticity (7–13), and triggered activity (46).

Our study also suggests that exploring bifurcation structures of model cells can reveal the conditions and ways for oscillatory behaviors to emerge or disappear, and possibly allow us to accurately predict and properly control the dynamics and bifurcation structures of real cells. Thus, the mathematical approach based on the bifurcation theory possibly leads to the appropriate design of a structurally stable pacemaker cell system. As suggested previously, it may be applicable to the engineering of biological pacemakers from native cardiomyocytes in vivo (47–49) or human embryonic stem cells ex vivo (17,50,51) for gene or cell therapy of bradyarrhythmias (for review, see (13,17,18)). Our findings regarding the regional differences in bifurcation structures of SA node cells would be useful as a theoretical background for the engineering of biological pacemakers with robust pacemaking and driving similar to the SA node.

Limitations and perspectives of study

Possible disadvantage of using simplified models

Limitations of our study include incompleteness of the models. The model systems used in this study were constructed as base models to reproduce the normal pacemaker activities of central and peripheral cells under basal conditions (14–16). These simplified models could reproduce the experimentally ob-

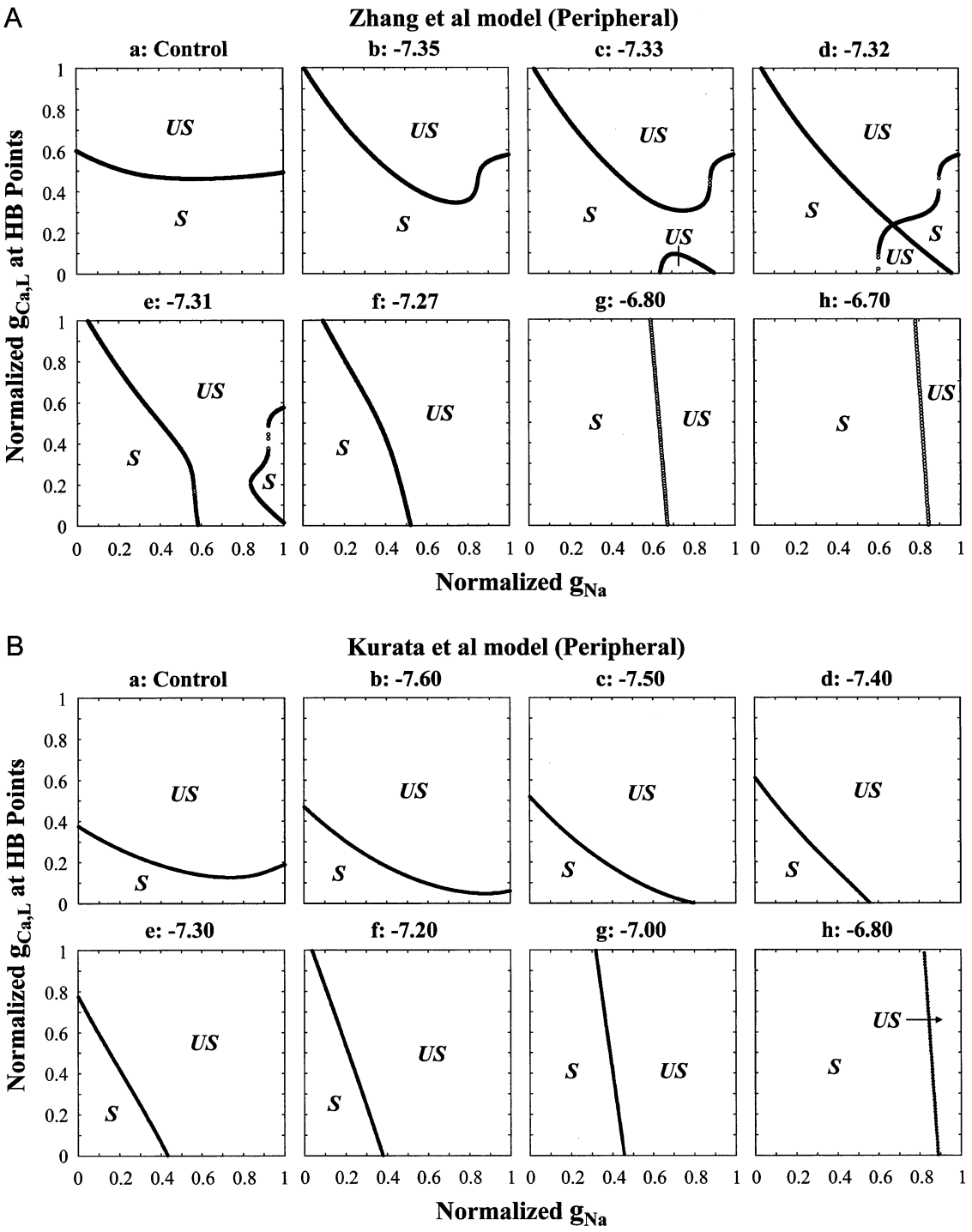

FIGURE 15 EP stability and bifurcation during decreases in $g_{Ca,L}$ and/or g_{Na} of the Zhang et al. (*A*) and Kurata et al. (*B*) peripheral models in the presence of ACh at various concentrations. Each panel shows a two-parameter bifurcation diagram for $g_{Ca,L}$ and g_{Na}, depicting the loci of Hopf bifurcation points. Values of [ACh] are shown at the top of each panel in log[M]. The normalized $g_{Ca,L}$ value was decreased from 1 to 0 at an interval of 0.001 for searching for bifurcations, with g_{Na} fixed at various values; the g_{Na} value was decreased from 1 to 0 at an interval of 0.001 (see Appendix C). Critical $g_{Ca,L}$ values at which Hopf bifurcations occurred were determined and plotted as functions of g_{Na}. The symbols *S* and *US* represent the stable and unstable EP regions, respectively.

served regional differences in dynamic properties of the central and peripheral cell pacemaking (15). However, they do not include detailed descriptions for intracellular Ca^{2+} dynamics, SR Ca^{2+} handling, or activities of other modulating factors. These intracellular factors are known to exert substantial effects on ion channel functions and pacemaker dynamics (e.g., see (52–55)) and possibly affect bifurcation structures as well. Moreover, the regional differences in the activity of Ca^{2+}

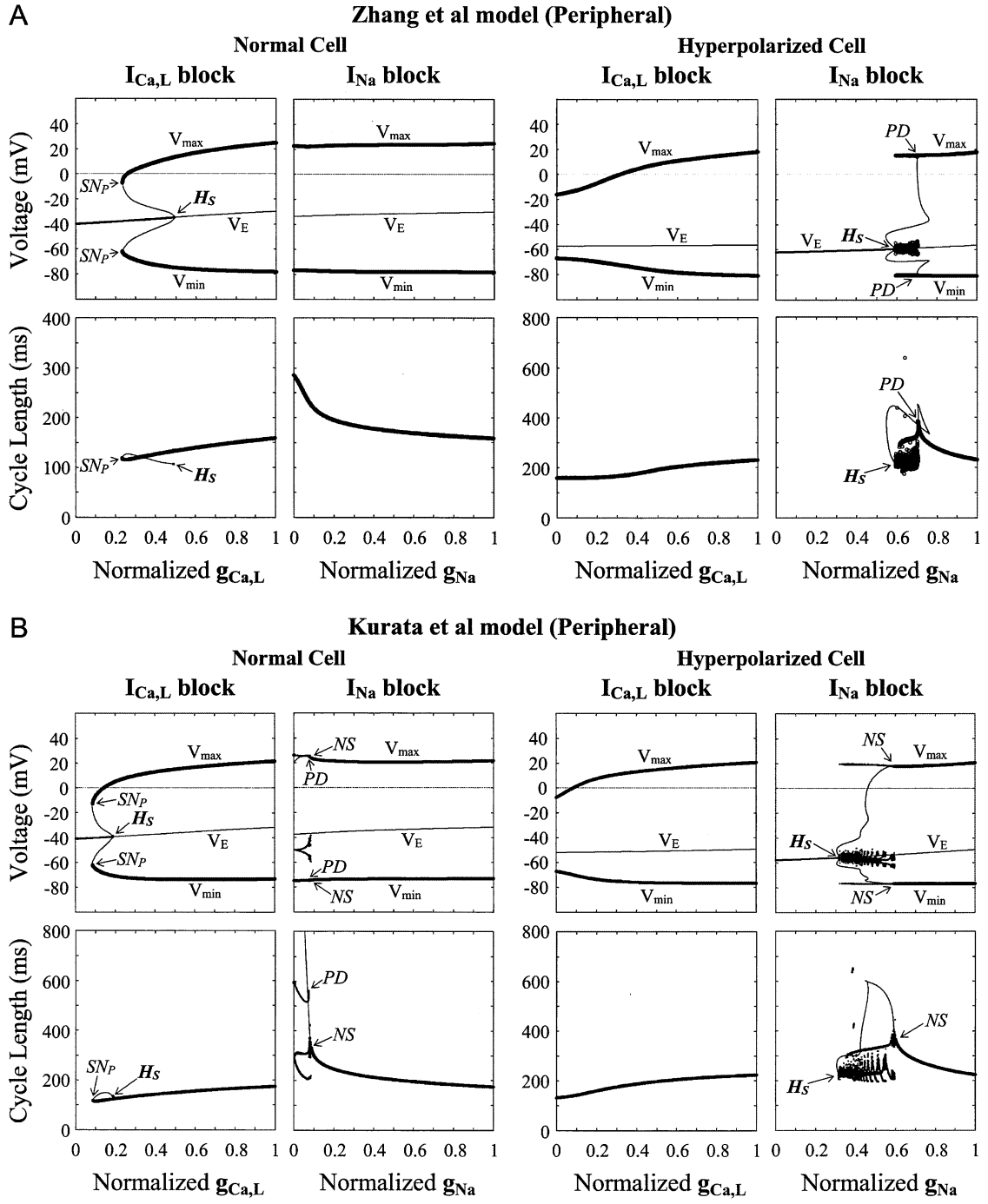

FIGURE 16 Bifurcation structures of the normal and hyperpolarized peripheral cells during the block of $I_{Ca,L}$ or I_{Na}. Both the Zhang et al. (*A*) and Kurata et al. (*B*) models were tested. One-parameter bifurcation diagrams for $g_{Ca,L}$ or g_{Na} depicting steady-state (V_E) and periodic (V_{min}, V_{max}) branches were constructed for the peripheral cells in the absence (*left*) and presence (*right*) of ACh (*top*); the CL of LCs is also shown as functions of $g_{Ca,L}$ or g_{Na} (*bottom*). The [ACh] values for the Zhang et al. and Kurata et al. models are $1 \times 10^{-6.8}$ and $1 \times 10^{-7.0}$ M (158.5 and 100 nM), respectively. Procedures of the calculations are the same as for Fig. 2. Hopf (H_S), saddle-node (SN_P), period-doubling (*PD*), and Neimark-Sacker (*NS*) bifurcations are located: *A*, H_S at $g_{Ca,L} = 0.4912$ (*normal*) and $g_{Na} = 0.5917$ (*hyperpolarized*); SN_P at $g_{Ca,L} = 0.2337$ (*normal*); *PD* at $g_{Na} = 0.7073$ (*hyperpolarized*); *B*, H_S at $g_{Ca,L} = 0.1891$ (*normal*) and $g_{Na} = 0.3178$ (*hyperpolarized*); SN_P at $g_{Ca,L} = 0.085$ (*normal*); *PD* at $g_{Na} = 0.074$ (*normal*); *NS* at $g_{Na} = 0.084$ (*normal*) and 0.595 (*hyperpolarized*).

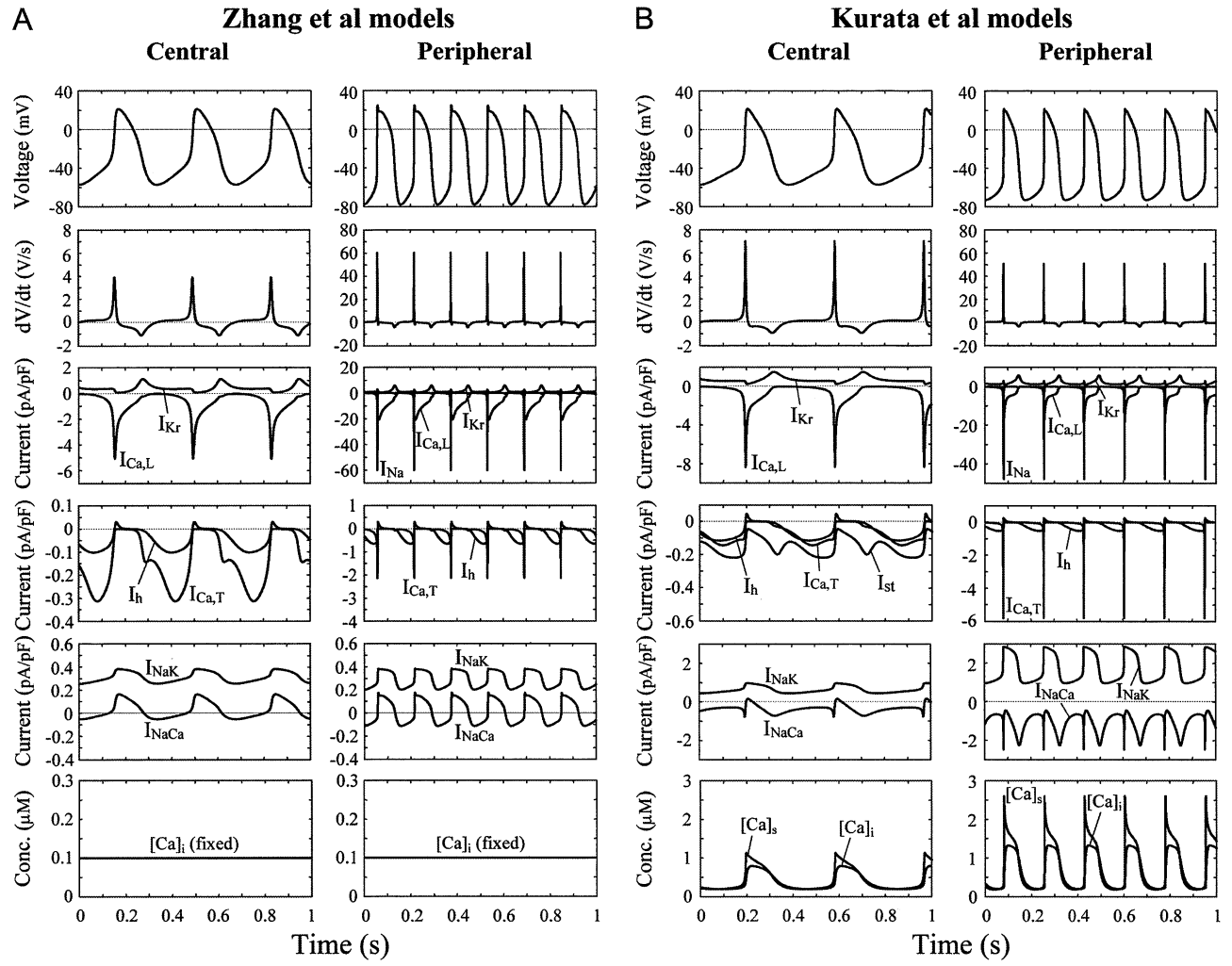

FIGURE 17 Steady-state behaviors of spontaneous APs, underlying transmembrane ionic currents, and intracellular Ca^{2+} dynamics simulated by the central and peripheral versions of the Zhang et al. (*A*) and Kurata et al. (*B*) models with the standard parameter values. Differential equations were numerically solved for 11 s (*A*) or 181 s (*B*) with initial conditions appropriate to an EP and a 1-ms stimulus of 1 pA/pF. Model cell behaviors during the last 1 s starting from maximum diastolic potential are depicted. Intracellular Ca^{2+} dynamics include the changes of Ca^{2+} concentrations in subspace ($[Ca^{2+}]_S$) and myoplasm ($[Ca^{2+}]_i$).

regulatory proteins including the Na^+/Ca^{2+} exchanger, SR Ca^{2+} release channel, and SR Ca^{2+} pump were not taken into account or not based on detailed experimental data; the densities and activities of these proteins are probably greater in the periphery than in the center (38,39).

Another shortcoming of our models may be the use of the classical Hodgkin-Huxley formalism for the kinetic formulation of the time-dependent currents including I_{Na}. More general and realistic schemes, i.e., Markovian state models have been developed for the Na^+ channel (56,57) as well as for other individual channels. However, we did not use these models for I_{Na}, because 1), no Markovian state scheme is available for the SA node Na^+ channel, 2), more detailed experimental data from SA node cells are required for the Markov scheme-based formulation of the SA node I_{Na} kinetics, and 3), such complex models are less suitable for bifurcation analyses. Nevertheless, further sophisticated models based on Markovian state schemes, such as for ventricular myocytes (58), need to be developed and tested for SA node cells in future investigations.

Influences of lacking Ca^{2+} clock

The most serious drawback of the models may be the lack of a "Ca^{2+} clock" that is defined as the spontaneous rhythmic Ca^{2+} release from the junctional SR. Blocking the Ca^{2+} clock by ryanodine or BAPTA dramatically increased CL and finally abolished pacemaker activity (59–63); thus, the Ca^{2+} clock may exert substantial effects on the dynamical properties of SA node cells. Nevertheless, we assumed that the basal pacemaking of SA node cells is attributable to the interplay of sarcolemmal ionic currents such as $I_{Ca,L}$, I_{Na}, I_h, and I_{Kr} (i.e., "membrane clock"), for the following reasons:

1. Experimental reports on the effects of eliminating SR Ca^{2+} release or intracellular Ca^{2+} transient were controversial. In other experimental studies, ryanodine or BAPTA did not abolish, but only slowed, SA node pacemaking (38,

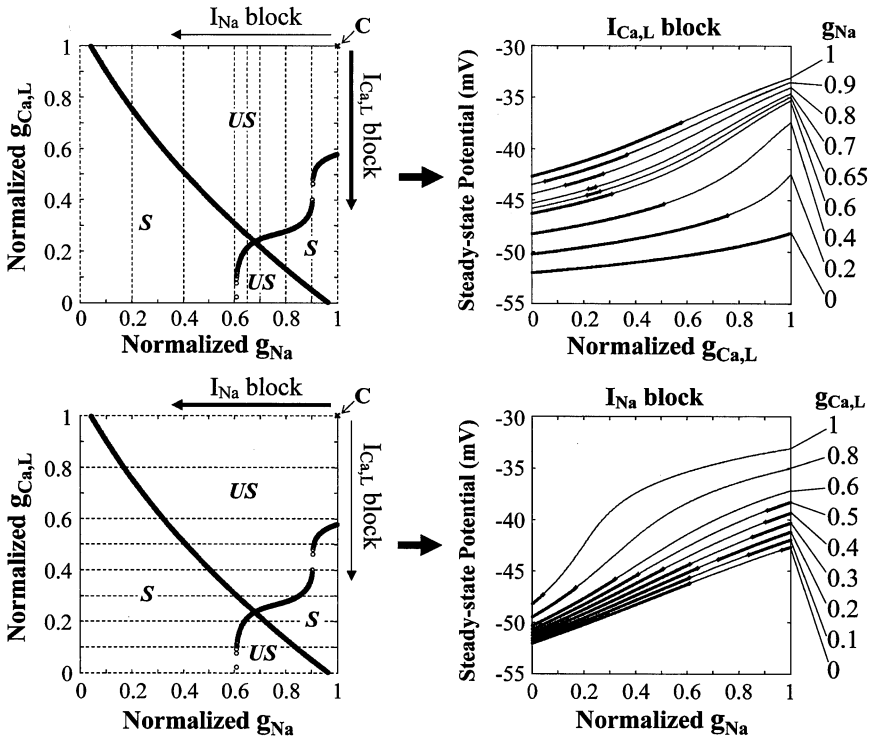

FIGURE 18 How to construct the two-parameter bifurcation diagram for $g_{Ca,L}$ and g_{Na} (Fig. 15) from one-parameter bifurcation diagrams for $g_{Ca,L}$ or g_{Na}. (*Left*) The two-parameter bifurcation diagram for the Zhang et al. peripheral model with the [ACh] of $1 \times 10^{-7.32}$ M (47.863 nM). The point labeled *C* corresponds to the control condition. The leftward and downward shifts from *C* indicate the block of I_{Na} and $I_{Ca,L}$, respectively (shown by the *arrows*). Dashed lines designate the points of g_{Na} (*top*) or $g_{Ca,L}$ (*bottom*) for the construction of the one-parameter bifurcation diagrams shown on the right. (*Right*) One-parameter bifurcation diagrams depicting V_E and its stability as functions of $g_{Ca,L}$ (*top*) or g_{Na} (*bottom*). The normalized $g_{Ca,L}$ (*top*) or g_{Na} (*bottom*) value as the first parameter was decreased from 1 to 0 at an interval of 0.001 for searching for Hopf bifurcations, with the second parameter g_{Na} (*top*) or $g_{Ca,L}$ (*bottom*) fixed at various values as shown on the right of each panel. Critical values of the first parameter $g_{Ca,L}$ (*top*) or g_{Na} (*bottom*) at which Hopf bifurcations occurred were determined by the stability analysis. The thick and thin segments are the stable and unstable V_E regions, respectively; the boundaries between the two segments correspond to the bifurcation points. The two-parameter bifurcation diagram can be constructed by plotting these bifurcation values of the first parameter $g_{Ca,L}$ (or g_{Na}) as functions of the second parameter g_{Na} (or $g_{Ca,L}$).

64,65); thus, the Ca^{2+} clock is not necessarily required for pacemaker generation.

2. Ryanodine and BAPTA are known to affect not only the Ca^{2+} clock but also the membrane clock (40); their secondary (or direct) effects on the membrane clock, rather than the elimination of the Ca^{2+} clock, may result in the dramatic responses.

3. Spontaneous Ca^{2+} release was local (not global), stochastic, and transient in the pacemaker potential range (60); thus, the manner in which the Ca^{2+} clock contributes to the stability and bifurcation structures of SA node cells is unclear. In our opinion, the Ca^{2+} clock is not a prerequisite for basal SA node pacemaking, although it would significantly modulate pacemaker activity and is possibly involved in the regional differences in pacemaker dynamics (38).

As already mentioned, neither SR Ca^{2+} cycling nor intracellular Ca^{2+} dynamics exerted substantial effects on the stability and bifurcation of SA node model cells, with their effects being too small to alter our conclusions. The simplified models used in this study are therefore valuable and highly appropriate for exploring the bifurcation structures of pacemaker cells and essential mechanisms of basal SA node pacemaking. Nevertheless, our models do not incorporate the real Ca^{2+} clock defined as the spontaneous rhythmic Ca^{2+} release from the junctional SR to trigger the membrane clock. We could produce a model with the spontaneous SR Ca^{2+} release (and a transient increase in $[Ca^{2+}]_{sub}$ and the forward-mode I_{NaCa}) during phase 4 depolarization by further increasing SR Ca^{2+} uptake and release rates (data not shown). However, such a model was not used because an excess increase of the SR Ca^{2+} uptake and release rates resulted in very small CL (<150 ms in the peripheral model) and often induced irregular dynamics. Maltsev et al. (66) developed a modified version of the Kurata et al. model (14) to exhibit the spontaneous local Ca^{2+} release from the junctional SR during phase 4. However, their formulas were based on phenomenological representation to approximate the experimental pattern of Ca^{2+} signals in the subspace, which were not suitable for bifurcation analysis. More elaborate models incorporating detailed descriptions of the intracellular Ca^{2+} handling as well as other modulating factors need to be developed for future investigations regarding the role of the Ca^{2+} clock in SA node pacemaking in terms of nonlinear dynamics and bifurcation theory.

Requirement of multicellular models

We used the single-cell or coupled-cell systems to investigate the robustness of SA node pacemaking against hyperpolarization and the roles of I_{Na} in peripheral cell pacemaking. However, the real intact SA node has complex architectures to facilitate optimization of the electrical loading by the surrounding atrial tissue (36,67–69). Previous studies suggest that electrotonic interaction is involved in the pacemaker mechanisms of the intact SA node (5,69). Thus, multicellular models including central and peripheral SA node cells and also atrial myocytes are required for further investigating how electrotonic interactions, as well as I_{Na}, contribute to the pacemaking and driving ability of the intact SA node in vivo. Modeling SA node tissues would also be useful in exploring

the mechanisms of pacemaker shifts (36,37), pacemaker synchronization (70), and abnormal rhythms such as the exit block and intranodal reentry (42).

Lack of experimental evidence

The conclusions in this study are, of course, the predictions from the model cell systems; thus they must be verified and supported by experimental works using real SA node cells. Fundamental properties of the model cell behaviors have been verified by Zhang et al. (15). Inconsistent with our result, however, pacemaker activity of the peripheral cell was not abolished by blocking $I_{Ca,L}$ in either their simulation or in experiments (3). We could not find experimental evidence for the cessation of peripheral cell pacemaking by the inhibition of $I_{Ca,L}$ as predicted by the models in Figs. 1 and 2, although the I_{Na} block was observed to abolish pacemaker activity of the peripheral SA node region with electrotonic loads of the atrium in mice (41,42). Whether an $I_{Ca,L}$ blocker can abolish peripheral cell pacemaking should be reexamined in future experiments. To the best of our knowledge, there is no systematic study regarding the bifurcation structures of SA node cells to clarify the regional differences in the dynamical mechanism and the robustness of pacemaker activity. We hope that this study provides a stimulus to further experimentation on these issues.

APPENDIX A: MODEL EQUATIONS

Mathematical expressions, definitions of the symbols, and standard parameter values used in this study are essentially the same as those in the original articles (14–16). The formulas for $I_{Ca,L}$, I_h, and $I_{K,ACh}$ with ACh modifications of Dokos et al. (29), as well as those for I_{Na} adopted from Garny et al. (16), are given below for convenience. Units are mV, pA, nS, ms, pF, mM, and L (pA/pF and nS/pF for ionic currents and conductance, respectively). Dynamics of the model cells with standard parameter values (for the Kurata et al. models; see Table 1) are shown in Fig. 17.

Na^+ channel current (I_{Na}):

$$I_{Na} = g_{Na} \times [Na^+]_o \times F \times (F/RT) \times V \times \{\exp[(V - E_{Na}) \times F/RT] - 1\}/[\exp(V \times F/RT) - 1] \times m^3 \times [(1 - F_{Na}) \times h_1 + F_{Na} \times h_2] \quad (A1)$$

$$m_\infty = \{1 + \exp[-(V + 30.32)/5.46]\}^{-1/3} \quad (A2)$$

$$h_\infty = \{1 + \exp[(V + 66.1)/6.4\}^{-1} \quad (A3)$$

$$\tau_m = 0.6247/\{0.8322166 \times \exp[-0.33566 \times (V + 56.7062)] + 0.6274 \times \exp[0.0823 \times (V + 65.0131)]\} + 0.04569 \quad (A4)$$

$$\tau_{h1} = 0.003717 \times \exp[-0.2815 \times (V + 17.11)]/\{1 + 0.003732 \times \exp[-0.3426 \times (V + 37.76)]\} + 0.5977 \quad (A5)$$

$$\tau_{h2} = 0.00003186 \times \exp[-0.6219 \times (V + 18.8)]/\{1 + 0.00007189 \times \exp[-0.6683 \times (V + 34.07)]\} + 3.556 \quad (A6)$$

$$F_{Na} = 0.09518 \times \exp(-0.06306 \times (V + 34.4))/\{1 + 1.662 \times \exp[-0.2251 \times (V + 63.7)]\} + 0.08693. \quad (A7)$$

L-type Ca^{2+} channel current ($I_{Ca,L}$) for modified Zhang et al. models:

$$I_{Ca,L} = g_{Ca,L} \times \{1 - 0.0037 \times [ACh]/(0.007 \times [ACh] + 0.0000006)\} \times (V - 46.4) \times (d_L \times f_L + 0.006/\{1 + \exp[-(V + 14.1)/6]\}) \quad (A8)$$

$g_{Ca,L}$=0.2752(central) or 0.9630 (peripheral)

$$d_{L\infty} = \{1 + \exp[-(V + 22.3 + 0.8 \times F_{Cell} - 5)/6]\}^{-1} \quad (A9)$$

$$f_{L\infty} = \{1 + \exp[(V + 45 - 10)/5]\}^{-1} \quad (A10)$$

$$\tau_{dL} = 2000 \times (\alpha_{dL} + \beta_{dL})^{-1} \quad (A11)$$

$$\alpha_{dL} = -28.39 \times (V + 35)/\{\exp[-(V + 35)/2.5] - 1\} - 84.9 \times V/\{\exp[-0.208 \times V] - 1\} \quad (A12)$$

$$\beta_{dL} = 11.43 \times (V - 5)/\{\exp[0.4 \times (V - 5)] - 1\} \quad (A13)$$

$$\tau_{fL} = 1000 \times (1.2 - 0.2 \times F_{Cell}) \times (\alpha_{fL} + \beta_{fL})^{-1} \quad (A14)$$

$$\alpha_{fL} = 3.75 \times (V + 28)/\{\exp[(V + 28)/4] - 1\} \quad (A15)$$

$$\beta_{fL} = 30/\{1 + \exp[-(V + 28)/4]\} \quad (A16)$$

$$F_{Cell} = 1.0309347 \times d_{Cell}/\{1 + 0.7745 \times \exp[-(3 \times d_{Cell} - 2.05)/0.295]\} \quad (A17)$$

$$d_{Cell} = 0 \text{ (central) or } 1 \text{ (peripheral)}.$$

L-type Ca^{2+} channel current ($I_{Ca,L}$) for Kurata et al. models:

$$I_{Ca,L} = g_{Ca,L} \times \{1 - 0.0037 \times [ACh]/(0.007 \times [ACh] + 0.0000006)\} \times (V - 45) \times d_L \times f_L \times f_{Ca} \quad (A18)$$

$$d_{L\infty} = \{1 + \exp[-(V + 14.1)/6]\}^{-1} \quad \text{(A19)}$$

$$f_{L\infty} = \{1 + \exp[(V + 30)/5]\}^{-1} \quad \text{(A20)}$$

$$f_{Ca\infty} = 0.00035/(0.00035 + [Ca^{2+}]_{sub}) \quad \text{(A21)}$$

$$\tau_{dL} = (\alpha_{dL} + \beta_{dL})^{-1} \quad \text{(A22)}$$

$$\alpha_{dL} = -0.02839 \times (V + 35)/\{\exp[-(V + 35)/2.5] - 1\} - 0.0849 \times V/\{\exp[-V/4.808] - 1\} \quad \text{(A23)}$$

$$\beta_{dL} = 0.01143 \times (V - 5)/\{\exp[(V - 5)/2.5] - 1\} \quad \text{(A24)}$$

$$\tau_{fL} = 257.1 \times \exp[-(V + 32.5)^2/13.9^2] + 44.3 \quad \text{(A25)}$$

$$\tau_{fCa} = 1/(0.021 + 60 \times [Ca^{2+}]_{sub}). \quad \text{(A26)}$$

Hyperpolarization-activated cation current (I_h):

$$I_h = [g_{h,Na} \times (V - E_{Na}) + g_{h,K} \times (V - E_K)] \times y \quad \text{(A27)}$$

$$y_\infty = \alpha_y/(\alpha_y + \beta_y) \quad \text{(A28)}$$

$$\tau_{dL} = 1000 \times (\alpha_y + \beta_y)^{-1} \quad \text{(A29)}$$

$$\alpha_y = \exp[-(V + 78.91 - dV_y)/26.63] \quad \text{(A30)}$$

$$\beta_y = \exp[(V + 75.13 - dV_y)/21.25] \quad \text{(A31)}$$

$$dV_y = -10 \times \{[ACh]/([ACh] + 0.0000025)\}^4. \quad \text{(A32)}$$

Muscarinic K^+ channel current ($I_{K,ACh}$):

$$I_{K,ACh} = 0.031 \times [K^+]_o^{0.41} \times \{[ACh]/([ACh] + 0.000057447)\}^4 \times \{[K^+]_I - [K^+]_o \times \exp(-V \times F/RT)\}. \quad \text{(A33)}$$

APPENDIX B: STABILITY ANALYSIS BASED ON THE LINEAR STABILITY THEORY

We evaluated the stability of EPs according to the linear stability theory, i.e., by linear approximation of a nonlinear system at an EP (see (71,72)). For simplicity, first consider the two-dimensional autonomous system of the form

$$dx_1/dt = f_1(x_1, x_2), \quad dx_2/dt = f_2(x_1, x_2), \quad \text{(A34a)}$$

or the vector form

$$d\mathbf{x}/dt = \mathbf{f}(\mathbf{x}), \mathbf{x} = (x_1, x_2)^T, \quad \mathbf{f}(\mathbf{x}) = [f_1(x_1, x_2), f_2(x_1, x_2)]^T \quad \text{(A34b)}$$

(T denotes transpose). Suppose that the EP to be (x_{1E}, x_{2E}), so that $f_1(x_{1E}, x_{2E}) = f_2(x_{1E}, x_{2E}) = 0$. We can therefore write, by a Taylor series expansion of the vector field $f_i(x_1, x_2)$ around the EP,

$$f_1(x_1, x_2) = \partial f_1/\partial x_1(x_{1E}, x_{2E}) \times (x_1 - x_{1E}) + \partial f_1/\partial x_2(x_{1E}, x_{2E}) \times (x_2 - x_{2E}) + O(\text{tho}),$$
$$f_2(x_1, x_2) = \partial f_2/\partial x_1(x_{1E}, x_{2E}) \times (x_1 - x_{1E}) + \partial f_2/\partial x_2(x_{1E}, x_{2E}) \times (x_2 - x_{2E}) + O(\text{tho}), \quad \text{(A35)}$$

where the symbol O stands for the term of higher order (tho). Thus, the linear approximation to Eq. A34 in the neighborhood of the EP is defined as the system for $h_1(= x_1\text{-}x_{1E})$ and $h_2(= x_2\text{-}x_{2E})$:

$$dh_1/dt = \partial f_1/\partial x_1(x_{1E}, x_{2E}) \times h_1 + \partial f_1/\partial x_2(x_{1E}, x_{2E}) \times h_2,$$
$$dh_2/dt = \partial f_2/\partial x_1(x_{1E}, x_{2E}) \times h_1 + \partial f_2/\partial x_2(x_{1E}, x_{2E}) \times h_2. \quad \text{(A36a)}$$

This linearized system is also written in the vector form

$$d\mathbf{h}/dt = \mathbf{Df}(\mathbf{x_E}) \times \mathbf{h}, \mathbf{h} = (h_1, h_2)^T,$$
$$d\mathbf{h}/dt = [dh_1/dt, dh_2/dt]^T, \quad \text{(A36b)}$$

where $\mathbf{Df}(\mathbf{x_E})$ is the Jacobian matrix of first-order partial derivatives of $\mathbf{f}(\mathbf{x})$, denoted by:

$$\mathbf{Df}(\mathbf{x_E}) = \begin{bmatrix} \partial f_1/\partial x_1(x_{1E}, x_{2E}), \partial f_1/\partial x_2(x_{1E}, x_{2E}) \\ \partial f_2/\partial x_1(x_{1E}, x_{2E}), \partial f_2/\partial x_2(x_{1E}, x_{2E}) \end{bmatrix} \quad \text{(A37)}$$

We can expect in most cases that the solutions of Eq. A36 will be geometrically similar to those of Eq. A34 near the EP. It is well known that there are solutions of Eq. A36 of the form

$$h_1(t) = C_1 \times r_{11} \times \exp(\lambda_1 \times t) + C_2 \times r_{12} \times \exp(\lambda_2 \times t),$$
$$h_2(t) = C_1 \times r_{21} \times \exp(\lambda_1 \times t) + C_2 \times r_{22} \times \exp(\lambda_2 \times t), \quad \text{(A38a)}$$

or the vector form

$$\mathbf{h}(t) = C_1 \times \mathbf{r}_1 \times \exp(\lambda_1 \times t) + C_2 \times \mathbf{r}_2 \times \exp(\lambda_2 \times t),$$
$$\mathbf{h}(t) = [h_1(t), h_2(t)]^T, \quad \mathbf{r}_1 = (r_{11}, r_{21})^T, \quad \mathbf{r}_2 = (r_{12}, r_{22})^T, \quad \text{(A38b)}$$

where λ_1 and λ_2 are the eigenvalues (roots of the characteristic equation) for the Jacobian matrix $\mathbf{Df}(\mathbf{x_E})$. C_1 and C_2 are arbitrary constants to be complex in general. The approximation $\mathbf{h}(t)$ describes the local behavior of the solution, indicating how the process evolves when the initial state deviates slightly from the EP. When λ_i is complex, represented as

$$\lambda_I = \text{Re}[\lambda_i] + j \times \text{Im}[\lambda_i], \quad \text{(A39)}$$

we obtain

$$h_1(t) = \sum C_i \times r_{1i} \times \exp(\text{Re}[\lambda_i] \times t) \times [\cos(\text{Im}[\lambda_i] \times t) + j \times \sin(\text{Im}[\lambda_i] \times t)],$$
$$h_2(t) = \sum C_i \times r_{2i} \times \exp(\text{Re}[\lambda_i] \times t) \times [\cos(\text{Im}[\lambda_i] \times t) + j \times \sin(\text{Im}[\lambda_i] \times t)] (i = 1, 2). \quad \text{(A40)}$$

Here $\text{Re}[\lambda_i]$ and $\text{Im}[\lambda_i]$ are respectively the real and imaginary part of λ_i. For a more general case of an n-dimensional autonomous system of the form

$$d\mathbf{x}/dt = \mathbf{f}(\mathbf{x}), \mathbf{x} = (x_1, x_2, \ldots, x_n)^T, \mathbf{f}(\mathbf{x}) = [f_1(x_1, x_2, \ldots, x_n), f_2(x_1, x_2, \ldots, x_n), \ldots, f_n(x_1, x_2, \ldots, x_n)]^T, \quad \text{(A41)}$$

the linearized form around an EP of $\mathbf{x_E} = (x_{1E}, x_{2E}, \ldots, x_{nE})^T$ is

$$d\mathbf{h}/dt = \mathbf{Df}(\mathbf{x_E}) \times \mathbf{h}, \quad \mathbf{h} = (h_1, h_2, \ldots, h_n)^T,$$
$$d\mathbf{h}/dt = [dh_1/dt, dh_2/dt, \ldots, dh_n/dt]^T. \quad \text{(A42)}$$

Then, the solution of Eq. A42 is given by

$$\mathbf{h}(t) = [h_1(t), h_2(t), \ldots, h_k(t), \ldots, h_n(t)]^T,$$
$$h_k(t) = \sum C_i \times r_{ki} \times \exp(\lambda_i \times t) = \sum C_i \times r_{ki} \times \exp(\mathrm{Re}[\lambda_i] \times t) \times [\cos(\mathrm{Im}[\lambda_i] \times t) + j \times \sin(\mathrm{Im}[\lambda_i] \times t)](i, k = 1, 2, \ldots, n). \quad \text{(A43)}$$

Thus, $\mathrm{Re}[\lambda_i]$ represents the rate constant of a solution beneath the EP to be attracted to or go away from the EP. The EP is stable if all of the $\mathrm{Re}[\lambda_i]$ values are negative because the system is asymptotically attracted to the EP; it is unstable if at least one of $\mathrm{Re}[\lambda_i]$ values is positive because the system goes away from the EP.

APPENDIX C: CONSTRUCTION OF TWO-PARAMETER BIFURCATION DIAGRAMS FOR $G_{CA,L}$ AND G_{NA}

The two-parameter bifurcation diagrams for $g_{Ca,L}$ and g_{Na} (Fig. 15) show how the stability of EPs reverses via Hopf bifurcations during the inhibition of $I_{Ca,L}$ and/or I_{Na}. One-parameter bifurcation diagrams for $g_{Ca,L}$ of 0–1 were first constructed with various g_{Na} values of 0–1 (with intervals of 0.001) by the stability analysis for EPs; those for $g_{Na} = 1$, 0.9, 0.8, 0.7, 0.65, 0.6, 0.4, 0.2, and 0 are shown in Fig. 18 (*top-right*). To construct the two-parameter bifurcation diagrams as shown in Fig. 15, the critical $g_{Ca,L}$ values at Hopf bifurcations in the one-parameter bifurcation diagrams were plotted as functions of g_{Na} (Fig. 18 *top-left*). This two-parameter bifurcation diagram can also be constructed from one-parameter bifurcation diagrams for g_{Na} determined with various $g_{Ca,L}$ values (see Fig. 18 *bottom* for $g_{Ca,L} = 1$, 0.9, 0.8, 0.7, 0.6, 0.5, 0.4, 0.2, and 0).

This work was supported in part by the Ministry for Education, Science, Sports and Culture of Japan Grant-in-Aid for Scientific Research (C) 17590192 (to Y.K. and T.S.), Kanazawa Medical University Grant for Collaborative Research C2005-1 (to Y.K. and T.S.), and Kanazawa Medical University Grant for Promoted Research S2006-6 and S2007-2 (to Y.K.).

REFERENCES

1. Noma, A. 1996. Ionic mechanisms of the cardiac pacemaker potential. *Jpn. Heart J.* 37:673–682.
2. Kurata, Y., I. Hisatome, S. Imanishi, and T. Shibamoto. 2003. Roles of L-type Ca^{2+} and delayed-rectifier K^+ currents in sinoatrial node pacemaking: insights from stability and bifurcation analyses of a mathematical model. *Am. J. Physiol. Heart Circ. Physiol.* 285:H2804–H2819.
3. Kodama, I., M. R. Nikmaram, M. R. Boyett, R. Suzuki, H. Honjo, and J. M. Owen. 1997. Regional differences in the role of the Ca^{2+} and Na^+ currents in pacemaker activity in the sinoatrial node. *Am. J. Physiol. Heart Circ. Physiol.* 272:H2793–H2806.
4. Kreitner, D. 1985. Electrophysiological study of the two main pacemaker mechanisms in the rabbit sinus node. *Cardiovasc. Res.* 19:304–318.
5. Zhang, H., and M. Vassalle. 2000. Role of dual pacemaker mechanisms in sinoatrial node discharge. *J. Biomed. Sci.* 7:100–113.
6. Zhang, H., and M. Vassalle. 2001. Role of I_K and I_f in the pacemaker mechanisms of sino-atrial node myocytes. *Can. J. Physiol. Pharmacol.* 79:963–976.
7. Chay, T. R., and Y. S. Lee. 1985. Phase resetting and bifurcation in the ventricular myocardium. *Biophys. J.* 47:641–651.
8. Chay, T. R., and Y. S. Lee. 1990. Bursting, beating, and chaos by two functionally distinct inward current inactivations in excitable cells. *Ann. N. Y. Acad. Sci.* 591:328–350.
9. Guevara, M. R., and H. J. Jongsma. 1992. Three ways of abolishing automaticity in sinoatrial node: ionic modeling and nonlinear dynamics. *Am. J. Physiol.* 262:H1268–H1286.
10. Landau, M., P. Lorente, D. Michaels, and J. Jalife. 1990. Bistabilities and annihilation phenomena in electrophysiological cardiac models. *Circ. Res.* 66:1658–1672.
11. Varghese, A., and R. L. Winslow. 1994. Dynamics of abnormal pacemaking activity in cardiac Purkinje fibers. *J. Theor. Biol.* 168:407–420.
12. Vinet, A., and F. A. Roberge. 1990. A model study of stability and oscillations in the myocardial cell membrane. *J. Theor. Biol.* 147: 377–412.
13. Kurata, Y., I. Hisatome, H. Matsuda, and T. Shibamoto. 2005. Dynamical mechanisms of pacemaker generation in I_{K1}-downregulated human ventricular myocytes: Insights from bifurcation analyses of a mathematical model. *Biophys. J.* 89: 2865–2887.
14. Kurata, Y., I. Hisatome, S. Imanishi, and T. Shibamoto. 2002. Dynamical description of sinoatrial node pacemaking: improved mathematical model for primary pacemaker cell. *Am. J. Physiol. Heart Circ. Physiol.* 283:H2074–H2101.
15. Zhang, H., A. V. Holden, I. Kodama, H. Honjo, M. Lei, T. Varghese, and M. R. Boyett. 2000. Mathematical models of action potentials in the periphery and center of the rabbit sinoatrial node. *Am. J. Physiol. Heart Circ. Physiol.* 279:H397–H421.
16. Garny, A., P. Kohl, P. J. Hunter, M. R. Boyett, and D. Noble. 2003. One-dimensional rabbit sinoatrial node models: benefits and limitations. *J. Cardiovasc. Electrophysiol.* 14:S121–S132.
17. Gepstein, L., Y. Feld, and L. Yankelson. 2004. Somatic gene and cell therapy strategies for the treatment of cardiac arrhythmias. *Am. J. Physiol. Heart Circ. Physiol.* 286:815–822.
18. Kurata, Y., H. Matsuda, I. Hisatome, and T. Shibamoto. 2007. Effects of pacemaker currents on creation and modulation of human ventricular pacemaker: theoretical study with application to biological pacemaker engineering. *Am. J. Physiol. Heart Circ. Physiol.* 292: H701–H718.
19. Guckenheimer, J., and P. Holmes. 1983. Nonlinear Oscillations, Dynamical Systems, and Bifurcations of Vector Fields. Springer-Verlag, New York.
20. Parker, T. S., and L. O. Chua. 1989. Practical Numerical Algorithms for Chaotic Systems. Springer-Verlag, New York.
21. Kuznetsov, Y. A. 2003. Elements of Applied Bifurcation Theory, 3rd edition. Springer-Verlag, New York.
22. Zhang, H., Y. Zhao, M. Lei, H. Dobrzynski, J. H. Liu, A. V. Holden, and M. R. Boyett. 2007. Computational evaluation of the roles of Na^+ current, I_{Na}, and cell death in cardiac pacemaking and driving. *Am. J. Physiol. Heart Circ. Physiol.* 292:H165–H174.
23. Wilders, R., H. J. Jongsma, and A. C. G. van Ginneken. 1991. Pacemaker activity of the rabbit sinoatrial node: a comparison of mathematical models. *Biophys. J.* 60:1202–1216.
24. Demir, S. S., J. W. Clark, C. R. Murphey, and W. R. Giles. 1994. A mathematical model of a rabbit sinoatrial node cell. *Am. J. Physiol.* 266:C832–C852.
25. Dokos, S., B. Celler, and N. Lovell. 1996. Ion currents underlying sinoatrial node pacemaker activity: a new single cell mathematical model. *J. Theor. Biol.* 181:245–272.
26. Sarai, N., S. Matsuoka, S. Kuratomi, K. Ono, and A. Noma. 2003. Role of individual ionic current systems in the SA node hypothesized by a model study. *Jpn. J. Physiol.* 53:125–134.
27. Baruscotti, M., D. DiFrancesco, and R. B. Robinson. 1996. A TTX-sensitive inward sodium current contributes to spontaneous activity in newborn rabbit sino-atrial node cells. *J. Physiol.* 492:21–30.
28. Muramatsu, H., A.-R. Zou, G. A. Berkowitz, and R. D. Nathan. 1996. Characterization of a TTX-sensitive Na^+ current in pacemaker cells isolated from rabbit sinoatrial node. *Am. J. Physiol.* 270:H2108–H2119.
29. Dokos, S., B. G. Celler, and N. H. Lovell. 1996. Vagal control of sinoatrial rhythm: a mathematical model. *J. Theor. Biol.* 182:21–44.
30. Zhang, H., A. V. Holden, D. Noble, and M. R. Boyett. 2002. Analysis of the chronotropic effect of acetylcholine on sinoatrial node cells. *J. Cardiovasc. Electrophysiol.* 13:465–474.

31. Beau, S. L., D. E. Hand, R. B. Schuessler, B. I. Bromberg, B. Kwon, J. P. Boineau, and J. E. Saffitz. 1995. Relative densities of muscarinic cholinergic and beta-adrenergic receptors in the canine sinoatrial node and their relation to sites of pacemaker activity. *Circ. Res.* 77:957–963.
32. Roberts, L. A., G. R. Slocum, and D. A. Riley. 1989. Morphological study of the innervation pattern of the rabbit sinoatrial node. *Am. J. Anat.* 185:74–88.
33. Watanabe, E. I., H. Honjo, T. Anno, M. R. Boyett, I. Kodama, and J. Toyama. 1995. Modulation of pacemaker activity of sinoatrial node cells by electrical load imposed by an atrial cell model. *Am. J. Physiol. Heart Circ. Physiol.* 269:H1735–H1742.
34. Dhooge, A., W. Govaerts, Yu. A. Kuznetsov, W. Mestrom, A. M. Riet, and B. Sautois. 2006. MATCONT and CL_MATCONT: Continuation Toolboxes in MATLAB. http://www.matcont.ugent.be/matcont.html.
35. Fukai, H., S. Doi, T. Nomura, and S. Sato. 2000. Hopf bifurcations in multiple-parameter space of the Hodgkin-Huxley equations I. Global organization of bistable periodic solutions. *Biol. Cybern.* 82:215–222.
36. Boyett, M. R., H. Honjo, and I. Kodama. 2000. The sinoatrial node, a heterogeneous pacemaker structure. *Cardiovasc. Res.* 47:658–687.
37. Shibata, N., S. Inada, K. Mitsui, H. Honjo, M. Yamamoto, R. Niwa, M. R. Boyett, and I. Kodama. 2001. Pacemaker shift in the rabbit sinoatrial node in response to vagal nerve stimulation. *Exp. Physiol.* 86:177–184.
38. Lancaster, M. K., S. A. Jones, S. M. Harrison, and M. R. Boyett. 2004. Intracellular Ca^{2+} and pacemaking within the rabbit sinoatrial node: heterogeneity of role and control. *J. Physiol.* 556:481–494.
39. Musa, H., M. Lei, H. Honjo, S. A. Jones, H. Dobrzynski, M. K. Lancaster, Y. Takagishi, Z. Henderson, I. Kodama, and M. R. Boyett. 2002. Heterogeneous expression of Ca^{2+} handling proteins in rabbit sinoatrial node. *J. Histochem. Cytochem.* 50:311–324.
40. Boyett, M. R., H. Zhang, A. Garny, and A. V. Holden. 2001. Control of the pacemaker activity of the sinoatrial node by intracellular Ca^{2+}. Experiments and modelling. *Philos. Trans. R. Soc. Lond. A Math. Phys. Sci.* 359:1091–1110.
41. Lei, M., S. A. Jones, J. Liu, M. K. Lancaster, S. S.-M. Fung, H. Dobrzynski, P. Camelliti, S. K. G. Maier, D. Noble, and M. R. Boyett. 2004. Requirement of neuronal- and cardiac-type sodium channels for murine sinoatrial node pacemaking. *J. Physiol.* 559:835–848.
42. Lei, M., C. Goddard, J. Liu, A. L. Leoni, A. Royer, S. S. Fung, G. Xiao, A. Ma, H. Zhang, F. Charpentier, J. I. Vandenberg, W. H. Colledge, A. A. Grace, and C. L. Huang. 2005. Sinus node dysfunction following targeted disruption of the murine cardiac sodium channel gene Scn5a. *J. Physiol.* 567:387–400.
43. Benson, D. W., D. W. Wang, M. Dyment, T. K. Knilans, F. A. Fish, M. J. Strieper, T. H. Rhodes, and A. L. George, Jr. 2003. Congenital sick sinus syndrome caused by recessive mutations in the cardiac sodium channel gene (SCN5A). *J. Clin. Invest.* 112:1019–1028.
44. Smits, J. P., T. T. Koopmann, R. Wilders, M. W. Veldkamp, T. Opthof, Z. A. Bhuiyan, M. M. Mannens, J. R. Balser, H. L. Tan, C. R. Bezzina, and A. A. Wilde. 2005. A mutation in the human cardiac sodium channel (E161K) contributes to sick sinus syndrome, conduction disease and Brugada syndrome in two families. *J. Mol. Cell. Cardiol.* 38:969–981.
45. Satin, J., I. Kehat, O. Caspi, I. Huber, G. Arbel, I. Itzhaki, J. Magyar, E. A. Schroder, I. Perlman, and L. Gepstein. 2004. Mechanisms of spontaneous excitability in human embryonic stem cell derived cardiomyocytes. *J. Physiol.* 559:479–496.
46. Gibb, W. J., M. B. Wagner, and M. D. Lesh. 1994. Effects of simulated potassium blockade on the dynamics of triggered cardiac activity. *J. Theor. Biol.* 168:245–257.
47. Miake, J., E. Marbán, and H. B. Nuss. 2002. Gene therapy: biological pacemaker created by gene transfer. *Nature.* 419:132–133.
48. Qu, J., A. N. Plotnikov, P. Danilo, Jr., I. Shlapakova, I. S. Cohen, R. B. Robinson, and M. R. Rosen. 2003. Expression and function of a biological pacemaker in canine heart. *Circulation.* 107:1106–1109.
49. Plotnikov, A. N., E. A. Sosunov, J. Qu, I. N. Shlapakova, E. P. Anyukhovsky, L. Liu, M. J. Janse, P. R. Brink, I. S. Cohen, R. B. Robinson, P. Danilo, Jr., and M. R. Rosen. 2004. Biological pacemaker implanted in canine left bundle branch provides ventricular escape rhythms that have physiologically acceptable rates. *Circulation.* 109: 506–512.
50. He, J.-Q., Y. Ma, Y. Lee, J. A. Thomson, and T. J. Kamp. 2003. Human embryonic stem cells develop into multiple types of cardiac myocytes: action potential characterization. *Circ. Res.* 93:32–39.
51. Xue, T., H. C. Cho, F. G. Akar, S.-Y. Tsang, S. P. Jones, E. Marbán, G. F. Tomaselli, and R. A. Li. 2005. Functional integration of electrically active cardiac derivatives from genetically engineered human embryonic stem cells with quiescent recipient ventricular cardiomyocytes: insights into the development of cell-based pacemakers. *Circulation.* 111:11–20.
52. Demir, S. S., J. W. Clark, and W. R. Giles. 1999. Parasympathetic modulation of sinoatrial node pacemaker activity in rabbit heart: a unifying model. *Am. J. Physiol.* 276:H2221–H2244.
53. Greenstein, J. L., and R. L. Winslow. 2002. An integrative model of the cardiac ventricular myocytes incorporating local control of Ca^{2+} release. *Biophys. J.* 83:2918–2945.
54. Saucerman, J. J., L. L. Brunton, A. P. Michailova, and A. D. McCulloch. 2003. Modeling β-adrenergic control of cardiac myocytes contractility *in silico*. *J. Biol. Chem.* 278:47997–48003.
55. Shannon, T. R., F. Wang, J. Puglisi, C. Weber, and D. M. Bers. 2004. A mathematical treatment of integrated Ca dynamics within the ventricular myocyte. *Biophys. J.* 87:3351–3371.
56. Clancy, C. E., and Y. Rudy. 1999. Linking a genetic defect to its cellular phenotype in a cardiac arrhythmia. *Nature.* 400:566–569.
57. Irvine, L. A., M. S. Jafri, and R. L. Winslow. 1999. Cardiac sodium channel Markov model with temperature dependence and recovery from inactivation. *Biophys. J.* 76:1868–1885.
58. Iyer, V., R. Mazhari, and R. L. Winslow. 2004. A computational model of the human left-ventricular epicardial myocyte. *Biophys. J.* 87:1507–1525.
59. Lakatta, E. G., V. A. Maltsev, K. Y. Bogdanov, M. D. Stern, and T. M. Vinogradova. 2003. Cyclic variation of intracellular calcium: a critical factor for cardiac pacemaker cell dominance. *Circ. Res.* 92: e45–e50.
60. Vinogradova, T. M., Y.-Y. Zhou, V. A. Maltsev, A. E. Lyashkov, M. Stern, and E. G. Lakatta. 2004. Rhythmic ryanodine receptor Ca^{2+} releases during diastolic depolarization of sinoatrial pacemaker cells do not require membrane depolarization. *Circ. Res.* 94:802–809.
61. Vinogradova, T. M., V. A. Maltsev, K. Y. Bogdanov, A. E. Lyashkov, and E. G. Lakatta. 2005. Rhythmic Ca^{2+} oscillations drive sinoatrial nodal cell pacemaker function to make the heart tick. *Ann. N. Y. Acad. Sci.* 1047:138–156.
62. Lakatta, E. G., T. M. Vinogradova, A. Lyashkov, S. Sirenko, W. Zhu, A. Ruknudin, and V. A. Maltsev. 2006. The integration of spontaneous intracellular Ca^{2+} cycling and surface membrane ion channel activation entrains normal automaticity in cells of the heart's pacemaker. *Ann. N. Y. Acad. Sci.* 1080:178–206.
63. Maltsev, V. A., T. M. Vinogradova, and E. G. Lakatta. 2006. The emergence of a general theory of the initiation and strength of the heartbeat. *J. Pharmacol. Sci.* 100:338–369.
64. Li, J., J. Qu, and R. D. Nathan. 1997. Ionic basis of ryanodine's negative chronotropic effect on pacemaker cells isolated from the sinoatrial node. *Am. J. Physiol.* 273:H2481–H2489.
65. Honjo, H., S. Inada, M. K. Lancaster, M. Yamamoto, R. Niwa, S. A. Jones, N. Shibata, K. Mitsui, T. Horiuchi, K. Kamiya, I. Kodama, and M. R. Boyett. 2003. Sarcoplasmic reticulum Ca^{2+} release is not a dominating factor in sinoatrial node pacemaker activity. *Circ. Res.* 92:e41–e44.
66. Maltsev, V. A., T. M. Vinogradova, K. Y. Bogdanov, E. G. Lakatta, and M. D. Stern. 2004. Diastolic calcium release controls the beating

rate of rabbit sinoatrial node cells: numerical modeling of the coupling process. *Biophys. J.* 86:2596–2605.

67. Boyett, M. R., H. Dobrzynski, M. K. Lancaster, S. A. Jones, H. Honjo, and I. Kodama. 2003. Sophisticated architecture is required for the sinoatrial node to perform its normal pacemaker function. *J. Cardiovasc. Electrophysiol.* 14:104–106.
68. Joyner, R. W., Y.-G. Wang, R. Wilders, D. A. Golod, M. B. Wagner, R. Kumar, and W. N. Goolsby. 2000. A spontaneously active focus drives a model atrial sheet more easily than a model ventricular sheet. *Am. J. Physiol. Heart Circ. Physiol.* 279:H752–H763.
69. Verheijck, E. E., R. Wilders, and L. N. Bouman. 2002. Atrio-sinus interaction demonstrated by blockade of the rapid delayed rectifier current. *Circulation.* 105:880–885.
70. Michaels, D. C., E. P. Matyas, and J. Jalife. 1987. Mechanisms of sinoatrial pacemaker synchronization: a new hypothesis. *Circ. Res.* 61:704–714.
71. Jordan, D. W., and P. Smith. 1987. Nonlinear Ordinary Differential Equations, 2nd edition. Oxford University Press, New York.
72. Seydel, R. 1994. Practical Bifurcation and Stability Analysis: From Equilibrium to Chaos, 2nd edition. Springer-Verlag, New York.

１．研究課題名：血管新生を制御する可溶型 VEGF 受容体の mRNA 選択的スプライシング機構の解明（研究番号　S2006-7）

２．キーワード：１）血管新生（Angiogenesis）
２）内皮細胞増殖因子（VEGF）
３）VEGF 受容体（Flt-1）
４）mRNA 選択的スプライシング（mRNA alternative processing）

３．研究代表者：鶴岡　直樹・医学部・助教・ゲノム医科学（生化学）

４．研 究 目 的

血管新生は、重要臓器の発生や機能維持などに生理的に必須であるとともに、ガンの増殖・転移や成人病など病的状態の発生にも密接に関わっている。また、再生医療においても血管新生技術は必須である。したがって、その制御機構の解明は血管異常による疾病のリスク予知・予防・治療法開発に大きく貢献するとともに、次世代医療の基盤確立に繋がる重要な課題である。

血管新生を誘起する最も主要な因子は内皮細胞増殖因子（VEGF）であり、数種の膜結合型VEGF受容体(Flt-1, KDR)を介して血管内皮細胞増殖･血管管腔形成を誘導する。Flt-1 遺伝子からはmRNAの選択的スプライシングによって分泌型として産生されるタンパク質（可溶型 Flt-1）が存在し、この可溶型 Flt-1 は内皮細胞に作用する VEGF 濃度を調整することで血管新生制御に大きく寄与している。しかしながら、可溶型 Flt-1 の mRNA 選択的スプライシングの制御機構はほとんど解明されていない。よって本研究では、新規な血管新生制御法開発への応用を目指して、VEGF 受容体の mRNA 選択的スプライシング機構の解明を行うこととした。

５．研 究 計 画

可溶型 Flt-1 は，Flt-1 mRNA 前駆体の第 13 イントロン中に存在するポリ A シグナルが選択的に使用されてイントロン配列が残存し、同配列中に存在するストップコドンで翻訳が停止することにより生成する。可溶型 Flt-1 は膜型 Flt-1 の膜貫通領域を欠失しているため、可溶型として細胞外に分泌される。VEGF 結合領域は含まれているため VEGF を細胞外でトラップし遊離の VEGF 濃度を制御することができる（Fig. 1)。本研究では、以下のようにして可溶型と膜結合型の生成を調整する Flt-1 mRNA の選択的 3’端プロセシングの制御機構の解析を試みた。

(1) ヒト初代培養微小血管内皮細胞（HMVEC）で発現する可溶型 Flt-1 mRNA の選択的 3’端プロセシング部位を 3’-RACE 法により同定する。
(2) ヒトFlt-1のミニ遺伝子とHMVECを用いたmRNA 3’端プロセシング解析系を確立する。

(3) Flt-1 遺伝子の選択的 3’端プロセシング部位周辺に変異を導入して解析し、膜型と可溶型の産生比率を制御する配列を同定する。

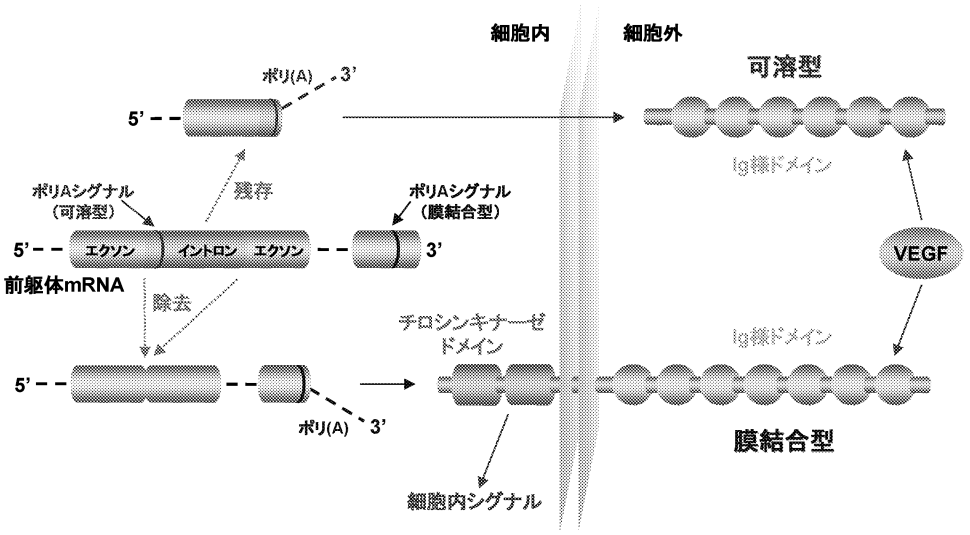

Fig. 1, 3’端選択的プロセシングにより生成する可溶型 / 膜結合型 VEGF 受容体

６．研 究 成 果

1) 可溶型 Flt-1 mRNA の 3’端プロセシング部位の解析

HMVEC の全 RNA を鋳型とし、イントロン 13 の配列からなるプライマーと Poly dT プライマーを使用して 3’Race-PCR を行い可溶型の 3’端プロセシング部位を決定した。可溶型が生成する場合は、主としてイントロン 13 の 5’端から 111 番目の位置でプロセシングされており、プロセシング部位上流にはポリ A シグナルのヴァリアント配列である AUUAAA が 2 箇所存在していることがわかった。

2) 選択的 3’端プロセシング機構の解析系の構築

可溶型 Flt-1 のプロセッシング部位が明らかになったことから、プロセシング部位を含んだエクソン 12-14 で構成されるヒト Flt-1 のミニ遺伝子を作製して、選択的 3’端プロセシング機構の解析系の構築を試みた。ミニ遺伝子の転写産物においても内在性の Flt-1 と同様に選択的 3’端プロセシングとスプライシングが起これば、膜型はエクソン 12-14 を含む mRNA が、可溶型はエクソン 12、 13 とイントロン 13 の一部を含む mRNA が生成することになる。これらの mRNA は、ベクターの配列からなるプライマーとアンカーを付加したポリ dT プライマーを用いた RT-PCR により同時に増幅、検出した(Fig. 2)。

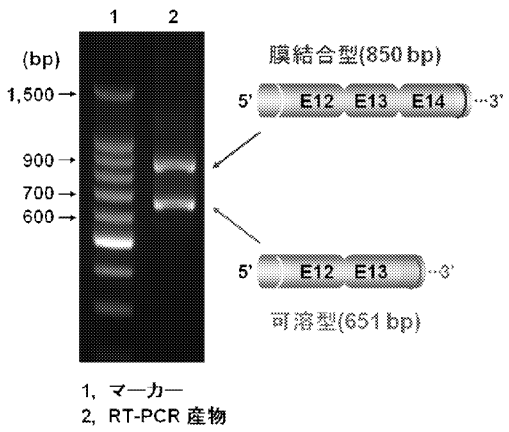

Fig. 2, Flt-1 ミニ遺伝子による選択的 3’端プロセシング機構の解析系

3) 選択的 3’端プロセシング機構の制御配列の解析

選択的 3’端プロセシングを制御する Flt-1 mRNA 上の配列の同定を試みた。候補として、制御に関与する可能性のある RNA 結合タンパク質の認識配列モチーフを検索した。また、Flt-1 と同様、選択的 3’端プロセシングによって可溶型を生成する NRP-1 においても、共通の制御配列が保存されている可能性があると考え、両遺伝子間で相同な配列も検索した。検索された配列に変異を導入したミニ遺伝子をそれぞれ作製し (m1-m8)、選択的 3’端プロセシングのアッセイを行った。この結果、イントロン 13 の 133-135 の UUU を AAA に置換したミニ遺伝子 (m6) において可溶型の生成量が優位に減少した。可溶型/膜型の比ではコントロールミニ遺伝子の約 1/5 となったことから、m6 の変異導入部位が 3’端プロセシング制御配列の一つであると考えられた (Fig. 3)。

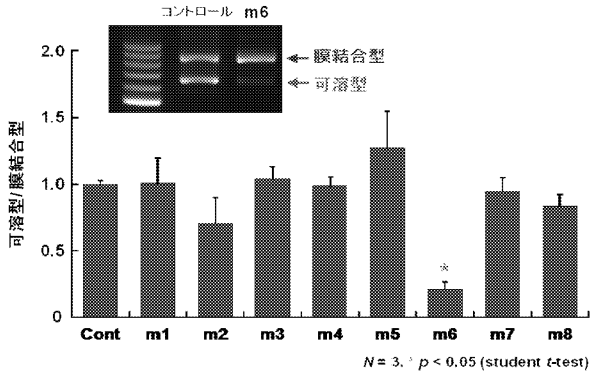

Fig. 3, **変異体ミニ遺伝子の選択的3’端プロセシングのアッセイ**

７．研究の考察・反省

本研究により、微小血管内皮細胞で発現する可溶型 Flt-1 mRNA の選択的 3’端プロセシング部位を 3’-RACE 法により同定し、ヒト Flt-1 のミニ遺伝子と HMVEC を用いた mRNA 3’端プロセシング解析系を確立した。また、Flt-1 遺伝子の選択的 3’端プロセシング部位周辺に変異を導入して解析し、膜型と可溶型の産生比率を制御する配列を同定した。制御配列と推定された m6 の変異導入部位は，hnRNP ファミリーの A2/B1、D1/D2、 A0 や、ELAVL1 タンパク質などの因子の結合モチーフとなっている。これらの RNA 結合タンパク質が実際に血管内皮細胞内で発現しているか、Flt-1 mRNA の選択的 3’端プロセシングの制御に関与するかを検証する必要がある。また、同部位はプロセシング部位下流 20-40 に含まれ、比較的 U が多い領域となっていることから、プロセシングに必要な切断刺激因子 (CstF) の結合部位である可能性が高い。推定された RNA 結合タンパク質が CstF と拮抗して標的配列に結合することで、可溶型の生成を制御している可能性も考えられる。今後、Flt-1 遺伝子の選択的 3’端プロセシングにおけるこれらの因子の機能を解明し、新規な血管新生制御法の開発を目指したい。

８．研 究 発 表

未発表

１．研究課題名：マウス敗血症・エンドトキシンショック病態の細動脈膜電位への影響
（研究番号　S2006-8）

２．キーワード：１）循環系（circulatory system）
２）低血圧（hypotension）
３）ショック（shock）
４）血管平滑筋（vascular smooth muscle）
５）膜電位（membrane potential）

３．研究代表者：高野　博充・医学部・助教・生理機能制御学（生理学Ⅱ）

４．研 究 目 的

敗血症や細菌のエンドトキシンによって起こる循環ショック時には、血管の弛緩反応や神経伝達物質に対する反応低下がみられ、低血圧への関与が示唆されている。同時に血管の静止張力を決定する静止膜電位が正常よりも深くなっていることがラットで報告されている。一方、全身の血圧の決定には抵抗血管である細動脈の収縮弛緩が重要な役割を演じている。ところが、これまでのショックの研究では単離血管標本としては大動脈を用いられることが多く、末梢の細動脈レベルでの研究は少ないのが現状である。

しかしながら、大動脈と細動脈では、たとえば内皮依存性弛緩のメカニズムなど多くの性質が異なっていることが知られている。また、研究対象の実験動物としてラットが多く用いられてきた。そこで今回申請者は将来的に遺伝子操作が容易であるマウスの細動脈の膜電位に注目して敗血症・エンドトキシンショックのメカニズムの解明を行う。

５．研 究 計 画

1) 膜電位測定：モデル動物から単離した腸間膜動脈（直径 200μm）を、生理食塩水を灌流し 37℃に保ったチャンバーに固定する。bolocilicate グラスキャピラリーを用いたガラス微小電極法による細胞内導出を行い、細胞膜の電気生理学的変化を記録・解析する。

2) エンドトキシンモデル動物の作成：マウス（Balb/c 6-7 週齢　体重 22.3±5 g）の尾静脈内にエンドトキシン（E-coli LPS、5mg/Kg）を投与して作成。6 時間後、腸間膜動脈を取り出し、実験に供する。

3) 実験プロトコル：細胞膜上チャネル抑制剤および神経伝達物質を灌流溶液中に投与しその膜電位に対する作用を記録解析する。今回は ATP 感受性 K チャネル、Ca 感受性 K チャネル、電位依存性 K チャネルおよび内向き整流性 K チャネルに着目して実験を行う。また内皮細胞除去標本に対し、上記のプロトコルを行い、エンドトキシンショック・敗血症時の膜電位上の変化が内皮細胞と平滑筋細胞のどちらにあるのかを明らかにする。

６．研 究 成 果

Balb/c マウス腸間膜動脈を漿膜側からガラス微小電極を刺入すると-51 ± 1 mV の膜電位が記録された。内皮を除去した腸間膜動脈では-47.8 ± 0.6 mV の膜電位が記録された。α受容体刺激薬である phenylephrine（PE 0.1, 0.3, 1, 3, 10 μM）を投与すると、腸間膜動脈は濃度依存的に脱分極を示した（control −53 ± 2 mV、PE 0.1 μM -53 ± 1 mV、PE 0.3 μM −50 ± 1 mV、PE 1 μM −48 ± 1 mV、PE 3 μM −42 ± 3 mV、PE 10 μM −40 ± 4 mV）。ATP 感受性カリウムイオンチャネル阻害剤である glibenclamide は腸間膜動脈の膜電位を変化させなかった。ムスカリン受容体刺激薬 Acetylcholine （ACh; 10 μM）は腸間膜動脈の膜電位をほとんど変化させなかった（control −51 ± 1 mV、ACh −52 ± 0.6 mV）。ホスホジエステラーゼを阻害して細胞内 cAMP を増やす Forskolin 10 μM を投与すると腸間膜動脈は 5.5± 2 mV 過分極した。

一方、SD rat の腸間膜動脈では漿膜側からガラス微小電極を刺入すると-50 1 mV の膜電位が記録された。Acetylcholine （ACh 10 μM）は rat の腸間膜動脈の膜電位を大きく過分極させた（-69 ± 3 mV）。Phenylephrin による脱分極、Forskolin による過分極はマウスと同程度であった。

７．研究の考察・反省

マウス腸間膜動脈はラットの腸間膜動脈とほぼ同じ静止膜電位を持っていた。しかし、Acetylcholine に対する反応性は異なっており、ラットでは Acetylcholine 投与により大きな過分極反応を示したが、マウスでは Acetylcholine はほとんど膜電位を変化させなかった。一方、細胞内 cAMP が増えると過分極し、phenylephrine による脱分極反応はマウス、ラットともに違いがないことが分かった。マウス腸間膜動脈は内皮を除去することにより脱分極したので、内皮が腸間膜動脈の静止膜電位の形成に影響を与えていることが分かった。また、静止膜電位には ATP 感受性カリウムイオンチャネルは関係していないことが分かった。

以上の結果を踏まえ、エンドトキシン投与モデル動物への実験を行う予定である。

８．研 究 発 表

現在結果解析を含めて準備中である。

1. 研究課題名：共役リノール酸異性体によるラット大腸発がん抑制効果とその機構解析
（研究番号　S2006-9）

2. キーワード：　1）　共役リノール酸（conjugated linoleic acid）
2）　大腸発がん（colon carcinogenesis）
3）　前がん病変（aberrant crypt foci）

3. 研究代表者：安井　由美子・総合医学研究所・研究員・共同利用部門

4. 研 究 目 的

我が国において、がんの発症は増加の一途を辿っており、ここ 20 数年病気による死亡原因の第一位となっている。中でも大腸がんと乳がんの増加は著しく、その対策は国民的課題となっている。その対策の一つとして、近年、天然物によるがんの化学予防効果に関する研究が注目されている。ところで、三大栄養素の一つである脂質はエネルギー源としての役割のみならず、脂質を構成する脂肪酸が特有の生理機能を発現し、各種の疾病の発症や予防に深く関わっている。より興味深い生理活性を有する脂質として研究が急激に進んでいるのは共役脂肪酸であり、その代表的なものに共役リノール酸（CLA）がある。CLA は反芻動物の肉や乳製品中に存在し、その生理作用としては抗肥満、抗動脈硬化、抗腫瘍作用などが報告されている。CLA の有する抗腫瘍作用に関しては、乳がんでの研究は多いが、大腸がんに関しての報告は極めて少ないのが現状である。そこで本研究では、CLA によるヒト大腸がん抑制のための基礎的資料を得る目的で、ラット大腸発がんモデルを用いた CLA の発がん抑制作用を詳細に検討し、その抑制メカニズムについても明らかにする。

5. 研 究 計 画

CLA の有する大腸発がん抑制効果について、大腸がん誘発物質 Azoxymethane（AOM）を投与した F344 ラットを用いた検討を行い、その作用機構の解析を行う。具体的には、雄の F344 ラットを 1 週間予備飼育の後、4 週間 0.01%、0.1%、1% CLA（9t,11t-CLA）を混餌投与する。その間、AOM を 2 回皮下投与する。4 週間後、屠殺し、大腸と肝臓を摘出する。摘出した大腸をホルマリン固定し、大腸粘膜の前がん病変、腫瘍組織の病理組織学的解析、免疫組織化学的解析（アポトーシスの発現など）および分子生物学的解析（COX-2、PPARγ、cyclin D1 などの発がん関連遺伝子の発現）を行い、また脂質代謝に及ぼす影響も検討するため、摘出した大腸および肝臓の脂肪酸組成分析を行う。

6. 研 究 成 果

9*t*,11*t*-CLA の混餌投与によりラット大腸 ACF 数は AOM のみの群に比べて 0.01%投与で約 60%に、そして 0.1%および 1%投与では 40%に抑制された。さらに、悪性腫瘍形成と相関の高い 4 つ以上の ACs から成る ACF に関しては、0.01%投与で約 12%、0.1%投与で約 9%、1%投与では 3%にまで抑制される強い効果が見られた。また、9*t*,11*t*-CLA は大腸粘膜のアポトーシスを濃度依存的に誘導し、PCNA および cyclin D1

の発現を抑制した。更に、大腸粘膜中の PPARγ発現が増加し、COX-2 発現が抑制された。さらに、9*t*,11*t*-CLA 投与による大腸粘膜および肝臓中の 9*t*,11*t*-CLA の蓄積、加えて、肝臓脂質含量が濃度依存的に減少していることが観察された。

7. 研究の考察・反省

9*t*,11*t*-CLA は、大腸粘膜に対してアポトーシス誘導や細胞増殖抑制、さらに COX-2 や PPARγなどの発がん関連遺伝子の発現を調節することにより大腸 ACF 形成を顕著に抑制することが示された。また、9*t*,11*t*-CLA の混餌投与は脂質代謝系にも影響を及ぼすことが明らかとなった。今後は、この発がん抑制機序について詳細について検討していく。

8. 研 究 発 表

Yasui Y, Suzuki R, Kohno H, Miyamoto S, Beppu F, Hosokawa M, Miyashita K, Tanaka T. 9trans,11trans conjugated linoleic acid inhibits the development of azoxymethane-induced colonic aberrant crypt foci in rats. Nutr Cancer. 2007; 59(1):82-91. (MLDB)

NUTRITION AND CANCER, 59(1), 82–91

9trans,11trans Conjugated Linoleic Acid Inhibits the Development of Azoxymethane-Induced Colonic Aberrant Crypt Foci in Rats

Yumiko Yasui, Rikako Suzuki, Hiroyuki Kohno, Shingo Miyamoto, Fumiaki Beppu, Masashi Hosokawa, Kazuo Miyashita, and Takuji Tanaka

Abstract: *We investigated the effects of 9trans,11trans (9t,11t)-conjugated linoleic acid (CLA) isomer on azoxymethane (AOM)-induced colonic aberrant crypt foci (ACF) in rats. Male F344 rats were given 2 weekly subcutaneous injections of AOM (20 mg/kg bw) to induce colonic ACF. They also were fed a diet containing either 0.01%, 0.1%, or 1% 9t,11t-CLA for 4 wk starting 1 wk before the first dosing of AOM. The group that received a diet supplemented with 9t,11t-CLA had a significantly lower number of ACF/colon in comparison to the AOM alone group in a dose-dependent manner up to 0.1%. Furthermore, treatment with 9t,11t-CLA induced apoptosis and suppressed cell proliferation activity in the non-lesional crypts. The downregulation of cyclooxygenase-2 and cyclin D1 and the activation of peroxisome proliferators activated receptor γ were observed in the colonic mucosa of rats fed a diet supplemented with 9t,11t-CLA. Our findings thus provide some novel insight into the chemopreventive effect of 9t,11t-CLA against preinitiation as well as postinitiation stages of colorectal carcinogenesis.*

Introduction

Colorectal cancer (CRC) is one of the most prevalent causes of cancer-related deaths in both males and females in the Western world (1) and eastern Asia (2). Epidemiological studies have indicated that the risk of developing colon cancer may be attributable to the combined effects of environmental and endogenous factors (3). It has also been reported that the amount and type of dietary fat consumed are of particular importance for the development of this malignancy (4–6). The fatty acid composition of dietary fat is more closely associated to the development of colon cancer than the total amount of fat consumed (7). For example, diets rich in n-3 fatty acids reduce the risk of chemically induced colon carcinogenesis in comparison to diets high in n-6 fatty acids and/or saturated fatty acids (8). Docosahexaenoic acid or eicosapentaenoic acid also inhibit colon tumor development by the inhibition of cell proliferation and the induction of apoptosis (9,10). The disruption of gene networks involved in the regulation of cell proliferation, differentiation, cell cycle, and cell death results in cancer development. For example, adenomatous polyposis coli (APC); p53; cyclooxygenase (COX)-2; β-catenin; and K-ras are involved with the development and progression of colon cancer (11). In particular, COX-2 has attracted attention as one of the key target genes involved in the early stage of colorectal tumorigenesis (12). It has also been reported that the overexpression of the cyclin D1 gene occurs early in the process of carcinogenesis and plays an important role in rat colorectal carcinogenesis (13).

Conjugated linoleic acid (CLA) is a collective term referring to a mixture of positional genometric isomers of linoleic acid [9cis (c), 12c-octadecanoic acid] in which the double bonds are conjugated. CLA is primarily found in food derived from ruminants such as beef and lamb as well as the dairy products from these sources. CLA concentrations in dairyproducts typically range from 2.9 to 8.92 mg/g fat, of which the 9c,11-trans (t) isomer [Fig. 1(a)] makes up to 73% to 93% of the total CLA. Furthermore, low concentrations of CLA are found in human blood and tissues (14). For example, content of CLA is 2.7 ± 0.5 mg/g human milk lipid (15). Also, blood CLA levels increases when human subjects consume CLA-rich diets (14). Although there are numerous isomers of CLA in natural products, 9c,11t-CLA and 10t,12c-CLA [Fig. 1(b)] have received the most attention because of their biological activity against disease development including the development of cancer. In fact, CLA has been reported to reduce the risk of various types of cancers including skin, gastric, breast, and colon cancers (16). Both CLA isomers are principle isomers of synthetic CLA via alkali isomerization. 10t,12c-CLA isomer also possesses certain biological activities (17). Therefore, a synthetic mixture of CLA

Y. Yasui, R. Suzuki, H. Kohno, S. Miyanoto, and T. Tanaka are affiliated with the Department of Oncologic Pathology, Kanazawa Medical University, 1-1 Daigaku, Uchinada, Ishikawa 920–0293, Japan. S. Miyamoto is also affiliated with the Division of Food Science and Biotechnology, Graduate School of Agriculture, Kyoto University, Kyoto 606–8502, Japan. F. Beppu, M. Hosokawa, and K. Miyashita are affiliated with the Graduate School of Fisheries Sciences, Hokkaido University, 3-1-1 Minato, Hakodate, Hokkaido 041-8611, Japan.

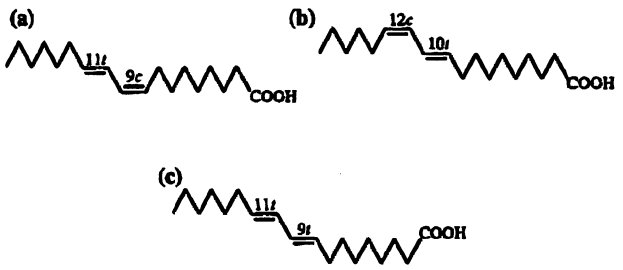

Figure 1. Structures of conjugated linoleic acid isomers. (a): 9cis,11trans-conjugated linoleic acid. (b): 10trans,12cis-conjugated linoleic acid. (c): 9trans,11trans-conjugated linoleic acid.

that contains 9c,11t-CLA (43%) and 10t,12c-CLA (45.3%) potently inhibits carcinogenesis (18,19). Although 9c,11t-CLA has been implicated as the most active CLA because of its predominant isomer incorporated into the phospholipids of cell membrane (20), a minor isomer, 9t,11t-CLA [Fig. 1(c)], may have certain biological activity. In fact, our previous study demonstrated apoptosis-inducing ability of 9t,11t-CLA in human colon cancer cell lines (21). Also, 9t,11t-CLA isomer is preferentially incorporated into the liver phospholipid and triglyceride, whereas the incorporation of c,t-CLA isomers is partial discrimination (22). However, there are no detailed in vivo studies on the biological activity and nutritional significance of 9t,11t-CLA because of the difficulty involved with a large-scale separation of the 9t,11t-isomer from the CLA mixture. 9t,11t-CLA are present at infinitesimal quantity in dairy products: commercial cheeses (100 g) contain 0.12 g of total CLA and 0.0084 g of t,t CLA (23). Kishino et al. (24,25) has recently demonstrated the bacterium production of 2 CLA isomers, 9c,11t- and 9t,11t-CLA, from ricinoleic acid (24) and linoleic acid (25). We therefore used this technique to assess the biological activity of 9t,11t-CLA in experimental carcinogenesis.

In this study, we investigated whether 9t,11t-CLA influences the preinitiation as well as postinitiation stages of azoxymethane (AOM)-induced rat colon carcinogenesis by assessing aberrant crypt foci (ACF) that are putative precursor lesions for CRC (26). We also analyzed the expression of several genes that are involved in colon carcinogenesis including COX-2, peroxisome proliferators activated receptor (PPAR) γ and cyclin D1.

Materials and Methods

Preparation of CLA

Free fatty acids of 9t,11t-CLA (98.46% pure) produced by bacteria (24,25) were obtained from Meiji Seika Co., Ltd. (Tokyo, Japan).

Animals, Chemicals, and Diets

Male F344 rats (4 wk old; Charles River Japan, Inc., Kanagawa, Japan) were used for the ACF assay. The animals were maintained in the Kanazawa Medical University Animal Facility according to the Institutional Animal Care Guidelines. All animals were housed in plastic cages (4 rats/cage) with free access to drinking water and a basal diet, American Institute of Nutrition (AIN)-76A (LSG Corporation, Tokyo, Japan) (27), under controlled conditions of humidity (50 ± 10%), lighting (12-h light/dark cycle), and temperature (23 ± 2°C). Experimental diets containing 3 different dose levels (wt/wt) of 9t,11t-CLA (0.01%, 0.1%, and 1%) based on the AIN-76 formulation (28) were stored at –20°C under a nitrogen atmosphere in airtight containers. The animals were quarantined for 7 days after arrival and randomized by body weight into experimental and control groups. Beginning at 5 wk of age, they were fed with experimental diets for 4 wk. The rats in Groups 1 (8 rats) and 6 (4 rats) were fed the AIN-76A alone. Groups 2 through 4 (8 rats each) were fed diets containing 0.01%, 0.1%, and 1% 9t,11t-CLA, respectively. Group 5 (4 rats) was fed a diet containing 1% 9t,11t-CLA alone. All rats were provided with the experimental diets and tap water ad libitum and weighed weekly. At 6 wk of age, the animals in Groups 1 through 4 were given 2 weekly subcutaneous injections of AOM (20 mg/kg body weight; Sigma-Aldrich Chemical Co., St. Louis, MO). All animals were killed 2 wk after the last administration of AOM, and complete necropsies were performed. The colons of 5 rats each from Groups 1 through 4 and those of 1 rat each from Groups 5 and 6 were examined for the presence of ACF. The lipid composition was also analyzed in the livers (5 rats each from Groups 1–4 and 4 rats each from Groups 5 and 6) and the colons (3 rats each from the groups).

Determination of ACF

The frequency of ACF was determined according to the method described in our previous report (29). At autopsy, the colons were flushed with saline, excised, cut open longitudinally along the main axis, and washed with saline again. They were cut and fixed in 10% buffered formalin for at least 24 h. The fixed colons were dipped in a 0.5% solution of methylene blue in distilled water for 30 s, briefly washed with the distilled water, and placed on a microscope slide with the mucosal surface facing up. The ACF were counted using a light microscope (Olympus BX41, Olympus Optical Co., Ltd., Tokyo, Japan) at a magnification of ×40.

Immunohistochemistry

An immunohistochemical analysis for the proliferating cell nuclear antigen (PCNA), apoptotic nuclei, and cyclin D1 was performed on 4-μm-thick paraffin-embedded sections from the colons of rats in each group by the labeled streptavidin biotin method using a LSAB KIT (DAKO Japan, Kyoto, Japan) with microwave accentuation. The paraffin-embedded sections were heated for 30 min at 65°C, deparaffinized in xylene, and rehydrated through graded ethanol at

Table 1. Body and Liver Weight (g) of the Rats Fed the Control Diet or the 9t,11t-CLA Diet[a]

Group no.	Treatment (No. of rats examined)	Body weight (g)	Liver weight (g)	Relative liver weight (g/100 g body weight)
1	AOM alone (8)	210 ± 12[b]	8.14 ± 0.53	3.88 ± 0.24
2	AOM + 0.01% 9t,11t-CLA (8)	199 ± 6	7.10 ± 0.43	3.57 ± 0.18
3	AOM + 0.1% 9t,11t-CLA (8)	219 ± 10	8.95 ± 0.42	4.09 ± 0.08
4	AOM + 1% 9t,11t-CLA (8)	215 ± 7	9.45 ± 0.79[c]	4.39 ± 0.34[c]
5	1% 9t,11t-CLA (4)	216 ± 5	8.29 ± 0.69	3.83 ± 0.24
6	None (4)	207 ± 0.5	9.14 ± 0.27	4.42 ± 0.13

a: Abbreviations are as follows: 9t,11t, 9trans,11trans; CLA, conjugated linoleic acid; AOM, azoxymethane.
b: Mean ± SD.
c: Significantly different from group 1 by Tukey multiple comparison posttest ($P < 0.01$).

room temperature. Tris HCl buffer (0.05 M, pH 7.6) was used to prepare the solutions and was used for washes between the various steps. The incubations were performed in a humidified chamber. To determine the extent of PCNA-incorporated nuclei, PCNA immunohistochemistry was performed according to the method described by Watanabe et al. (30). The apoptotic index was also evaluated by immunohistochemistry for single-stranded DNA (ssDNA) (30). The sections were treated for 40 min at room temperature with 2% bovine serum albumin and incubated overnight at 4°C with primary antibodies. The primary antibodies included anti-PCNA mouse monoclonal antibody (diluted 1:50; PC10, DAKO Japan), anti-ssDNA rabbit polyclonal antibody (diluted 1:300; DAKO Japan), and anticyclin D1 mouse monoclonal antibody (diluted 1:100; Novocastra Laboratories, Newcastle upon Tyne, UK). Horseradish peroxidase activity was visualized by treatment with H_2O_2 and 3,3′-diaminobenzidine for 5 min. During the last step, the sections were weakly counterstained with Mayer's hematoxylin (Merck Ltd., Tokyo, Japan). For each case, negative controls were performed on serial sections. The incubation with the primary antibodies was omitted in the control sections. The intensity and localization of immunoreactivities against all the primary antibodies were examined on the sections using a microscope, Olympus BX41. The PCNA, apoptotic, and cyclin D1-positive indexes were determined by counting the number of positive cells among at least 200 cells in the lesional crypts and were expressed as percentages.

Lipid Extraction and Analysis of the Fatty Acid Composition

The specimens of the colon and liver sublobes except the caudate lobe that was used for histopathology were frozen at −80°C until the lipid analyses were performed. The liver and colon lipids were extracted with chloroform/methanol (2:1, vol/vol) as described previously by Folch et al. (31). The component peaks were identified by comparisons with standard fatty acid methyl ester and quantified by a Shimazu Chromatopac C-R6A integrator (Shimazu Seisakusho Co., Ltd., Kyoto, Japan). The identification of CLA isomers was confirmed by gas chromatography mass spectrometry after conversion of the methyl ester to dimethyloxazoline derivatives (23). The analysis of fatty acid composition was done more than 2 times for each sample, and there were no significant differences among the results for the same sample.

Real-Time Quantitative Reverse Transcriptase Polymerase Chain Reaction (RT-PCR) Analysis

Total RNA was extracted from the colon mucosa by an acidic phenol method and further purified by using an RNeasy Mini Kit (Qiagen, Chatsworth, CA) according to the manufacturer's instructions. The extracted total RNA was subjected to reverse transcription by using a High Capacity cDNA Archive Kit (Applied Biosystems, Foster City, CA) according to the manufacturer's instructions. 1 ml of cDNA solution (adequate concentration) was mixed with 1.25 μl TaqMan probe, 12.5 μl TaqMan Master Mix, and 10.25 μl water, and quantitative RT-PCR reaction was subsequently performed in an ABI PRISM 7000 Sequence Detection System (Applied Biosystems, Ltd., Tokyo, Japan). The thermal cycling conditions were as follows: 50°C for 2 min, 95°C for 10 min, followed by 40 cycles of denaturation at 95°C for 15 s, and annealing and extension at 60°C for 1 min. The TaqMan probes, COX-2 (Rn00568225), PPARγ (Rn00440945), and β-actin (Rn00667869) of TaqMan® Gene Expression Assays were purchased from Applied Biosystems.

Statistical Evaluation

Where applicable, the data were analyzed using a Tukey multiple comparison posttest with $P < 0.05$ as the criterion of significance.

Results

General Observations

The mean body, liver, and relative liver weights (g/100 g body weight) of all the groups are summarized in Table 1.

Table 2. Effect of 9t,11t-CLA on AOM-Induced ACF Formation in Male F344 Rats[a]

Group no.	Treatment (No. of rats examined)	Total no. of ACF/Colon	Total no. of ACs/Colon	No. of ACs/Focus	% of ACF containing 4 or more ACs
1	AOM alone (5)	101 ± 32[b]	301 ± 77	3.02 ± 0.22	33.31 ± 4.53
2	AOM + 0.01% 9t,11t-CLA (5)	64 ± 27[c]	111 ± 52[d]	1.71 ± 0.12[d]	4.95 ± 3.18[d]
3	AOM + 0.1% 9t,11t-CLA (5)	40 ± 8[d]	62 ± 16[d]	1.52 ± 0.11[d]	2.98 ± 0.73[d]
4	AOM + 1% 9t,11t-CLA (5)	41 ± 9[d]	63 ± 11[d]	1.57 ± 0.13[d]	1.11 ± 1.55[d]
5	1% 9t,11t-CLA (1)	0	0	0	0
6	None (1)	0	0	0	0

a: Abbreviations are as follows: 9t,11t, 9trans,11trans; CLA, conjugated linoleic acid; AOM, azoxymethane; ACF, aberrant crypt foci; AC, aberrant crypts.
b: Mean ± SD.
c: Significantly different from Group 1 by Tukey multiple comparison post test, $P < 0.05$.
d: Significantly different from Group 1 by Tukey multiple comparison post test, $P < 0.01$.

All animals remained healthy throughout the experimental period. Although the mean body weight did not significantly differ among the groups, the mean liver and relative liver weights of Group 4 ($P < 0.01$ for each) were significantly greater than those of Group 1. However, there were no histological alterations (including fatty liver) in the rats of all the groups.

Frequency of ACF

Table 2 summarizes the data on colonic ACF analysis. All rats belonging to Groups 1 through 4 developed ACF. The mean number of ACF in the colons of the rats in Group 1 was 101 ± 32. The dietary administration of 9t,11t-CLA at all the dose levels caused significant inhibition of ACF formation, 0.01% 9t,11t-CLA administration caused a 37% reduction ($P < 0.05$), 0.1% 9t,11t-CLA administration resulted in a 60% reduction ($P < 0.01$), and 1% 9t,11t-CLA administration caused a 59% reduction in ACF ($P < 0.01$). There were significant decreases in the total number of aberrant crypts (ACs) per colon ($P < 0.01$) and the number of ACs per focus ($P < 0.01$) in these groups. In addition, the percentages of ACF that consisted of more than 4 crypts in Groups 2 through 4 were significantly smaller than those in Group 1 ($P < 0.01$). There were no microscopically observable changes, including ACF, in the colons of rats in Groups 5 and 6.

PCNA-Labeling Index

The PCNA-labeling indexes in the nonlesional colon mucosa are presented in Fig. 2(a). The mean PCNA-labeling indexes in Groups 1 through 4 were higher than those of Groups 5 and 6. The supplementation of 9t,11t-CLA to the diet at various doses reduced the mean PCNA-labeling indexes in comparison to the indexes in the absence of 9t,11t-CLA in a dose-dependent manner ($r = -0.67$, $P < 0.0005$), and the reduction observed in Groups 4 ($P < 0.01$) and 6 ($P < 0.001$) was statistically significant in comparison to the reduction in Group 1 (24.6 ± 5.59).

Apoptosis Labeling Index

The mean apoptosis indexes in the colon mucosa with nonlesional crypts are presented in Fig. 2(b). The mean apoptosis index of Group 4 (7.0 ± 1.73, $P < 0.05$) was significantly greater than that of Group 1 (3.8 ± 0.84), and apoptosis was induced in a dose-dependent manner ($r = 0.84$, $P < 0.005$).

Cyclin D1-Positive Cell Rate

As illustrated in Fig. 2(c), the AOM alone group (Group 1) had the highest cyclin D1-positive ratio among the groups. The mean cyclin D1-positive ratios of Groups 3 ($P < 0.01$), 4 ($P < 0.001$), and 6 ($P < 0.001$) were significantly lower than the ratio in Group 1. The diets supplemented with 9t,11t-CLA lowered the cyclin D1-positive ratio in a dose-dependent manner ($r = -0.81$, $P < 0.005$).

Total Lipid Contents and Lipid Composition in the Liver and Colon Mucosa

Total lipid contents and lipid composition of liver and colon mucosa are given in Tables 3 and 4. The total lipid contents of liver were decreased as the dose of CLA was increasing. The value of Group 4 was significantly smaller than Group 1. The total lipid contents of colon mucosa did not significantly differ among the groups. From the data on fatty acid compositions of the lipids in the liver and colonic mucosa, 9t,11t-CLA derived from the experimental diets was detected in both tissues, and the contents correlated to the dose in the diets. The percent compositions of CLA in the colonic mucosa were greater than those in the liver. The CLA diets did not affect the amounts of n-6 polyunsaturated fatty acid, linoleic acid, or arachidonic acid (AA).

Expression of COX-2 and PPARγ mRNA

The expression of COX-2 mRNA in the colonic mucosa from all the groups is shown in Fig. 3(a). The COX-2 expression level of the rats treated with AOM alone (Group 1)

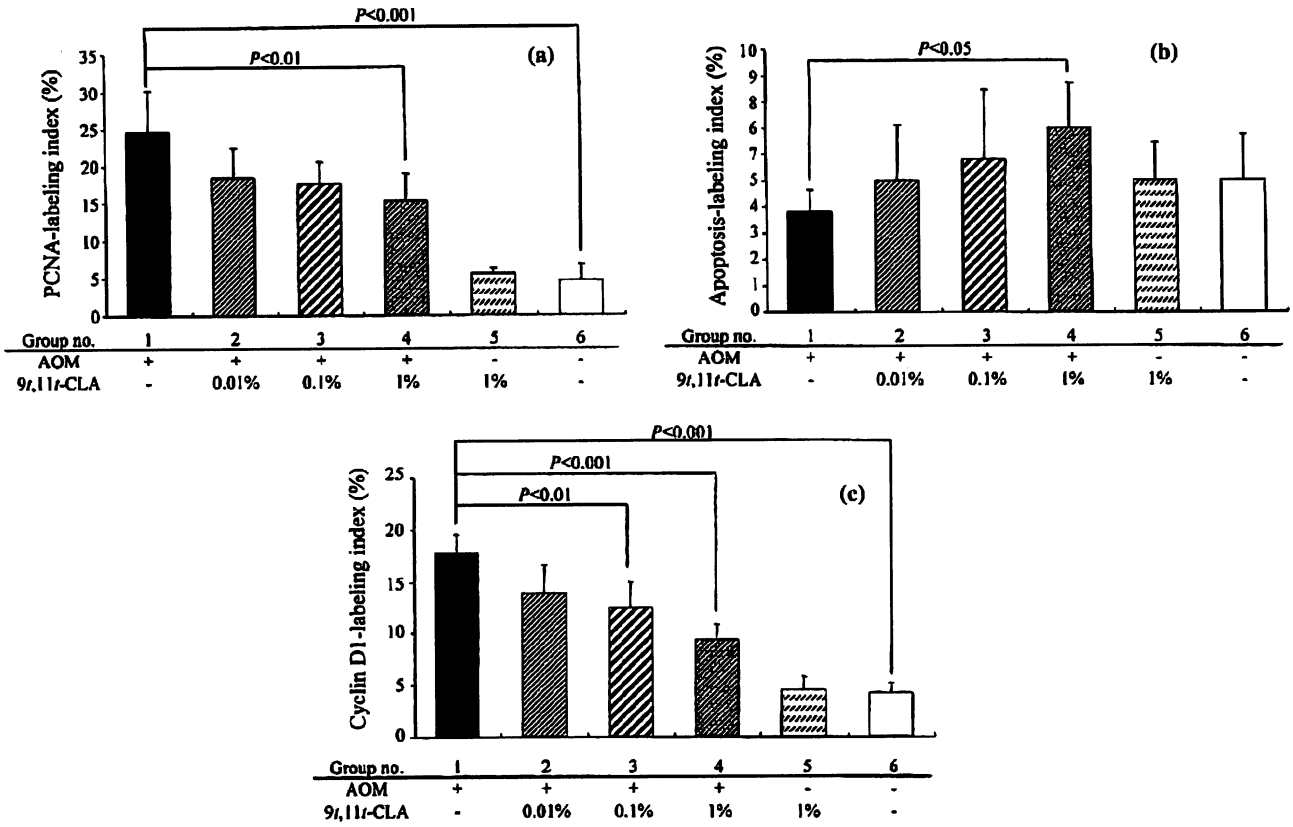

Figure 2. Effects of dietary 9t,11t-conjugated linoleic acid (CLA) on proliferating cell nuclear antigen (PCNA) expression, apoptosis induction (ssDNA expression), and cyclin D1 expression in rat colonic mucosa by immunohistchemistry. Data are expressed as the mean percentage of (a) PCNA labeling and (b) apoptosis indexes [bars; SD (Group 1–4, $n = 5$; Group 5 and 6, $n = 2$)] and (c) cyclin D1-positive index in the nonlesional crypts [bars; SD (Group 1–4, $n = 8$; Group 5 and 6, $n = 4$)]. AOM, azoxymethane.

showed an 1.5-fold increase in comparison to the expression level in untreated rats. However, the COX-2 expression level of the CLA-treated rats (Groups 3 and 4) was downregulated and was comparable to that of rats who did not receive AOM. The expression was dose-dependently decreased in rats fed 9t,11t-CLA containing diets. The PPARγ expression level [Fig. 3(b)] of the rats treated with AOM alone (Group 1) was almost half of that of the untreated group. Conversely, the expression of PPARγ mRNA was dose-dependently increased by feeding with 9t,11t-CLA.

Discussion

In this study, the administration of 9t,11t-CLA significantly inhibited the development of large ACF (4 or more aberrant crypts) in conjunction with a dose-dependent effect on the indexes of PCNA, apoptosis, and cyclin D1. In our recent study, 9t,11t-, 10t,12c-, and 9c,11t-CLA isomers induced apoptosis in human colon cancer cells (9t,11t- > 10t,12c- > 9c,11t-CLA) (21). Our results thus suggest that 9t,11t-CLA has a potent chemopreventive effect on CRC occurrence, and the optimum concentration of 9t,11t-CLA is less than 1%. Whereas liver and relative liver weights in rats treated with AOM and 1% 9t,11t-CLA (Group 4) were significantly greater than those in rats given AOM alone (Group 1), the treatment with 1% 9t,11t-CLA alone (Group 5) did not affect both values when compared to untreated rats (Group 6). Importantly, histopathological examination revealed no toxicity, including fatty liver, in the tissues of rats that received 9t,11t-CLA containing diets, suggesting future studies on cancer chemoprevention and nutritional importance of 9t,11t-CLA. In addition, it is worthy of further study to determine whether the doses of 9t,11t-CLA higher than 1% further enhance the efficacy.

CLA has received considerable attention from the findings of animal experiments, which have demonstrated anticarcinogenic (32), antiatherosclerotic (33), and antidiabetic (34) effects. There have been many reports describing the chemopreventive ability of CLA in chemically induced carcinogenesis, especially in the mammary glands (35). In the colon, CLA administrated by gavage at a dose level of 0.5% of the diet (wt/wt) reduced the formation of heterocyclic amine-induced ACF in the colons of Fisher 344 rats (36). Cheng et al. (37) also reported that 1,2-dimethylhydrazine-induced ACF was suppressed by feeding with 1% CLA. Those studies have demonstrated the preventive effects of CLA

Table 3. Total Lipids Content and Fatty Acid Composition of Lipids in the Liver[a]

Group no.	Treatment (No. of rats examined)	Total lipids (mg/g liver)	Fatty acid composition (wt%)								
			16:0	16:1 n-7	18:0	18:1 n-9	18:2 n-6	20:4 n-6	22:6 n-3	9c,11t-CLA	9t,11t-CLA
1	AOM Alone (5)	111 ± 36[b]	23.6 ± 0.8	5.7 ± 1.1	13.6 ± 1.2	13.9 ± 2.5	10.8 ± 1.4	17.3 ± 1.4	2.5 ± 0.4	ND	ND
2	AOM + 0.01% 9t,11t-CLA (5)	92 ± 9	23.2 ± 0.8	4.2 ± 1.0	14.4 ± 1.0	12.6 ± 1.3	12.0 ± 1.9	19.1 ± 1.6	2.9 ± 0.2	0.01[c]	0.02
3	AOM + 0.1% 9t,11t-CLA (5)	79 ± 12	23.7 ± 1.5	4.7 ± 1.0	14.1 ± 1.0	10.9 ± 0.8	11.3 ± 0.7	18.2 ± 1.6	2.5 ± 0.4	ND	0.17
4	AOM + 1% 9t,11t-CLA (5)	60 ± 18[d]	23.4 ± 1.0	4.7 ± 0.6	14.0 ± 0.4	11.1 ± 0.4	11.0 ± 0.8	17.7 ± 0.7	2.7 ± 0.1	0.01	1.2 ± 0.1
5	1% 9t,11t-CLA (4)	77 ± 12	23.5 ± 1.6	4.9 ± 1.3	14.3 ± 1.3	12.7 ± 2.3	10.6 ± 1.8	19.5 ± 2.1	3.4 ± 0.4	ND	0.9 ± 0.2
6	No. Treatment (4)	79 ± 6	26.9 ± 1.2	6.7 ± 0.7	12.2 ± 1.4	19.4 ± 2.1	9.4 ± 0.2	15.0 ± 2.0	2.8 ± 0.4	ND	ND

a: Abbreviations are as follows: wt, weight; 9c,11t, 9cis,11trans; 9t,11t, 9trans,11trans; CLA, conjugated linoleic acid; AOM, azoxymethane; ND, Not detected.
b: Mean ± SD.
c: Mean.
d: Significantly different from Group 1 by Tukey multiple comparison test, $P < 0.01$.

Table 4. Total Lipids Content and Fatty Acid Composition of Lipids in the Colonic Mucosa[a]

Group no.	Treatment (no. of rats examined)	Total lipids (mg/g colonic mucosa)	Fatty acid composition (wt%)								
			16:0	16:1 n-7	18:0	18:1 n-9	18:2 n-6	20:4 n-6	22:6 n-3	9c,11t-CLA	9t,11t- CLA
1	AOM alone (3)	180 ± 137[b]	28.3 ± 1.2	8.9 ± 1.2	3.1 ± 0.5	28.0 ± 0.6	21.0 ± 0.4	1.3 ± 0.8	ND	0.1[c]	0.1
2	AOM + 0.01% 9t,11t-CLA (3)	151 ± 42	29.4 ± 0.7	8.7 ± 0.7	3.3 ± 0.3	28.2 ± 0.4	20.4 ± 0.9	1.0 ± 0.3	0.02	0.1	0.1
3	AOM + 0.1% 9t,11t-CLA (3)	159 ± 45	28.5 ± 0.7	9.5 ± 0.7	2.8 ± 0.4	27.3 ± 0.3	20.5 ± 0.3	1.1 ± 0.3	0.03	0.1	0.5
4	AOM + 1% 9t,11t-CLA (3)	169 ± 86	28.7 ± 1.4	9.7 ± 1.4	2.3 ± 0.2	25.7 ± 0.2	19.6 ± 0.8	0.9 ± 0.4	ND	0.1	4.1 ± 0.3
5	1% 9t,11t-CLA (3)	67 ± 32	30.0 ± 0.8	10.8 ± 0.8	3.9 ± 0.7	25.4 ± 0.4	14.7 ± 1.4	2.3 ± 0.9	0.1 ± 0.1	0.04	2.8 ± 0.5
6	No treatment (3)	155 ± 31	31.1 ± 0.3	10.1 ± 0.3	3.2 ± 0.1	29.6 ± 0.3	17.4 ± 0.9	1.0 ± 0.1	0.03	0.1	0.1

a: Abbreviations are as follows: wt, weight; 9c,11t, 9cis,11trans; 9t,11t, 9trans,11trans; CLA, conjugated linoleic acid; AOM, azoxymethane; ND, Not detected.
b: Mean ± SD.
c: Mean.

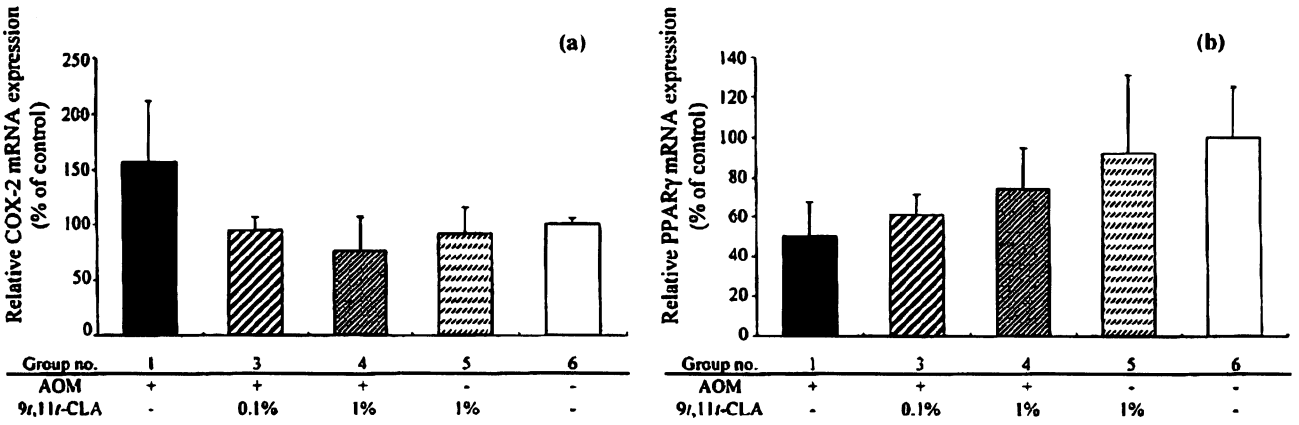

Figure 3. Expression levels of (a) cyclooxygenase (COX)-2 mRNA and (b) peroxisome proliferators activated receptor (PPAR)γ mRNA in the colonic mucosa. Data are expressed as the mean percentage (of Group 6) ± SD (bars) of 3 independent experiments. AOM, azoxymethane; CLA, conjugated linoleic acid.

supplementation containing mainly the 9c,11t and 10t,12c forms in almost equal proportions and much lower concentrations of other CLA isomers. In this study, we observed the chemopreventive effects of 9t,11t-CLA, which is a minor component of CLA isomers, on the number of AOM-induced colonic ACF in rats. We also observed the inhibitory effect of 9t,11t-CLA in the development of large ACF with 4 or more ACs, which are correlated with the incidence of colonic adenocarcinoma induced by AOM (38). Ealey et al. (39) reported that CLA mixture did not affect the average crypt multiplicity (crypts/ACF) or the average number of ACF-induced AOM in colons of male Sprague-Dawley rats. This is the first report clearly demonstrating the inhibitory effects of 9t,11t-CLA during the early phase of rat colon carcinogenesis. This inhibitory effect of 9t,11t-CLA on ACF formation is similar to that of 9c,11t,13t-conjugated linolenic acid (CLN) in our previous study (40).

The analysis of the fatty acid profiles of the lipids in the colonic mucosa and liver demonstrated that 9t,11t-CLA isomers had accumulated in both tissues. Linoleic acid is known to biosynthesize to AA by desaturation and elongation (41). Furthermore, there is a positive association between carcinogenesis and the dietary intake of both the n-6 fatty acid precursor linoleic acid and its product AA (42). In this study, neither AA nor linoleic acid was significantly decreased in the tissue specimens as a result of 9t,11t-CLA administration. Therefore, we presume that 9t,11t-CLA could modulate certain gene pathways involved in the formation of ACF without affecting the fatty acid composition, as did 9t,11t,13c-CLN (43). Interestingly, the liver lipid content was decreased by feeding with 9t,11t-CLA diets in this study, although Alasnier et al. (44) described the unchanged content in total lipids and fatty acid composition in liver of male Wistar rats fed 9t,11t-CLA (150 mg/day) for 6 days.

Colon carcinogenesis is a multistep process involving multiple genetic alterations such as the mutations of K-ras (45), β-catenin (45), and APC (46) and the altered gene expressions of COX-2 (11,45,47), inducible nitric oxide (45), and cyclin D1 (48). In this study, the CLA diet lowered the expression level of COX-2 mRNA (which was increased by AOM treatment) to the level of the group not treated with AOM. In particular, 9t,11t-CLA inhibited the expression level of COX-2 in a dose-dependent manner. Recently, COX-2 has attracted attention as a key target gene involved in the early stage of colorectal tumorigenesis (12). Our findings regarding altered COX-2 expression were consistent with the reduction in the percentage of large ACF due to the administration of 9t,11t-CLA.

PPARs are ligand-activated nuclear receptors that are responsible for the regulation of cellular events including apoptosis (49). It has been shown that PPARγ is expressed at high levels in normal colonic mucosa (50) and colon cancer (51). PPARγ-selective ligands inhibit cellular proliferation in colon cancer cell lines (52) and retard the growth of human colon tumor xenografts (52). Treatment with a selective PPARγ ligand (ciglitazone) downregulates the expression of COX-2 proteins and induces apoptosis in HT-29 human colon cancer cells (53). In our previous studies, synthetic ligands for PPARγ effectively inhibited chemically induced ACF formation in rats (54,55), and these findings were consistent with those in the study conducted by Osawa et al. (56). Furthermore, findings from in vitro studies have demonstrated that certain naturally occurring polyunsaturated fatty acids and their metabolites are endogenous PPARγ ligands (57). CLA is reported to act as a high affinity ligand and activator of PPARγ (34). We recently demonstrated that seed oils containing 9c,11t,13t- or 9c,11t,13c-CLN suppress AOM-induced colon carcinogenesis via the increased expression of PPARγ protein in the colon mucosa (58,59). Although we did not determine expression of PPARγ protein level in this study, our results were consistent with previous results (58,59). In this study, treatment with 9t,11t-CLA upregulated the PPARγ mRNA expression, which suggested that the inhibition of ACF formation by CLA administration was partly due to the activation of PPARγ caused by the downregulation of COX-2 expression.

Several studies have been conducted to reveal the prognostic significance of cyclin D1 overexpression in various

carcinomas including CRC (60). Cyclin D1 is a G1 cyclin that regulates the transition from the G1 phase to the S phase because its peak level and maximum activity are attained during the G1 phase of cell cycle. In the former study, cyclin D1 was aberrantly accumulated in a significant subset of human CRC cases that were dependent on cyclin in their cell cycle progression (61). Furthermore, another investigator reported that the overexpression of cyclin D1 was detected in 30% of adenomatous polyps. This finding indicated that cyclin D1 overexpression is a relatively early event in colon carcinogenesis and is possibly responsible for the pathological changes in the mucosa that precede neoplastic transformation (62). Recently, Lampen et al. (63) demonstrated that 9c,11t-CLA inhibits cell proliferation and suppresses the mRNA expression of proliferation genes such as c-myc, cyclin D1, and β-catenin in human colon cancer cells. In this study, the cyclin D1-positive cell ratio was significantly inhibited in a dose-dependent manner by the administration of 9t,11t-CLA. Because cyclin D1 is one of the important target genes for cancer chemoprevention (64), our results indicate that the inhibition of ACF formation by 9t,11t-CLA may be due to the downregulation of proliferation genes such as cyclin D1.

In summary, this study demonstrated that 9t,11t-CLA inhibits AOM-induced ACF formation in rats. Furthermore, 9t,11t-CLA demonstrated a dose-dependent beneficial effect on the early phase of colon carcinogenesis. These effects may occur through the induction of apoptosis and the suppression of cell proliferation on colonic mucosa. The effects were also partially mediated by the inhibition of the expression of COX-2 and cyclin D1 and the activation of PPARγ. Our findings suggest that 9t,11t-CLA may be useful for the chemoprevention of CRC.

Acknowledgments and Notes

We would like to express our thanks to the staff of the Research Animal Facility, Kanazawa Medical University. This study was supported by the Grants-in-Aid for Cancer Research and the Grants-in-Aid for the 3rd Term Comprehensive 10-Year Strategy for Cancer Control from the Ministry of Health, Labour and Welfare of Japan; the Grants-in-Aid for Scientific Research (Nos. 18880030, 18592076, and 00120029) from the Ministry of Education, Culture, Sports, Science and Technology of Japan; and the Grants (S2006-9, H2006-6, and C2006-3) from Kanazawa Medical University. Address correspondence to Yumiko Yasui, Department of Oncologic Pathology, Kanazawa Medical University, 1-1 Daigaku, Uchinada, Ishikawa 920-0293, Japan. Phone: +81-76-286-2211. FAX: +81-76-286-6926. E-mail: y-yasui@kanazawa-med.ac.jp.

Submitted 28 December 2006; accepted in final form 25 April 2007.

References

1. Parkin DM, Bray F, Ferlay J, and Pisani P: Global cancer statistics, 2002. *CA Cancer J Clin* **55**, 74–108, 2005.
2. Kono S: Secular trend of colon cancer incidence and mortality in relation to fat and meat intake in Japan. *Eur J Cancer Prev* **13**, 127–132, 2004.
3. Giovannucci E and Willett WC: Dietary factors and risk of colon cancer. *Ann Med* **26**, 443–452, 1994.
4. Reddy BS, Tanaka T, and Simi B: Effect of different levels of dietary trans fat or corn oil on azoxymethane-induced colon carcinogenesis in F344 rats. *J Natl Cancer Inst* **75**, 791–798, 1985.
5. Bartsch H, Nair J, and Owen RW: Dietary polyunsaturated fatty acids and cancers of the breast and colorectum: emerging evidence for their role as risk modifiers. *Carcinogenesis* **20**, 2209–2218, 1999.
6. Rao CV, Hirose Y, Indranie C, and Reddy BS: Modulation of experimental colon tumorigenesis by types and amounts of dietary fatty acids. *Cancer Res* **61**, 1927–1933, 2001.
7. Caygill CP, Charlett A, and Hill MJ: Fat, fish, fish oil and cancer. *Br J Cancer* **74**, 159–164, 1996.
8. Caygill CP and Hill MJ: Fish, n-3 fatty acids and human colorectal and breast cancer mortality. *Eur J Cancer Prev* **4**, 329–332, 1995.
9. Anti M, Armelao F, Marra G, Percesepe A, Bartoli GM, et al.: Effects of different doses of fish oil on rectal cell proliferation in patients with sporadic colonic adenomas. *Gastroenterology* **107**, 1709–1718, 1994.
10. Chen ZY and Istfan NW: Docosahexaenoic acid is a potent inducer of apoptosis in HT-29 colon cancer cells. *Prostaglandins Leukot Essent Fatty Acids* **63**, 301–308, 2000.
11. Srivastava S, Verma M, and Henson DE: Biomarkers for early detection of colon cancer. *Clin Cancer Res* **7**, 1118–1126, 2001.
12. Takahashi M, Mutoh M, Kawamori T, Sugimura T, and Wakabayashi K: Altered expression of beta-catenin, inducible nitric oxide synthase and cyclooxygenase-2 in azoxymethane-induced rat colon carcinogenesis. *Carcinogenesis* **21**, 1319–1327, 2000.
13. Otori K, Sugiyama K, Fukushima S, and Esumi H: Expression of the cyclin D1 gene in rat colorectal aberrant crypt foci and tumors induced by azoxymethane. *Cancer Lett* **140**, 99–104, 1999.
14. MacDonald HB: Conjugated linoleic acid and disease prevention: a review of current knowledge. *J Am Coll Nutr* **19**, 111S–118S, 2000.
15. Chardigny JM, Wolff RL, Mager E, Sebedio JL, Martine L, et al.: Trans mono- and polyunsaturated fatty acids in human milk. *Eur J Clin Nutr* **49**, 523–531, 1995.
16. Lee KW, Lee HJ, Cho HY, and Kim YJ: Role of the conjugated linoleic acid in the prevention of cancer. *Crit Rev Food Sci Nutr* **45**, 135–144, 2005.
17. Sebedio JL, Gnaedig S, and Chardigny JM: Recent advances in conjugated linoleic acid research. *Curr Opin Clin Nutr Metab Care* **2**, 499–506, 1999.
18. Ip C, Chin SF, Scimeca JA, and Pariza MW: Mammary cancer prevention by conjugated dienoic derivative of linoleic acid. *Cancer Res* **51**, 6118–6124, 1991.
19. Pariza MW and Hargraves WA: A beef-derived mutagenesis modulator inhibits initiation of mouse epidermal tumors by 7,12-dimethylbenz[a]anthracene. *Carcinogenesis* **6**, 591–593, 1985.
20. Chen BQ, Xue YB, Liu JR, Yang YM, Zheng YM, et al.: Inhibition of conjugated linoleic acid on mouse forestomach neoplasia induced by benzo (a) pyrene and chemopreventive mechanisms. *World J Gastroenterol* **9**, 44–49, 2003.
21. Beppu F, Hosokawa M, Tanaka L, Kohno H, Tanaka T, et al.: Potent inhibitory effect of *trans*9, *trans*11 isomer of conjugated linoleic acid on the growth of human colon cancer cells. *J Nutr Biochem* in press, 2006.
22. Yang L, Yeung SY, Huang Y, Wang HQ, and Chen ZY: Preferential incorporation of trans, trans-conjugated linoleic acid isomers into the liver of suckling rats. *Br J Nutr* **87**, 253–260, 2002.
23. Sehat N, Kramer JK, Mossoba MM, Yurawecz MP, Roach JA, et al.: Identification of conjugated linoleic acid isomers in cheese by gas chromatography, silver ion high performance liquid chromatography and mass spectral reconstructed ion profiles: comparison of chromatographic elution sequences. *Lipids* **33**, 963–971, 1998.
24. Kishino S, Ogawa J, Ando A, Omura Y, and Shimizu S: Ricinoleic acid and castor oil as substrates for conjugated linoleic acid production by washed cells of Lactobacillus plantarum. *Biosci Biotechnol Biochem* **66**, 2283–2286, 2002.
25. Kishino S, Ogawa J, Ando A, Iwashita T, Fujita T, et al.: Structural analysis of conjugated linoleic acid produced by Lactobacillus plantarum,

and factors affecting isomer production. *Biosci Biotechnol Biochem*, **67**, 179-182, 2003.
26. Bird RP: Role of aberrant cypt foci in understanding the pathogenesis of colon cancer. *Cancer Lett* **93**, 55–71, 1995.
27. Reeves PG, Nielsen FH, and Fahey GCJ: AIN-93 purified diets for laboratory rodents: final report of the American Institute of Nutrition ad hoc writing committee on the reformulation of the AIN-76A rodent diet. *J Nutr* **123**, 1939–1951, 1993.
28. Nutrition Alo: Report of the American Institute of Nutrition ad hoc Committee on Standards for Nutritional Studies. *J Nutr* **107**, 1340–1348, 1977.
29. Tanaka T, Kawabata K, Kakumoto M, Makita H, Hara A, et al.: Citrus auraptene inhibits chemically induced colonic aberrant crypt foci in male F344 rats. *Carcinogenesis* **18**, 2155–2161, 1997.
30. Watanabe I, Toyoda M, Okuda J, Tenjo T, Tanaka K, et al.: Detection of apoptotic cells in human colorectal cancer by two different in situ methods: antibody against single-stranded DNA and terminal deoxynucleotidyl transferase-mediated dUTP-biotin nick end-labeling (TUNEL) methods. *Jpn J Cancer Res* **90**, 188–193, 1999.
31. Folch J, Lees M, and Sloane Stanley GH: A simple method for the isolation and purification of total lipides from animal tissues. *J Biol Chem* **226**, 497–509, 1957.
32. Belury MA: Conjugated dienoic linoleate: a polyunsaturated fatty acid with unique chemoprotective properties. *Nutr Rev* **53**, 83–89, 1995.
33. Nicolosi RJ, Rogers EJ, Kritchevsky D, Scimeca JA, and Huth PJ: Dietary conjugated linoleic acid reduces plasma lipoproteins and early aortic atherosclerosis in hypercholesterolemic hamsters. *Artery* **22**, 266–277, 1997.
34. Houseknecht KL, Vanden HJP, Moya-Camarena SY, Portocarrero CP, Peck LW, et al.: Dietary conjugated linoleic acid normalizes impaired glucose tolerance in the Zucker diabetic fatty fa/fa rat. *Biochem Biophys Res Commun* **244**, 678–682, 1998.
35. Ip MM, Masso-Welch PA, and Ip C: Prevention of mammary cancer with conjugated linoleic acid: role of the stroma and the epithelium. *J Mammary Gland Biol Neoplasia* **8**, 103–118, 2003.
36. Liew C, Schut HA, Chin SF, Pariza MW, and Dashwood RH: Protection of conjugated linoleic acids against 2-amino-3- methylimidazo[4,5-f]quinoline-induced colon carcinogenesis in the F344 rat: a study of inhibitory mechanisms. *Carcinogenesis* **16**, 3037–3043, 1995.
37. Cheng JL, Futakuchi M, Ogawa K, Iwata T, Kasai M, et al.: Dose response study of conjugated fatty acid derived from safflower oil on mammary and colon carcinogenesis pretreated with 7,12-dimethylbenz[a]anthracene (DMBA) and 1,2-dimethylhydrazine (DMH) in female Sprague-Dawley rats. *Cancer Lett* **196**, 161–168, 2003.
38. Pretlow TP, O'Riordan MA, Somich GA, Amini SB, and Pretlow TG: Aberrant crypts correlate with tumor incidence in F344 rats treated with azoxymethane and phytate. *Carcinogenesis* **13**, 1509–1512, 1992.
39. Ealey KN, el-Sohemy A, and Archer MC: Conjugated linoleic acid does not inhibit development of aberrant crypt foci in colons of male Sprague-Dawley rats. *Nutr Cancer* **41**, 104–106, 2001.
40. Kohno H, Suzuki R, Noguchi R, Hosokawa M, Miyashita K, et al.: Dietary conjugated linolenic acid inhibits azoxymethane-induced colonic aberrant crypt foci in rats. *Jpn J Cancer Res* **93**, 133–142, 2002.
41. Garg ML, Keelan M, Thomson AB, and Clandinin MT: Desaturation of linoleic acid in the small bowel is increased by short-term fasting and by dietary content of linoleic acid. *Biochim Biophys Acta* **1126**, 17–25, 1992.
42. Phinney SD: Metabolism of exogenous and endogenous arachidonic acid in cancer. *Adv Exp Med Biol* **399**, 87–94, 1996.
43. Suzuki R, Yasui Y, Kohno H, Miyamoto S, Hosokawa M, et al.: Catalpa seed oil rich in 9t,11t,13c-conjugated linolenic acid suppresses the development of colonic aberrant crypt foci induced by azoxymethane in rats. *Oncol Rep* **16**, 989–996, 2006.
44. Alasnier C, Berdeaux O, Chardigny JM, and Sebedio JL: Fatty acid composition and conjugated linoleic acid content of different tissues in rats fed individual conjugated linoleic acid isomers given as triacylglycerols. *J Nutr Biochem* **13**, 337–345, 2002.
45. Takahashi M and Wakabayashi K: Gene mutations and altered gene expression in azoxymethane-induced colon carcinogenesis in rodents. *Cancer Sci* **95**, 475–480, 2004.
46. Kinzler KW and Vogelstein B: Lessons from hereditary colorectal cancer. *Cell* **87**, 159–170, 1996.
47. Kishimoto Y, Morisawa T, Hosoda A, Shiota G, Kawasaki H, et al.: Molecular changes in the early stage of colon carcinogenesis in rats treated with azoxymethane. *J Exp Clin Cancer Res* **21**, 203–211, 2002.
48. Bissonnette M, Khare S, von Lintig FC, Wali RK, Nguyen L, et al.: Mutational and nonmutational activation of p21ras in rat colonic azoxymethane-induced tumors: effects on mitogen-activated protein kinase, cyclooxygenase-2, and cyclin D1. *Cancer Res* **60**, 4602–4609, 2000.
49. Rosen ED and Spiegelman BM: PPARγ: a nuclear regulator of metabolism, differentiation, and cell growth. *J Biol Chem* **276**, 37731–37734, 2001.
50. Fajas L, Auboeuf D, Raspe E, Schoonjans K, Lefebvre AM, et al.: The organization, promoter analysis, and expression of the human PPARγ gene. *J Biol Chem* **272**, 18779–18789, 1997.
51. Sarraf P, Mueller E, Jones D, King FJ, DeAngelo DJ, et al.: Differentiation and reversal of malignant changes in colon cancer through PPARγ. *Nat Med* **4**, 1046–1052, 1998.
52. Brockman JA, Gupta RA, and Dubois RN: Activation of PPARγ leads to inhibition of anchorage-independent growth of human colorectal cancer cells. *Gastroenterology* **115**, 1049–1055, 1998.
53. Yang WL and Frucht H: Activation of the PPAR pathway induces apoptosis and COX-2 inhibition in HT-29 human colon cancer cells. *Carcinogenesis* **22**, 1379–1383, 2001.
54. Kohno H, Yoshitani S, Takashima S, Okumura A, Hosokawa M, et al.: Troglitazone, a ligand for peroxisome proliferator-activated receptor γ, inhibits chemically-induced aberrant crypt foci in rats. *Jpn J Cancer Res* **92**, 396–403, 2001.
55. Tanaka T, Kohno H, Yoshitani S, Takashima S, Okumura A, et al.: Ligands for peroxisome proliferator-activated receptors alpha and gamma inhibit chemically induced colitis and formation of aberrant crypt foci in rats. *Cancer Res* **61**, 2424–2428, 2001.
56. Osawa E, Nakajima A, Wada K, Ishimine S, Fujisawa N, et al.: Peroxisome proliferator-activated receptor γ ligands suppress colon carcinogenesis induced by azoxymethane in mice. *Gastroenterology* **124**, 361–367, 2003.
57. Hwang D: Fatty acids and immune responses—a new perspective in searching for clues to mechanism. *Annu Rev Nutr* **20**, 431–456, 2000.
58. Kohno H, Yasui Y, Suzuki R, Hosokawa M, Miyashita K, et al.: Dietary seed oil rich in conjugated linolenic acid from bitter melon inhibits azoxymethane-induced rat colon carcinogenesis through elevation of colonic PPARγ expression and alteration of lipid composition. *Int J Cancer* **110**, 896–901, 2004.
59. Kohno H, Suzuki R, Yasui Y, Hosokawa M, Miyashita K, et al.: Pomegranate seed oil rich in conjugated linolenic acid suppresses chemically induced colon carcinogenesis in rats. *Cancer Sci* **95**, 481–486, 2004.
60. Maeda K, Chung YS, Kang SM, Ogawa M, Onoda N, et al.: Overexpression of cyclin D1 and p53 associated with disease recurrence in colorectal adenocarcinoma. *Int J Cancer* **74**, 310–315, 1997.
61. Bartkova J, Lukas J, Strauss M, and Bartek J: he PRAD-1/cyclin D1 oncogene product accumulates aberrantly in a subset of colorectal carcinomas. *Int J Cancer* **58**, 568–573, 1994.
62. Arber N, Hibshoosh H, Moss SF, Sutter T, Zhang Y, et al.: Increased expression of cyclin D1 is an early event in multistage colorectal carcinogenesis. *Gastroenterology* **110**, 669–674, 1996.
63. Lampen A, Leifheit M, Voss J, and Nau H: Molecular and cellular effects of *cis*-9, *trans*-11-conjugated linoleic acid in enterocytes: effects on proliferation, differentiation, and gene expression. *Biochim Biophys Acta* **1735**, 30–40, 2005.
64. Hur K, Kim JR, Yoon BI, Lee JK, Choi JH, et al.: Overexpression of cyclin D1 and cyclin E in 1,2-dimethylhydrazine dihydrochloride-induced rat colon carcinogenesis. *J Vet Sci* **1**, 121–126, 2000.

１．研究課題名：新規抗癌剤探索をめざした薬剤感受性検査システムの開発
（研究番号 S2006-10）

２．キーワード：１）膵臓癌（Pancreatic cancer）
２）塩酸ゲムシタビン（Gemcitabine）
３）グリコーゲン合成酵素 3β（GSK3β）
４）マイクロアレイ（Microarray）

３．研究代表者：島崎　猛夫・医学部・助教・腫瘍内科学

４．研 究 目 的

膵癌は難治性癌の代表であり、早期発見が難しく、転移浸潤能が高いという特徴を持つ。塩酸ゲムシタビン（GEM)は膵癌に対する標準的抗がん剤として使用されているが、その奏効率は 20%以下であり、その奏功率の向上は喫緊の重要課題である。そこで、①GEM の奏功率を改善するための作用メカニズム解明のための遺伝子解析を行ない、次に、新たな分子標的治療のための研究を行った。がんにおいて変化する多彩な分子群はいずれもがん分子標的の候補である。大腸癌におけるグリコーゲン合成酵素キナーゼ glycogen synthase kinase3β:GSK3βには、Wnt シグナルに関係しない新しい機能があり、がん治療の分子標的であることが発見されている。また、糖代謝経路で発見された GSK3βは基幹的細胞シグナルを制御し、正常細胞では Wnt シグナルを抑制するが、大腸癌において、GSK3β異常発現やリン酸化による活性調節の破綻が癌細胞の生存と増殖を維持・促進するという「がん促進機能」が見出されている。我々は、塩酸ゲムシタビン(GEM)が、糖代謝経路の多機能酵素 GSK3βのリン酸化を促進することを報告している。以上の背景のもと、②膵癌細胞に対する GEM と GSK3β阻害剤(GSKi:AR-A014418:Calbiochem)併用による抗腫瘍効果とその分子機構を解明することにより、分子標的治療確立のため研究を行った。

５．研 究 計 画

ヒト膵癌細胞株 PANC-1 の培地に GEM を添加し、生存細胞を計測し、PANC-1 に対する GEM の IC50 を計測し、濃度依存性・時間依存性に PANC-1 の生存・増殖を抑制するかどうかを検討する。DNA 断片化 ELISA にて、apoptosis の誘導能を検討する。PANC-1 に IC50 の濃度の GEM を作用させて、cDNA マイクロアレイ (Affymetrix 社　Human Genome U133 Plus 2.0 Array)により解析を行う。有意に変化した遺伝子群を抽出し、 Ingenuity System パスウエイ解析ツール（IPA）を用いて解析を行う。次に、ヒト膵癌培養細胞株 PANC-1 に対し 10-100 mg/L の GEM と 5 mg/L の GSKi を培地に添加し、非投与群、GEM あるいは GSKi 単独投与群，両者の併用群に分けて、増殖抑制効果を MTT assay にて評価する。 ヌードマウス（Balb/c）に 1×10^6 個の Panc-1 を皮下に移植した腫瘍マウスを作成。マウスを 4 群（コントロール DMSO 群、GEM 投与群、GSKi 単独投与群、GEM と GSKi 併用群）にわけ、約 2 ヶ月にわたり投与を行ない、PANC-1 腫瘍サイズを測定し、移植腫瘍の病理所見も検討する。

６．研 究 成 果

ヒト膵癌細胞株 PANC-1 の培地に GEM を添加し、生存細胞を計測すると、PANC-1 に対する GEM の IC50 は 16 mg/L であった。GEM は濃度依存性・時間依存性に PANC-1 の生存・増殖を抑制した。DNA 断片化 ELISA では、apoptosis の誘導が観察された。つぎに、PANC-1 に 16 mg/L（IC50）の GEM を作用させて、第１日目と第３日目における遺伝子発現を cDNA マイクロアレイ（Affymetrix 社　Human Genome U133 Plus 2.0 Array)により解析した。第１日目に 1.5 倍以上に、第３日目に３倍以上に発現増加した遺伝子群と、第１日目に 0.7 倍以下に、第３日目に 0.3 倍以下に低下した遺伝子群（372 個）を抽出し、 Ingenuity System パスウエイ解析ツール（IPA）を用いて解析した。 GEM により発現が変動していた遺伝子群の多くは gene expression、cell death、 DNA replication や cell cycle に関与するものであった。IPA による解析では, p53 との関連が示唆された。次にヒト膵癌培養細胞株 PANC-1 に対し 10-100 mg/L の GEM と 5 mg/L の GSKi を培地に添加し、無治療群、GEM あるいは GSKi 単独投与群、両者の併用群に分けて、増殖抑制効果を MTT assay にて評価した。 併用群では、GEM 単独群と比較して、GEM 濃度依存性に抗腫瘍効果の有意な増強を認めた。ヌードマウス（Balb/c）に 1×10^6 個の Panc-1 を皮下に移植した腫瘍マウスを作成。マウスを４群（コントロール DMSO 群、GEM 投与群、GSKi 単独投与群、GEM と GSKi 併用群）にわけ、約２ヶ月にわたり投与を行った。PANC-1 腫瘍サイズは、GEM と GSKi の併用腹腔内投与群及び GSKi 単独投与群で他の治療群に比べて、有意に小さいものであった。病理所見では、特に併用群において PCNA 免疫染色（細胞増殖）が有意に抑制されていた。また、Tunnel 染色法にて、併用群でもっともアポトーシスが誘導されていた。これら病理所見により、GEM と GSKi の併用療法は、細胞増殖を抑制し、アポトーシスを誘導することが作用機序として推定された。さらなる分子メカニズム解明のためにマイクロアレイ解析及び IPA 解析を行った。マイクロアレイ解析では、GEM により誘導される遺伝子で、GSK3βによりその発現が修飾される遺伝子群約 300 個を同定した。解析の結果、GEM+GSKi と最も関連するネットワークは、p53、Myc を中心としたネットワークであった。p53 の Westernblotting による蛋白発現解析では、GEM の投与により p53 の発現が増加し、GEM の併用により発現が減弱していた。GSKi により変動をうけた遺伝子のうち、既に GEM の治療効果と関連すると報告のある p8 や TP53INP1 なども GSKi により修飾を受けていることが明らかとなった。

７．研究の考察・反省

GEM の作用分子メカニズムについては、S 期の DNA 合成障害作用であること以外に、どのような分子メカニズムが影響しているかという点については不明な点が多い。我々は GEM の作用により PANC-1 細胞で発現変化する候補遺伝子を cDNA マイクロアレイ解析により 372 個へ絞り込み、パスウエイ解析ツールにて *p53* と *myc* の経路への関与を明らかにした。GEM の奏功率を向上させるための分子ターゲットとして我々は、以下の理由で、Wnt/β-catenin シグナルを構成する分子の一つである GSK3βに着目した。GSK3βはグリコーゲン合成酵素（GS）をリン酸化することにより不活性化させるセリン・スレオニンリン酸化酵素として年以上前に発見された。糖

代謝経路において、本酵素はインスリンシグナルにより不活性化され、その結果、GS の作用によりグルコースからグリコーゲン合成が進み、血糖が制御される。その後の研究により、本酵素は自身がリン酸化する基質に対応して、糖代謝のみならず細胞周期、増殖・分化、アポトーシスや細胞骨格、運動能など、基幹的な細胞機能を制御していることが明らかにされつつある。GSK3βは細胞増殖にかかわる種々の転写因子（c-JUN，c-Myc など）やプロトオンコプロテイン（β-catenin）などをリン酸化して不活化あるいは不安定化することから、がん抑制因子であると認識されることが多い。しかしこれは GSK3βの増殖シグナル抑制機能の一部が重点的に解析されてきた結果であり、がん抑制機能を大前提として理論が構築されてきた結果である。しかし、GSK3β は NFkappaB 細胞生存機構に必須のシグナル分子であることが報告され、最近になって、細胞の生存や増殖過程における GSK3βの機能が癌細胞を中心に解析され始めている。今回我々はこのような背景の下，GSK3βが膵癌治療の新しい分子標的になる可能性を検証すべく、研究を行った。今回の研究により、膵臓癌でも GSK3β が治療のターゲットであることが示唆され、その阻害剤と GEM の併用が臨床応用として強く期待されることが明らかになった。その作用機序についても、マイクロアレイ解析の結果、*p53* 及び *MYC* の経路の関与が推定され、GSK3βがこれらの経路に関与し、その発現を修飾しているという結果であった。最も関与が推定された p53 蛋白質はその多彩な活性により本来遺伝子の異常から生態を守る働きを担っている。その主な活性は、遺伝子異常発生細胞における、遺伝子転写制御を介した細胞周期進行の制御・遺伝子修復酵素の活性化・アポトーシス誘導能である。一方、*p53* 遺伝子自体に突然変異が生じるとこれらの *p53* 蛋白質の機能が欠損し、腫瘍の発生に至るというメカニズムが考えられており、ヒトがん細胞における *p53* 遺伝子の変異は、大腸・胃・乳腺・肺・脳・食道など多くの人の腫瘍において *p53* 遺伝子が突然変異を起こしていることが見出され、*p53* 蛋白質の異常な蓄積が多くの腫瘍組織において観察されている。さらにがん高発家系において p53 遺伝子に変異がみられることも報告されている（Li-Fraumeni 症候群）。正常細胞には、*p53* 蛋白はごく微量しか存在せず、*p53* 遺伝子の変異により半減期が延長し、変異 *p53* 蛋白質が細胞核内に蓄積することが示唆されており、また、がん化の初期段階で p53 の突然変異が起きることが推測されていることより、変異 *p53* 蛋白は癌促進物質である可能性も推定され、今回の我々の実験結果から、GSK3β阻害による *p53* 蛋白発現低下は、変異 *p53* 蛋白の発現を減弱させることによる抗腫瘍効果としての作用を示したものである可能性がある。今後 *p53* 蛋白の変異と抗癌剤感受性の関係の解析をさらに進めて行く予定であり，さらに新規抗癌剤として GSK3β阻害剤の臨床応用を目指している。

２００６　平成１８年度金沢医科大学共同研究成果報告書
奨励研究成果報告書

平成２０年１２月発行
編　集　研究業績評価委員会
発行所　金沢医科大学出版局
石川県河北郡内灘町大学１丁目１番地